Development of Novel Gamma Detector Arrays for Industrial and Medical Applications

By

Dawid M. Hampel

A thesis submitted to
the University of Birmingham
for the degree of
DOCTOR OF PHILOSOPHY

Nuclear Physics Group
Positron Imaging Centre
School of Physics and Astronomy
College of Engineering and Physical Sciences
University of Birmingham
February 2024

ABSTRACT

Positron emission particle tracking (PEPT) is a technique directly developed from positron emission tomography (PET) where the position of a positron-emitting radiotracer is calculated from the lines-of-response (LORs) of a PET scanner. First developed at the University of Birmingham in the 1980s to study fluid flow in heavy industrial machinery, the technique has been applied to study the behaviour of systems used in food, recycling, pharmaceutical, and medical industries, to name a few. From studying flow patterns to breakup of particles, data acquired through PEPT has been used to validate simulation models and help uncover the mysteries of systems for which no simulation model exists.

From chemical engineers to mathematicians, PEPT is a technique that brings many areas of study together. However, while most PEPT users pay great attention to the tracking algorithms, interpretation of the positional data, and comparison of data to their models and expectations, very few pay attention to the machines and physics that make PEPT work. Failure to understand the fundamental limits of the positron scanners used for PEPT has led to overestimated expectations and noisy or low amounts of data for proper position calculations.

This thesis begins forth a detailed discussion of the history of PET and PEPT in order to understand the fundamental physics limitations and design choices of the scanner technologies — in particular the technical aspects of all BGO-based ECAT series PET scanners. This information has been used for the development of novel, dedicated PEPT systems which is the main focus of this thesis work. The systems are built from parts of deprecated medical machines, pushing the technologies to their absolute limits. The most advanced, dedicated PEPT system to date, SuperPEPT, has exceeded expectations. It has displayed superior sensitivity, a very high 2.1 MHz data rate, a large 40.00 cm diameter and 53.50 cm long field-of-view (FOV), and a 5 mm PEPT spatial resolution providing the best tracking accuracy available in PEPT. Furthermore, the expansion of the Large Modular Array

(LaMA) for PEPT made it the only reconfigurable PEPT system of such scale which can accommodate uniquely shaped industrial systems through the largest FOV of any PEPT system to date.

Through the use of non-destructive design verification methods like PEPT, large datasets of verification data can be obtained for simulation and design verification. SuperPEPT's extreme sensitivity and large data rate further expand PEPT into tracking of sub-millimetre particles with lesser amounts of activity than possible with previous scanners at the Positron Imaging Centre (PIC). Furthermore, LaMA PEPT has already shown its ability to adapt and meet the demands of larger lab-scale industrial appliances. Its use to verify the behaviour of the FLSmith CoarseAIR™ fluidised bed flotation cell (FBFC) had show its ability to acquire data over an FOV that is over 2 m tall. With these two systems currently available on top of the other equipment at the PIC, the different possibilities to study industrial equipment have never before been so flexible.

TO FAMILY

ACKNOWLEDGMENTS

Throughout the course of my PhD, I have met many wonderful people who gave their support and expertise and have left their mark on this work. Without them, none of this would ever happen.

First of all, I must extend my deepest gratitude to my supervisors, Professor Tzany Kokalova Wheldon and Professor Carl Wheldon, for their trust, support, knowledge, encouragement, and access to materials, equipment, and facilities. They also provided a relaxed and enjoyable environment with more than enough personal freedom.

This thesis would also not be possible without the knowledge and expertise of Professor David Parker who supported me and answered all my weird questions about PEPT and Samuel Manger who also imparted all of his PEPT knowledge in me. It was a pleasure working together.

I would also like to thank Ben Phoenix, Robert Wheeler, and Tichaona Dauramanzi for running the cyclotron, producing all the tracers, access to tools and equipment, and just being great to hang around and learn from. Thanks also to Paul Jagpal for his electronics knowledge and support and Chaw and Paul for handling all of my weird queries at the physics stores.

With all my love I also want to thank my parents, Jacek and Agnieszka, for their continuous and unwavering support, encouragement, and always being there for me throughout my life. Who knows who would I be without you. All the hard work and effort that went into all of this research is for you.

Finally, I would like to thank all my fellow PhD colleagues, past and present, for the mutual support, encouragement, and all the fun experiences we shared along the way. Including but not limited to everyone at E318: Mark, Stephen, Sammy, Angus, Ross, Pedro, Stuart, Rebeckah, Simone, Kiran, Tony, and Håkan; and the guys at the PIC: Dominik, Jack, Matthew, and Leonard.

No individual is alone responsible for a single stepping stone along the path of progress, and where the path is smooth progress is most rapid.

Ernest Orlando Lawrence

Nobel Prize banquet speech

29 February 1940

LIST OF PUBLISHED WORKS

Journal Papers

1. *SuperPEPT: A new tool for positron emission particle tracking; first results*, **D. M. Hampel**, S. Manger, D. J. Parker, Tz. Kokalova Wheldon, Nuclear Instruments and Methods in Physics Research Section A, Volume 1028, (2022), 10.1016/j.nima.2021.166254

2. *Performance Evaluation of the Current Birmingham PEPT Cameras*, D. J. Parker, **D. M. Hampel**, Tz. Kokalova Wheldon, Applied Sciences, Volume 12, (2022), 10.3390/app12146833

3. *Monte Carlo Model of the Large Modular Array for Positron Emission Particle Tracking*, M. Herald, **D. M. Hampel**, Tz. Kokalova Wheldon, J. P. K. Seville, C. R. K Windows-Yule, IEEE Access, Volume 11, (2023), 10.1109/ACCESS.2023.3255505

4. *Characterisation of the multiphase fluid dynamics of the CoarseAIR™ fluidised bed flotation cell using the Large Modular Array (LaMA) for positron emission particle tracking (PEPT)*, D. Mesa, **D. M. Hampel**, S. J. Neethling, Tz. Kokalova Wheldon, P. R. Brito-Parada, Minerals Engineering, in press, (2024)

Contents

List of Figures

List of Tables

Chapter One

Introduction to Positron Emission Tomography (PET)

Positron emission tomography (PET) is an imaging technique which combines principles of both nuclear and functional imaging. Through the detection of radioactive tracers (radiotracers) over a period of time, PET imaging can produce a quantitative distribution of the tracer concentration in the subject. It is through the use of these radiotracers and how the subject responds to their presence that functional effects, metabolic processes, physiological activities, and compositional differences can be studied and measured. This is unlike most other imaging techniques like X-ray imaging, X-ray computed tomography (CT), and magnetic resonance imaging (MRI) which only image the physical structure of the subject.

PET is dependent on the use of radiotracers that decay through the $\beta+$ process. As generalised in Figure 1.1, these radiotracers emit a positron (and an electron neutrino) which subsequently undergoes an annihilation process with an electron to emit two annihilation gamma rays. Due to the laws of conservation, each of these gamma photons has an energy equal to the mass of an electron or 511 keV. Due to the low energy that this interaction occurs at, these photons are emitted virtually back-to-back or 180° apart (see Section 1.7.2).

It's this back-to-back correlation of annihilation photons and their predictable energy that makes PET a very powerful technique [1].

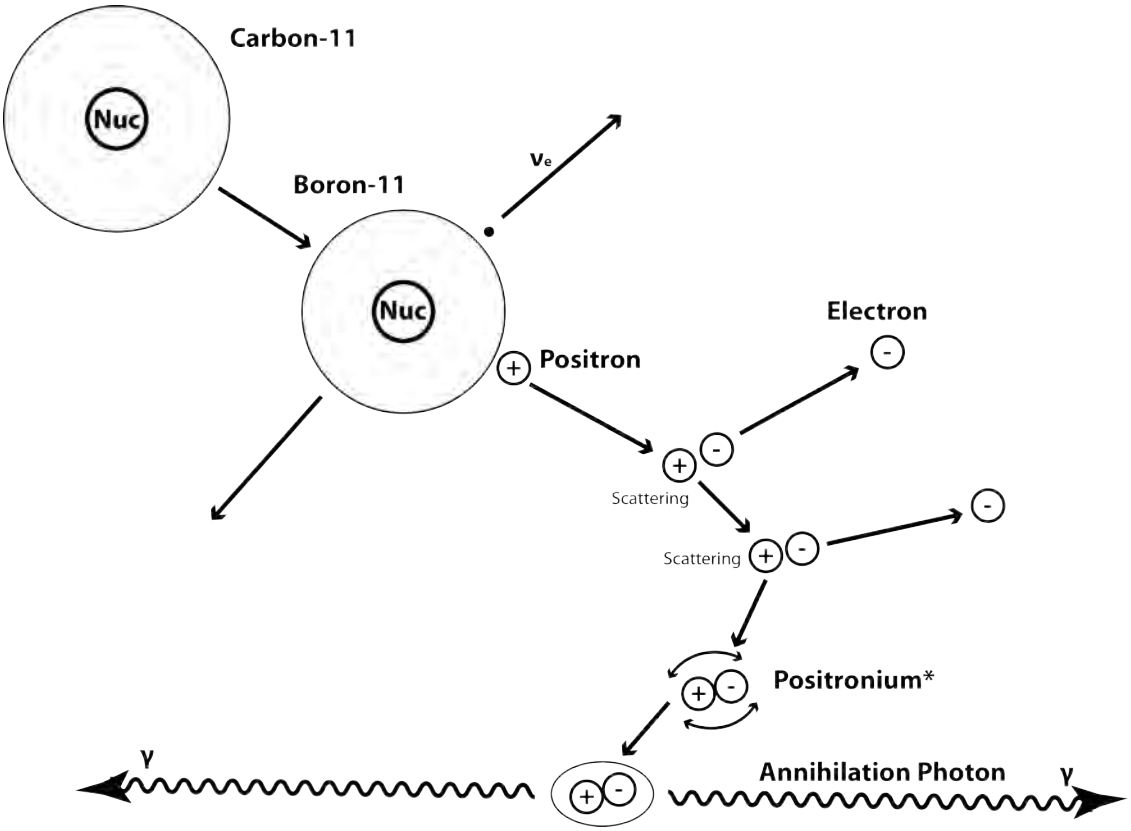

Figure 1.1: A generalised diagram of the positron emission or $\beta+$ decay and subsequent positron-electron annihilation for ^{11}C. After the positron is emitted, it undergoes multiple inelastic scattering events as it starts to loose its excess kinetic energy and thermalise. About 60 % of the time, the positron will directly annihilate with an electron. However, about 40 % of the time, the positron will form an exotic atom, an onium, called positronium. Depending on the spin alignment of the electron and the positron, positronium will decay between 0.12 ns and 140 ns. During positronium decay there is a small chance that three gamma rays will be emitted and not the usual two [2]. Figure not to scale.

Using detector systems to detect the back-to-back photons in coincidence, defines what is known as a line-of-response (LOR) within the field-of-view (FOV) of the system. It is assumed that along this LOR the annihilation occurred and the original radiotracer was located, as shown in Figure 1.2. This is unlike Single Photon Emission Computed Tomography (SPECT) which depends only on single emitted gamma rays for its imaging. However, to know from which direction the single gamma ray originated, SPECT systems

rely on heavy parallel-hole multichannel collimators that guarantee the gamma ray enters the detector tangentially to its face.

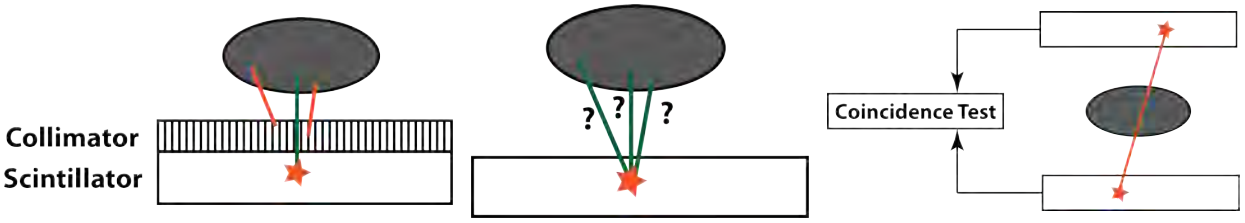

Figure 1.2: (Left, Center) In a single photon system like SPECT, for the system to be able to define a line of response it needs to know the position of the interaction of the gamma ray in the scintillator and the direction the gamma ray came from. This is accomplished through the use of a collimator which ensures the gamma rays enter the detector perpendicular to its surface. (Right) In a positron coincidence detection system like PET, when the two back-to-back gamma rays are detected, then the location of the annihilation can be said to be on the formed line of response.

The LORs are then stored in a special two-dimensional (2D) histogram called a sinogram (see Section 1.2) which represents the total concentration of a radiotracer across all possible LORs in a given plane. Postprocessing of one or more of these sinograms using reconstruction algorithms like the Fourier-transformation-based Filter Back Projection (FBP) [3–5] or an iterative-based Algebraic Reconstruction Technique (ART) [6–11] yields the tomographic images which can then be quantitatively and qualitatively analysed. Recently, the development of multimodal PET systems including PET/CT and PET/MRI allows the PET images to be overlaid with structural details to further aid in diagnosis.

When compared to other imaging modes, PET does not have the highest spatial and temporal resolution. The need to acquire data for a noticeable amount of time to produce a complete data set for image reconstruction and the time needed to perform image reconstruction, prevent PET from being used for dynamic studies. However, very recent developments in high-power computing, high-speed data storage, and fast detector technology, have reduced the minimum time required for each image acquisition. This enables studies to perform many short acquisitions over a period of time to produce a series of images between

which changes in radiotracer distribution can be studied.

Advantages of PET include the use of the relatively high-energy 511 keV photons for imaging. These annihilation photons have more penetrating power than X-rays which have energies up to 150 keV and SPECT radioisotopes' gamma rays which are typically 50–300 keV. The correlated back-to-back gamma rays that have to be detected in coincidence, natively collimate and improve the signal-to-noise ratio and spatial resolution when compared to SPECT [1, 12].

1.1 Imaging Planes and Septa (2D vs 3D Scanners)

Historically, PET can be conducted in two modes of operation: 2D and 3D. When PET scanners were first designed, like PET III or ECAT I, they featured a single ring of detector elements. These systems could only produce a single image plane. However, as technology improved, more detector rings were added. A two-ring scanner was able to produce three image planes: two direct planes consisting of coincidences between detectors within each of the rings and a single cross plane consisting of coincidences between the two rings. Using ECAT 831/12-08 as an example, the system had eight detector rings and featured septa or thin collimators that separated each ring of detector elements from one another. These septa prohibited coincidences from occurring between detector rings not adjacent to one another. In the case of eight detector rings as in Figure 1.3, the scanner had eight direct and seven cross image planes. This is known as the 2D mode. As septa were permanently installed in the scanner gantry, the ECAT 831 was only able to operate in 2D mode. This should not be confused with 3D image reconstruction which scanners operating in 2D mode are still capable of doing.

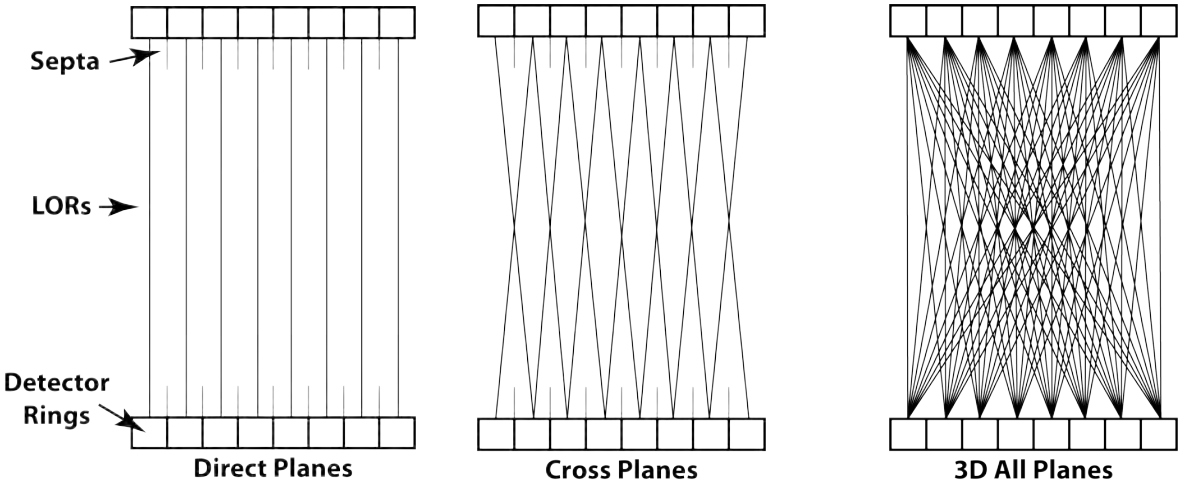

Figure 1.3: An axial cutaway of an eight-ring tomograph demonstrating the 2D mode direct and cross planes and the 3D mode using all possible planes with the septa removed.

The 2D mode and use of septa were indicative of early PET scanners. This limitation reduced the amount of memory required to record all the LORs as every image plane requires a whole new sinogram (see below) and increased image reconstruction times. Septa also reduced noise and scatter coincidences improving the signal-to-noise ratio and reducing system dead time. However, as data storage costs decreased and available computation power increased, a new 3D imaging mode was introduced (see Section 7.1.6). In this mode, septa are completely removed or withdrawn from the gantry and every detector ring is in coincidence with all other detector rings. For an eight-detector ring scanner in a 3D mode shown in Figure 1.3, the scanner acquired 64 image planes: eight direct, seven cross, and 49 oblique planes. The 3D mode increased the scanner's sensitivity, data rates five to ten times, and the signal-to-noise ratio in reconstructed images although they acquired significantly more noise and scatter coincidences. For quite a while, scanners from the ECAT 951 to the ECAT EXACT HR+ had to ability to automatically withdraw the septa from the FOV of the scanner for a dual 2D and 3D mode. This was selected by the operator and depended on the imaging procedure being conducted. The 2D and 3D modes of operation were also electronically controlled in the coincidence processor. Additionally, in 2D mode, a test was conducted during coincidence testing which removed any stray oblique coincidences. Today,

all modern PET scanners operate in 3D-only mode [12].

1.2 Types of Data Storage

To efficiently store and later process the coincidence data produced by a PET scanner, a stored data array called a sinogram is used. A sinogram is a two-dimensional array that represents all possible LORs produced by the system in a single image plane. Therefore, 3D PET scans with 64 image planes requires 64 sinograms to be concurrently recorded while the same system in 2D mode with 15 image planes requires only 15 sinograms. Each element or pixel of the sinogram represents the number of times a specific LOR was detected during the acquisition. One axis of the array represents the perpendicular displacement of the LOR from the centre of the FOV of the scanner while the second axis represents the angle of

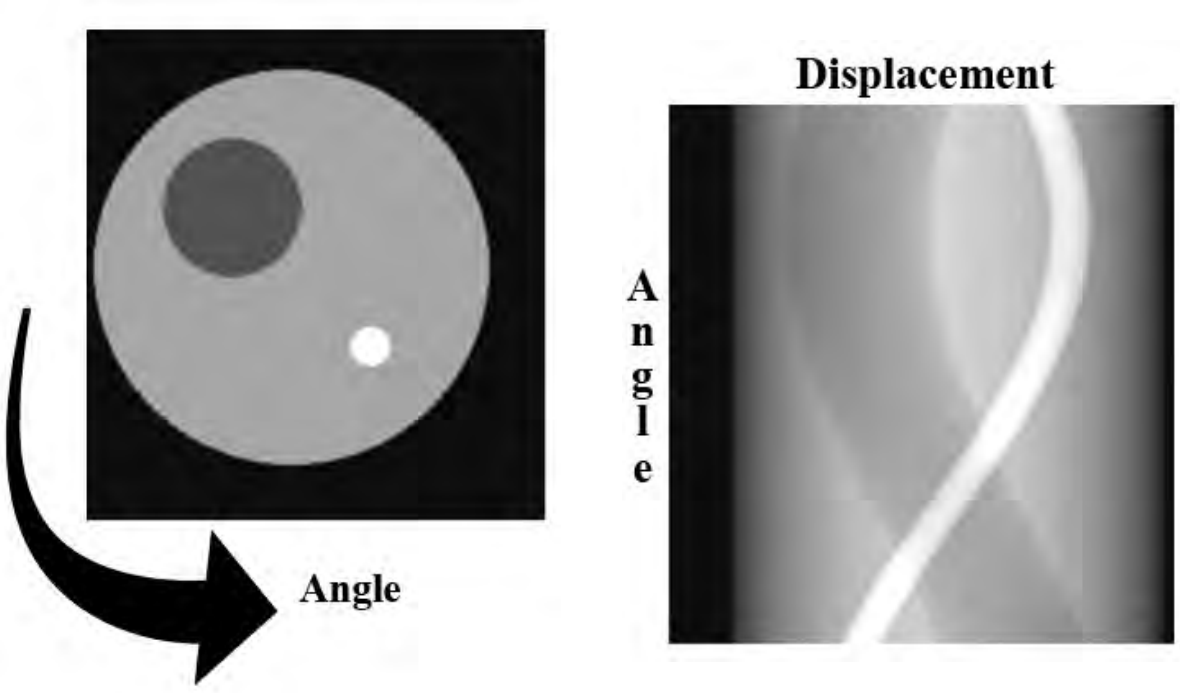

Figure 1.4: The resulting sinogram (right) after 180° worth of projection views around the test object (left) are acquired [12].

the LOR to the horizontal axis of the system. This is known as the angle/displacement notation where each row of displacement data at a given angle represents the projection of the activity present within the FOV of the scanner upon the detector from that angle. Therefore, as shown in Figure 1.4, a sinogram contains all projections of the activity volume in that plane [12]

Most scanners can additionally record the raw data in what is called the list mode. This mode of operation bypasses the formation of histograms and directly writes the event data in either the angle/displacement form or in a special data form which identifies the two detector elements that formed the coincidence with additional status bits to the hard drive. This mode of operation is extremely storage dependent not only on the amount but the write speed of the storage device. Usually, each list mode data event is 4 B in size with scanners acquiring coincidences at rates up to a few million per second. Therefore, a scanner acquiring three million coincidences per second would require at least 720 MB of storage per minute and the ability to handle such a data rate.

1.3 Data Acquisition

To properly image a distribution of a radionuclide located within the FOV of a PET scanner, the detector position, detected gamma-ray energy, and the relative interaction time have to be known to the system. The method by which position is acquired by the system depends on the type of scanner used. In most cylindrical, full-ring tomographs that use an array of individual crystal elements, the position of the crystal element the gamma ray interacted with is known by its hardwired connection to the system (see Section 6). In these systems, a subarray of crystal elements (32 or more) is grouped into a detector block system (see Section 6.1.1) which is usually viewed by four photomultiplier tubes (PMTs) in the older

systems. The signal output of the four PMTs is then analysed to identify in which crystal element the interaction occurred. Then, the location of the detector block itself in the ring is known to the system through the physical electronic connection of the detector block to the rest of the system as the ring geometry never changes. After the coincidence test, the system uses the position of the two detector blocks and crystal elements to determine the sinogram the coincidence belongs to and the angle/displacement the formed LOR represents.

If a dual-head coincidence Anger camera system is used for PET acquisition, the position of the interaction that occurred within the crystal is determined using Anger logic (see Section 4.2.4). As a single crystal is viewed by many PMTs, the output from all the PMTs in the detector head is analysed by the camera's logic to identify where the gamma ray interacted in the two dimensions. Later when a coincidence is found, the LOR formed by the two positions is used to determine the image plane and the displacement of the LOR. The angle of the LOR is simply the rotational position of the detector heads around the FOV of the scanner.

The energy of the gamma ray is much simpler to determine. It is the sum of all PMT outputs in the two systems described above. This energy signal is then processed by an energy discriminator which produces a logic pulse if the energy is within an allowed energy window. The system quickly discards any events that fall outside those limits, most of which are scattered gamma rays and noise.

Finally, the relative time of interaction is calculated using the cycles of a system clock. Like most digital systems, a PET scanner is orchestrated by a single oscillator from which the main system clock and other clock signals are derived (see Section 6.1.3). The master clock is usually the slowest in the whole system as it orchestrates the main stages of the event processing pipeline. A time-keeping clock which runs at a much higher frequency than the main clock is used for determining the offset in counts to the next main clock cycle where

each count is equal to Δt or the time resolution of the PET scanner. In BGO-based ECAT systems Δt is 4 ns.

1.4 Coincidence Testing

Coincidence testing in PET systems is a highly orchestrated procedure (see Section 6.2). Once an interaction occurs in one or more detector elements, the whole event processing pipeline is set in motion. As mentioned earlier, energy discrimination is performed on each single event which discards any gamma rays outside the energy limits. At the same time, a clock pulse counter is started acquiring the offset to the next master clock cycle. Once the master clock cycle occurs, the offset count along with some positional information is passed to the coincidence processor. As the single event arrives at the coincidence processor, a series of tests and shuffling occurs. It would be very inefficient to test for coincidence between every single detector element, so the coincidence processor follows module pair combinations (see Section 8.3.1). These module pairs specify which areas of the scanner can be in coincidence together. They are established during the scanner's development to minimalise detector parallax effects (see Section 1.7.4) and prevent any improbable coincidences between neighbouring detectors.

The coincidence processor then distributes the single event information to various coincidence-testing subsections based on the allowed module pair number. Here the offset count is compared between the detected events and if two events fall within a coincidence window of one another they are said to be in coincidence producing a valid LOR. The coincidence window in a BGO-based ECAT PET scanner is equal to 2τ which is equal to $3\Delta t$ where Δt is the time resolution of the system and τ is the half-width of the coincidence window [13]. For a coincidence window of 12 ns, the time resolution of a PET scanner is

4 ns. Also at this time, the LOR's plane information is analysed. If a scanner is in 2D mode, then certain plane combinations are not allowed and the coincidence status of such a pair is retracted. Finally, a multiple coincidence test is conducted which tests if two or more LORs were produced. If that happens, a special multiple event flag is raised and one of the LORs is chosen at random to be passed to the data acquisition system. Once all the checks are completed, the LOR information is passed to an external computational unit responsible for sinogram management [12].

1.5 Coincidence Types

In PET, there are a few different types of coincidences that can occur. In an ideal world, all detected coincidences would be true coincidences or coincidences whose two detected photons originate from the same annihilation and have not undergone any interactions that would alter their trajectory and/or energy, as shown in Figure 1.5. However, that is not the case and true coincidences are mixed with scattered, random, and multiple coincidences. All of these coincidences are considered noise and need to be rejected or corrected by the

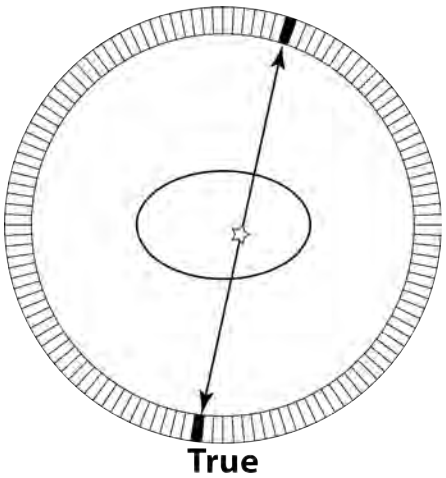

Figure 1.5: A true coincidence is where both annihilation photons from the same annihilation were detected by a PET scanner.

scanner. Most of these coincidence types are due to single events or where only one of the two annihilation photons is detected by the system. Single events also include contributions from the environment, space, and other gamma rays released by the radiotracers. These single events are important as they are in part responsible for random and multiple coincidences and significantly contribute to the dead time of the system (see Section 1.7.5). Prompt coincidences are also mentioned in literature and are simply all types of coincidences summed together. They include all true, random, scatter, and multiple coincidences detected by the system. Prompt coincidences can also be called uncorrected coincidences [12].

1.5.1 Random Coincidences

Random coincidences are formed when two uncorrelated gamma rays are detected within the timing window of the system as shown in Figure 1.6. This type of coincidence is one of the biggest sources of noise in a PET system. The random coincidence rate (R) is related to the single count rate in each detector (S_1 and S_2) and the coincidence window width (2τ) such that

$$R = 2\tau S_1 S_2, \tag{1.1}$$

and if the count rates in both detectors are approximately the same then

$$R = 2\tau S^2. \tag{1.2}$$

Therefore, the random coincidence rate increases quadratically with an increase in the singles count rate, which increases with the amount of activity. Similarly, the random coincidence rate can be lowered by shrinking the coincidence window width, shielding from the environment, or using lower amounts of activity [12].

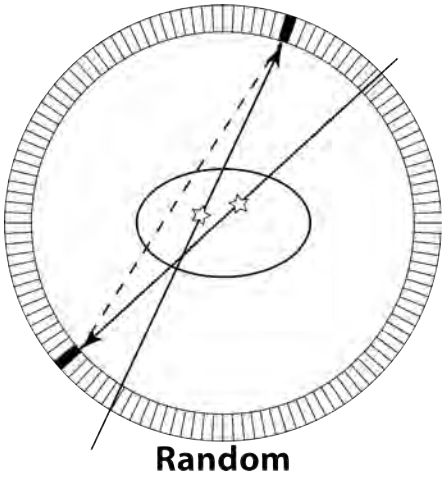

Figure 1.6: A random coincidence is where the detected photons originate from different annihilations.

1.5.2 Scatter Coincidences

Scatter coincidences happen when one or both of the annihilation photons undergo Compton scattering changing their energy and direction, as shown in Figure 1.7. When detected as a true coincidence by the system, these coincidences produce false LORs which further degrade image quality. These coincidences are dependent on the amount of activity, the type of scanner, and the shape of the patient making them some of the hardest to correct

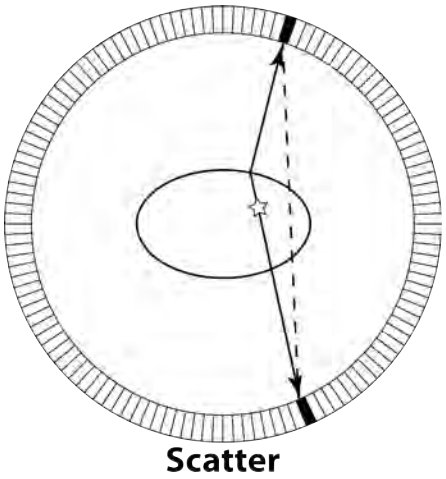

Figure 1.7: A scatter coincidence is where one or both of the annihilation photons interact with the environment altering their direction and energy.

for. Anywhere between 15% and 50% of detected coincidences can be scattered coincidences [12].

1.5.3 Multiple Coincidences

Multiple coincidences occur when three or more gamma rays are detected by the system within the coincidence window, as shown in Figure 1.8, and occur mostly during high-activity acquisitions. This causes ambiguity in the system as it is not clear which gamma rays belong to which annihilation. These types of coincidences are very easy to detect by the coincidence circuit and can be discarded. However, in the case of three detected photons, most likely two of these photons belong to a true coincidence such that one of the three possible LORs is correct. In some systems, one of these LORs is randomly selected and passed through as it may be more beneficial to take the random chance of obtaining a true LOR than indiscriminately discarding them all [12].

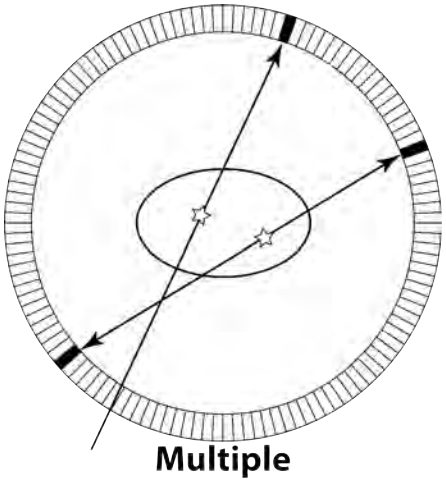

Figure 1.8: A multiple coincidence is where three or more annihilation photons are detected by the system causing ambiguity in determining the true coincidence.

1.6 False Coincidence Correction Methods

Of the three types of false coincidences mentioned above, only random and scatter coincidences need to be actively corrected.

1.6.1 Random Coincidence Correction

Random coincidences are the easier of the two types to correct for and therefore a few different methods have been developed for their correction. The oldest and most common correction method is the online subtraction of delayed coincidences. This method leverages the fact that random coincidences are randomly distributed and therefore a coincidence between two photons can occur even when separated by a large delay (see Section 6.2). Here, after the single photon events are tested for a true coincidence, they are checked for a possible delayed coincidence where another 2τ wide coincidence window is established a large amount of time from the true coincidence window (like 128 ns). Since this coincidence could not happen due to true or scatter coincidences, it must be due to random coincidences. The LOR is then determined for that coincidence as if it were a true coincidence and is passed to the sinogram which contains all prompt coincidences. However, instead of adding a count to the channel corresponding to that LOR, it subtracts one from that channel. This creates what is known as a prompt–delay sinogram. Unfortunately, this method of random correction results in the creation of statistical noise in the sinogram. This is insignificant in acquisitions with high prompt-to-delayed coincidence ratios but becomes significant for ones with a low ratio which is usually the case for quick acquisitions [12, 14].

The effect of noise on the sinogram due to the subtraction of delayed coincidences can be estimated using the noise equivalent counts (NEC) of a sinogram:

$$NEC = \frac{T^2}{T + S + f_{FOV}(1+k)R}, \tag{1.3}$$

where T is the true coincidence rate, S is the scattered coincidence rate, f_{FOV} is the fraction of the FOV occupied by the patient, R is the random coincidence rate, and k is a factor dependent on the method of random coincidence correction. $\sqrt{NEC}$ is also proportional to the signal-to-noise ratio (SNR) of a sinogram. Therefore, the SNR can be calculated for a sinogram and a value of k can be calculated to indicate how much noise a correction method introduces. For a noise-generating approach like the one listed above $k = 1$ and for a noiseless approach $k = 0$. Using NEC, one can compare the various methods of random coincidence correction [12, 14].

Another correction method for random coincidences is known as the smooth-delay estimation. This method uses delayed coincidences as described above but instead of actively subtracting them from the prompt coincidence sinogram, a separate delayed sinogram is formed. After the acquisition is complete, a smoothing algorithm is passed over the delayed sinogram before it is subtracted from the prompt sinogram. This method yields a value of k such that $0 < k \ll 1$. A singles-based approach can also be used to correct for random coincidences. This requires the system to measure the average singles rate at an appropriate time and point during the acquisition for every single detector element. Then using Equation 1.1, a random coincidence rate is calculated for every single possible LOR that is then used to correct the prompt coincidence sinogram [14].

1.6.2 Scatter Coincidence Correction

Scatter coincidence correction is a lot less intuitive than random coincidences. The simplest method to remove scatter coincidences is through the use of energy discrimination. It can then be said that it is advantageous to have a very narrow energy acceptance window centred around 511 keV. However, due to the energy resolution of the detectors and counting statistics, gamma rays that are 511 keV in energy will have a Gaussian distribution centred

around 511 keV with the full width at half maximum (FWHM) dependent on the energy resolution of the scintillator. Therefore, the discriminator energy windows cannot be set too tight as it risks rejecting many more true coincidences than scatter coincidences. The energy resolution of a scintillator is directly correlated to the scintillator light yield per unit of energy deposited. The higher the yield, the more scintillation photons are produced, improving counting statistics. See Table 1.3 for light yields of various PET scintillators. Usually, for a BGO-based scanner, the lower level discriminator (LLD) is set between 300-350 keV and the upper level (ULD) is set to 650 keV. For a NaI(Tl)- or GSO-based system LLD is usually 435 keV and ULD is between 590-665 keV [12, 15].

As most annihilation photons will scatter via Compton scattering, any significantly scattered photons will have a significant energy reduction. However, low-angle scatters usually will not lose enough energy to be caught by the discriminator. To correct for these low-energy scatters, many methods have been devised. Some estimate the scatter component by convolving the images with deblurring filters while others use Monte Carlo simulations [15]. For methods used by the BGO-based ECAT PET scanners see Section 6.1.3; however, these scanners do not have a method for low-angle/low-energy scatter correction.

1.7 Spatial Resolution of PET and Its Limitations

The spatial resolution of a PET scanner expresses the ability of the system to differentiate small radioactive sources from one another. It is presented in terms of FWHM of the point spread function (PSF). A PSF can be acquired with a point source placed in free air in the centre of the scanner, reconstructing the image, and measuring the count distribution across the produced point on the image. Importantly, it is acquired using a low-activity source to prevent contributions from random and scattered events. It is affected by many aspects of

the scanner design, the reconstruction algorithm, and the nature of positrons [12].

1.7.1 Positron Range

The ultimate limit on PET spatial resolution is the range of the positron. As the radioisotope undergoes $\beta+$ decay, a proton in its nucleus is converted into a neutron by releasing a positron and an electron neutrino. The energy released by the decay is shared by the daughter nucleus and the two particles. This means that the emitted positron can have anywhere from 0 to E_{max}, as shown in Table 1.1, which is dependent on the parent nucleus or the difference in masses of the daughter and parent nucleus. The average kinetic energy of the positron can then be approximated to be $0.33 \times E_{max}$. However, for the positron to undergo annihilation,

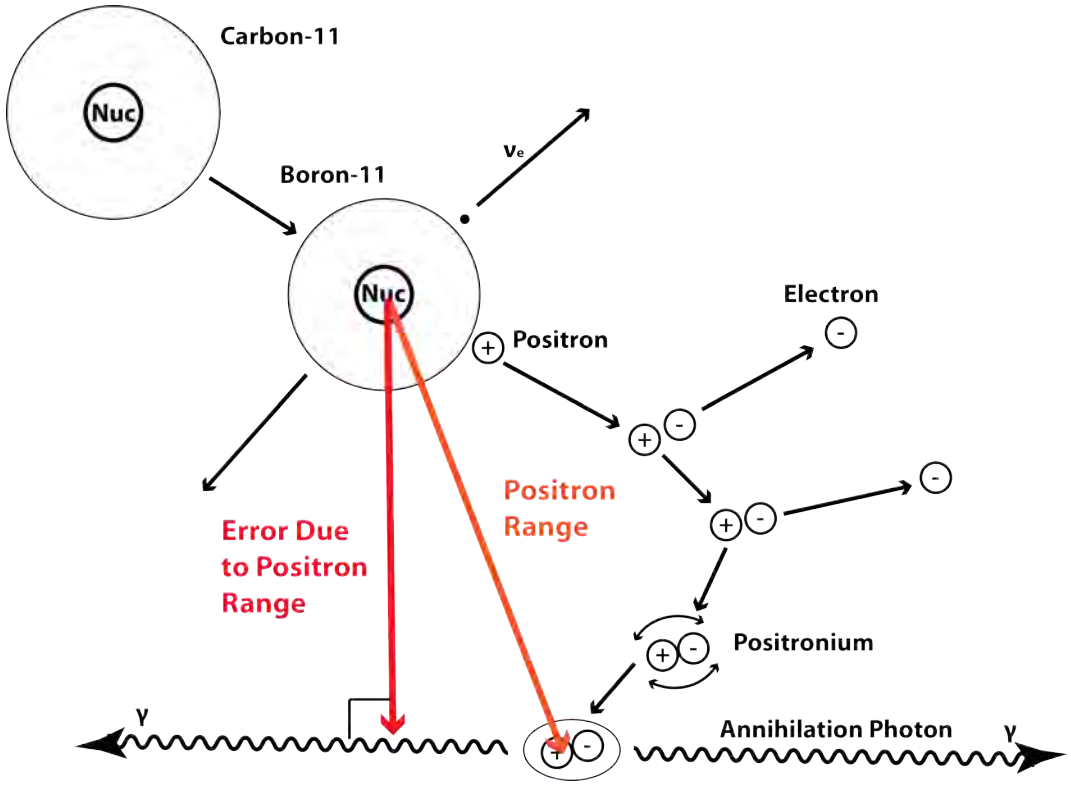

Figure 1.9: A diagram demonstrating the error in determining the position of the radionuclide due to the positron range as the positron travels away from the decay site to its annihilation site. Not to scale.

it needs to lose almost all of its kinetic energy. In its short lifespan, it undergoes many inelastic scattering interactions, especially in electron-dense materials like tissue. Therefore, depending on the medium and the positron energy, the positron can travel anywhere up to a few centimetres as shown in Table 1.1 [12, 15, 16].

As shown in Figure 1.9, due to the positron's many interactions, the overall distance it travels is a lot longer than what is perceived. In PET the positron range is measured as the average distance between the decay and annihilation site but the actual error due to the positron range is the shortest perpendicular distance from the recorded LOR to the decay site. In water and tissue, the effect due to the positron distance is negligible in body-sized tomographs when used with radioisotopes that emit a positron with low maximum kinetic energy. However, its effect is noticeable when imaging small animals with high-resolution animal PET scanners and using radioisotopes emitting high-energy positrons in the order of a few MeV [12, 15, 16].

1.7.2 Positron Noncollinearity

The second limit on the PET spatial resolution is due to the nature of the positron non-collinearity. This effect is independent of the parent radioisotope and it is due to the positron and the electron carrying a small net momentum when they annihilate. The positron loses most of its kinetic energy but not all before it combines with an electron. About 60 % of the time, the positron will directly annihilate with an electron. However, about 40 % of the time, the positron will form an exotic atom, an onium, called positronium. Depending on the spin alignment of the electron and the positron, positronium will decay around 0.12 ns or 140 ns. During annihilation, the mass of the positron and electron is converted into electromagnetic energy. Most of the time, this causes two annihilation photons to be emitted; however, about 0.5 % of the time, during positronium decay, three photons will be emitted [2]. During the

Table 1.1: Properties of positrons emitted by various PET isotopes. Positron ranges were calculated using the continuous slowing down approximation [17].

Isotope	Half-Life [18]	β^+ Branching Ratio (%) [18]	$\beta^+ E_{max}$ (MeV) [18]	$\beta^+ E_{mean}$ (MeV) [18]	$\beta^+ R_{max}$ Liquid Water (mm) [17]	$\beta^+ R_{mean}$ Liquid Water (mm) [17]	X- and γ-Rays $> 0.25\,\mathrm{MeV}$ [18]
$^{11}_{6}\mathrm{C}$	20.364 min	99.77	0.9604	0.3857	4.16	1.22	No
$^{13}_{7}\mathrm{N}$	9.965 min	99.80	1.1985	0.4918	5.44	1.73	No
$^{15}_{8}\mathrm{O}$	122.24 sec	99.90	1.7320	0.7353	8.33	2.96	No
$^{18}_{9}\mathrm{F}$	109.77 min	96.73	0.6335	0.2498	2.44	0.64	No
$^{22}_{11}\mathrm{Na}$	2.6018 yr	89.96	1.8212	0.2164	8.82	0.51	Yes
$^{52}_{25}\mathrm{Mn}$	5.591 d	29.4	0.5753	0.242	2.14	0.61	Yes
$^{62}_{29}\mathrm{Cu}$	9.673 min	97.83	2.9369	1.3190	14.77	6.10	Yes
$^{64}_{29}\mathrm{Cu}$	12.701 h	17.49	0.6526	0.2780	2.54	0.75	Yes
$^{66}_{31}\mathrm{Ga}$	9.49 h	57	4.153	1.75	21.20	8.43	Yes
$^{68}_{31}\mathrm{Ga}$	67.71 min	88.91	1.8991	0.8295	9.24	3.46	Yes
$^{72}_{33}\mathrm{As}$	26.0 h	87.8	3.334	1.170	16.90	5.29	Yes
$^{76}_{35}\mathrm{Br}$	16.2 h	47.0	3.941	1.11	20.09	4.96	Yes
$^{82}_{37}\mathrm{Rb}$	1.2575 min	95.4	3.382	1.481	17.16	6.98	Yes
$^{86}_{39}\mathrm{Y}$	14.74 h	31.9	3.141	0.66	15.86	2.58	Yes
$^{89}_{40}\mathrm{Zr}$	78.41 h	22.74	0.902	0.3955	3.84	1.27	Yes
$^{124}_{53}\mathrm{I}$	4.1760 d	22.7	2.1376	0.82	10.54	3.41	Yes

most common case of two photon emission, they are emitted with a distribution of angles $180 \pm 0.25°$ as shown in Figure 1.10. As the distribution is roughly Gaussian in shape with a FWHM of about 0.5°, the blurring effect due to noncollinearity, Δ_{nc}, can be estimated to be:

$$\Delta_{nc} = 0.5D \tan(0.25°) \approx 0.0022D, \tag{1.4}$$

where D is the detector diameter of the scanner [12]. Therefore, as shown in Table 1.2, the effect increases with the scanner diameter but is essentially negligible in scanners of all sizes due to the detectors' finite element size which is usually greater than 2 mm [12, 15, 16].

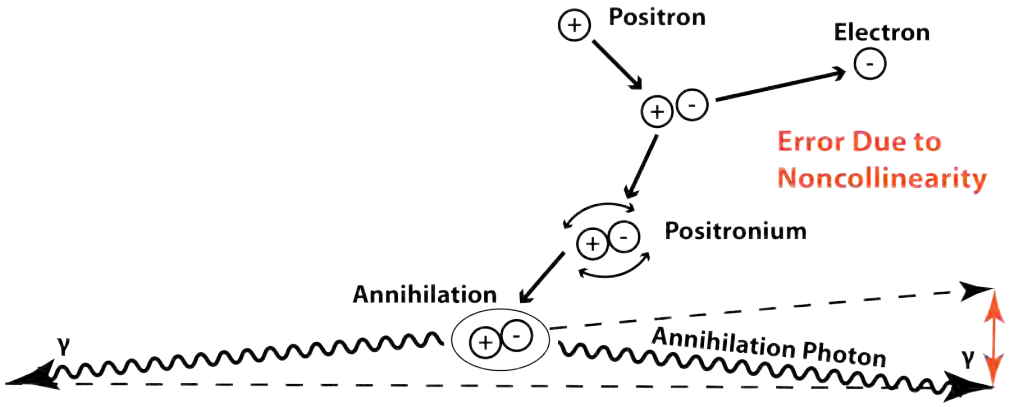

Figure 1.10: An idealised diagram demonstrating the error on possible identification of the LOR due to the $180 \pm 0.25°$ separation of the annihilation photons, due to the conservation of momentum. Not to scale.

Table 1.2: Resolution loss due to noncollinearity for various tomograph ring diameters.

Ring Diameter D (cm)	Resolution Loss Δ_{nc} (mm)
50	1.1
60	1.3
70	1.5
80	1.7
90	2.0
100	2.2

1.7.3 Detector Element Size

Perhaps the largest effect on PET spatial resolution is the intrinsic spatial resolution of the crystal element in a multi-crystal scanner. As the gamma ray can interact anywhere within the volume of the crystal, the resulting LOR that connects the two detector elements in coincidence is not a line but a volume within which the origin of the annihilation can lie. The geometric resolution of such a system can then be approximated by a triangular point spread function with $FWHM = w/2$ where w is the size of the detector element when the source is midway between the two detector elements. This function becomes trapezoidal as the source is moved off-centre towards one of the detectors as shown in Figure 1.11. This means that the probability of detecting the coincidence is not uniform throughout that volume between the two detector elements, contributing some nonuniformity to the sensitivity of the system. For purposes of PET, it is always assumed that the LOR connects the centre of the face of one detector element to the centre of the face of the other detector element [12].

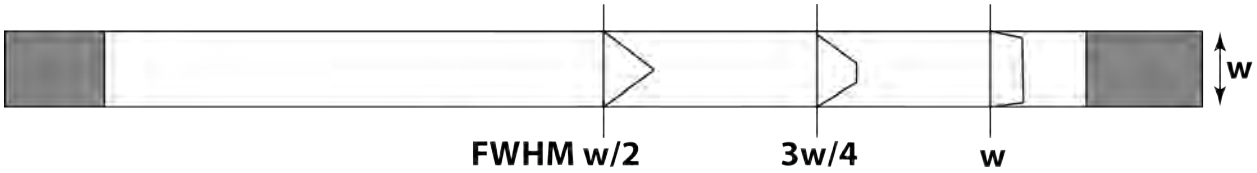

Figure 1.11: The effect of the finite detector element size on the spatial resolution of the system as a point source is moved between the two detector elements at different locations [12].

1.7.4 Detector Parallax

Detector parallax, also known as the depth of interaction effect, is the degradation of spatial resolution of a PET system due to the annihilation photons being able to interact anywhere within the volume of a thick scintillator detector element. This occurs when a source is positioned with a large axial offset such that the gamma ray will interact with the detector

face at a shallow angle; compared to entering the detector at angles perpendicular to the face when the source is positioned in the centre of FOV as shown in Figure 1.12. This shallow angle of attack may allow the gamma ray to penetrate the first detector and interact with its adjacent neighbour. This effect broadens and causes the coincidence response function to become asymmetrical with increasing radial offset. This may lead to the misidentification of the LOR and its mispositioning toward the centre of the FOV when the LOR is projected to the face of the detector. The intensity of this effect depends on the type of scintillator, size of detector elements, detector separation, scanner geometry and many more factors which are considered when designing a PET scanner. To reduce the effects of parallax, scanners have restrictions on which detectors can be in coincidence to avoid these shallow angled coincidences. However, developments in PET scanner technology have brought forth various methods for the measurement or estimation of the depth of interaction within the detector element (see Section 1.9). This estimation of the depth of interaction can help correctly associate the coincidence event and a LOR [12, 16].

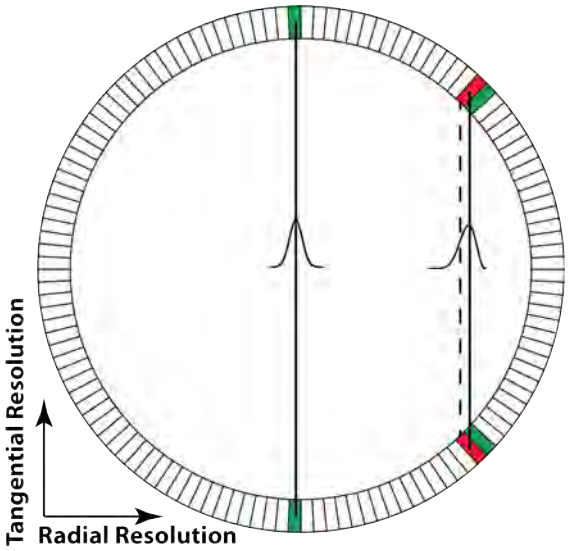

Figure 1.12: Due to the lack of depth of interaction information and shallow angle of interaction, the gamma ray can enter through one detector element and interact in another leading to degradation of spatial resolution by increasing the radial offset of the actual LOR to the reported LOR.

1.7.5 Dead Time and Pile Up

About 90 % of all detected events by the scanner are single events. This is an important statistic to understand as all single events contribute to the dead time of the system. The dead time of a system is the time during which a detector cannot collect new gamma rays because it is processing the previous one and/or waiting for the scintillator to decay. Dead time can lead to a significant loss of events, especially during high-activity acquisitions. Unfortunately, due to the nature of scintillators and processing electronics, dead time is necessary as the charge pulse from the detector has to be integrated for an appropriate amount of time to determine the energy of the incident gamma ray. It can be reduced by using fast scintillators which have a very fast decay time (like LSO, see Table 1.3) and fast electronics which can quickly process the energy signals.

As dead time cannot be avoided, mathematical methods have been developed which can estimate the system dead time and apply a multiplicative factor to the measured count, but these methods usually break down at very high counting rates. Using high amounts of activity can also lead to pile-up where two gamma rays interact in the scintillator at almost the same time producing a charge pulse equal to the total energy of both rays. This type of event should be rejected by the energy discriminator but as one of these two gamma rays could be part of a true coincidence, it can lead to loss of sensitivity. Therefore, it might be advantageous to reduce the activity given at any single time during the scan in favour of longer or multiple individual scans [12, 16].

1.8 Time of Flight PET

Time of flight (TOF) PET imaging is a recently reintroduced development of commercial PET in the late 2000s due to the availability and reduced cost of high-speed electronics

Table 1.3: Properties of various PET scintillators [1, 15, 16, 19–22]. Legend: ρ - Density, Z_{eff} - Effective Z, λ_{em} - Peak Emission Wavelength, $R_{\lambda_{em}}$ - Refractive Index at Peak Emission Wavelength, τ_{decay} - Scintillation Decay Constant, $E_{resolution}$ - Energy Resolution.

Scintillator	Formula	Hygro-scopic	ρ (g/cm^3)	Z_{eff}	$R_{\lambda_{em}}$	λ_{em} (nm)	Yield x1000 (MeV^{-1})	τ_{decay} (ns)	$E_{resolution}$ @ 662 keV (% FWHM)
NaI:Tl	NaI:Tl	Yes	3.7	51	1.9	410	38	230	6
BGO	$Bi_4Ge_3O_{12}$	No	7.1	74	2.2	480	8.2	300	8
GSO	Gd_2SiO_5:Ce	No	6.7	59	1.9	430	9	65	7
BaF_2	BaF_2	Slightly	4.9	54	1.5	220	1.3-1.4	0.8	8
$CeBr_3$	$CeBr_3$	Yes	5.2	46	2.1	380	57-66	17	4
CsF	CsF	Yes	4.6	52	1.5	390	1.9-2.0	3	~ 20
GAGG:Ce	$Gd_3Al_2Ga_3O_{12}$:Ce	No	6.6	53	1.9	520	42-57	50-120 + 200-400	5
	$Gd_3Al_{5-x}Ga_{x<3}O_{12}$:Ce	No	6.5	53	1.9	520	50-58	140-200 + >600	4
	$Gd_3Al_{5-x}Ga_{2.4<x<3}O_{12}$:Ce,Mg	No	6.6	53	1.9	520	43-47	40-50 + 100-200	6
	$Gd_3Ga_3Al_2O_{12}$:Ce (cer)	No	6.6	53	1.9	~ 550	30-70	50-170 + slow	~ 5
GLuGAG:Ce	$(Gd,Lu)_3(Al,Ga)_5O_{12}$:Ce (cer)	No	6.7-6.9	53	1.8	~ 550	20-50	40-90 + slow	~ 7
$LaBr_3$:Ce	$LaBr_3$:Ce(5%)	Yes	5.1	45	2.0-2.3	380	64-76	16	3
	$LaBr_3$:Ce(>10%)	Yes	5.1	45	2.0-2.3	380	68-70	16-18	3
	$LaBr_3$:Ce(5%),Sr	Yes	5.1	45	2.0-2.3	380	~ 78	18 + slow	2
LSF-3	$Ce_xLu_{2+2y-x-z}A_zSiO_{5+y}$ A=Ca,Gd,Sc,Y,La,Eu,Tb	No	7.3	65	1.8	420	~ 38	35-40	8
LGSO	$Lu_{2(1-x)}Gd_xSiO_5$:Ce(0.025%)	No	7.2	66	1.8	420	~ 34	30-34	8
LSO:Ce	Lu_2SiO_5:Ce	No	7.4	66	1.8	420	26-32	39-43	8
	Lu_2SiO_5:Ce,Ca	No	7.4	66	1.8	420	32-39	31-37	8
LYSO:Ce	$Lu_{2(1-x)}Y_xSiO_5$:Ce	No	7.1	65	1.8	420	26-34	38-44	8
	$Lu_{2(1-x)}Y_xSiO_5$:Ce,Ca	No	7.1	65	1.8	420	33-40	33-39	8
LuI_3:Ce	LuI_3:Ce	Yes	5.6	60	—	~ 500	~ 100	~ 30	~ 3

required to take advantage of this method. The method was initially explored in the 1980s for cardiac and brain imaging with very short-lived ^{11}C, ^{15}O, and ^{82}Rb isotopes. Due to their short half-life, high activities of the radioisotope are used which initially can overwhelm a scanner and result in increased dead time. This is where TOF can be used to extract more information from the already low number of true coincidences and improve the signal-to-noise ratio. However, the introduction of ^{18}F-Fluorodeoxyglucose (FDG) and the high cost of these systems caused the technology to be shelved until this century [23].

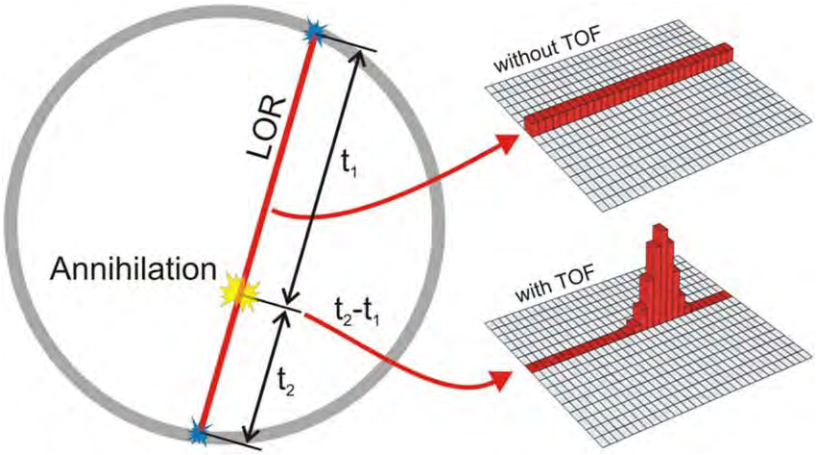

Figure 1.13: A diagram illustrating the principle of TOF PET where the location of the annihilation can be narrowed down to a subsection of the LOR rather than treating the whole LOR as of equal probability [19].

TOF uses the difference in time of arrival of the two annihilation photons at the detector to estimate where along the LOR the annihilation had occurred. As shown in Figure 1.13, in regular PET, when a LOR is determined it is assumed that the annihilation has an equal probability of occurring anywhere along it. In TOF PET, the difference in time of arrival can show towards which of the two detectors the annihilation occurred and the offset from the centre of the FOV d can be calculated as:

$$d = \frac{(t_2 - t_1)c}{2}, \tag{1.5}$$

where t_1 and t_2 are the times of arrival and c is the speed of light. However, the uncertainty

on that offset Δd is:

$$\Delta d = \frac{c\Delta t}{2}, \tag{1.6}$$

where Δt is the coincidence resolving time of the scanner. Modern TOF PET scanners have a coincidence resolving time of 200-400 ps which means the uncertainty on the position is 3-6 cm. While not ideal, with the use of a proper TOF reconstruction algorithm, these scanners see improved image quality, spatial resolution, and improved signal-to-noise ratio [12, 19, 23].

1.9 Depth of Interaction PET

The depth of interaction (DOI) PET scanner is a system which uses a detector that can in some way estimate the depth of interaction of the gamma ray in their thick scintillator. This area of PET saw its first development in the 1990s with the HRRT research tomograph (see Section 7.8.2). As this is an area of current development, many novel detector designs and methods of achieving DOI estimation have been proposed and tested as shown in Figure 1.14; however, above all two methods stood out as the most promising [12, 24].

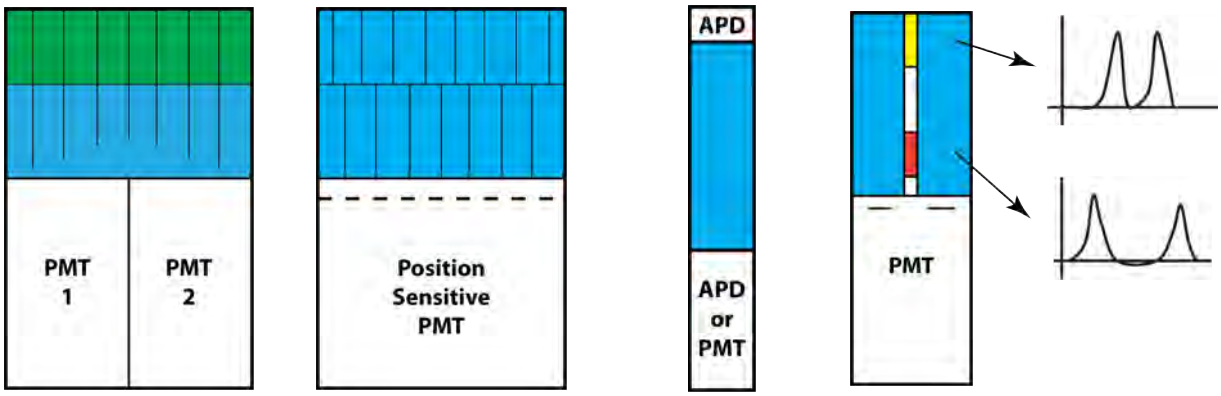

Figure 1.14: Some of the most widely discussed and promising DOI detector block designs. From left to right: The layered phoswich detector design used in the HRRT. The offset crystal matrix detector block design. The sandwiched crystal design. The light sharing crystal pair design.

The first method is through the use of a phoswich detector design. This is the method first developed for the HRRT which involves layering of different scintillator types or scintillators of the same type but with slightly different compositions such that their decay time is measurably different. Combined with electronics for pulse shape discrimination (PSD), the measurable difference in the decay time of the scintillation can be used to identify in which layer the gamma ray interacted and estimate the DOI to that layer. In the HRRT, the detector used two layers of a scintillator although modern designs have been proposed that use three or four layers [12, 24].

The second method of DOI estimation is to use photodetectors at both ends of the crystal. In this method, the ratio of the two signals can be used to estimate the DOI within the full crystal element. However, to prevent attenuation of the gamma rays, the detector on the inside of the scanner has to be very thin. This was made possible with the development of semiconducting photodetectors like the PIN photodiode, avalanche photodiode (APD), and silicon photomultiplier (SiPM). While a single detector on the inside of the ring needs to be used per individual detector element, the detector used on the outside of the detector can be a PMT and even shared among a few detector elements in a detector block design [16].

Some other novel methods of achieving DOI involve stacking crystal arrays with small positional offsets on top of a position-sensitive PMT such that the crystal centres do not overlap one another. Associations of the event to one of these crystal centres can then be used to associate the event to a certain layer of the detector and estimate the DOI. The last method worth mentioning to estimate DOI uses individual crystal elements that instead of using a reflective material between them use different absorber materials at different depths that also permit some light sharing between a pairs of these crystals. Analysis of the resulting signal produced by the pair can then identify which element the gamma ray interacted with and roughly estimate the DOI through pulse shape analysis [16].

Chapter Two

Positron Emission Particle Tracking (PEPT)

Positron emission particle tracking (PEPT) is an industrial imaging/particle tracking adaptation of the PET imaging technique. The PEPT technique was conceived at the University of Birmingham in the late 1980s and reported in 1988 by C. R. Bemrose et al. as a possible way of tracking single radiolabelled particles in the FOV of a positron camera rather than imaging a volume of radiolabelled fluid [25]. Positron emission was chosen over single photon imaging due to the relatively high energy and high penetration of the 511 keV annihilation photon. This allows the study of processes normally invisible to other particle-tracking techniques due to its ability to penetrate thick metal structures usually found in industrial machinery. Further energy discrimination and electronic collimation reduce the high levels of scatter coincidences found when imaging metal-containing machinery.

The development of PEPT at the University of Birmingham stemmed from the 1986 development of the Birmingham positron camera shown in Figure 2.1 and described by M. R. Hawkesworth et al. which is a larger and improved version of the Rutherford Appleton Laboratory (RAL) Mk.I multiwire proportional counter (MWPC) [26]. The camera was used

at the University of Birmingham initially for PET imaging of industrial systems to study the distribution of fluids within them and later for the first PEPT data acquisitions. The method was properly established in 1993 by D. J. Parker et al. with the development of the Birmingham Method for particle triangulation and tracking (see Section 2.1) [27].

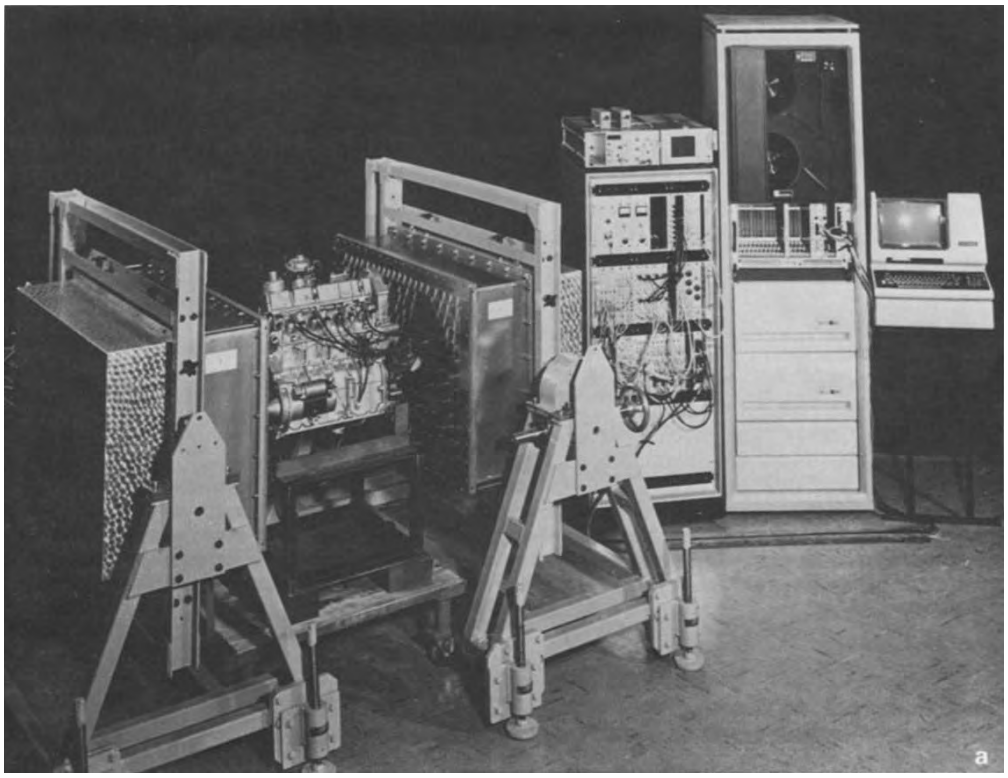

Figure 2.1: The Birmingham positron camera with a small automotive engine under study. The left electronics rack houses all the camera electronic modules and an analogue computer. The right electronics rack houses a CAMAC system and a DEC 11/23 computer [26].

In PEPT, instead of producing images acquired over long periods showing the integrated distribution of the radionuclide in the system, the individual LORs are grouped into batches representing a small period of acquisition (usually under 1 ms) that are then used to calculate a single position through triangulation. Repeated throughout the whole acquisition, the individual positions are used to build a track representing the motion of the particle in the system. Further analysis and post-processing of many of these tracks can yield industrial data representing velocity fields and particle occupancy in 3D. To obtain the individual LOR data, the PET scanner acquisition needs to be specially modified or

configured to output the list mode data that then can be converted to real-world units and processed using a PEPT algorithm.

Particle tracking algorithms and applications of PEPT to engineering, physics, and medicine have been under constant development for over 35 years at the University of Birmingham Positron Imaging Centre (PIC). With a constant need to apply the technique to track faster and smaller particles, the development of specialised positron camera systems for PEPT has been undertaken for several years at the PIC. Recently developed, highly-sensitive SuperPEPT demonstrates high data rates capable of tracking smaller and less active particles (see Section 10) while the expanded Large Modular Array (LaMA) for PEPT has allowed the study of very large and long engineering systems which was not possible before (see Section 11).

2.1 The Birmingham Method

The earliest and most widely applied PEPT algorithm was developed by David J. Parker et al. in 1993 at the University of Birmingham acquiring the name Birmingham Method [27]. In its simplest form, the algorithm tries to locate a point-like positron-emitting source which minimises the average perpendicular distance from all LORs in a given group. If all the LORs were due to true coincidences, then the average perpendicular distance from all the LORs in every group would be within the spatial resolution of the scanner. However, as the recorded LORs contain random and scatter coincidences, the algorithm is run iteratively by calculating the minimum distance point and rejecting the furthest LOR(s) from it. This is repeated until a predefined fraction of the original set of LORs is left. Then the final position of the point source is produced and the algorithm starts all over again with the next subset of LORs.

PEPT scanners record LORs in list mode as a sequential list of lines or trajectories such that $L_1, L_2, L_3, ...$ From that list, a subset, S, of $N(S)$ number of LORs in S is consecutively chosen such that $S = L_1, L_2, ...L_N$. The sum of perpendicular distances between all LORs in the subset S and any point m_S is then:

$$D_S(m_S) = \sum_S \delta_i(m_S), \tag{2.1}$$

with $\delta_i(m_S)$ as the perpendicular distance for the ith LOR to point m_S. The minimum distance point, m_S, for the set S of LORs can be calculated by solving the above equation such that:

$$\nabla D_S(m_S) = 0. \tag{2.2}$$

The mean deviation of the LORs from the point m_S is then:

$$d(S) = \frac{D_S(m_S)}{N(S)}. \tag{2.3}$$

To calculate the final position, the algorithm follows these steps:

1. Calculate m_S for the set S.
2. Remove LORs for which $\delta_i(m_S)$ is larger than $kd(S)$, where k is a fixed multiplication factor usually set between 1.0 and 1.5.
3. The removal leaves a new subset S_1 of LORs which should have a smaller $d(S_1)$ and an improved m_{S_1}; these are now calculated.
4. The original set S is then rechecked using m_{S_1} in case any of the rejected LORs lie closer to m_{S_1} then m_S. So, again remove any LORs from S for which now $\delta_i(m_{S_1})$ is larger than $kd(S_1)$.
5. The algorithm iterates over the above steps creating smaller subsets S_2, S_3, etc....
6. When $N(S_n) = N(S_{n-1})$, the trajectory with the largest $\delta_i(m_{S_n})$ is removed.

7. The algorithm stops when $N(S_n) = fN(S)$.

8. The final position m_{S_n} with mean deviation $d(S_n)$ is written to a file.

9. A new set S of the next N LORs is taken from the list mode file and the algorithm starts over.

The size of N is chosen by the user and it highly depends not only on the scanner but on the experimental measurement itself as discussed in Section 2.2, below. The value of f is also dependent on the scanner and the experimental setup, or the amount of noise being recorded. A good starting value of f is usually 0.4 and is discussed in Section 10.4.

The mean deviation $d(S)$ for each position is also referred to as the PEPT error or the uncertainty on the position and can be referred to as d or Δx, like in the section below, depending on the context. To calculate the PEPT spatial resolution ω in Equation 2.5 below, Δx should be taken as the average of all $d(S)$ of all positions calculated for a stationary particle over a period of time. Birmingham Method is the preferred tracking algorithm for simple characterisation of PEPT systems. Its simple, mesh-free yet intuitive data processing pipeline and its ultra efficient use of computer resources makes it a perfect candidate to process large quantities of list mode data to simply extract its statistics. It is one of the best algorithms when tracking relatively normal speed, normal activity, single particles in a PEPT experiment [28].

2.2 PEPT System Characterisation

To calculate a valid particle position using any PEPT algorithm, it is important to understand the limitations posed by each PEPT camera. Camera properties such as the coincidence rate and sensitivity limit the maximum speed of a tracer particle it can precisely

locate. Due to fundamental limitations on the positron emission process and limitations of the detector systems themselves, the true LORs will be distributed at varying distances from the actual tracer location. This can be characterised by the standard deviation or spatial resolution ω of the system. If the tracer particle does not move significantly, the uncertainty on the position Δx calculated using N number of LORs is:

$$\Delta x = \frac{\omega}{\sqrt{N}}. \tag{2.4}$$

However, as stated before, the group of LORs contains random, scattered, and multiple coincidences which need to be discarded by the algorithm. When using the Birmingham Method, the algorithm rejects the corrupt LORs until a fraction f of the original group of N LORs remains. The above relationship can then be written as:

$$\Delta x = \frac{\omega}{\sqrt{fN}}. \tag{2.5}$$

This relationship can then be used to determine the spatial resolution, ω, of a PEPT system averaged in 3 dimensions. However, due to the anisotropic placement of detectors in most PEPT systems, the system can resolve a particle's position more accurately in some directions than others. For example, using a full ring tomograph, the position of a particle in the dimensions represented by the transverse plane of the scanner can be determined more accurately than along the dimension represented by the axis of the scanner.

This relationship can be further expanded to calculate the optimum N for the scanner for a particle moving with velocity v. Substituting $\Delta x = v\Delta t$ and $N = R\Delta t$ where Δt is the time interval in which the particle would move a distance equal to the stationary particle position uncertainty Δx and R is the coincidence rate:

$$\Delta x = v\Delta t \approx \frac{\omega}{\sqrt{fN}} = \frac{\omega}{\sqrt{fR\Delta t}}. \tag{2.6}$$

Rearranging this equation, to solve for the time interval:

$$\Delta t \approx \left[\frac{\omega^2}{v^2 f R}\right]^{\frac{1}{3}}, \tag{2.7}$$

which can be substituted back into $v\Delta t$ such that the position uncertainty is:

$$\Delta x \approx \left[\frac{v\omega^2}{fR}\right]^{\frac{1}{3}}. \tag{2.8}$$

Therefore, the optimum number of LORs used for every position triangulation for a particle moving with velocity v is:

$$N = R\Delta t \approx \left[\frac{\omega^2 R^2}{v^2 f}\right]^{\frac{1}{3}}. \tag{2.9}$$

This equation can be used as a rule of thumb to check before the experiment if the selected PET scanner will be able to handle the velocities present in the system under study. If the calculated N is too small (< 100 depending on the system) this can result in a large standard deviation on the calculated position [29, 30].

Another way of checking if a system is the right one for an experiment is using Equation 2.5. For example, ADAC Forte is a two-headed positron camera whose head separation can be adjusted to fit a range of industrial machines. Its ease of use makes it a commonly used PEPT system at the PIC although it has a low data rate. The camera can record coincidences at around 100,000 coincidences per second and has a spatial resolution of about 10 mm. Using an $f = 0.5$, it can produce positions every 1 ms with an uncertainty of about 1.4 mm. If an experiment is expected to have particles moving at a maximum 3 m/s, then the particle will move 3 mm in that 1 ms which is over twice our uncertainty. This means the particle is too fast to be located with 1.4 mm precision, using the above specified parameters. It will have to be located more often with increased loss of precision. In the above example, producing positions every 0.5 ms results in an uncertainty of 2 mm when the particle travels 1.5 mm which can be an acceptable trade-off. If the experiment requires a better position uncertainty, then considerations in selecting the right f have to be made, the particle has to be slowed down (when possible/acceptable), or a different PEPT system with a higher sensitivity/coincidence data rate needs to be used.

Besides the ADAC Forte, the SuperPEPT and LaMA PEPT are also available PEPT systems at the PIC and are discussed in Sections 8 - 11. Both of these systems have their pros and cons but they both outperform the ADAC Forte. LaMA PEPT has a higher sensitivity and data rate than the ADAC Forte and, most importantly, its shape can be adapted to fit a variety of PEPT experiments that cannot be imaged with the standard square head or cylindrical scanner geometries. Its biggest drawbacks are the high variations in sensitivity (depending on the custom geometry) and its relatively high data noise. On the other hand, SuperPEPT has a very high data rate, low data noise, and very high sensitivity. Perhaps, its only drawback is the set cylindrical geometry which can be troublesome for positioning and fitment of various heavy-duty machines.

Chapter Three

Developments Leading to Nuclear Imaging

Nuclear imaging is a process which utilises gamma rays emitted during the radioactive decay of radiopharmaceuticals or radiotracers from within the subject being imaged to obtain information on the location and distribution of the radionuclides within. Nuclear imaging can be used to show changes in functions of processes through the distribution of the radiotracer in the system and its change over time. The field of nuclear imaging can be traced back to the development of X-ray imaging, scintillation detectors, and radiopharmaceuticals. The multidisciplinary aspect of nuclear imaging makes it very hard to pinpoint its historical beginning. Contributions from physics, medicine, chemistry, and engineering concurrently led to its beginning.

Without the advancements in science and electronics presented in this section, the modern PET and PEPT systems would not exist. Without the Crookes tube leading to the discovery of electrons, X-rays, and gamma rays, the advancements in radiation detection, counting, and imaging would not lead to the development of the photomultiplier tube, electronic readout devices, and scintillation detectors. Further, without X-ray imaging be-

coming a safe, everyday occurrence, use and manufacture of radiation-containing compounds to study biological functions and eventually locate cancer tumours in the body, nuclear imaging as a whole would not be developed and commonly used today. In order to understand the basic function and development of PET and PEPT systems, one needs to comprehend the history behind such complex systems.

3.1 Electrons and X-rays

The development of medical imaging goes hand-in-hand with the discovery of the X-ray. Observations of X-rays, can be traced as far back as 1785 to William Morgan's experiments with electrical current in partially evacuated glass tubes that emitted an unknown glow [32]. In 1875, William Crookes invented what is known as a cold cathode or Crookes tube shown in Figure 3.1 and described the negatively charged cathode rays. Since then, the effects of, unknown at the time, X-rays started to appear in literature [31]. Later in 1897, Joseph John Thomson, John Sealy Edward Townsend, and Harold Albert Wilson identified cathode rays as negatively charged particles giving the first estimate of the charge and mass of the electron [33]. All of these early scientists working with cathode rays described the glow of

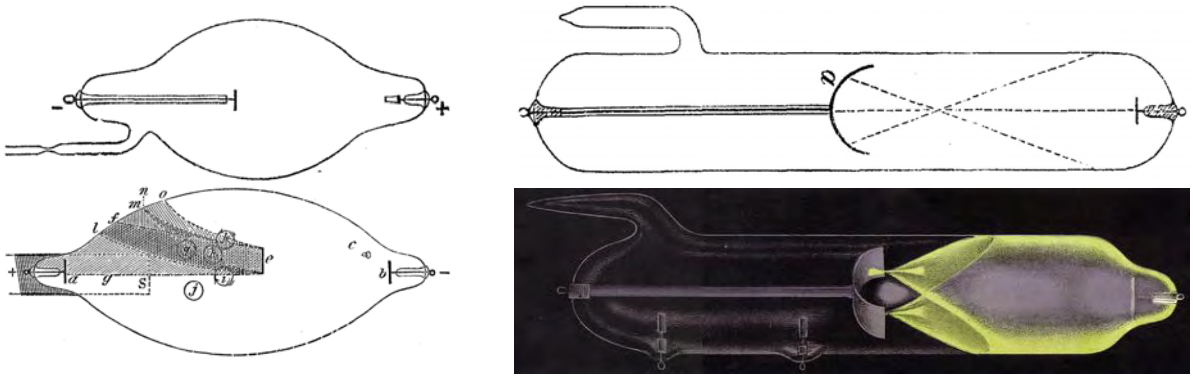

Figure 3.1: A selection of tubes William Crookes presented in his groundbreaking article demonstrating the glowing effect and the deflection of the beam in a magnetic field among other experiments [31].

the tube due to the acceleration of the electrons and their ionising effect in the Crookes tube leading to the production of X-rays and the glow.

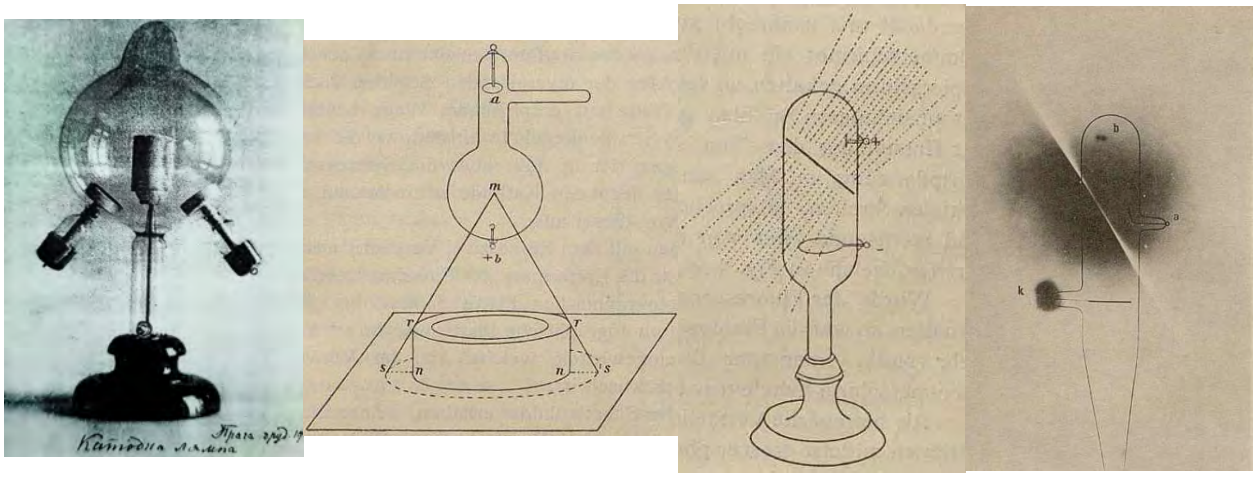

Figure 3.2: An image of one of Puluj's early X-ray tubes [34] followed by one of his experimental setups used to determine the distribution of X-rays in space, and finally ending on a film exposure of one of his tubes showing the high amounts of X-rays being produced [35, 36].

In late December 1895, Wilhelm Conrad Röntgen discussed his observations of this unknown radiation that caused the Crookes tube glow. He termed the radiation "X" rays to mean unknown rays that caused a fluorescent screen to glow when he covered his Crookes tube in cardboard to prevent the glow from activating the screen in the first place. As the cardboard would have prevented any stray cathode rays from activating the screen, unknown invisible radiation had to be causing the fluorescence [37–40]. The actual circumstances in the way Röntgen observed the first X-rays are a mystery as he had his lab notes burnt after his death [41]. Although, recently uncovered documents and studies thereof have presented a challenge to Röntgen's claim of the title of discovering X-rays as Ivan Puluj, who was acquainted with Röntgen, is said to have shown the effects Röntgen later described in his paper. Although Puluj published two papers on X-rays right after Röntgen's first paper [35, 36], it is said that they were based on work that pre-dated Röntgen's discovery and used Puluj's custom-designed X-ray tube, see Figure 3.2, one of which Puluj supposedly gave Röntgen before his discovery [34]. As the rediscovery of facts in this area is still ongoing,

only time will tell who is right if enough evidence has survived the test of time.

3.1.1 X-ray Imaging

First medical X-ray images were also taken by Röntgen of his wife's hand shown in Figure 3.3 in 1895, by exposing a photographic plate with X-rays [37–39]. After the publication, the X-ray field exploded with everyone wanting to experience them. The use of X-rays in an actual clinical setting was first accomplished in January 1896 by John Francis Hall-Edwards working at the Birmingham General Hospital in the UK. He took an X-ray of a colleague's hand to help find a needle stuck under their skin and a month later he used the technique in a surgical setting to guide surgery [42]. The first medical X-rays in the USA were done at Dartmouth College in 1896. Gilman DuBois Frost and Edwin Brant Frost took images of a broken wrist of Eddie McCarthy, as seen in Figure 3.4, whom Gilman treated earlier at the College taking USA's first X-ray using a tube of Puluj's superior design [43, 44].

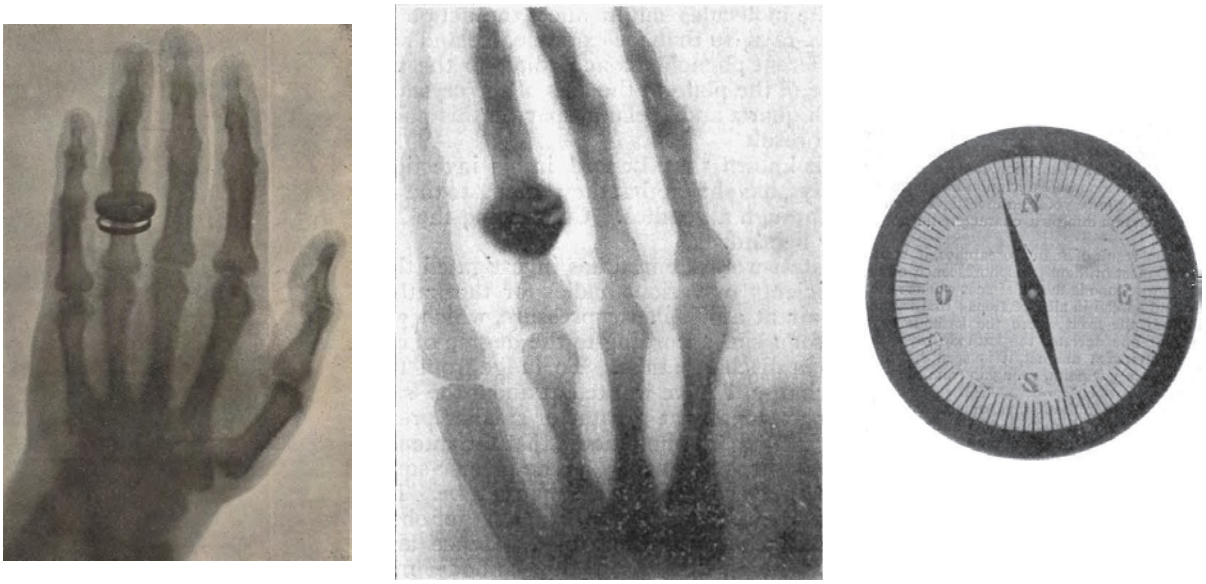

Figure 3.3: X-ray images of Röntgen's wife's hand (or another person's) and of a pocket compass which accompanied the various editions of his publications [38, 39].

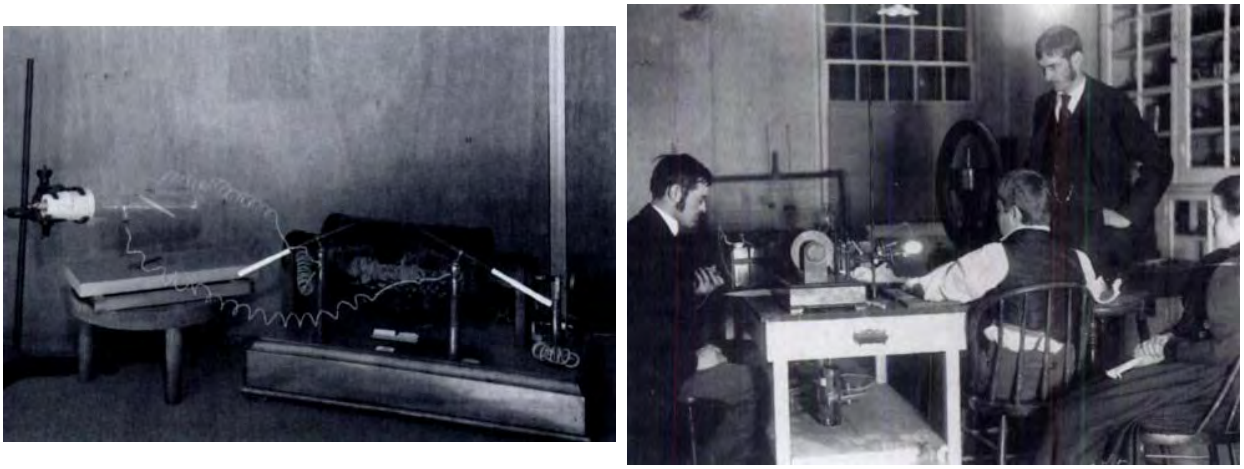

Figure 3.4: (Left) The Puluj's tube and induction coil that were used to take the first X-rays in the US at Dartmouth College. (Right) The moment the first X-ray was taken at Dartmouth College with (Left to Right) Edwin Frost, patient Eddie McCarthy, Gilman Frost, and Margaret Mead Frost [43].

3.1.2 Fluoroscopy

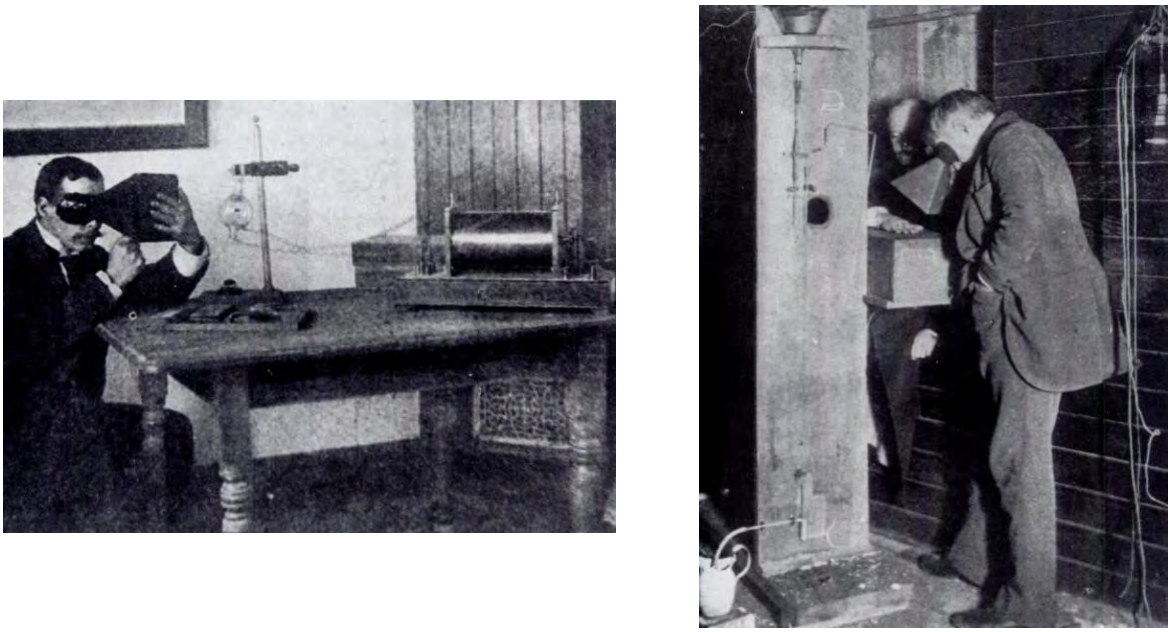

Figure 3.5: Early uses of fluoroscopes by a scientist checking the intensity of a X-ray tube using his hand and Thomas Edison using his Vitascope [45].

It was quickly made apparent that it was possible to view X-rays "live" using a luminescent screen. Röntgen noticed that barium platinocyanide ($Ba[Pt(CN)_4]$) fluoresced when

exposed to X-rays. This material was then used by Enrico Salvioni in the cryptoscope and William Francis Magie in the Skiascope who concurrently in February 1896 developed the live imaging devices. Thomas Alva Edison also studied various materials' X-ray fluorescence identifying scheelite (calcium tungstate, $CaWO_4$) as the most effective and used it to develop his Vitascope, shown in Figure 3.5, the first commercial mass-produced live imaging device in May 1896 [45]. A major improvement in X-ray technology came in 1913 when the principle of a hot cathode vacuum tube developed by John Ambrose Fleming in his 1904 thermionic diode [46], shown in Figure 3.6, was applied to the Crookes tube by William David Coolidge. The Coolidge tube shown in Figure 3.6 was a more reliable, controllable, and continuous source of X-rays compared to the troublesome cold cathode tubes used at the time [47, 48]. To this day, the design principles used in the Coolidge tube are still used in modern X-ray tubes although they are now heavily shielded and use rotating anodes.

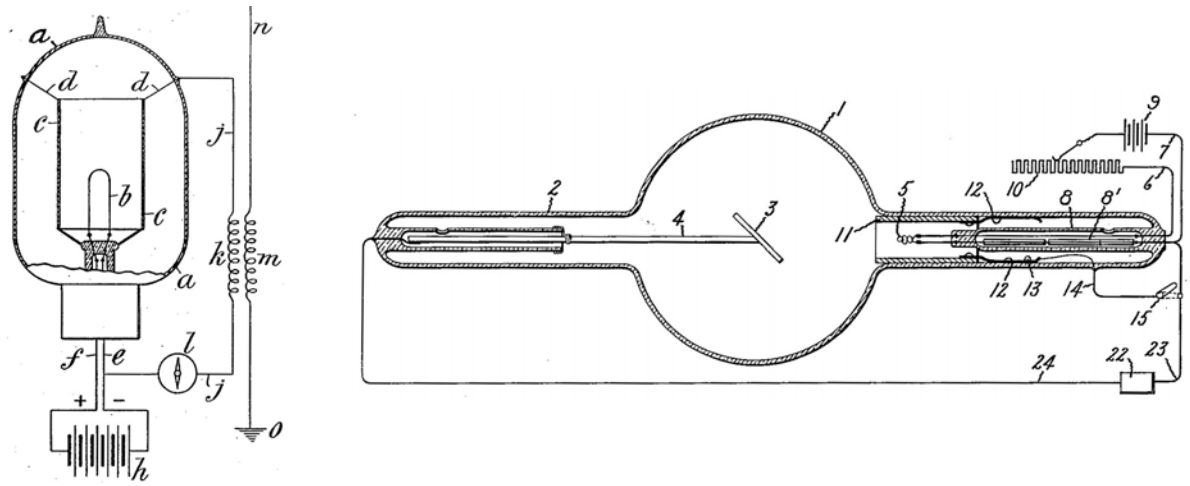

Figure 3.6: (Left) John Fleming's thermionic diode schematic diagram [46]. (Right) William Coolidge's hot cathode X-ray tube [48].

At this moment in time, X-rays became cemented as the dominant medical imaging type. They are easy to generate and control through the use of X-ray tubes and can be easily imaged using standard photography films and luminescent screens. Although the lack of shielding, radiation safety, and the high dose acquired, especially by operators, after multiple X-ray images/experiments would lead to cancer, this method made it possible to

view the structure of the human body as never seen before. As the effects of X-rays and radiation in general started to be understood, it became important to properly shield and isolate the X-ray source, decrease the dose/time required for each exposure, and to increase the sensitivity of the film and screens. Therefore, it became vital for the development of modern medical imaging devices to develop high sensitivity radiation detectors and films that could acquire higher resolution, quality, and contrast images with as little radiation as possible. However, this development in detection sensitivity would be mostly lead by the discovery of the gamma ray.

3.2 Discovery of the Gamma Ray

The gamma ray itself was first discovered and observed by Paul Ulrich Villard in 1900 studying radiation given off by natural radium samples [49]. It was later named by Ernest Rutherford in 1903 who theorised that they are high-speed beta particles, but because they were not deflected by magnetic fields, they had no charge [50]. It was not until 1914 when Ernest Rutherford and Edward Neville da Costa Andrade observed gamma rays diffracting from a rock-salt crystal and measured their wavelengths that gamma rays were classified as electromagnetic radiation with a wavelength shorter than that of X-rays [51]. While general observations and measurements of particles were possible at this time, individual particle counting and measurement techniques were starting to be developed.

3.3 Developments in Radiation Counting

In the early days of nuclear science, there were very limited instruments available for radiation detection and observation. Besides the use of photographic plates and early ionisation

chambers, materials which experienced scintillation or luminescence caused by ionising radiation were also used as the earliest radiation counters.

3.3.1 Spinthariscope

The earliest of the widely used scintillators was zinc sulfide (ZnS) whose luminescent properties were first observed in 1866 by Théodore Sidot and presented by Alexandre-Edmond Becquerel [52]. ZnS is only made as a polycrystalline solid and cannot be grown in a single crystal, as a result, it can only be used in very thin layers [1]. It was widely used in early X-ray screens, cathode-ray tubes, and radium watches where it could be applied and used in thin quantities. In 1903, William Crookes used a ZnS screen to observe a sample containing radium which he said uniformly illuminated the screen. However, when he spilt a tiny bit of the rare sample onto the screen, he observed tiny, individual flashes of light rather than a uniform exposure [53]. This observation led to his invention of the Spinthariscope or a small vacuum tube filled with a tiny amount of radium salt that had a ZnS screen on one end and a lens that could be used to view it [54, 55]. This was essentially the first manual scintillation counter that at the time was marketed more as a toy and a curiosity (still is) rather than a piece of scientific equipment.

It was not until 1908, that Erich Rudolf Alexander Regener described the visual scintillation counting technique of alpha particles using ZnS scintillator, which involved manual counting of light flashes in a dark room, that the technique gained wider scientific use [56]. It was almost immediately recognised that pure ZnS does not scintillate and that impurities present in the originally produced samples were the cause of the effect. ZnS specifically produced for nuclear applications had to be "activated" with copper or manganese compounds [57] but today it is widely activated with silver [1]. At the time, the technique was strenuous and highly susceptible to human error.

3.3.2 Gas-Filled Electronic Counter Tubes

In the same year, Ernest Rutherford and Johannes Wilhelm "Hans" Geiger designed a gas-filled electronic counter tube. The tube was part of a larger experimental apparatus shown in Figure 3.7 that featured a brass tube anode, capped with ebonite stoppers, with a thin cathode wire running through it, and a thin mica entrance window at the other end. As alpha particles were introduced from a different part of the apparatus, the tube's sharp response could be viewed on a quadrant electrometer [58]. The design was based on the Townsend discharge principle discovered by John Sealy Townsend in 1901 where free electrons accelerated by an electric field can collide with gas molecules in a low-pressure environment and free more electrons which then in an avalanche effect can undergo more collisions [59]. The ionised gas molecules would then travel to the cathode where they would recombine with the electrons. The source of the initial free electrons in the case of the counter was ionising radiation.

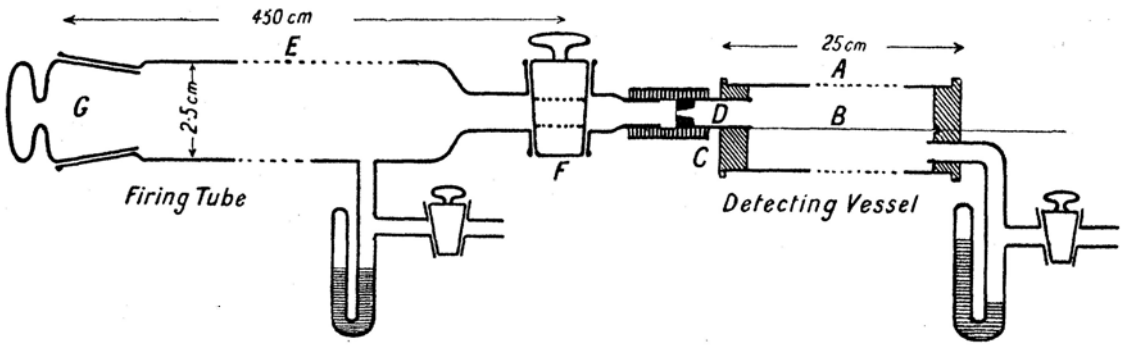

Figure 3.7: Rutherford's and Geiger's gas-filled electronic counter apparatus [58].

By 1912, Geiger and Rutherford changed the quadrant electrometer for a string electrometer where they were able to use photography film to record the movement of the string and achieve up to 1,000 counts per minute [60]. Geiger further redesigned the tube as a standalone module shown in Figure 3.8 which consisted of a brass tube capped at one end and a mica entrance window on the other. The central cathode wire was only suspended on one end and sharpened to a point on the other such that it ended right before the mica

window. The tube was only able to record alpha and beta particles at the time [61].

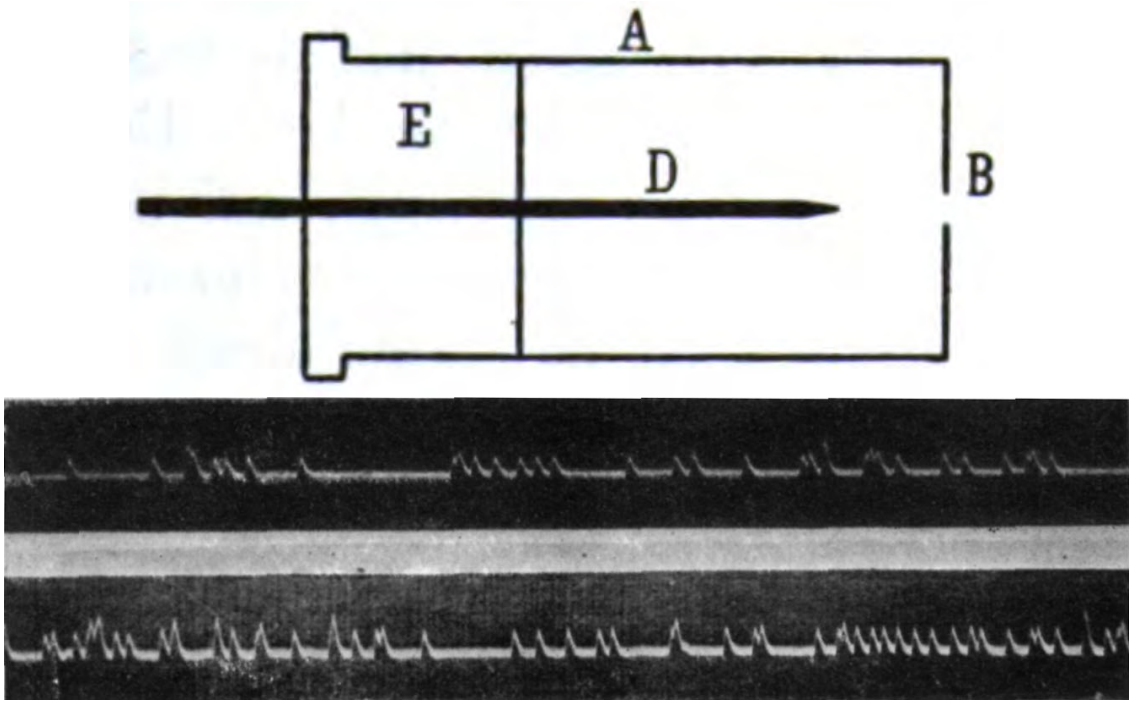

Figure 3.8: Geiger's standalone counter tube with a sharpened central cathode and a thin mica window [61]. Following, is the photographic registration of the string electrometer showing a response to alpha particles at a rate of 600 per minute and 900 per minute [57].

In 1928 came the first big improvement to the tube. Geiger and Otto Ernst Heinrich Klemperer realised that by switching the tube's polarity such that the central wire was the anode and adding a small ball to its tip to prevent unintentional discharges, see Figure 3.9, the tube was able to not only detect alpha and beta but also gamma particles. Having access to new high-voltage power supplies, they also described the loss of proportionality of the tube as it entered the Geiger region [62]. In the same year, Geiger and Walther Müller incorporated the above changes and powered the tube in the Geiger region creating the Geiger-Müller (GM) detector [63, 64].

The tube suffered from repetitive pulses caused by electrons released by the positive ions smashing into the anode. This was resolved in 1937 by Adolf Trost who discovered that small additions of ethanol to quench the avalanche prevented multiple pulses from occurring.

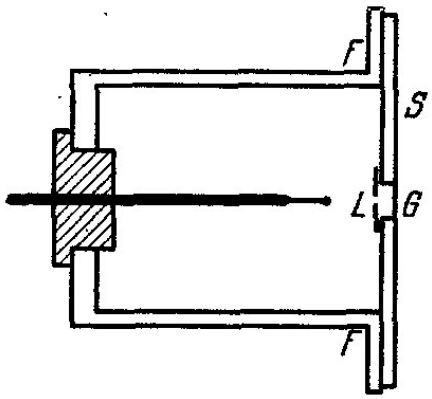

Figure 3.9: The improved Geiger counter tube with the central anode wire [62].

During the quenching process, the positive gas ions interact with the ethanol molecules which transfer the electron back to the gas ion and then they knock into the anode. However, when they knock into the anode, the ethanol molecule neutralises and disintegrates absorbing a portion of the kinetic energy and preventing free ion ejection [65]. This meant that using a quenching gas gave the tube a limited lifespan. This was addressed in 1948 by Sidney H. Liebson and Herbert Friedman who used inorganic halogen quench gases giving in theory a limitless life to the GM tube [66].

Although, advanced ways of recording the signal pulses from the GM tube using physical media were developed, these were still hindered by the need to manually count the recorded pulses and were limited by the response time and resolution of each of these methods. However, in 1932, Charles Eryl Wynn-Williams introduced the first thyratron-tube-based scale-of-two (binary) counter which was able to register electronic impulses at high rates shown in Figure 3.10, finally allowing for easy signal counting [67]. This capability permitted the studies of high activity or purity samples which would lead to the saturation of the older techniques. Further, higher count rate meant higher temporal resolution which not only made it possible to distinguish particles which were emitted quickly one after another during a decay, but increased the overall efficiency of the system allowing for more precise, higher resolution studies. In a way, this binary counter contributed to the development

of all modern digital electronics. With all of these developments, visual scintillation was quickly made redundant and replaced by Geiger counters and ionization chambers with binary counters until the development of the photomultiplier tube.

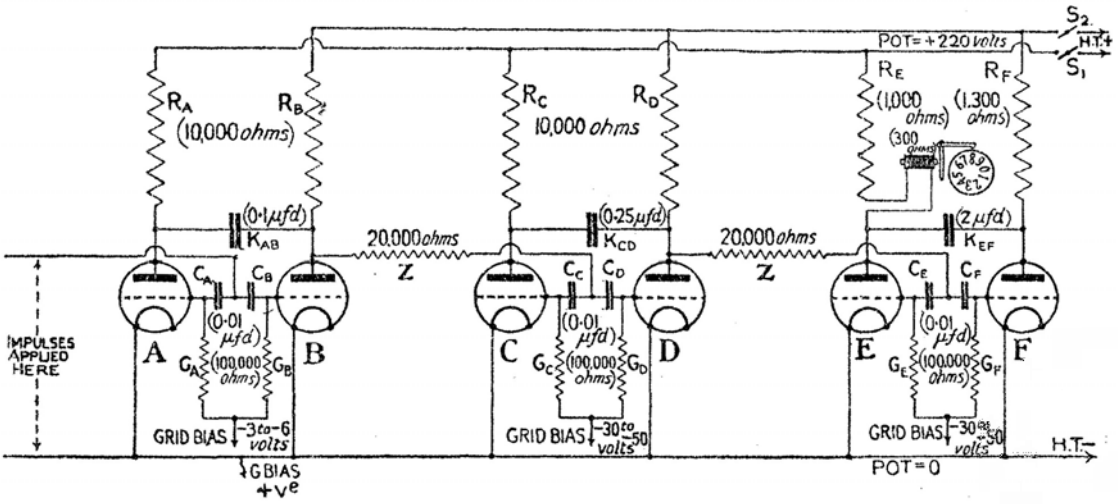

Figure 3.10: Schematic diagram of the repeatable, thyratron-tube-based, scale-of-two counter designed by Charles Wynn-Williams [67].

3.4 Development of the Photomultiplier Tube (PMT)

The history of the development of the photomultiplier tube (PMT) is a long one. It involves discoveries of key physics principles over a 50 year span. A PMT could not exist without the photoelectric effect, secondary emission, and use of vacuum tubes. The combination of these principles to build the first multistage photomultiplier tube will be discussed.

3.4.1 The Vacuum Tube and Signal Amplification

There is a lot of controversy surrounding the history of the development of the first amplifying electronic device. One of the first electronic detecting glass tube devices was the Audion, developed by Lee de Forest in 1906 which was used as a radio receiver detector [68–70]. It

essentially was a diode in a low-pressure gas-filled glass tube which, unknown at the time, gave it erratic performance issues. De Forest continued to file multiple patents with some minor and seemingly insignificant improvements. However, in 1908, he patented the first triode after a few modifications to his diode design, see Figure 3.11 [71]. Unknown to him, the triode, besides being a signal detector, was the first device capable of signal amplification. By 1912, other researchers realised the potential of the triode and began building amplifying radios and the first oscilloscopes [72].

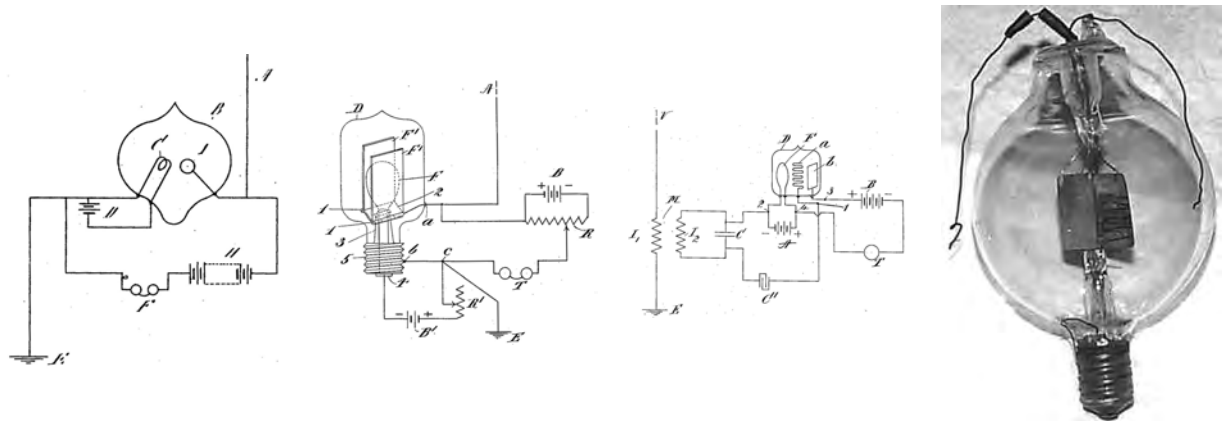

Figure 3.11: A few of de Forest's Audions. The first two are the diode-like devices used at the time as radio receiver detectors [68, 69]. The last two are the triodes which lead to the development of signal amplification [71, 72].

During his career, de Forest battled many patent-related lawsuits because many of his parts and circuit designs bear many similarities to systems developed earlier by other researchers. His first diode, the Audion, closely resembled that patented by Fleming in 1905 during his research into the thermionic valve [46]. The only defence de Forest had was that his Audions were gas-filled and Fleming's thermionic valves were under vacuum. In fact, in 1914 a student at Columbia University, Edwin Howard Armstrong, documented the theoretical principles of the Audion [73] and later when he and de Forest faced off over a patent dispute, Armstrong was able to prove that de Forest did not even understand how "his inventions" worked [72].

Soon, observations and developments by Irving Langmuir in 1913 revealed that to

fix the performance issues of the tube, a true vacuum had to be used. Langmuir not only demonstrated that a vacuum is needed for valve tubes to work properly, but the metal purity is also very important. This led to the development of the first pure, true vacuum amplification tube, the Pliotron, shown in Figure 3.12. He even went on to improve Edison's lightbulb by concluding that to be more efficient they should be filled with a low-pressure inert gas that is meticulously scrubbed of any impurities, greatly extending the bulb's lifespan [74]. By the early 1920s, de Forest's Audion was rendered obsolete and the true vacuum triode became the staple of the growing home radio market.

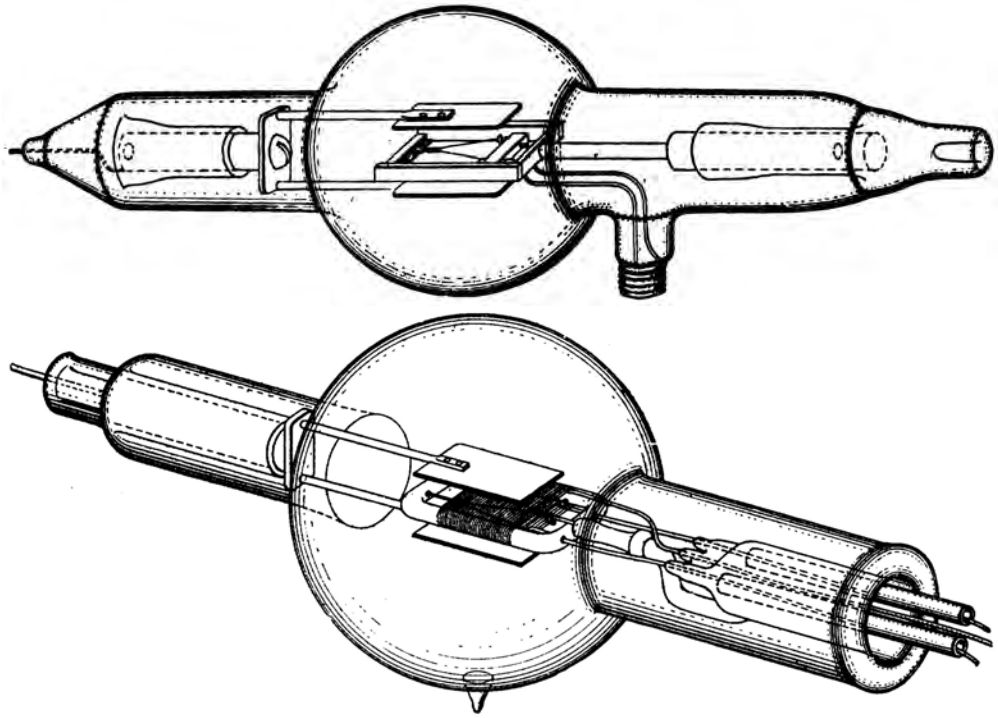

Figure 3.12: Languir's vacuum tubes. On top is the Kenotron used for high voltage rectification and on the bottom is the Pliotron used for audio and radio amplification [74].

3.4.2 The Single-Stage Photomultiplier

By the 1920s, the stage was set for the development of the PMT. Based on the extensive work of Julius Johann Phillipp Ludwig Elster and Hans Friedrich Karl Geitel on different

photoemissive materials, it was apparent that no single element at the time had the efficiency to be a useful photocathode material [75]. In 1929, Lewis Richard Koller and Norman Robert Campbell working for the General Electric Company developed the first photoemissive compound material the Ag-O-Cs (silver oxygen caesium) also called the S-1 [76, 77]. The material showed a two-order-of-magnitude increase in sensitivity over previous materials, it was also a good secondary emitter, and had 0.4% quantum efficiency at 800 nm [78]. Finally, in 1934, the first single-stage photomultiplier was developed. It was accomplished by Harley Iams and Bernard Salzberg of the Radio Corporation of America (RCA) when they combined the Ag-O-Cs photocathode and a single secondary emission dynode in a vacuum tube shown in Figure 3.13. The single-stage tube only had a gain of around eight [79]. To improve the gain of the photomultiplier, a new radical design using multiple secondary emission dynodes would have to be used.

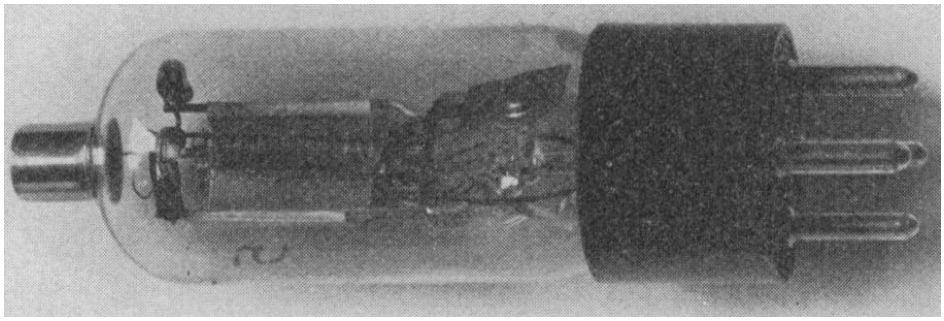

Figure 3.13: The first gain of 8 sing-stage photomultiplier tube which used an Ag-O-Cs photocathode and a single secondary stage in a vacuum tube [79].

3.4.3 The Multi-Stage Photomultiplier

Now the story is a bit complicated as for years the RCA was credited with the first multi-stage photomultiplier, but recent rediscoveries say it was developed in the Soviet Union. It is hard to say who is right as few Russian documents are available online from those times. It has been recently [80] reported that in 1930, a soviet scientist Leonid Aleksandrovitch Kubetsky received a Soviet author's certificate #24040 for his proposed design of a multi-

staged photomultiplier tube. In his design, Kubetsky proposed a single photocathode with multiple secondary electron emitters each of which was supplied with a higher potential than the previous. Between 1933 and 1934, he developed multiple of these devices using Ag-O-Cs photocathodes and dynodes, one of which is shown in Figure 3.14. Kubetsky used constant magnets for electron focusing between the multiple stages and was able to achieve gains in the order of $10^3 - 10^4$. In the Soviet Union, these tubes became known as Kubetsky's tubes [80–83].

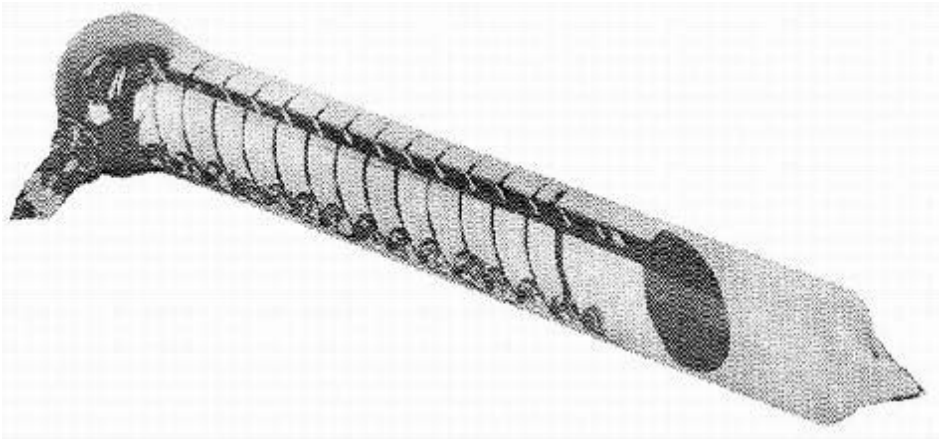

Figure 3.14: Kubetsky's multi-stage photomultiplier tube that supposedly predates the developments at RCA [80].

In the 1930s, Stalin was investing heavily in RCA-made radio equipment to build radio broadcast centres throughout the Soviet Union. As part of the investment, RCA sent scientific staff to the Union on multiple occasions to train staff and gauge their needs. Vladimir Kosma Zworykin of RCA was part of one of these trips in September 1934 when he visited Moscow and Leningrad, read various lectures at local universities, and visited laboratories one of which was Kubetsky's lab where he was shown the tubes and even used some of them. Supposedly after that visit, Zworykin noted down the details of the multi-staged photomultiplier and it was only after September 1934 that his dated personal and lab notes began showing details of the tube he and his team supposedly designed [80]. So, in 1935, Zworykin, George A. Morton, and Louis Malter of RCA published their famous paper

about the multi-dynode tube shown in Figure 3.15 [84]. No matter who designed the first muti-dynode tube, all the tubes used constant magnets for electron guidance between the different stages. In practice, this was problematic as changing the bias voltage of the tube to adjust its gain required the magnetic field to be precisely adjusted, making the tube's operation a complicated one [78].

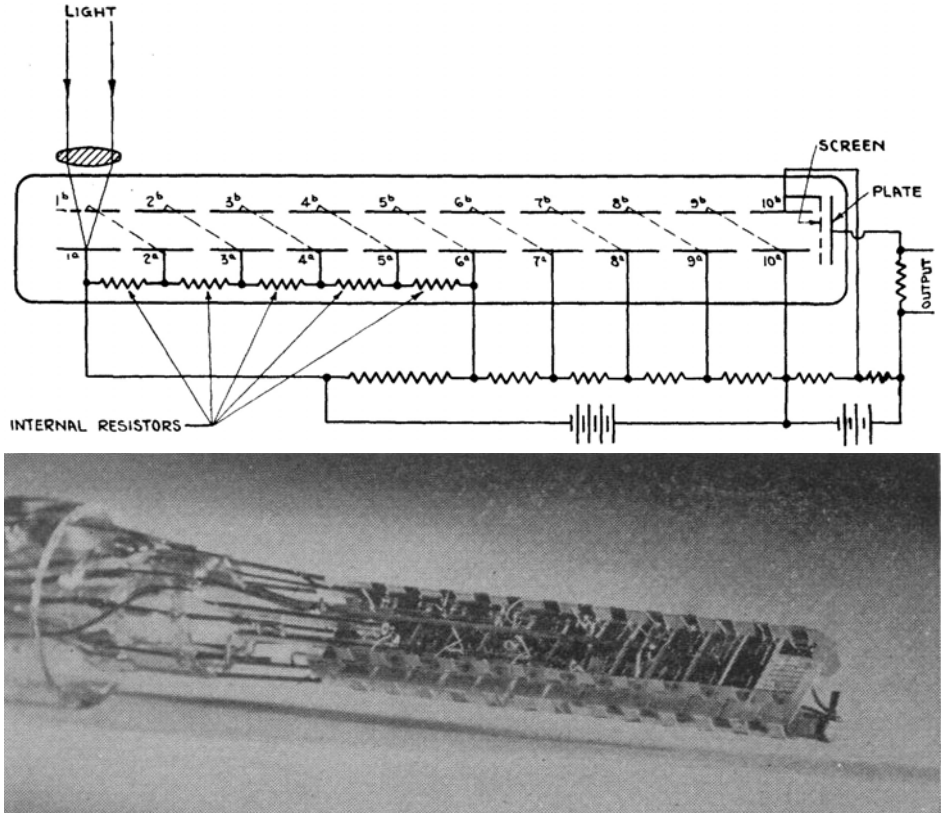

Figure 3.15: The multi-stage photomultiplier tube developed at RCA by Zworykin et al. [84] The linear design looks similar to that of Kubetsky's tube in Figure 3.14.

In the late 1930s, a few more advances made the tube into the basic design of what we know today. John R. Pierce [85] of Bell Laboratories and Jan A. Rajchman [86–88] of RCA both, independently experimented with the design and came up with a linear dynode arrangement that depended only on electrostatics for electron focusing, as shown in Figure 3.16. This allowed the tube bias voltage to be changed without a need to stabilise any magnetic fields. Another advancement came in 1936 with the development of a new photocathode material Sb-Cs (antimony caesium) by P. Görlich [89]. This material had a high

quantum efficiency of 12% at 400 nm [78]. With those inventions, Zworykin and Rajchman developed the RCA Type 931 photomultiplier tube in 1939 [90]. The 931 initially featured the Ag-O-Cs photocathode but was soon changed to the Cs-Sb photocathode. It was a fully electrostatic-focusing tube that featured nine dynodes and became one of the earliest mass-produced PMTs [78, 88].

Figure 3.16: The electrostatically focused photomultiplier tube designed by Rajchman of RCA. The design is more compact than that of the original multi-stage PMT with increased gain [88].

3.5 Development of Scintillators and Scintillation Detectors

The PMT was not immediately recognised as an important device for use in nuclear physics. At first, in 1938, an electron multiplier, which is a photomultiplier without the photocathode or just the dynode array on its own, was used by Zoltán Lajos Bay to measure the current

of an electron beam [91]. Conversely, in 1942, Russell Morgan used an RCA Type 929 phototube, a photomultiplier without the dynode array just containing the photocathode directed at the anode, as an exposure meter for X-ray studies using a scheelite scintillator, shown in Figure 3.17 [92]. It was during the Manhattan Project in 1944 that Samuel Crowe Curran and William Robert "Bill" Baker used an RCA Type 1P21 PMT to record alpha scintillations produced by a ZnS(Ag) screen [93, 94]. As their report was classified and only published in 1948, others have been credited with this accomplishment. Marietta Blau and B. Dreyfus have been credited with the accomplishment of using an electronic alpha scintillator detector's current to measure the intensity of alpha radiation in 1945 [95] or John W. Coltman and Fitz-Hugh B. Marshall who used it to count individual pulses in 1947, as shown in Figure 3.18 [96]. Similarly, in 1947, Rubby Sherr developed the first PMT-based alpha survey meter as most systems to this point were immovable [97].

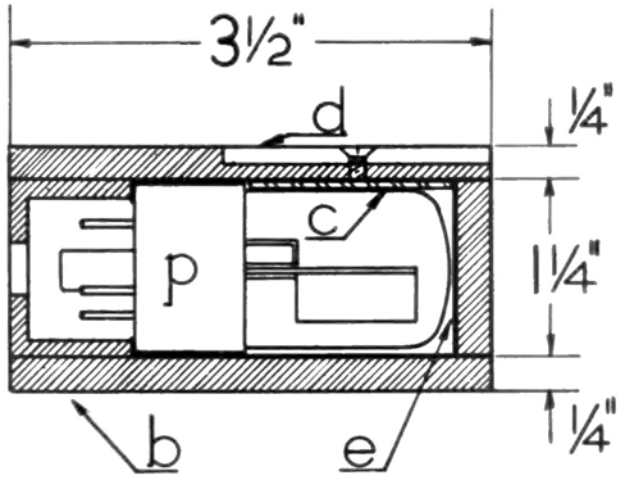

Figure 3.17: A diagram of the X-ray exposure meter designed by Russell Morgan using a shielded phototube and a scheelite scintillator [92]. The phototube (p) was housed in a Bakelite enclosure (b) lined with aluminium foil (e) for electrostatic protection. The scintillator (c) was housed inside the assembly in front of which a decorator screen (d) could be placed to decrease the amount of X-rays reaching the scintillator. This type of detector design was indicative of the times with little stray radiation protection.

Up to 1945, most scintillators were only good at detecting alpha and beta radiations. This was due to the opaque and/or polycrystalline nature of the early materials which

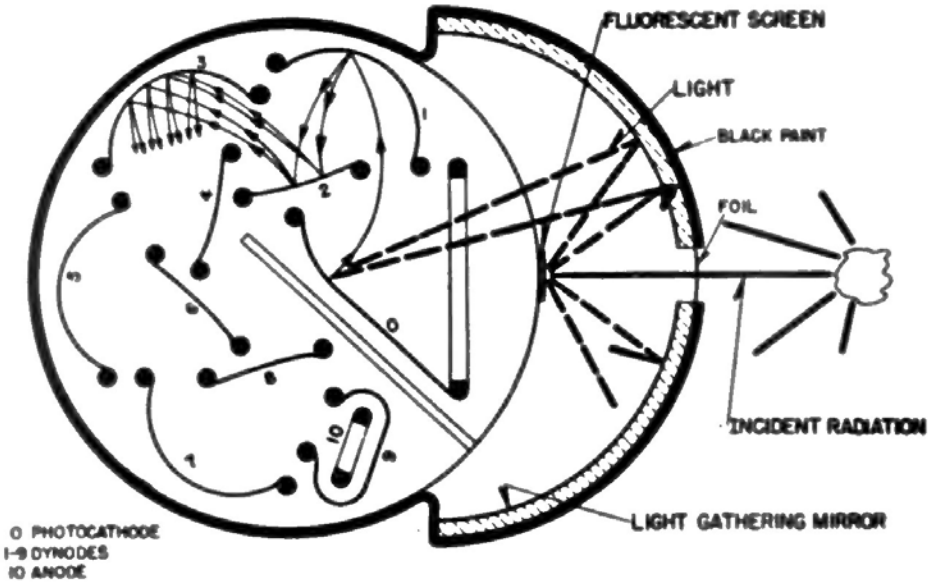

Figure 3.18: A diagram of a scintillation counter designed by Coltman and Marshall showing the path of incident radiation and the production and multiplication of the electrons in an RCA photomultiplier tube [92].

prevented proper light propagation through their volume. This meant that these scintillators could only be used in limited thicknesses which were too thin to stop most gamma rays. The first usable gamma-ray scintillator was naphthalene ($C_{10}H_8$) and was developed by Hartmut Kallmann who made the scintillator block from melted down moth-balls in post-war Germany around 1945. Coupled with an RCA PMT which was cooled to sub-zero Celsius temperatures, he was able to detect gamma rays while minimising noise and dark currents. He was unable to publish his findings first-hand but sent them to his colleagues in the US who confirmed and published them in his name [98, 99].

The most influential of the newly discovered scintillators in the 1940s is thallium-activated sodium iodide (NaI(Tl)). It was first synthesised by Robert Hofstadter in 1948 who observed the intense scintillation light from NaI crystal to which he added "a pinch of thallium" [100, 101]. What made NaI(Tl) so special was its extremely high light output as noted in Table 1.3, and its high gamma absorption or stopping power. The high brightness/light output of the NaI(Tl) resulted in a scintillator with a high signal-to-noise ratio

as any real signal would produce many more scintillation photons than those produced by noise. The high effective Z of the crystal meant that high-energy gamma rays, up to a few MeV, could be captured by it and resulted in an overall high efficiency of gamma detection. Further, the high efficiency made it sensitive to lower sample activities and made it easier to record gammas emitted with a very low branching ratio. Realising this, Hofstadter recorded and published spectra for most radionuclides accessible at the time and for the first time discussed backscatter, escape, and annihilation peaks visible in them while patenting his discovery, as shown in Figure 3.19 [102, 103]. Although NaI(Tl) was known to be hygroscopic and degraded quickly over time in a normal atmosphere, it was not until the 1950s when methods of hermetically sealing the crystal were developed that its popularity started to rise.

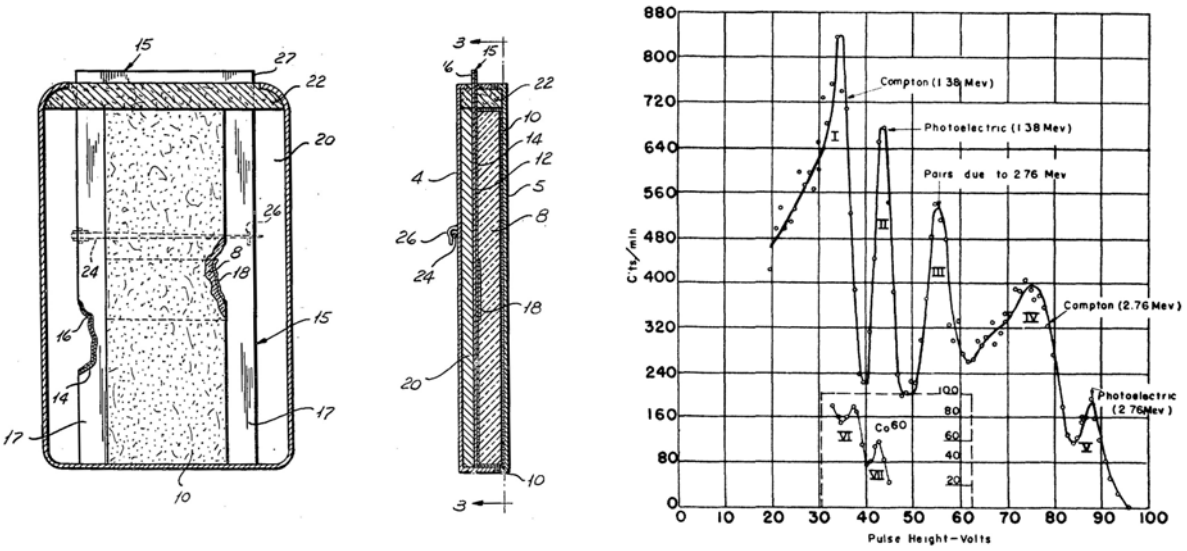

Figure 3.19: (Left) Hofstadter patented NaI(Tl) scintillator along with a few radiation detector designs. Here is shown a personal badge detector utilising a piece of NaI(Tl) scintillator in various coatings to expose a piece of film [103]. (Right) ^{24}Na spectrum obtained by Hofstadter using a detector with a NaI(Tl) scintillator and describing the origin or cause of the various peaks including the Compton peaks and spectrum. In the lower centre is a mini reference spectrum of ^{60}Co obtained using the same method [102].

As the popularity of PMTs and scintillators increased, the 1940s saw a great development in organic and inorganic scintillators. By the end of the 1940s, organic scin-

tillators such as anthracene ($C_{14}H_{10}$), stilbene ($C_{14}H_{12}$), naphthalene ($C_{10}H_8$), phenanthrene ($C_{14}H_{10}$), and fluorene ($(C_6H_4)_2CH_2$) and inorganic scintillators such as scheelite (calcium tungstate, $CaWO_4$), cadmium (II) tungstate ($CdWO_4$), silver-activated zinc sulfide (ZnS(Ag)), thallium-activated sodium iodide (NaI(Tl)), fluorite (fluorspar, CaF_2), and thallium-activated potassium iodide (KI(Tl)) have been explored and documented [104, 105]. The 1950s saw the development of the first liquid organic and plastic scintillators while the 1960s ushered in the era of semiconducting detectors.

3.6 Discovery of the Positron

The positron or an anti-electron is the antimatter counterpart of an electron, having the same metrics as an electron but with an opposite, positive charge. The existence of the positron was not theorised until 1928 when Paul Adrien Maurice Dirac introduced his famous Dirac equation to explain the Zeeman effect [106]. The equation and the article did not directly state the existence of the positron but it could be solved such that the electron energy could have both a negative and positive solution. This was pointed out in a 1929 paper by Hermann Klaus Hugo Weyl who discussed the implications of the equation [107]. Since quantum mechanics did not allow for the negative solution to be simply rejected as was done in classical mechanics, there needed to be an explanation. In 1930, Dirac tried to explain his theory that an electron with a negative energy must behave in an external magnetic field as if it had a positive charge [108]. Some suggested that the proton must be the solution but that was quickly argued against by Julius Robert Oppenheimer as it would mean the proton would have to quickly decay [109]. Weyl then proved in his book that the positive anti-particle must have the same mass as the electron [110]. With their support, in 1931 Dirac predicted the existence of what he called an anti-electron with the mass of an electron but an opposite charge. He also stated that the particle would annihilate if it came in contact

with an electron [111].

With the theory in place, a few scientists realised that they most likely observed the positron before but either dismissed it or accounted it to human error. The first of them was Dmitri Vladimirovich Skobeltsyn who is said to have observed the positron as early as 1923 when working with a modified Wilson cloud chamber with an electromagnet magnetic field generator installed to study the Compton effect [112, 113]. He observed particles that behaved like electrons but curved in the opposite direction and even presented the image shown in Figure 3.20 in a 1928 conference before Dirac published his paper [114]. Skobeltsyn's efforts were not for nothing as his modified magnetic Wilson cloud chamber [113] and discovery of charged cosmic rays [114] led to the positron discovery. It is even likely that he observed positrons in his 1931 images but did not identify them at the time [115]. Similarly, in 1929 Chung-Yao Chao observed positron-electron annihilation while a graduate student at Caltech, but as the effect was unknown at the time, the observations were branded inconclusive [116]. Also, Jean Frédéric Joliot-Curie and Irène Joliot-Curie found evidence in their old photographs they previously dismissed as protons [117].

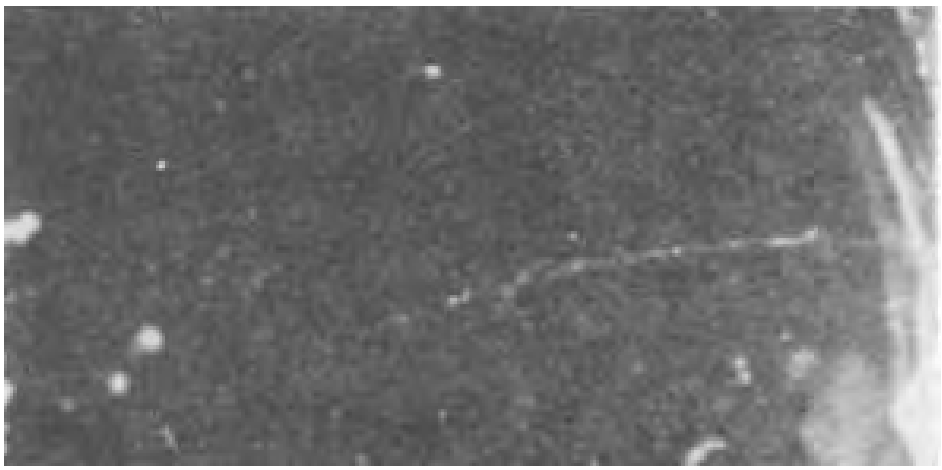

Figure 3.20: An image of the track of an unknown (at the time) particle that Skobeltsyn observed in his Wilson cloud chamber. He argues that it is too heavy to be a photon and can't be an electron or proton [114].

In the end, Carl David Anderson of Caltech was credited with the discovery and

proper identification of positrons in August 1932 naming them positrons after the journal editor suggested the name [118]. The cloud chamber image is shown in Figure 3.21. They were also concurrently identified by Patrick Maynard Stuart Blackett and Giuseppe Paolo Stanislao "Beppo" Occhialini but supposedly they delayed their publication to obtain more evidence such that Anderson ended up being the first one to publish [117, 119].

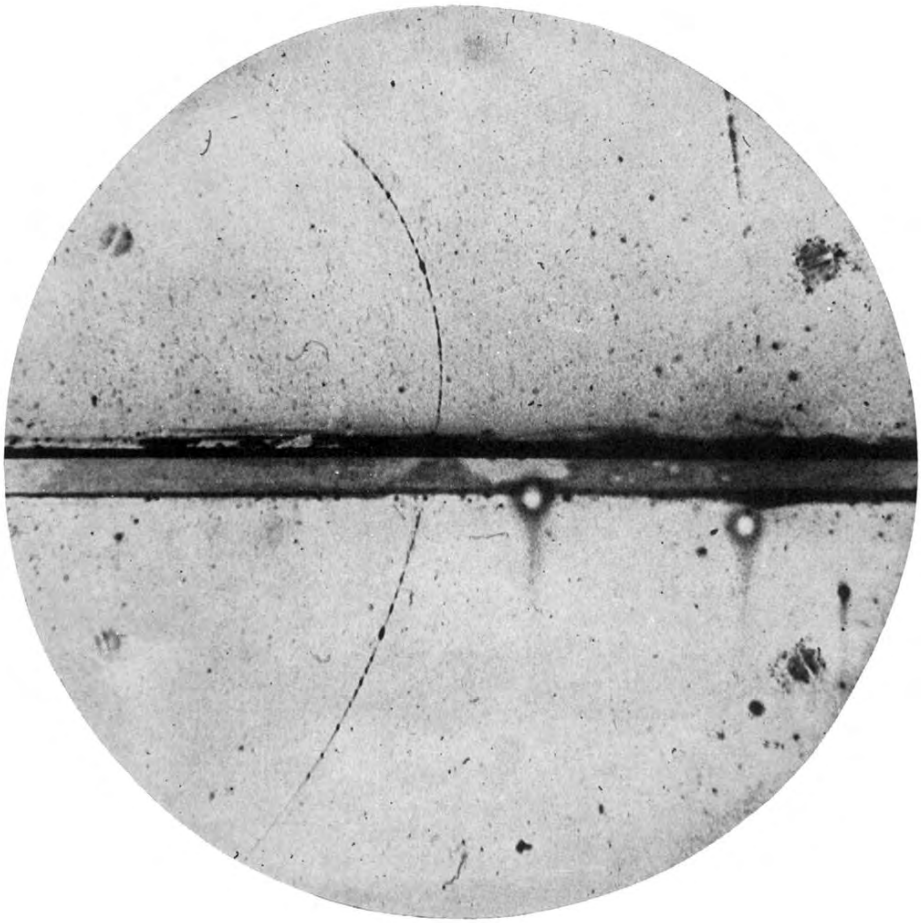

Figure 3.21: Image of the Wilson cloud chamber taken by C. D. Anderson showing a positron penetrating a 6 mm piece of lead and losing some of its energy while generating a very long track. A proton would not be able to produce such a long track in the chamber [118].

3.7 Development of Radionuclides for Medicine

The development of nuclear imaging systems directly stems from the development of nuclear medicine and radiopharmaceuticals. The origin of nuclear medicine and the use of radionuclides as pharmaceuticals date back to 1923 when George Charles de Hevesy first used naturally-occurring, radioactive ^{212}Pb to study the uptake of lead by plants [120–123]. Later in 1924, with his colleagues Jens Anton Christiansen and Svend Lomholt, he used ^{210}Bi to label and trace bismuth-containing medicines in rabbits to study their distribution and circulation within the body. Later they used ^{210}Pb to study lead distribution in various organs and its excretion. These were the first animal-based experiments involving radiochemistry [121-125].

Figure 3.22: Picture of George Charles de Hevesy, nicknamed "The Father of Nuclear Medicine," who was the first to use radioactive isotopes for tracking and studying various biological processes in plants and animals [121].

Perhaps the most important milestone in nuclear medicine occurred in February 1934

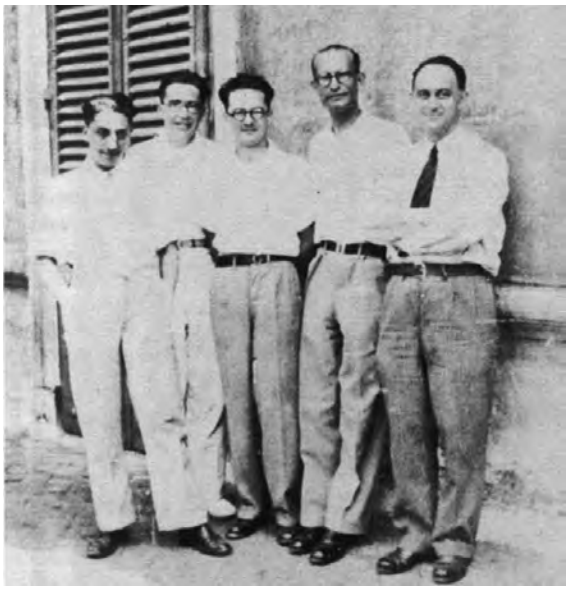

Figure 3.23: (Left) Frédéric Joliot-Curie and Irène Joliot-Curie pictured working at their laboratory at the Institut du Radium in Paris, France [126]. (Right) Fermi's group at the University of Rome, Italy, 1934. From left to right: Oscar D'Agostino, Emilio Segrè, Edoardo Amaldi, Franco Rasetti, and Enrico Fermi [126].

when Frédéric Joliot-Curie and Irène Joliot-Curie, pictured in Figure 3.23 left, discovered the artificial production of radioisotopes. They produced ^{30}P, ^{13}N, and ^{27}Si after they irradiated aluminium, boron, and magnesium with polonium (technically with its emitted alpha particles) and noticed that the emission of radioactivity did not end after the polonium was removed [127–129]. With the news of alpha-induced reactions, other researchers began applying the technique to other elements and with different particles. The biggest development occurred only a few months later when Enrico Fermi and his students, pictured in Figure 3.23 right, used a radon-boron neutron source to irradiate most natural elements known at the time. Their quick and systematic approach yielded new isotopes like ^{16}N, ^{24}Na, ^{28}Al, ^{31}Si, ^{32}P, ^{52}V, ^{56}Mn, ^{76}As, ^{80}Br, ^{82}Br, and ^{128}I to name a few and proved neutron induced reactions possible [126, 130–132]. Realising the potential of the new radioisotopes, in 1935 de Hevesy in collaboration with Otto Chiewitz used radioactive ^{32}P to study its metabolism in

rats. This was the first time a man-made radionuclide was used for *in vivo* studies [121–123, 133].

3.7.1 Medical Isotopes at Lawrence Berkeley National Laboratory

The rest of the early development of nuclear medicine can be said to originate from the well-known Lawrence Berkeley National Laboratory (LBNL), or the Radiation Laboratory as it was known at the time. This is where Ernest Orlando Lawrence, pictured in Figure 3.24, with the help of his students, especially Milton Stanley Livingston, developed the cyclotron, pictured in Figure 3.24, between 1929 and 1930 and built various devices throughout the 1930s [134, 135, 137, 138]. With a well-established laboratory and great radionuclide production potential, in 1936 John Hundale Lawrence (Ernest's brother), pictured in Figure 3.25, decided to leave his position at the Yale Medical School and work with his brother to study the potential of isotopes and radioactive beams in medicine. He started a program that led to the establishment of the Donner Laboratory and the birth of modern nuclear

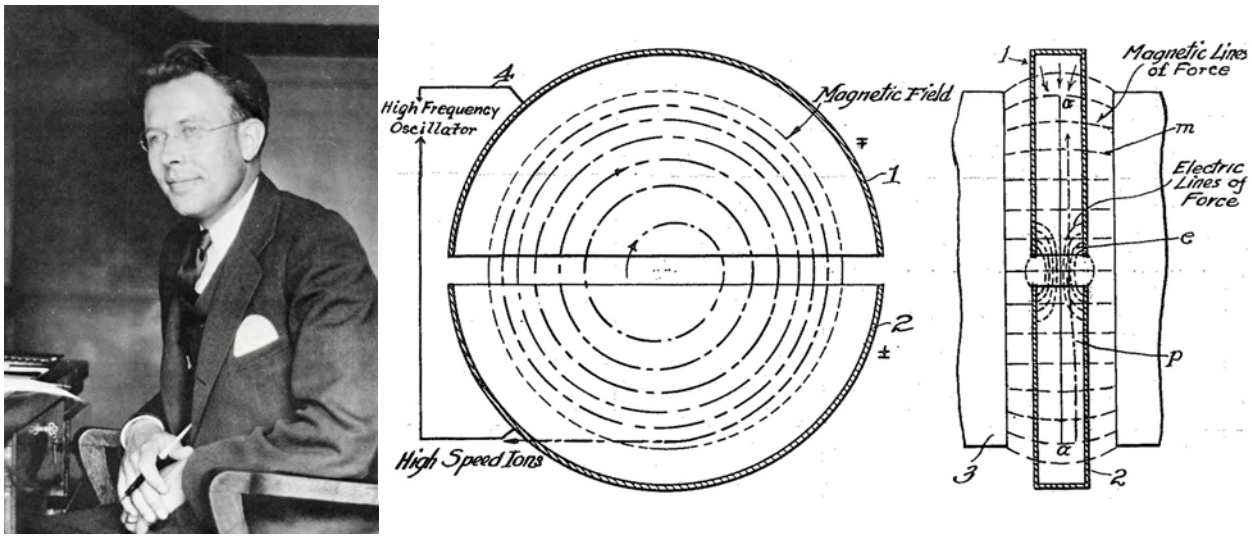

Figure 3.24: Ernest Orlando Lawrence who in 1930 developed the cyclotron next to a diagram of the cyclotron from his original patent showing the path of the accelerated ions and the magnetic field lines [134, 135].

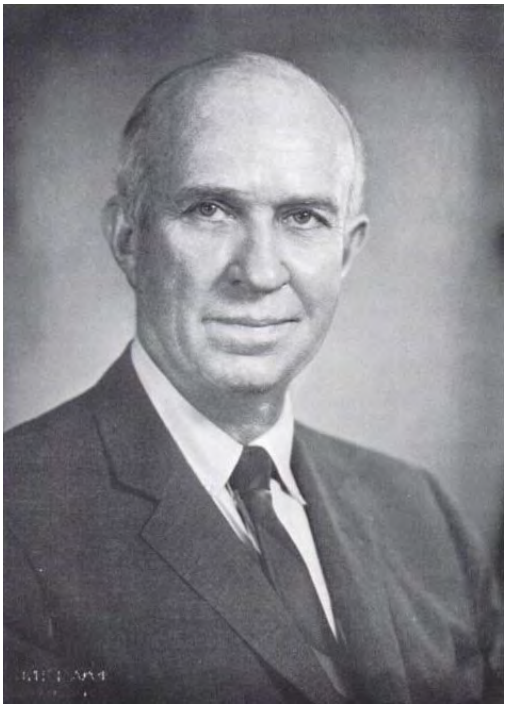

Figure 3.25: John Hundale Lawrence the pioneer of nuclear medicine who established the Donner Laboratory and was the first to use radioisotopes for diagnosis and treatment of human diseases [136].

medicine [134, 136, 139].

With the newly discovered ^{32}P, after meticulous studies of its biological distribution, John Lawrence used it to treat leukaemia and polycythemia vera, the former being the first time a radioisotope was used to treat a human disease. Later in 1937, he began using ^{59}Fe, first synthesised at LBNL by Glenn Theodore Seaborg and Emilio Gino Segrè, pictured in Figures 3.26 and 3.23 respectively, to study bone marrow [140, 141]. At the same time, Joseph Gilbert Hamilton working at the laboratory began using ^{24}Na to study sodium absorption in humans [142, 143]. In 1938, Hamilton realised that to minimise any side effects, he needed isotopes with relatively short half-lives of around a week. Setting his sights on the thyroid, he asked Seaborg to find him a shored-lived isotope of iodine. Seaborg working with John Jacob Livingood, pictured in Figure 3.26, and using the 37-inch cyclotron, bombarded a tellurium target with deuterons and neutrons and later extracted the still-commonly-used

^{131}I with a half-life of 8 days [144, 145], ideal for thyroid studies [134, 136, 139].

Figure 3.26: John Jacob Livingood (left) and Glenn Theodore Seaborg (right) in a hurry to the post office to send their latest manuscript to the *Physical Review* [134].

3.7.2 Technetium-99m

In 1938, Seaborg and Segrè isolated the metastable ^{99m}Tc by irradiating molybdenum with deuterons in the 37-inch cyclotron. Its isolation was very problematic due to the unknown at the time isomerism technetium experienced [134, 146, 147]. ^{99m}Tc is the most important nuclear medicine isotope still used in around 80% of nuclear diagnostic procedures around the world [148]. However, the isotope did not see much medical use until the 1960s when Powell Richards of the Brookhaven National Laboratory (BNL) suggested its use in medicine. That was after in 1958 it was discovered by Walter Tucker and Margaret Greene that it could be easily produced using a research nuclear reactor to produce ^{99}Mo which then could be used

to make a ^{99m}Tc generator [149–152].

3.7.3 Fluorine-18

In 1937, Arthur Hawley Snell working at LBNL was the first to synthesise ^{18}F, perhaps the most important PET imaging isotope ever [153]. Its popularity only began in the 1970s when in 1962 Josef Pacák, Zdeněk Točík and Miloslav Černý first synthesised fluorodeoxyglucose (FDG) which is a marker for tissue uptake of glucose and therefore can be used to study tissue metabolism and pinpoint certain types of cancers [154]. In 1978, Tatsuo Ido and Al Wolf at BNL succeeded in labelling FDG with ^{18}F ushering in the rise of the popularity of PET imaging. Images taken with ^{18}F-FDG can provide a diagnosis of a wide range of medical conditions [155]. ^{18}F is also used alone and in various other chemical compounds used in medical imaging [148].

3.7.4 Carbon-11

Another nuclear medicine and PET imaging isotope developed at LBNL is ^{11}C whose short 20-minute half-life made it ideal for quick metabolism studies, especially when used to label carbon dioxide gas. Its first biological use occurred in 1938 by Samuel Ruben and Martin David Kamen who synthesised it to study photosynthesis in plants [156]. It was later used in 1945 to study carbon dioxide in the human body [136, 157]. As ^{14}C became more readily available with a longer half-life, ^{11}C stopped being used until the 1960-1970s when it became useful for PET studies and more readily available due to the availability of small medical cyclotrons worldwide [158].

3.7.5 Carbon-14

^{14}C was also first synthesised at LBNL in 1940. It was achieved by Kamen and Ruben who struggled to synthesise it for over a year until they decided to leave a block of graphite to be irradiated by deuterons and stray radiation for a month at the 37-inch cyclotron. The block was constantly irradiated by deuterons during the day and only taken out to give way to other samples that had to be processed that day. Eventually, the effort yielded results and traces of ^{14}C were discovered and initial measurements of its long half-life were taken [159–161]. The ^{14}C produced was later used by them to study photosynthesis even further. Eventually, ^{14}C's use as a tracer became a reality when it was discovered it could be produced at a large scale in a nuclear research reactor [162].

3.7.6 Gallium-67 and -68

One of the later medical isotopes used predominately in PET is ^{68}Ga. In the 1940s, gallium was one of those elements which did not have many industrial applications and therefore its biological characteristics were unknown. With the proposition to use gallium as a coolant in naval reactors, studies of its toxicology finally began. In 1949 it was shown that natural gallium can concentrate in areas associated with bone formation but concluded that metallic gallium is non-toxic while some of its compounds are [163–165]. Later studies with the reactor-produced radioactive ^{72}Ga had shown its possible application in radiation therapy and diagnosis [166–168]. However, by 1951 its clinical benefits were outweighed by its overall poor performance and problems with detection (which was attributed to poor detector technology available at the time and the low specific activity of the reactor produced isotope) [169–171]. Further studies were conducted with the much longer-lived accelerator-produced ^{67}Ga. ^{67}Ga's high cost of production meant that its initial clinical use was low. Its major advantage over ^{72}Ga was its high specific activity due to the isotopic purity of the target

material [172].

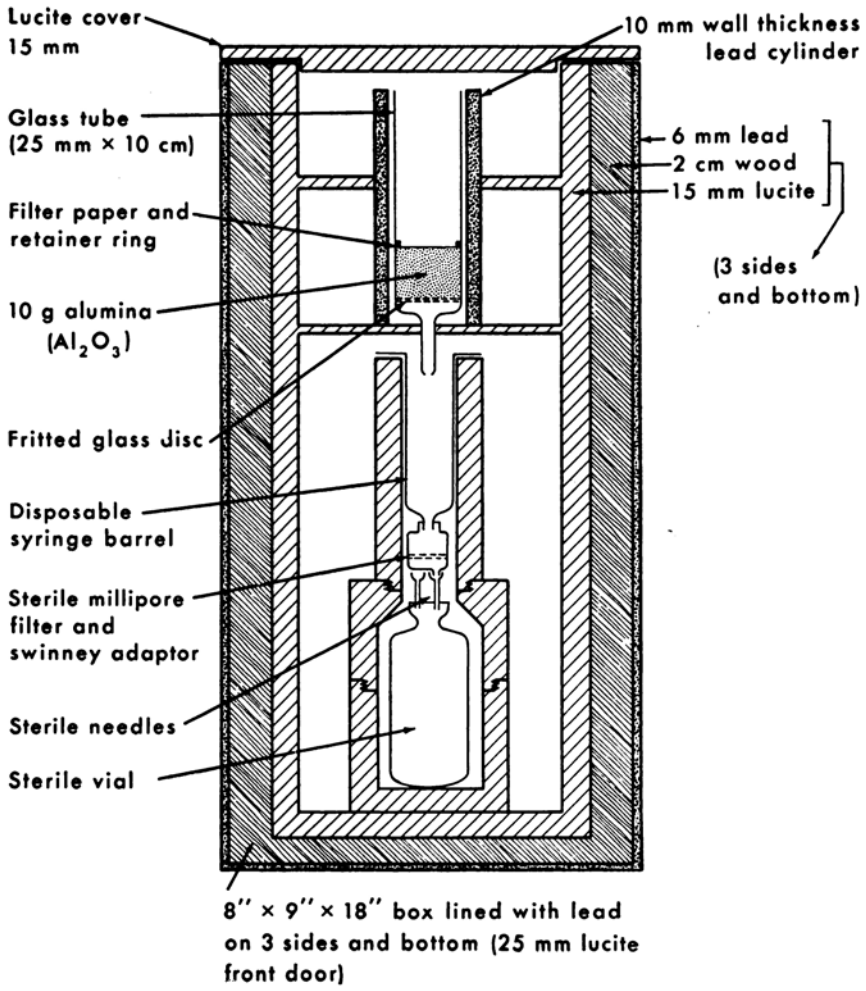

Figure 3.27: An early ^{68}Ga-EDTA generator setup containing a replaceable glass cartridge with ^{68}Ge in EDTA solution trapped in the alumina matrix. To milk the column/cow, 10 mL of EDTA solution is added to the top of the column which binds with the generated ^{68}Ga to form ^{68}Ga-EDTA which drips out the bottom of the column and is collected. The solution is then neutralised and filtered before it can be used for medical purposes [173, 174].

Eventually, in the 1960s, the development of the positron-emitting ^{68}Ga-EDTA (ethylene-diamine tetra-acetic acid) generator (once called a positron cow, see Figure 3.27), from the accelerator-produced ^{68}Ge, made it an ideal isotope for medical imaging. Furthermore, ^{68}Ga could be freed from the EDTA complex using simple chemistry allowing it to be processed into other chemical forms. The on-demand availability of this 68-minute half-life ^{68}Ga-EDTA from a generator that can be used multiple times a day over a long period has not only made

nuclear imaging more accessible but also provided easy and very low-cost access to radioisotopes used during the early development of new imaging systems [173–176]. Today, ^{68}Ga is predominantly used for short PET scans while ^{67}Ga is still used for long, multi-day, whole-body SPECT imaging [177, 178].

3.7.7 Other PET Isotopes

Besides the common PET isotopes listed above, other important positron-emitting medical isotopes later proven to be useful in PET imaging include ^{13}N and ^{15}O. These are used to label natural compounds such as ammonia and water, and have half-lives of 10 and 2 minutes, respectively, which requires them to be produced on-site. While some of the first PET isotopes that are not commonly used today, include ^{74}As and ^{64}Cu. However, ^{64}Cu is still a commonly used therapy isotope [148].

Since the 1940s, the use of radioisotopes for PET has evolved past their use in elemental or basic molecular forms into large, bio-active molecules. Therefore, an ideal PET isotope, first of all, has to emit positrons and not be very toxic to humans. Its properties should make it easy to handle, without much special equipment. Its half-life needs to be long enough to be properly processed, distributed, and administered to the patient, but short enough such that the patient can be safely released to the public after the procedure without the isotope accumulating for a long time in their body. Finally, a desirable PET isotope should be easily produced using a cyclotron or another accelerator in high specific activities. This means that its parent material should have high isotopic purity which will further decrease processing time required to separate the desired isotope from the parent material and other produced isotopes. Its ability to be produced by cyclotrons would make it accessible in places were nuclear reactors are not present. Further, due to the growing popularity of accelerators and their higher availability means that the isotopes can be readily

produced.

Any of the of the PET isotopes can be used for industrial PEPT studies. Further, isotopes of elements or molecules that are toxic to humans can also be used. Besides the basic necessity that the isotope is a positron emitter and safe to handle, the physical requirements of the delivery of the isotope via a tracer particle are more important. PEPT tracers can be whole particles directly irradiated in the beam line and used as-is, can be whole particles with a modified surface treatment or coating, or coated resin beads which are used to absorb ions of radioactive isotopes present in a solution, to name a few. Therefore, in PEPT, more attention is spent on matching the physical characteristics of the tracer particle to the medium used in the experiment than on the radioisotope selection and production.

Chapter Four

Rise of Nuclear Imaging

Until the end of the 1940s, the field of nuclear medicine had little to do with nuclear imaging as no detector technology existed that could take an image of the distribution of a radionuclide in a body. Measurements of only specific areas, averaged as a whole could be performed

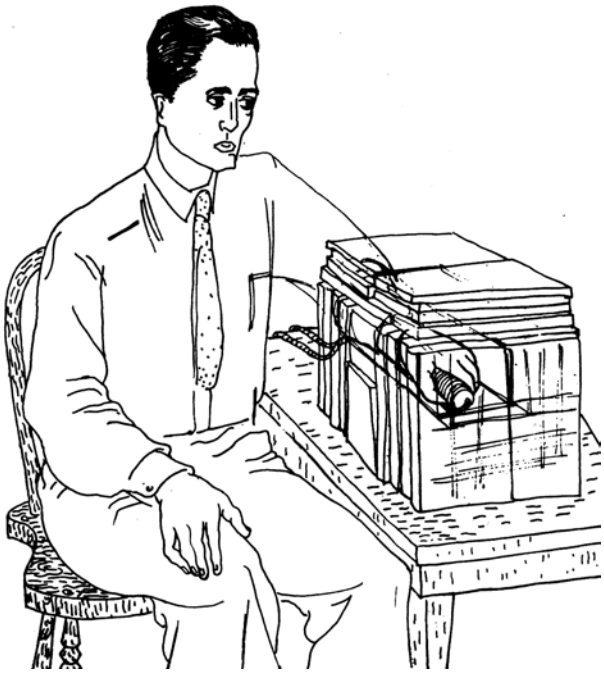

Figure 4.1: An early radionuclide distribution study conducted by Joseph Hamilton using a GM counter housed in a shielded box used to study ^{24}Na distribution in a human body [142].

which started to become a major drawback in the advancements of radioisotopes for diagnosis and cancer localisation. Most studies up to this point utilised GM counters and some early scintillators to measure the amount of radiation and its change over time over a specified area. Pin-point probes could measure radiation in specific areas while specially built enclosures could measure the radiation of a whole limb or a wider area as shown in Figure 4.1. This drawback led to the development of multiple different nuclear imaging techniques all of which can trace their beginning to the end of the 1940s.

4.1 The Rectilinear Scanner

The first of the nuclear imaging systems was the rectilinear scanner. In 1949, Benedict Cassen, Lawrence Curtis, and Clifton W. Reed working at the University of California Los Angeles (UCLA) built and described the first scintillator-based system for the localisation and measurement of radioactivity in a subject. The system featured two different probes, both of which used a photomultiplier directly coupled to a calcium tungstate scintillator. The regular probe shown in Figure 4.2 featured a side-on photomultiplier which was enclosed in

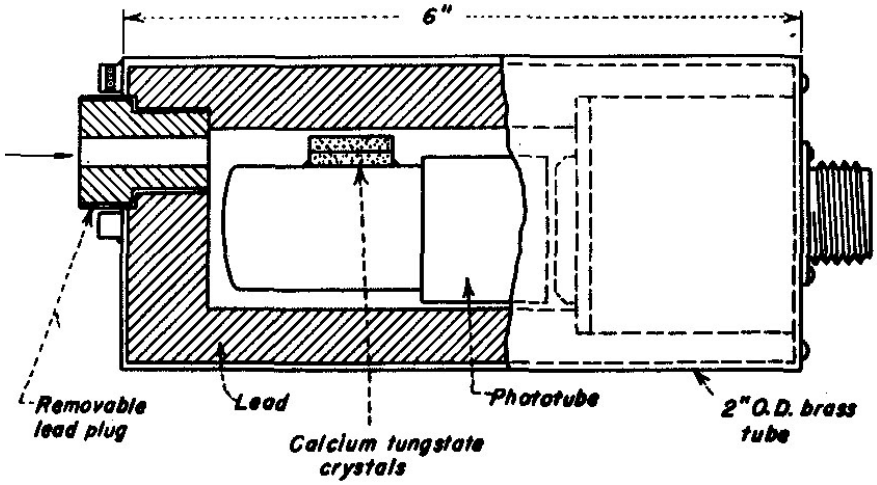

Figure 4.2: A cut-away view of the regular collimated probe used on the Rectilinear Scanner [179].

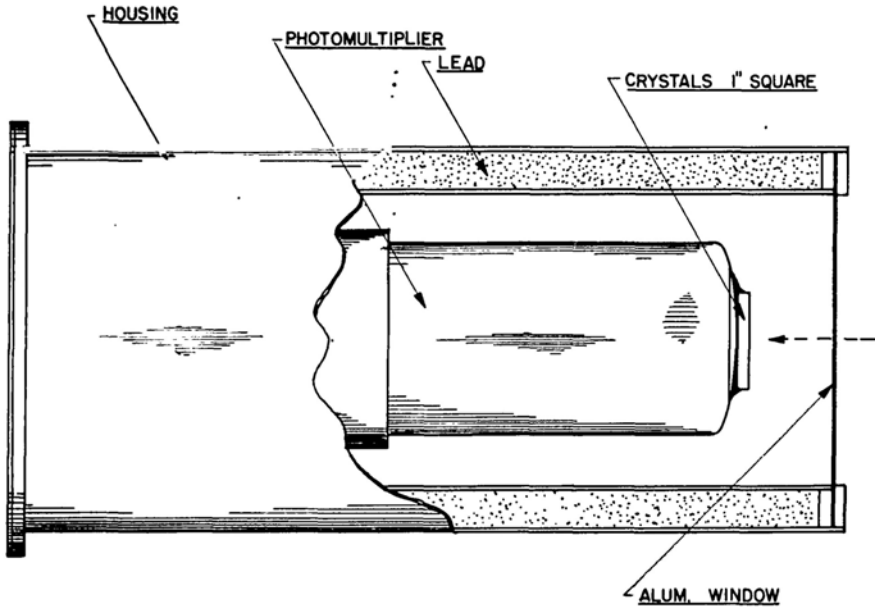

Figure 4.3: A cut-away view of the wide-angle probe used on the early version of the Rectilinear Scanner [180].

Figure 4.4: An early version of the Rectilinear Scanner used to take a scan of the distribution of ^{131}I in the thyroid. The scanner is manually positioned by the doctor with the aid of a chart [179].

a lead container with an opening at its bottom where a lead collimator could be inserted for more precise measurements. The wide-view probe shown in Figure 4.3 was developed using a head-on PMT with a thin aluminium foil window into the assembly which did not

have a collimator. The probe was mounted to a manually movable gantry that held the detector steady and vertically during the measurement. The system was quickly used to perform studies of the morphology of the thyroid using ^{131}I. To help position the counter, a pre-printed chart with 400 counting points was positioned on the patient, the scanner was manually moved from point to point, as shown in Figure 4.4, and the results were manually written down. As each of these scans took up to two hours to perform, the first version of the rectilinear scanner proved to be very labour-intensive for the operator [179, 180].

Soon after that, Cassen, Curtis, and Reed further improved their scanner into a truly automatic system shown in Figure 4.5. Two motors were used to move the probe in the horizontal plane and a readout system was controlled by a scalar circuit. The scanner controlled a printer which moved over a piece of paper in a proper spatial relation to the probe and the signal was used to control an electromagnet with an ink pen. As the scanner

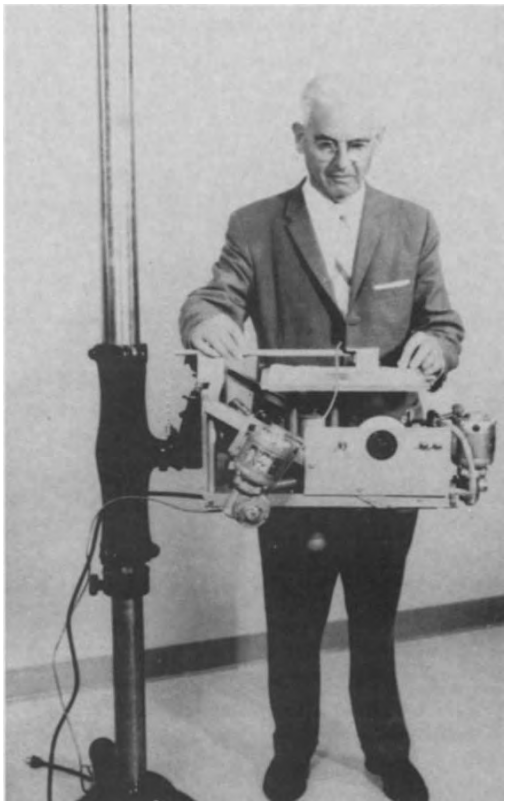

Figure 4.5: Ben Cassen and his automatic Rectilinear Scanner [179].

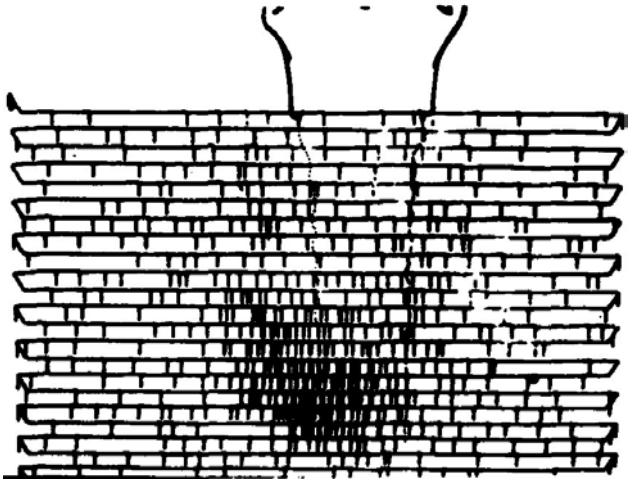

Figure 4.6: An example scan of a thyroid using ^{131}I taken using an automatic rectilinear scanner [179].

moved, the ink pen marked the paper with the path taken. Whenever sufficient events were detected, the electromagnet was tripped and a small mark/bump was drawn in the location the pen was currently at, as shown in Figure 4.6 [181, 182]. Eventually, in 1950, Curtis and Reed left UCLA to start the RC Scientific Instrument Company (Playa Del Ray, California, USA) which specialised in scintillation detectors and rectilinear scanners like the one shown in Figure 4.7. The relay printer mechanism was replaced by an electrosensitive printer based on the Teledeltos conductive paper developed for early photo transmission. The paper featured a carbon-coated, electrosensitive front side. A metal stylus was used to trace the movement of the scanner and the circuit formed by the probe and a conductive aluminium backing plate part of the printer was used to pass a current proportional to the count rate of the probe. This current caused the electrosensitive coating to develop and mark the paper where the stylus was located [183]. This not only increased the speed of the scanner, which decreased the overall procedure time and meant that more patients could be processed in a day, but produced higher-quality images which could more accurately pinpoint any abnormalities in the thyroid. While a remarkable advancement at the time, the rectilinear scanner was predominately used for thyroid studies as other organs like the liver failed to create quality images [179, 184–187].

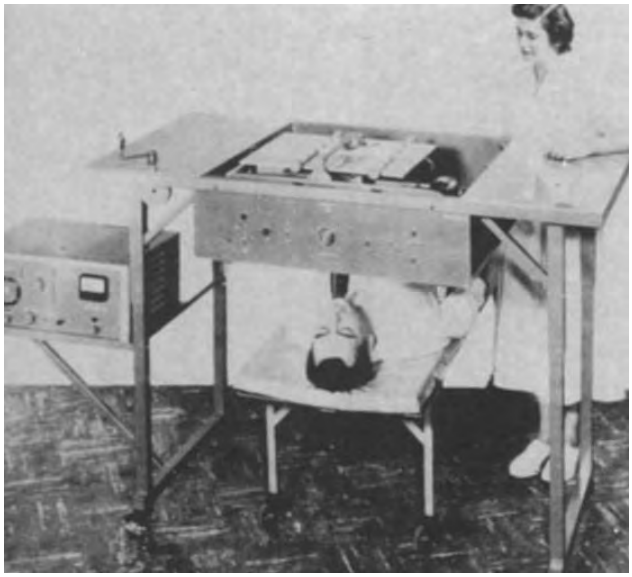

Figure 4.7: A commercial version of the automatic Rectilinear Scanner marketed by the RC Scientific Instrument Company [179].

The final modification to the scanner came in 1956 when David Edmund Kuhl changed the printer mechanism for a glow lamp. The glow lamp's intensity was dependent on the count rate of the scanner as it moved over a piece of X-ray film in a light-proof box. This

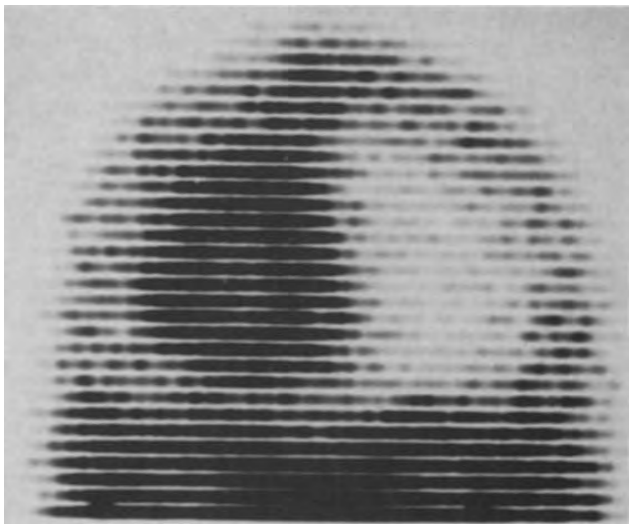

Figure 4.8: A photoscan conducted using the Picker Photoscanner of a brain with a grade III astrocytoma [179]. The scanner used a superior shading technique to present its information when compared to the line marking technique of the earlier scanner version shown in Figure 4.6.

not only increased the resolution and sensitivity of the system but the lamp created shades of grey on the film rather than marks of the same colour, as shown in Figure 4.8. Once the film was developed, it could be analysed similarly to a regular X-ray image with the varying intensity of grey convening more information. Also, the calcium tungstate scintillator was replaced with a hermetically sealed NaI(Tl) scintillator as the sealing technology was recently developed. Kuhl's modified scanner design was then sold as the Picker Photoscanner by the Picker International Corporation (Highland Heights, Ohio, USA) [188]. By 1973, the system had reached the peak of its popularity as new imaging technologies were being developed and released, with some of the models being used into the 1990s [179, 189].

4.2 Nuclear Imaging Systems Developed by Hal Anger

Figure 4.9: Hal Anger next to his whole-body scanner at the Donner Laboratory circa 1965 [190].

Hal Oscar Anger pictured in Figure 4.9 started working at the Donner Laboratory in 1948. He graduated from the University of California Berkeley in 1943 with a bachelor's degree in electrical engineering after working on radar technology at Harvard's Radio Research

Laboratory during World War II. At the beginning of his work at the Donner Laboratory, he was assigned to engineer and modify the 184-inch cyclotron at LBNL from the wartime production of uranium to a medical facility where the deuteron beam could be used for cancer treatment. Later his true calling as the designer of scintillation cameras was discovered [191].

4.2.1 The Pinhole Camera

In 1951, the news of Cassen's rectilinear scanner began to spread. Studying the design, Anger quickly recognised the serious limitations and the inefficiency of using so much radiation to just record the emissions at a single point at a time. So, he started to develop a camera that could capture the emissions from a larger area at a time [192]. He continued the development of the idea of a pinhole camera that Donald Eugene Copeland and Emanuel W. Benjamin built in 1949. The pinhole principle was developed in general photography where an image can be focused and projected onto an imaging plane without the use of any optics. They used a conical lead collimator with a pinhole aperture that they placed directly between the radiation sample and a piece of an X-ray film. This apparatus had very low sensitivity with the gamma rays being used to directly expose the film, showing the distribution of radiation in the source [193].

Anger's pinhole camera pictured in Figure 4.10 used a thick-walled lead pinhole collimator that ensured only gamma rays that passed through the pinhole made it to the imaging plane. However, to greatly increase the efficiency of the device and produce usable images, Anger's version exchanged the X-ray film to a regular photographic plate which was behind a 2-inch by 4-inch by 5/16-inch thick piece of NaI(Tl) scintillator. The gamma rays produced scintillations in the crystal which then would expose the photographic plate appropriately. The initial testing of the device proved successful with it being able to locate an ^{131}I contain-

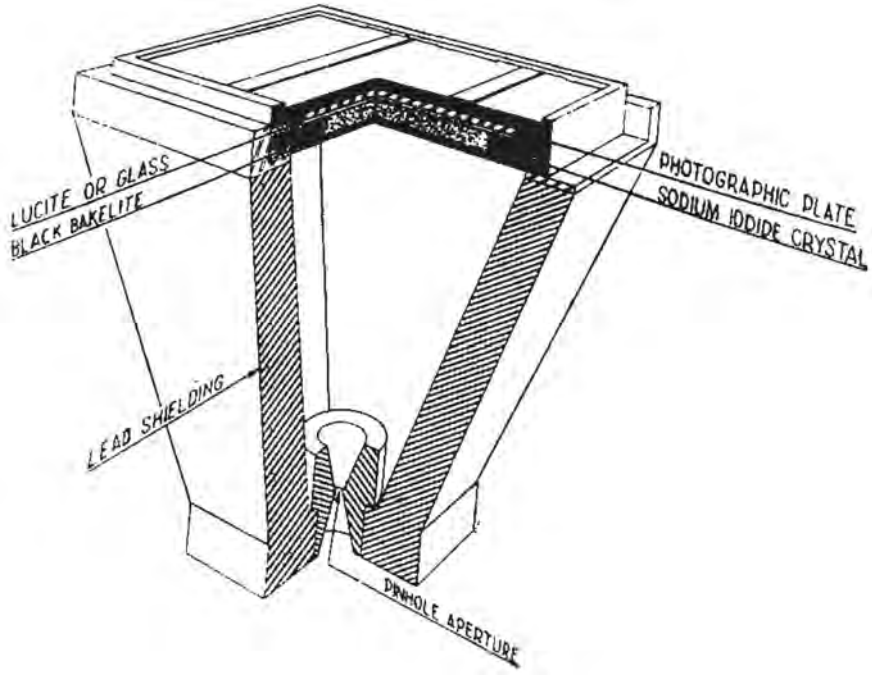

Figure 4.10: Anger's first gamma camera, the pinhole camera. It utilised the pinhole principle developed in general photography where an image can be focused and projected onto an imaging plane without the use of any optics [194].

ing thyroid carcinoma. The major drawback of the device was that it was indiscriminate in the energy and type of radiation that produced scintillations in the crystal. Also, Compton scattering within the body, the camera, and the crystal itself and light scattering within the singular piece of the crystal itself caused the distribution to be blurred and led to the loss of resolution [194].

4.2.2 The Whole-Body Scanner

Concurrently, as he developed the pinhole camera, Anger developed the first whole-body hybrid scanner system, the Mark I Whole-Body Scanner in 1953 pictured in Figure 4.11. The system consisted of a head scanning a 7-inch-wide area of the patient from side to side, an image-generating printer, and a patient indexing system which moved the camera assembly in 7-inch steps along the length of the patient. The head contained 10 3/8-inch

square and 11/16-inch-thick NaI(Tl) crystals arranged in a 7-inch-wide line with each one coupled to an RCA 1P21 PMT, an amplification circuit, and terminating with a glow lamp. Each of the 10 glow lamps were arranged in a straight line in a light-proof box and they were moved proportionally to the movement of the scanning head in front of a long piece of photography film [192, 195, 196].

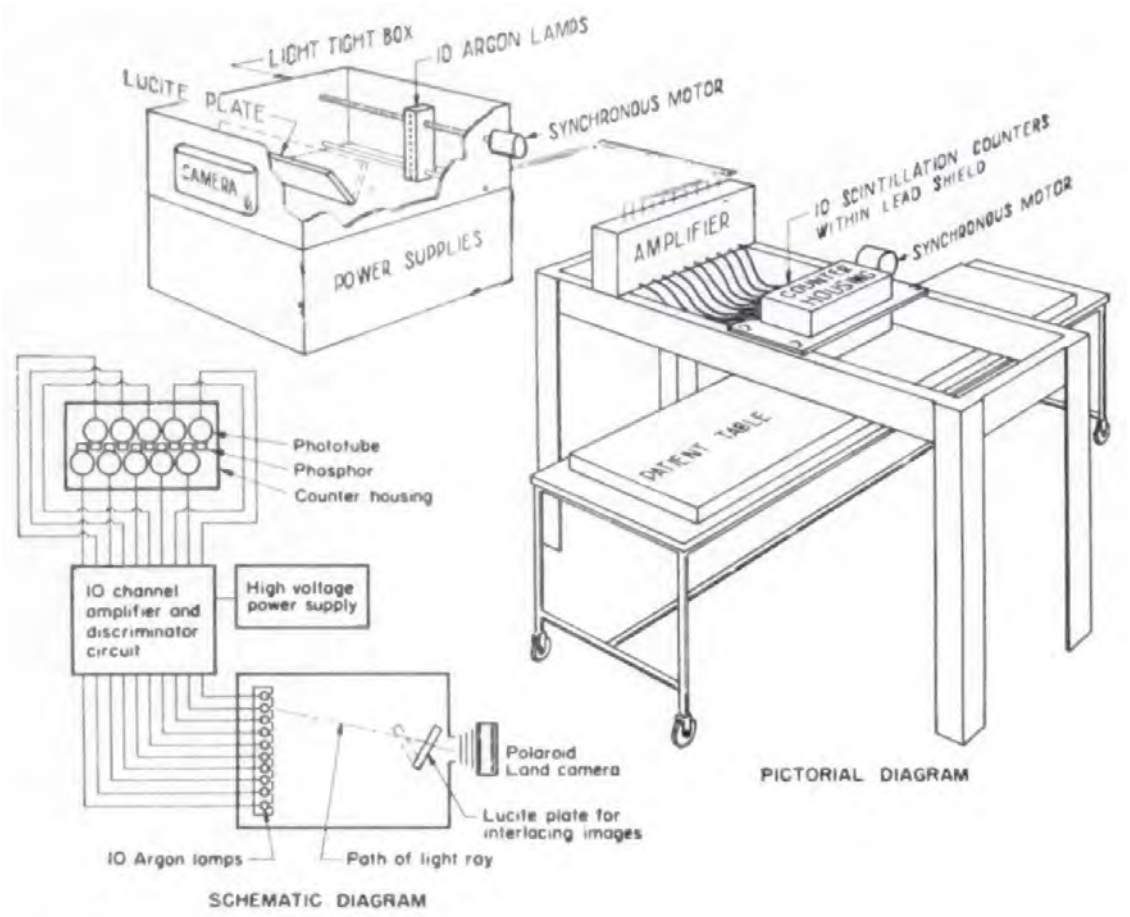

Figure 4.11: The Whole-Body Scanner Mark I, designed by Anger scanned a whole human body in 7-inch strips at a time [195].

The glow lamps exposed the film with their intensity varying with the count rate observed by each of the scintillators. As the image produced featured pronounced gaps between each of the lines, the scanner featured an early image interlacing system where the patient could be moved by 1/2, 1/3, or 1/4 the pitch of the scintillator crystals to produce a 20-, 30-, or 40-line scan, respectively, instead of the normal 10-line scan for each 7-inch

region of the body. Instead of shifting the lamps to expose the additional lines, a linear Lucite lens was used which bent the light from each lamp so it would expose the film in the appropriate place between the normal lines. Once one of the 7-inch-wide regions was scanned, the film was switched out and the patient shifted by 7 inches to acquire the next region. A whole-body scan usually required 10 to 11 of these 7-inch scans and the images were later manually aligned and stitched together as shown in Figure 4.12. This created a postprocessing problem. The images lacked any alignment marks which caused misalignment problems and clear discontinuities at the boundaries of the slices. The long imaging time also meant that by the time the scanner imaged the other end of the body, the isotope was given enough time to noticeably decay and change the exposure of the image. The system was successful at localising tumours and many unsuspected metastases using ^{131}I [195, 196].

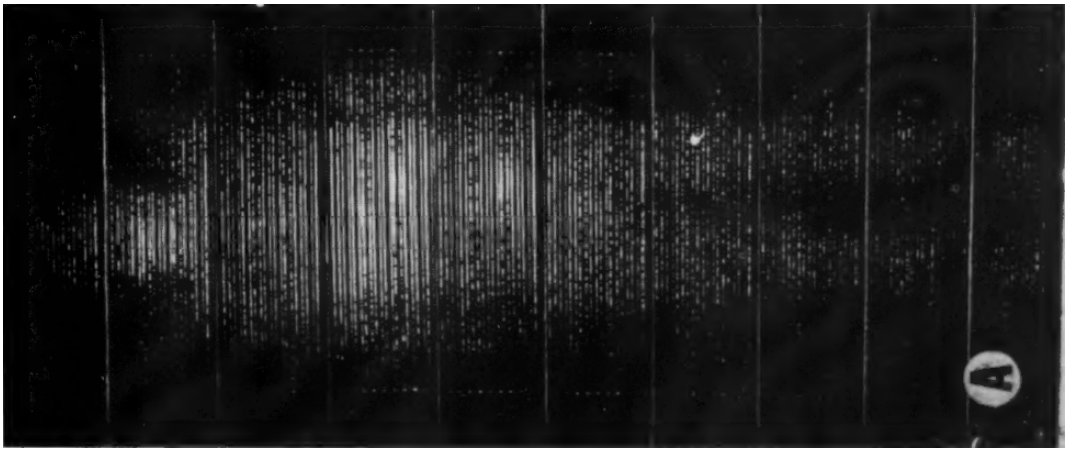

Figure 4.12: The whole-body scan taken using the Whole-Body Scanner Mark I. The individual 7-inch strips of film can be easily identified [195].

Anger continued working on this scanner design and by 1966 he designed the Mark II which featured 64 detectors in four rows of 16 such that the detector head was 30-inches in length or the width of a patient. The staggered row design removed the need for interpolation and the addition of energy discrimination allowed the scanner to focus on only select gamma energies, drastically reducing the noise in the image. Energy discrimination was an especially important development as it allowed for rejection of any scattered and background photons;

a major source of image noise and blurring. It ensured that only gamma rays within a set energy window would be used for the imaging and therefore ensured that they originated from the area under the scanner head. The primitive glow bulb system was also exchanged for a cathode-ray display with a scrolling roll of film in front of it. As gamma rays were detected, the cathode-ray tube fired a beam in the spot corresponding to the detector location exposing the film. These modifications allowed the scanner to do a single pass over the whole body in under six minutes, solving the major problems presented by the Mark I [197]. Variations of this design were sold as Picker Dynapix by Picker Int Corp and provided some competition to his Anger Camera until the end of the 1960s [191].

4.2.3 The Pinhole Camera with Multi-Crystal Image Amplification

Seeing the drawbacks of using a mobile system which cannot capture a whole organ at the same moment, Anger further developed the pinhole camera design in 1954 by using many small NaI(Tl) scintillator crystals to form a screen and an image-intensifying tube to amplify the image as illustrated in Figure 4.13. To solve the loss of resolution due to the

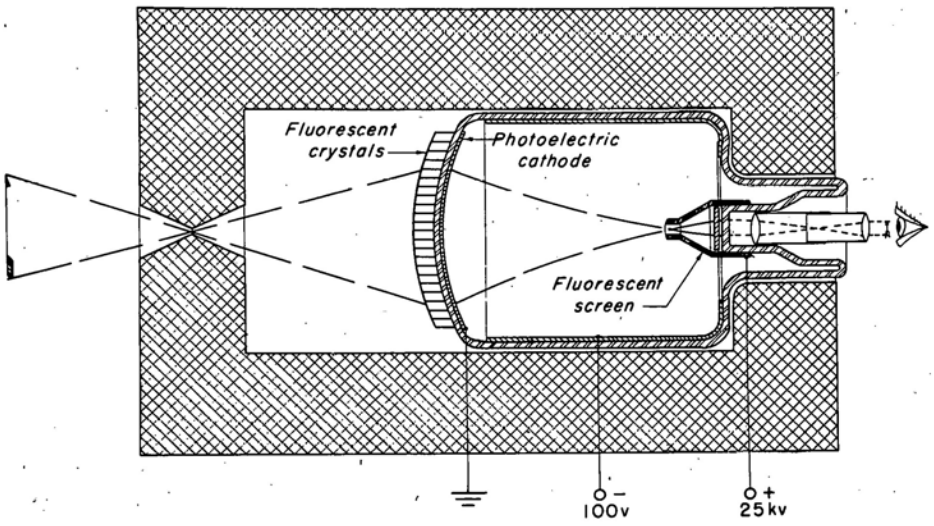

Figure 4.13: The pinhole camera with an image amplifier tube designed by Philips and 241 individual NaI(Tl) crystals used as the gamma screen [198].

scintillation light scattering within a single crystal, Anger used 241 1/4-inch-diameter and 1/2-inch-thick NaI(Tl) crystal elements arranged in a 5.5-inch-diameter circle such that each crystal was optically isolated and held in place by an aluminium holder from one another. The holder followed the curvature of an image-intensifying tube specially made at Philips for Anger without the ZnS screen. The tube's 5-inch-diameter photocathode converted the scintillation light into photoelectrons that were then focused onto a phosphor screen that produced visible light further magnified by an inbuilt lens. This version of the camera was more suitable for live viewing rather than capturing images on film. Its major drawback was the inability to take images due to it requiring additional lenses, resulting in loss of sensitivity and increased imaging time [190, 191, 198].

4.2.4 The 4-Inch Anger Camera

Working on his imaging systems, Anger finally described the first version of the Anger Camera in 1957. It was made up of a 4-inch-diameter and 1/4-inch-thick NaI(Tl) scintillator coupled to seven 1.5-inch-diameter PMTs using a transparent optical liquid as illustrated in Figure 4.14. The seven PMTs were connected to a signal matrix circuit that produced the x- and y-position signals based on the ratios of scintillation photons detected by each of the PMTs and a total energy signal. This process/logic of using the ratios of detected scintillation photons by an array of PMTs from a single piece of scintillator and/or light guide to obtain the position of the source of the scintillation photons became known as the Anger logic. The energy signal then passed through a pulse-height energy discriminator that was used to select a range of allowed energies improving the resolution of the image by rejecting any background or scattered events. A cathode-ray tube (CRT) screen was used with a photo camera mounted in front of it to acquire the image. The x- and y-position signals positioned the cathode-ray beam while the signal from the pulse-height discriminator

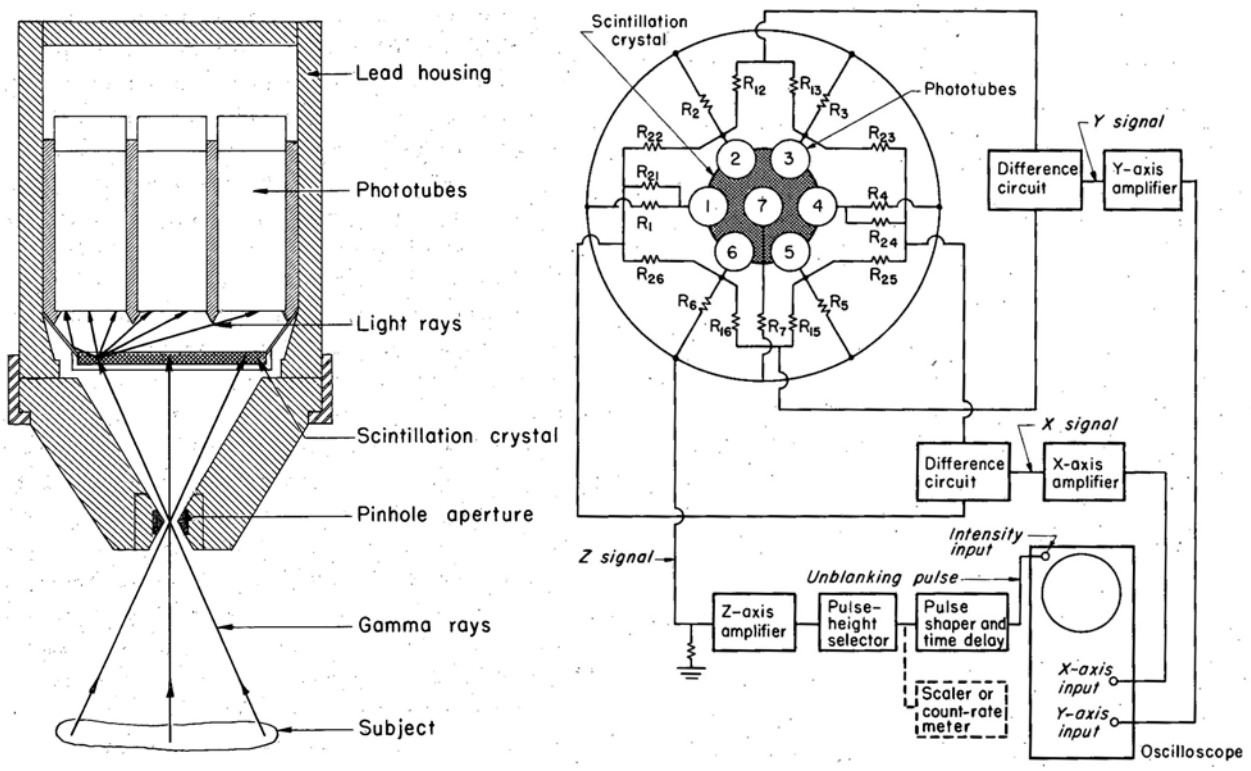

Figure 4.14: The 4-inch Anger Camera featuring a pinhole collimator and a 4-inch NaI(Tl) scintillator viewed by 7 PMTs with a block diagram of the Anger logic circuit used to calculate the position of the interaction in the crystal [200].

fired it when the energy was within the acceptable range. This exposed a small dot on the photography film and over time produced the image of the radionuclide distribution. The first design still featured the pinhole collimator but it was mounted such that it could be positioned at almost any angle to the patient. Initial thyroid images shown in Figure 4.15 and taken with ^{131}I proved the design was on the right track [199–201].

With developments still needed to tackle, the design was further improved through the initial testing of a multi-channel collimator, see Figure 4.16 left, with results which were very promising. It was concluded that the multi-channel collimator has to be further refined or moved around to prevent any image distortions. At this time, Anger also mentioned that the camera could be used for transmission scans or images with a source placed behind the patient or object that was to be imaged, the first time this principle was suggested in nuclear

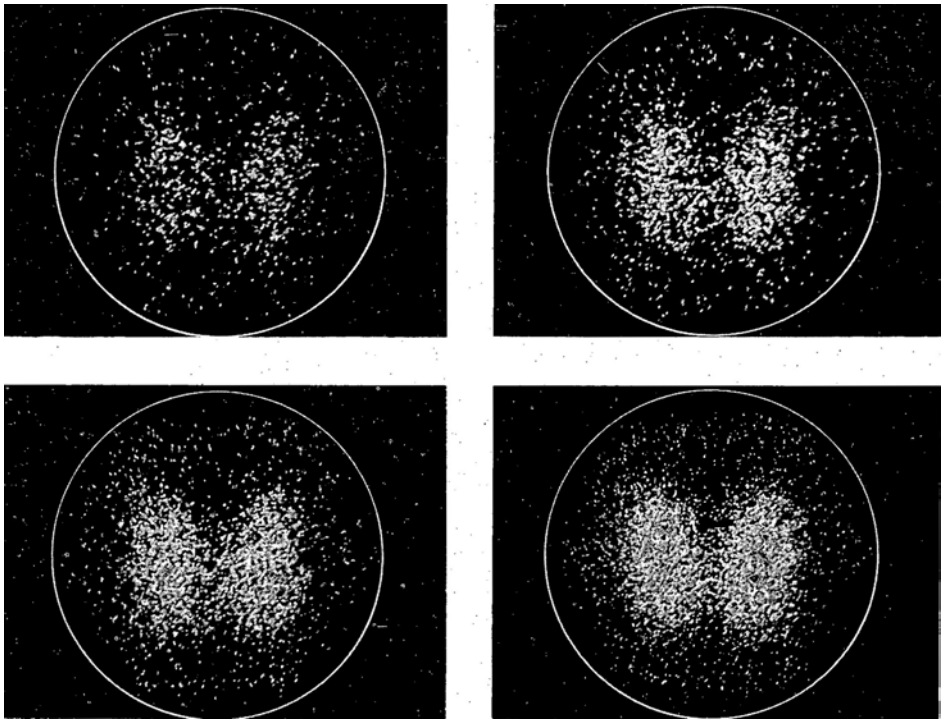

Figure 4.15: Pictures of a thyroid phantom taken with the 4-inch Anger Camera at four different exposures [200].

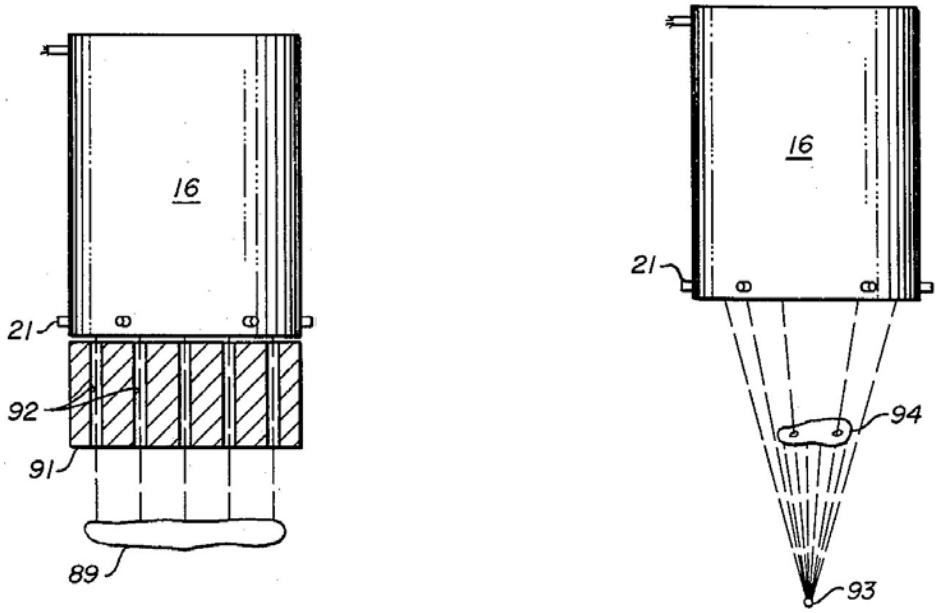

Figure 4.16: (Left) The 4-inch Anger Camera with one of the first parallel multichannel collimators. (Right) The 4-inch Anger Camera's suggested use for transmission imaging of objects [202].

imaging, see Figure 4.16 right [202–204].

4.2.5 The 11-Inch Anger Camera

In 1963, the camera was upgraded to feature an 11.5-inch-diameter by 1/2-inch-thick NaI(Tl) scintillator viewed by 19 3-inch-diameter PMTs arranged in a hexagonal array, as shown in Figure 4.17 left. The electronics were also improved besides being expanded to accommodate the 19 PMT signals. With the advances in collimator design and the development of a mathematical basis on how they affect image resolution and quality, the single-aperture pinhole collimator was finally dropped from further development as its conical shape made it inefficient for imaging of large organs and required the camera to be position further away from the subject. New custom-designed collimators that could be exchanged between procedures became the new norm. A triple-aperture thyroid collimator that produced a frontal and two oblique views of the thyroid became a standard for thyroid imaging, see Figure 4.17 right, while parallel multichannel collimators were used for general organ imaging.

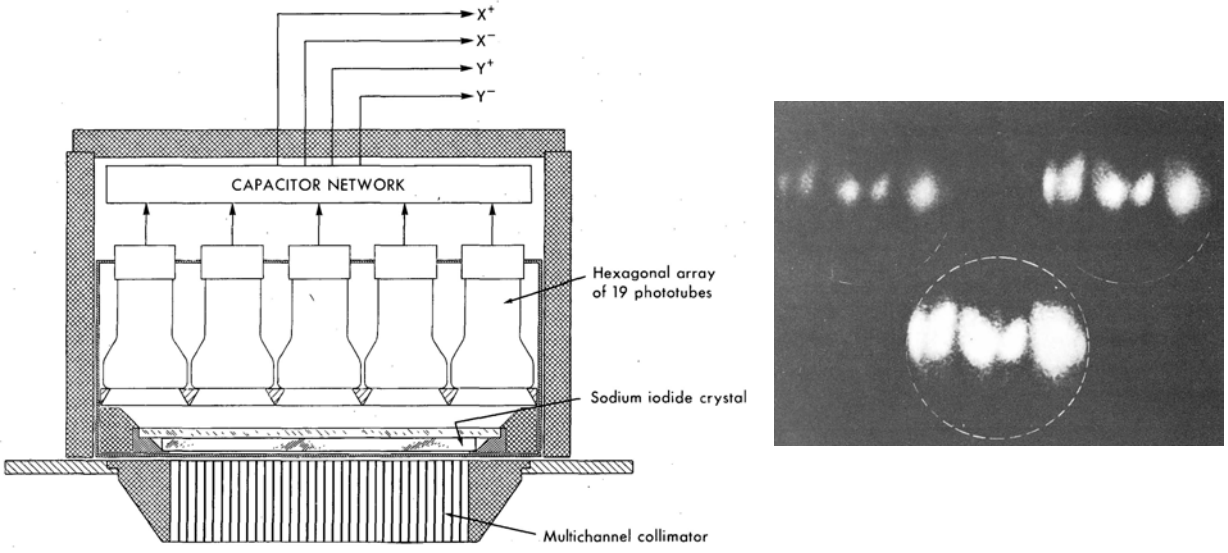

Figure 4.17: (Left) The head assembly of the 11-inch Anger Camera [205]. (Right) The 3-view images of the thyroid were taken at 3 exposures using the triple-aperture thyroid collimator mounted to an 11-inch Anger Camera [206].

These multichannel collimators provided higher resolution and sensitivity for imaging over larger and deeper positioned organs, like the liver and kidneys, that a pinhole collimator struggled to image [191, 205–207].

Further improvements in oscilloscope cameras resulted in cameras with multiple lenses, apertures, and even shutter-like-mechanisms that could image the oscilloscope screen using different aperture gradients, for different amounts of time, at different times from the start of acquisition, and/or different locations of the screen itself. Multi-lens cameras with grated apertures were especially useful as they produced the same oscilloscope image but at different intensities which prevented over- and under-exposures as demonstrated in Figure 4.18 left. Further, 80-lens cameras were developed that could take rapid sequences of images for dynamic imaging as shown in Figure 4.18 right [191, 208–210].

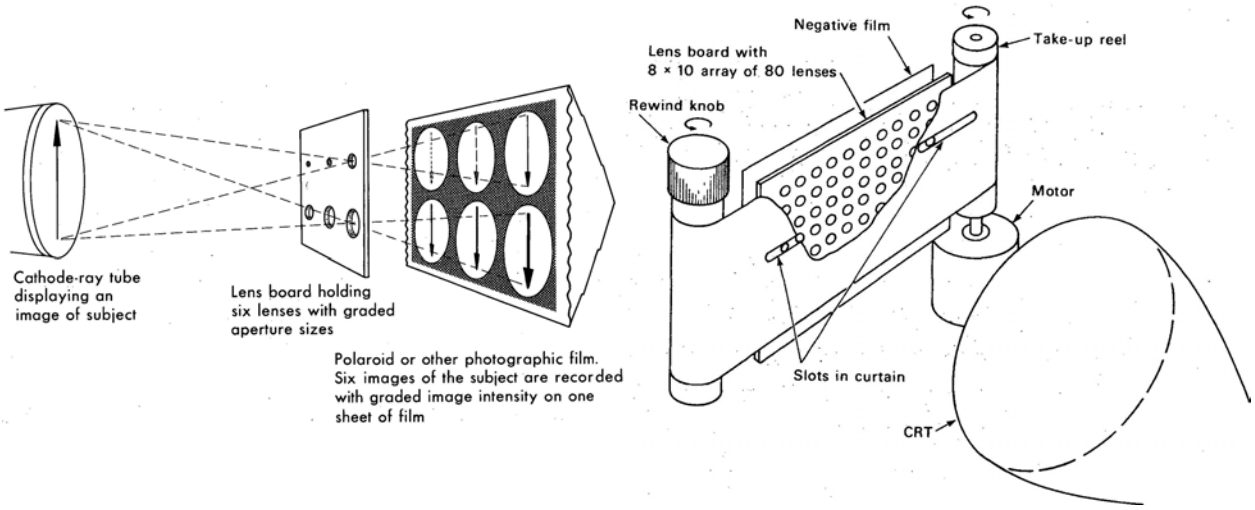

Figure 4.18: (Left) A general design of a six-lens oscilloscope camera used by Anger to capture scintigraphs at varying intensities to mitigate unwanted over- and under-exposures. Some of the images were over- or under-exposed but a few were always about right [209]. (Right) An advanced 80-lens oscilloscope camera that could capture many series of exposures over a long acquisition time [206].

While his cameras saw great potential and development at the Donner Laboratory, it was not until 1963 that they saw proper medical use. That is the year Alexander Gottschalk, a medical doctor with clinical expertise joined the Donner Laboratory. Working closely with

Anger and using his medical connections, he was able to acquire patients for imaging trials at the Donner Laboratory and eventually oversaw the camera's first use at the Alta Bates Hospital (Berkeley, California, USA). He was also a key player in popularising the ^{68}Ga generator use in the production of ^{68}Ga-EDTA for imaging before ^{99m}Tc became a country-wide standard in the United States of America [174, 190–192].

4.2.6 Beyond the 11-Inch Anger Camera

The camera system was constantly improved and modified with crystals 12- and 16-inches in diameter and up to an inch thick. Eventually, in 1966, the first gamma-camera-based longitudinal tomographic scanner based on the tomographic principle described by David Edmund Kuhl and Roy Q. Edwards in 1963 was built [212]. The camera named the Tomoscanner Mark I, shown in Figure 4.19, was based on an 8.5-inch NaI(Tl) scintillator viewed by seven

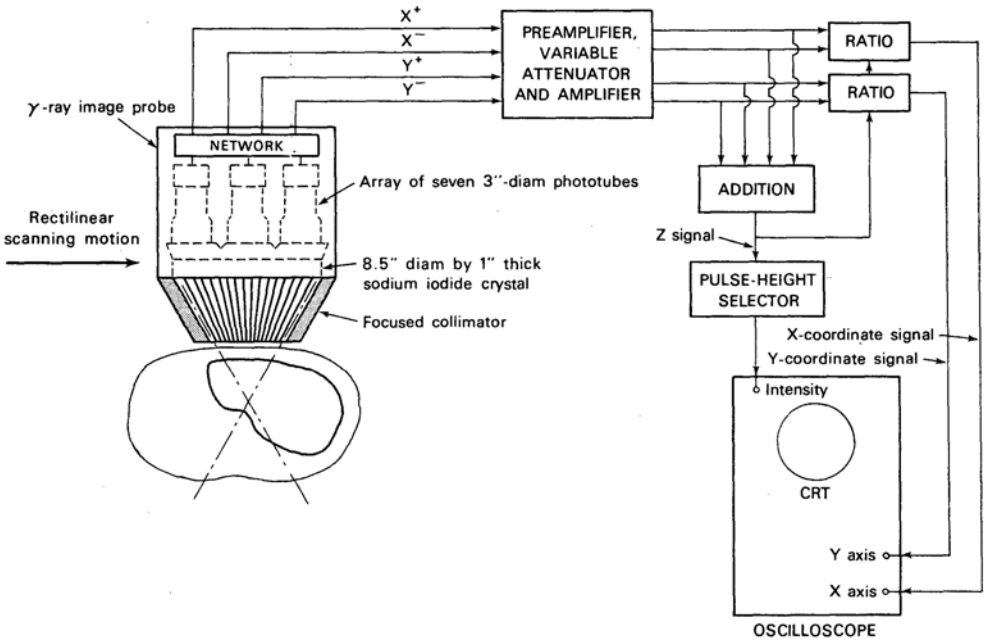

Figure 4.19: A functional diagram of Anger's Tomoscanner Mark I. The scanner utilised an Anger Camera based on an 8.5-inch scintillator with a converging collimator. The system was able to move in a rectilinear fashion producing the tomographic images using a specialised CRT camera [211].

3-inch PMTs. It used a focused, converging, multichannel collimator and moved in a rectilinear fashion to scan the area under study and produce five and later six tomographic planes on the film. It featured a very complex cathode-ray display camera to reproduce the tomographic images on film as shown in Figures 4.20 and 4.21. This was possibly the most advanced version of Anger's cameras that incorporated advancements from all the previous versions. The system was used to scan a liver with metastatic lesions demonstrating its high resolution and ability to relatively indicate the depth of the lesions [190, 191, 211, 213–215].

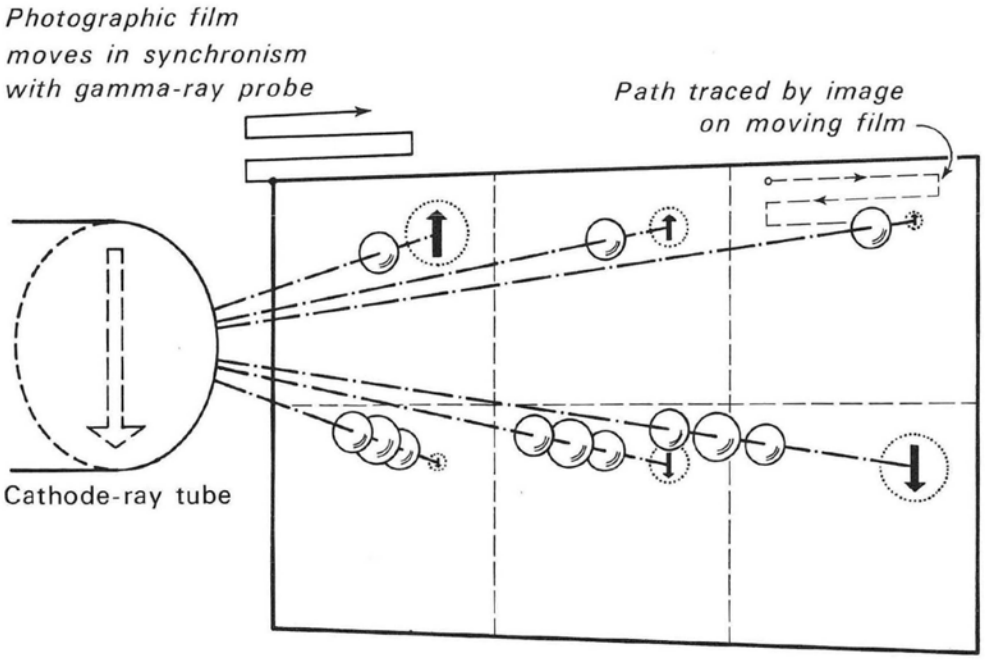

Figure 4.20: A functional diagram of Anger's Tomoscanner Mark I oscilloscope camera showing the size arrays of lenses used to reproduce the tomographic planes on film from the oscilloscope screen output [215].

Finally, in 1968 Anger began trials of transmission imaging with his large cameras which he suggested in his original patents as shown in Figures 4.16 right and 4.22. This imaging method was useful for imaging larger and hard-to-image organs such as the lungs, diaphragm, and heart that border air-filled areas. Transmission scans also produce a clear organ outline, something that is hard to achieve with many emission scans [202, 215–217].

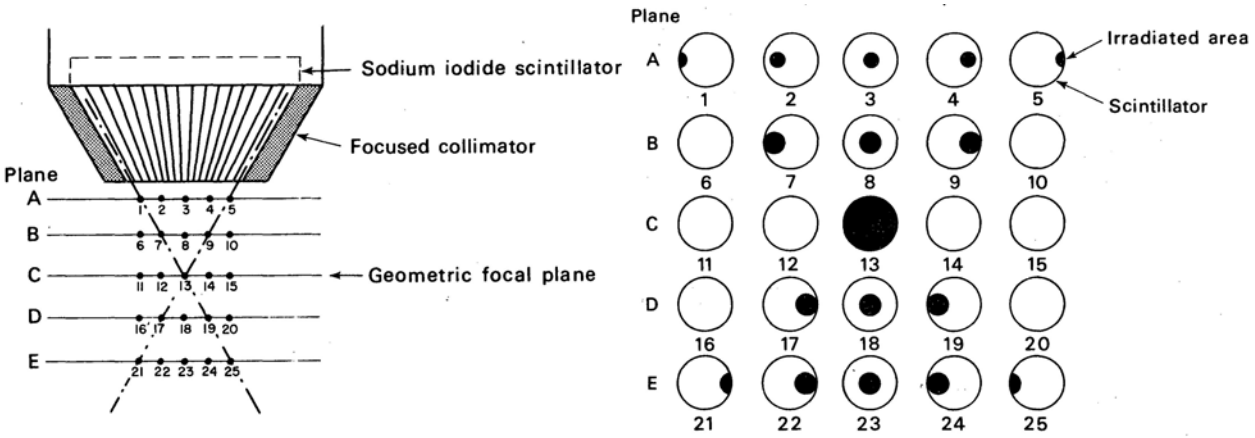

Figure 4.21: A diagram illustrating the principle of the Tomoscanner. If a source is placed at any of the 25 points on the left, a response of the scintillator is shown on the right where the shaded area corresponds to the area irradiated by the source. As the scanner scans across the subject and the oscilloscope camera projects the screen onto the moving film as shown in Figure 4.20, the crystal response is projected onto the film at different sizes influencing how fast the adjacent responses blend reproducing the tomographic planes [211].

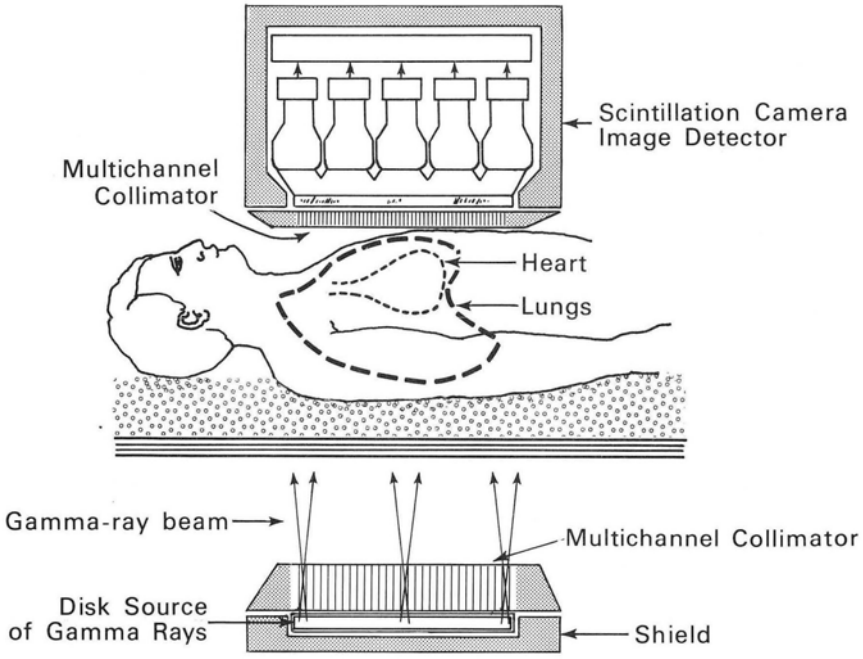

Figure 4.22: Transmission imaging with an 11-inch Anger Camera using a collimated source of gamma-rays located under the patient to image organs such as the lungs and the heart [215].

4.3 Early Positron Coincidence Imaging

Positron coincidence imaging, like normal gamma imaging, began in the early 1950s with the advent of nuclear medicine. However, unlike scintigraphy which has its roots in the need to image the thyroid, positron coincidence imaging originated with the need to study and locate tumours in the brain. Due to the amount of bone and tissue found in the area, any radiation emitted in the head is very prone to scattering and therefore presents an imaging problem.

4.3.1 The Early Coincidence Detection Setups

The methods of tumour localisation in the head using radionuclides and coincidence detection were first described in 1951 by two different groups after the angular distribution of the two-photon annihilation was refined [218]. Frank R. Wrenn Jr., Myron L. Good, and Philip Handler published a study on the effects on the count rate of two NaI(Tl) detectors set in coincidence when used with and without a collimator. They used ^{64}Cu and ^{65}Zn as the radiotracer which at the time were identified as possible brain tracers [219]. Similarly, William Herbert Sweet of the Massachusetts General Hospital (MGH) described the current state of the art at the hospital used for the localisation of brain tumours using specialised GM counter probes and ^{32}P and ^{42}K radiotracers but mentioned positron coincidence detection as a future way of localising brain tumours using external probes [220].

In 1953, Gordon Lee Brownell and Sweet at MGH developed the first positron coincidence imaging device dedicated to brain tumour localisation shown in Figure 4.23. The system featured two collimated NaI(Tl) detectors placed on either side of the patient's head that were then moved rectilinearly. This device recorded the coincidence and unbalanced counts using a tapper mechanism marking a piece of paper as shown in Figure 4.24 [222,

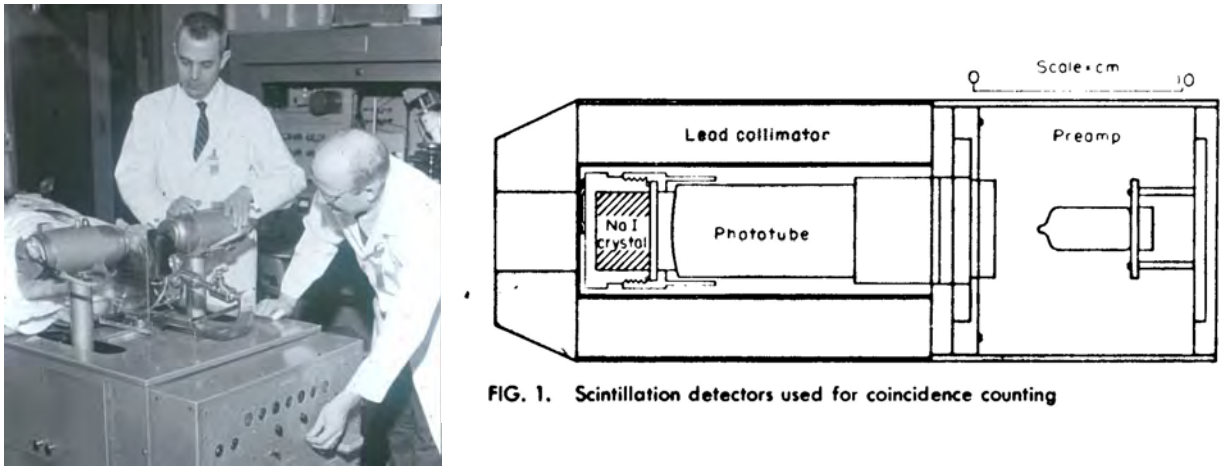

Figure 4.23: The first position coincidence scanner built by Brownell and Sweet at MGH was used to rectilinearly scan a patient's head. It was made up of a pair of collimated NaI(Tl) detectors that moved in tandem on opposite sides of the head [221, 222].

223]. Later in 1961, a group at BNL started to plan what can be said to be the first full-ring positron camera. It was going to consist of 32 NaI(Tl) detectors arranged in a single ring around the head to take a single tomographic image at a time as illustrated in Figure 4.25. The device was going to use a 2D pulse-height analyser with a magnetic drum memory to store the coincidence counts while rejecting single counts and multiple coincidences, setting the stage for nuclear electronics developments. However, the device was not built until a decade later in 1973 (see Section 4.5.1) [221, 224, 225].

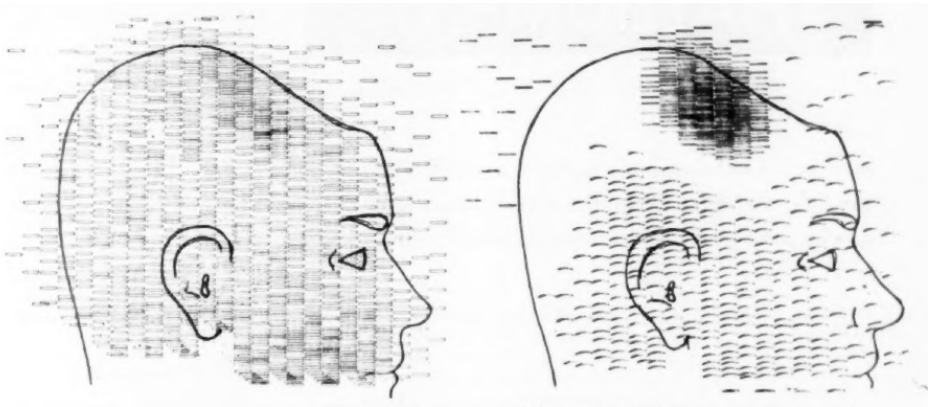

Figure 4.24: An early positron scan conducted at MGH by Brownell and Sweet of a post-operation patient showing cancer recurrence in the coincidence (left) and unbalanced (right) images [222].

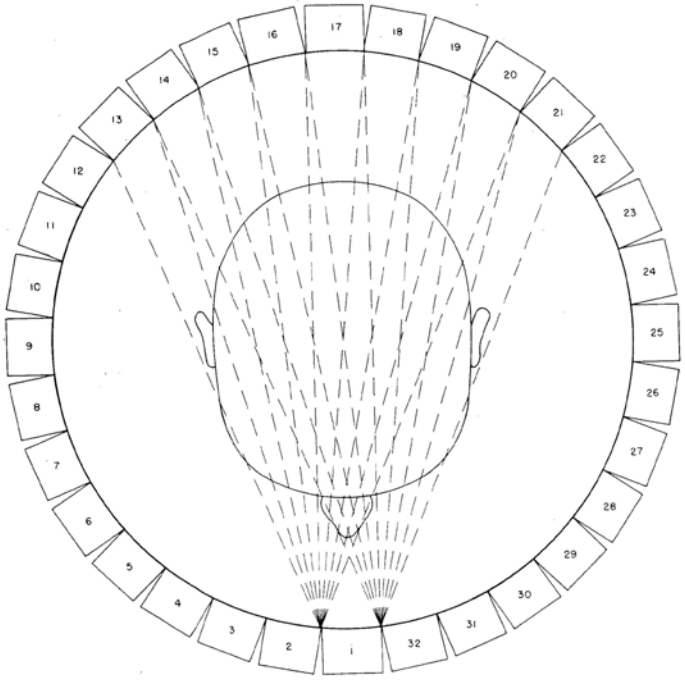

Figure 4.25: Rankowitz et al. design of the 32-detector brain tumour scanner at BNL. This was the first design to feature a full-ring detector array [224].

4.3.2 Anger's 4-Inch Positron Camera

In 1957, as Anger developed his first Anger Camera system based on the 4-inch NaI(Tl) scintillator, he also started to experiment and develop positron cameras based on these assemblies. The first of these systems was a Single-Crystal Positron Camera which simply used a 4-inch uncollimated camera as an image sensor and a single NaI(Tl) detector positioned directly opposite it, on the other side of the patient as shown in Figure 4.26 left. If both detectors detected a 511 keV gamma ray in coincidence, it would simply allow the Anger Camera to pass the detected event to the output system. At the same time, Anger also experimented with a Twin-Crystal Positron Camera which used two 4-inch uncollimated cameras simply set in coincidence as illustrated in Figure 4.26 right. This system was more advanced as all the circuits were doubled and it can be said to be the first dual-head scintillation camera. This began to present a growing problem that increasing the detector modules corresponds to a rapidly increasing amount of electronics and the scanners price. As the

methods used in tomography were still under development and the output was limited to immediate plotting through the CRT system, this camera system was severely limited to imaging thin objects positioned perfectly on the plane in between the two head assemblies. The position signals were weighted together such that their output always indicated where the line-of-response (LOR) produced by the pair of gamma rays crossed the central plane of best definition. Therefore, if the gamma rays originated anywhere outside of that central plane, they would be plotted in the wrong place contributing to a loss of definition in the final image [204, 226].

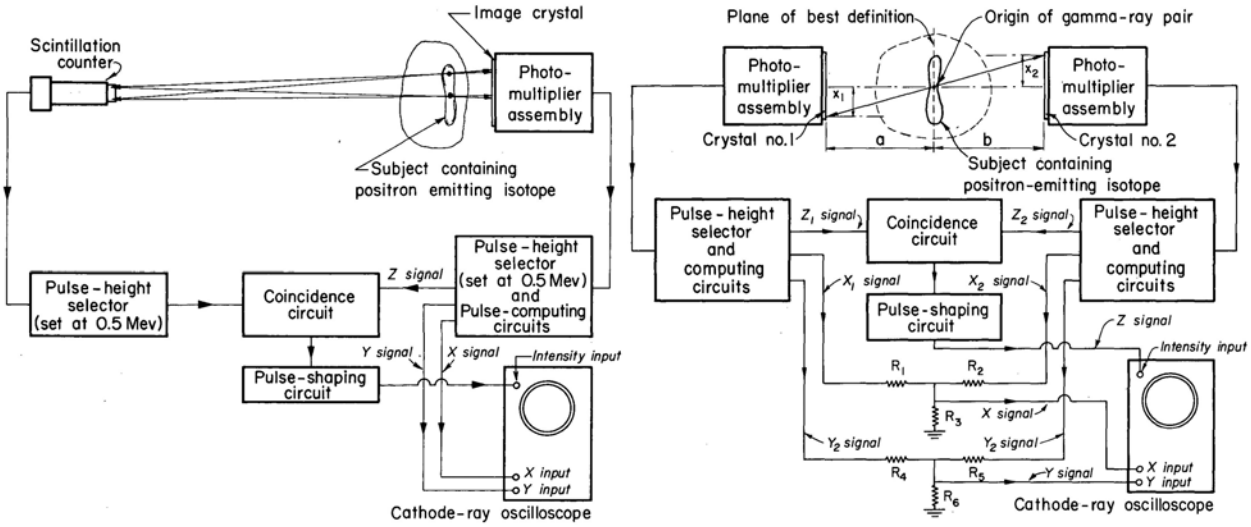

Figure 4.26: Functional diagrams of the Single-Crystal Positron Camera (left) and the Twin-Crystal Positron Camera (right) which utilised the 4-inch Anger Camera as the main imaging sensor [204].

4.3.3 Anger's 11-Inch Positron Camera

By 1963, Anger built and tested his 11-inch camera which he developed with positron coincidence imaging in mind. The camera could be set in both single and coincidence mode and featured a curved, hexagonal, 19 NaI(Tl) detector array called the positron focal detector in addition to the image detector as shown in Figure 4.27. The positron focal detector, when enabled, applied a correction signal to the gamma camera position output. If the gamma ray

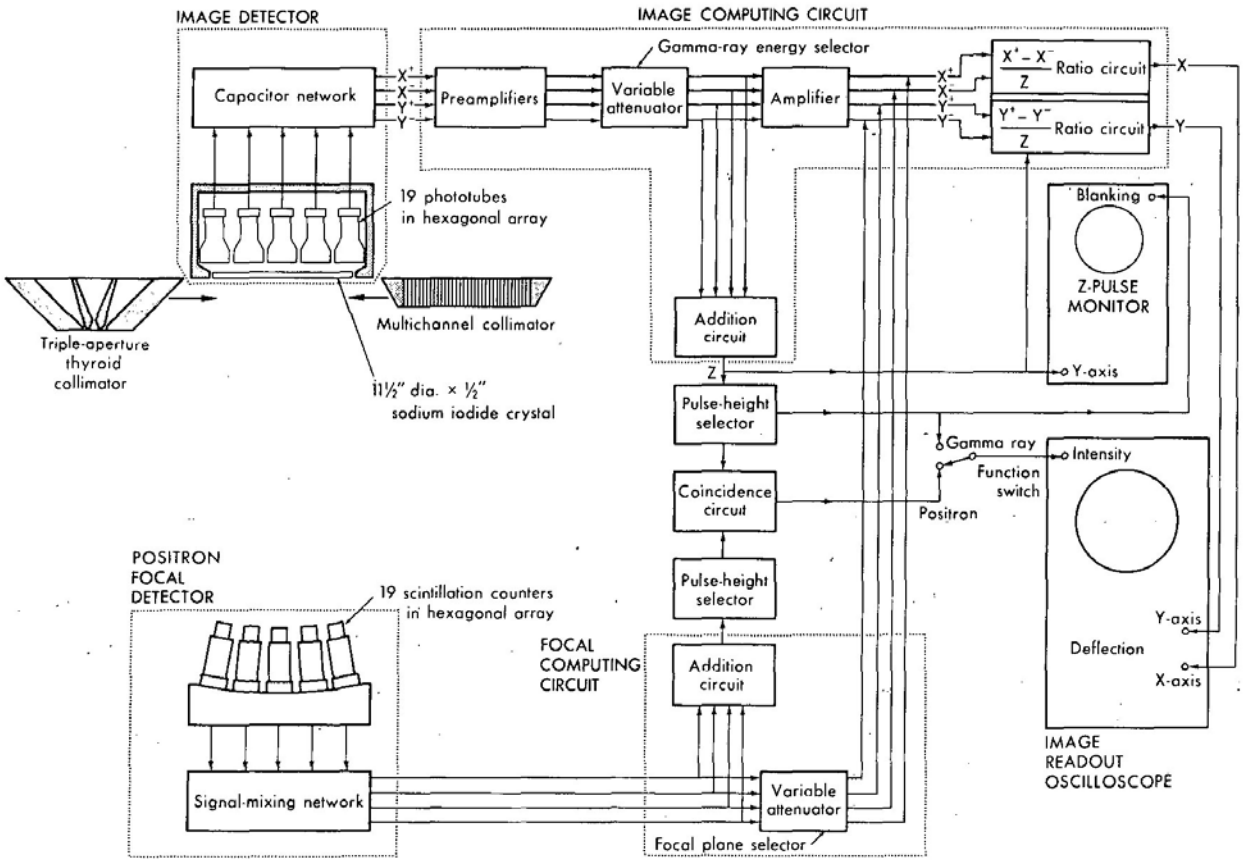

Figure 4.27: Anger's 11-inch Positron Camera which utilised the 11-inch Anger Camera as an image sensor and a Positron Focal Detector array for generating a correction signal that allowed the camera to focus on various tomographic planes [206].

was detected in the central of the 19 detectors, no position correction was applied; and, if it was detected in the other 18 detectors, appropriate x and y correction signals were generated by the array. The operator of the system was also able to choose the focal plane of the system at set intervals from the face of the gamma camera which simply varied the intensity of the correction signals produced by the positron focal detector. Initially, the system was run without any collimation on the gamma camera, but with the refinement of the parallel multichannel collimator, it began being used to collimate positron images further increasing their definition [206, 215]. This 11-inch positron camera system was shown to be effective at detecting simulated brain tumours using ^{68}Ga-EDTA and ^{203}Hg-Neohydrin [192, 227–230]. Similarly, the system was also used to conduct studies of the distribution of bone marrow

and the effects of various conditions on it using ^{52}Fe [231, 232].

4.3.4 The Hybrid Positron Scanner

By 1968, Brownell et al. at MGH started to construct a multi-crystal positron coincidence scanner. The first of them was named the Hybrid Positron Scanner, shown in Figure 4.28, and featured a two-head design with nine 2.22 cm x 4.13 cm by 5.08-cm-deep NaI(Tl) scintillators in a column per head, each with a trapezoidal collimator. The heads were then moved rectilinearly to obtain the final image data that could be recorded on a tape and printed using the classic CRT camera method. A feature of this scanner was that each crystal was in coincidence with three crystals opposite it and it was able to focus on different planes parallel to the heads [221, 225, 233, 234].

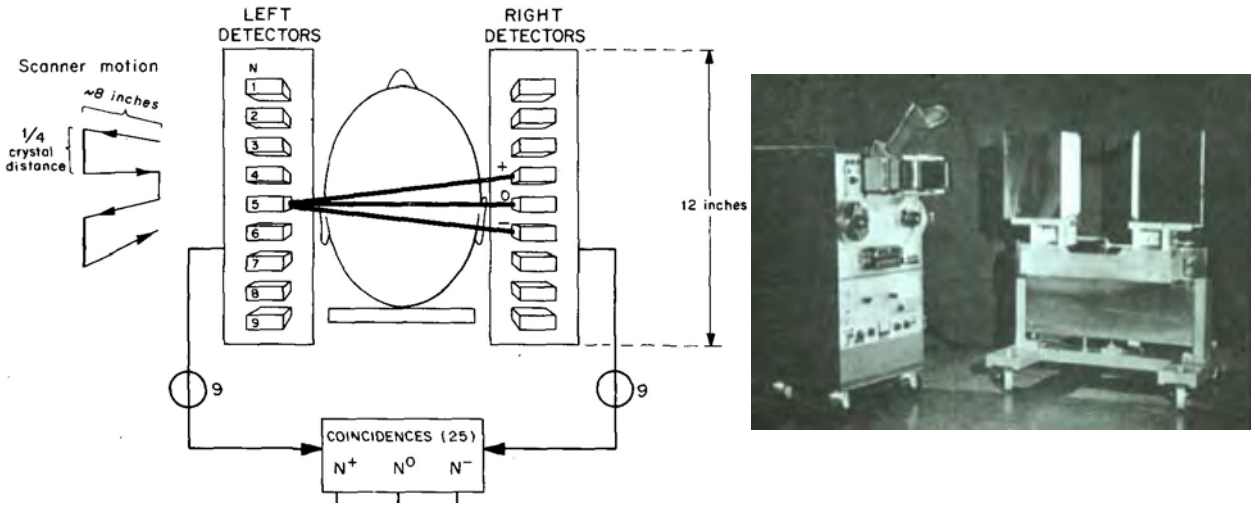

Figure 4.28: The Hybrid Positron Scanner built at MGH scanned the patient's head in a rectilinear fashion and, due to its multicrystal design, allowed the system to efficiently use the emitted radiation [221, 233].

4.4 Transverse Axial Tomography

Throughout the early 1970s, Kuhl, Edwards, Budinger, Gullberg, and many others continued to develop the principle of transverse tomography. Transverse tomography would allow imaging of the human body in slices that would ease imaging of organs and tumours located deep within the body; something that the scanners up to this point had troubles doing repetitively, quickly, and accurately. Kuhl and Edwards further studied the method using a Mark II device of their own design that was like a positron version of a rectilinear scanner with two NaI(Tl) detectors that could be rotated at any angle around the subject. They also used the Mark II for transmission tomography by replacing one of the detectors with an ^{241}Am source [212, 237–239]. However, this device did not use a computer to form the images but rather an optical integrator which, similarly to a CRT screen read-out, had its limitations due to producing the final image during the scan. At this time, the lack of ability to record raw data and postprocess it at a later time was becoming a problem as all the scanner setting had to be initially set up correctly otherwise the scan results could be unreadable. Unlike the Mark II, their later Mark III and Mark IV scanners shown in Figure

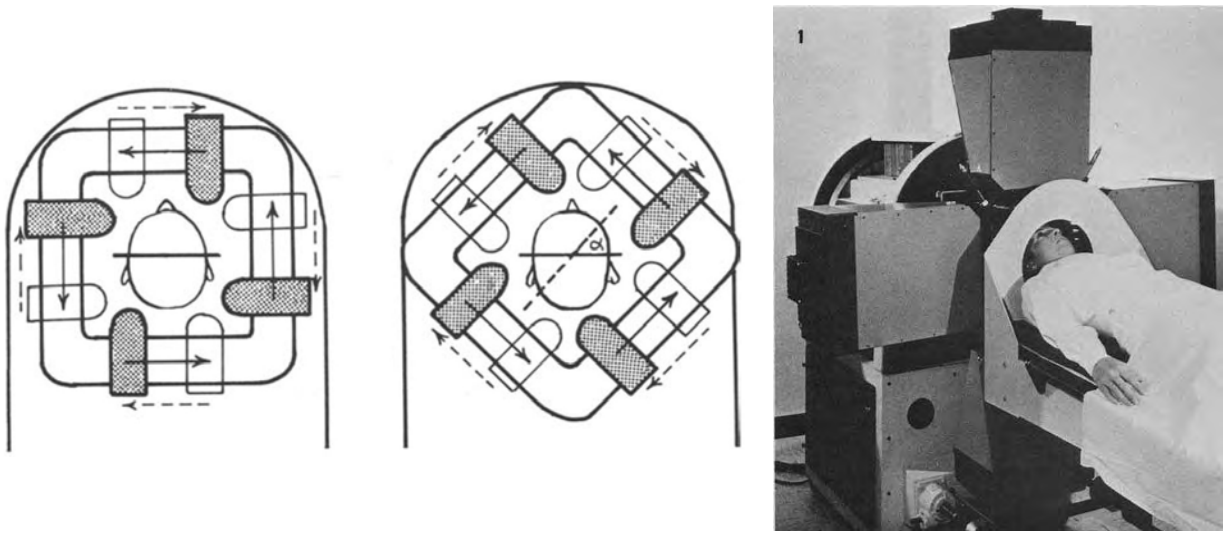

Figure 4.29: The Mark III (left) and Mark IV (right) tomographic scanners designed by Kuhl and Edwards for early SPECT acquisitions [235, 236].

4.29 were gamma scanners with four head assemblies that eventually led to the establishment of Single Photon Emission Computerised Tomography (SPECT) [235, 236]. Budinger and Gullberg also contributed greatly to the formation of SPECT by using an Anger Camera for scans rather than individual or arrays of individual detectors like Kuhl, Edwards, and Brownell did in their designs [221, 225, 240, 241].

4.4.1 The PC-I

By 1970, Brownell et al. working at the MGH continued to develop the design of the hybrid scanner and built the Multi-Crystal Positron Camera, also known as the PC-I, which had a 27 cm by 30 cm field-of-view (FOV) through the use of a novel method of crystal multiplexing. At the time, this camera had one of the largest FOVs. This large of an FOV allowed not only to acquire a larger volume of the patients body without having to move it, but to process patients faster than other cameras at the time. However, unlike earlier transverse tomography scanners, it was able to image the body of an adult and not just the head. Instead of using a single large crystal, many smaller NaI(Tl) crystal disks were used in the two-head camera design. The 127 crystal disks in each head were arranged in a square, planar array viewed by 72 PMTs. Each PMT would view four halves of four different crystals and each crystal was viewed by two adjacent PMTs, see Figure 4.30. Each crystal was in coincidence with the crystal opposite it and 24 of its nearest neighbours. The ratio of energies from adjacent PMTs would then be used to calculate in which crystal element the interaction occurred. This not only reduced the cost of the camera, but also improved its spatial resolution when compared to earlier multi-crystal systems. The two-head system had to rotate through 180° to acquire all the needed views for a tomographic reconstruction. This cut down the scanning time in half when compared to a single-headed system that had to roate through the full 360°. While acquiring each view, the heads did not rotate but translated or shifted linearly

to acquire data at more positions than the number of individual crystal elements in the head assembly. This function increased the image resolution and quality of reconstructed images than would normally be possible [242, 243]. This device was designed to easily acquire both regular tomographic images on planes located between the two heads and, for the first time, transverse tomographic images on planes located within the subject [221, 225, 244].

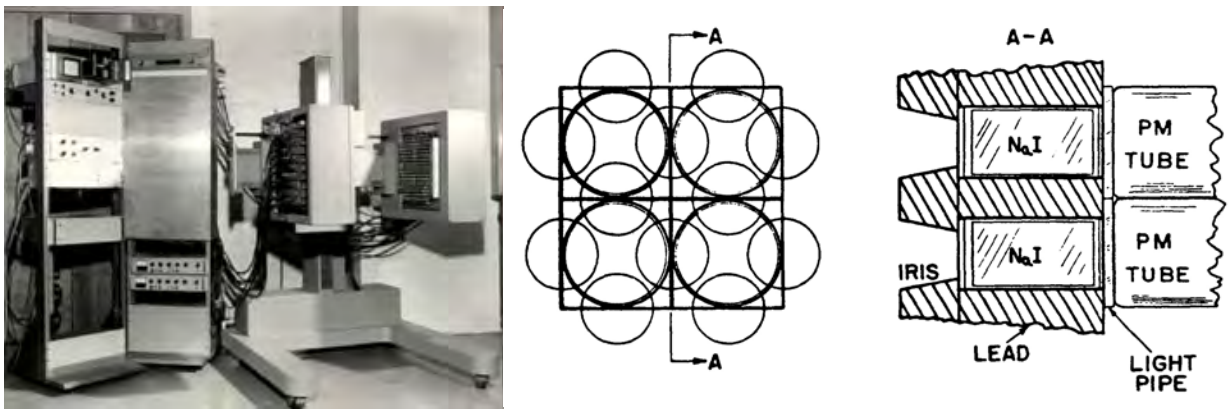

Figure 4.30: The Multi-Crystal Positron Camera was developed by Burnham and Brownell at Massachusetts General Hospital. (Left) The Multi-Crystal Positron Camera at MGH [221]. (Right) The light-sharing technique of the camera. The larger circles are the PMTs and the smaller circles are the NaI(Tl) crystal elements [242].

4.4.2 Developments in Computing Allow for Algorithmic Postprocessing

At the same time as PC-I was being developed, David Alan Chesler, who was also part of the MGH group, was working on computer-based image reconstruction methods and developed one of the most influential image reconstruction methods in PET, the filtered back projection (FBP). Using a simple desktop PET scanner, he acquired the needed emission and transition test data. After a bit of postprocessing using his computer, he was successful in the reconstruction of the emission, transmission, and absorption-corrected emission images [3, 4]. His method was immediately applied to the PC-I data yielding the first positron emission tomographs as shown in Figure 4.31 [5, 221, 225]. It was also later applied to

X-ray computer tomography (CT) which was concurrently developed by Godfrey Newbold Hounsfield and Allan MacLeod Cormack in 1973 using an iterative reconstruction method [7–11, 245, 246].

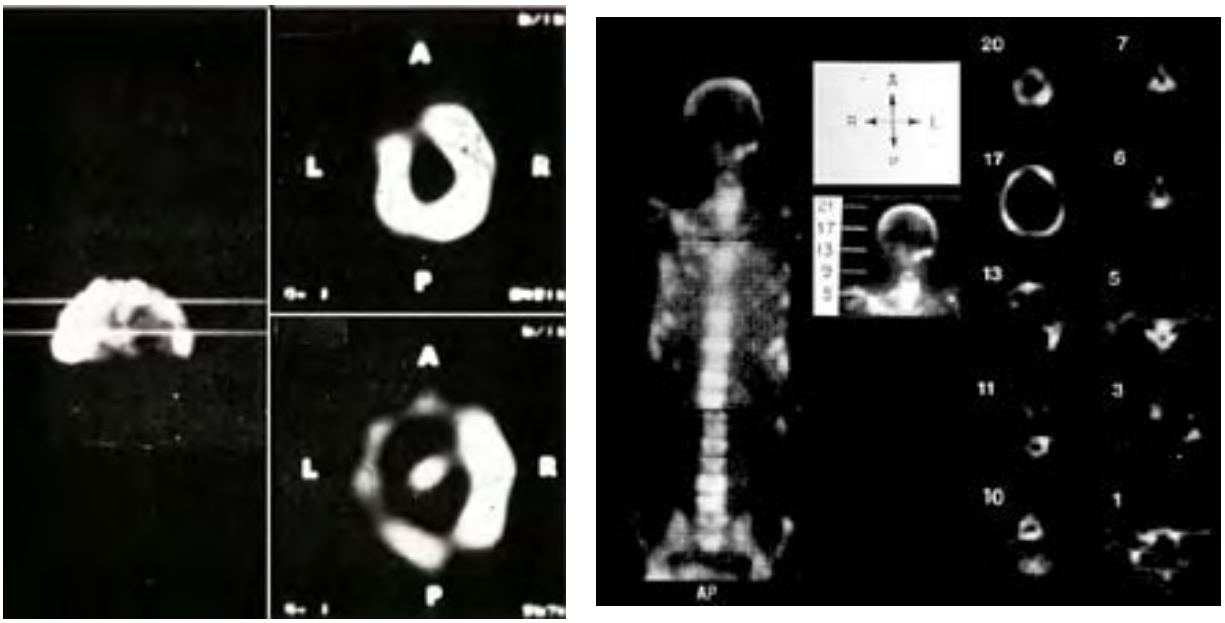

Figure 4.31: Some of the first filtered back projection reconstructed images taken using the PC-I. (Left) A brain study was conducted using ^{68}Ga. The two white lines on the left image indicate the position of the transverse slices shown on the right. A tumour is visible in the centre of the lower slice. (Right) A bone scan was conducted using Na^{18}F. The left image shows the anteroposterior view with multiple bone metastases. The centre view shows the locations of the reconstructed transverse tomographic slices shown on the right side [221].

4.4.3 The PC-II

By the mid-1970s, the group at MGH developed the PC-II which was largely similar to PC-I but featured a larger, more sensitive detector assembly. With the development of the FBP algorithm, the PC-I and PC-II were modified to natively reconstruct images using this algorithm, as shown in Figures 4.31 and 4.32. However, to fully take advantage of the algorithm and make transverse axial tomography as efficient as possible, a new system design would have to be developed [247–250]. The PC-II was later commercialised by The Cyclotron

Corporation (Berkeley, California, USA) as the Positron Camera Model 4200, which for a while was the only system on the market that could take normal plane tomographs, multi-slice transverse axial tomographs, and perform some dynamic studies. However, it did not perform FBP reconstruction but used an iterative approach. This meant that for a while the PC-I and PC-II at MGH were the only positron cameras capable of taking FBP reconstructed human PET images [221].

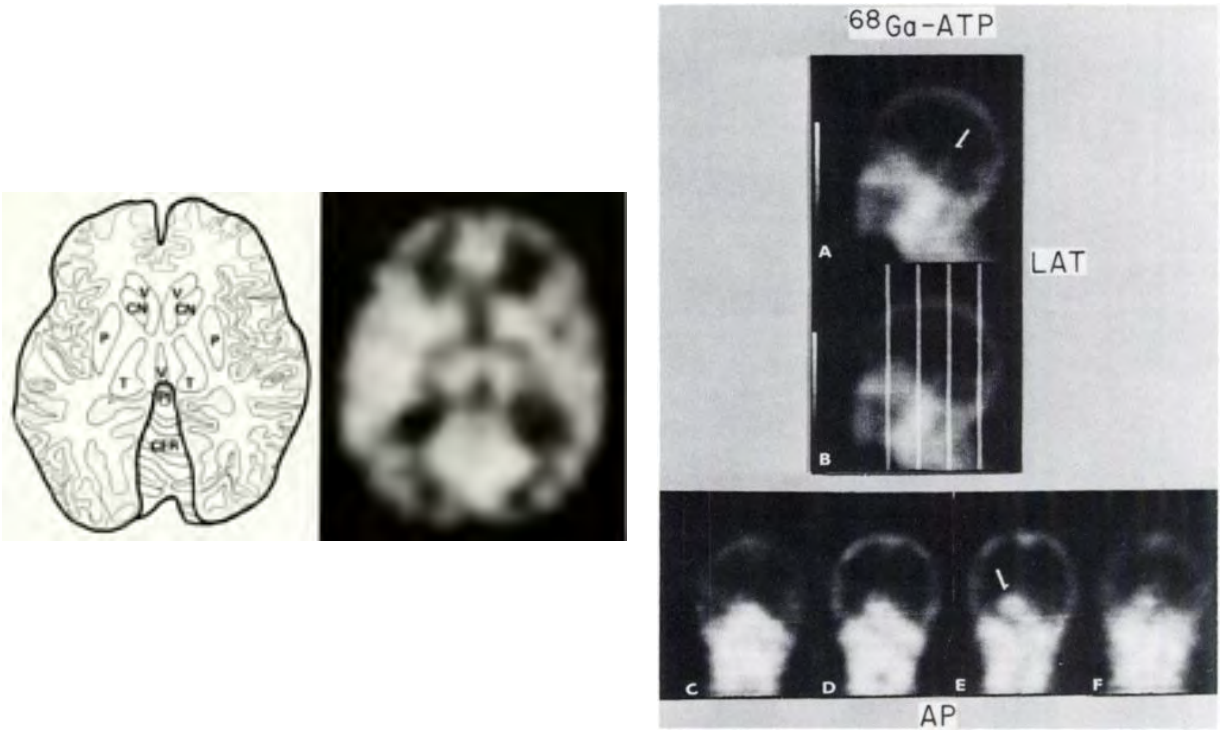

Figure 4.32: Some filter back projection reconstructed images taken using PC-II. (Left) An image of a normal control human brain taken using ^{18}F [221]. (Right) A brain scan was performed using ^{68}Ga-ATP with an arrow pointing to a tumour [248].

4.5 Development of the Full Ring Tomograph

With the development of the filtered back projection algorithm and the progress in integrated circuit design and miniaturisation, the goal of future PET development became focused on improving instrumentation by reducing scan times, providing quantitative results, and

reducing all sources of noise. Cameras produced up to this point did not have any provisions for accounting for detector dead time and random coincidence correction, both of which are important to yield quantitative results. However, a few more failures had to occur to bring the PET designers together.

4.5.1 Road to PETT

In 1973, J. S. Robertson et al. of BNL built the 32 NaI(Tl) detector full-ring positron camera to take individual transverse images of the brain. This system, shown in Figure 4.33, was first designed by S. Rankowitz in 1961 to localise brain tumours but it was not built until 1973 [224, 251]. However, with its limited sampling and lack of random coincidence correction, attenuation correction, and a proper image reconstruction algorithm, it failed to produce proper tomographic images and was transferred to the Montreal Neurological Institute. At the Institute, Chris Thompson, Ernst Myer, and Lucas Yamato continued

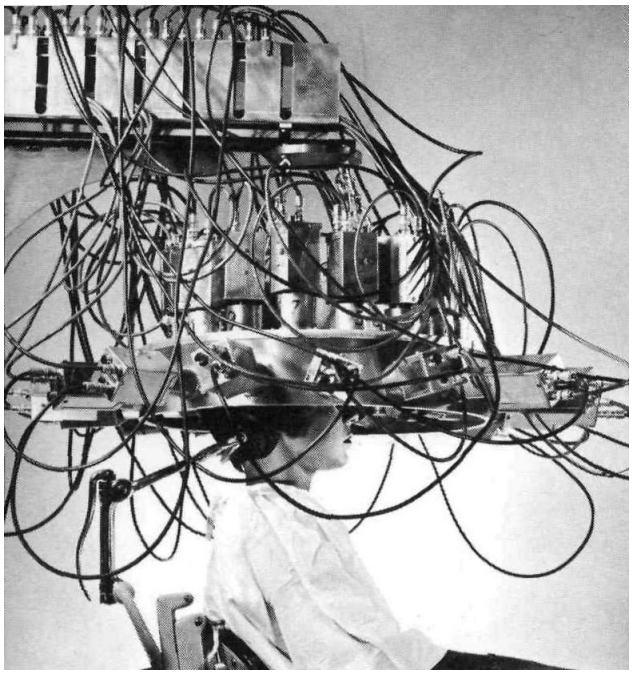

Figure 4.33: The Brookhaven National Laboratory 32-detector positron camera built by Robertson et al. and designed to take tomographs of the brain [251].

further development of the system into the late 1970s as Positome [252, 253].

That same year, working at Washington University, Michael Edward Phelps, Edward Joseph Hoffman, and Nizar A. Mullani built the Positron Emission Transaxial Tomography (PETT) system. While not much was published about it, the device was the first full-ring positron camera that featured a Fourier-transform-based reconstruction algorithm. While a step in the right direction, the system failed to produce quantitative images as it did not account for any attenuation, used collimators which degraded the spatial resolution, and had a low spatial sampling. With all the recent failures to produce a quantitative tomograph, the group at Washington University including Michael Matthew Ter-Pogossian and Terry Jones sat down and discussed the development of a new scanner that was able to produce quantitative tomographic images [225, 244].

Filled with ideas on how to build the first proper PET scanner, Phelps and Hoffman travelled to Oak Ridge, Tennessee, USA to meet with EG&G ORTEC group which is known for its detector and nuclear electronics knowledge. Meeting James Kelly Milam, Charles W. Williams, Terry D. Douglas, and Ronald Nutt, Phelps and Hoffman presented their design ideas for a hexagonal tomograph made up of 24 NaI(Tl) detectors with attenuation correction, coincidence detection, and a system using FBP for image reconstruction. With the EG&G ORTEC's expertise and provision of some electronic modules, the PETT II was built in under a month and ready to acquire data in early 1974. PETT II was a small benchtop scanner able to fit small animals and phantoms as shown in Figure 4.34 left. A month later a second scanner was built, the PETT II 1/2 was identical to the PETT II except that it featured a computer-operated rotating table for easy and precise placement and indexing of phantoms and animals, as shown in Figure 4.34 centre [254]. Both PETT II and PETT II 1/2 were used to develop the mathematics and physics behind quantitative PET before a full-sized model was built. The established principles of PET were finally published by Phelps et al. discussing how to design a PET scanner, how resolution,

sensitivity, attenuation, and contract are virtually depth independent, attenuation can be easily corrected for using a transmission scan, efficiency of a system is dependent on the number of possible coincidence pairs, compared reconstruction algorithms and how they are able to remove noise, and described how all of that lead to quantitative results ushering in the new era of PET [225, 244, 255].

Figure 4.34: (Left) The PETT II system built at EG&G ORTEC and used for obtaining test data used to establish the principles of PET. (Centre) The PETT II 1/2 system which was identical to PETT II but featured a computerised platform used for positioning phantoms and small animals. (Right) The PETT III/PET III or a full-sized version of PETT II was built at Washington University with double the amount of detectors that were able to produce the first quantitative results in human PET scans [244].

4.5.2 The First Full-Sized Tomograph

Returning to Washington University armed with all the necessary knowledge, the group constructed the PETT III or PET III as one of the Ts standing for transaxial was removed because a tomograph can reconstruct images in all planes. PET III was a full-sized version of PETT II, shown in Figure 4.34 right, with 48 NaI(Tl) detectors in a hexagonal bank array that, at the time, had an unmatched spatial sampling. The ring rotated through 60° to acquire all the necessary rotational views while each of the six detector banks was able to translate linearly to produce more sampling positions than physical detectors. The system had a dedicated computer for the gantry rotation, detector translation, patient bed positioning, and image reconstruction operations. EG&G ORTEC designed the electronics

while Mullani created the coincidence logic. The heavy shielding and the closed-in nature of the ring design heavily reduced noise due to scattered coincidences. Due to all of these developments and the use of FBP algorithm, quantitative measurements of the regional tissue concentration of a radionuclide were made possible. For the first time ever, quantitatively, ratios of radionuclide uptake could be calculated between different organs and fluids. Quantitative dynamic studies of various fluids in the body as well as studies of distribution of various molecules were undertaken. This is the moment in history that PET became an actual measurement tool and not just a fancy camera. The scanner was quickly put to work acquiring many first human images of brain oxygen flow, blood flow, glucose metabolism (shown in Figure 4.35), and ^{18}F bone scans marking a new era of functional nuclear imaging [244, 256, 257].

Figure 4.35: A first human PET scan of the metabolism of glucose in the brain taken using ^{11}C-D-Glucose [244].

Chapter Five

Development of the Modern PET Scanner System Architecture

With the establishment of PET principles and tomographic image acquisition and reconstruction methods through a long period of trial and error, the first human-sized tomograph was built and immediately started to acquire human physiological data. In this section, the story of the development of the detector block will be presented. From the development and use of the BGO scintillator to the limitations placed on detector design by the PMTs, the various PET scanners designed during this period to try and overcome each of the challenges will be discussed. In the end, the formation of Computer Technology and Imaging Inc. (CTI) with the sole goal of making PET scanners viable for manufacturing, with the inspiration of these previous research scanners, the detector block was developed.

5.1 Before the BGO Scintillator

The Emission Computed Axial Tomograph (ECAT) dates back to 1976 when Michael E. Phelps and Ed Hoffman moved from Washington University to UCLA and set out on a joint

venture with EG&G ORTEC to improve on their PET III design. The new system aimed to take transaxial tomographic images, improve image contrast, and produce true quantitative images that reflected actual amounts of radiation present in an area while optimising its physical design and flexibility.

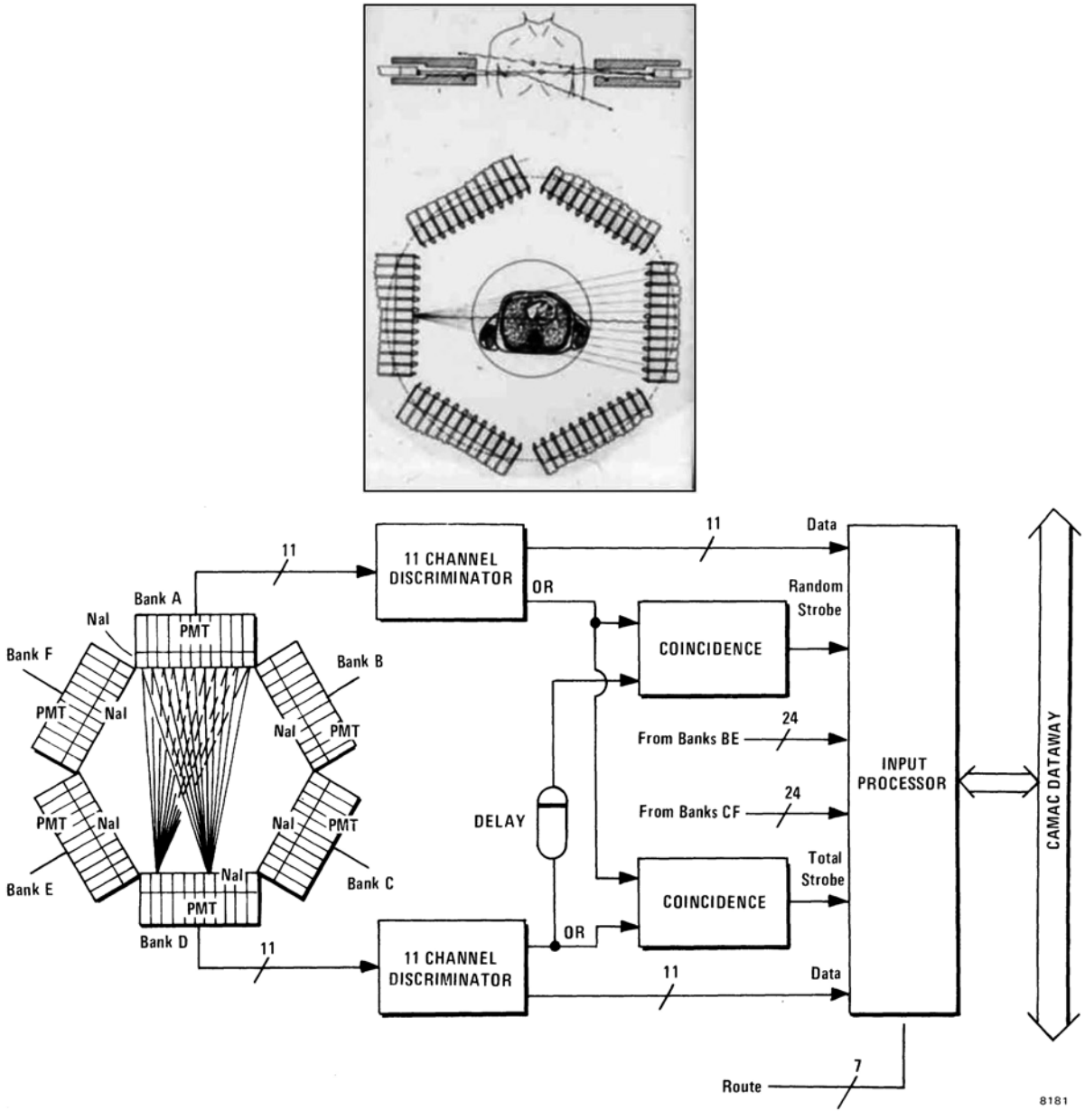

Figure 5.1: ECAT II system structure. (Top) The ECAT II gantry layout. It was the same as the ECAT I [225]. (Right) The ECAT II data acquisition and processing flow diagram [258].

The ECAT (also known as the ECAT I) was the first production prototype of a PET scanner that helped kick-start the worldwide PET research programs [225, 244]. The scanner was of a hexagonal bank design with opposite banks positioned 1 m apart. Due to the limitations of early electronics, only banks directly opposite of one another were in coincidence. Each bank consisted of 11 in-line 3.8 cm diameter and 7.5 cm thick NaI(Tl) crystal discs each viewed by a single PMT; effectively forming a single ring. The processing electronics mostly consisted of off-the-shelf NIM (Nuclear Instrumentation Module) and CAMAC (Computer Automated Measurement and Control) electronic modules controlled by a Digital Equipment Corporation (DEC) PDP-11/45 (Programmed Data Processor) computer [259]. The ECAT I prototype was quickly upgraded to resolve any immediate issues, leaving the overall design the same. The upgraded version began commercial production as the ECAT II, shown in Figure 5.1, and sold to various clinics in the USA, Europe, and Japan with an option to add a second ring of detectors. The single ring version cost over $3.5M of today's US dollars [225, 244, 258].

Perhaps the epitome of the NaI(Tl) scintillator-based PET scanners was the Donner 280-crystal high-resolution positron tomograph developed at the Donner Laboratory in the late 1970s. It was based on 280 8 mm by 30 mm and 50 mm deep NaI(Tl) scintillator blocks packed in 9.7 mm by 33 mm stainless steel cans arranged in a single ring resulting in a 92 cm diameter scanner with 10.3 mm crystal pitch. To accommodate the fine crystal pitch, quartz light guides were used to distribute the scintillation light to each of the PMTs assemblies in an alternating order as shown in Figure 5.2. In this geometry, each crystal in the ring is in coincidence with 105 crystals opposite it. However, due to the small nature of the crystals and the sealing technique used, the NaI(Tl) began to yellow and lose its properties [260]. As such, two years later, all the NaI(Tl) crystals were switched out for the BGO scintillator increasing the sensitivity of the scanner 2.3 times [261].

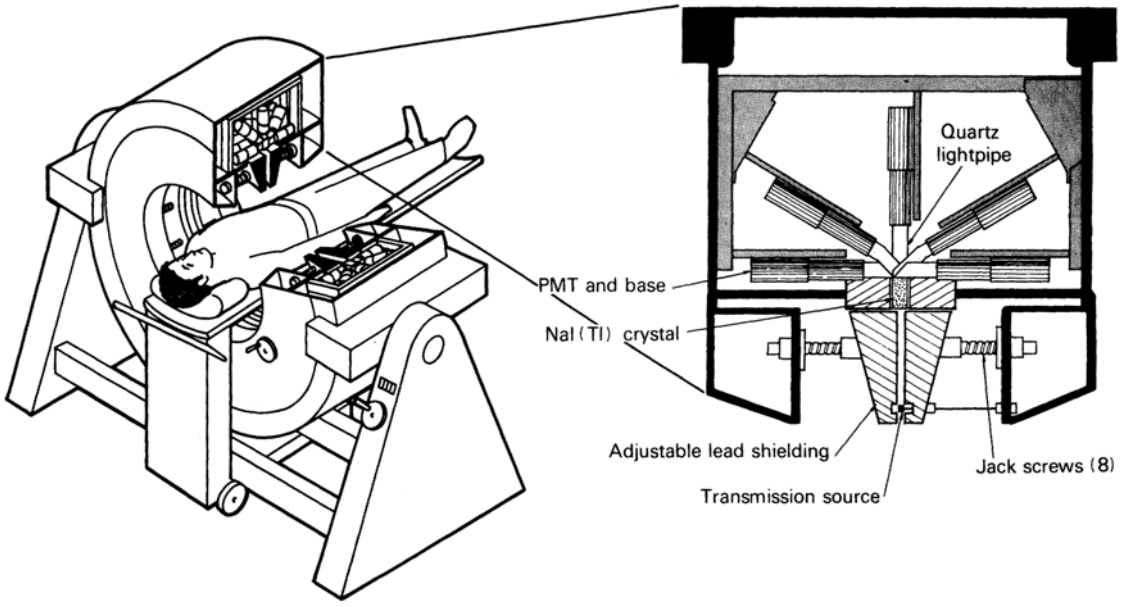

Figure 5.2: The Donner 280-crystal high-resolution positron tomograph built at the Donner Laboratory [260].

5.2 Development of the BGO Scintillator Tomograph

At this time, the limiting factors of using NaI(Tl) as the PET scintillator became apparent. Its hygroscopic nature made it difficult to work with and shape into custom geometries. Due to the sealing, few millimetre-sized crystal elements were impractical to produce. It was at this time that the first luminescence reports of bismuth germanate (BGO, $Bi_4Ge_3O_{12}$), a heavy-metal-containing crystal with an effective atomic number of 83, were published by Marvin J. Weber in 1973 [262]. In 1975, O. H. Nestor and C. Y. Huang further characterised BGO's scintillation properties describing it as non-hygroscopic as well as chemically and mechanically durable, directly suggesting its use in PET scanners [263]. Then in 1977, Z. H. Cho and M. R. Farukhi further analysed the BGO properties as applied to PET systems and compared it to the currently used NaI(Tl) [264]. The only problem with BGO was its relatively long decay time and poor light propagation (see Table 1.3). However, at the time, the pros immensely outweighed the cons.

As such, the first tomograph to use a BGO scintillator was constructed at the Montreal Neurological Institute by Chris J. Thompson, Y. L. Yamamoto, and E. Meyer as the Positome II in 1978. It was loosely based on the NaI(Tl)-based Positome I they developed from the failed BNL positron camera (see Section 4.5.1). The new scanner was based on a trapezoidal BGO crystal shape that was 3.0 cm tall and 3.0 cm deep but it was 1.8 cm wide on the inside of the ring and 2.2 cm wide on the outside of the ring. Each of these crystals was directly coupled to a 3/4-inch PMT with a dedicated amplification unit as shown in Figure 5.3. The whole ring tomograph was then formed of 64 of these detector modules separated by tungsten septa for a detector ring diameter of 42 cm. The system demonstrated excellent performance and efficiency which allowed for quicker patient processing and acquisitions of only 1 s per frame. The system was soon updated to the Positome III by the addition of a

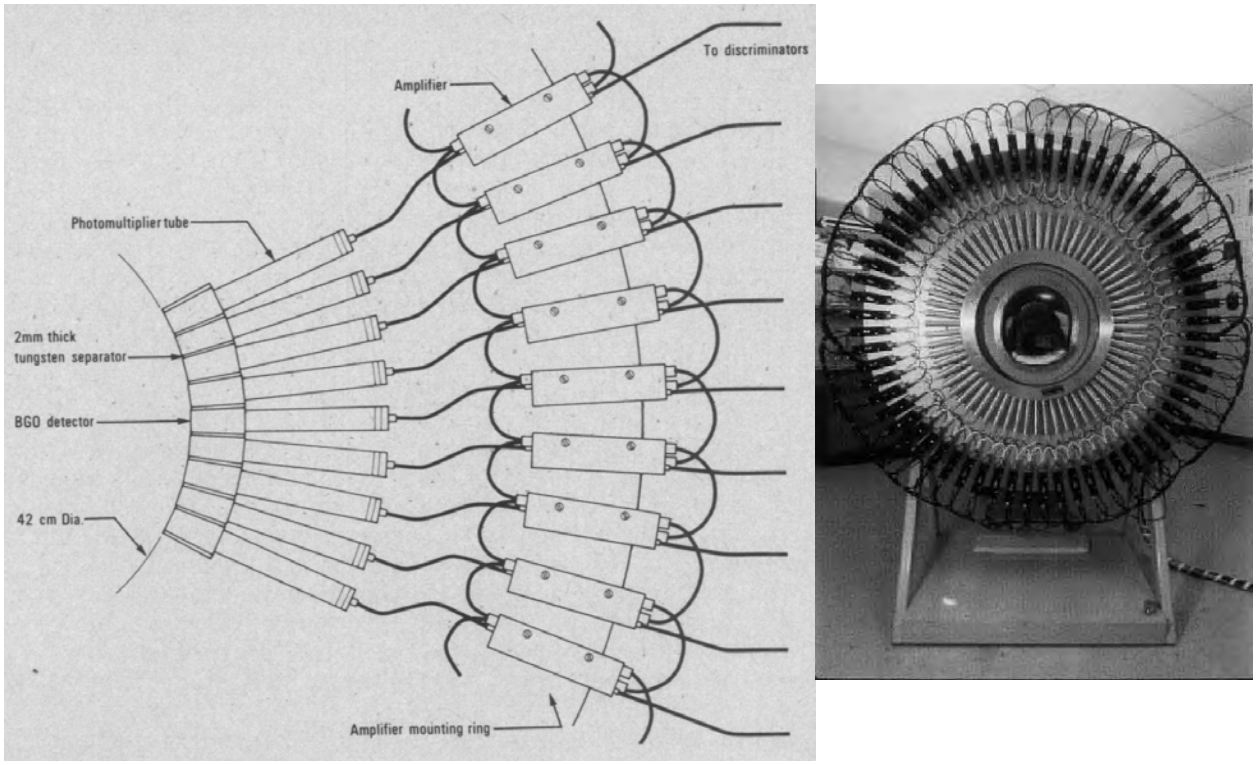

Figure 5.3: The Positome II system developed by C. J. Thompson et al. at the Montreal Neurological Institute. It used trapezoidal-shaped BGO scintillator blocks directly coupled to 3/4-inch PMTs and an amplification system for a 64-detector full-ring tomograph [244, 265].

second identical ring of detectors to produce a three-slice PET scanner [265].

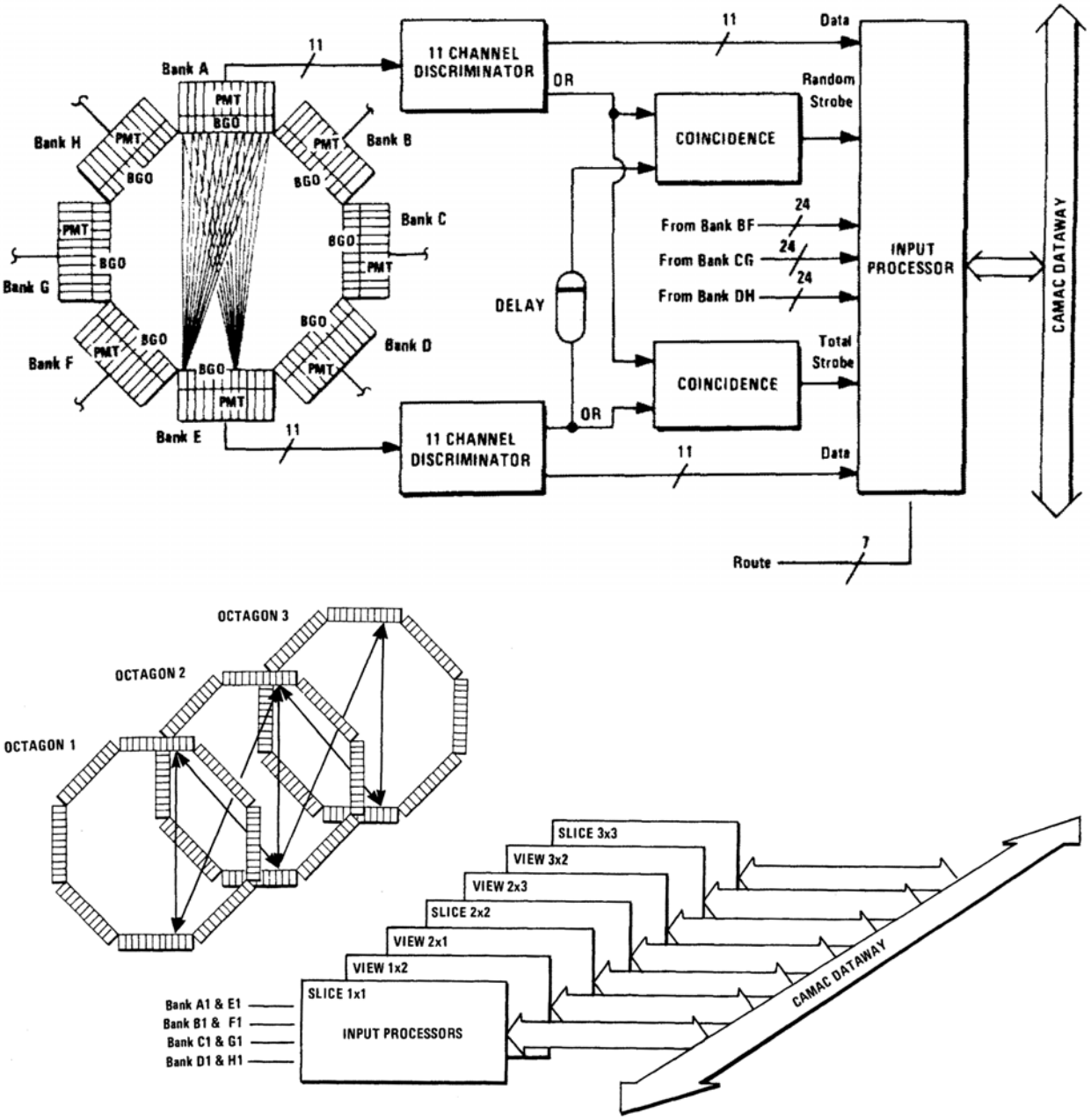

Figure 5.4: NeuroECAT system structure and data acquisition flow diagram. The top diagram shows the function block diagram for each ring or imaging plane while the bottom diagram shows how this functional unit is repeated to process all allowed coincidence pairs [266].

Concurrently as the Positome II was being developed, the group at UCLA developed NeuroECAT (model 828) [266, 267], the first commercial BGO PET scanner. It was a

smaller scanner with a 30 cm patient portal diameter designed for high-resolution and low-noise measurements of the adult head or a child's torso. The gantry was of an octagonal design with an internal diameter of 65 cm, eight linear banks of detectors, and three whole rings as a standard for a total of 264 detectors, as illustrated in Figure 5.4. Each linear bank of detectors contained 11 17 mm by 27 mm and 29 mm deep blocks of BGO individually coupled to 20 mm PMTs and separated by 3 mm thick lead shielding from one another. The whole gantry was able to tip/tilt 20° forwards and backwards to allow for optimal image plane positioning. To further remove noise and increase image resolution, the system featured shadow shields and interplane septa shown in Figure 5.5. Both of these could be individually engaged on demand by the user. The interplane septa were designed to remove unwanted scattered and random coincidences between the planes while the shadow shields were used to cover some of the exposed face area of the detectors to improve image resolution

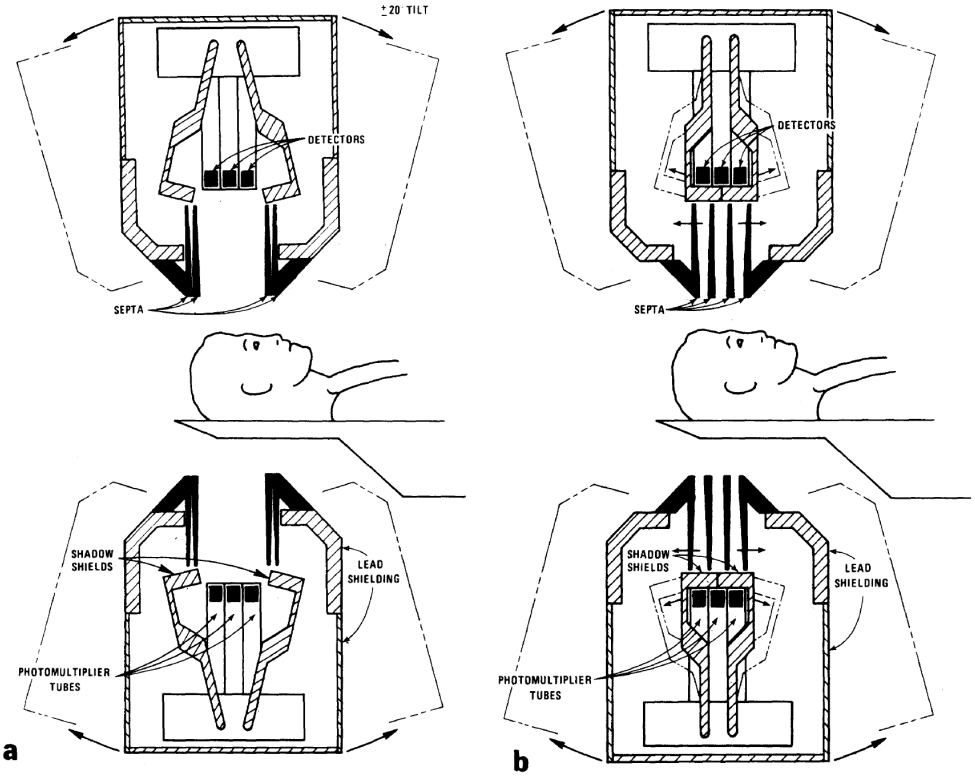

Figure 5.5: NeuroECAT in the high-sensitivity but low-resolution mode (a) and in the low-sensitivity but high-resolution mode [266].

at a cost of sensitivity. The scanner was able to achieve a 10.5 mm resolution without the shadow shields and 8 mm resolution with the shadow shields engaged. This scanner design solidified BGO's position as the main PET scintillator for the next two decades.

5.3 Foundation of CTI

By the 1980s, it had become clear that to properly use a PET scanner, a ready supply of short-lived PET isotopes is needed, a supply of which is mostly possible for clinics and hospitals with easy access to a cyclotron. To solve that problem, Phelps and some of his associates from EG&G ORTEC formed Computer Technology Imaging (CTI) Incorporated (Knoxville, Tennessee, USA) in 1983 intending to provide medical isotope-producing cyclotron systems and PET scanners as a package. In 1984, CTI acquired the ECAT trademark and technology from EG&G ORTEC and a large stake in The Cyclotron Corporation (TCC) (Berkeley, California, USA) which was on the brink of bankruptcy from producing large therapy cyclotrons. Edging TCC out of bankruptcy, in 1986, CTI acquired the rest of the company renaming it CTI Cyclotron Systems and started the development of the mini-cyclotron system known as the Radioisotope Delivery System (RDS). The RDS was designed for the on-site production of specific medical radioisotopes and the system is sold and marketed to date. That same year, CTI signed a partnership with Siemens Medical Systems Incorporated (Iselin, New Jersey, USA) to form CTI PET Systems (CPS) Incorporated (Knoxville, Tennessee, USA) where CTI, a 50.1% stock owner, would design and build PET systems that were then marketed and sold by Siemens around the world [268].

Following the partnership formation, they released their first full-body PET scanner an ECAT III (model 911). The design was started in 1983 under EG&G ORTEC by Phelps and Hoffman based on the NeuroECAT. The scanner now featured a single imaging plane

cylindrical geometry made up of 512 detectors divided into 16 banks of 32. The gantry had a patient portal diameter of 65 cm and a detector diameter of 100 cm. Each BGO crystal was 5.6 mm wide, 30 mm high, and 30 mm deep. This advancement increased the axial resolution of the system not only due to the smaller element width of 5.6 mm but also due to the 0.5 mm spacing between the crystal elements themselves. This was the first ECAT to feature the wobble function (see Section 6.4) to increase the system resolution. Without the wobble function, the scanner had a resolution between 5.5 mm and 6 mm and with the wobble enabled, the system had a resolution between 4.5 mm and 5 mm. Furthermore, the system incorporated dynamic data gating to acquire clear heart images at different pumping stages, list mode data acquisition for short periods of dynamic data acquisitions that then could be manipulated by the user, a 125 MHz main system clock, and a first gantry consisting of custom-made digital electronics going away from the standardised NIM and CAMAC modules [13, 269]. These digital electronics would also be used in some of the later scanners as discussed in Section 7.1. The scanner also came equipped with an updated DEC VAX-11/780 computer for data acquisition and scanner control. It was available in one- to four-ring geometries but it quickly became evident that using a one-to-one crystal to PMT coupling effectively doubled the system cost with each additional ring and made the system excessively large. This became a problem for many clients who could not afford a system this expensive and limited the crystal size to the smallest available PMT [270, 271].

Therefore, CTI set out to develop a method which would decrease the number of electronic data channels while increasing the number of individual crystals and decreasing their size. Another important consideration for their new design was decreasing the scan time by increasing the axial FOV of the system. This would ultimately decrease a patient's dose.

5.4 Analogue Coding

At this moment in time, the group at MGH has started to develop their new series of positron cameras. Brownell and Burnham et al. set to develop their high-resolution cylindrical scanner. However, seeing the same drawback of using a direct crystal-to-PMT coupling, they started to study ways of multiplexing the crystals to a small array of PMTs. Therefore, in 1979, Burnham et al. patented the analogue coding method. This method involved using an array of discrete scintillator crystals but coupling them to a singular light guide spanning the whole circumference of the scanner. This light guide was then viewed by fewer, larger PMTs than the crystal elements themselves, as shown in Figure 5.6. Anger-like logic (see Section 4.2.4) was then used to determine which crystal element the interaction occurred in [272, 273].

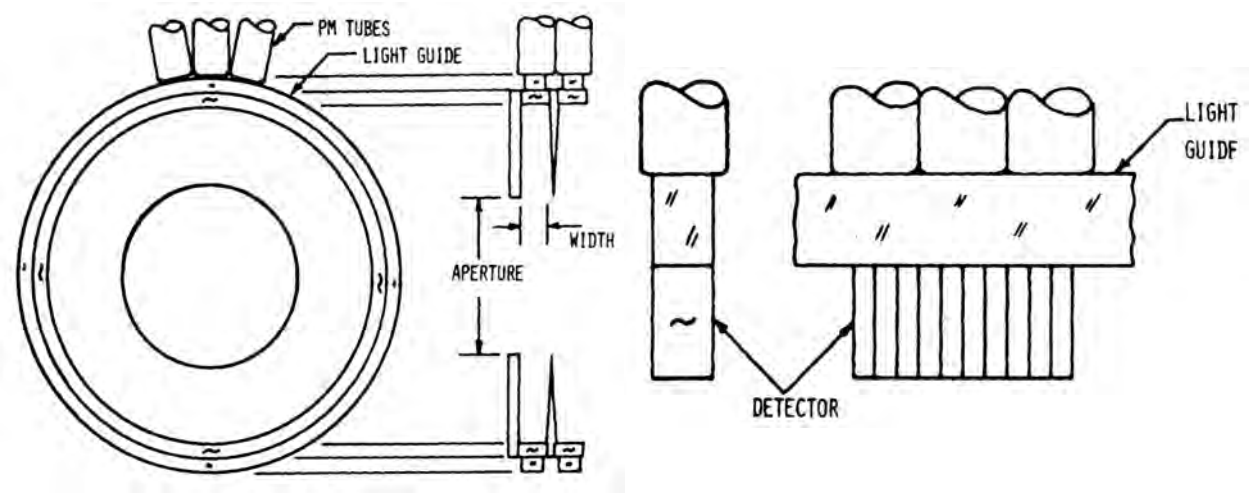

Figure 5.6: Burnham et al. developed the analogue coding technique at MGH which utilised a continuous, solid light guide that coupled many small detector crystals to a smaller amount of bigger PMTs. The crystal in which the interaction occurred was then identified using Anger-like light-sharing logic [272].

Following Monte Carlo simulations and small-scale tests, the group built a single-ring scanner called the PCR-I (Positron Camera Ring Tomograph) using the analogue coding technique, shown in Figure 5.7. The scanner was made out of 360 BGO 2-cm-high by 3-

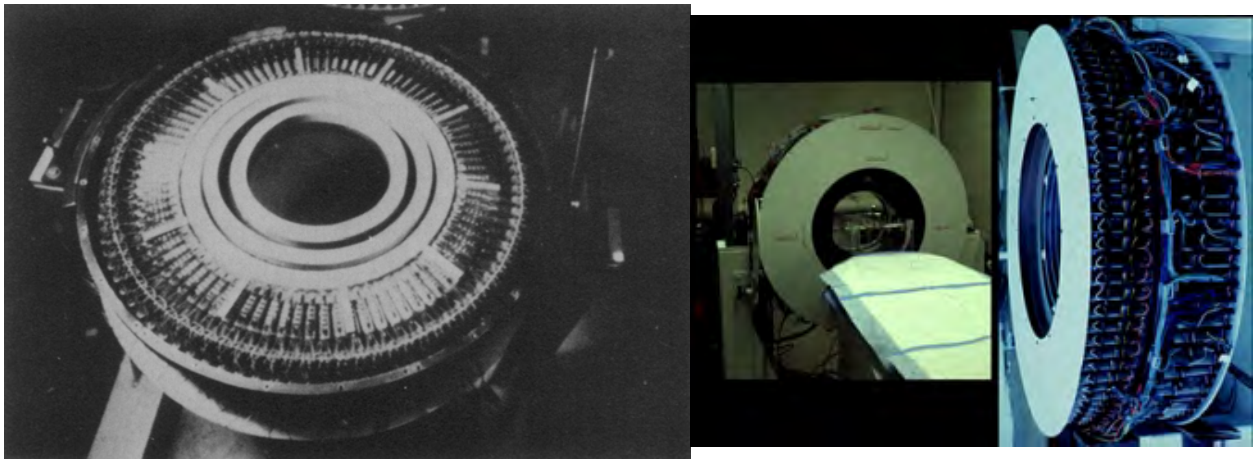

Figure 5.7: The PCR-I tomograph during the assembly showing the various concentric layers of the scanner and then as assembled and used at MGH [221, 274].

cm-long and tapered from 0.45-cm- to 0.4-cm-wide trapezoidal crystals. The crystals were coupled to a 0.9-cm-thick and 1.6-cm-wide solid Lucide light guide ring which was then

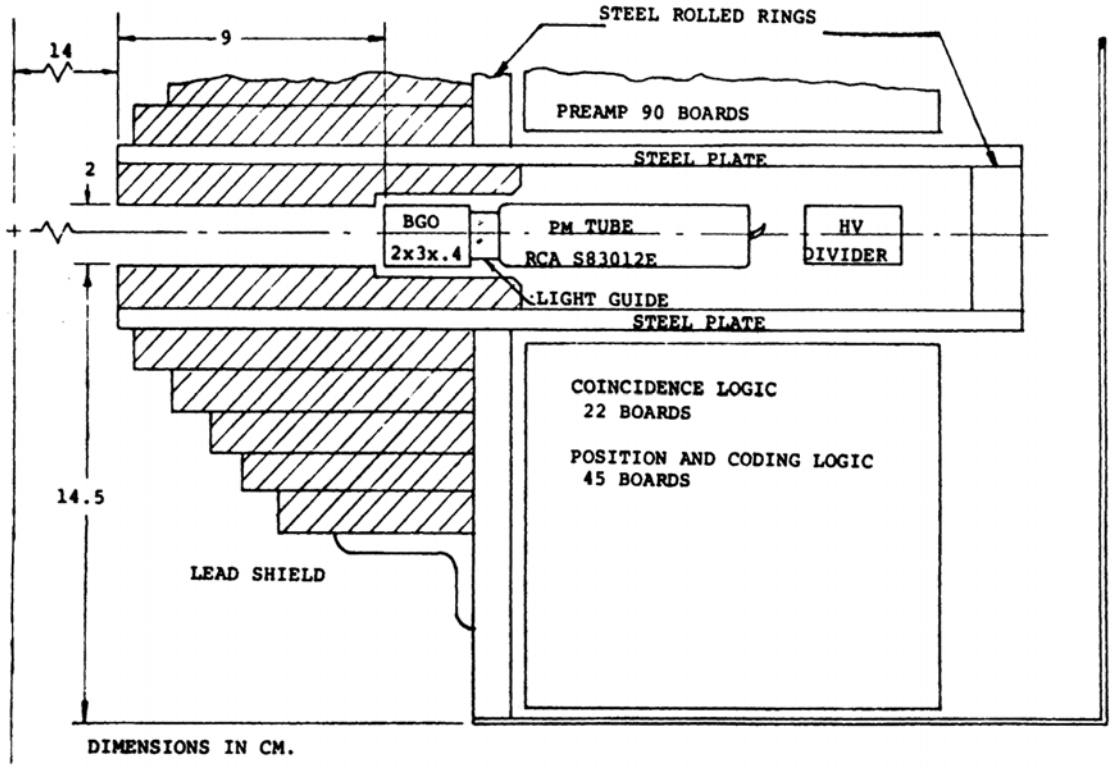

Figure 5.8: The cutaway view of the PCR-I displaying the BGO scintillator coupled to the PMT through the Lucide light guide alongside heavy lead shielding and the ring support frame [274].

viewed by 90 2-cm-diameter PMTs, as shown in Figure 5.8. This whole assembly created a tomograph with a detector diameter of 46 cm. To locate the crystal in which an interaction occurred, signals from adjacent PMTs in the ring were used which resulted in a 4.8 mm special resolution for the system [274, 275]. This analogue coding design was later developed into the PCR-II, also known as the MGH Cylindrical PET, shown in Figure 5.9 by around 1992. The PCR-II used a cylindrical design made out of 3 mm by 5.7 mm and 30-mm-deep BGO scintillator elements arranged in 20 rings of 640 elements for a total of 12,800 crystal elements in the whole scanner. This array was then coupled using a continuous light guide to a hexagonal array of 1,760 1/2-inch PMTs mounted in small subblocks shown in Figure 5.10. The final scanner created a cylindrical tomograph 60 cm in diameter and 11.5-cm-wide [275–278].

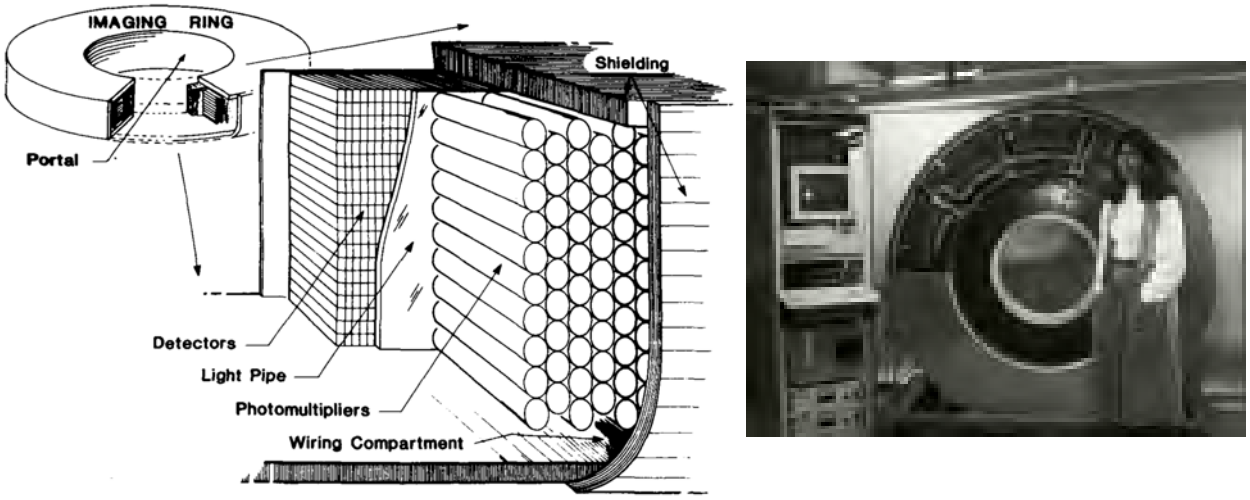

Figure 5.9: (Left) A cutaway view of the PCR-II or MGH Cylindrical PET displaying the 20 rows of BGO detector elements coupled via a light guide to a hexagonal array of PMTs [279]. (Right) The PCR-II in the late stages of development at MGH [221].

With the state-of-the-art development in PET tomographs occurring at MGH, Casey and Nutt of CTI visited the Physics Research Laboratory in 1984. They concluded that while the technique was very promising, it would be expensive and difficult to manufacture. Knowing that they needed to use a similar principle to multiplex their detector assemblies but in an easy-to-manufacture form, they developed the detector block system in 1986, forever

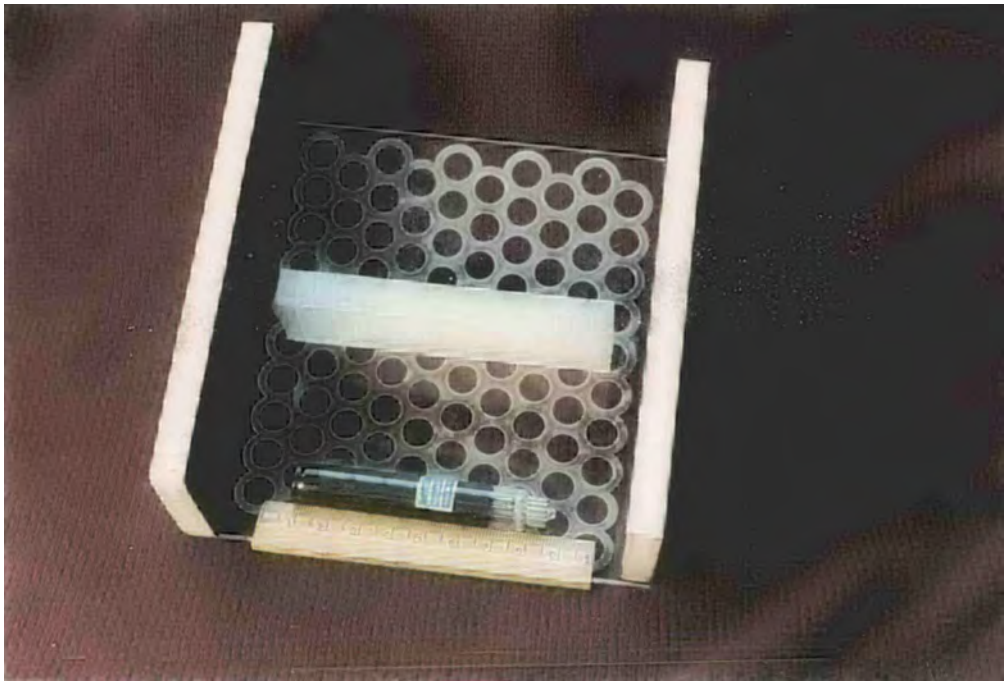

Figure 5.10: A subsection of the PCR-II showing the curved light guide with machined index locations for the 1/2-inch PMTs one of which is shown by the wooden ruler. The white bar in the centre is an 18x4 array of BGO crystal elements to be mounted [279].

changing the PET scanner architecture [225, 244, 280].

5.5 Development of the Detector Block

From the research done by Anger on his camera, it was well established that when an interaction occurs in a scintillator block viewed by many PMTs, the light intensity (i.e. the number of scintillation photons which is proportional to the energy measured) will vary across the neighbouring PMTs. Light intensity will be the strongest in the closest PMT and the weakest in the furthest PMT due to light propagation within the crystal and the light guide. This difference in the number of photons collected by each PMT (i.e. the charge/current produced by the PMT, signal) can then be used to pinpoint the location of the interaction. With this idea in mind, experiments with a fully segmented BGO scintillator

block coupled to a normal light guide and four PMTs had shown that the crystal element in which the interaction occurred could be identified by the unique signal signature it produced across all the PMTs. The problem with this approach was that the effect was very subtle as the light was allowed to propagate uncontrollably in the light guide leading to a blurring effect [281, 282]. Furthermore, the PMT gain drift due to its age and differences in the manufacturing would constantly change the signal output requiring the signature to be often experimentally calibrated; a very slow and possibly costly endeavour. Following this research, Casey and Nutt developed a novel slotted light guide that would in turn limit in a controllable manner, the scattering of light, producing a more well-defined distribution. This effect is demonstrated in Figure 5.11 [280, 283].

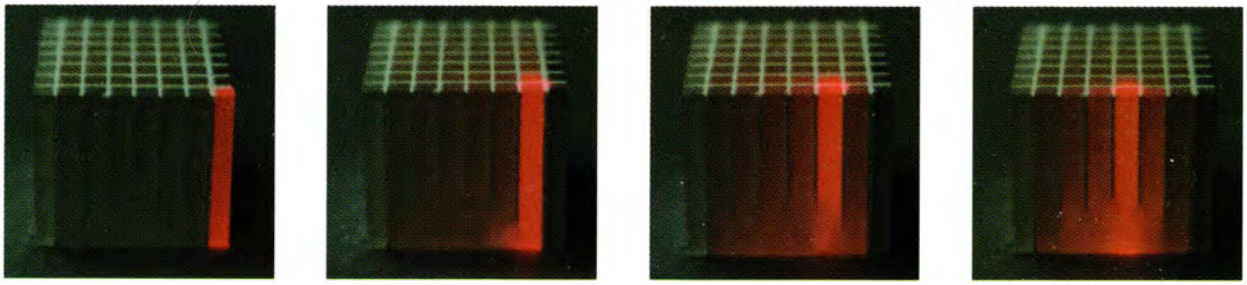

Figure 5.11: An idealised demonstration of the light distribution in a variably slotted BGO detector block design. The crystal is lit using a red laser for the demonstration. As can be seen, the variable slotting is designed to allow more light to be propagated through the crystal the closer the crystal element is to the centre of the array. Going from left to right, the edge crystal element almost exclusively deposits all of its photons in the PMT right below it. The next crystal element over allows a bit of its photons to escape and be picked up by the adjacent PMT. The next crystal element allows even more of its light to be shared. The most central crystal element almost equally shares all of its light, with the PMT under it receiving just a bit more of it. See Figure 5.12 for the PMT positions. Note: The block shown is of the updated design with 64 crystal elements while the original design only contained 32 crystal elements. [284].

The detector block itself, shown in Figure 5.12, was made up of an 8x4 array of light-isolated BGO scintillator crystal elements 5.6-mm-wide by 13.5-mm-high and 30-mm-deep. The crystal was coupled to a Lucite light guide segmented into the same grid as the crystal. However, the light guide was slotted to various depths with the slots closest to the outside

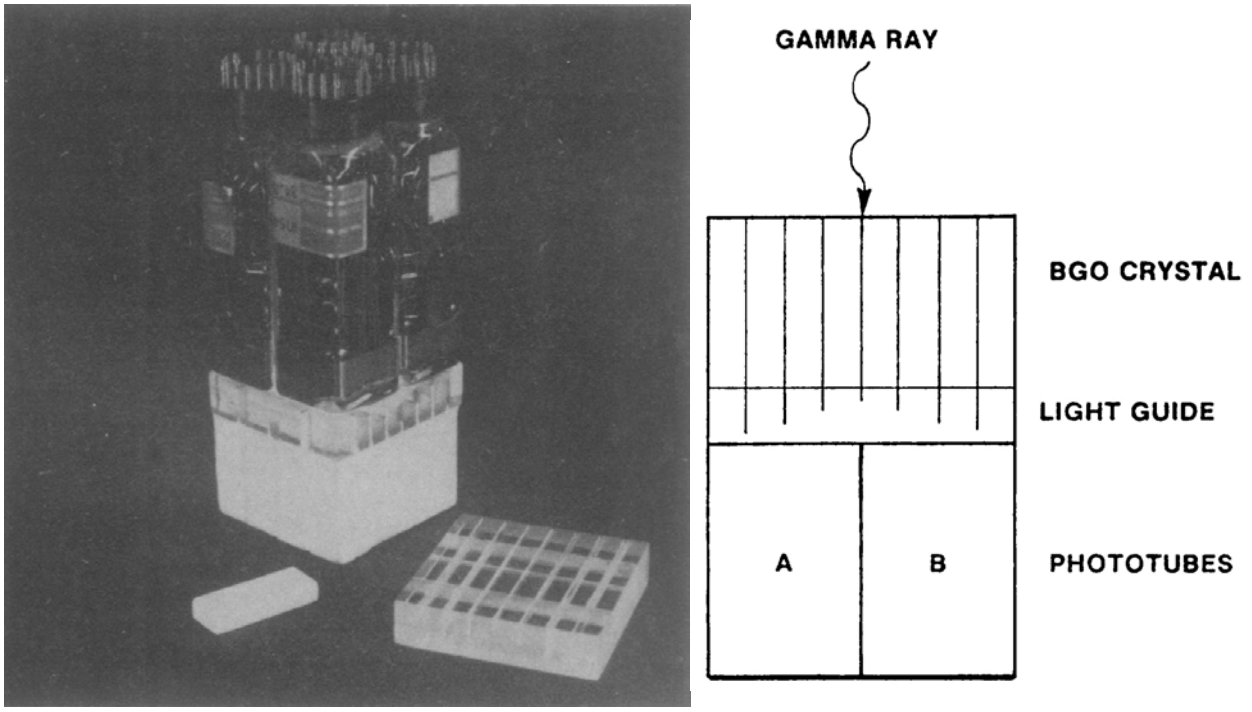

Figure 5.12: The original detector block design by Casey and Nutt. This detector block design features the fully segmented BGO scintillator block and the variably-slotted light guide [280].

of the block being the deepest and the ones in the centre being the shallowest. The slots were then filled with a light-isolating compound. This light guide was then bonded with clear epoxy to four PMTs and the whole assembly was placed in a metal can and filled with self-vulcanising rubber compound for stability. A small circuit containing the voltage divider for proper biasing of the PMT was then attached to each of the PMTs. With this system under study, they discovered that the ratio of light photons collected by one PMT and another in the system is simply dependent on the probability that a photon will be collected. However, this probability of photon collection while in theory should be the same for each PMT of the same design, varies sometimes substantially due to manufacturing differences and quality. Therefore, normalising the signal ratios between pairs of PMTs by the total signal intensity recorded by the four PMTs can be used to identify the crystal element in which the interaction occurred independent of any small variations in the system. For the system to produce statistically accurate and reproducible results, the time the event/interaction

occurred and the total charge/current from each of the tubes would have to be accurately measured [280, 283].

The creation and measurement of the fast timing and slow energy signals were achieved through the use of fast pre-amplifiers and gated integrators. The fast pre-amplifiers produced a fast-timing signal for each of the PMTs that were then summed together and sent to a constant fraction discriminator (CFD). The CFD produced a statistically accurate, walk-free time mark for the system. The gated integrators were then triggered by the CFD signal to sum the charge produced by each of the PMTs, producing the slow energy signal. The length of the integration was controlled by a set timer triggered by the CFD pulse. The slow energy signal was then adjusted by a multiplying digital-to-analogue converter (DAC) effectively setting the gain for each of the tubes. The digital inputs were set by a microcontroller as determined during a simple calibration procedure. This ability to vary the gain would ensure that the light-to-charge ratio was equal for each of the four tubes in the block, correcting for any tube drift over time [280].

All the energy signals were then summed to produce the total energy signal used for the normalisation of the ratios and the scatter test. Finally, the energy signals from two adjacent tubes in a column were summed to produce the transaxial energy signal and two adjacent tubes in a row were summed to produce the axial energy signal. The total energy signal was then digitised against a set reference value using a flash analogue to digital converter (ADC) and the two positional energy signals were digitised against the total energy signal used as a reference. A lookup table was used into which the two positional signals were fed and a digitised crystal element number was given. As these were signal ratios, the lookup table would only have to be made once for a particular block design when prototyping the system. Using this signal processing design, Casey and Nutt were able to narrow 32 crystal elements into only four signal channels, greatly decreasing the amount of electronics and allowing the use of crystal elements smaller than a PMT [280].

With the discovery of BGO as a good PET scintillator, at the time, the physical limitations of NaI(Tl) were suddenly gone. BGO can be cut into any size imaginable and, due to not being affected by moisture, it does not have to be hermetically sealed. As the Positome II had demonstrated BGO use in a PET scanner architecture, the NeuroECAT became the first production BGO PET scanner which cemented BGO's use in PET scanners for the next few decades. With the growing demand for PET scanners, CTI was formed as a separate entity to the research-based EG&G ORTEC and released the ground-breaking ECAT III, a commercial production BGO-based full-body scanner which began using custom-made digital electronics going away from the standard NIM and CAMAC modules. Finally, as it became clear that by using more and ever smaller crystal elements in a scanner, it greatly increases the amount and complexity of electronics needed to process the coincidence data. Therefore, CTI developed the detector block based on the ideas of analogue coding they observed used in the MGH's PC-I and PCR-I systems. With their patented detector block concept, CTI began to develop ever complex PET scanners each bringing new advancements in electronics and detector technology.

Chapter Six

Generalised Design of the ECAT System

In this section, a discussion of the functionality of the CTI-produced BGO-based ECAT systems will be undertaken. Parts of various scanners, discussed in detail in Section 7, were made available to me through the Positron Imaging Centre (PIC) and parts thereof were used in some way to develop the PEPT systems (Sections 8 and 9) during my research PhD. While electronic technology advancements through the decades of PET scanners represented here vary greatly, the overall concepts down to the ways these systems communicate mostly remained unchanged. This section will focus on the detectors, data acquisition, and processing parts of the scanners.

Overall, the ECAT system can be broken down into two subsystems: data acquisition & handling, and gantry control. Gantry control systems are only discussed partially as they are unimportant in the PEPT systems; only data acquisition and handling will be explained in detail. This subsystem consists of the bucket assembly containing the detectors and positioning logic, the coincidence processor testing for coincidences in the system, the Advanced Computational System (ACS) for saving and manipulating the raw data into images, and the clock generator for orchestrating the whole system. An operator's console computer is also discussed briefly as that is where the user would normally interact with the

scanner. An idealised block diagram of the ECAT system data and communication lines is shown in Figure 6.1.

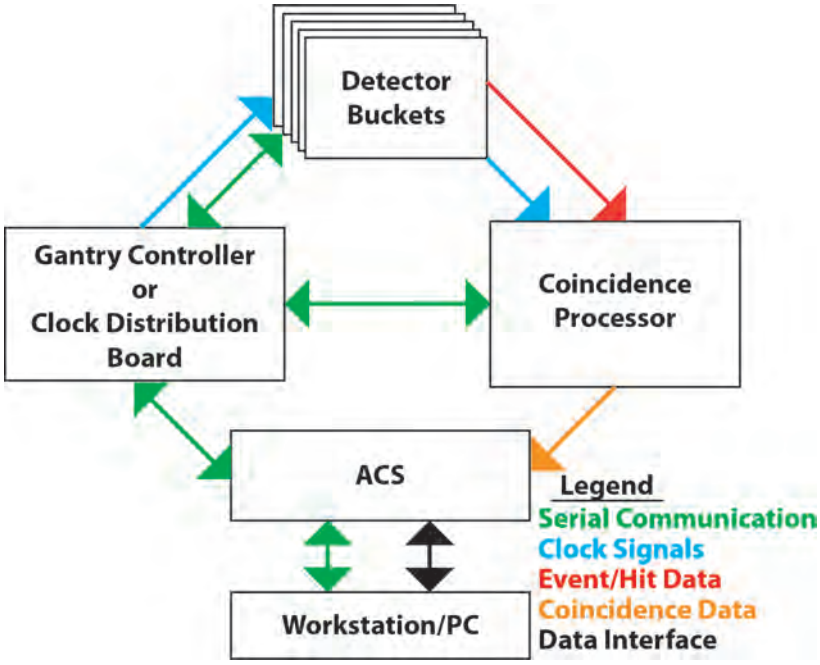

Figure 6.1: The ECAT system data and communication flow block diagram. The diagram does not include any quality-of-life systems such as patient handling, safety, and gantry control.

6.1 The Bucket

The bucket is the term used to describe the smallest assembly of detector electronics in the system which handles detector control, communication, and position, time, and energy processing. Each assembly typically supports four detector blocks in the early systems and twelve detector blocks in the later systems. The bucket receives a 3.90625 MHz (256 ns period) master clock signal (often referred to as 4 MHz), a 62.5 MHz (16 ns period) 16 ns clock signal, and serial communication data in and out over four twisted-pair differential emitter-coupled logic (ECL) connections from the gantry controller/clock generator. Each assembly also receives 5 V and −5.2 V logic power supplies, 1500 V for PMT bias, and a

system common ground from the main power bus of the scanner. The assembly distributes the high-voltage (HV) bias and receives signal pulses back through a four-pin connector leading to each PMT in each of the detector blocks. One of the pins is blanked over to provide extra separation of the HV line from the signal line and as an indexing pin to prevent any wrong connections.

Each detector block has an independent analogue processing section that produces the energy signals required for the crystal identification and a CFD time mark for time calculation, as discussed in Section 5.5. The data from the analogue section are then passed to the digital section which digitises the energy signals, uses them to determine the hit crystal element, determines the type of interaction, digitises the time of interaction as an offset from a master clock pulse, and stages the data for arbitration and sending to the coincidence processor. All of the bucket's functions are controlled by a microcontroller and a re-programmable sequencer located on the main bucket controller board. The microcontroller is responsible for mode selection, self-testing and diagnosis, calibration data management, event type statistics tracking, and receiving and sending commands and diagnostic data over the serial communication lines.

6.1.1 The Detector Block

As stated before, the detector block is the fundamental element of the ECAT system. The version of the detector block described by Casey and Nutt in their pioneering paper was only used on the ECAT 931 series of scanners [280]. This was also the only series of detector blocks to have a four axial by eight transaxial segmented BGO scintillator and to be available in three different crystal element axial sizes (see Section 7.1). All the detector blocks produced since have an 8x8 segmented BGO scintillator and are only available in a single crystal element size per scanner. However, the biggest change incorporated was the removal of the

light guide. Now, the crystal itself serves as the light guide and is slotted to varying depths. There are no sources of information on why that was done but most likely the loss of photons at the boundary between the scintillator and light guide was significant. Every photon that reaches the PMT and produces a signal increases the accuracy of correctly determining the right crystal element. CTI did submit a new patent for the block without the separate light guide only half a year after the original patent in 1985 [283, 285]. The two versions of the detector block are shown below in Figure 6.2 [280].

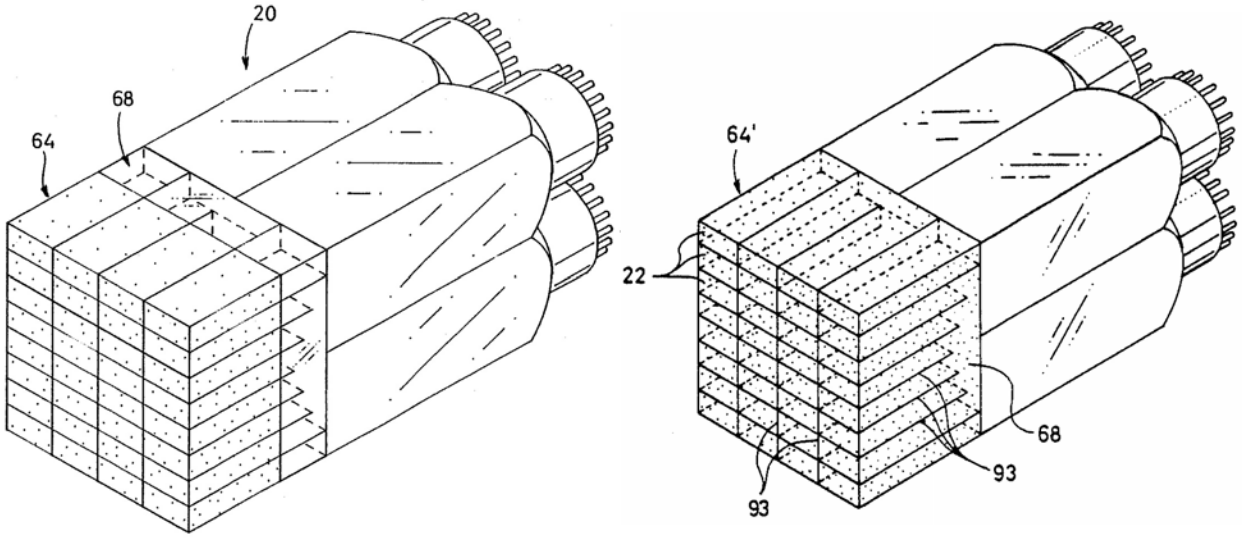

Figure 6.2: Comparison of the drawing of the two versions of the detector block. On the left is the first version utilising a separate light guide to distribute the scintillation photons to the PMTs and on the right is the later version without the separate light guide [283, 285].

The crystal is sliced such that the grove produced by the saw is around 0.5-mm-wide and then filled in with an unknown, white, powder-like reflector material, most likely a Teflon-based compound. The crystal array is then permanently bonded to four square PMTs with square photocathodes each with their high voltage biasing circuit and a short four-pin lead for HV bias, signal output, and common ground. This whole assembly is then placed in a thin, wedge-shaped aluminium casing and filled with a self-vulcanising rubber compound. The front of the crystal is covered to prevent ambient light from entering the assembly. This was initially done with pieces of glued-on flexible rubber padding but evolved into the use

of hard, thin carbon fibre composites. An important detail to mention is that the crystal elements on the edge of the matrix are thinner by about 0.3 mm. This is done to keep the crystal pitch the same between adjacent blocks while making space for the aluminium housing and potting compound.

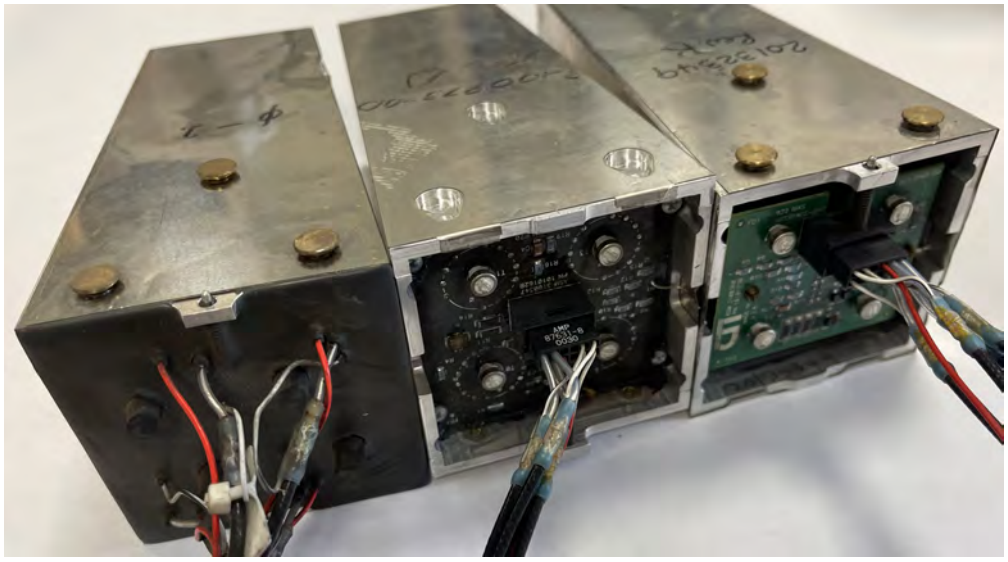

Figure 6.3: The evolution of the HV and signal distribution board in the ECAT EXACT series of detector blocks. Left to right: An early detector block design with a fully potted board. A detector block with an exposed board and removable leads. The latest ECAT EXACT detector block with a removable board and leads.

The biggest issue with the design of the detector block is that the HV biasing circuit is also potted under the rubber compound. While it does provide an extra layer of security to the circuit, it makes any repair extremely hard to perform due to the difficulty in removal of that compound. Normally that would not be a problem but the highest mode of failure in the whole ECAT system is the burning out of the HV resistors and capacitors which in this instance render the whole block useless. CTI addressed this issue in the ECAT EXACT series of detector blocks by placing the circuit on a small, removable, external board that slots in at the back of the detector block. The design progression can be seen in Figure 6.3 where the first block is fully potted, the second one has an exposed board which is not removable, and the final block has a fully removable board. This design also unified the HV

supply for the block to a single connector where before each lead had its own HV cable. This advancement finally allowed the replacement of the small board, saving the expensive crystal and PMT array or the cost of block refurbishment.

When assembling the system, it is most important to know how to connect the four PMT leads to the bucket. As shown in Figure 6.4 left, all CTI four-PMT-based detector blocks follow this PMT numbering scheme. While it does not matter if the block is right side up or upside down, the PMTs need to be connected to the bucket in that order for the logic to produce crystal element position data that matches the physical position of the detector block.

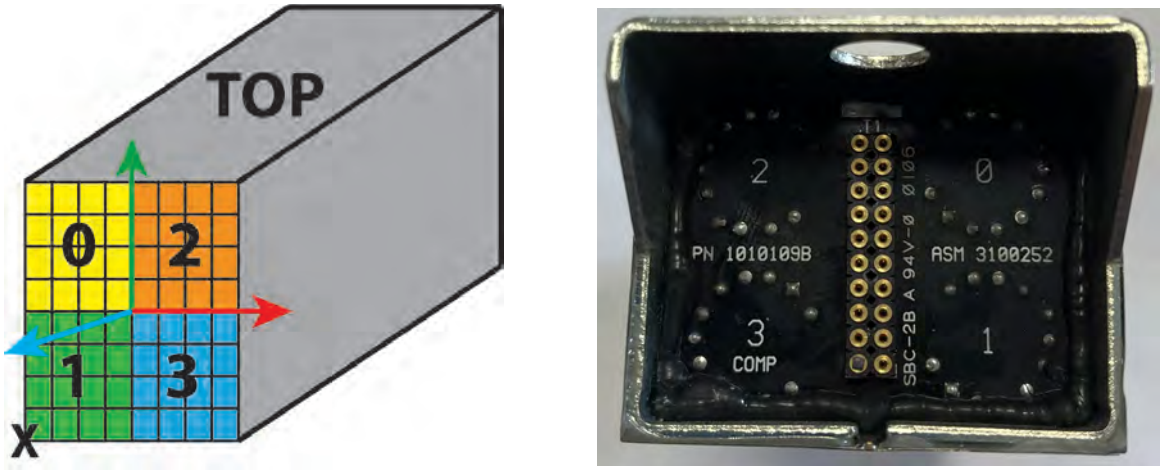

Figure 6.4: Left: A generalised front view of the detector block showing the PMT numbering scheme. The X in the lower left corner denotes the origin of the detector block as described by the systems where the 0 crystal element row and 0 crystal element column will always be located, increasing in count up and to the right, respectively. The axis corresponds to the centre of the detector block face where red is the +x-axis, green is the +y-axis, and blue is the +z-axis. This is the origin of the block as referenced in data processing in PEPT (see Section 8.3.2). Right: Back view of an ECAT EXACT HR+ detector block showing the PMT numbers noted on the back. They can also sometimes be found written on the individual PMT leads in older detector blocks.

6.1.2 The Analogue Processing Section

The analogue section design of the bucket, as shown in Figure 6.5, has not changed much over the whole ECAT series. No matter what technology the circuit is implemented in, the same signal flow is still represented. One trait of this section is that it is implemented on a separate PCB from the rest of the bucket controller and that it is repeated for each block in the bucket. This circuit directly receives the charge pulse from the anode of each of the PMTs which is immediately passed to a fast variable gain preamplifier. The gain of the amplifier is set by a DAC whose value is set on startup by the microcontroller as listed in its memory. This so-called fast signal produced by the pre-amplifier is then used by various sections of this circuit. In later models, it feeds an Op-Amp-based baseline restore circuit which feeds back into the pre-amplifier and ensures any DC offset is minimised before signal processing occurs. This function is disabled and the correction factor is held constant when an event is detected by the CFD to prevent any corrections from occurring during the signal integration stage.

The fast signal from all four tubes is summed by an RC summing circuit and is fed into a CFD. The CFD provides a walk-free, statistically repeatable timing signal that is then passed to the digital section and is also used to signal the start of the integration to the gated integrators. Then, the fast signal for each of the tubes is passed to the gated integrators that will produce the slow, energy signal. As mentioned above, the start of the integration is signalled by the CFD pulse and it is terminated after a set time by the sequencer located on the bucket controller board. The CFD threshold, just like the pre-amplifier gain, is set by a DAC whose value is set by the microcontroller at startup from a value stored in its memory. The slow energy signals are then summed together to produce a total block energy signal and the energy signals from tubes 0 and 1 and tubes 0 and 2 are summed to produce the transaxial and axial energy signals, see Figure 6.5. The energy signals are then latched into

three six-bit flash ADCs. The total energy is digitised referenced to a set voltage level and the axial and transaxial energies are digitised referenced to the total energy signal, producing the required signal ratios as a digital value. These digital values and the CFD signal are then passed to the energy and position processing section.

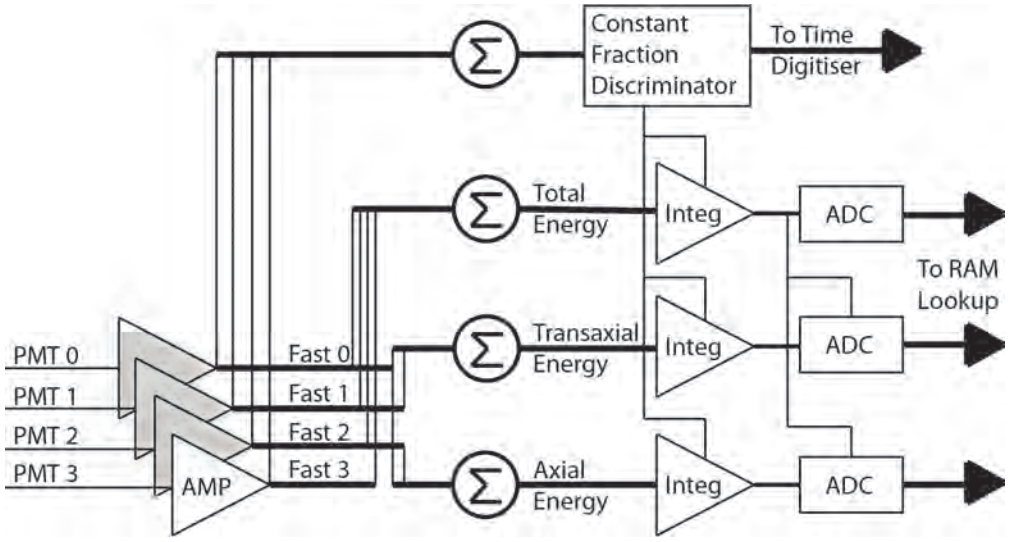

Figure 6.5: The idealised analogue processor block diagram. The analogue section receives the four PMT signals and produces a CFD timing mark and three energy signals used in the energy and position processing section.

6.1.3 The Energy and Position Processing Section

The energy and position processing section which is also known as the digital section of the bucket is where the time and the actual crystal element in which the interaction occurred are determined through the data path shown in Figure 6.6. Most importantly, the time the interaction occurred is calculated with respect to the master clock pulse. The clocking/synchronisation of the ECAT system is one of the areas that remained the same from the ECAT 931 to ECAT EXACT HR+. The two clock signals governing the system are all produced from a single 125 MHz oscillator which is part of the gantry control system. There the signal is divided to produce the 16 ns clock and the master clock signals which are then distributed to each bucket controller through equal-length cables. The bucket controller uses these sig-

nals to produce other signals the board requires, including a 31.25 MHz (32 ns period) 32 ns clock signal used for serialising 8 bits of data in a single master clock cycle.

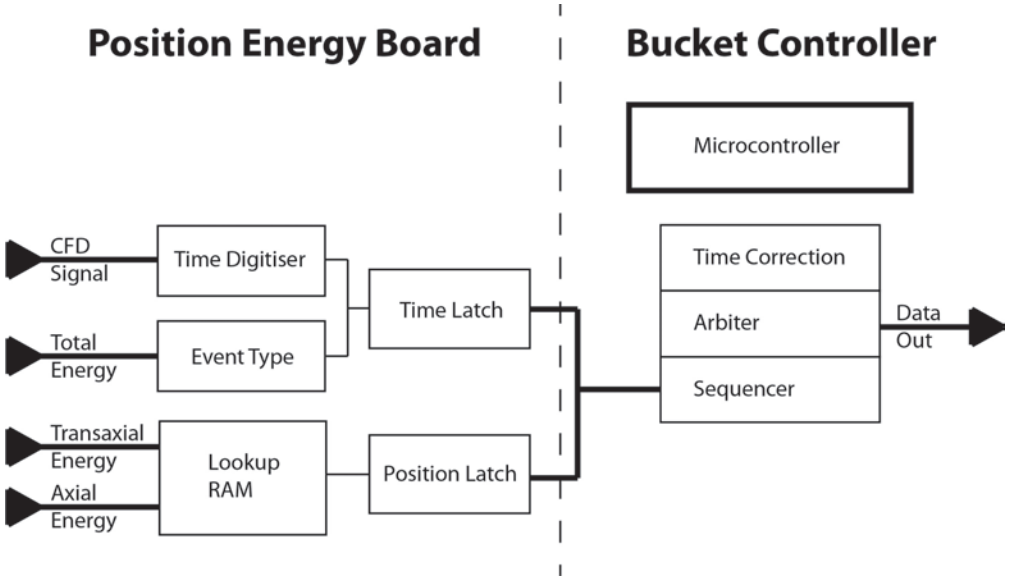

Figure 6.6: A block diagram of the digital part of the bucket data processing pipeline and the bucket controller. This section accepts data from the analogue processor section shown in Figure 6.5.

The time digitizer passes the CFD signal through a 2 ns segmented delay line whose outputs are sampled by a buffer every 16 ns clock cycle. If any of the outputs are high, the output is latched preventing successive clock pulses from clearing the value. Also, that same signal starts a count of the successive 16 ns clock pulses until the next master clock cycle passes the time information further down the processing timeline and clears the system for another hit to occur.

The digitised axial and transaxial energy ratios are passed to a random-access memory (RAM) based lookup table producing a binary word describing the crystal position in the block. The lookup table itself is loaded from the microcontroller memory on startup and can be modified during detector calibration procedures. The only exception to this lookup table system is the ECAT 931 series of scanners that have the lookup table set at the factory in a programmable array logic (PAL) chip, see Section 7.1. Next, the total energy value is tested

against a set of lower and upper energy discriminator values as well as the scatter energy limit which determines if a valid energy or a scattered/low-energy event had occurred. With the positional, timing, and energy data processed, they are ready to be transferred to the bucket controller so an event-ready flag is raised if a valid energy or a scatter event has occurred. If a scatter event occurs, a low-energy flag is also raised which will be passed down to the coincidence processor with the rest of the data in the next section.

6.1.4 The Bucket Controller

The bucket controller is the main orchestrator of all the data-processing steps in a bucket and consists of a microcontroller and various PAL and generic array logic (GAL) chips for handling and sequencing the data. The microcontroller handles the boot sequence, bucket mode selection, calibration data acquisition, memory handling, diagnostic data tracking, event count statistics, sequencer programming, and serial communication. It has access to an erasable programmable read-only memory (EPROM), electronically erasable programmable read-only memory (EEPROM), and static random-access memory (SRAM). The EPROM is usually only accessed at startup and contains the bootstrap code, serial communication program, various boot time self-tests, and an EEPROM cyclic redundancy check (CRC) code. The EEPROM contains the actual microcontroller firmware which can be updated over the serial communication line, the PMT gain values, the energy discriminator settings, the crystal position lookup tables which are uploaded to the energy position sections of the bucket at boot, and any other changeable bucket setting. The SRAM is used to store various run-time statistics, bucket statistics, and calibration histograms when calibration is being performed. The serial address of the bucket is physically set using DIP switches located on the board itself which is only used for addressing the board over serial communication.

The 16 ns clock signal, the master clock signal, and the serial-in and -out signals

arrive from the gantry controller/clock distribution board and are immediately converted into transistor-transistor logic (TTL) format. The clock signals are further divided and distributed throughout all parts of the board including the sequencer. The sequencer is a GAL chip that is programmed by the microcontroller and organises the data processing stages of the bucket. During normal operation mode, the sequencer passes the data through all the stages of digitising the energy and time signals, decoding the crystal position, and finally sending those data to the coincidence processor where the bucket microcontroller never touches the energy and position data. In other modes of operation like during the position or energy histogram acquisition, the sequencer directs the digitised energy values before they are used in a lookup table straight to the microcontroller which bins them into a histogram and then sends the data back over the serial communication line to be used for calibration, diagnosis, etc. The sequencer is also assisted by an arbiter chip which in case of multiple subsections/detector blocks registering an event concurrently, randomly selects which event to choose for further processing.

With an event selected and given the go-ahead to be passed on to the coincidence processor, a final time correction is applied to the calculated time value. The correction value is recalled from the EEPROM and it can be set in 2 ns increments for each crystal element individually or during calibration. This correction is implemented to further compensate for any variations in PMTs, data path clock skew, and pre-amplifier time skew. The block number from which the event originated is also added to the positional data. Finally, the time and position data along with some other status bits are latched into 8-bit TTL serialisers. The TTL signal is then converted into differential ECL and sent over equal-length twisted-pair cable to the coincidence processor. The master clock signal and the 32 ns clock signal produced by the bucket controller board are also converted to differential ECL and sent over twisted-pair cables to the coincidence processor for coincidence processor synchronisation. The data, when available, can only be sent to the coincidence processor once every master

clock cycle effectively limiting the throughput of each bucket to 3.90625 million events per second or once every 256 ns.

The microcontroller also collects single count rates based on the flags raised by each of the energy processing subsections. The uncorrected singles are counted when any of the event request flags are raised, even concurrently. This count does not account for any events lost due to the reset of the detector electronics (dead time) but accounts for all single events even those that happened in multiples. Then the corrected singles rate is a statistically calculated rate which is compensated for the dead time of the electronics. This provides an estimate of the data rate that could be happening if the system was always processing data without the need to reset itself every cycle. A final counter is selected by the microcontroller depending on its mode of operation. It can count scatter, multiple/pileup, and CFD transition events. The microcontroller provides various status LEDs, can sense the supply voltage levels, and determine board temperature among a few other miscellaneous diagnostic features.

6.2 The Coincidence Processor

The coincidence processor is the single most important assembly in the scanner whose shape and size were changed with every scanner iteration. All coincidence processors can be simplified into three stages as shown in Figures 6.7 and 6.8: input buffering and segregation; coincidence testing; and output word formation and buffering. In the early ECAT 931 and 951 scanners, the coincidence processor took up half of a cabinet and was made up of many large boards. Each ring had its own receiver board and multiple coincidence processing boards all communicating over a very large, custom backplane. See figures in Section 7.1 for examples. Eventually, with the use of very large-scale integrated (VLSI) application-specific integrated circuit (ASIC) chips, all of those boards were condensed to a single board.

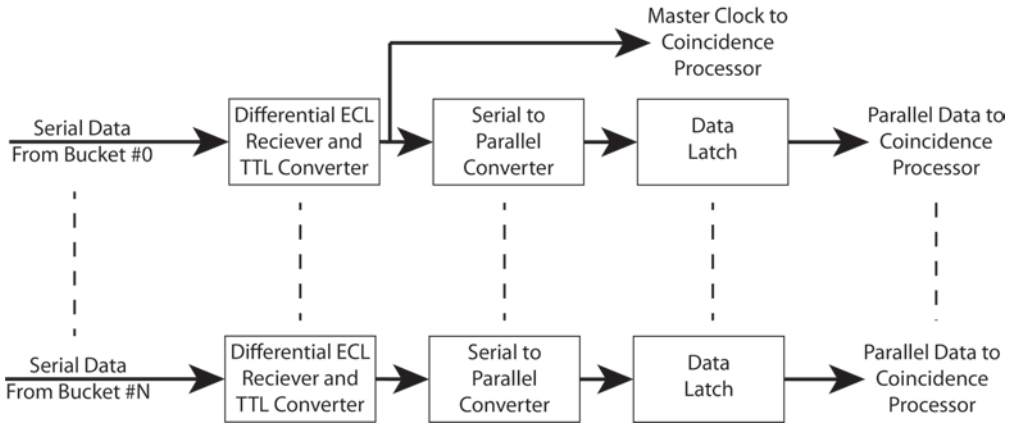

Figure 6.7: A generalised block diagram of the coincidence processor receiver showing the data flow and the master clock signal sampling from the first channel.

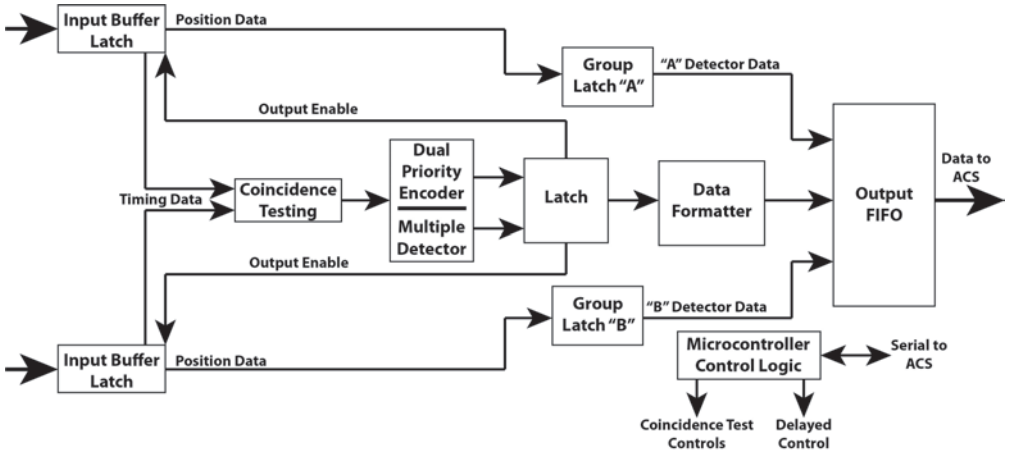

Figure 6.8: A generalised block diagram of the coincidence processor showing the various stages of the data processing.

Like the bucket controller, the coincidence processor also contains a microcontroller and various types of memories. It sends and receives serial commands over twisted-pair differential ECL to and from the gantry controller. Most of the time, the microcontroller only keeps track of various coincidence event types as they are processed; however, it can also set the plane mode of the coincidence processor. The plane mode determines which individual crystal planes can be in coincidence and makes the coincidence logic reject all others. The three plane modes are parallel planes, cross planes, and all planes. Parallel plane and cross plane modes are used in 2D imaging while all planes mode with septa removed essentially enables 3D imaging mode.

The data from each of the buckets is immediately converted into TTL format, as can be seen in Figure 6.7. The position and timing data are fed into shift registers which deserialise it. The clock signals used for timing the coincidence processor are also passed through from each of the buckets, as mentioned in Section 6.1.4. However, depending on the number of boards and/or the number of major subsections of the coincidence processor, the clock signals can only be accepted from one of the buckets per each of the coincidence boards and/or subsections. Usually, the clock signals are taken from the first bucket and its opposite and/or the last bucket and its opposite per each physical detector ring. This is important during debugging of the system as unplugging one of these buckets will stop the coincidence processor from functioning. The only datum not being sent over from the bucket is the bucket number itself. The coincidence processor assumes the bucket number from the physical connection of the data cable to the coincidence processor board. Therefore, while assembling the system, it is important to make sure the right bucket is plugged into the right socket on the coincidence processor board.

After deserialisation, the data are latched into a first set of input latches that hold the data from all the buckets. Input processing PAL chips read the plane data contained within the position data for each bucket and check for possible coincidence pairs between the permitted bucket module pairs. The plane check is also conducted based on the selected plane mode of the coincidence processor as mentioned above. Module pairs are used to describe the modules which are permitted to be in coincidence. Examples are shown in Tables 8.1 and 9.1. This is done to reduce the amount of electronics used and prevent testing of coincidences that cannot be true; like between neighbouring buckets. Therefore, a bucket in a ring can only be in coincidence with the bucket opposite it, 3 buckets to each side of that one, and the 7 buckets similarly positioned in each of the other rings of the scanner. Module pair numbers also efficiently describe and encode all the possible bucket pairs in a system. The module pair scheme differs across scanners with different maximum numbers of

buckets per detector ring. In order not to repeat any bucket combinations, the bucket with the smaller number/ID in a ring is known as the "A" or "master" bucket and the other one is the "B" or "slave" bucket. This is very important for decoding the coincidence data later on.

The input processors, having identified possible coincidence pairs between permitted module pairs and having valid plane combinations, now shift the paired data to various parallel, coincidence test sections. The timing data from each of the buckets in coincidence is presented to the coincidence test GAL chip while the positional data are latched into "A" and "B" data latches to be stored during the coincidence time test, see Figure 6.8. The coincidence test is done using a 12 ns coincidence window which is formed from the original hit pulse being 4 ns wide and an additional 4 ns before and after that event. If the pair of events occurred in that time window, a prompt coincidence is detected and passed for further testing. To account for random coincidences, a delayed coincidence window is used. This coincidence window is also 12 ns wide and offset from the prompt window by a set time which was reported to be either 128 ns [286] or 48 ns [13]. Valid prompt and delayed coincidence windows for the 128 ns delay offset are shown in Table 6.1. If a delayed coincidence occurs, a delayed flag is raised and passed with the event data.

Having identified valid coincidences in time, the outputs of the coincidence test sections drive two circuits. The first circuit checks if a bucket is in coincidence with more than one other bucket. This raises a multiple flag for those coincidences. The other circuit is a dual-priority encoder which decides which of the coincidence events to pass through as the coincidence. This is due to the same restriction as the buckets observe which is that the coincidence processor can only form a single coincidence every master clock cycle. The dual-priority encoder essentially tries to eliminate any non-uniformities which may form due to this restriction. The processed event data are then latched into a formatting circuit which formats the various events flags, the "A" and "B" bucket positional data, and assigns the

Table 6.1: A table showing the 12 ns coincidence windows for prompt (green) and delayed (orange) events with a 128 ns delay window offset. Here the time is discretised into a 6-bit counter counting from 0 to 63 between each master clock cycle yielding each count equal to 4 ns. The top row corresponds to bucket "A" time and the left column corresponds to bucket "B" time.

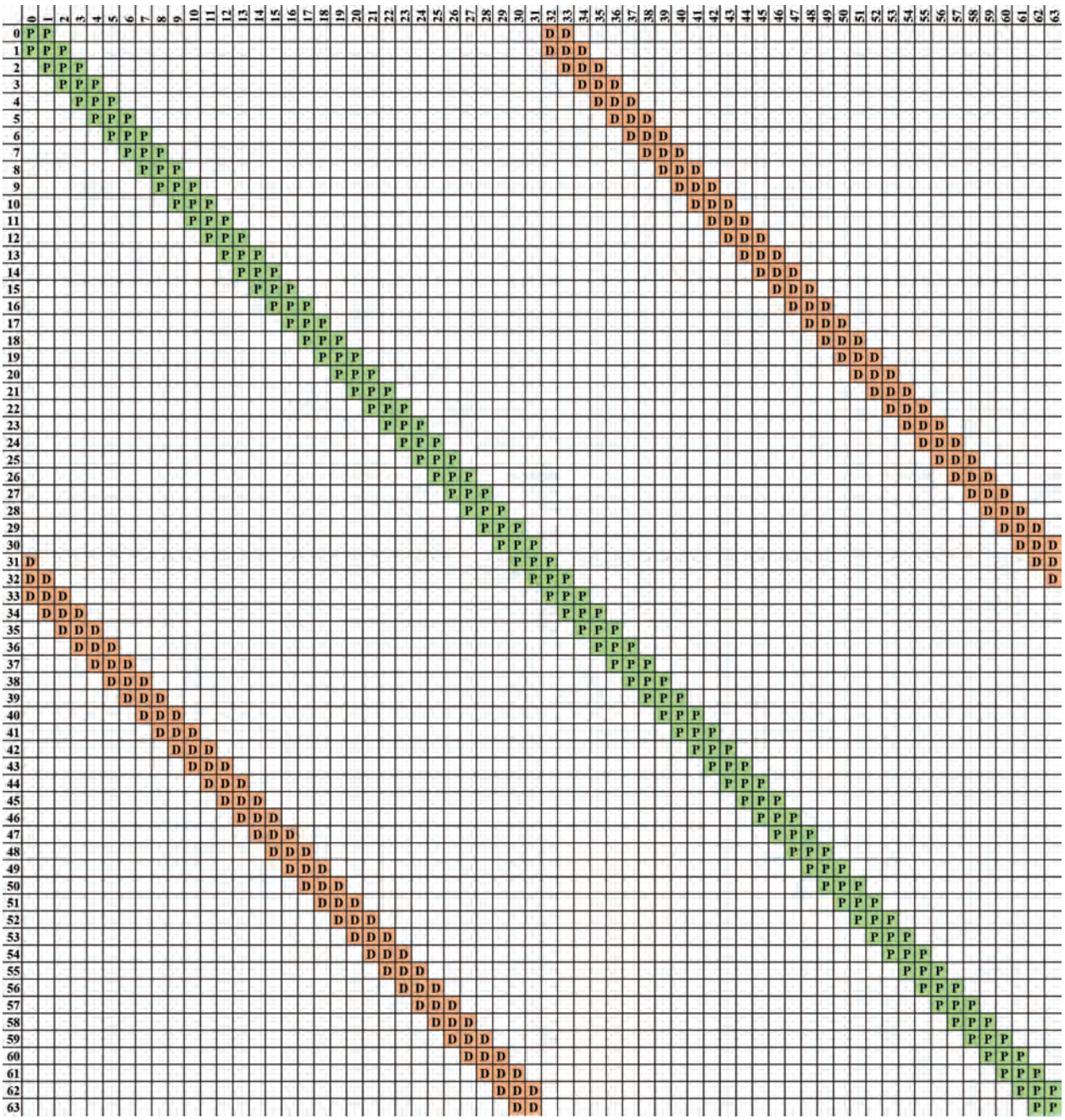

module pair number and the ring number. This information is arranged into a 32-bit wide word, with some blank bits, describing between which two crystal elements the coincidence

has occurred. Finally, the word is staged into a FIFO (first-in, first-out) memory to be transmitted to the advanced computational system (ACS) real-time sorter (RTS). The coincidence processor does not assign any timing information to the final word produced.

6.3 The Advanced Computational System (ACS) and Host CPU

The advanced computational system (ACS) is a Versa Module Eurocard (VME) bus (VMEbus) based control computer for the ECAT system. It consists of a host CPU, VMEbus arbiter, the real time sorter (RTS) system, VME memory, interface cards for various storage media, and a data interface to the operator's workstation. The host CPU in all of the ECAT ACSs is a Motorola 68000 series CPU (68000, 68020, and 68030 in the later models) that manages the gantry operations. It performs various control and configuration tasks to prepare the gantry for whatever type of acquisition the operator wants to conduct and communicates with the operator's workstation and the rest of the gantry via a serial command line. It is also able to send the sinogram data from its memory to the computer via the data interface. It manages the bus memory by reserving space for the various sinograms it will need to acquire and then stores them along with patient attenuation and normalisation data by offloading them from memory onto optical or tape drives. The ACS also processes the sinograms to form FBP images that subsequently are passed for analysis to the operator's workstation. It can also manage list mode data acquisition operation by constantly using the memory as a FIFO for the raw data as it slowly offloads it to an optical drive. The ACS also features a VMEbus arbiter, the job of which is to allocate the bus as requested on a first come, first served basis preventing bus jams.

The ACS receives the data directly from the coincidence processor through its RTS

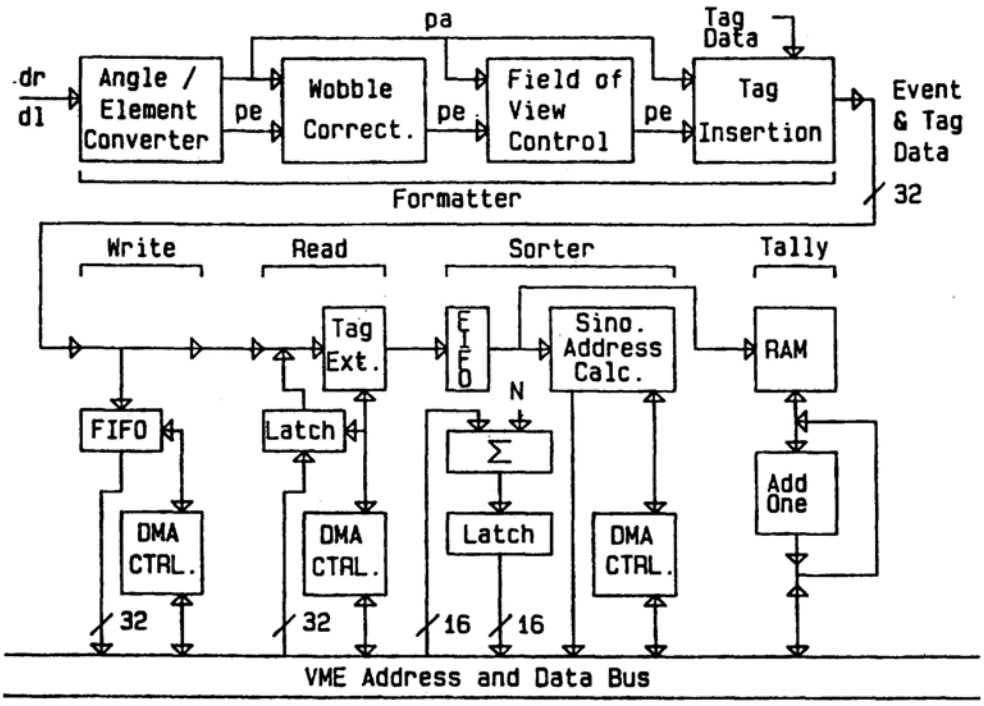

Figure 6.9: The real time sorter (RTS) (version I) data flow block diagram as integrated in the ECAT 931 and 951 series [269]. The RTS II is extremely similar in design with the write and read cards being incorporated into the neighbouring cards, the wobble function removed, and an additional rotating rod converter card. Legend: dr and dl are the detector right and left or data representing the crystal elements in coincidence, pa is the calculated sinogram projection angle, and pe is the calculated sinogram projection element or displacement.

system shown in Figure 6.9. The RTS is made up of a few different cards on the VMEbus with the job of translating and segregating the 32-bit word from the coincidence processor into a sinogram or pass it to memory if in list mode data acquisition mode. The RTS is also able to replay list mode data from memory to form sinograms. These cards are interconnected in the front to not take up the VMEbus bandwidth. The RTS only uses the VMEbus when it has to communicate with the memory. The first element of the RTS is the coincidence input/adapter board which receives the data from the coincidence processor and latches them into an input buffer before passing them to the next section. The biggest function of this board is the handshake controller which checks if data are available at the coincidence processor output and requests them to be transmitted. This is implemented because the ACS works asynchronously to the coincidence processor and it is the master of

the interface. The handshaking procedure for the ECAT 931 and 951 scanners is described in Section 9.4.1. Next, the data are passed to the RTS formatter card where they are latched into an angle/element converter which converts the coincidence processor data word into an angle/displacement sinogram position. Here, timing and gating event words can be inserted into the data stream which is especially useful for list mode acquisitions. In later versions, the data are passed to an RTS rotating rod converter card which, when transmission or blank scans are performed, checks if a coincidence originated from a transmission event and marks it as such, otherwise it just passes the data through to the RTS sorter card. The RTS sorter card first latches the word into a FIFO before sending it to a sinogram base address and bin address calculator which finds where in memory the sinogram bin for this angle/displacement is located, as set up by the host CPU. With the address obtained, the sorter uses a VME direct memory access (DMA) controller to transfer the sinogram data to memory via a read-modify-write process. Finally, the data word is passed to an RTS injection monitor card which simply keeps a running tally of all event types for all planes during an acquisition.

The last important part of the ACS in the later scanner models is the array processor. In earlier models (ECAT 931 - early 951), the array processor was part of the operator's console computer. The array processor is just a specialised processor board which can hold projection data during reconstruction and perform the same operation in parallel over many data points. Here, during reconstruction, a view of the projection data is loaded from the memory that is then normalised and corrected for attenuation. Finally, user-selected filters can be applied. In the end, the filtered view is sent back to memory where it is scaled and/or rebinned and then sent to the operator's console computer for storage and analysis.

6.4 Gantry Control Electronics

The gantry control electronics encompass essentially every other aspect of the scanner gantry control outside of the data acquisition. Generic input monitoring, generic output control, motor control, clock and serial communication fanout, power monitoring and control, front panel user displays and IO, and bucket performance monitoring are some of the main functions this area performs.

The most important of the gantry electronics is the clock generation and distribution system which uses a single 125 MHz oscillator to produce the 16 ns and master clock signals that sync the buckets and the coincidence processor together. Without it, the scanner would cease to operate. Next, the current loop converter converts the RS-232 based serial command interface from the ACS and into a differential ECL format. These signal lines are then distributed to the various other control boards in the gantry that accept serial commands, the coincidence processor, and the clock distribution section to be distributed to all the buckets. On some of the older systems, a gating input board is also available providing 2 to 4 user-defined TTL gating signal inputs mostly used during dynamic cardiac imaging. This gating input controls how sinograms are acquired for the different stages of a heartbeat. The older scanners also could wobble or rotate the detector ring. This increased the resolution of the earlier scanners by producing a finer sinogram; however, this function would cause blurring when imaging moving organs like the heart and lungs and was soon removed.

The early ECAT 931 and 951 gantries could also be rotated and tilted by the user and therefore included gantry tilt and rotation sensors and motors. Modern gantries are stationary with the only motor controller being required for rod source movement, patient bed positioning, and septa movement. Other generic inputs include emergency stop buttons, temperature sensors, cooling air/water flow sensors, and DIP switch gantry settings. The

temperature monitoring section almost continuously samples temperatures around the gantry and of each bucket to ensure efficient operation of the system and an emergency shutdown in case of overheating. Similarly, voltage levels are monitored by each of the buckets and at the power supplies and in case of over or under voltage the system can be safely shut down. The generic outputs include power supply relays, status LEDs, and laser control relays.

In the newer scanners, quite a few of these individual boards merged into one gantry controller board managed by a single microcontroller. The gantry controller board now encompasses clock generation and distribution, continuous bucket monitoring, current loop converter and serial communication distribution, motion control communication, front panel communication, and temperature and voltage monitoring. While some of these functions still have dedicated driver boards, they interface directly with the gantry controller board.

6.5 Operator's Workstation

The operator's workstation is the only normal user interface to the scanner. It is made up of a computer system which runs the proprietary ECAT software and various other runtime scripts. In general, the user can enter and select all sorts of scan parameters, views, and patient information to set up the scanner for acquisition. It can save and recall scan data for processing, reconstruction, slicing, and further analysis. It tracks and performs daily maintenance tasks. And finally, it can manage database organisation as well as data archiving. It also had a suite of diagnostic software which technicians could use for scanner diagnosis, system set up, and calibration.

The early ECAT scanners, up-to ECAT 951, used a somewhat complicated Digital Equipment Corporation (DEC) computer system. Here, a MicroVAX II (Virtual Address eXtension) computer system was used based on its proprietary Q-bus (LSI-11 bus) to inter-

face to the CPU, memory, serial interface, and disk storage. A DEC MicroVERTER was used to interface the Q-bus to an older DEC UNIBUS which interfaced with the display processor/driver, the array processor (see Section 6.3), and provided DMA; a high-speed interface to the ACS via the DEC DR11-W interface. The computer ran the VAX/VMS operating system.

The later versions of ECAT 951 and later scanners switched to a Sun Microsystems workstation system. Besides being a lot more compact than the DEC MicroVEX II, the Sun system provided a greater choice of storage devices and interfaces that were not natively supported in the DEC system. The Sun system featured a colour display, early 2D and 3D graphics accelerators, a laser printer, an optical mouse, a floppy drive interface, a disk drive interface, and a tape drive interface to name a few. The Sun system directly interfaced with the ACS using an Ethernet connection for data transfer and ran the SunOS operating system.

Chapter Seven

The ECAT Scanners

In this section, I will describe the differences/advancements from each ECAT system to another as the series was developed from the early ECAT 931 series through to the ECAT EXACT HR++, the last scanner in the series to use BGO as the scintillator.

7.1 The ECAT 931

The ECAT 931 (model 931) PET scanner released between 1985-1986 was the first scanner to feature the detector block system designed to facilitate whole-body scans. It was built upon the success of the NeuroECAT (model 828), the first commercial BGO-based PET scanner [267], and the ECAT-III (ECAT 911, model 911), the first digital gantry PET scanner [270, 271]. The ECAT 931 was similar to the ECAT III and was able to perform 2D static, dynamic, transmission, and gated acquisitions through its fine interplane septa, retractable ring sources, wobble functionality, and gate inputs. The gantry was able to be rotated and tilted by the operator to get better images of certain organs. It was air-cooled and featured digital bucket controllers similar to those used on the ECAT III except that they now accepted inputs from detector blocks. The patient bed was controlled by

the operator's computer to allow for precise patient localisation within the scanner. The coincidence processor and the ACS were also very similar in theory of operation to those used on the ECAT III but were adapted to accept a lot more image planes. The ACS still interfaced with the DEC UNIBUS system through a high-speed interface which featured an off-the-shelf array processor and a display processor used for the FBP reconstruction of slices and user display control, respectively. However, the VAX-11 computer was updated to the more modern MicroVAX II Q-bus-based computer. The UNIBUS was interfaced with the Q-bus through the MicroVERTER interface. The Q-bus contained the rest of the computer peripheral interfaces, CPU, memory, and disk drivers. It ran the VAX/VMS operating system and sported a full suite of the VAX/VMS-based ECAT software [225, 286–288].

7.1.1 Detector Block and Gantry Options

The ECAT 931 was the first implementation of the detector block principle and therefore came with some interesting options. This was the only generation of the detector block to be sliced into an 8 transaxial and 4 axial array, as shown in Figure 7.1, and be offered in 3 different axial crystal element sizes. This was possible due to the use of a variably slotted light guide which was removed in the next version of the detector block in favour of a variably slotted BGO scintillator itself. However, to keep the detectors closely packed with the best transaxial resolution, the transaxial crystal element size was kept the same at 5.6 mm wide with a 6.1 mm pitch and the depth was always 30 mm. The three axial crystal element sizes were:

- 12.9 mm high with a 13.5 mm pitch for the /12 version.
- 15.4 mm high with a 16.0 mm pitch for the /16 version.
- 19.4 mm high with a 20.0 mm pitch for the /20 version.

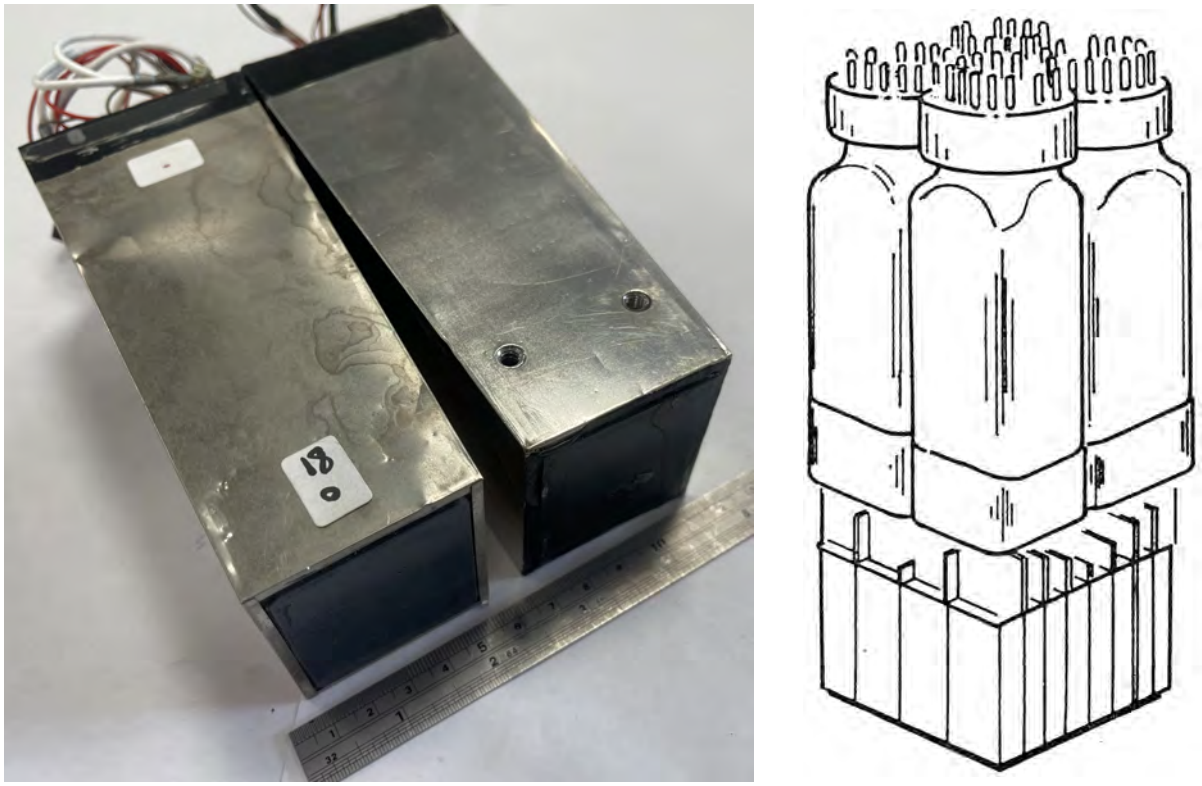

Figure 7.1: Right: Two ECAT 931/12 detector blocks. The left one is oriented right side up and the right one is upside down showing the threaded inserts used for mounting the block to the bucket assembly plate. Left: The ECAT 931/12 detector block drawing with clearly visible 8x4 division and a light guide coupled to 4 square PMTs [287].

The /12 version crystal array was the only one that would match one-to-one with the active array of the four square PMTs, all the other versions' crystal array would expand beyond the PMT view and required the light guide to guide the scintillation light back into their view [287, 288].

The gantry itself was available in single- or double-ring versions, with the -04 version having a single ring of detector blocks or four rings of crystal elements and the -08 version having two rings of detector blocks or eight rings of crystal elements. It was also available in three ring diameters:

- Model 831 had 10 buckets or 40 detector blocks per ring forming a detector diameter of 64 cm and a patient portal diameter of 35 cm and was intended for brain scans.

- Model 933 had 12 buckets or 48 detector blocks per ring forming a detector diameter of 76 cm and a patient portal diameter of 51.4 cm and could be used for lower-precision whole-body scans.
- Model 931 had 16 buckets or 52 detector blocks per ring forming a detector diameter of 102 cm and a patient portal diameter of 56.7 cm and was intended for high-quality whole-body scans and included retractable transmission sources not available in the other options.

This meant that the scanner was offered in 18 different versions even though the most commonly bought detector block arrangement was the -08/12 version with two rings of detector blocks and the smallest axial crystal element size for higher axial resolution scans [287, 288].

The ECAT 931 bucket electronics while similar in operational theory to the ECAT III bucket, were very different. This was the first bucket controller to use the crystal element position lookup table design [280]. The bucket consisted of a main block controller board which, as mentioned in Section 6.1.4, contained the microcontroller (Intel 8031, eight-bit processor) for the control of the bucket functions and serial communication. Unlike the later versions of the bucket controller, this bucket was unable to perform position calibration due to the table being pre-programmed into a permanent PAL chip. The microcontroller was still able to acquire calibration data and set gains, upper-level discriminator (ULD) level, lower-level discriminator (LLD) level, time correction, and CFD thresholds for the detector blocks [287, 289].

As there was no need to reprogram the lookup tables and set them on boot, the overall bucket design was very simple. The repeatable functional blocks of the data processing pipeline were discretised into small vertical boards that were soldered into the main controller board that also served as a data bus between the different sections, see Figure 7.2. Each of

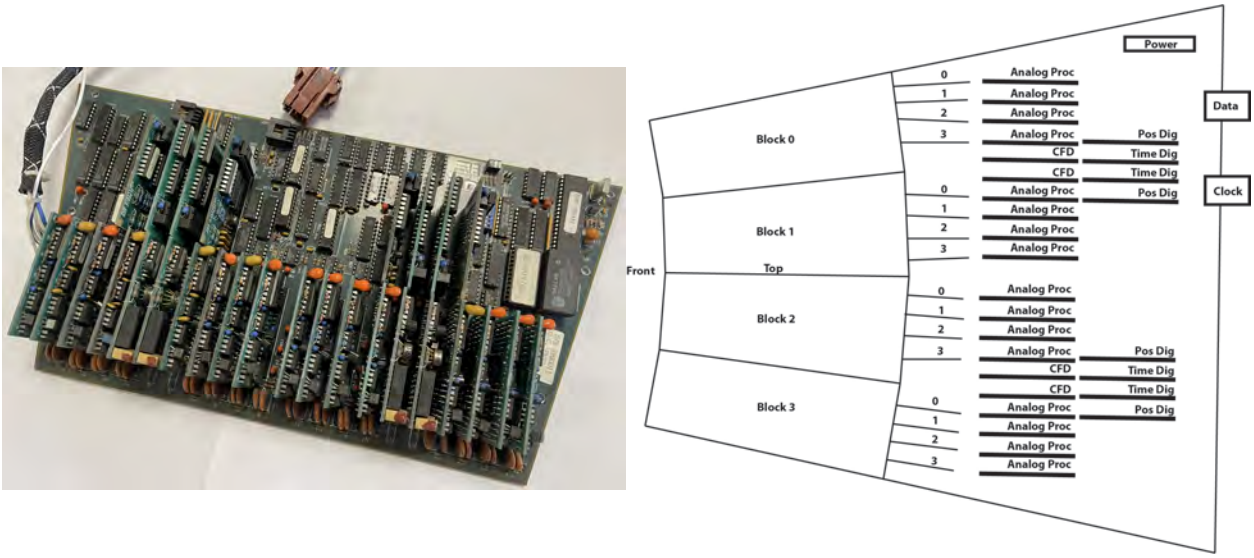

Figure 7.2: The ECAT 931 bucket assembly electronics and layout. Left: The ECAT 931 block controller board with all the subsection boards (Block Controller PN: 1010016B, Analogue Processor PN: 1000016A/B, Position Decoder PN: 1000020C, Time Digitiser PN: 1000021A, Constant Fraction Discriminator PN: 1000018A). Right: A labelled layout drawing of the ECAT 931 block controller assembly including the detector blocks and identifying all the functions of the sub-boards.

the PMTs in a detector block had their own analogue processor sub-board that contained the pre-amplifier and DAC gain control circuits. The board received the PMT charge pulse as its input and produced a fast timing and a slow energy signal. The fast-timing signal from each of the analogue boards was passed to a single CFD board per detector block that produced the time mark for the time digitiser board and the energy integration mark for the analogue processor. The time digitiser board produced a digitised time stamp referenced to the next master clock cycle. Finally, the slow energy signals were passed to the position decoder board to be summed together and produce inputs for the pre-programmed PAL chip. The chip used the digitised energy values to determine the plane and column number of the crystal element that was hit as well as if the event was a true event based on the LLD and ULD setting [289].

At the end of the pipeline, the block controller board added any time correction to the digitised time and formatted the final data to be sent to the coincidence processor. The

data were sent over four twisted-pair wires in differential ECL logic where one of the lines sent the six-bit timing word, a valid hit flag, and a scatter event flag and the second one sent over one free bit, three bits describing the column number, two bits describing the plane number, and two bits describing the block number. That was all the information needed to describe which exact crystal element the interaction occurred within the scope of the bucket. The other two lines passed on the clock signals described in Section 6.1.3 [289].

7.1.2 The Coincidence Processor

The ECAT 931 coincidence processor was fully incorporated in PAL and GAL chip logic due to which scale it had to be designed in a modular card style shown in Figure 7.3 left. The whole assembly consisted of a custom backplane shown in Figure 7.3 right, a ring receiver board per each ring shown in Figure 7.4, and one or more Image Plane Coincidence Processor (IPCP) boards shown in Figure 7.5.

A ring receiver board was used for each of the rings to receive the signals from the buckets, convert them to TTL format via translator buffers, deserialise data via shift registers, and latch it onto the backplane which distributed it to the appropriate IPCP boards. The ring receiver also fed the clock signals from the number 0 and 8 buckets in each ring to the IPCP boards. While a single-ring scanner only required a single IPCP board to handle all the coincidences, a double-ring scanner required four IPCP boards: one per ring to handle coincidences within that ring and two to handle coincidences between the two rings. Each of the IPCP boards worked as described in Section 6.2 and used an Intel 8031 eight-bit microcontroller to manage each board and set its mode of operation. However, each one of the IPCP boards had its own FIFO output section and was daisy-chained with a 64-pin twisted-pair flat cable which brought the coincidence data to the ACS upon its request, as seen in Figure 7.3. The cable carried 24 data lanes and four ACS handshake signals shown in

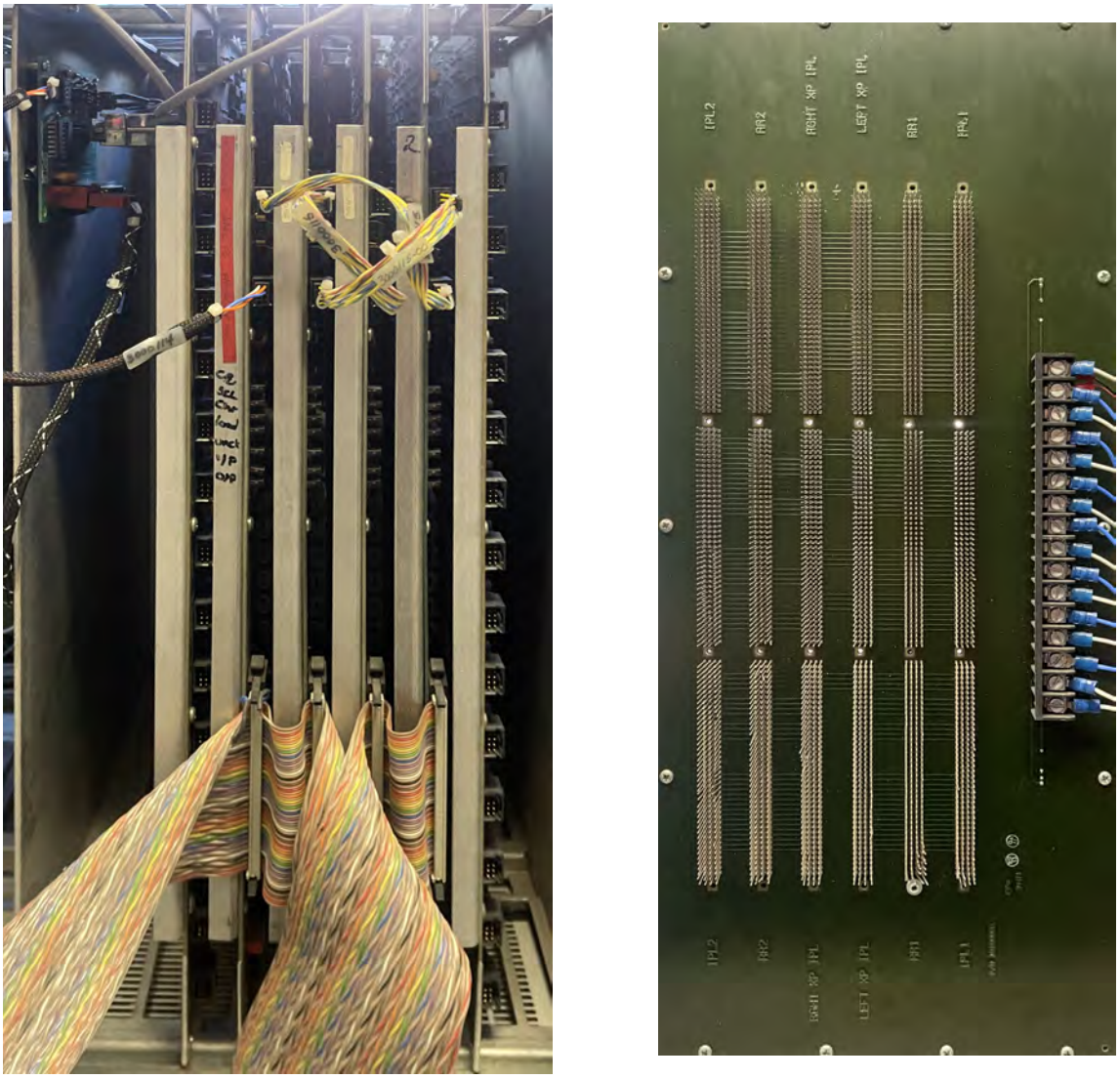

Figure 7.3: ECAT 931 coincidence processor assembly. Left: ECAT 931 coincidence processor card cage. The individual cards from left to right are the ring 1 receiver (all bucket cables disconnected for clarity), the ring 1 IPCP, the ring 1x2 IPCP, the ring 2x1 IPCP, the ring 2 IPCP, and the ring 2 receiver (all bucket cables disconnected). The IPCP boards are daisy-chained together and connected to the ACS with the large, flat, twisted-pair ribbon cable. The IPCP boards are also daisy-chained at the top to pass through the serial communication which leads to the current loop converter seen in the top left corner of the card cage. (931 Ring Receiver PN: 1010009A, 931 IPCP PN: 1010010B) Right: The back view of the coincidence processor backplane (PN: D1010008P1) shows the giant card edge connectors and the power distribution strip.

Figure 9.6. Each of the three scanner gantry diameter configurations shared the same backplane but had a custom ring receiver that had 10, 12, or 16 bucket connectors. Two of the

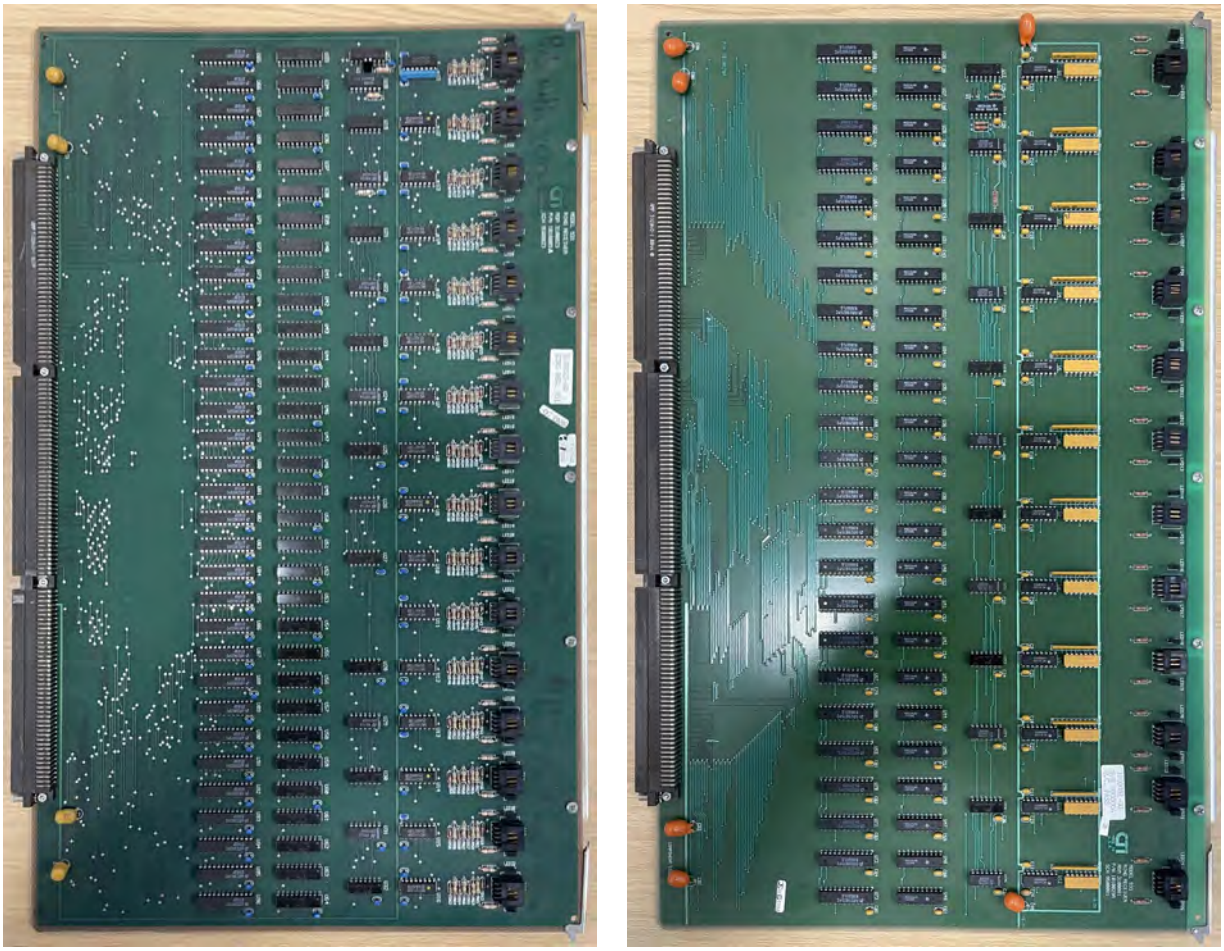

Figure 7.4: ECAT 931 ring receiver boards. Left: An ECAT 931 ring receiver board for 16 buckets per ring gantry (PN: 1010009A). Right: An ECAT 933 ring receiver board for 12 buckets per ring gantry (PN: 1010029A).

ring receiver boards are shown in Figure 7.4 for the model 931 scanner with 16 buckets per ring and the model 933 scanner with 12 buckets per ring. The IPCP boards were the same for each of the versions except they were not fully populated for the smaller ring geometries. Chips used for the coincidence testing of module pairs not used by the smaller geometries were not installed. A fully populated model 931 IPCP board is shown in Figure 7.5 and a partially populated later model 953 IPCP board is shown in Figure 7.8.

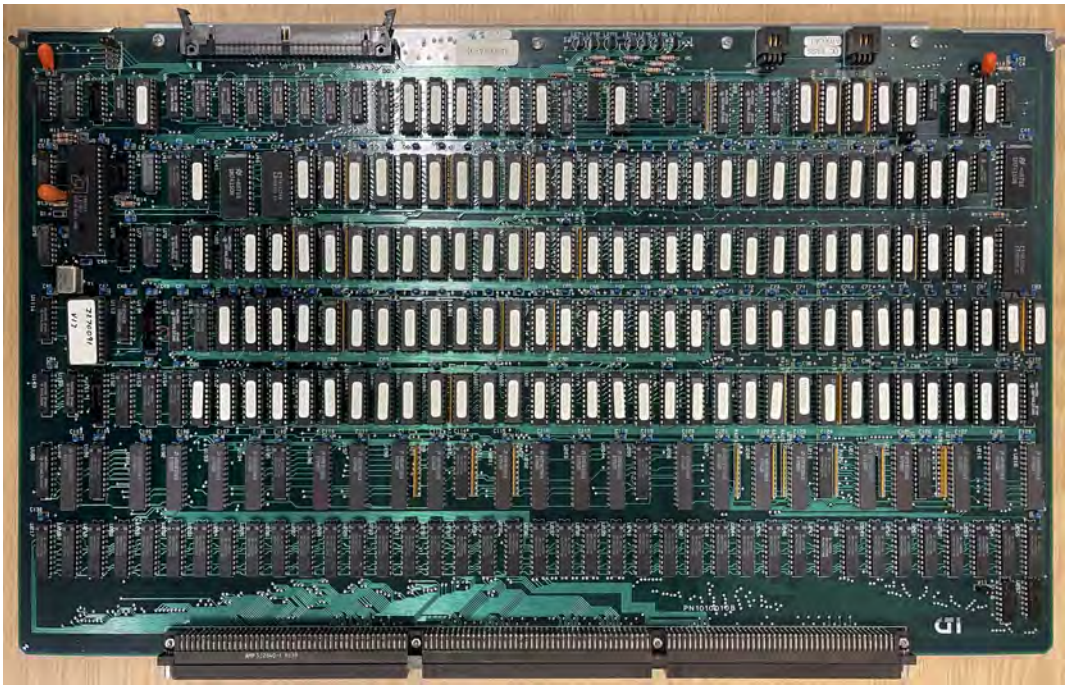

Figure 7.5: ECAT 931 image plane coincidence processor (IPCP) board fully populated for 16 buckets per ring geometry. (PN: 1010010B)

7.1.3 The ACS

The advanced computational system (ACS) (version I) used in the ECAT 931 closely matched that of the ECAT III in the number and types of RTS boards that were only modified to properly interpret and bin the data from the additional rings. The ACS used a Motorola 68000 single-board computer running the VxWorks operating system to orchestrate its functions, a few VME memory cards to contain the sinograms and/or the list mode data, and an arbiter as described in Section 6.3. Unlike later models, the array processor was part of the operator's workstation [287].

The coincidence data was latched into the RTS adaptor board responsible for the handshaking and initial buffering of the data. Then using a front-end interconnection, the data was passed to the RTS formatter board which took the positional data from the adaptor and converted it into a sinogram angle/displacement format. The formatter also corrected

the angle/displacement data for the wobble movement when it was enabled, applied selectable field-of-view (FOV) conditions rejecting data between buckets outside of the selected FOV, and inserted any timing and gating information, if used. The angle/displacement data, tag information, and the original coincidence word were then passed to the RTS write controller board which when list mode data acquisition was selected wrote the data along with the tag information to the VME memory. If the list mode data mode was disabled, the data was passed to the RTS read controller board which enabled "play-back" of the list mode data for histogramming. In normal mode, the data simply passed these two boards and continued to the RTS sorter board. The RTS sorter board took the angle/displacement data, calculated the VME memory address which holds the appropriate sinogram index, and incremented or decremented the bin count via DMA. Finally, only the event tag data was passed to the RTS injection monitor board or a tally which kept the statistics about the event types observed by the system for each image plane. Once the sinogram acquisition was finished or during the list mode data acquisition, the data was offloaded to a tape or disk storage device under the ACS CPU supervision to free up the fast VME memory [269].

7.1.4 Operator's Workstation

As mentioned before, the operator's workstation consisted of a DEC UNIBUS which was connected through a high-speed interface to the ACS to quickly receive the sinogram data held in the VME memory or on the VME-connected drives. An array processor on the UNIBUS was used to reconstruct the FBP images and a display processor was used to show the images to the operator along with the ECAT software UI. The UNIBUS was interconnected to the DEC Q-bus which housed the MicroVAX II computer that run the VAX/VMS operating system and the ECAT software suite [288].

7.1.5 Other Gantry Electronics

Some of the other electronic boards which make up the gantry are worth mentioning here. The most important of them all is the clock distribution and fanout boards shown in Figure 7.6. As the name suggests, they generate the clock signals described in Section 6.4 and distribute them along with the serial communication lines to all the buckets. The board connects to the current loop converter board, shown in Figure 7.7, which receives the RS-232 serial from the operator's console via the ACS and converts them to the differential ECL logic as used by the boards. While the current loop converter board only acts as a logic converter, the clock distribution and fanout board contains an Intel 8031 microcontroller responsible for starting and stopping the clock signal [289].

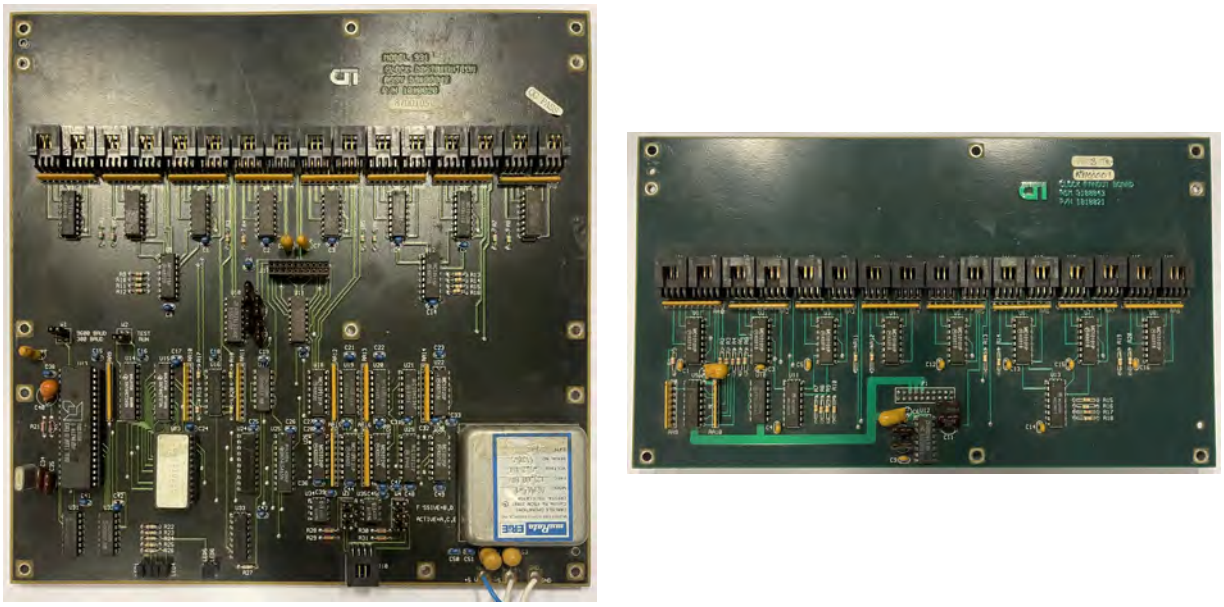

Figure 7.6: Left: ECAT 931 clock distribution board which contains the 125 MHz oscillator, generates the required clock signals, and distributes them to 16 buckets. This board is connected to the current loop converter for serial communication and, for a two-ring system, a clock fanout board via the interboard connector in the centre of the board (PN: 1010020). Right: ECAT 931 clock fanout board which mounts on top of the clock distribution board and provides 16 additional bucket connections (PN: 1010021).

A big subsection of the gantry electronics includes the gantry motion electronics responsible for wobble control, transmission source positioning, motor driver boards for

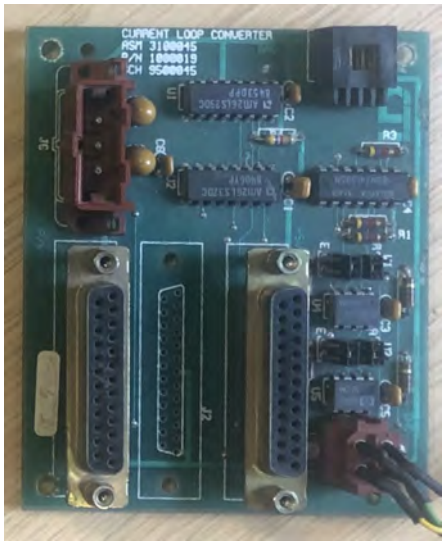

Figure 7.7: ECAT 931 current loop converter board which converts the RS-232 serial from the ACS into differential ECL signal that is then distributed to the various boards in the gantry (PN: 1000019).

gantry tilt, gantry rotation, patient bed positioning, phantom positioning, gating input board, and various IO boards for emergency stop and limit switches. All of these boards resided in a separate card cage and on a separate bus appropriately named the "Motion Control Processor" card cage. The card cage used a DEC Q-bus system under the control of a DEC SBC-11/21 single-board computer. The SBC-11/21 is a T-11 16-bit microprocessor-based system also known as the KXT11-AA and nicknamed the Falcon. The SBC-11/21 received serial commands from the operator's computer, the MicroVAX II, and interpreted them to properly position and control the various gantry elements. It collected positional data to verify all motions were done correctly and sent them back to the ACS to be included in coincidence data formatting or used as tag words and simply inserted into the data stream, as discussed in Section 7.1.3; especially important for the source and wobble position and gating information [289].

What might not be apparent here is that all of the electronics described needed a lot of space, 4 cabinets worth to be exact which had to be housed in their own electronics room [288]. The MicroVAX II itself took 2 cabinets for its electronics and peripherals.

Another cabinet housed the coincidence processor card cage and the last one housed the motion control card cage and the ACS. As a result of the coincidence processor being in a separate room from the gantry, this required all of the data cable from each of the buckets to be individually run in a big bundle from the gantry to the electronics room producing a very long cable loom where each cable had to be the same length to prevent any clock skew between the data lines.

7.1.6 3-Dimensional Imaging/Septa Removal

The ECAT 931 was sold as a 2D scanner capable of acquiring cross-plane and parallel-plane coincidences for a full set of 15 sinograms as standard, for the two-ring -08 option, with no user-removable septa. The coincidence processor, as mentioned in Section 6.2, already featured the possibility of enabling all plane coincidences for 3D scan acquisition. Enabling all coincidence planes and setting the ACS accordingly produced a total of 64 sinograms to account for all the possible planes. At the time, 3D scans were not a new idea but were simply impossible to perform with the early scanners having up to three crystal rings. While 2D acquisition with septa helps reduce scatter and noise coincidences, it also removes a lot of valid data that could be used during reconstruction for a more accurate image. Having removable septa was also not a new idea with the NeuroECAT having automatically retractable septa. With the septa retracted, NeuroECAT worked more efficiently when taking low-dose scans which produced less scatter and random noise, resulting in a higher-quality image than 2D scans [266]. Since the ECAT 931 was the first PET scanner with up to eight crystal rings, it became a test bed in 1988-1989 for 3D acquisition in large bore scanners. While septa removal was very inconvenient and took over three hours to complete, the data showed promising results for the incorporation of 3D scan functionality in future scanner designs [225, 290].

7.2 The ECAT 951

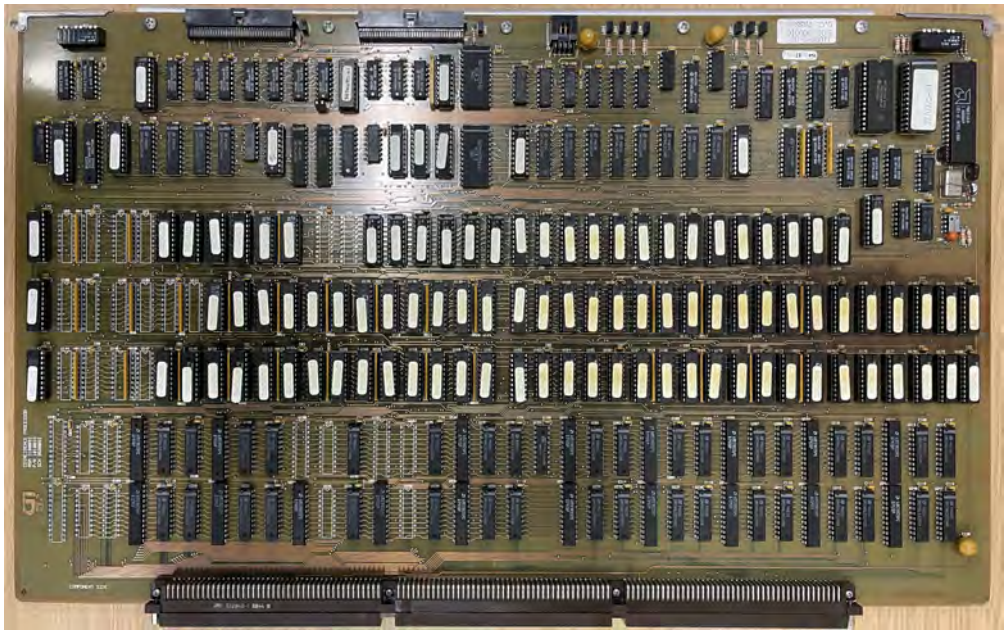

Figure 7.8: ECAT 953 image plane coincidence processor board for 12 detectors per ring scanner. The board is the same as for the ECAT 951 geometry except it is missing chips used for the unneeded module pair combinations (PN 1010033).

The ECAT 951 series of scanners released between 1989 and 1990 was designed as the successor and direct replacement of the ECAT 931 series with an improved axial resolution and doubling of crystal rings. It was almost the same as the ECAT 931 sharing many common functions and parts. Both scanners featured a rotating, tilting, air-cooled gantry that could perform static, dynamic, transmission, and gated scans with the use of the wobble function, extendable transmission sources, and gate inputs. The ECAT 951 was initially released as a 2D scanner but later updates incorporated the 3D functionality as described in Section 7.2.1. The major changes came due to the use of an updated detector block with an 8x8 array crystal element array. The bucket controller electronics were also updated with new features as discussed in Section 7.2.2. Besides those two changes, the coincidence processor, the ACS, the motion control electronics, and the other gantry electronics' design and implementation remained virtually the same. Only small changes were made to the IPCP boards functionally

to pass along and recognise the additional bit describing the 8 crystal planes the detector block now featured and perform appropriate coincidence rejection based on the plane setting. The new IPCP board for the smaller ECAT 953 scanner can be seen in Figure 7.8.

Figure 7.9: ECAT 951 coincidence processor assembly which works very similarly as the ECAT 931 coincidence processor assembly and uses the same backplane. The IPCP cards use a new 80-pin flat ribbon cable to connect to the ACS which also distributes the serial communication between the boards. The updated current loop converter, shown in Figure 7.16, can be seen mounted in the upper left corner of the card cage.

The cable connecting the coincidence processor to the ACS was also switched to an IDE-like, 80-pin, flat, ribbon cable. It now contained two lines used for a cable connection test, 27 lines for the coincidence data, four lines for the ACS handshaking, and four lines for the serial communication lines between the coincidence boards as can be seen in Figures 7.9

and 9.7. Similarly, the ACS remained the same as in the ECAT 931 except that it featured a new RTS adaptor and formatter boards that were able to interpret the additional plane data and an updated Motorola 68020 CPU. The operator's console was also initially advertised to be of the DEC MicroVAX II design; however, it was soon updated to feature a Sun Microsystems SPARC-V workstation. With this update, an Intel i860-based array processor was also introduced which was now located in the ACS cabinet under the Motorola CPU control with an Ethernet adaptor used as the data interface to the Sun workstation. This offloaded the image reconstruction from the operator's computer to the ACS which was more than capable of handling the reconstruction requests. With the new SunOS operating system, the ECAT software suite was updated to run under SunOS which it continued to do throughout all the scanner versions described in this section.

7.2.1 Detector Block and Gantry Options

The detector block used in the ECAT 951 series of scanners underwent an important development since its use in the ECAT 931 system. Most importantly, the light guide was removed and replaced with a variably slotted BGO scintillator block acting as its own light guide directly coupled to the PMTs. This also meant that producing crystal arrays larger than the area of the 4 PMTs became impractical, but as most 931 series scanners were acquired with the smallest axial size crystal elements, the /12 version, there was no need to develop additional larger detector blocks for this model. Also, the crystal was now sliced into eight axial crystal planes which greatly increased the axial resolution of the system and the number of image planes produced. Therefore, the ECAT 951 was only available in a single detector block size shown in Figure 7.10. The block had the same transaxial element size of 5.6 mm with 6.1 mm pitch and 30 mm depth as the ECAT 931 blocks, but only had a 6.2 mm high with 6.7 mm pitch axial element size. Similarly to the ECAT 931 series, the ECAT 951

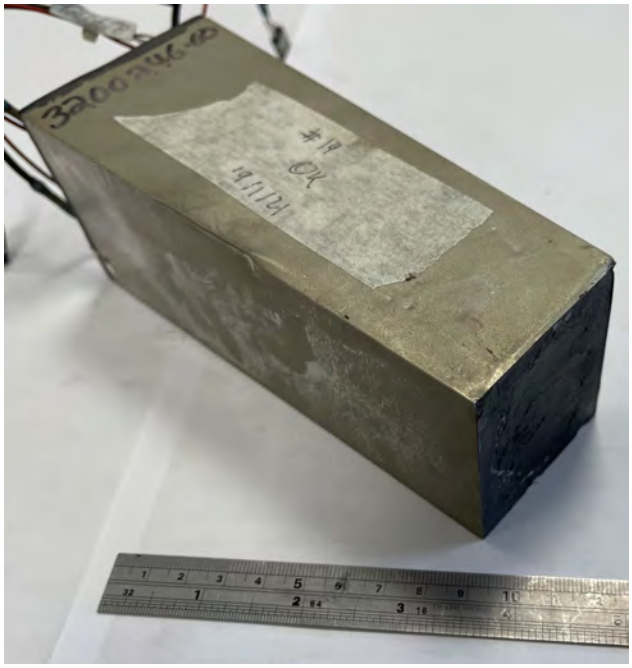

Figure 7.10: ECAT 951 series detector block.

series was available in a single ring /15 version and a double ring /31 version; where the /# notation represents the number of possible 2D image planes. The wedge bucket assembly with the detector blocks from the ECAT 951 scanner is shown in Figure 7.11.

The gantry was also offered in the same 3 diameter options as the 931:

- ECAT 951 was the 16 buckets per ring version like the ECAT 931.
- ECAT 953 was the 12 buckets per ring version like the ECAT 933.
- ECAT 851 was the 10 buckets per ring version like the ECAT 831.

Technically, the ECAT 953 was sold as the ECAT 953B as a dedicated brain scanner and was initially the only scanner of the series to feature retractable interplane septa with an allowance for full 3D scans. It also was the first scanner in the world to take a full 3D brain scan in 1991 [225, 284, 291]. With the success of the ECAT 953B as a 3D scanner and the experiments on the ECAT 931 scanner as mentioned in Section 7.1.6, the ECAT 951 scanner

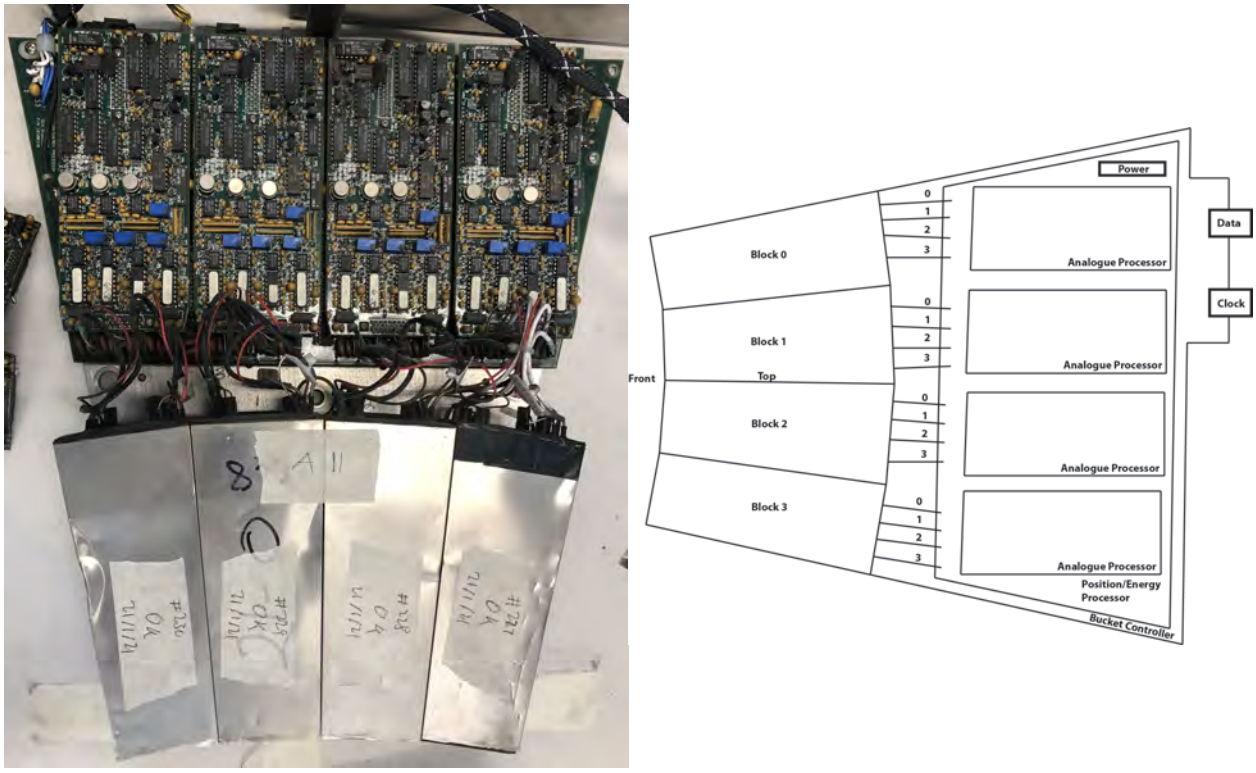

Figure 7.11: ECAT 951 bucket wedge assembly. Left: ECAT 951 bucket assembly showing the four detector blocks mounted to a bucket bracket with the bucket electronics attached behind them. Right: A labelled drawing of the ECAT 951 bucket assembly including the detector block numbers and identifying all the subsections of the stacked board, see Figure 7.12.

was eventually amended to include retractable septa as standard in the ECAT 951R version [292].

7.2.2 The New Bucket Controller

The bucket controller underwent a total overhaul with the introduction of the ECAT 951 series. The greatest change to the system came in the form of the implementation of the functionality to acquire calibration histograms and change the position lookup tables. This was most likely done to extend the life of the detector block as not all system changes due to age can be fixed by simply modifying the pre-amplifier gain. The updated bucket

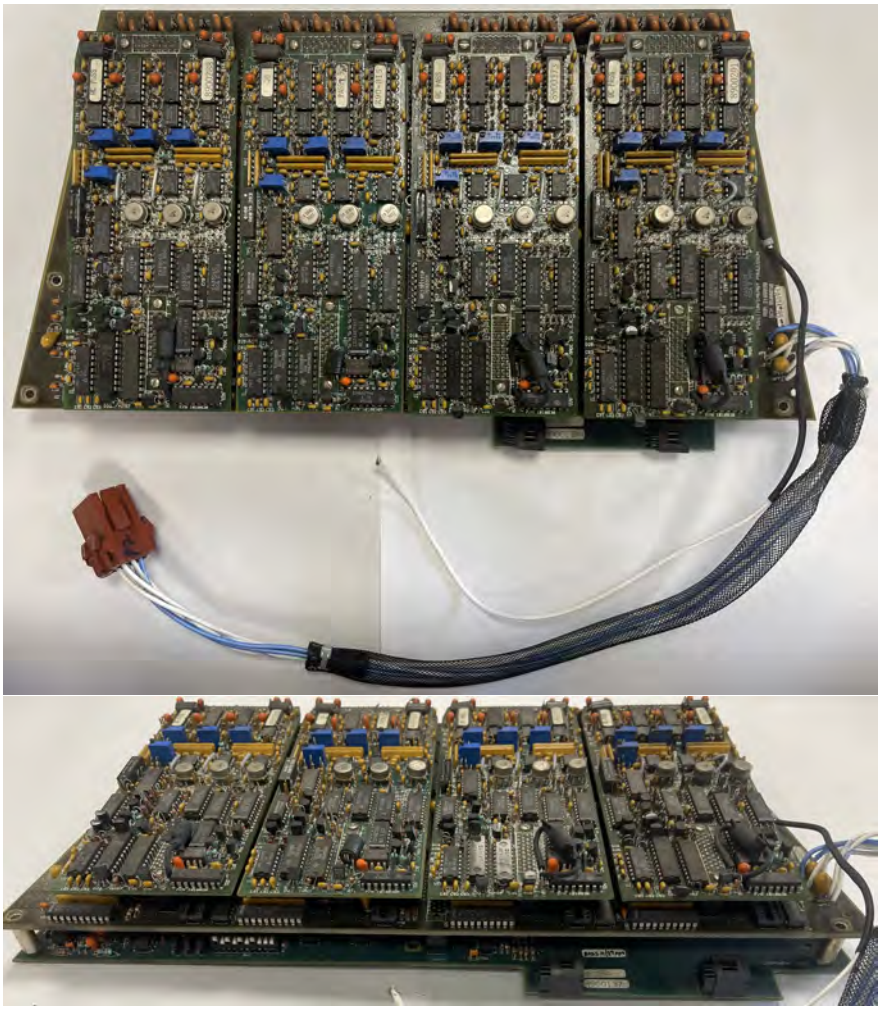

Figure 7.12: ECAT 951 bucket electronics assembly shown from the top and side. The side view shows the layered nature of the assembly with the boards being attached via inter-board connectors.

controller incorporated additional memory for the storage of the position lookup tables and used reprogrammable GAL chips instead of PAL chips for comparison. It also needed to accommodate data bus lines and drivers to move the lookup table data to the appropriate GAL chips from the microcontroller's EEPROMs at boot. Furthermore, the microcontroller needed a way to intercept the raw digitised timing and the transaxial, axial, and total energy values before they were used in the lookup tables to form histograms for user interpretation or to be used during an automatic block calibration routine. As a result, the electronics were reshuffled and regrouped on the various boards. Therefore, the bucket assembly shown

in Figure 7.12 is now made up of three different boards: a single bucket controller board shown in Figure 7.13 on the bottom, a single position and energy processor board shown in Figure 7.14 in the middle, and four analogue processor boards shown in Figure 7.15 (one per detector block) on the top of the stack.

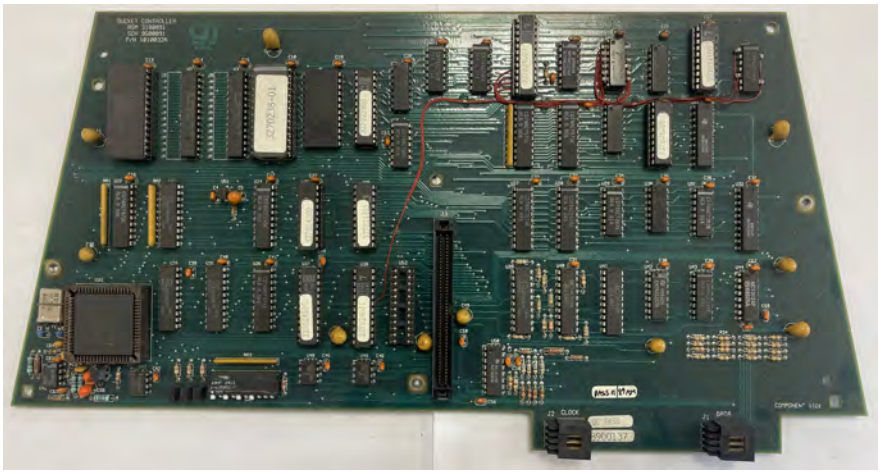

Figure 7.13: ECAT 951 bucket controller board containing the Intel 80C196 microcontroller in the bottom left corner and the clock and data connectors on the bottom right (PN: 1010032A).

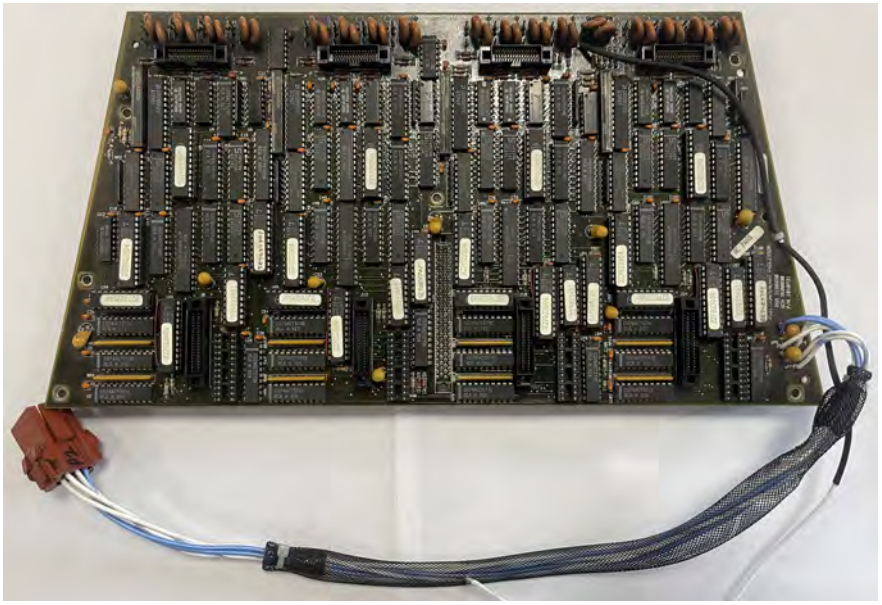

Figure 7.14: The ECAT 951 bucket position and energy processor board which contains the time digitiser and the GAL crystal element position lookup logic. The board also features the power supply lead and the PMT connectors lined along the top edge of the board (PN: 1010031).

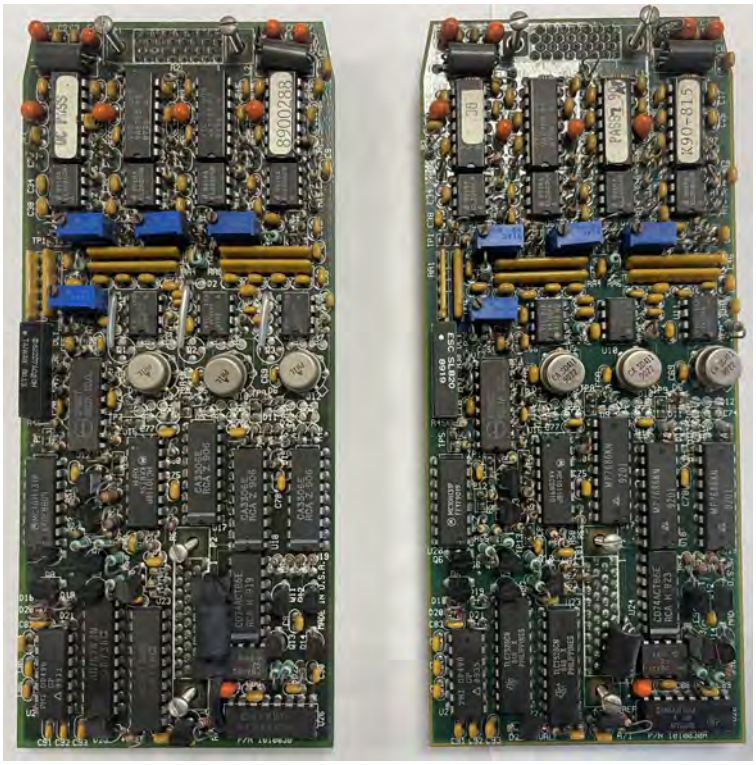

Figure 7.15: The ECAT 951 bucket analogue processor boards are mounted on top of the position and energy processor board via the top horizontal and the bottom vertical inter-board connectors. Two versions of the board are shown here. Left: (PN: 1010030) Right: (PN: 1010030A) The newer right version is missing pads for various unpopulated components found in the earlier left version.

The various boards were sandwiched together and used inter-board connectors to create a low-profile board assembly. On top of the bucket controller board sits the position and energy processor board which accepts the digitised energy signals and the timing pulse from each of the four analogue processing sections. The board is connected using a single inter-board connector to the bucket controller and it is responsible for distributing the logic power throughout the bucket and the HV directly to each of the PMTs' three-pin connectors also located on this board. The PMT signal is taken from that connector and passed to the analogue processor board it uses. The analogue processor boards sit on top of the position and energy processor board and connect to it via two inter-board connectors: one predominately handling the data inbound to the analogue section and the other handling the outbound data. Otherwise, the analogue section works as described in Section 6.1.2.

Unlike the ECAT 931 system where the vertical boards were permanently soldered together, this design allowed for easy troubleshooting and replacement of faulty boards thanks to the connectors [293].

Unlike the ECAT 931 bucket controller, the ECAT 951 controller used the Intel 80C196 16-bit microcontroller which is part of the Intel MCU-96 family. It is a commercial derivative and upgrade of the Intel 8061 used in the ECAT 931 bucket controller. It is important to note here that from this point on the Intel 80C196 became a microcontroller of choice at CTI as it will be used everywhere a microcontroller needs to be used in future scanners. It will eventually replace the microcontrollers on the coincidence processor board, various motor driver boards, and various sensor boards around the scanner. The bucket controller board also featured extra EEPROMs to store the calibration settings and lookup tables. It received the same timing signals and communication lines as the ECAT 931 bucket from the same clock fanout/gantry controller board shown in Figure 7.6; however, it sent slightly different data. It still used four twisted-pair differential ECL lines to send data to the coincidence processor where two of the lines were used to send the usual clock signals as

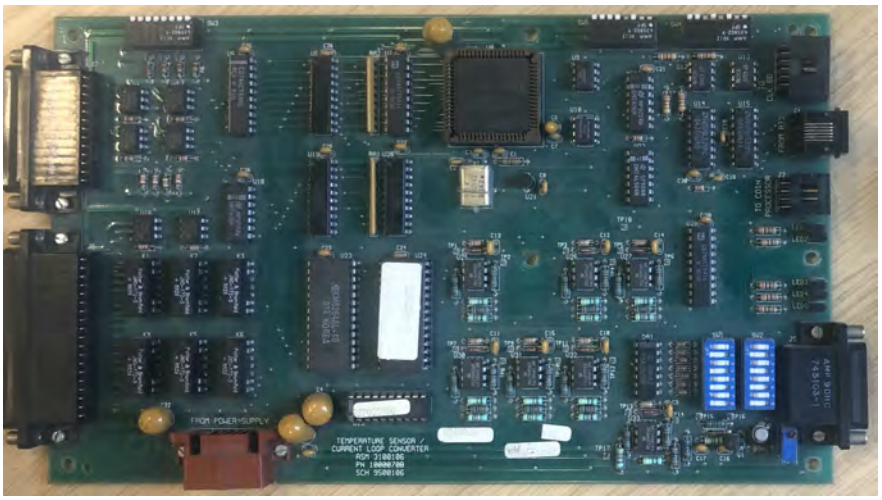

Figure 7.16: The ECAT 951 temperature sensor and current loop converter board. This upgraded board features the Intel 80C196 microcontroller (top dead centre) and integrates the temperature sensor interface for the scanner gantry (PN 1000070B).

described before. One of the data lines sent the same six-bit timing word, a valid hit flag, and a scatter event flag like in the ECAT 931 bucket. However, the other data lane now sent the three bits describing the column number, three bits describing the plane number, and two bits describing the block number in which the hit occurred. This is the same as the ECAT 931 board except for an additional plane bit. The ECAT 951 also featured the newly upgraded and integrated current loop converter board shown in Figure 7.16 that now included the gantry temperature sensor interface.

7.3 The ECAT EXACT

The ECAT EXACT released between 1991 and 1992 was the first multi-ring scanner truly designed for whole-body 2D and 3D emission and transition scans. As a result of many advances in this generation of the scanner, which features a wide axial FOV due to up to three rings of detector blocks and native 3D data acquisition, many features of the gantry were redesigned. The wobble functionality was removed as it was intended to improve image resolution which now was possible through the use of 3D scans. Therefore, the gantry came with retractable septa and retractable transmission rotating rod sources as a standard. Due to the wider axial FOV, the need to position the gantry and patient at weird compound angles to each other to obtain clearer images of certain organs disappeared. As a result, this was the first ECAT gantry to be fully stationary. The gantry could not rotate, tilt, or wobble. The gate input functionality was also removed from the system [284, 294].

With a system so densely filled with electronics to support the three detector rings, the gantry was water-cooled. Water cooling was provided through the use of an external water chiller which pumps the chilled water into two heat exchangers within the gantry. Two powerful, yet quiet, fans blew the hot gantry air through the heat exchangers and blew

out chilled air in such a way as to create a vortex within the gantry directly cooling all the electronics [294].

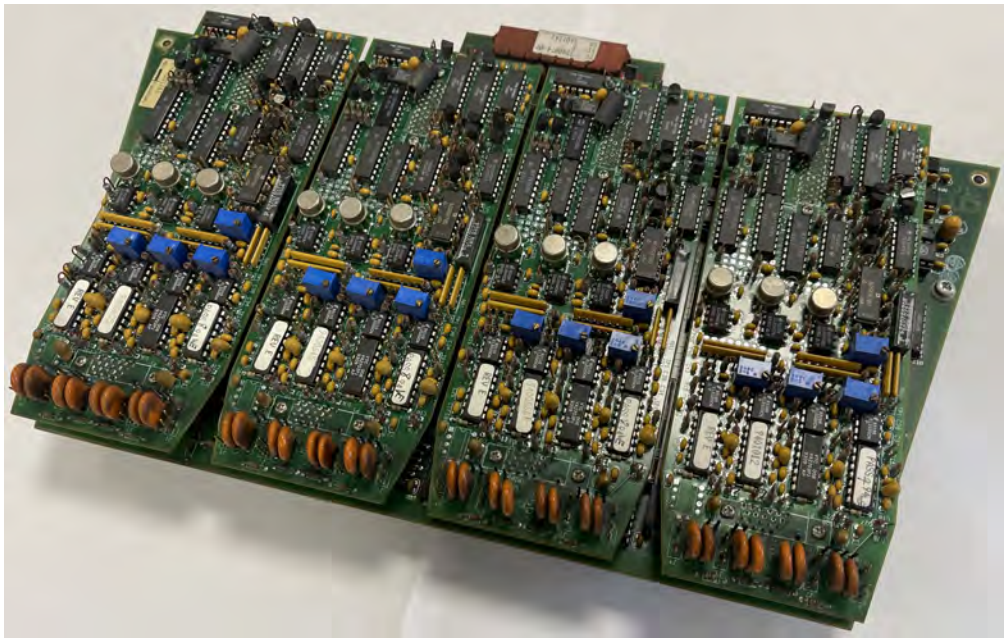

Figure 7.17: The ECAT EXACT bucket electronics are very similar to the ECAT 951 bucket electronics shown in Figure 7.12. The design features a power connector seen in the back instead of a power lead for the logic power and the analogue processor boards now hold the PMT socket pins. (Bucket Controller PN: 1010050A, Position Energy Processor PN: 1010049B, Analogue Processor PN: 1010048B)

With this scanner generation, the bucket controller did not change much, as shown in Figure 7.17. The only notable change was the redesign of the power connector and the move of the PMT connectors to the analogue processor boards. The biggest change of all the assembles happened to the coincidence processor board. Using digital VLSI ASIC technology, most of the coincidence testing functions were incorporated into these chips replacing hundreds of custom-programmed PAL and GAL logic chips. With this miniaturisation, all the coincidence processor functions from the ring receiver to the testing of coincidences between all the rings and the final output of data to the ACS were now located on a single board smaller than an IPCP board from the ECAT 951 [294].

The ACS also underwent a small redesign mostly to concentrate certain RTS cards

together and remove unneeded wobble correction logic among a few other things to form the RTS II. The operator's console also did not change much. An updated Sun SPARCStation IPX workstation was provided with the system running the latest SunOS and ECAT software [295].

7.3.1 Detector Block and Gantry Options

The detector block used in the ECAT EXACT stayed in principle the same as the ECAT 951 block except for a new mounting system as seen in Figure 7.18. The ECAT EXACT was also only offered with a single detector block size where the scintillator crystal was divided into an 8x8 crystal element array with each element being 6.45 mm by 6.45 mm square and 20 mm deep with a pitch of 6.75 mm in each direction. Unlike the previous scanners, the ECAT EXACT was offered in a single gantry diameter option of 82.4 cm detector diameter and 56.2 cm patient portal diameter. This gantry diameter supported only 12 buckets per

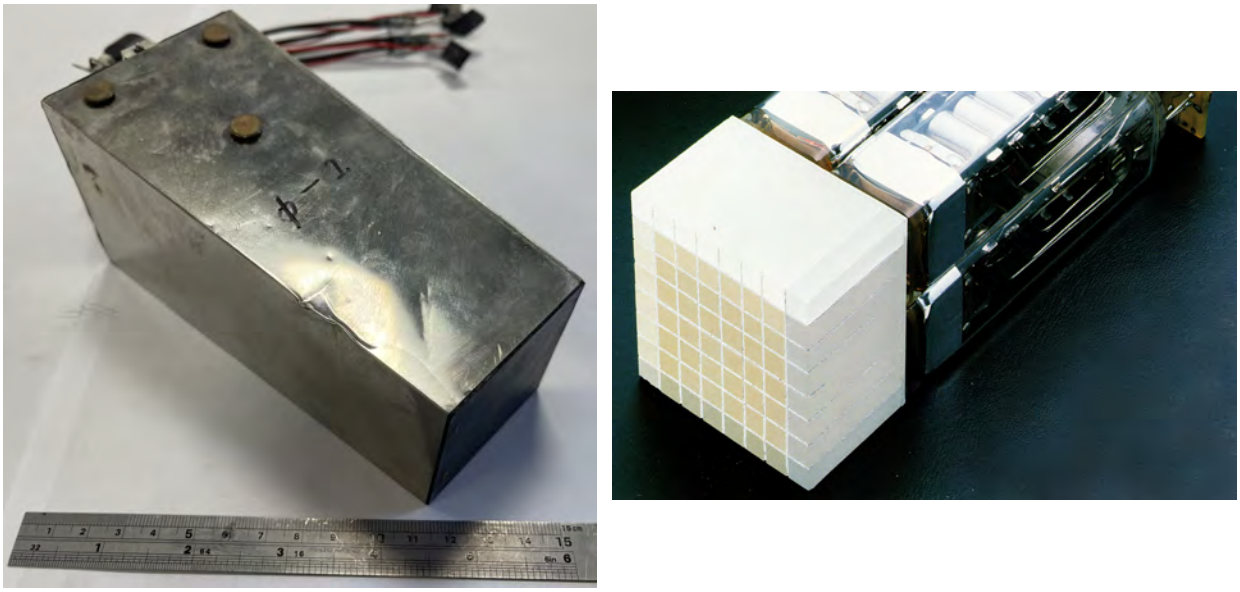

Figure 7.18: Left: The ECAT EXACT detector block shown with the new stud-based mounting system. The opposite side has holes into which these studs can lock in. Right: A promotional picture of the EXACT block showing the square BGO element matrix [284].

ring, but the scanner was offered as standard with a two-ring gantry in its EXACT 31 variant (model 921) and was also available in a three-ring gantry in the EXACT 47 variant (model 922). Therefore, unlike the ECAT 951, the EXACT was only available in two different variants, the 31 and 47, the numbers simply based on the number of 2D image planes [284, 294, 296].

7.3.2 The ASIC Coincidence Processor

Perhaps the most significant development to emerge with the ECAT EXACT was the so-called Three Ring Coincidence Processor shown in Figure 7.19. Like the previous versions of the coincidence processor, this one receives signals from each of the buckets as described before. The clock signals are only used from the first and last bucket in each of the first two ring inputs: buckets 0, 11, 12, and 23. The ECL signals are converted to TTL, the data is deserialised, and it is latched into appropriate input PALs ready for processing. Unlike previous versions, this coincidence processor groups the three physical rings into two logical rings. This is achieved through the use of a smart virtual ring.

The coincidence processor is divided into four test sections: two testing coincidences within a ring and two testing coincidences between adjacent rings. This is similar to how the ECAT 931 and 951 coincidence processors had four IPCP boards to handle the coincidences. In this setup, events from rings one and three have priority in the system as they are directly linked to each coincidence processor subsection. However, ring two events are distributed between the sections depending on which one has an event waiting for processing. Labelling the subsections as A, B, C, and D, subsection A always processes events occurring within ring one and subsection D always processes events occurring within ring three. Now depending on the system load, events occurring within ring two will be either guided to subsection A or D depending if either of them has an event to process. If both subsections are busy

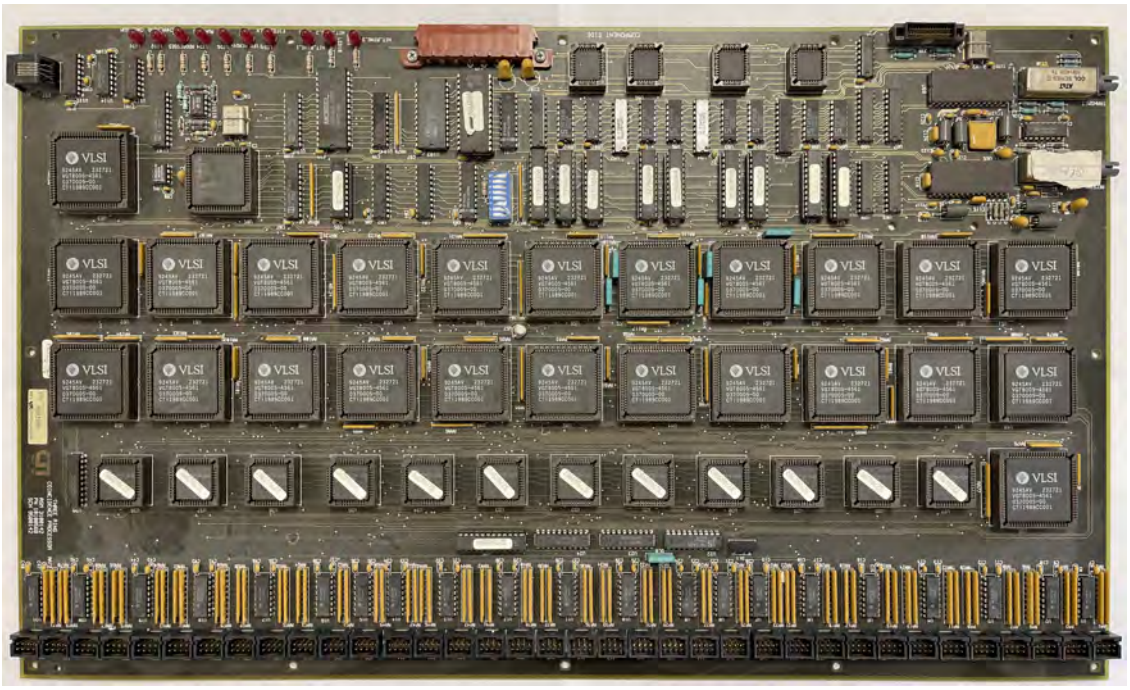

Figure 7.19: ECAT EXACT three ring coincidence processor featuring the ASIC chips miniaturising a cabinet worth of electronics onto a single board. The coincidence processor accepts the data from all three rings using the sockets at the bottom of the board and sends the coincidence data over the fibre optic serial in the top right corner of the board to the ACS (PN: 1010056B).

with ring one and three events, the ring two event is lost. Similarly, subsection B always processes cross-plane events from ring one to two and sometimes events from ring two to three, and subsection C always processes cross-plane events from ring three to two and sometimes events from ring two to one. With this trick, it is possible to fit three rings into a two-ring coincidence processor. The same board is used for the two-ring (/31 version) system except that it only has two-thirds of the buckets plugged in. With the third ring missing, the second ring is always guaranteed to have a free subsection for event processing [294].

With the data being latched into the input PALs and grouped into the appropriate logical two rings, they are tested for coincidence. The testing is done for each subgroup by six custom VLSI ASIC coincidence chips where each of the chips is the same and tests a different set of allowed module pairs simply through its hard-wired position on the board.

Therefore, all the VLSI ASIC chips can be interchanged with one another. The coincidence testing is done in the same way as described in Section 6.2. Finally, the coincidence data is formatted into a 32-bit word, serialised, and sent over to the ACS RTS II coincidence input board via a fibre optic cable. As the coincidence processor is now a single board, it is mounted inside the gantry itself removing the need for the extremely long data cables which used to run to a separate electronics room.

7.3.3 The ACS II

The ACS received some minor updates consolidating some of its boards into a more modern design described in Section 6.3. In summary, the ACS still contains an arbiter, a Motorola 68020 CPU-based single-board computer, an Intel-based array processor, SCSI for disk and tape drives, multiple VME memory cards, and an Ethernet interface to the Sun workstation. The RTS II coincidence input board now incorporates the memory read back function which was previously part of the RTS read controller board. Then, the staged coincidence word is passed to the RTS formatter card which simply converts the coincidence data word into a sinogram angle/displacement and inserts tags like timing words into the data stream. The functionality to add wobble correction was removed with the removal of the feature from the scanner and the insertion of the rotating rod transmission event was moved into its own card. The data was next passed from the RTS formatter card to the RTS rotating rod converter card which, when enabled during transmission scans, modifies the event tag data to identify events from a transmission source, otherwise, the data simply passes through the board to the RTS sorter card. The RTS sorter card now besides converting the angle/displacement data through the bin address calculator to find the sinogram bin in memory and modify it using direct memory access (DMA) via read-modify-write procedure also incorporates the feature of the RTS write controller and can write the original coincidence word along

with any tag information and event words for list mode data acquisition. Finally, the RTS injection monitor card like before keeps a tally of all the event types for the various image planes [294].

7.3.4 The Gantry Controller

With this scanner model, various functions that were previously delegated to many small boards located all around the gantry and different cabinets were finally consolidated into a single board. The removal of various gantry motion functions also meant the removal of the motion control cabinet and the incorporation of the leftover motion functions into this board.

The gantry controller now acts as the main function orchestrator within the gantry. It is managed by an Intel 80C196 microcontroller which acts as the main interface and command interpreter. The gantry controller incorporates the current loop converter and the clock distribution and fanout boards receiving RS-232 serial communication from the operator's workstation via the ACS. The board generates the clock signals described in Section 6.4, distributes them to the bucket controllers, and creates and manages the motion serial bus which connects to the rotating rod motion controller board, the septa motion controller, and the bed motion controller boards. Each of these boards has its own Intel 80C196 microcontroller responsible for interpreting the motion commands sent to it and monitoring the various limit and emergency switches and motor motion and position. They not only drive the appropriate motors but also verify that the motion was correctly executed. If any problem occurs, they send error codes to the gantry controller or simply raise an emergency stop alarm.

The gantry controller also controls the LCDs and user inputs located on the outside

of the gantry as well as monitors various emergency stop signals and dead man's switches. Again, as with the coincidence processor, the miniaturisation allows it to be mounted inside the gantry further reducing the footprint of the scanner [294].

7.4 The ECAT EXACT HR

The ECAT EXACT HR (model 961) scanner was released around 1993-1994 and was the first PET scanner to feature a resolution better than 4 mm [284]. Unfortunately, it seems to be a rare scanner with possibly only a couple of gantries ever produced. There is little to no information available about it and only a couple of papers name it as a scanner used in an experiment. From what's available, the scanner was made up of a unique detector block whose crystal was cut into an eight axial by seven transaxial array of 30 mm deep crystal elements that measured 5.9 mm in the axial direction and only 2.9 mm in the transaxial direction making up eight rings with very fine crystal elements. Due to the small size of the crystal block in the transaxial dimension, the detector block was only viewed by 2 PMTs that featured double photocathodes still producing four signals per detector block [225, 297, 298].

The scanner gantry was made up of three rings, each having 112 detector blocks with a detector diameter of 80 cm and a patient portal diameter of 56 cm. Overall, the system is described as being almost the same as the previous ECAT EXACT system just with a lot more detector blocks that were capable of 2D and 3D scans with its retractable septa and transmission rod sources. As not much else is said about the scanner, if it used the same bucket controller as the ECAT EXACT then that would mean that each detector ring would contain 28 buckets [225, 297, 298].

7.5 The ECAT ART

The ECAT ART or Advanced Rotating Tomograph (model 925) is a partial-ring full-body PET scanner that was designed with the sole purpose of providing an affordable scanner to the wider medical and research community. It was the first PET scanner to cost under a million US dollars at the time [284]. Its design began around 1992 as a partnership between CTI and the University of Geneva to develop the RPT-1 or the Rotating Positron Tomograph. The group used a mix of available electronics from CTI to build the scanner with a detector block divided into an eight by eight array of 5.6 mm axial height, 6.45 mm transaxial width, and 30 mm depth crystal elements. It was arranged such that it was made out of two detector rings in two opposite banks where each bank was only two buckets wide, containing 16 detector blocks as can be seen in Figure 7.20 left. The group conducted many tests including 2D and 3D scans in a rotate-stop-shoot fashion taking readings at between 6 and 48 consecutive angular positions. With their data, they realised that with this scan method, 3D scans were of comparable sensitivity to a 2D scan using a full-ring scanner.

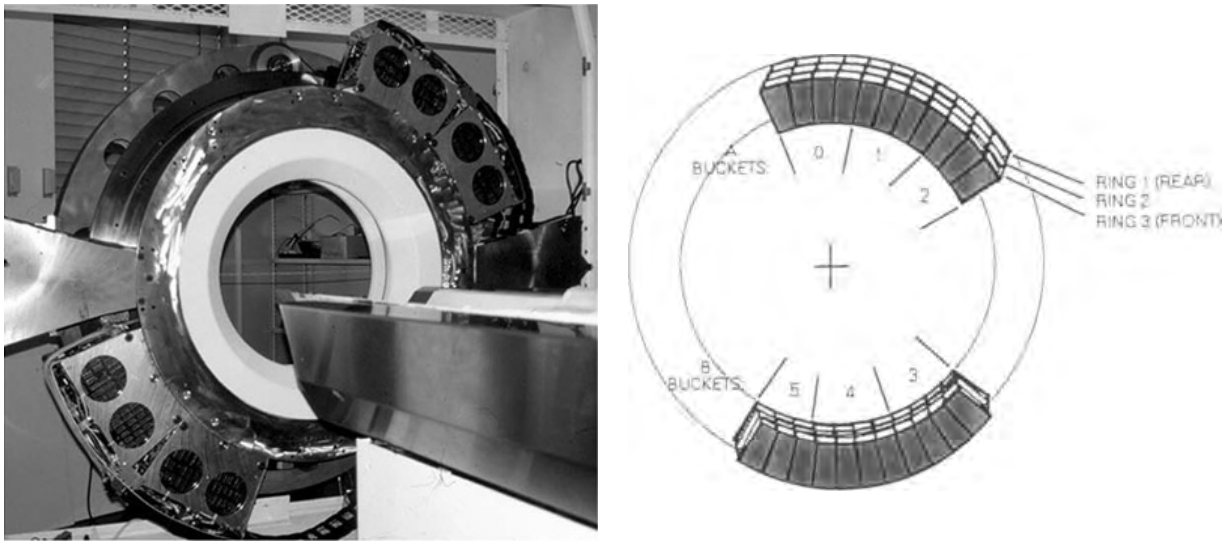

Figure 7.20: Left: The PRT-1 with its covers removed showing the opposite banks made out of four buckets each (in two rings) [225]. Right: The ECAT ART gantry layout with its three-ring design and banks containing 2.75 buckets worth of detectors asymmetrically opposed to each other [299].

However, to improve image quality and sensitivity, they recommended three detector rings to be used in the next prototype [300].

Soon after they built a second prototype, the RPT-2, with suggested modifications to the buckets with no septa for a full 3D scanner. They started to use the same detector blocks as found in the ECAT EXACT scanner and arranged them into three rings of 10 detector blocks per ring per bank, needing to use two and a half bucket controllers per bank per ring. This created a gantry with a detector diameter of 82 cm and each bank covering 75° of the full gantry. This scanner was comparable to the ECAT EXACT 47 full-ring scanner and fit into the same footprint incorporating its water-cooling features but only containing 40% of the detectors. An interesting feature incorporated in the RPT-2 was the ability to offset one of the buckets by 37.5° as a measure to increase the FOV of the scanner. The study concluded that the RPT-2 provided comparable results to a full-ring scanner made up of the same number of detectors and when compared to a proper full-ring scanner like the ECAT EXACT it did show a bit of a performance loss which was acceptable to produce proper quality medical images. Eventually, the details were finalised and the ECAT ART was released around 1994 [284, 299, 301].

The production ECAT ART was a fully 3D scanner with no septa, included retractable rod sources, and added back the gating functionality. The gantry had a detector diameter of 82 cm and a patient portal diameter of 60 cm. It featured a few modern advances most important of which was the VLSI ASIC-based bucket controllers. Both the analogue and the digital sections had separate ASIC chips produced which greatly minimised the bucket's footprint but most importantly allowed each bucket to now host 12 detector blocks instead of the four in the older versions. Like in the RPT-2, the ECAT ART used the same detector blocks as the ECAT EXACT. With the new bucket design, there was no longer a need to have separate bucket assemblies to manage a few blocks in each of the rings. Instead, the 12 detector blocks were now stacked in three axial and four transaxial arrays to produce

the three rings. Each bank was made out of two full buckets of 12 detector blocks and a final partial bucket which only contained 9 detector blocks for a total of 3 by 11 bank of detector blocks. Each of the banks spanned 82.5° of the gantry and the two banks were now permanently asymmetrically opposed to each other to increase the FOV of the system, as shown in Figure 7.20 right [299].

Besides the bucket controller and the detector block, all other parts of the ART electronics were specially designed and included features only found in this rotating scanner. The coincidence processor still operated on the same principle as all the others, but it only required a single coincidence ASIC chip to process all the coincidences. Due to a bucket now spanning multiple rings, the input drivers would assign the data from the physical buckets into virtual rings to divide the 12 blocks into smaller test sections. The coincidence processor also contained the clock generation and serial fanout to all the buckets and the rod source controllers. This made it the only ECAT coincidence processor to generate the clock and both send and receive signals to the bucket controller. The communications controller, or the ART version of the gantry controller, mostly incorporated similar features as the EXACT. It sent and received serial commands from the ACS and passed them to all the other boards in the gantry. It interfaced with the coincidence processor, bed controller, front panel IO, gantry rotation controller and position readback, gating inputs, and various safety switches [302].

The ACS was also modified and updated appropriately. First of all, it featured two single-board computers. The first one was a Sun SPARC-based computer which interfaced with the CSPI SC-4 quad array processor, it was predominantly occupied with image reconstruction, and it connected via an Ethernet link to the Sun workstation. The rest of the ACS and the RTS were under the control of a Motorola 68030 CPU-based computer which also interfaced with the Sun workstation via a second Ethernet connection. The coincidence data arrived at the ART translator card which received the data and translated them into

angle/displacement format. The data were then passed to the RTS VSB (VME Subsystem Bus) Sorter card which calculated the sinogram bin address and through the use of DMA performed the appropriate bin increment or decrement operation in VME memory. The VSB sorter leveraged the VSB bus system to free up and bypass the VMEbus so it is free for image reconstruction operations. Finally, as always, the event tag was passed to the injection monitor which kept the event tally [302].

7.5.1 The ASIC Bucket Controller

One of the most important advancements introduced with the ECAT ART was the development of the extremely simplified, VLSI ASIC-based, 12-detector-block bucket controller. This bucket was made up of a single bucket controller board which contained the bucket microcontroller and the digital ASIC chips responsible for position lookup and data staging. It had vertical supports for six analogue processor boards each of which processes analogue data from 2 detector blocks before passing it to the digital ASICs, see Figure 7.24.

The Analogue Processor Board

The analogue processor board is the simplest element of the bucket assembly and is shown in Figure 7.21. The board receives logic and HV power from the bucket controller board which is passed through a small board containing HV resistors that act as replaceable fuses. This is a welcome change from the previous designs as it adds an extra layer of protection to the whole board and makes it easier to repair in case of an overload. The HV is then distributed to the eight three-pin connectors for each of the PMTs from the two detector blocks the board supports. The signals from each of the detector block's PMTs are taken to the analogue ASIC chip which runs all the analogue functions. The analogue ASIC contains the variable gain amplifiers, the DACs for offset and gain control, the CFD, the position/energy integrators,

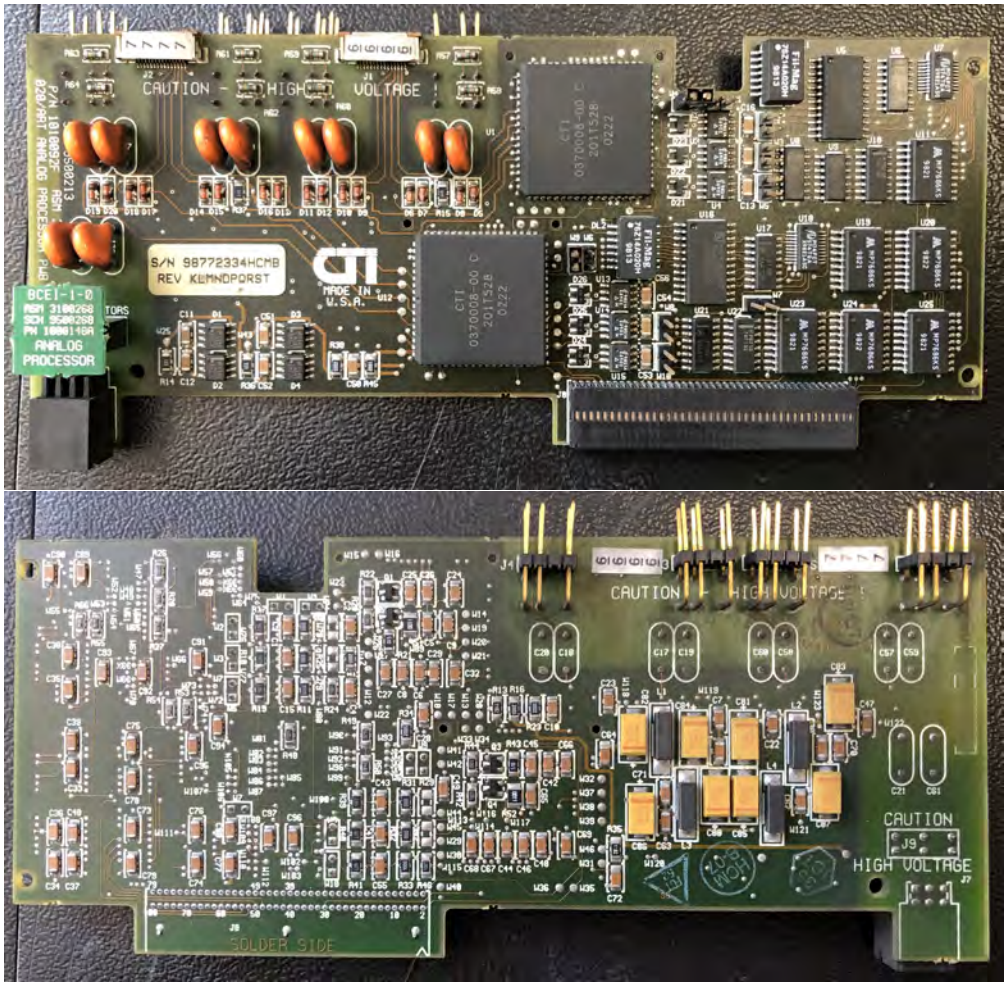

Figure 7.21: The analogue ASIC processor board from the front and back. The two big analogue ASICs are visible on the front as well as the small green removable HV resistor/fuse board (PN: 1010092F).

and circuitry for self-testing and communication with the bucket controller as can be seen in Figure 7.22. The analogue ASIC produces the CFD time mark and the transaxial, axial, and total energy signals. These energy signals are processed by flash ADCs elsewhere on the board and the time mark is interpreted into a seven-bit timing word through the same method, as described in Section 6.1.2, and are latched into output buffers ready to be sent to the main board. The circuit is exactly duplicated for the second detector block. The analogue ASIC can communicate with the microcontroller on the bucket controller board through the use of a common I2C serial bus to all the analogue ASICs. Each chip's I2C

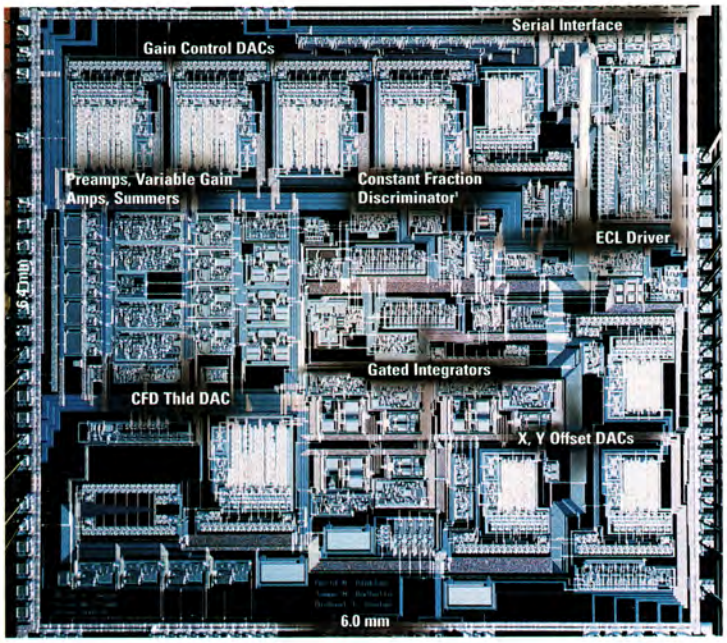

Figure 7.22: A microphotograph of the analogue ASIC chip die. The analogue ASIC was implemented in the 2 µm CMOS technology with 3,600 analogue CMOS transistors [284].

address is assigned by the slot they are inserted into on the bucket controller board and therefore the boards and the ASIC chips are interchangeable. The I2C bus is used to upload the preamplifier gains, offsets, and CFD adjustments from the microcontroller memory on boot.

The Bucket Controller Board

The bucket controller board, shown empty in Figure 7.23 and fully populated in Figure 7.24, in essence, works as described in Section 6.1.4. An Intel 80C196 microcontroller manages all the boot activities and board mode settings, and it has a memory/IO manager that gives it access to many different data buses located within the bucket. It can interface with an EPROM containing the bootstrap, low-level communication program, and basic self-tests. The EEPROMs contain the firmware and the various calibration settings the microcontroller uploads to each of the ASICs at startup. There is also additional RAM for

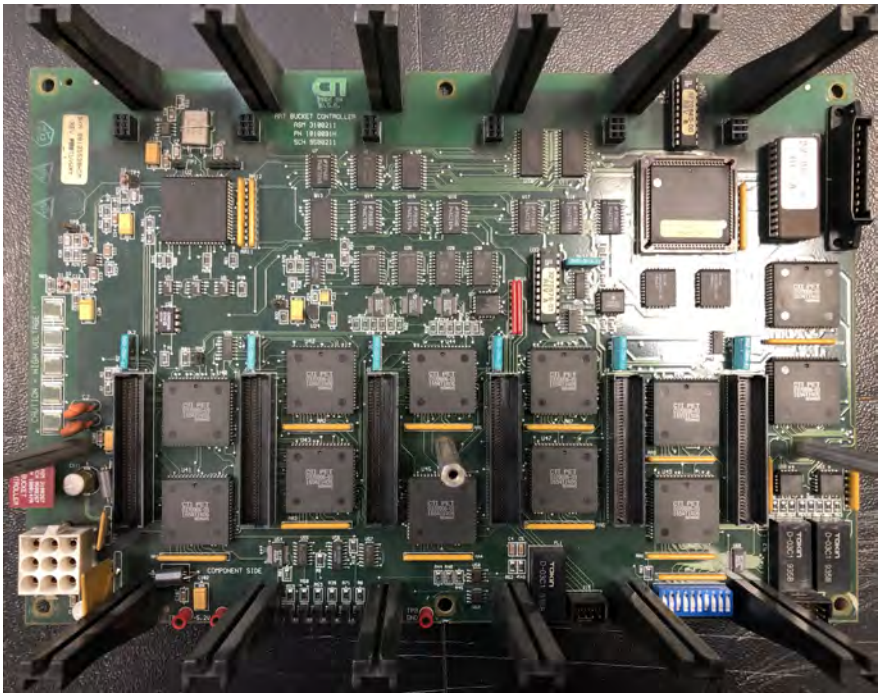

Figure 7.23: The ASIC bucket controller board. The 80C196 microcontroller can be seen in the upper left corner, the sequencer in the upper right corner, the power connector and HV resistors/fuses in the bottom left corner, and the 12 digital ASIC chips all along the bottom half of the board between the analogue processor boards' inter-board connectors. The board also features vertical guides/supports for the analogue boards.

use during calibration and histogram formation modes to store the data as well as to store the various tallies the microcontroller keeps during normal runtime. The microcontroller also monitors the different voltage levels, board temperatures, and has direct access to the analogue ASICs' I2C bus. As with all the bucket controllers before, the board receives the serial communication lines and the two clock signals via differential ECL as described in Section 6.1.4. The board then distributes these clock signals and derives its own to drive the ASICs [302].

The digital ASIC chips are based on a 37,000 gate array made in 1.2 µm CMOS technology and perform the rest of the functions in the bucket controller pipeline. They receive the digitised time and energy signals upon their request from the analogue ASIC and use a lookup table with threshold values to determine the crystal element in which the

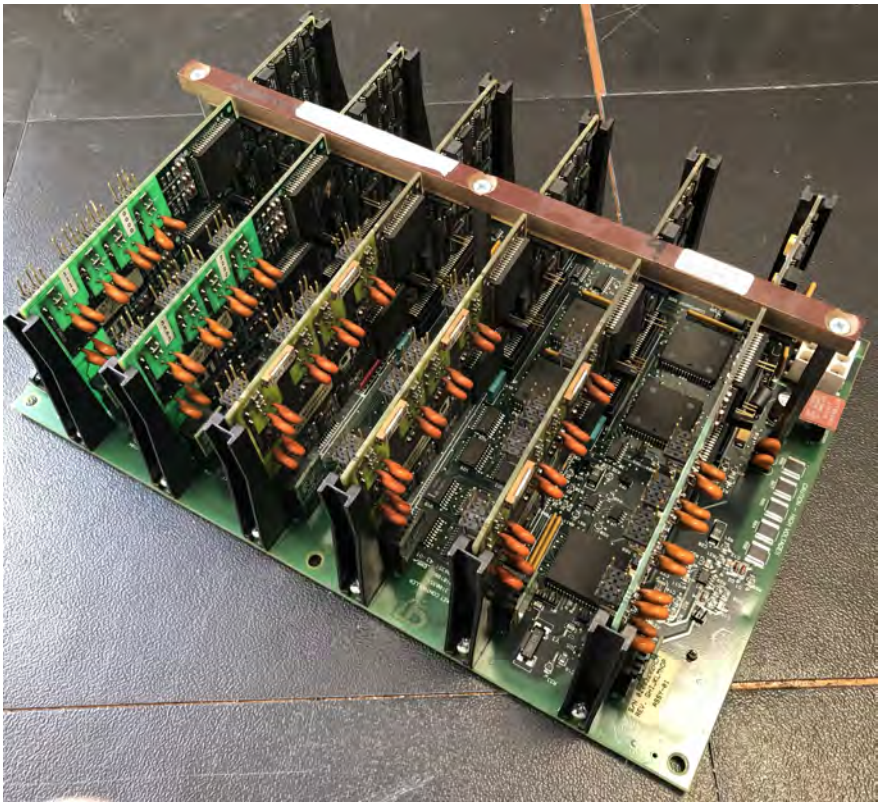

Figure 7.24: The ASIC bucket assembly with all 6 analogue processor cards populated. From left to right, the first two and the last card are of a newer HR+/ACCEL update which removed some unnecessary/development parts (PN: 1010172). The other 3 cards are of the first ART version shown in Figure 7.21. Functionally, the two versions of the analogue cards are the same.

hit occurred. Time correction and energy discrimination are also performed by this chip before the data are formatted into three eight-bit serial words. To reduce the number of data lines on the board, the digital ASICs are all daisy-chained together through three serial lines and two control lines. The data are buffered from the topmost chip to the lowest chip until they reach the output buffer and are sent to the coincidence processor over twisted-pair differential ECL. However, for the first time, this connection has been changed. Now instead of four signal lines the cable carries five signal lanes. Two of the lanes carry the same clock signals as described in Section 6.1.4 while the other three data lanes carry the time, detector, and the new ring information [302].

One important difference from the previous bucket controllers is that each digital ASIC has a built-in sequencer that can be reprogrammed through a set of internal latches set by the microcontroller. These latches allow the microcontroller firmware to not only change the timing of certain parts of the digital ASIC functionality but also the order of events that occur within for maximum flexibility. All of these settings along with the lookup table data, time correction, and discriminator level settings are programmed into the digital ASICs at startup by the microcontroller. This is done through a special eight-bit wide interface that uses two control signals. This interface is only connected to the topmost chip and the setting data are cascaded down the chain through the same serial lines that later carry the interaction data. The ASIC can also be set into a histogram mode where it does not do any position lookup or corrections to the data and simply passes it down the data chain. At the last chip, during the histogram mode, the microcontroller can read the raw data to produce the various position and energy calibration histograms [302].

7.5.2 ART to PET/CT

In the end, the ECAT ART sold fewer units than expected simply because PET studies were starting to be covered by certain insurances which enticed clinics to invest in higher-quality and faster scanners [225]. The ART gantry design was not a total loss. The rotating gantry made it a perfect opportunity to mount a spiral CT system. As a result, in a partnership with the University of Pittsburgh, CTI developed the first PET/CT to be mounted on the same rotating gantry shown in Figure 7.25 in 1998 [303]. One advantage of the system was that both PET and CT scans could be performed at the same time and that the CT scans could be used for attenuation correction in PET scans which otherwise required an additional transmission PET scan to be performed. Therefore, a combined PET/CT greatly increased the patient throughput and provided PET/CT combined images that not only showed the

physiological structure of the patient but overlaied the radioisotope distribution for easier identification of any problem areas. This ART was later developed into the LSO-based Biograph PET/CT system released in 2001, see Section 7.8.4. The PET/CT development eventually led to the end of the clinical PET-only scanners by around the mid-2000s when no major manufacturer was offering one for sale [225, 304, 305].

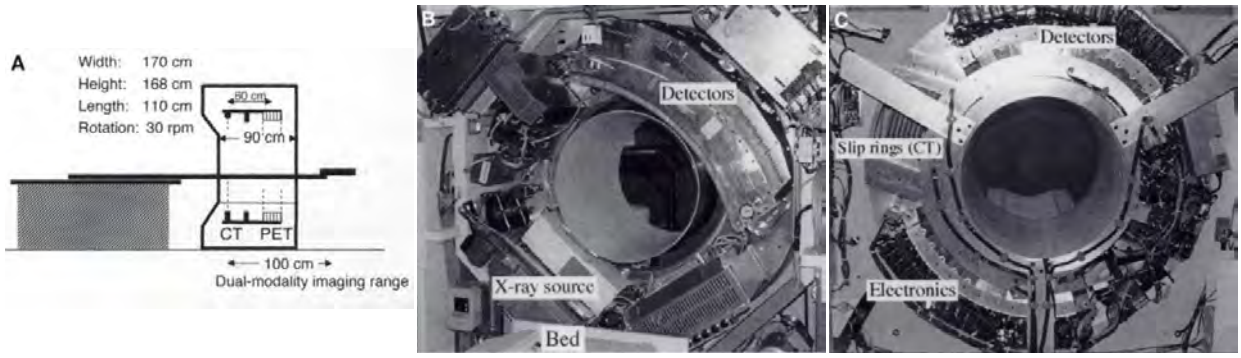

Figure 7.25: The first PET/CT system developed by Beyer et al. [303] combined the ECAT ART (C) system with a helical Somatom AR.SP CT scanner (B) mounted in the same gantry offset 60 cm axially (A).

7.6 The ECAT EXACT HR+

The ECAT EXACT HR+ (model 962) released around 1996 was the last commercially produced ECAT scanner with the BGO-based detector blocks. The scanner featured retractable septa, rod sources, an automated patient bed, and a water-cooled gantry. It contained one of the smallest 8x8 BGO detector blocks shown in Figure 7.26 for an ECAT system with a crystal element axial height of 4.39 mm with a 4.85 mm pitch and the transaxial width of 4.05 mm with a 4.51 mm pitch and a 30 mm depth. Like the ECAT EXACT block, the HV divider circuit for the PMT is located on a small removable board that connects to the back of the detector block [298, 306].

This scanner incorporates the ASIC bucket design introduced with the ECAT ART

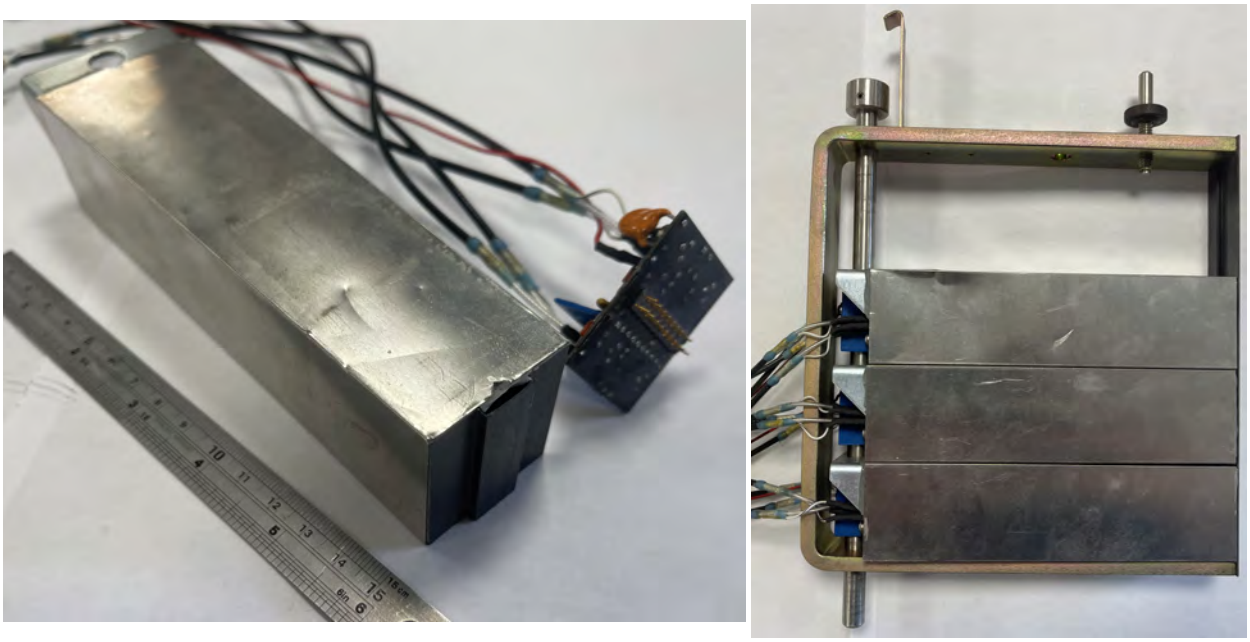

Figure 7.26: ECAT EXACT HR+ detector block. Left: ECAT EXACT HR+ detector block with its removable HV distribution board disconnected and placed to the side. Right: ECAT EXACT HR+ detector block assembly for a single column of four blocks, with one block removed. Three of these assembles were joined to a single bucket assembly that was then inserted into the scanner gantry.

described in Section 7.5.1. With this bucket, the 12 detector blocks were stacked to produce a 4x3 detector block array with four detector rings. The full gantry contained 24 of these buckets for a total of 72 detector blocks per ring for a detector diameter of 82.4 cm. Many other electronics have not changed functionally since the ECAT EXACT version. The gantry controller shown in Figure 7.27 handles the same functions except that it was adopted for 24 buckets. The operator's console is still based on a Sun workstation and the ACS II contains an additional SPARC CPU for the array processor like in the ART. The RTS II system is similar to that of the ECAT EXACT except it supports the ECAT EXACT HR+ coincidence word structure and can bin it appropriately. It also contains an additional RTS write controller board like in the old ECAT versions so it could support quicker list mode data acquisitions without relying on one of the other boards for that task [298, 306].

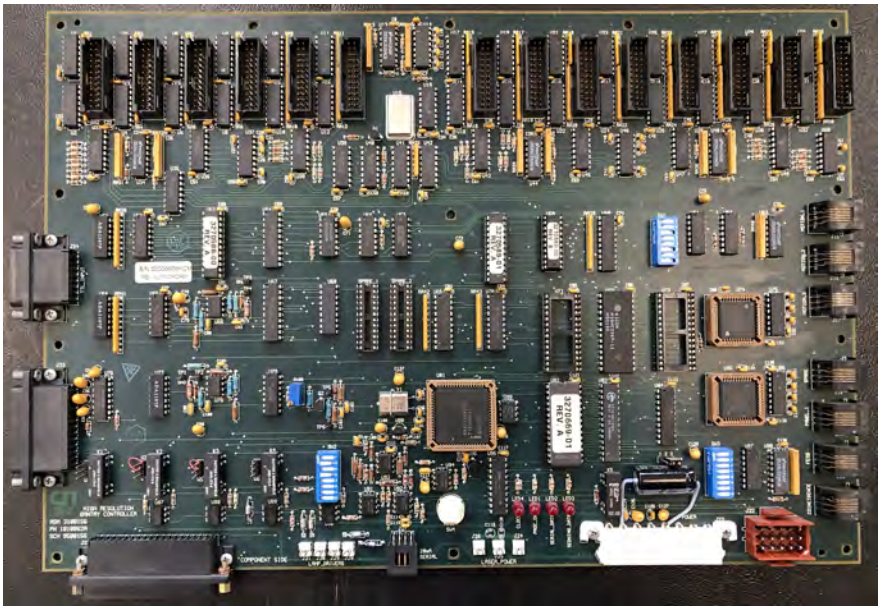

Figure 7.27: ECAT EXACT HR+ gantry controller board (PN: 1010062A). The connectors on the top of the board are for the bucket communication and between them, in the centre, is the 125 MHz main oscillator. On the left side are various IO/sensor connectors. On the right side are serial interfaces to the various motion and other gantry control boards. Right below the centre of the board is the Intel 80C196 microcontroller.

7.6.1 The Lossless Coincidence Processor

The ECAT EXACT HR+ coincidence processor is the only board that was functionally redesigned to accept all the detector inputs and check their coincidences. Similarly, as in the ART, the coincidence processor uses so-called virtual rings to reshuffle the data coming from the buckets. Since the process is fully controlled by the input PAL logic and there are no physical rings which would take priority, the coincidence processor always processes all the coincidence pairs with an equal priority [307]. This is different than in the ECAT EXACT coincidence processor where it was possible to lose some coincidences; therefore, this coincidence processor is called the lossless coincidence processor and can be seen in Figure 7.28.

This implementation of a fully virtual coincidence processor introduced a new module pair numbering scheme. As the scanner is essentially made of a single ring of 24 buckets

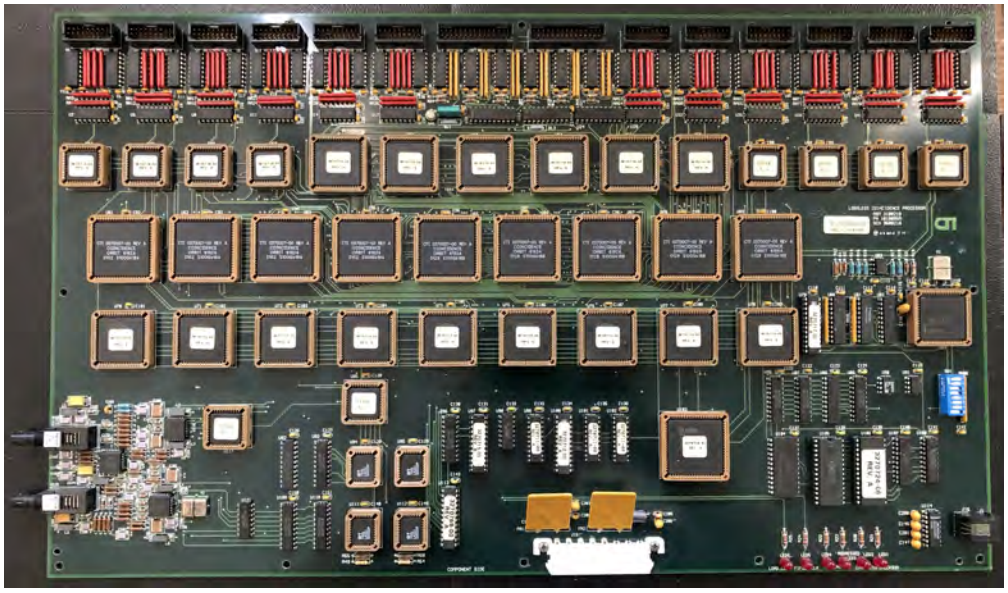

Figure 7.28: ECAT EXACT HR+ lossless coincidence processor board (PN: 1010095A). The top of the board contains the bucket pair data inputs. The bucket pairs are connected in order from left to right and the board takes the clock signals from the two larger connectors (number seven and eight) in the centre of the pack. The coincidence data is output over a serial fibre optic connection in the lower left corner of the board.

that are arranged in even-odd neighbouring pairs, this reinterprets the gantry as having 12 bucket pairs where each one has four detector block rings and six detector blocks per ring. Each of these bucket pairs can be in coincidence with the bucket pair opposite it and three to each side whereas bucket pair zero is in coincidence with bucket pairs three through nine. Then each of the four rings is identified by a ring number and the six detector blocks in each of the rings of the bucket pair are treated the same. This means that if a hit occurs in the same detector and the same crystal element in a detector block in ring one and ring two the bucket controller describes them in the same way except for the ring number. Now unlike previous numbering schemes in the ECAT EXACT or earlier scanners, the bucket controller does not identify the crystal element by the plane, row, and block number. It now uses a crystal plane to identify in which of the eight crystal planes the event occurred and a crystal segment number which is a sum of all the columns of the six detector blocks. So crystal segment zero is the first column in the first detector block in that ring and crystal segment

47 is the last column of the last of the six detector blocks in a ring.

The virtual ring system was designed to allow testing of all the practical coincidences with very minimal hardware. So after being split into the virtual rings, the bucket pairs are split into odd and even buckets and are guided to different test sections to efficiently process all the coincidence possibilities. Another interesting point is that the buckets are no longer connected to the coincidence processor through an exclusive socket on the board, but rather the data cables coming from the odd-even bucket pairs are connected to the same plug which then plugs into the coincidence processor treating them as one.

7.7 The ECAT EXACT HR++

The ECAT EXACT3D also known as the HR++ (model 966) is a version of the HR+ with an extended axial FOV. Only one of these scanners was ever produced containing only the retractable rod sources and no septa for a 3D-only scanner. The scanner has the same gantry diameter and uses the same electronics and detector blocks as the HR+, but is simply a restacked version of the HR+ where instead of 12 detector blocks being stacked in a four axial by three transaxial arrangement, they are now stacked in a six axial by two transaxial arrangement. This increases the number of rings from four to six while keeping the same number of detector blocks per ring. However, instead of 24 buckets, the HR++ has 50% more or 36 buckets which still connect to the same coincidence processor just running a different firmware [308]. Here instead of the buckets being treated as pairs they are treated as triplets and three data cables now connect to a single socket on the coincidence processor. This was the last BGO-based PET scanner designed and produced by CTI before it switched to producing only LSO-based scanners.

7.8 The ECAT Series Beyond BGO

While it might seem from the description above that CTI only took time to develop BGO-based scanners, they started their research early on the new LSO series of detector blocks. Cerium-activated lutetium oxyorthosilicate (LSO, LSO(Ce)) is a fast scintillator that has both higher light yield and a faster decay time than the BGO but does not have the same efficiency in stopping a 511 keV photon, see Table 1.3. The higher light yield also improves the energy resolution and therefore provides for better scatter and noise event rejection than BGO. This made it a perfect option for a new generation of PET scanners.

LSO was synthesised and characterised in 1992 by Charles L. Melcher and Jeffrey S. Schweitzer during their pursuit to find a new, better scintillator [309]. They chose to pursue LSO based on previous oxyorthosilicate scintillator advances, the first of which was cerium-activated gadolinium oxyorthosilicate (GSO, GSO(Ce)) characterised in 1983 and showed promising characteristics but was very fragile [310]. Later in 1986, further studies led to the characterisation and growth of cerium-activated yttrium oxyorthosilicate (YSO, YSO(Ce)) which was more rugged than GSO [311]. Most of these compounds were synthesised before as polycrystalline powders but never as a single crystal. Some oxyorthosilicates like lanthanum oxyorthosilicate and cerium oxyorthosilicate could not be grown as they just decomposed when melting to grow a single crystal [311]. In fact, LSO was first patented and used in equipment used to inspect oil wells for cracks and defects and was soon licensed to CTI for PET purposes such that their competitors still have to use lutetium yttrium oxyorthosilicate (LYSO, LYSO(Ce)) or LSO with a pinch of yttrium [284, 312, 313].

7.8.1 The microPET

The first PET scanner to use LSO as the main scintillator was the microPET, shown in Figure 7.29, designed for 3D-only small animal imaging. It was composed of 30 8x8 LSO blocks with crystal element size of 2 mm by 2 mm by 10 mm deep. This resulted in 17.2 cm detector diameter gantry [314]. Each of the tiny crystal elements was coupled via an optical fibre to a Philips XP1722 64-channel PMT [315]. These 64 signals were then used to produce the four position-encoding signals that then could be used to calculate the crystal position in a similar way to a classic BGO-based detector block. Although a costly system due to the multi-channel PMTs, microPET showed vast improvements in image quality over the clinical systems like the ECAT EXACT HR+ with a resolution of 2 mm or better in all directions [314].

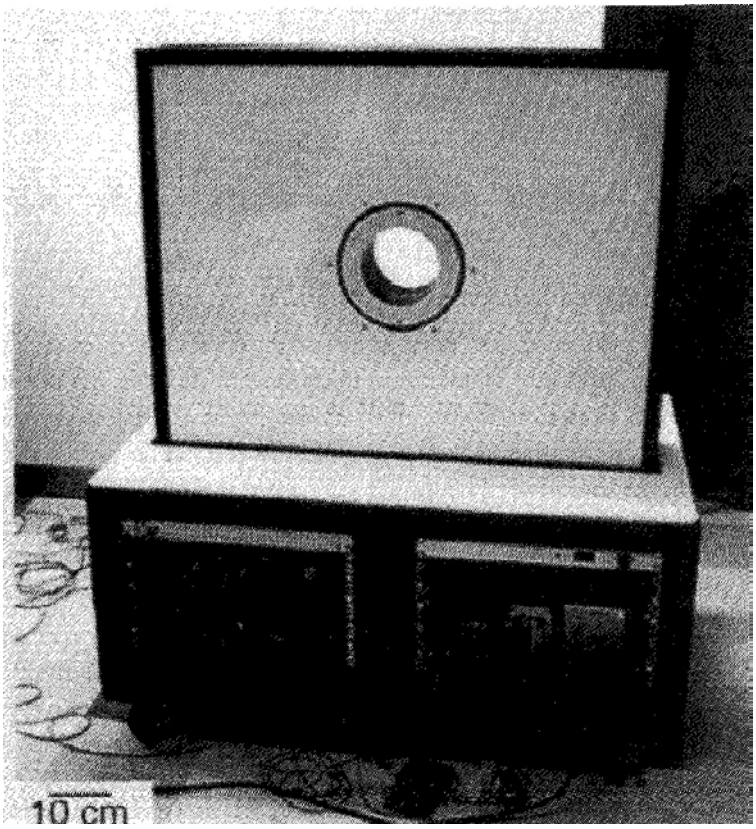

Figure 7.29: The first LSO-based PET scanner. The first microPET system as designed and built at UCLA before its commercialisation [314].

The microPET was developed at UCLA under a partnership agreement with CPS who provided their expertise and parts. With the development of the microPET, Concorde Microsystems, Inc. (Knoxville, Tennessee, USA) was formed around 1999. The company was 50.1% owned by CPS and managed by Ronald Nutt's children. They had a 5-year agreement with CPS to use their technology and materials to develop animal PET scanners and market and sell them. The companies remained in partnership with UCLA to further develop the platform until 2004 when the 5-year agreement ended and CTI bought the company to form CTI Concorde Microsystems, a CTI subsidiary [316, 317].

7.8.2 The ECAT HRRT

The first ever LSO clinical PET scanner was the ECAT HRRT (High-Resolution Research Tomograph) made in 1999 as a collaboration effort between CTI and Max Plank Institute. It was a 3D-only brain scanner and the first clinical scanner to achieve 2.5 mm resolution due to its depth of interaction (DOI) capability [284]. The research started back in 1997 with an investigation into different combinations of LSO, GSO, and YSO scintillators to obtain their pulse-shape characteristics. This led to the discovery that different LSO crystals exhibit different light emission patterns not only with differences in the cerium concentration but also with the way the activator atoms distribute and occupy various cerium sites in the crystal matrix during its growth [318]. This meant that greater quality control was needed to obtain uniform crystals from batch to batch but also that two LSO crystal arrays with different cerium content could be stacked on top of one another and the decay time difference could be pronounced enough to be easily identifiable with pulse shape discrimination (PSD) analysis.

Later in 1998, the detector block design was evaluated for the novel DOI design. The research focused on GSO/LSO and LSO/LSO comparison and concluded that the 7 ns

difference in decay time achieved by using different Ce-activated LSO crystals is enough for PSD with excellent, uniform positioning of the crystal photopeaks. The excellent timing resolution of the LSO also meant that a 5 ns coincidence window could be used in the new system compared to the 12 ns in BGO systems. A shorter coincidence window would reduce noise through better scatter and multiple event rejection [24].

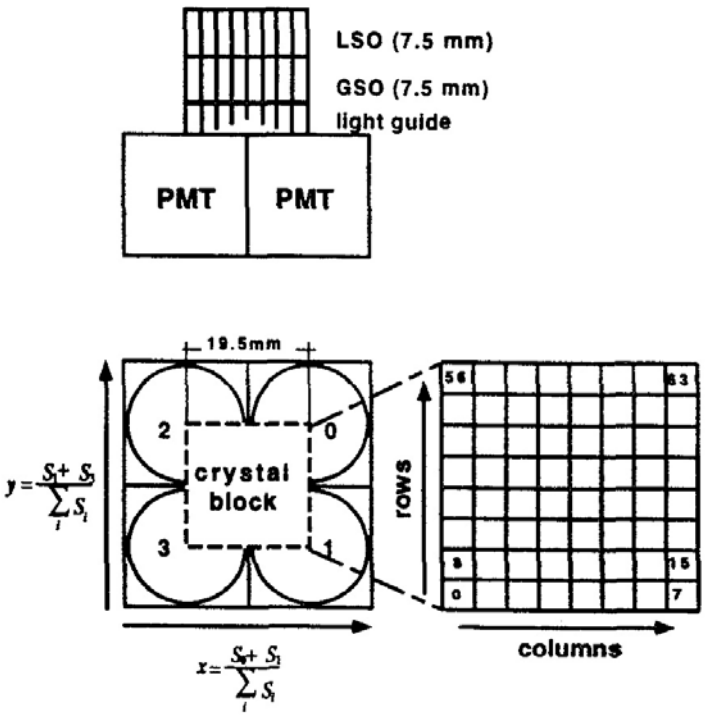

Figure 7.30: The ECAT HRRT quadrant shearing block design [24].

The final LSO/LSO detector design used two layers of 8x8 2.1 mm by 2.1 mm by 7.5 mm deep crystal element arrays joined together with no offset. The block used a dedicated light guide that was sliced to variable depths, similar to the original BGO detector block design discussed in Section 5.5. The crystal block sandwich was positioned over 4 Hamamatsu R-1450 PMTs in a quadrant sharing arrangement, which unlike in the original detector block design the crystal block only covered a quarter of each PMT with half of the PMT dimension sicking out in each direction as shown in Figure 7.30; a design similar in principle to the MGH positron camera mentioned in Section 4.4.1 [24, 319]. This meant that individual

quadrant shearing detector blocks were impossible to make and a linear bank design similar to that of the NeuroECAT or earlier scanners was used.

So, the ECAT HRRT was of a linear octagonal bank design with each bank containing 117 LSO/LSO blocks in a 9x13 array viewed by 140 PMTs in a 10x14 array. Each bank was 46.9 cm from a bank opposite it for a scanner with a patient portal diameter of 35 cm. The scanner featured a new coincidence processor that operated in a 4 ns wide coincidence windows which could be increased in 4 ns steps. To handle the high data rates, a new ACS III was designed based on the Intel Pentium PRO CPU. The resulting design was a compromise of resolution and sensitivity with higher noise levels than usual. The 2.5 mm resolution over a whole brain volume was ground-breaking but with the current design could not be achieved in routine scans. The image reconstruction times were greatly increased due to the high resolution; therefore, the data was usually compressed losing up to 20% of axial resolution in the process. The high noise ratio was improved through increased shielding and the use of novel noise correction methods [320, 321].

7.8.3 The ECAT ACCEL

The first clinical commercial whole-body LSO-based PET scanner was released by CTI around 1999 as the ECAT ACCEL for 2D and 3D whole-body imaging. It was of a very similar design to the ECAT EXACT 47 featuring 8x8 LSO-based detector blocks with a crystal element size of 6.45 mm by 6.45 mm and 25 mm deep in an 82.4 cm detector diameter gantry. The coincidence processor used a 6 ns coincidence window. When compared to the ECAT EXACT HR+, the ECAT ACCEL displayed similar characteristics with a slight improvement in noise equivalent counts. However, this improvement was more pronounced with high-dose imaging as the LSO-based detector was better suited for noise rejection [305, 322]. The system was a great first stepping stone in whole-body, clinical scanner design and

ushered in both the end of the BGO PET scanner era and PET-only scanners.

7.8.4 Rise of the Multimodal Imaging Systems

The turn of the century ushered in a new era of medical imaging systems. Less single-mode imaging systems were being produced in favour of the multimodal systems. The first commercial PET/CT was announced by GE Medical Systems (Milwaukee, Wisconsin, USA) as Discovery LS in early 2001. This was immediately followed by an announcement by CTI releasing their PET/CT system, marketed as a Reveal by CTI or Biograph by Siemens. This system used the Siemens Somatom Emotion 2-slice CT scanner merged with an ECAT EXACT HR+. Soon they also released the Reveal RT and Biograph LSO with an ECAT ACCEL as the PET scanner. Then in 2002, CTI released an LSO-based ART scanner called the ECAT EMERGE, the last PET-only CTI scanner. That same year, they released a PET/CT scanner only based on an ECAT ACCEL with an upgraded 16-slice CT scanner called the Reveal XVI by CTI or Biograph Sensation 16 by Siemens [225]. This pattern of merging existing PET architectures with ever newer CT systems continued through the early 2000s.

With over 20 years in the industry, in 2005, Siemens Medical Solutions USA, Inc. (Malvern, Pennsylvania, USA) bought CTI Molecular Imaging, Inc. and formed Siemens Healthcare Molecular Imaging, still located in Knoxville, Tennessee, USA [268]. That same year, avalanche photodiode (APD) based LSO pre-clinical PET scanners started to be built becoming the first PET scanners not affected by magnetic fields. With these advances, in 2006 Siemens Healthcare Molecular Imaging built five small bore, brain-only PET/MR scanners further expanding the multimodal imaging options [225].

In 2008, Philips Medical Systems, Inc. (Andover, Massachusetts, USA) released the

Gemini TF (TrueFlight), the first commercial time-of-flight (TOF) PET/CT scanner. This was quickly followed by the Siemens Biograph mCT, an APD-based LSO TOF PET/CT scanner. With further improvements in TOF, in 2010 Siemens released the Biograph 6 Truepoint and a bit later the Biograph mMR, the first APD-based LSO PET/MR scanner with 3T MR simultaneous imaging capability. At the same time, silicon photomultipliers (SiPM) have emerged with much faster timing than APDs making them more desirable for PET systems. So in 2013, Philips produced the first PET/CT, the Veros, that featured a fully digital SiPM-based PET/CT scanner [225].

Today all the new scanners have complementary CT or MR systems and the TOF functionality with a timing resolution of 500 ps for PMT-based and less than 400 ps for solid-state photomultiplier-based detectors [225].

7.9 Intercompatibility of Various ECAT Parts

The ECAT series of PET scanners was designed from the ground up to be a fully modular system with identical subsets of parts that could easily be exchanged when needed. As discussed throughout the previous sections in this section, it is clearly evident that certain parts and operational principles of the system were never changed. Therefore, it is possible to exchange certain parts between the different types of ECAT scanners. However, in most cases, for the data to flow through properly, the coincidence processor must be set to all planes mode, the data must be saved as list mode by the ACS, and/or the ACS has to be bypassed or removed. In any case, these modifications will break the sensitivity of the scanner and are only useful for PEPT purposes.

7.9.1 The Detector Block

The detector block is the most exchangeable piece of the whole system. The 8x8 detector blocks found in the ECAT 951, EXACT, HR+, and HR++ can all be interchanged since the crystal element size does not really matter, only the ratio of energies that the four PMTs produce. A setup and calibration procedure has to be run when mixing the detector blocks so new lookup tables are established and since the detector blocks do not contain any smart electronics, there are no problems with firmwares.

The oddly divided detector blocks found in the ECAT 931 and HR are a bit different. From personal experimentation, I observed that it is possible to use the ECAT 931 8x4 detector block in an 8x8 system only if the bucket is calibrated with the ECAT 951 8x8 detector block first. Depending on the calibration, the system will either split the hits occurring in one of the four planes between two of the eight planes or it will preferentially assign that hit to one of the two. Obviously, this cannot be done when trying to acquire image-worthy data, but for PEPT where the data will not be interpreted by the ACS, these detector blocks can be used and the events coming from detector planes one and two, three and four, five and six, and seven and eight just have to be treated as coming from plane one, two, three, or four of a four plane detector. Similarly, when using an 8x8 detector block with the ECAT 931 8x4 bucket, the opposite happens and the 8x8 detector block becomes an 8x4 detector block with the hits occurring in the plane pairs being summed into a single plane. Unfortunately, due to the rarity of the HR system and the 8x7 detector block, I was unable to verify its compatibility.

7.9.2 The Bucket Electronics

The compatibility of the buckets between the different scanner versions can be broken into two categories: the 4 and the 12 detector block systems. All the buckets, no matter how many detector blocks they support, always take in the same serial data and clock signals of the same frequency, over the same type of cable, use the same pin layout, and they even use the same connectors. Therefore, it is possible to use any of the clock generator boards found in the ECAT 931 and 951 scanners or any of the gantry controllers found in the ECAT EXACT, ART, HR+, and HR++ scanners to communicate with and orchestrate the system.

On the other hand, the bucket data lines underwent a modification between the 4 and 12 detector block bucket systems. The 12 detector block bucket system now has a third data line for transferring the ring information. So, it is not possible to interchange the two types of buckets between the systems.

The four detector block buckets can be interchanged between one another, especially between the ECAT 951 and EXACT scanners. The ECAT 931 bucket is the odd one of the bunch. Due to it supporting an 8x4 detector block, the bucket uses two bits instead of three to describe the detector plane in which the hit occurred. But, as the detector information is passed to the coincidence processor as an eight-bit word, five of which describe the block number and the crystal segment, the ECAT 931 board has an empty bit left that the other boards used for the third plane bit. Therefore, the ECAT 931 bucket and the later four detector block buckets can be mixed only if the coincidence processor is set to all planes mode. This will prevent the coincidence processor from reading the plane numbers incorrectly and discarding valid coincidences.

The 12 detector block buckets, on the other hand, cannot be readily interchanged between one another unless they use the same detector block layout. This is due to the

virtual ring coincidence processor system where the bucket is responsible for assigning the ring number to describe in which ring the detector block is located. However, this function is controlled by the bucket's microcontroller so if the firmware contained within the EPROM is changed to the one with the correct geometry, the bucket can be used.

7.9.3 The Coincidence Processor

The coincidence processors cannot really be interchanged with one another because each of them contains some sort of function special to that scanner. The ECAT EXACT HR+ and HR++ coincidence processors could be interchanged as they are the same board but only after their firmware is updated to the correct one. The only coincidence processors that can be exchanged together are the ECAT 931 and 951 coincidence processors if run in all-plane mode which is due to the extra bit describing the detector plane incorporated with the 8x8 detector block design. What is kind of surprising is that the newer ECAT 951 8x8 bucket can be used with the ECAT 931 IPCP as it passes the empty bit that describes the third plane bit in the ECAT 951 bucket through to the coincidence output. This can be seen in Section 9.4.2 and Figures 9.6 and 9.7 describing the coincidence processor output connector mapping for the LaMA PEPT.

As the ECAT 931 and 951 coincidence processors are made out of individual cards in a card cage that shares exactly the same backplane, the ring receiver boards can be switched between the two series and can be used as a ring one or two receivers without a problem as they are electronically the same. The IPCP boards can be interchanged to be either ring one, two, or one of the cross-plane boards. As a matter of fact, the way the backplane functions, it is possible to run the system using any combination of boards. The system can be converted from a two-ring scanner to a single-ring scanner by removing one of the receivers and three of the IPCP boards. It is also possible to remove the two cross-plane IPCP boards and run

the scanner as if the two rings were independent of one another or vice versa keeping only the two cross-plane boards and only producing cross-ring coincidences. The only problem is the different front end of the IPCP boards between the ECAT 931 and 951 so to daisy-chain the output, the boards need to be of the same series or a special adaptor needs to be made.

7.9.4 Application to PEPT

Throughout this whole section, all of CTI's BGO-based PET scanners have been discussed and their characteristics and features are summarised in Tables 7.1 and 7.2. All of these scanners share some similarities, with some of the neighbouring versions being the most compatible, parts wise. As discussed in the section above, the detector blocks can be widely interchanged while coincidence processors mostly cannot be. Therefore, to design a PEPT system, one has to first choose the coincidence processor they want and the number of detectors per bucket, as these are tied together. Finally, the detector block type is chosen per section of the PEPT scanner; if it has different subsections. Following this idea of starting with a coincidence processor and building the system outwards, the SuperPEPT and LaMA PEPT have been designed and built with parts sourced from various different ECAT scanners.

Table 7.1: Physical characteristics of CTI's BGO-based ECAT PET scanners as discussed in Sections 5 through 7. References are listed in those sections. Legend: DB - Detector Block, Dia - Diameter, T - Transaxial, A - Axial, D - Depth, P - Partial, H - Head, FB - Full-Body, Oct - Octagonal, Cyl - Cylindrical.

Released (around)	Name	Model No.	Usage	Geometry	Portal Dia (cm)	Detector Dia (cm)	Buckets per Ring	Crystal Size (T-A-D) (mm)	DB Crystal Layout (T-A)	Crystal Rings per DB	Bucket DB Layout (T-A)	Number of Independent Rings	Total Crystal Rings
1978	NeuroECAT	828	H	Oct	30	65	8	17-27-29	1-1	1	11-1	3	3
1983	ECAT III	911	FB	Cyl	65	100	16	5.6-30-30	1-1	1	32-1	1-4	1-4
1985-86	ECAT 931	931	FB	Cyl	56.7	102	16	/12 - 5.6-12.9-30	8-4	4	4-1	-04 - 1 -08 - 2	4 8
		933	FB		51.4	76	12	/16 - 5.6-15.4-30					
		831	H		35	64	10	/20 - 5.6-19.4-30					
1989-90	ECAT 951	951	FB	Cyl	56.7	102	16	5.6-6.2-30	8-8	8	4-1	/15 - 1 /31 - 2	8 16
		953B	FB/H		51.4	76	12						
		851	H		35	64	10						
		951R	FB		56.7	102	16						
1991-92	ECAT EXACT 31	921	FB	Cyl	56.2	82.4	12	6.45-6.45-20	8-8	8	4-1	1 2	8 16
	ECAT EXACT 47	922											
1993-94	ECAT EXACT HR	961	FB	Cyl	56	80	?	2.9-5.9-30	7-8	8	?	3	?
1994	ECAT ART	925	FB	P Cyl	60	82	6	6.45-6.45-20	8-8	8	4-3/3-3	1	24
1996	ECAT EXACT HR+	962	FB	Cyl	56.2	82.4	24	4.05-4.39-30	8-8	8	3-4	1	32
1996-99	ECAT EXACT HR++	966	FB	Cyl	56.2	82.4	36	4.05-4.39-30	8-8	8	2-6	1	48

Table 7.2: System features of CTI's BGO-based ECAT PET scanners as discussed in Sections 5 through 7. References are listed in those sections. Legend: R - Retractable, C - Changeable, F - Fitted, V - VMEBus.

Released (around)	Name	Model No.	Adjustable Gantry	Septa	Wobble	Transmission Sources	Gating	Bucket Logic	Coincidence Processor Logic	ACS Logic	Gantry Logic	Cooling	Interface OS
1978	NeuroECAT	828	Yes	R	No	Yes	Yes	NIM	NIM	NIM	CAMAC	Air	RSX-11M
1983	ECAT III	911	Yes	C	Yes	?	Yes	Digital	Digital	V	Q-bus	Air	VAX/VMS
1985-86	ECAT 931	931				Yes							
		933	Yes	F	Yes	No	Yes	Digital	Digital	V	Q-bus	Air	VAX/VMS
		831				No							
1989-90	ECAT 951	951		F									
		953B		R									
		851	Yes	F	Yes	Yes	Yes	Adj Digital	Digital	V	Q-bus	Air	SunOS
		951R		R									
1991-92	ECAT EXACT 31	921											
	ECAT EXACT 47	922	No	R	No	Yes	No	Adj Digital	ASIC	V	Digital	Water/Air	SunOS
1993-94	ECAT EXACT HR	961	?	R	?	Yes	?	?	?	?	?	?	?
1994	ECAT ART	925	No	R	No	Yes	No	ASIC	ASIC	V	Digital	Water/Air	SunOS
1996	ECAT EXACT HR+	962	No	R	No	Yes	Yes	ASIC	ASIC	V	Digital	Water	SunOS
1996-99	ECAT EXACT HR++	966	No	R	No	Yes	Yes	ASIC	ASIC	V	Digital	Water	SunOS

Chapter Eight

SuperPEPT

SuperPEPT is a custom-designed positron camera with the simple purpose of producing a high-resolution, high-sensitivity, extended axial FOV, dedicated PEPT system. It solves the biggest challenge in PEPT by providing a large circular FOV that is 53.50 cm long and 40.00 cm in diameter. This was achieved through the use of small transaxial and axial gaps to strategically space the detector blocks apart. These gaps produce variations in sensitivity within the FOV of the scanner, but unlike in imaging, PEPT does not need a uniform area of sensitivity to work properly.

My contributions to the system predominately include everything from its initial assembly to its continued operation. When I joined the project, the gantry and the general layout have already been designed and in the process of being manufactured. The new MiE hardware was also purchased before I joined the project and partially incorporated. Initial system behaviour tests have already been underway and I continued with them trying to understand how the system works and how we can communicate with it and modify its settings. Myself, I have done a lot of its final assembly and testing, I set the detector connection scheme, designed and assembled the power distribution system, developed calibration methods, and, most importantly, I spent countless hours troubleshooting broken electronics

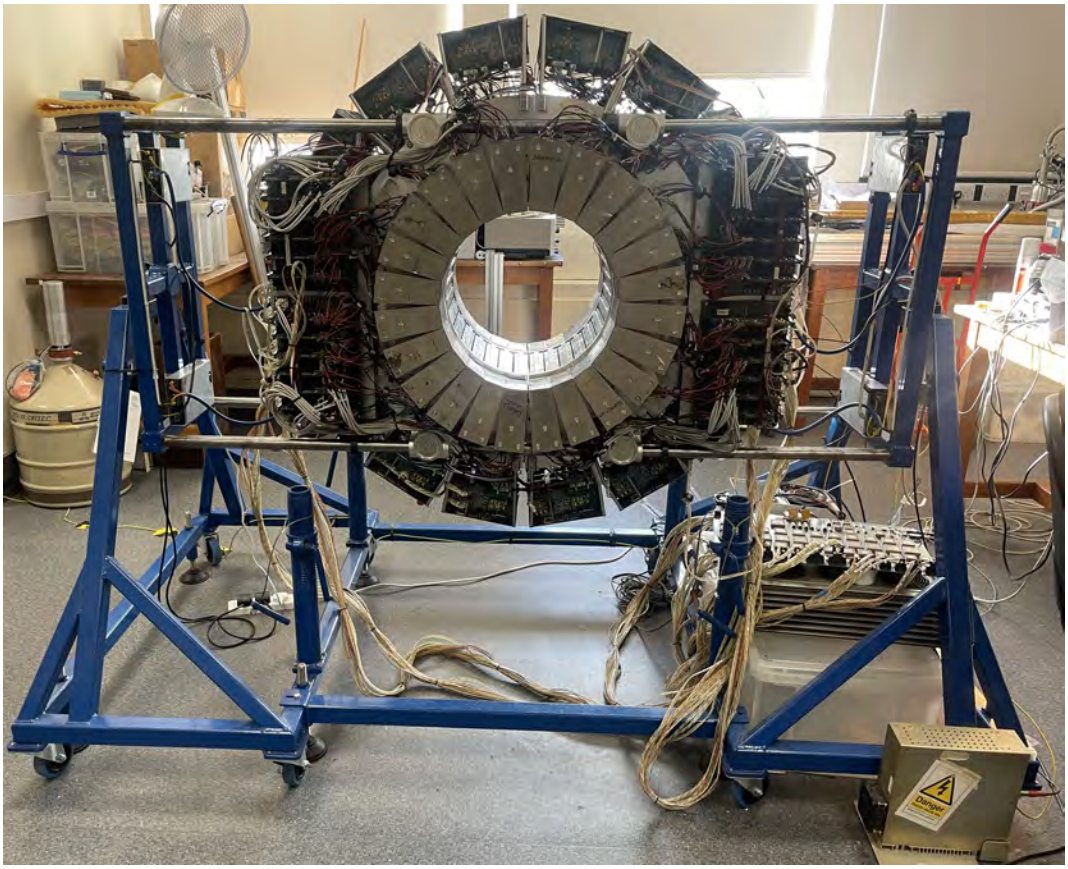

Figure 8.1: SuperPEPT gantry in its horizontal orientation as viewed from the front. The top-end section with its four bucket controllers is visible first followed by the centre section with its bucket controllers surrounding the whole gantry. The bottom end section is the least visible with some of its blocks showing when looking through the portal. The coincidence processor, gantry controller, and MiE Scintron are resting on top of the crates in the bottom right, behind the high-voltage power supply. The logic power supplies are mounted to the four corners of the rotating gantry frame, two per each half. The gantry is split vertically in the middle.

boards and detectors that were producing odd signals/data. Besides handling all the initial hardware issues that come from using multiple scrap/broken-down systems to build a single working one, I have also written many pieces of software including serial communication programs, troubleshooting and maintenance programs, and data visualisation and processing programs. Almost a full year of my PhD has been given to the development of this system; not including support of the various student and external PIC user experiments that use it.

8.1 Geometry and Assembly

The system was designed primarily based on the ECAT EXACT HR+ scanner system described in Section 7.6. The geometry and the number of buckets used are dictated by the HR+ coincidence processor, which allows 24 buckets in the whole system. As can be seen in Figures 8.1 and 8.2, the system also uses BGO-based detector blocks from the ECAT EXACT 31 (see Section 7.3) and ECAT ART (see Section 7.5) and bucket electronics from the ECAT ART. These were redundant scanners that were replaced by newer systems. The ECAT EXACT HR+ was acquired from the Hammersmith Imanet, the ART from Hammersmith Hospital, and the EXACT 31 from the University of Aberdeen at various points in the past by the PIC. To achieve the high-sensitivity and long axial FOV, the scanner was divided into three sections as shown in Figure 8.2: a high-resolution, high-sensitivity centre section and two end sections tasked with the extension of the axial FOV.

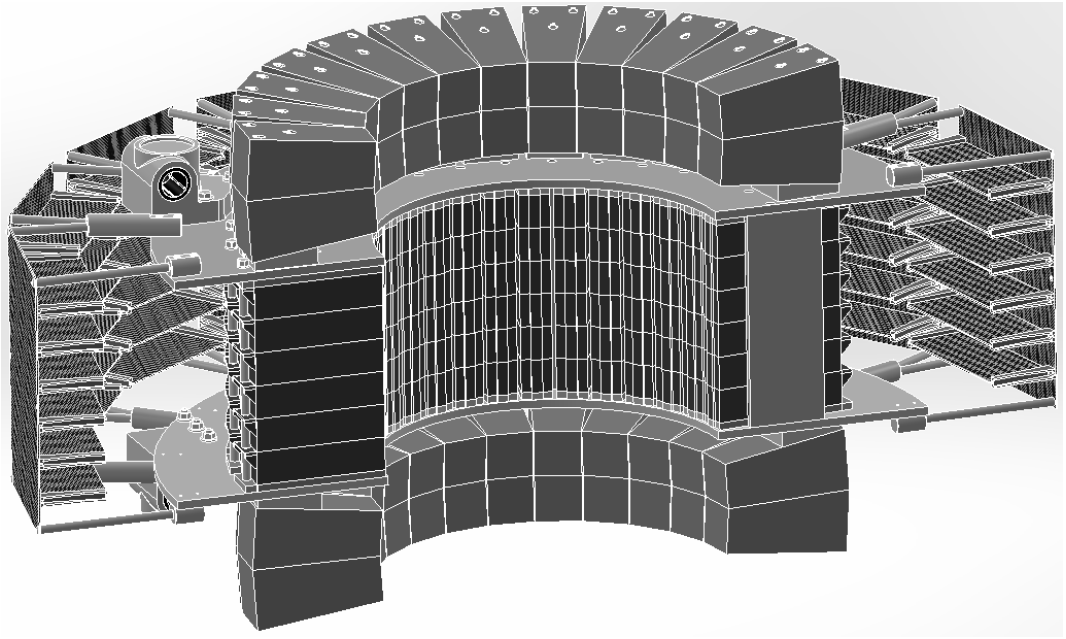

Figure 8.2: The SuperPEPT cutaway CAD view displaying the detector block arrangement. The bigger, lighter-coloured EXACT blocks make up the two outer sections and the block-coloured, smaller HR+ blocks make up the centre section of the SuperPEPT. The bucket controller boards for the end sections are not shown in this design.

The centre section is made out of 192 HR+ detector blocks that are stacked into six rings with 32 blocks per ring. The 32 columns formed give the central section an axial extent of 23.30 cm. Each of the columns is separated by a small gap of about 5 mm from the edge of one detector block to its neighbour. The column arrangement was possible due to the flat wedge design of the HR+ detector block shown in Figure 7.26. Unlike the EXACT blocks shown in Figure 7.18, the HR+ block is flat in the vertical direction and a wedge in the horizontal direction while the other blocks are wedge-shaped in all directions.

The two end sections of SuperPEPT are composed of 48 EXACT/ART detector blocks each in two rings of 24 detector blocks. Since the blocks are wedge-shaped in all directions, they were mounted to the gantry at a slight angle such that the plane formed between the two rings is parallel to the transverse plane of the scanner (see Figure 8.2 and 8.3). The axial extent as measured from the end of one detector block face to the other is 10.60 cm. Each of the outer rings is separated by 4.50 cm from the end of the centre section which results in the total sensitive axial length of the scanner being 53.50 cm long. The 4.50 cm gap is due to the gantry frame and the adaptors attaching the wedge-shaped outer detector blocks to the gantry taking up space. As shown later in Section 10, the gap does not cause any significant and non-uniform drop in sensitivity on the axis of the scanner.

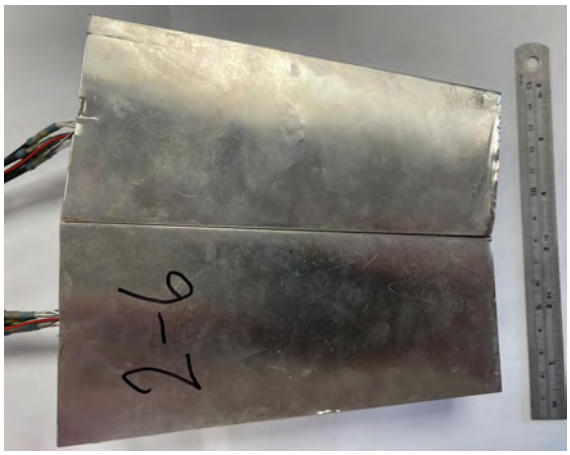

Figure 8.3: SuperPEPT end section EXACT detector block wedge assembly demonstrating the angle of the detector block faces.

The gantry frame assembly shown in Figure 8.1, custom-built at the University of Birmingham, supports all of the detector blocks and bucket controllers. The gantry is made up of two aluminium disks which sandwich the centre section with struts separating each column of the detector blocks. To these plates, small adaptor blocks are attached to which the outer detector blocks lock in using their built-in studs visible in Figure 7.18. The bucket controller boards for the centre section are attached to standoffs on the outside of the ring. In contrast, the ones for the outer sections are held on external plates attached to the sides of the gantry visible in Figure 8.1 for the top-end section. The gantry is designed to rotate and lock while facing vertically or horizontally and to split into two halves that can be easily spread apart to help position and centre larger pieces of equipment under observation.

8.2 Data Acquisition

SuperPEPT uses the HR+ coincidence processor (see Section 7.6.1 and Figure 7.28) orchestrated by the HR+ gantry controller (see Figure 7.27) for clock and serial communication distribution. All other systems and control boards have been removed. The list mode data was originally planned to be acquired using the original HR+ ACS II system; however, due to unfortunate circumstances, the HR+ ACS II was damaged during experimentation and is irreparable. To fix that issue, a Scintron 7.2 system produced by MiE GmbH was acquired to replace the broken ACS II system. The Scintron is a third-party replacement and upgrade system for the ECAT EXACT 47, HR+, and ACCEL PET scanners. The system replaces the whole ACS assembly with a custom system designed by MiE. The system provides an updated operator's workstation based on a modern Windows PC running the MiE Scintron PET software used for the operation of the scanner. With the special help of MiE, we were able to disable the various safety systems which are no longer present on this bare-bones machine and we were able to enable almost indefinite list mode data acquisitions, only lim-

ited by the available space and throughput of the HDD. The list mode data acquisition is controlled by the Scintron software and it is saved to the HDD part of their custom system. The files are then offloaded from the internal HDD via the operator's PC and processed using in-house custom-designed software.

8.3 Deciphering the List Mode Data

Due to the overwhelming help we received from MiE to modify their system, we are not allowed to discuss the proprietary format of the list mode data written by their software. However, the crystal element numbering scheme used to identify the individual crystal elements as designed by CTI and produced by the original coincidence processor is discussed below.

8.3.1 The ECAT EXACT HR+ Crystal Element Numbering System

As initially discussed in Section 7.6.1, due to the virtual ring design of the coincidence processor, the scanner can be described as a single ring of 24 buckets. These buckets are arranged in even-odd neighbouring bucket pairs illustrated in Figure 8.4. These 12 bucket pairs can then be interpreted as having four detector rings and six detector blocks per ring. Each of the bucket pairs is in coincidence with the bucket pair opposite it and three to each side; whereas bucket pair zero is in coincidence with bucket pairs three through nine as shown in Figure 8.5. Following this scheme, bucket pair one is in coincidence with bucket pairs four through ten and so on.

To describe all possible coincidence combinations, a numbering scheme called the

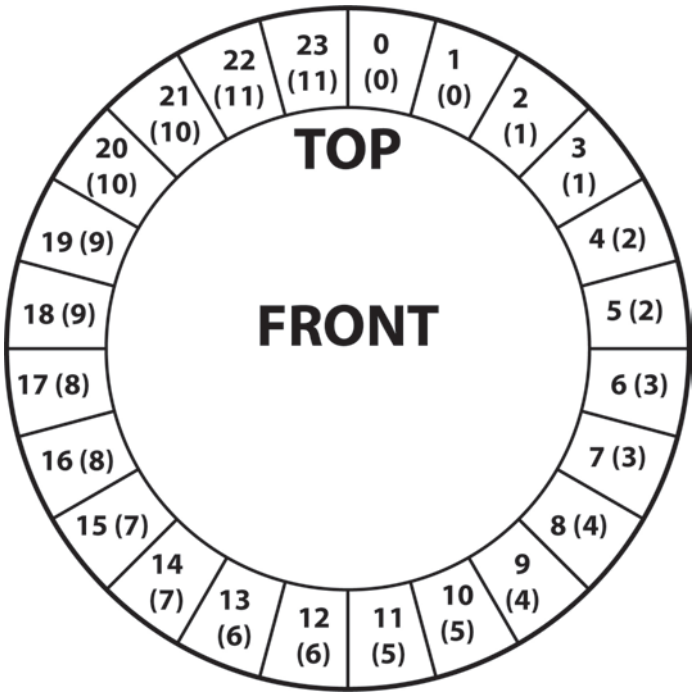

Figure 8.4: The ECAT EXACT HR+ bucket numbering scheme shows the bucket number and the bucket pair number in parentheses. The top indicates the top of the original scanner gantry and the front is the side from which the patient was normally inserted.

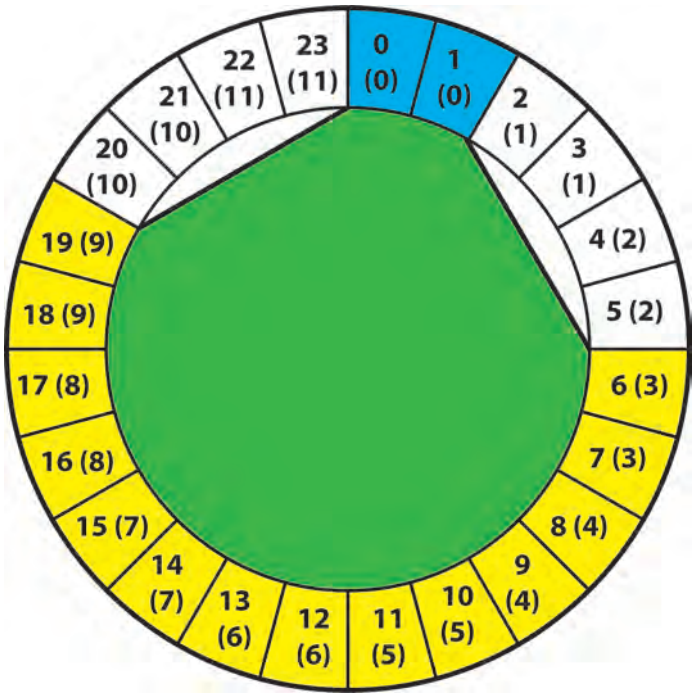

Figure 8.5: The ECAT EXACT HR+ buckets pair coincidence range. Here bucket pair 0 is shown to be in coincidence with bucket pairs 3 through 9. The ring is shown in the same orientation as in Figure 8.4.

module pair numbers is used. While in the older systems, the module pairs pointed to singular modules/buckets, in the HR+ the module pair numbers describe the bucket pair pairs. The scheme does not repeat any pairs as the coincidence between bucket pair zero and six is the same as between six and zero. This is also the only describing number that is not zero-based but starts at one. The module pair scheme is shown in Table 8.1.

Table 8.1: The ECAT EXACT HR+ module pair numbering scheme uses the "A" master bucket pair and "B" slave bucket pair notation. The green fields indicate possible coincidence pairs and the orange fields indicate impossible coincidence pairs.

		The "A" Bucket Pair											
		0	1	2	3	4	5	6	7	8	9	10	11
The "B" Bucket Pair	0	X											
	1		X										
	2			X									
	3	1			X								
	4	2	8			X							
	5	3	9	15			X						
	6	4	10	16	22			X					
	7	5	11	17	23	28			X				
	8	6	12	18	24	29	33			X			
	9	7	13	19	25	30	34	37			X		
	10		14	20	26	31	35	38	40			X	
	11			21	27	32	36	39	41	42			X

Now, each of the four rings is identified by a ring number and the six detector blocks in each of the rings of the bucket pair are treated the same. For the numbering scheme to be correctly interpreted, the blocks need to be connected in a certain order to the bucket

controller. The connection scheme is shown in Figures 8.6 and 8.7.

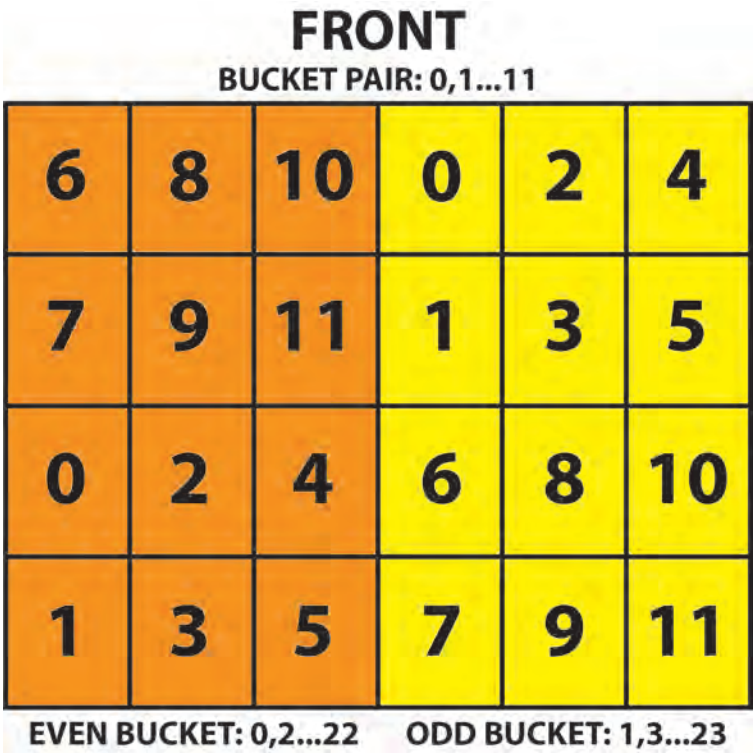

Figure 8.6: The ECAT EXACT HR+ detector block connection scheme to the ASIC bucket controller as done in the original gantry geometry. The front indicates the front of the ring and the numbering scheme is as-viewed from the inside of the ring or front of the detector blocks. See Figure 8.7 for the corresponding numbered connections on the ASIC bucket controller assembly.

Unlike previous schemes in the ECAT EXACT or earlier scanners, the bucket controller does not identify the crystal element by the crystal plane, row, and block number. It now uses a crystal plane to identify in which of the eight crystal rows the event occurred and a crystal segment number which is a sum of all the six detector blocks. This is such that crystal segment zero is the first column in the first detector block in that ring and crystal segment 47 is the last column of the last of the six detector blocks in a ring. The zero plane, zero column crystal element is still located in the lower left corner of the detector block as previously shown in Figure 6.4. This numbering scheme is shown in Figure 8.8 for the original scanner gantry.

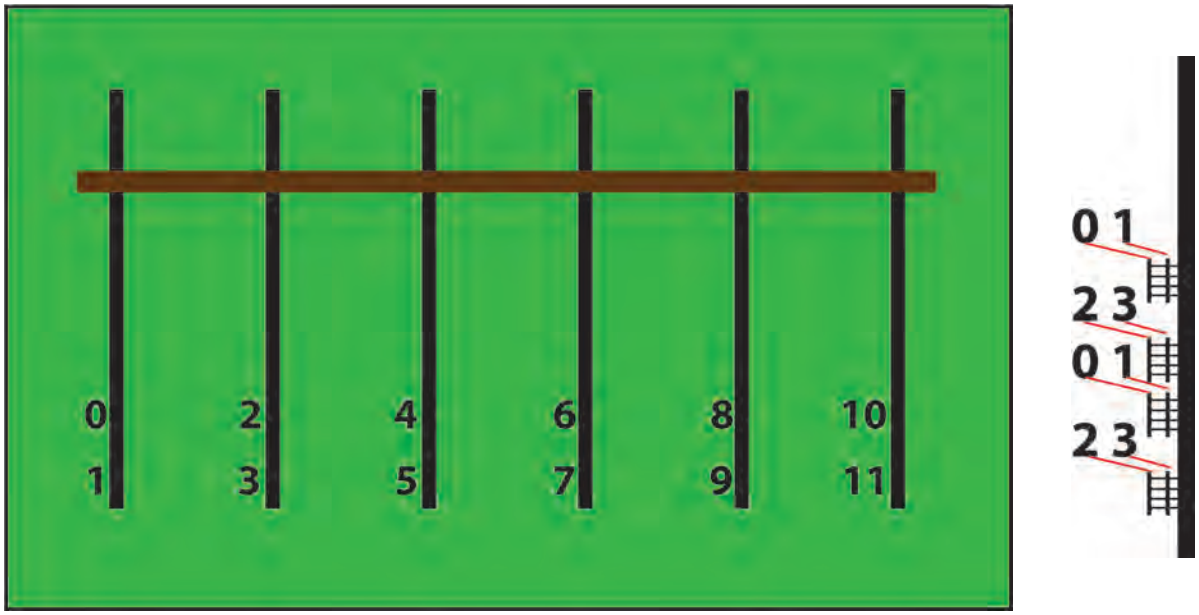

Figure 8.7: The ECAT EXACT HR+ bucket controller detector block connector numbering scheme. On the left is a simplified view of the bucket controller board with the six analogue processor boards and the detector block connectors numbered appropriately. See Figure 7.24 for the assembly. On the right is a simplified view of the analogue processor board itself with the 8 (4 per detector block) PMT connectors numbered according to the PMT number of the detector block.

With the numbering scheme properly described, the coincidence processor outputs a 32-bit word which describes the coincidence using these numbers along with some event-type flags. The word includes the six-bit module pair number describing not only which two bucket pairs are in coincidence but also defines which bucket is the "A" and which is the "B" bucket as the bucket-related numbers are given in a certain order. For each of the buckets a three-bit ring number, three-bit plane number, and six-bit segment number are given. This leaves two-bits free for event-type flags.

8.3.2 SuperPEPT Crystal Element Numbering System

SuperPEPT crystal element numbering scheme is the same as that of the original ECAT EXACT HR+, the only difference is the physical location of the individual detector blocks

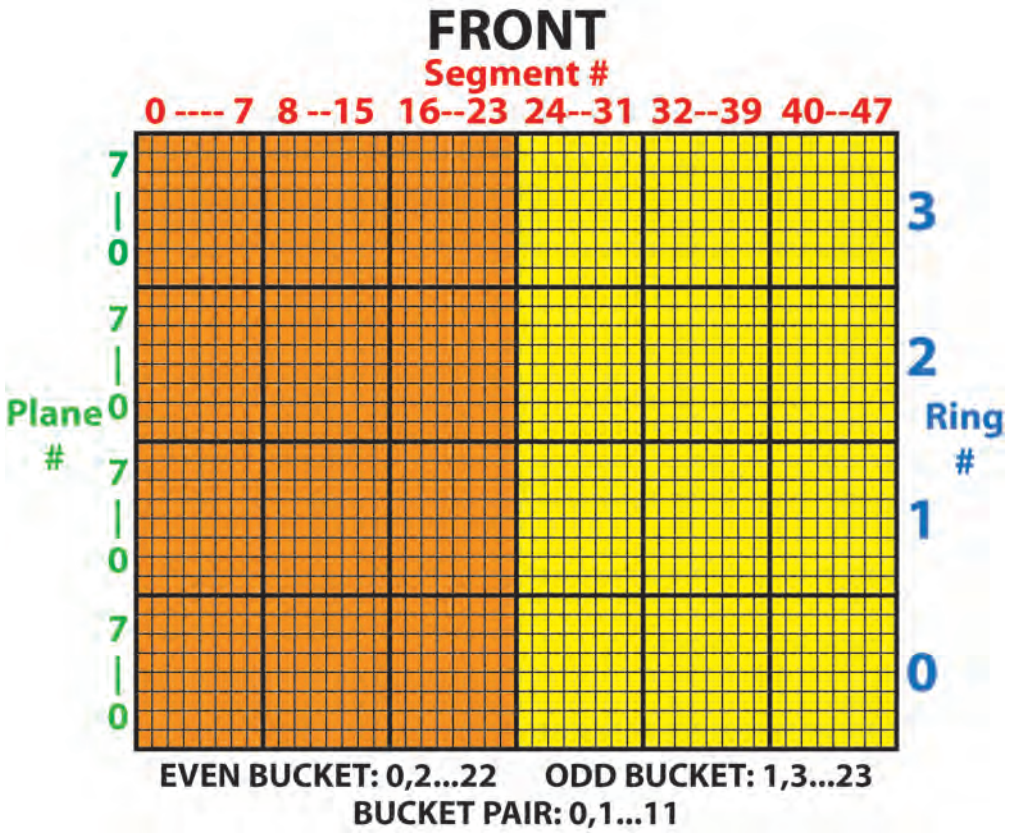

Figure 8.8: The ECAT EXACT HR+ detector block crystal element numbering scheme shows the ring number defining the rings formed by the detector blocks, the plane number describing the crystal plane within each detector block ring, and the segment number describing the crystal columns across the set of 6 detector blocks per each ring.

and buckets within the three sections of the system. As can be seen in Figure 8.9, the centre section contains bucket pairs zero, two, three, five, six, eight, nine, and eleven and the end sections contain bucket pairs one, four, seven, and ten but the buckets are split such that the top-end section has the odd bucket and the bottom-end section has the even bucket of each pair. This bucket arrangement is such that in the centre section, each bucket pair is in coincidence with five bucket pairs opposite it and two bucket pairs in the end sections. On the other hand, the end sections are such that each bucket pair is in coincidence with the three other bucket pairs within the section. Due to the splitting of the bucket pairs between the top and bottom sections, both end sections are fully in coincidence allowing as many cross coincidences through the FOV of the system as possible. On top of that,

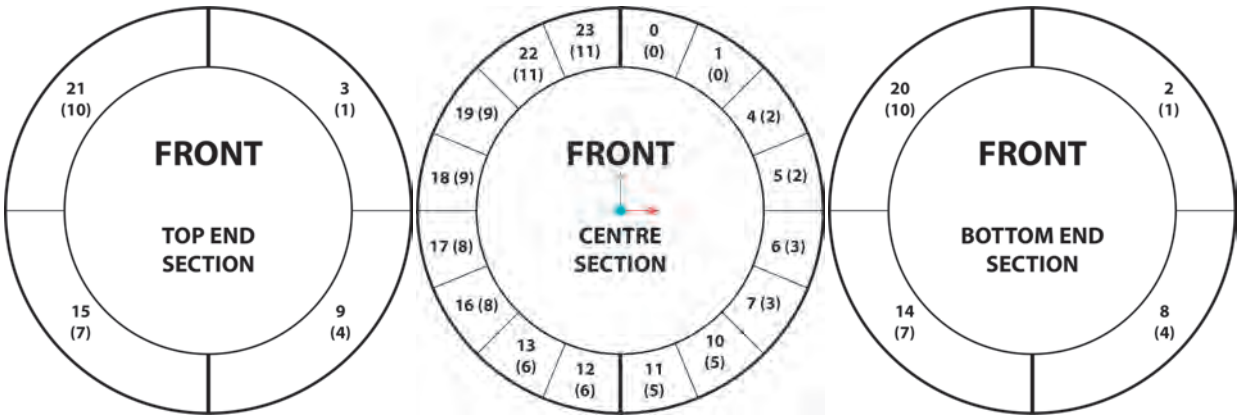

Figure 8.9: SuperPEPT bucket numbering/layout scheme showing the bucket pair numbers in parenthesis. The gantry is split along the thicker vertical line. The end sections split the bucket pairs between them such that the top end section always has the odd bucket and the bottom has the even bucket of the pair. The centre point axis is also shown where the +x-axis is red, the +y-axis is green, and the +z-axis is blue (out of the page).

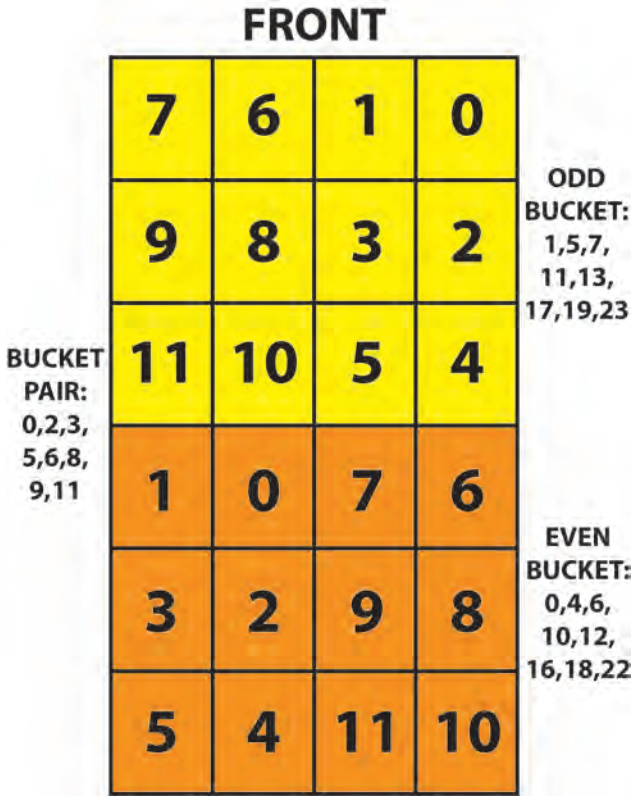

Figure 8.10: SuperPEPT detector block connection scheme for the centre section. The front indicates the front of the ring and the numbering scheme is shown as viewed from the inside of the ring or the front of the detector blocks.

each of the end section bucket pairs is in coincidence with four bucket pairs in the centre section. This combination offers the best LOR coverage through the FOV for such a long and constrained system. However, this combination also offers a few oddities. Because each of the bucket pairs is in coincidence with all the other bucket pairs in the end section, there is a possibility of getting some very short coincidences due to noise. For example, coincidences between neighbouring detector blocks between buckets three and nine in the end sections. These coincidences are easily discarded by the PEPT algorithms and are not a problem for a dedicated PEPT system.

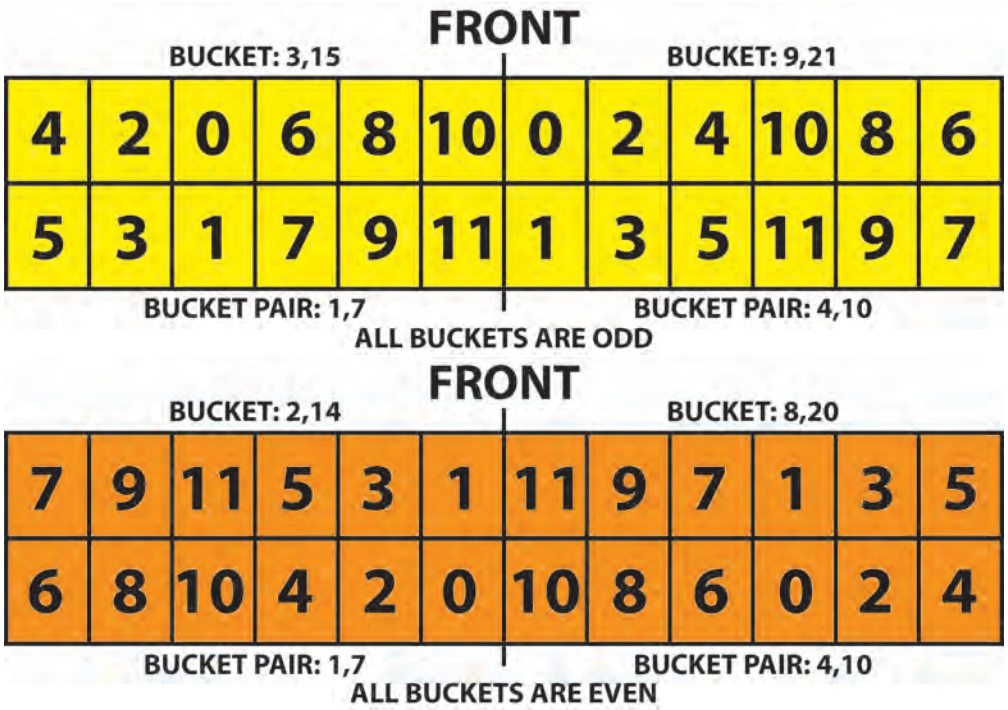

Figure 8.11: SuperPEPT detector block connection scheme for the end sections. The top end section is shown on the top and made up of the odd buckets and the bottom section is shown on the bottom and made up of the even buckets. Due to the use of the mounting studs located on the detector blocks for mounting, the top-end section detector blocks are mounted upside down which is evident in Figure 8.13. The front indicates the front of the ring and the numbering scheme is viewed from inside of the ring or the front of the detector blocks.

The detector block connection scheme for the sections is a bit unusual due to the splitting of the gantry into multiple sections. As shown in Figure 8.10, the centre section is

essentially the regular detector block layout scheme as used in the original gantry (see Figure 8.6) but rotated clockwise on its side with the odd and even buckets switching place. The individual blocks were rotated back in their place such that they were right side up. The end sections' detector block connection scheme is shown in Figure 8.11. Here, compared to the original scheme, the bucket pairs are split into the top and bottom sections and then the individual buckets' detector blocks are split in half and placed by one another. Since the detector blocks are mounted to the gantry using their stud system, the detector blocks in the top section are mounted upside down. This is not a problem, it just reverses the block's crystal numbering scheme.

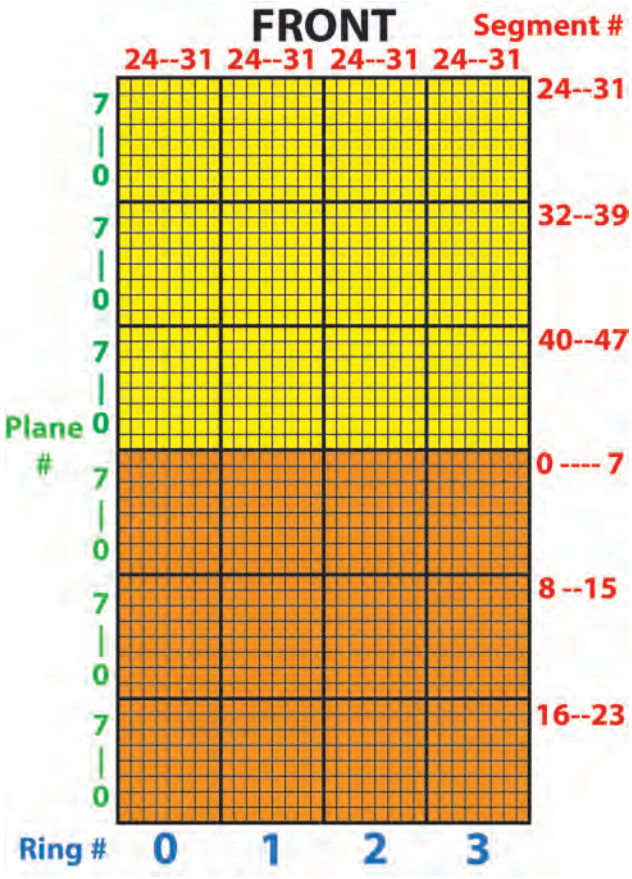

Figure 8.12: SuperPEPT centre section detector block crystal element numbering scheme. In this orientation, the ring numbers define the detector block column, the segment number defines the crystal column which is the same across a row of detector blocks and varies between the rows, and the plane number defines the crystal plane in the detector block.

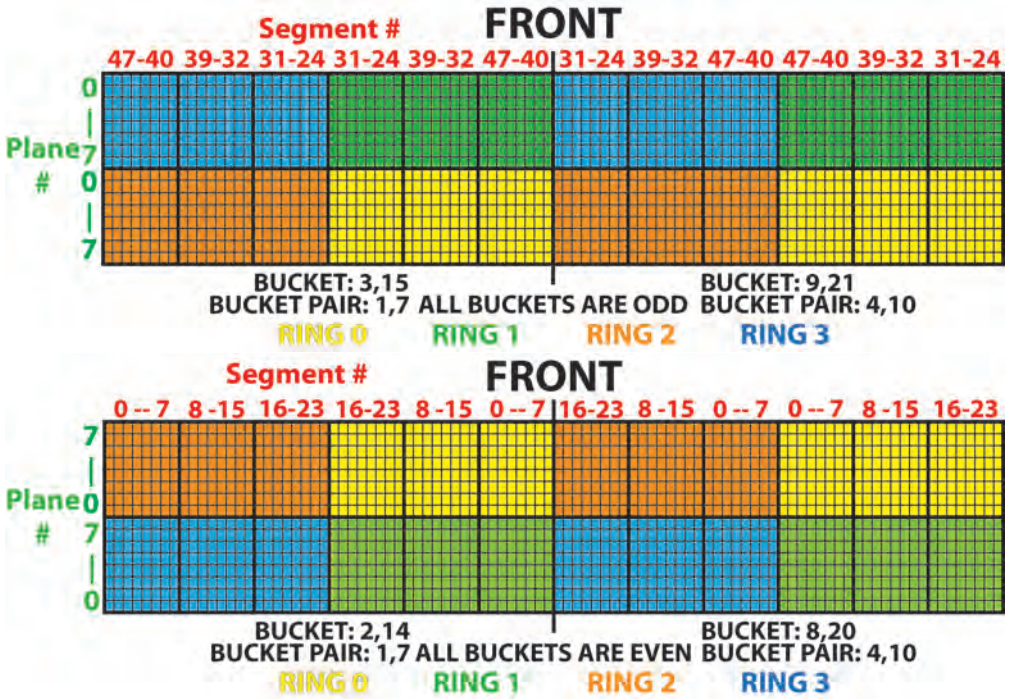

Figure 8.13: SuperPEPT end sections' detector block crystal element numbering scheme. The top end section is shown on the top and made up of the odd buckets and the bottom section is shown on the bottom and made up of the even buckets. Notice the reverse numbering in the top-end section due to the upside-down mounting of the detector blocks. The front indicates the front of the ring and the numbering scheme is viewed from inside of the ring or the front of the detector blocks.

The crystal element numbering scheme is shown in Figure 8.12 for the centre section and Figure 8.13 for the end sections. Unlike in the original version, here the numbering scheme becomes somewhat confusing, especially in the end sections. In the centre section, the ring numbers now indicate a column of detector blocks, the segment number indicates the column within a detector and is the same in each row of detector blocks, and the plane number indicates the crystal plane within the detector block. In the end sections, the ring number now indicates a subset of three detector blocks, the plane number still defines a crystal plane within a detector block, and the segment number indicates the crystal column within the detector block but that number is now shared between two columns of the detector blocks in that bucket.

Following these numbering schemes, it is now possible to fully identify the unique crystal element in coincidence in both buckets.

8.3.3 Crystal Element Numbers to a Real Position

There are many ways of translating the crystal element numbers into a real position in a lab/gantry frame. Most of them involve a combination of geometric and linear algebra methods. An explanation of how this is accomplished for SuperPEPT is presented below. This method for SuperPEPT is a lot more complex due to the novel block numbering scheme which has a lot of exceptions, gaps, and few useful patterns. The overall process can be divided into three major sections:

1. Calculation/derivation of missing geometric dimensions from known ones.
2. Determination of SuperPEPT section the detector block is located in.
3. Forming the transformation matrices and calculating the crystal element centre position.

The (0,0,0) centre position of SuperPEPT is the centre of the ring on the central transaxial plane of the gantry. Facing the gantry from the front, the +x-axis is in the 3:00 o'clock direction, the +y-axis is in the 12:00 o'clock direction along the split of the gantry, and the +z-axis is out towards the front of the gantry, establishing a right-handed axis as shown in Figure 8.9.

Calculation of Missing Geometric Dimensions

First, lets establish what is already known about the geometry. The ECAT EXACT HR+ detector blocks have a nominal crystal pitch of 4.85 mm axially and 4.51 mm transaxially. This

establishes the HR+ detector block height at the face of 38.80 mm and width of 36.08 mm when the pitch is multiplied by the eight crystal elements. Similarly for the ECAT EXACT detector blocks, their crystal elements are square and their nominal axial and transaxial pitch is 6.75 mm with a detector block height and width of 54.00 mm at the face. The 32 detector block columns in the centre section form an icosidodecagon (32-gon) and the 24 detector blocks per ring form an icositetragon (24-gon) for the end sections. With this information, it is possible to use the inscribed circle (incircle) for each of the sections to calculate the x and y coordinates on the transaxial plane of the gantry for each detector block using plane polar coordinates. Since the gantry is a cylinder, the z position of each detector block is calculated as a simple offset using the measured values for the spaces and the number of detector blocks. The distance from the topmost centre section detector block edge to the bottom edge of the end section detector block measures at 45.00 ± 0.01 mm giving the z spacing between the centre and end sections.

To use the incircle method, the inradius of each of the sections' polygon has to be calculated. The inradius could be measured across the gantry using a tape measure but this method leads to a large source of error due to the tape measure inaccuracies. A more accurate way is to use callipers to measure the detector faces and use the polygon side length to calculate the inradius. For the centre section, this is difficult due to the spaces between the detector blocks, so the actual side length will have to be extrapolated from the detector block width and the measured spacing between the adjacent detector block columns. The end section is a bit more straightforward. The bottom edges of the detector blocks meet each other which can be used for the polygon side length; but, due to the angle of the detector block faces, the inradius that passes through the detector block centre is larger than that calculated by the bottom edge. So, the length the inradius has to be extended by needs to be calculated. The final problem is due to how the gantry is split in half. The end sections are split exactly between the detector blocks; however, the centre section is split unevenly

due to the presence of the vertical separator struts. As can be seen in Figure 8.2, on one end of the split the gantry has the full divider while the other end does not have one. This means that the centre section is rotated by a small offset equal to half of the angle of the sector created by the divider.

Centre Section Inradius To calculate the actual side length of the 32-gon forming the centre section, the gap distance from one edge of the detector block to the other in the neighbouring column is required. This is measured to be $4.78 \pm 0.01\,\text{mm}$.

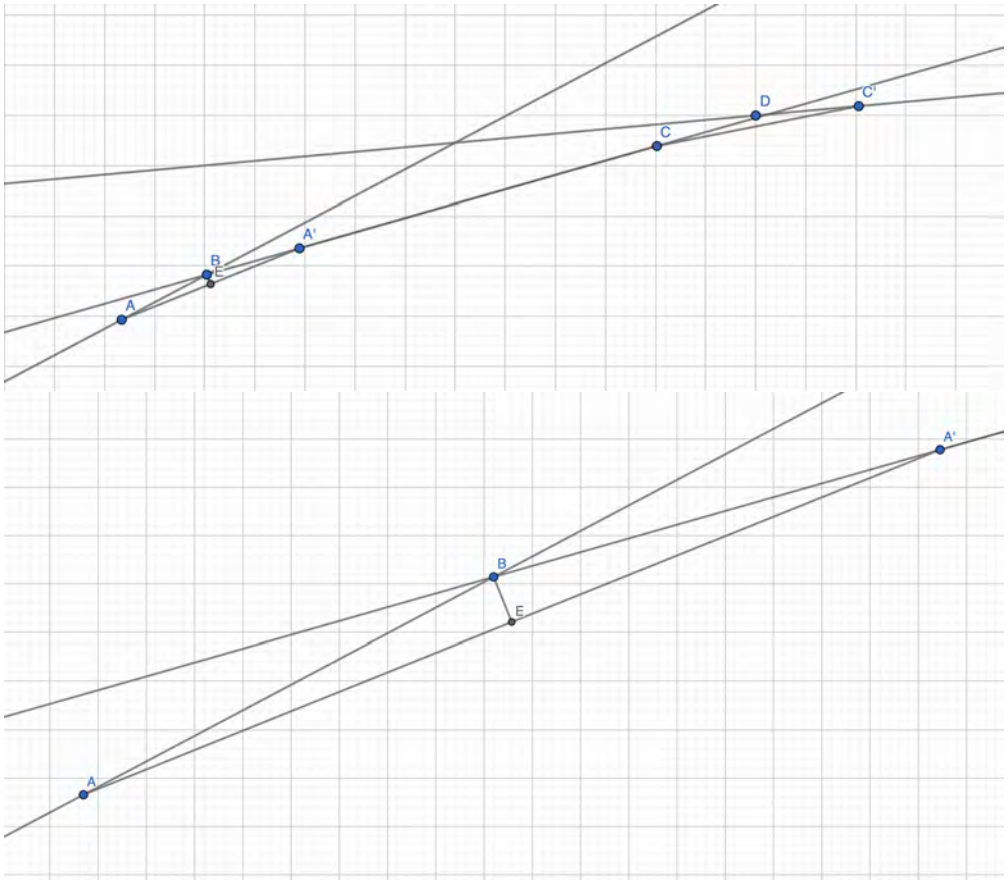

Figure 8.14: (Not to scale) A generalised view of SuperPEPT centre section face. $A'C$, A going to the left, and C' going to the right are the detector faces. AA' and CC' are the measured gaps between edges of adjacent detector block columns.

Using Figure 8.14, it can be seen that the actual side length of the 32-gon is BD which is equal to the sum of $A'C$ (the detector block face width), BA', and DC' which are

the face extensions due to the gaps and need to be calculated. All the gaps in the centre section are the same or $AA' = CC'$; therefore, $AB = BA' = CD = DC'$. $\angle ABA' = \angle CDC'$ are the interior angles of a 32-gon which are 168.75° exactly. As $AB = BA'$, $\triangle ABA'$ is an isosceles triangle such that $\angle BAA' = \angle BA'A$, height BE is perpendicular to AA', and E is the midpoint of AA'. Therefore, $AE = EA' = AA'/2 = 4.78 \pm 0.01\,\text{mm}/2 = 2.39 \pm 0.01\,\text{mm}$. Since, all interior angles of a triangle add up to 180.00°, $\angle BAA' = \angle BA'A = (180.00° - 168.75°)/2 = 5.625°$. Therefore, using trigonometric identities, $BA' = EA'/\cos(\angle BA'A) = 2.39 \pm 0.01\,\text{mm}/\cos(5.625°) = 2.40 \pm 0.01\,\text{mm}$. Finally, the side length can be calculated to be $2 \times 2.40 \pm 0.01\,\text{mm} + 36.08\,\text{mm} = 40.88 \pm 0.02\,\text{mm}$. Using an equation for inradius r of a regular polygon with n equal sides and s side length [323],

$$r = \frac{1}{2} s \cot\left(\frac{\pi}{n}\right), \tag{8.1}$$

the inradius of the centre section 32-gon is $207.53 \pm 0.10\,\text{mm}$.

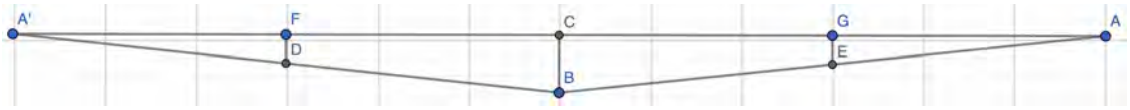

Figure 8.15: (Not to scale) A generalised view of SuperPEPT end section detector block face angle shown in Figure 8.3. $A'B$ and BA are the EXACT detector faces as viewed from the side. D and E are the centre points of the detector block faces.

End Section Inradius As shown in Figure 8.3 and generalised in Figure 8.15, due to the wedge shape of the EXACT detector blocks, the calculation for the inradius of a 24-gon based on the EXACT detector width will calculate the inradius from gantry axis to A or A' which is not to the centre of the detector block D or E. However, as the detector faces $A'B = BA$, $BC \perp A'A$, $A'A$ is parallel to the gantry axis, C is the midpoint of $A'A$, F is the midpoint of $A'C$, and G is the midpoint of CA, it can be proved that $A'D = DB = BE = EA$, $A'F = FC = CG = GA$, $DF \perp A'A$, $EG \perp A'A$, $DF = EG$, and $DF \parallel BC \parallel EG$. Therefore, the inradius to the detector face centre is the sum of the inradius to point A, which is based on side length equal to the EXACT detector block width or 54.00 mm nominal, and

length EG or DF. Using Equation 8.1, the inradius for 24-gon with 54.00 mm nominal side length is 205.09 mm.

To calculate EG or DF, more information about the wedge formation is needed. The easiest to measure dimension is distance $A'A$ which is 106.50 ± 0.01 mm. Therefore, CA is 53.25 ± 0.01 mm and GA is 26.625 ± 0.005 mm. Using trigonometric identities, we can calculate $\angle CAB = \angle BA'C = \cos^{-1}(CA/BA) = \cos^{-1}(53.25 \pm 0.01\,\text{mm}/54.00\,\text{mm}) = 9.56 \pm 0.06°$. Then, $EG = GA \times \tan(\angle CAB) = 26.625 \pm 0.005\,\text{mm} \times \tan(9.56 \pm 0.06°) = 4.48 \pm 0.03$ mm. Therefore, the inradius to the centre of the end section detector block is $205.09\,\text{mm} + 4.48 \pm 0.03\,\text{mm} = 209.57 \pm 0.03$ mm.

At this time it is also beneficial to calculate the detector half-height along the z-axis. This is equal to GA and it is just $A'A/4 = 106.50 \pm 0.01\,\text{mm}/4 = 26.625 \pm 0.003$ mm.

Centre Section Angular Offset The final piece of information needed is the angular offset of the centre section to account for the uneven split of the gantry. As the gantry should be split in the middle of the gap created by the separator but instead it is split such that the separator is fully moved to one side, the offset angle should be equal to the angle of the arc created from the edge of the detector block to the centre of the gap. This is the angle created by the extension to the detector face used to calculate the 32-gon inradius above.

Using the centre face geometry in Figure 8.16, DE is 36.08 mm nominal or the HR+ detector block width, AD and EC are the face extensions due to the gaps calculated to be 2.40 ± 0.01 mm, F is the detector face centre, and FB is the inradius of the centre section 32-gon or 207.53 ± 0.10 mm. $\angle ABC$ is the external angle of a 32-gon or 11.25° and $FB \perp AC$. The offset $\angle ABD$ is simply $\angle ABF - \angle DBF$. $\angle ABF = \angle ABC/2 = 11.25°/2 = 5.625°$. Using trigonometric identities, $\angle DBF = \tan^{-1}(DF/BF) = \tan^{-1}((36.08\,\text{mm}/2)/207.53 \pm 0.10\,\text{mm}) = 4.968 \pm 0.002°$. The centre section angular offset is then $5.625° - 4.968 \pm 0.002° =$

$0.657 \pm 0.002°$.

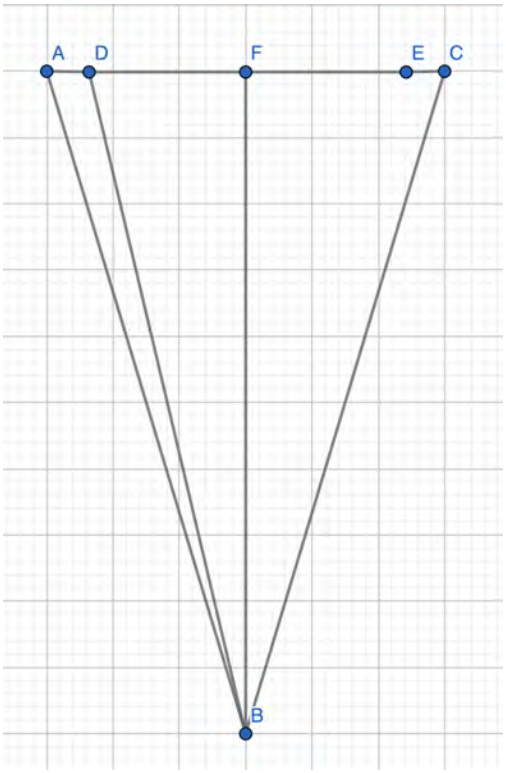

Figure 8.16: (Not to scale) A generalised view of SuperPEPT centre section face geometry used to calculate the centre section angular offset. DE is the HR+ detector block width, AD and EC are the face extensions due to the gaps, F is the detector block face centre, and FB is the inradius of the centre section 32-gon.

Calculating Crystal Element Positions in Detector Frame

To determine the section in which the detector block is located and therefore how further calculations will proceed depends on the bucket pair number and the segment number. This is done using a simple logic check:

- If the bucket pair number is not 1, 4, 7, or 10, the detector block is located in the centre section.
- Then if the segment number is larger than 23, the detector block is located in the top-end section.

- Otherwise, the detector block is located in the bottom end section.

Knowing the section the detector block is in, the detector block type used is also known. Therefore, it is possible to calculate the crystal element position in the detector block frame which is centred in the centre of its face, as shown in Figure 6.4. This position will later be transformed such that it is in the gantry frame. It is calculated using the following equation in a vector notation using the plane number and the segment number:

$$\underline{Pos_{detector\ block}} = \begin{pmatrix} ((\text{column number } \%\ 8) - 3.5) \times \text{pitch transaxial} \\ (\text{plane number} - 3.5) \times \text{pitch axial} \\ -10.0 \\ 1 \end{pmatrix}. \tag{8.2}$$

If the detector block is located in one of the end sections, the pitch values are taken for the EXACT block. If it is in the centre section, the HR+ block values are taken. Z is set to 10 mm as that is the depth at which 50% of 511 keV photons have interacted by in the BGO scintillator [324]. It is negative as the positive z-axis increases away from the detector face. The position is calculated as a 4-dimensional vector such that the following spatial transformation matrices are properly applied to it. The fourth dimension sometimes called the w describes if the vector is a vector or a position and is therefore 0 or 1, respectfully.

Calculating Crystal Element Positions in the Centre Section

To transform the position calculated in Equation 8.2 from the block frame to the gantry frame, one or more rotation and translation transformation matrices need to be applied. The first rotation applied is around the gantry x-axis such that the +y-axis of the block is facing up toward the +z-axis of the gantry. The matrix for the rotation around the x-axis

by an angle α is:

$$\underline{\underline{Rot_x}} = \begin{pmatrix} 1 & 0 & 0 & 0 \\ 0 & \cos\alpha & -\sin\alpha & 0 \\ 0 & \sin\alpha & \cos\alpha & 0 \\ 0 & 0 & 0 & 1 \end{pmatrix}. \tag{8.3}$$

For all blocks in the centre section, $\alpha = 90°$.

Another rotation is done around the gantry's z-axis such that the normal of the detector block face always points towards the gantry's centre axis. The matrix for a rotation around the z-axis by an angle γ is:

$$\underline{\underline{Rot_z}} = \begin{pmatrix} \cos\gamma & -\sin\gamma & 0 & 0 \\ \sin\gamma & \cos\gamma & 0 & 0 \\ 0 & 0 & 1 & 0 \\ 0 & 0 & 0 & 1 \end{pmatrix}. \tag{8.4}$$

To calculate the rotation angle γ, first, the overall column number of the detector block located in the centre section, when the detector ring is in its horizontal position, between 0 and 31 is calculated such that

$$\text{column number} = ([0, 2, 3, 5, 6, 8, 9, 11].\text{index}(\text{bucket pair}) \times 4) + \text{ring number}. \tag{8.5}$$

The rotation angle γ is then half of the 32-gon external angle, i.e. 5.625°, as the first column is not right on the gantry split but it starts between two columns. Then, the small angle offset of the centre section described earlier in the section is subtracted from that angle to rotate the section back to account for the uneven split. Finally, the 32-gon external angle or the angle of the sector taken by each of the sides, i.e. 11.25°, is multiplied by the column number and added to the rest. As this angle is calculated in the clockwise direction but the rotations are done in the counterclockwise detection, the whole value needs to be inverted such that the final angle γ is

$$\gamma = -(5.625° - \text{angular offset} + (11.25° \times \text{column number})). \tag{8.6}$$

The last matrix that needs to be determined is the translation matrix

$$\underline{\underline{M_{trans}}} = \begin{pmatrix} 1 & 0 & 0 & dx \\ 0 & 1 & 0 & dy \\ 0 & 0 & 1 & dz \\ 0 & 0 & 0 & 1 \end{pmatrix}. \tag{8.7}$$

In this instance, dx, dy, and dz describe the position of the centre of the detector block in the gantry frame. Since the detector block centres lie on a circle, planar polar coordinates can be used to calculate the dx and dy in the Cartesian coordinates using

$$\begin{aligned} dx &= r \times \cos(\Theta), \\ dy &= r \times \sin(\Theta). \end{aligned} \tag{8.8}$$

The inradius of this circle was calculated to be $207.53 \pm 0.10\,\text{mm}$ for the centre section. The angle Θ for planar polar coordinates is calculated from the +x-axis counterclockwise. This angle was already calculated above as γ which was calculated from the +y-axis so Θ is simply γ plus 90°. On the other hand, dz is calculated as a linear offset from the centre plane. The value is then multiplied by the height of the HR+ detector block to get the actual value. The equations for dx, dy, and dz are therefore

$$\begin{aligned} dx &= 207.53 \pm 0.10\,\text{mm} \times \cos(\gamma + 90°), \\ dy &= 207.53 \pm 0.10\,\text{mm} \times \sin(\gamma + 90°), \\ dz &= (2.5 - [3,4,5,0,1,2].\text{index}(\text{floor}(\text{segment number}/8))) \times \text{HR+ detector height}. \end{aligned} \tag{8.9}$$

Lastly, all the matrices have to be applied on the initial crystal position in the detector block frame from Equation 8.2 to yield the final crystal position in the gantry frame of view. The order is

$$\underline{Pos_{gantry}} = \underline{\underline{M_{trans}}} \cdot \underline{\underline{Rot_z}} \cdot \underline{\underline{Rot_x}} \cdot \underline{Pos_{detector\ block}}. \tag{8.10}$$

Calculating Crystal Element Positions in the Top End Section

A similar process as that used to calculate the centre section positions applies to the outer sections. Following the information in Figure 8.13 for the top section, it is apparent that there are practically no good patterns that can be exploited; therefore, the following methods will heavily depend on lookup tables.

First, the detector column number which numbers the detector columns from 0 to 5 clockwise in each bucket is calculated. Since the segment numbers in the top-end sections range from 24 to 47 and two columns always share the same range, the calculation will be best described with conditional statements:

- The detector column number is the segment number divided by 8 and rounded down.
- If the bucket pair number is 1 or 7 and the ring number is greater than 1, subtract 5 from the detector column number and take its absolute value.
- If the bucket pair number is 4 or 10, subtract 3 from the detector column number.
  - If the ring number is less than 2, subtract 5 from the detector column number and take its absolute value.

Another useful number to calculate is the quadrant number from the bucket pair number. It is simply

$$\text{quadrant} = \frac{\text{bucket pair} - 1}{3} \tag{8.11}$$

in the end sections. Then, the detector block angle can be calculated as:

$$\text{detector angle} = ((\text{detector column} + 0.5) + (\text{quadrant} \times 6)) \times 15^\circ, \tag{8.12}$$

where the 0.5 accounts for the ring being rotated such that the gantry splits between the detector blocks and not through its centre. 15° is the 24-gon external angle or the angle of the sector taken by each side of the polygon.

Having calculated the detector column, quadrant, and angle numbers, the detector block rotations can be derived. The top end section is the odd one out in a way that all of its detector blocks are mounted upside down. Therefore, all the detector blocks have to be rotated around the z-axis using the rotation matrix in Equation 8.4. The γ is simply 180°.

Next, like in the centre section, the detector block has to be rotated around the x-axis such that the detector block +y-axis is pointing in the same direction as the gantry's +z-axis. However, here the detector blocks are not simply rotated by 90° but by a bit less or more depending if they are in the top or bottom row. The small angle that the detector is rotated by was calculated earlier in the section, using Figure 8.15. It is $\angle CAB$ or $\angle BA'C$, which are equal to $9.56 \pm 0.06°$. Ring numbers can be used to find out which row the detector block is in, see Figure 8.13, such that rings 0 and 2 are in the bottom row and rings 1 and 3 are in the top row. The x rotation angle α used in Equation 8.3 is then calculated as

- If ring number is 0 or 2, $\alpha = 90° - 9.56 \pm 0.06°$.
- Otherwise, $\alpha = 90° + 9.56 \pm 0.06°$.

The third and final rotation is around the z-axis to point the detector block face normal toward the gantry centre axis. The z rotation angle γ used in Equation 8.4 is −detector angle because rotations are calculated in the counterclockwise direction but the detector angle was calculated in the clockwise direction.

Finally, the detector block centre position in the gantry frame is calculated to be used in Equation 8.7 to translate the detector block from the centre to its proper location. Like in the centre section, dx and dy can be calculated using the planar polar coordinates in Equation 8.8. The radius was calculated earlier to be $209.57 \pm 0.03\,\text{mm}$. The angle Θ is simply 90° − detector angle, because the detector angle is calculated from the +y-axis clockwise and Θ is calculated from the +x-axis counterclockwise. Therefore, the equations

dx and dy are

$$\begin{aligned} dx &= 209.57 \pm 0.03\,\text{mm} \times \cos\left(90^\circ - \text{detector angle}\right), \\ dx &= 209.57 \pm 0.03\,\text{mm} \times \sin\left(90^\circ - \text{detector angle}\right). \end{aligned} \tag{8.13}$$

On the other hand, dz is dependent on the row the detector is in, like angle α above. It is equal to the height of the HR+ detector blocks from the centre of the centre section to its end, the space between the centre and end section, and the half-height of the EXACT detector block calculated earlier. The half-height is 26.625 mm nominal and the space between the sections is 45.00 ± 0.01 mm as stated before.

- If ring number is 0 or 2, $dz = (3 \times \text{HR+ detector block height}) + 45.00 \pm 0.01\,\text{mm} + 26.625\,\text{mm}$,
- Otherwise $dz = (3 \times \text{HR+ detector block height}) + 45.00 \pm 0.01\,\text{mm} + (3 \times 26.625\,\text{mm})$.

Finally, the rotations and the translation matrices are applied in the order discussed or

$$\underline{Pos_{gantry}} = \underline{\underline{M_{trans}}} \cdot \underline{\underline{Rot_z}} \cdot \underline{\underline{Rot_x}} \cdot \underline{\underline{Rot_{z\,180}}} \cdot \underline{Pos_{detector\ block}}. \tag{8.14}$$

Calculating Crystal Element Positions in the Bottom End Section

Calculations for the bottom end section are the same as for the top end section with some exceptions:

1. The first, 180° rotation around the z-axis used to flip the detector block is not applied here as all detector blocks are not upside down.
2. The detector column is calculated differently as shown below.
3. The rotation angle α around the x-axis is also calculated differently.
4. The dz for the translation matrix is calculated the same as above but the value is inverted so $dz_{bottom} = -dz_{top}$.

Here, the detector column number is calculated following this logic.

- The detector column number is the segment number divided by 8 and rounded down.
- If the bucket pair number is 4 or 10, then subtract 2 from the detector column number and take its absolute value.
- If the ring number is less than 2, then subtract 5 from the detector column number and take its absolute value.

The x rotation angle α used in Equation 8.3 is then calculated using the following logic.

- If ring number is 0 or 2, $\alpha = 90^\circ + 9.56 \pm 0.06^\circ$
- Otherwise $\alpha = 90^\circ - 9.56 \pm 0.06^\circ$.

Finally, the rotations and the translation are applied in the following order

$$\underline{Pos_{gantry}} = \underline{\underline{M_{trans}}} \cdot \underline{\underline{Rot_z}} \cdot \underline{\underline{Rot_x}} \cdot \underline{Pos_{detector\ block}}. \tag{8.15}$$

In Summation

Combining the above sections, it is possible to calculate all the crystal element centres in the gantry frame. A sample Python code is presented in Appendix A. It iterates through all combinations of 12 bucket pair numbers, 4 ring numbers, 48 segment numbers, and 8 plane numbers producing all the crystal element centres present in SuperPEPT as shown in Figure 8.17. To make this position calculation run a lot faster when converting the raw list mode file into an LOR file, the user has the option to pre-calculate all the crystal element centre positions and store them in a lookup table. For very small files it is quicker to just calculate the position for each LOR as it's being processed, but for very large list mode files it is

beneficial to use pre-calculated lookup tables. They come at the expense of a few hundred kilobytes of memory, but omitting all the repeated calculations that have to be done for each end of the LOR, greatly decreasing processing time.

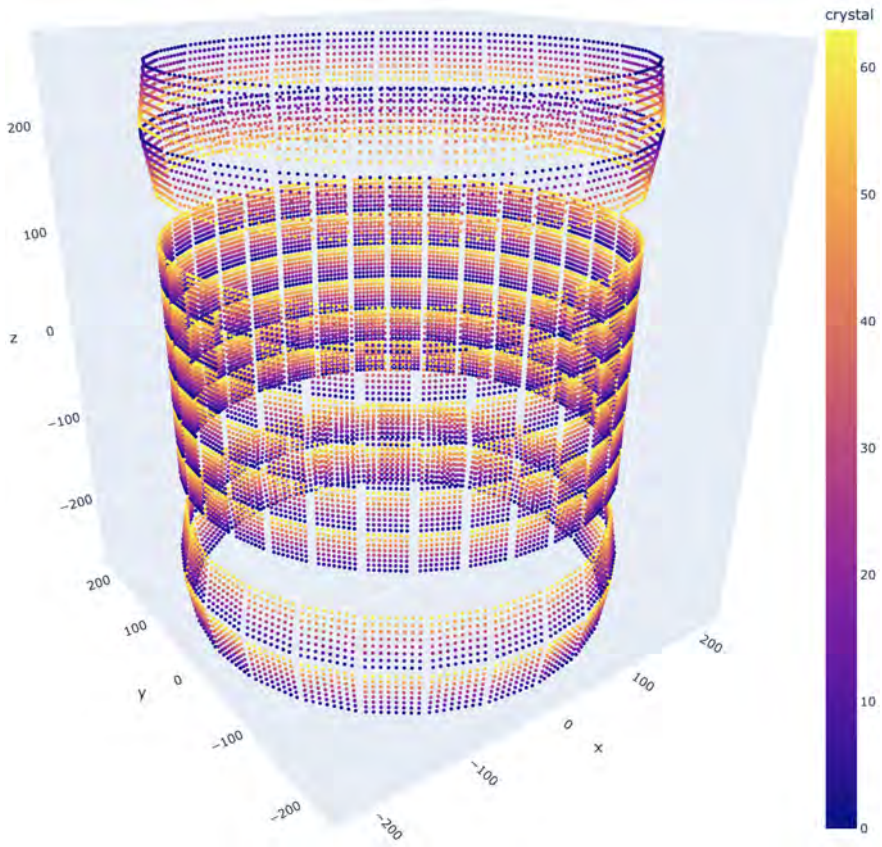

Figure 8.17: Calculated SuperPEPT crystal centre positions using the method discussed in Section 8.3.3 with the Python code in Appendix A. The colour scheme corresponds to the crystal element number in each detector block from 0 to 63.

8.3.4 Time Calculation

Like with most other PET scanner list mode file formats, the time is given as 1 ms tag words since the start of the acquisition. This means that each coincidence does not contain any timing information and that there is no way of knowing how the coincidences are distributed between the timing words besides their order. Due to this, SuperPEPT list mode file code gives the users multiple time calculation options. The quickest is to simply set the time of

all the LORs between timing words to be the previous full millisecond count. This method does not require the knowledge of the number of LORs between the timing words and is the quickest to process but one of the least accurate ones.

The other option is to evenly distribute the LORs between the two timing words. This means that the list mode file has to be read twice in chunks, once to find the count of LORs between timing words and then a second time to process the data and calculate the time from the start of the acquisition. Here the time is increased by 1 ms divided by the number of LORs between that timing word and the next timing word. Each LOR is then assigned a time since the start of the acquisition. There are other methods based on average coincidence rate as calculated based on a certain number of LORs at the start of the acquisition; however, these methods are not precise enough especially as the coincidence rate decreases over the long acquisition time due to the quick decay of the tracer or due to the tracer periodically leaving and entering the scanner FOV.

8.4 In Summary

The SuperPEPT has been built using parts from the ECAT EXACT HR+, ECAT EXACT 31, and ECAT ART; which have been discussed in detail in Section 7. The system was predominately based on the HR+ lossless coincidence processor with the bucket controller boards being sourced from the HR+ and ART. Due to the limited number of the working HR+ detector blocks and to further extend the axial FOV of the system, the centre section was assembled out of the small HR+ detector blocks and two end sections have been built out of the larger EXACT 31 and ART detector blocks. After initial troubleshooting and fixing/replacement of damaged parts, the appropriate data processing and management programs have been written. The mathematics of converting between the list mode data

format and real world values has been explained in Section 8.3.3 as incorporated in the data processing software. Next, the early characterisation of the system is presented in Section 10.

Chapter Nine

LaMA PEPT

LaMA PEPT or Large Modular Array for PEPT is a flexible geometry PEPT array dedicated to obtaining PEPT data from large and/or oddly-shaped systems. The camera began its life as the Modular Camera, first built in mid-2000 [325, 326]. The original system contained only 16 BGO-based buckets worth of mixed electronics from the ECAT 931 and 951 scanners. LaMA PEPT boxes the bucket electronics into individual aluminium boxes with all the required connections exposed at the back of the bucket. This transformed the original curved bucket layout shown in Figure 7.11 to a linearly distributed detector block system shown in Figure 9.1.

My contributions to the LaMA PEPT predominately include everything from the broken-down Modular Camera system I received to its continued operation. When I inherited the system, the initial 16 modules have been in a run down state needing calibration, heavy maintenance, and unification of the electronics to use the ECAT 951 bucket controllers and detector blocks. Further, I refurbished the coincidence processor initially used by the system and assembled a second one from spare parts, greatly reducing noise by cleaning the individual cards, sitting them properly, and fixing any damage. Next, I copied the original box design which was later used to built the new ones at the Physics Workshop. Finally,

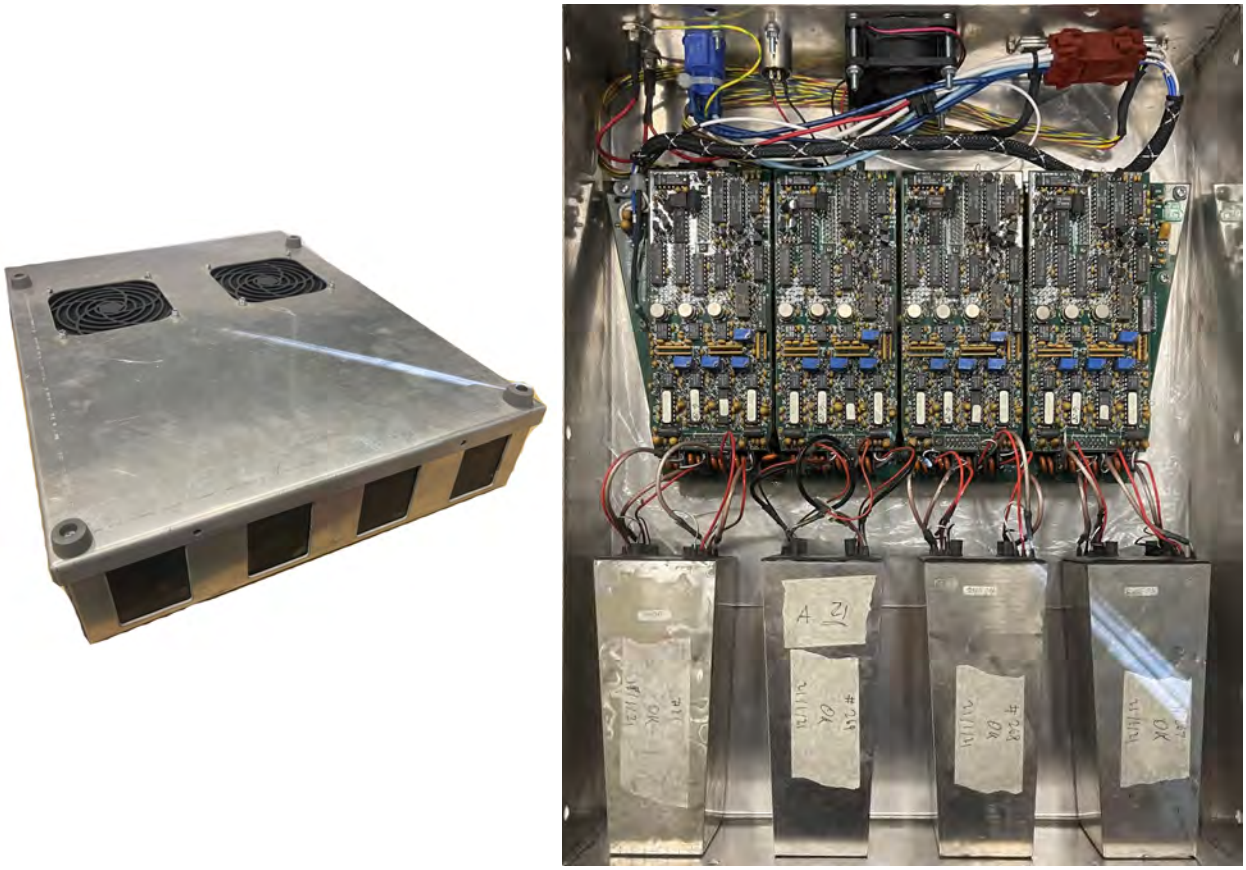

Figure 9.1: Left: The outside view of the modern LaMA bucket with installed air filters. Right: The inside view of the LaMA bucket with 4 ECAT 951 detector blocks and the ECAT 951 bucket electronics.

I assembled the 32 new modules, checking all the electronics and troubleshooting them if they did not work. The biggest time consuming task was the modification of the original data cables and assembly of the new power cables. This meant soldering over 1.5k individual wires which needed to be stripped, prepared for soldering, soldered, heat shrunk, and tested to make sure they will not short the system. I also built new power supplies which required heavy duty power bus-work to be done. Furthermore, I have designed and built various support frames and storage carts out aluminium structural profiles to support various experiments with this system. Finally, after solving majority of the hardware problems, I have also written many pieces of software including serial communication programs, troubleshooting and maintenance programs, and data visualisation and processing programs. Some of

these programs existed with the initial setup, but upon closer analysis, they needed to be modernised and many mistakes within them had to be corrected, especially in the parts converting the list mode data bits into real numbers. In the end, I choose to fully rewrite all of them. The manual labour on this system itself has taken up a good year of my PhD.

9.1 The Modular PEPT Concept

LaMA PEPT is based on a modular PEPT concept where the elements of the original scanner are discretised into the smallest pieces possible for efficient setup and data collection. All the unneeded pieces of the scanner like the patient handling systems, sources control systems, and original gantry are scraped. All the bucket assemblies are boxed into individual boxes, like the ones shown in Figure 9.1, with all the cables receiving new, user-friendly connectors. The original data and clock cables are also used. They have been cut and a DB-9 interconnect has been soldered in to create the interface at the bucket boundary. The coincidence processor, in the case of the large ECAT 931 and 951 card cage style coincidence processors, is housed in a ventilated standard 19-inch rack cabinet. The only fully redesigned part of the system is the power supply which swaps out the copper bus bars and old power supplies for individual cables and modern power supplies enclosed in their cases.

9.2 Updating the System

With the need to acquire data over large and tall volumes, the original modular camera system had to be expanded and any problems corrected or minimised. The system was expanded with an addition of 32 buckets for a total of 48 buckets in the whole system. The bucket electronics and detector blocks in the original 16 buckets were all switched out to

use the ECAT 951 components and a further 32 buckets were assembled. Two coincidence processors were also rebuilt for the system as a single one can only carry 32 buckets. So, an ECAT 931 and ECAT 951 two-ring, 16-bucket-ring coincidence processors were built and tested. They are shown in Figures 7.3 and 7.9 respectively. A lot of electronic noise in the system was eliminated during the rebuild. It was found that some of the boards were improperly setup with the DIP switches located on the board and the individual cards were not tightly inserted into the card cage. Due to the large IPCP card connectors, the cards are fastened with screws from the back of the backplane to pull in the cards tightly. Originally, this was done incorrectly with some of the screws simply missing or they were replaced with the wrong thread type and/or length. Replacing the missing screws and tightening them to an appropriate torque level greatly decreased the number of false coincidences in the system.

One of the issues with the original system was the excessive voltage drop over the thinner supply wires and improper power connectors. This caused some of the buckets to not boot properly and produce false event data. The power connectors were replaced from the generic XLR-type connectors which also began breaking apart with properly designed, heavy-duty, DC power connectors used in the music industry. The logic power supplies were fully replaced to include modern, lighter yet more efficient 5 VDC supplies shown in Figure 9.2. The power lines were also upgraded to a higher gauge and length, decreasing the voltage drop. The modern power supplies also allowed for a small degree of adjustment so that the voltage present at the bucket was corrected to be close to 5 VDC and -5.2 VDC, further minimising the effect of the voltage drop.

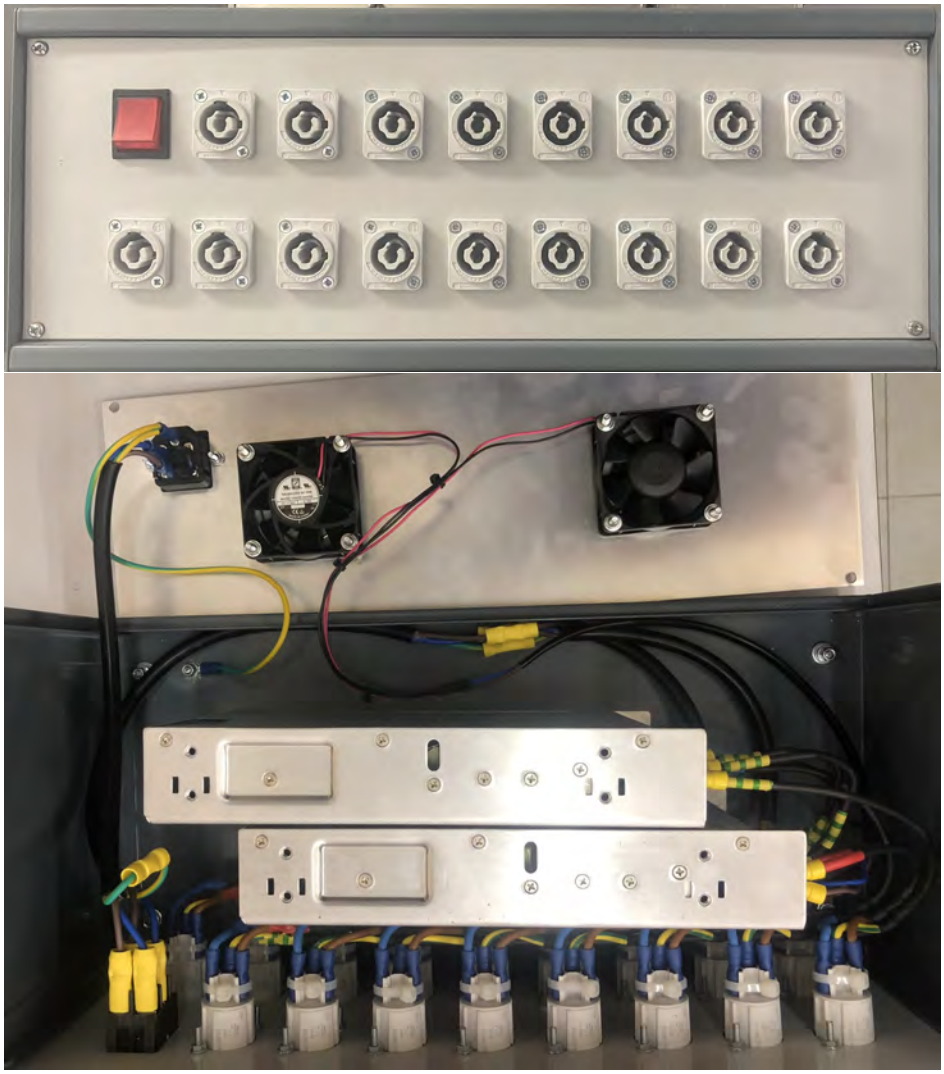

Figure 9.2: New logic power supplies for the LaMA PEPT. This is 1 of 3 modules made with each one being able to support 17 connections or 16 modules and 1 spare. The system uses commercial, heavy-duty Neutrik powerCON connectors with internal power distribution utilising solid copper conductors.

9.3 Geometry and Assembly

LaMA PEPT is perhaps the only PEPT system that does not have a set geometry. The smallest bucket module shown in Figure 9.1 can be arranged in many ways following some simple rules. These buckets can be placed at virtually any angle as long as they are physically supported. At least a single module pair needs to be connected to the system for it to record

coincidences, so the smallest geometry only has to have two buckets facing each other. The simpler geometries are formed by placing just a few buckets opposite of one another in two or four-stack arrangements around the equipment-under-test. More complex geometries are also achievable with the help of pre-built jigs or supports made up of structural profiles. As discussed later in Section 9.5.1, the only real limitation to the possible geometries are the module pairs or the set pairing of buckets that are in coincidence. It is important to keep them in mind and it is always recommended that buckets which were opposite of one

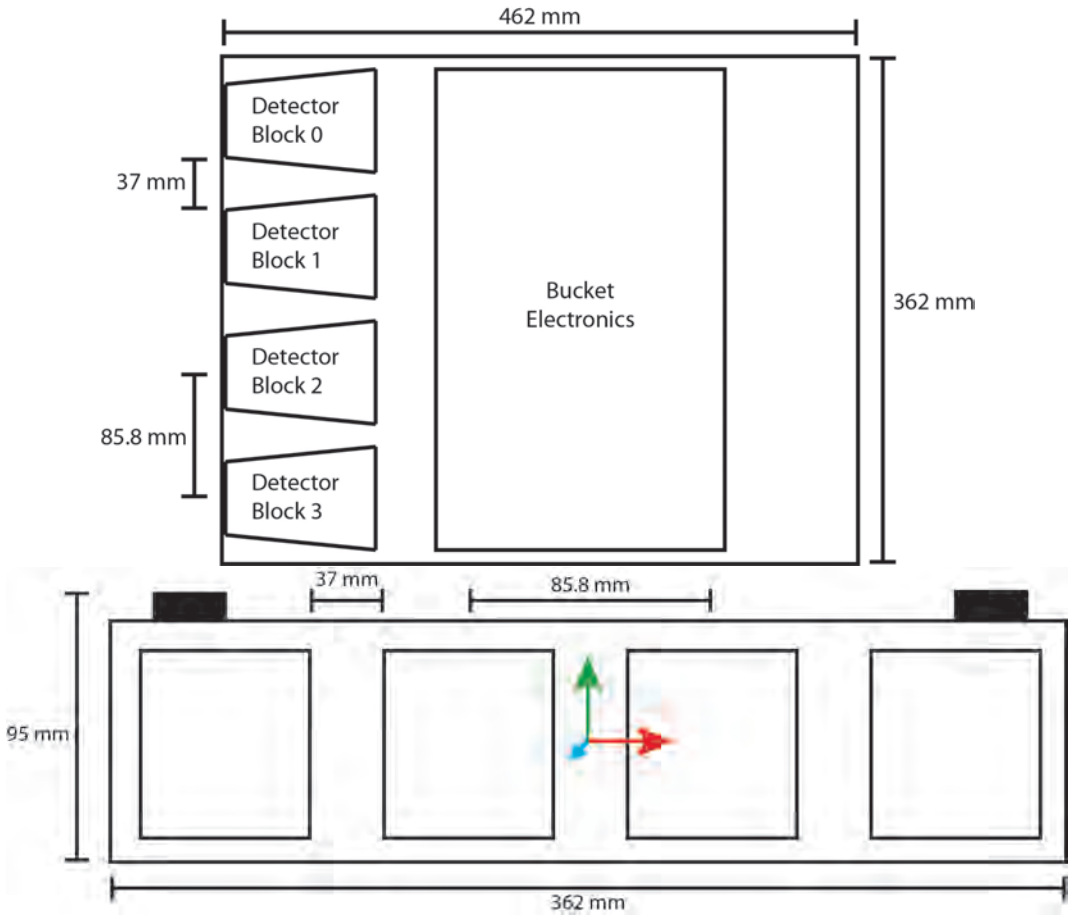

Figure 9.3: (Not to scale) Top: The inside view of the LaMA bucket showing the box dimensions and block spacing. Bottom: The front view of the LaMA bucket shows the box dimensions and the bucket origin that will be referred to later when calculating crystal positions. The red arrow is the +x-axis, the green arrow is the +y-axis, and the blue arrow is the +z-axis in the direction away from the bucket or out of the page. The black rectangles are the bucket feet which are mounted to the lid of the bucket as shown in Figure 9.1.

another in the original scanner ring geometry be placed opposite of one another in the custom geometry.

The bucket box dimensions are shown in Figure 9.3. The bucket box is 362 ± 1 mm wide, 462 ± 1 mm long, and 95 ± 1 mm high with the blocks being spaced 37 ± 1 mm apart. The bucket features easy-to-use connectors for connecting all the required power supplies and data lines as shown in Figure 9.4. The DB-9 connectors are different to those used on the bucket board itself. The original data cables were measured and cut such that a small piece of the line with the original connector stayed in each bucket and was soldered to the DB-9 sockets on the back of the bucket. The cut was performed at the same distance from the original plug each time such that the cables could be mixed without the danger of causing any clock skew between the different buckets. The leftover piece of the cable received the opposite DB-9 gender plug.

Figure 9.4: A view of the connectors available on the back side of the LaMA bucket. From left to right: female DB-9 connector for the differential ECL clock and serial communication line, male DB-9 connector for the differential ECL data connection to the coincidence processor, a cooling fan, male 4-pin XLR for 12 VDC supply for the fan, female Neutrik powerCON socket for a logic 5 VDC, −5.2 VDC, and common ground, and two SVH 1.5 kVDC sockets for daisy-chaining the HV supply through all the buckets.

9.4 Data Acquisition

Data acquisition for LaMA PEPT is achieved directly from the coincidence processor using the ACS data cable. The system fully replaces the ACS and is made up of a custom-designed

data acquisition board, shown in Figure 9.5, which handles the data line handshaking with the coincidence processor, inserts timing information, and shuffles the data such that they can be acquired using an Adlink PCI-7300A 32-channel digital I/O card. The PCI acquisition card is inserted into a Windows desktop PC which uses a custom C program written using the card's driver functions. Using the provided drivers, the data can be acquired using DMA into a series of buffers in the system memory. The buffers are then, in order, written to the HDD along with the buffer time since the start of acquisition. This system was first designed by Leadbeater et al. [327] and has gone through a few iterations since. Each of the two coincidence processors in the LaMA PEPT system uses its data acquisition setup and the

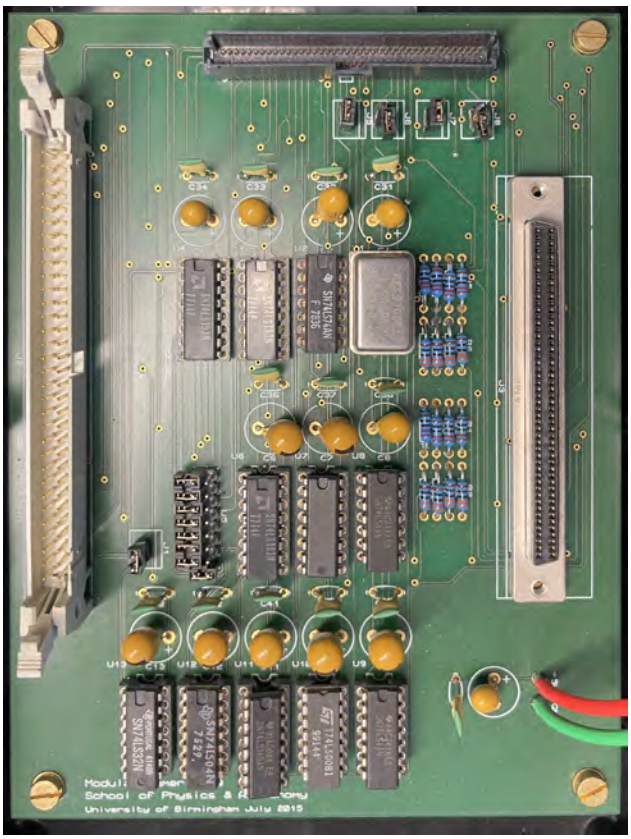

Figure 9.5: The acquisition board is designed to record coincidence data from the ECAT 931 and 951 coincidence processors. The left connector interfaces with the 931 coincidence processor. The top connector interfaces with the 951 coincidence processor. The right 100-pin SCSI-II connector interfaces with the Adlink PCI-7300A data acquisition card. The jumpers allow for the selection of the timing information clock frequency and the selection of status bits or insertion of custom TTL signals.

data are later combined in post-processing.

The data acquisition board features both connectors for the 931 and 951 coincidence processors due to their coincidence data output similarity (see Section 9.4.2) but only one of them can be plugged in at a time. The board also includes user-configurable jumpers. One set of jumpers samples the output of an 8-bit counter run by the board's 1 MHz clock. This divides the clock signal and allows the user to choose one of the lower frequencies as the clock for the timing information counter. The timing information is exposed to the PCI acquisition card as a 4-bit looping counter along with the 28-bits of data from the coincidence processor. A trigger signal is sent to the PCI card whenever the coincidence processor sends valid data or whenever the counter loops around. Later the data processing software uses these timing words to assign an accurate timing to each LOR. The program uses the looped-over timing words to keep time linearity whenever the particle exits the system FOV and no coincidences are produced. These timing-only words are then rejected as they do not contain valid coincidence data. A few more jumpers are used to select which delayed, multiple, or scatter flags are passed over to the PCI card or they can be used by the user to insert other sensor TTL level data into the data stream to be captured with the coincidences.

9.4.1 Handshaking

The handshaking procedure between the coincidence processor and the ACS is handled by a custom-programmed PAL chip in the ACS and decision circuits on each of the IPCP boards. The whole sequence and detailed timing information was reported by Leadbeater [328] and is summarised here. The handshaking procedure uses 4 signal lanes as shown in Section 9.4.2. Two signals are generated by the ACS: BSTB and BACK or the strobe and acknowledge signals, respectively. The other two signals are generated by the IPCPs: BREQ and BRPLY or the request and reply signals, respectively. Since the data bus interfaces with multiple

IPCP cards, the bus is run by 3-state logic devices. This means that the lines are normally pulled up high and actual signals are active low. A normal sequence of events is as follows:

1. When any of the IPCP boards have data available in the output FIFO, the FIFO produces an output-ready signal. The signal is then buffered, held, and presented to the ACS as a low request signal. Multiple IPCP boards can hold the request line low at the same time.
2. The ACS reads the low request signal constantly held down by the IPCP boards and when it is ready to receive data, it sends a short high-to-low pulse on the strobe line.
3. The strobe pulse is seen by all the IPCP boards at the same time. It is used by the first stage of a decision circuit. The decision circuit is a flip-flop which takes in the FIFO output-ready signal and the strobe pulse and produces an output when both are true. If the FIFO output ready signal is present, the strobe signal sets the flip-flop which then drives the next flip-flop in the second stage of the decision circuit.
4. After the strobe pulse, the ACS holds low the acknowledge line. This signal is seen in a particular order by the IPCP boards. The signal is first seen by the IPCP handling ring 1 coincidences only. If that IPCP board has data ready and the first stage flip-flop is set, the acknowledge signal is prevented from going to the next board and instead drives the second stage flip-flop. If that is not true, the signal is then passed to the IPCP board handling ring 2 coincidences, then the IPCP board handling ring 1x2 coincidences, and lastly the IPCP board handling ring 2x1 coincidences.
5. Using this priority selection method, only a single board can be selected. Now, that the second stage flip-flop was activated, it generates an unclock pulse and an output enable signal to the FIFO. This causes the FIFO to present its data to the ACS. The unclock pulse is then sent along the reply line to the ACS.
6. The reply pulse is then seen by the ACS, delayed a short time so the data can stabilise

on the cable, and it is used to latch data into a FIFO in the ACS. Once the data are latched, the ACS releases the acknowledge line.

7. The released acknowledge signal causes the IPCP boards to reset their decision circuits, disable the FIFO output, and release the request signal beginning the process from the beginning.

This handshaking procedure has a few issues especially when running the system at higher data rates than originally designed for clinical studies by using very active sources. This can cause multiple IPCP boards to hold low the request signal which is not a problem but only one of them will be handled using the acknowledge signal priority. After the reset, the boards that still have data present in their FIFO will again hold down their request lines low. However, at excessive data rates, it is possible for the ring 1 and ring 2 IPCP boards (the first and second IPCP to see the acknowledge signal, respectively) to overwhelm the system and prevent the other two or the last board from ever presenting its data. To alleviate this issue, each IPCP board has a cool-down period before it can send a request signal again after its data was read. The cool-down time is set manually using DIP switches located on the IPCP board itself.

Upon examination of the above handshaking sequence, it is evident that it is possible to fully ignore the IPCP initial request signal and simply query the coincidence processor at a constant rate. This is the method of handshaking used by the LaMA PEPT acquisition board. The handshaking sequence now follows these steps.

1. The acquisition board sends the strobe pulse to the IPCP boards.
2. The pulse is seen by all the IPCP boards and if any of them have data, the first stage flip-flop is set by the pulse.
3. After a short delay, the acquisition board holds the acknowledge signal low for a pre-

defined time.

4. If any of the IPCP boards have the first stage flip-flop set, the acknowledge signal sets the second stage flip-flop, unclocks the FIFO, and sends the reply pulse back to the acquisition board. The reply pulse is then delayed shortly and passed through to the Adlink PCI-7300A data acquisition card which saves the data.
5. After a pre-defined time, the acknowledge signal is released and the whole cycle begins again.

This handshaking method allows the user to select the rate at which the handshaking is conducted. While the acquisition board does not contain any jumpers to configure the frequency of the handshaking system, the user can switch out the main oscillator to set the desired frequency. However, there is a limit to this approach as the frequency selected needs to allow for all the signal delays and provide enough time for the data to stabilise on the bus.

9.4.2 IPCP Board to ACS Data Bus Connector Definitions

The format/pinout of the coincidence data lines from the coincidence processor to the ACS or LaMA PEPT acquisition board are shown in Figures 9.6 and 9.7. The two connectors are functionally the same except the 951 IPCP one carries the serial communication lines which in the 931 IPCP are run using a separate cable, see Figures 7.3 and 7.9. The 951 bucket also provides the additional "Plane 2" bits. Otherwise, the acquisition board simply connects the data signals for those two connector types together and directly guides them to the 100-pin SCSI-II connector used by the Adlink PCI-7300A digital data acquisition card.

1	A Segment 0
3	A Segment 1
5	A Segment 2
7	A Block 0
9	A Block 1
11	Spare
13	B Segment 0
15	B Segment 1
17	B Segment 2
19	B Block 0
21	B Block 1
23	Spare
25	Mod Pair 0
27	Mod Pair 1
29	Mod Pair 2
31	Mod Pair 3
33	Mod Pair 4
35	Mod Pair 5
37	BACK
39	BREQ
41	BSTB
43	BRPLY
45	Multiple
47	Delayed
49	A Plane 0
51	A Plane 1
53	B Plane 0
55	B Plane 1
57	IPCP Add 0
59	IPCP Add 1
61	Spare
63	Spare

1	A Segment 0
3	A Segment 1
5	A Segment 2
7	A Block 0
9	A Block 1
11	A Plane 2
13	B Segment 0
15	B Segment 1
17	B Segment 2
19	B Block 0
21	B Block 1
23	B Plane 2
25	Mod Pair 0
27	Mod Pair 1
29	Mod Pair 2
31	Mod Pair 3
33	Mod Pair 4
35	Mod Pair 5
37	BACK
39	BREQ
41	BSTB
43	BRPLY
45	Multiple
47	Delayed
49	A Plane 0
51	A Plane 1
53	B Plane 0
55	B Plane 1
57	IPCP Add 0
59	IPCP Add 1
61	Spare
63	Spare

Figure 9.6: The ECAT 931 IPCP coincidence data connector pinout when used with a 931 series bucket (left) and a 951 series bucket (right). The only difference between the two is that the two normally spare pins are used to communicate the additional plane bits when used with the 8x8 951 series bucket as discussed in Sections 7.9.2 and 7.9.3. The lines in light blue indicate the "A" bucket positional data, the light green lines indicate the "B" bucket positional data, the golden lines indicate the module pair number, the peach lines are the IPCP address, the grey lines are the coincidence type flags, the dark blue lines are the handshaking lines, and yellow lines are empty/spare. Only odd pins are shown as all even pins are grounded.

9.5 Deciphering the List Mode Data

Deciphering the list mode data for the LaMA PEPT setup is done in a very similar way to the SuperPEPT except that the geometry can be changed by the user. The original crystal numbering scheme is used to determine the bucket in which the detector block and ultimately

1	Cable Verifier
3	A Segment 0
5	A Segment 1
7	A Segment 2
9	A Block 0
11	A Block 1
13	Spare
15	B Segment 0
17	B Segment 1
19	B Segment 2
21	B Block 0
23	B Block 1
25	Spare
27	Mod Pair 0
29	Mod Pair 1
31	Mod Pair 2
33	Mod Pair 3
35	Mod Pair 4
37	Mod Pair 5
39	Multiple
41	Delayed
43	Scatter
45	A Plane 0
47	A Plane 1
49	A Plane 2
51	B Plane 0
53	B Plane 1
55	B Plane 2
57	IPCP Add 0
59	IPCP Add 1
61	Spare
63	Ser TXD
65	Ser RXD
67	Ser GND
69	FIFO Clr Req
71	BREQ
73	BSTB
75	BACK
77	BRPLY
79	Cable Verifier

1	Cable Verifier
3	A Segment 0
5	A Segment 1
7	A Segment 2
9	A Block 0
11	A Block 1
13	Spare
15	B Segment 0
17	B Segment 1
19	B Segment 2
21	B Block 0
23	B Block 1
25	Spare
27	Mod Pair 0
29	Mod Pair 1
31	Mod Pair 2
33	Mod Pair 3
35	Mod Pair 4
37	Mod Pair 5
39	Multiple
41	Delayed
43	Scatter
45	A Plane 0
47	A Plane 1
49	Spare
51	B Plane 0
53	B Plane 1
55	Spare
57	IPCP Add 0
59	IPCP Add 1
61	Spare
63	Ser TXD
65	Ser RXD
67	Ser GND
69	FIFO Clr Req
71	BREQ
73	BSTB
75	BACK
77	BRPLY
79	Cable Verifier

Figure 9.7: The ECAT 951 IPCP coincidence data connector pinout when used with a 951 series bucket (left) and a 931 series bucket (right). The only difference between the two is that the two plane bits are missing in the 4x8 931 bucket configuration as discussed in Sections 7.9.2 and 7.9.3. The lines in light blue indicate the "A" bucket positional data, the light green lines indicate the "B" bucket positional data, the golden lines indicate the module pair number, the peach lines are the IPCP address, the grey lines are the coincidence type flags, the dark blue lines are the handshaking lines, the dark green lines are the serial communication lines, the yellow lines are empty/spare, and the white lines are extra control signals. Only odd pins are shown as all even pins are grounded.

the crystal element are located. However, the bucket position and orientation itself need to be pre-entered into the source code for the conversion program requiring it to be recompiled for each experimental setup. This is unlike the SuperPEPT where the code can be compiled once.

9.5.1 ECAT 931 and 951 Crystal Element Numbering System

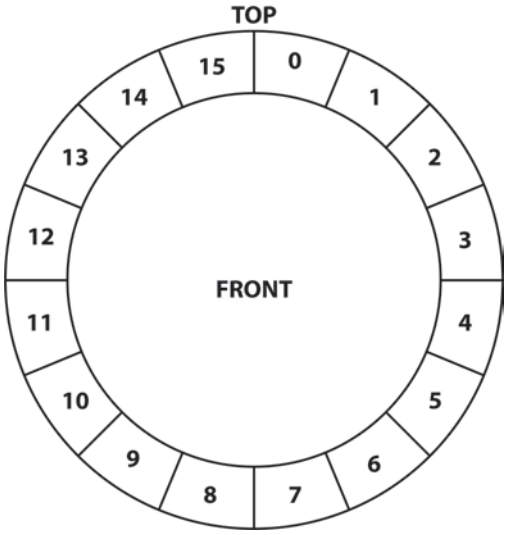

Figure 9.8: The ECAT 931 and 951 16-bucket-ring bucket numbering scheme. The top indicates the top of the original scanner gantry and the front is the side from which the patient was normally inserted. Buckets in the second ring are also numbered 0 to 15 by the system and can be distinguished by the IPCP board address as discussed in Section 9.5.1.

The electronics used in LaMA PEPT are based on the 16-bucket-ring geometry shown in Figure 9.8. As discussed in Sections 7.1 and 7.2, the ECAT 931 and 951 systems use the four-detector-block buckets such that each of the 16 bucket rings contains 64 detector blocks. Each ring, whether it be ring 1 or 2, numbers the buckets clockwise from 0 to 15. As shown in Figure 9.9, each bucket is in coincidence with the bucket opposite it, 3 to each side of that one, and the same 7 buckets in the adjacent ring.

To describe all the possible coincidence combinations, module pair numbers are used. Unlike in the SuperPEPT, the early ECAT systems are easier to describe as they do not

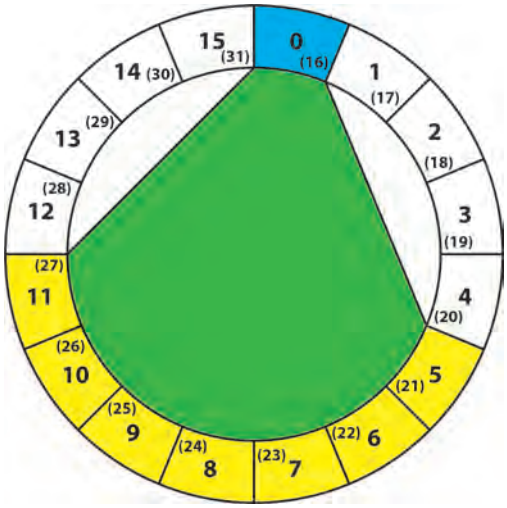

Figure 9.9: The ECAT 931 and 951 16-bucket-ring bucket coincidence range. Here bucket 0 or 16 (bucket 0 in the second ring) is in coincidence with the bucket opposite it, 3 buckets to each side of that one, and 7 buckets in the same position in the other ring or buckets 5 to 11 and 21 to 27 (5 to 11 in the second ring). Bucket numbers shown in parenthesis are buckets in the second ring and are only used by the conversion program to store the bucket positional data. The system does not use those numbers to identify buckets in the second ring, it also numbers them 0 to 15 and distinguishes between rings 1 and 2 by the IPCP board address.

use the bucket pairs acting as a single bucket. Therefore, the module pair describes two individual buckets and not two bucket pairs. The module pair numbers start at 1 but there are 56 of them compared to 42 in the HR+ system. The module pair scheme is shown in Table 9.1.

To differentiate between which ring the bucket belongs to, the ECAT 931 and 951 use the IPCP board address number. It is a 2-bit number with a range of 0 to 3 which describes which IPCP board produced the coincidence. As described in Section 7.1.2, the coincidence processor is made up of 4 IPCP boards each handling a specified set of coincidences in the full system. The board addressed 0 handles coincidences within ring 1 only. Therefore, buckets “A” and “B” are both in ring 1. Board addressed 1 handles coincidences between rings 1 and 2 such that bucket “A” is in ring 1 and bucket “B” is in ring 2. Board addressed 2 handles the opposite cross ring coincidences such that bucket “A” is in ring 2 and bucket

Table 9.1: The ECAT 931 and 951 module pair numbering scheme uses the “A” master bucket and “B” slave bucket notation. The green fields indicate possible coincidence pairs and the orange fields indicate impossible coincidence pairs.

The "B" Bucket \ The "A" Bucket	0	1	2	3	4	5	6	7	8	9	10	11	12	13	14	15
0	X															
1		X														
2			X													
3				X												
4					X											
5	1					X										
6	2	8					X									
7	3	9	15					X								
8	4	10	16	22					X							
9	5	11	17	23	29					X						
10	6	12	18	24	30	36					X					
11	7	13	19	25	31	37	42					X				
12		14	20	26	32	38	43	47					X			
13			21	27	33	39	44	48	51					X		
14				28	34	40	45	49	52	54					X	
15					35	41	46	50	53	55	56					X

“B” is in ring 1. Finally, the board addressed 3 handles coincidences purely within ring 2.

Next, each bucket provides the detector number or a 2-bit number in the range of 0 to 3 which describes the detector block containing the hit crystal element. The detector

blocks are numbered clockwise in the original gantry configuration or as numbered in Figures 7.11 and 9.3. Like in the HR+, the last two numbers are the plane number and the segment number. The plane number is either a 3-bit number in the range 0 to 7 when the 951 buckets are used or a 2-bit number in the range 0 to 3 when the 931 buckets are used. It describes the crystal ring that the crystal element is in. The segment number is a 3-bit number in the range 0 to 7 that defines the column the crystal element is in in a single detector block. This is unlike in the HR+ where the segment number describes the column across many detector blocks. The detector block number, plane number, and segment number scheme is shown in Figure 9.10. In the end, it is a straightforward numbering system to remember, especially when compared to the numbering scheme used in the ECAT EXACT HR+ system (Section 8.3.1).

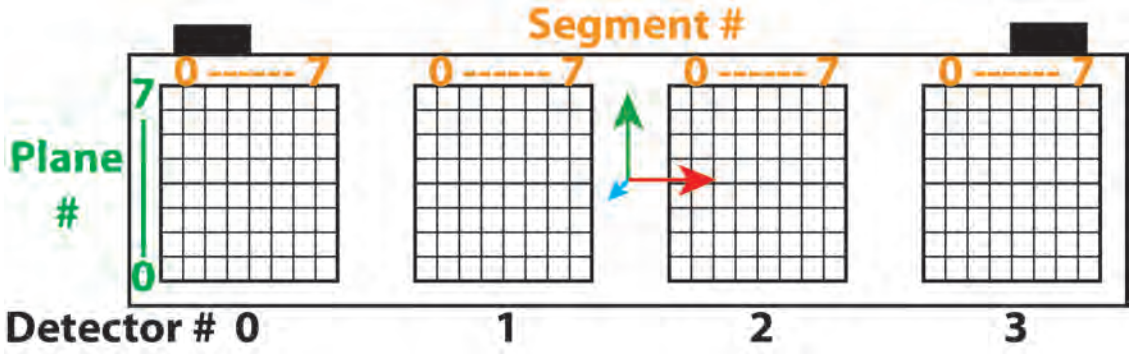

Figure 9.10: The ECAT 931 and 951 detector block crystal element numbering scheme.

9.5.2 Crystal Element Numbers to Real Position

Unlike the extremely complex SuperPEPT system, LaMA PEPT is very simple to calculate real positions for. Also, as LaMA PEPT is a flexible geometry system, it is not possible to fully describe the whole calculation in this work. As part of the geometry setup, the user needs to define the translation matrix and rotation matrices that describe the orientation of the bucket front centre face origin, shown in Figure 9.3, to the user-defined origin and axis orientation in the gantry/lab frame. These matrices are saved in code and looked up

using the bucket number that can be calculated using the module pair number and the IPCP board address number.

The final step is to calculate the crystal element position to the bucket origin and then have all the applicable transformations applied to it so it is in the gantry/lab frame. The crystal element position can be calculated using the block number, segment number, and plane number using the following equation when using the 951 detector blocks,

$$\begin{pmatrix} (6.1 \times (\text{segment number} - 3.5)) + ((48.8 + (37/2)) \times (\text{detector number} - 1.5)) \\ 6.7 \times (\text{plane number} - 3.5) \\ -10.0 \\ 1 \end{pmatrix}. \quad (9.1)$$

6.1 mm is the nominal 951 detector block transaxial crystal element pitch, 6.7 mm is the nominal 951 detector block axial crystal element pitch (Section 7.2.1), 48.8 mm is the nominal 951 detector block width, and 37 ± 1 mm is the detector spacing (Figure 9.3). A constant depth of 10 mm is also used as in the SuperPEPT.

9.6 In Summary

LaMA PEPT has been built as an upgrade to the old Modular Camera system. The existing 16 modules have been refurbished, calibrated, and unified to use the ECAT 951 bucket assemblies and detector blocks. Additionally, 32 new modules have been built to further extend the capabilities of the system. Two coincidence processors have been refurbished and troubleshoot to remove many sources of noise in the system. The power supplies have also been fully redesigned to use modern, efficient power supplies. Overall, the system has been further investigated to uncover points of compatibility between the ECAT 931 and 951 as discussed in Section 7. Most importantly, the meaning of each of the pins in the IPCP coincidence data cable for the ECAT 931 and 951 coincidence processor have been discussed

in Section 9.4.2. In Section 9.5, the logic on how to convert the list mode data to real world data has been undertaken. The biggest drive behind the development of this large array has been a very unique experiment discussed later in Section 11 that required a very large and tall PEPT array to record the necessary data. Formal characterisation of the LAMA PEPT is yet to take place.

Chapter Ten

SuperPEPT Early Characterisation Data

An initial characterisation of SuperPEPT has been carried out to assess the system's performance. This was carried out at a time when one of the end sections of the system was not assembled due to missing parts. Since then, the system has been fully assembled and at the time of writing, a full characterisation of the system is being conducted but will not be ready in time to be included in this thesis. Therefore, the initial characterisation data is presented below. For all the measurements, the lower-level discriminator has been set to 150 keV and the upper-level discriminator to 650 keV. This section includes figures and text taken in part from one of my journal articles referenced here [30].

Throughout this section, careful considerations were taken into account when positioning the particles for the positional tests. For the axial test the particle was lowered attached to a plum line positioned exactly in line with the centre axis of the SuperPEPT which was positioned with respect to the ring of detectors at the bottom and top of SuperPEPT. The distance the particle was moved by was then measured using a ruler with a millimetre accuracy. For the radial tests, the particle was also positioned manually, using a plum line on the centre axis and on the centre transaxial plane. The distance the particle was moved by linearly was then also measured using a ruler on a rail which was set parallel

to the transaxial plane of SuperPEPT. In these two cases, any initial small offset can be said to be within a millimetre. For all the experiments, the activity of the tracer particle was obtained using a calibrated Capintec CRC-15R Radioisotope Dose Calibrator and the time of measurements was recorded using the same mobile phone time with a seconds accuracy. For the rotational tests, the sources of error are discussed in that section.

10.1 Axial Sensitivity

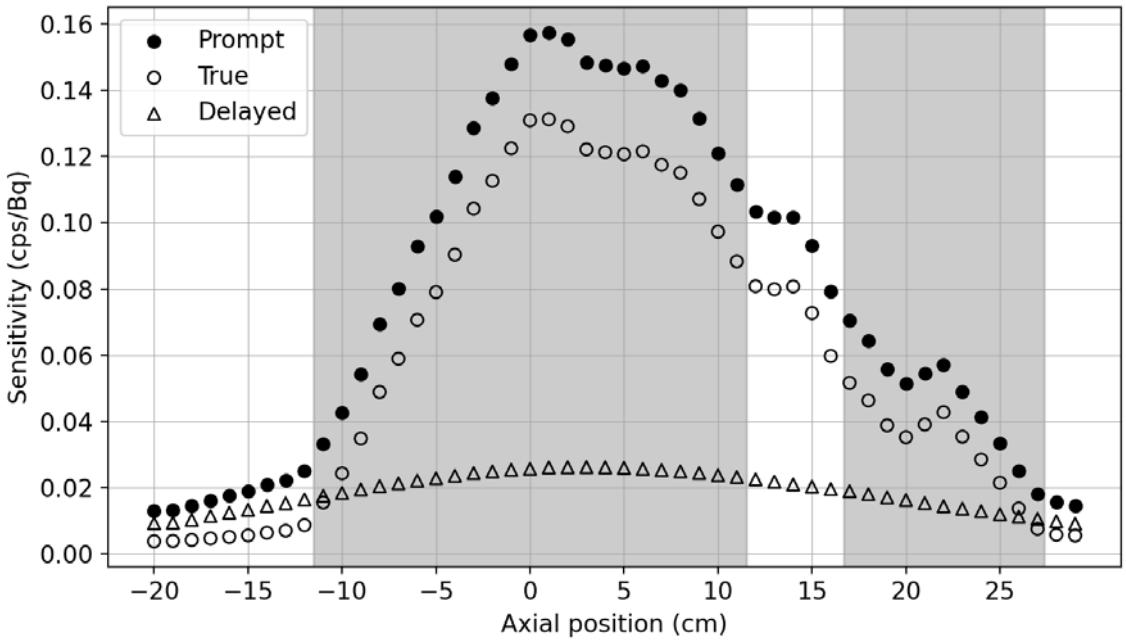

Figure 10.1: Variation in absolute axial sensitivity. The grey areas indicate the extent of the centre section and the top-end section. The errors are smaller than the markers used to display the data points. The position error is within a millimetre.

As can be seen in Figure 10.1, the absolute sensitivity of the system along the central axis was measured using a ^{18}F point source with an approximate 20 ± 1 MBq of activity at the start of acquisition. The exact activity at each recording point was used by correcting the initial activity for radioactive decay. The sensitivity is presented in units of coincidences per second per unit activity or cps/Bq. Here the sensitivity to true coincidences was calculated

by subtracting the contributions from delayed coincidences from the prompt coincidence rate.

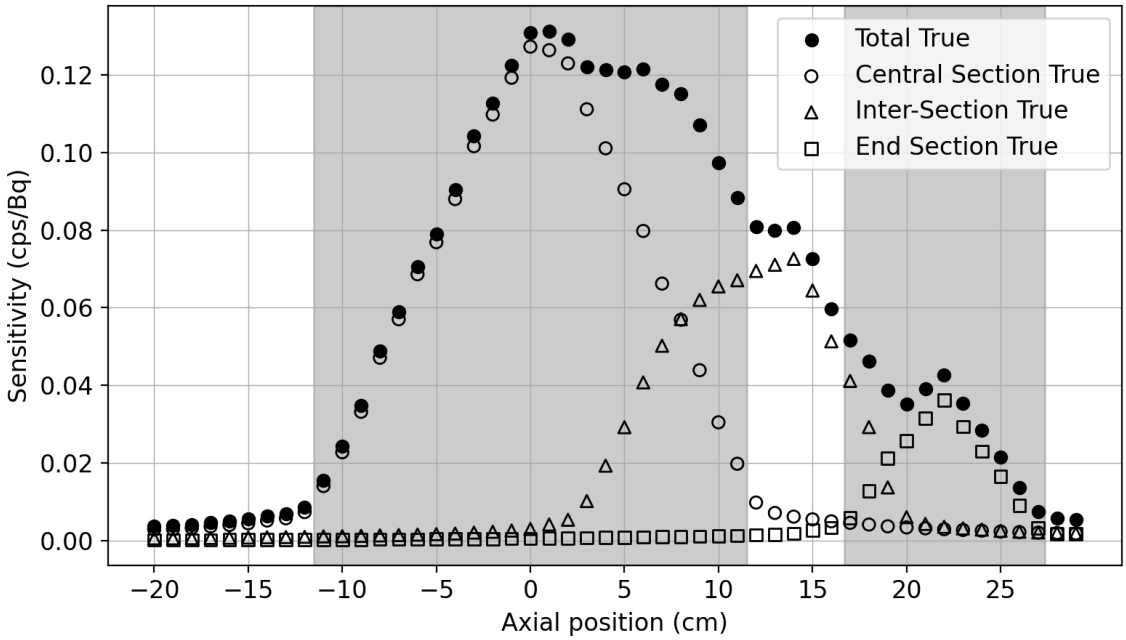

Figure 10.2: Variation in absolute axial sensitivity by the region the LOR originated in. The grey areas indicate the extent of the centre section and the top-end section. The errors are smaller than the markers used to display the data points. The position error is within a millimetre.

In Figure 10.2, the absolute sensitivity due to true coincidences is further divided according to the section where the coincidence occurred. The inter-section contribution is due to coincidences detected at one end by a detector in the centre section and at the other end by a detector in the end section. Analysing these figures, it can be seen that the addition on the end section extends the useful axial FOV of SuperPEPT out to about 23.0 cm from the centre compared to only 9.0 cm for the end without the end section present. This is where the true coincidence sensitivity has reached 30 % of the maximum. This gives the complete SuperPEPT system a useful axial FOV of 46.0 cm. This makes it an ideal system for studying of long/tall lab-scale industrial equipment and most importantly pipe flow as it is able to cover a long section of the pipe.

10.2 Radial Sensitivity

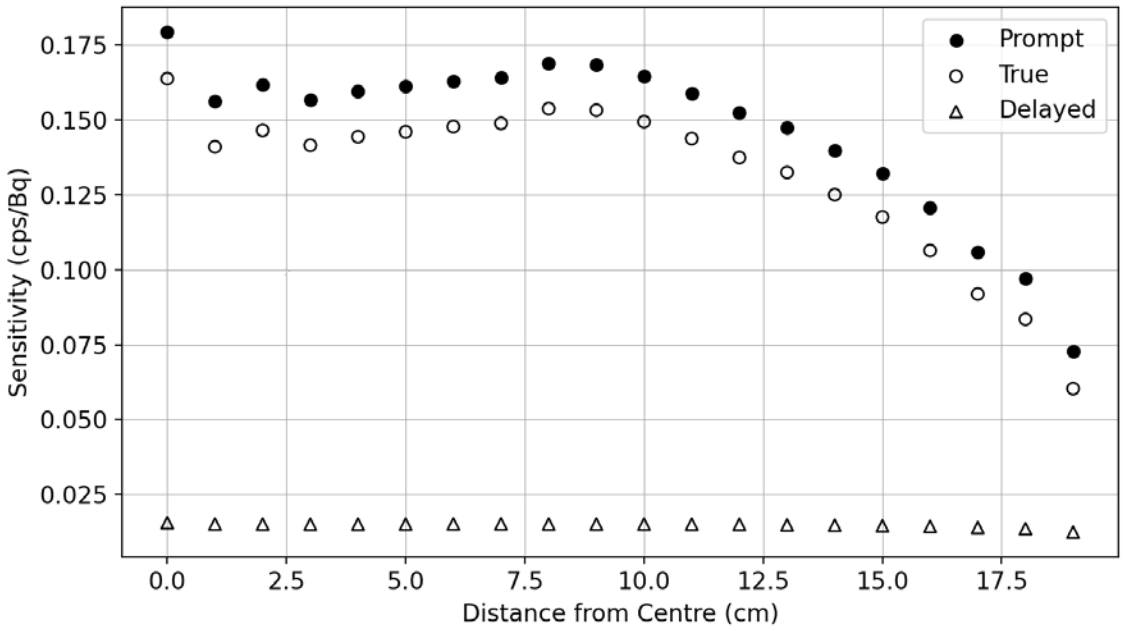

Figure 10.3: Variation in absolute radial sensitivity. The errors are smaller than the markers used to display the data points. The position error is within a millimetre.

In Figures 10.3 and 10.4, the absolute sensitivity of the system was measured on the middle transaxial plane radially from the centre to the detector face using a ^{18}F point source with an approximate 10 ± 1 MBq of activity at the start of acquisition. Like before, the activity was corrected for decay throughout the acquisition. As can be seen, the sensitivity gradually decreases towards the edge of the detector ring with only a factor of two difference in sensitivity. Therefore, the scanner can comfortably study apparatuses that are up to 38.0 cm in diameter. The temporary rise in radial sensitivity at 8.5 cm from the centre is due to the increasing inter-section coincidence contribution.

As can be observed in Figures 10.3 and 10.4, the drastic increase in sensitivity at the very centre of the ring is due to the interference from the small gaps between detector blocks in the centre section. For example, if the gaps between the detector blocks are uniformly distributed and account for about 12 % of the circumference of the centre section in 2D,

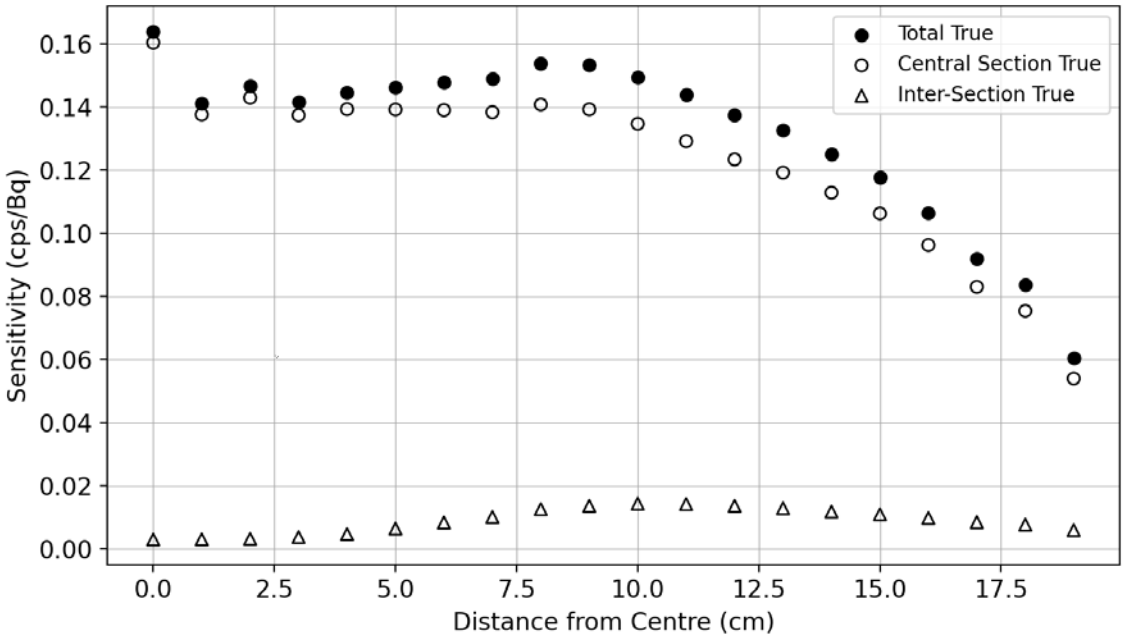

Figure 10.4: Variation in absolute radial sensitivity by the region the LOR originated in. The errors are smaller than the markers used to display the data points. The position error is within a millimetre.

when a positron source is located exactly in the centre on the axis of the scanner, the gaps are opposite of each other and the two annihilation photons will either always escape the scanner or hit a detector. This means that the sensitivity of the scanner is reduced by 12 % when compared to a gapless system. However, when the source is just slightly off the centre axis, the gap alignment is lost and the effect on the sensitivity is as if the detection efficiency of each photon is reduced by 12 %, which results in an overall reduction in coincidence sensitivity of about 23 % when compared to a gapless system. Therefore, for a system with gaps, the difference in sensitivity between an on centre axis and an off centre axis position is around 11 %.

10.3 Coincidence Data Rates

Next, the coincidence rate as a function of activity in the centre of the scanner was investigated using a ^{11}C source with an initial activity of approximately 120 ± 1 MBq. Figure 10.5 shows coincidence rates as reported by the coincidence processor in response to a query sent over the serial communication throughout the acquisition and Figure 10.6 shows the overlaid real coincidence rates as reconstructed from the list mode file. According to the values reported by the system, the maximum true coincidence rate for SuperPEPT is about 3.2 MHz at about 55 MBq of activity when the random/delayed coincidences begin to overwhelm the system. However, the actual maximum true coincidence rate is about 2.1 MHz at about 18.6 MBq of activity. This decrease is due to the hardware limitations and the write data rate limits of the disk drive of the data acquisition computer which itself was never designed to handle these extreme activities.

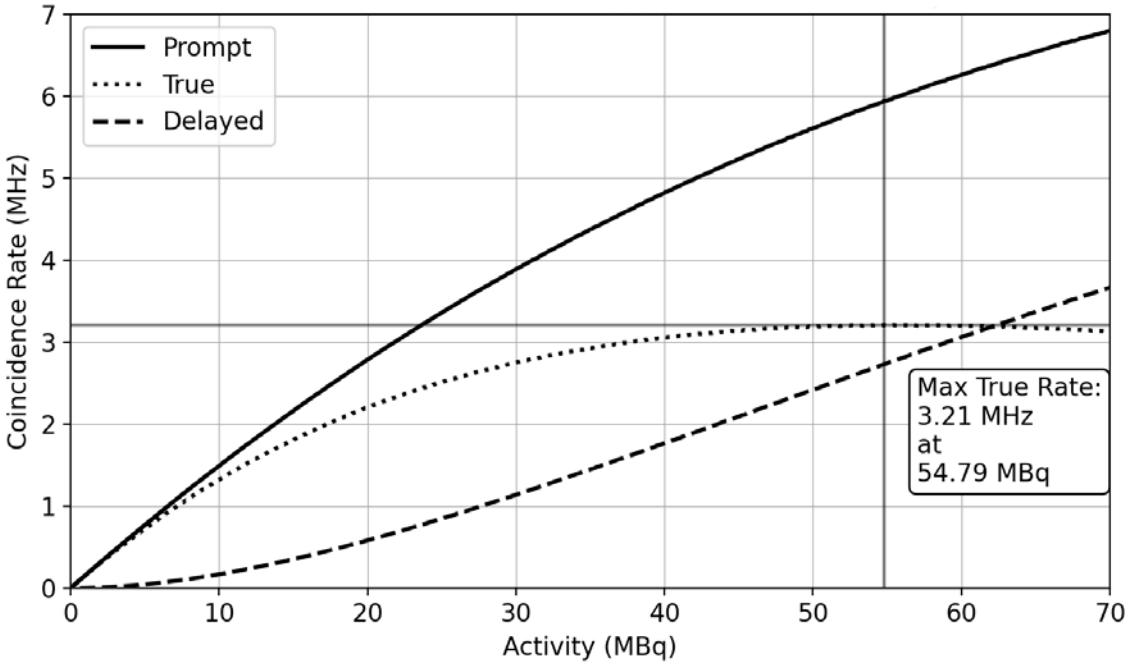

Figure 10.5: Coincidence data rate variation as a function of particle activity as reported by the scanner serial interface statistics.

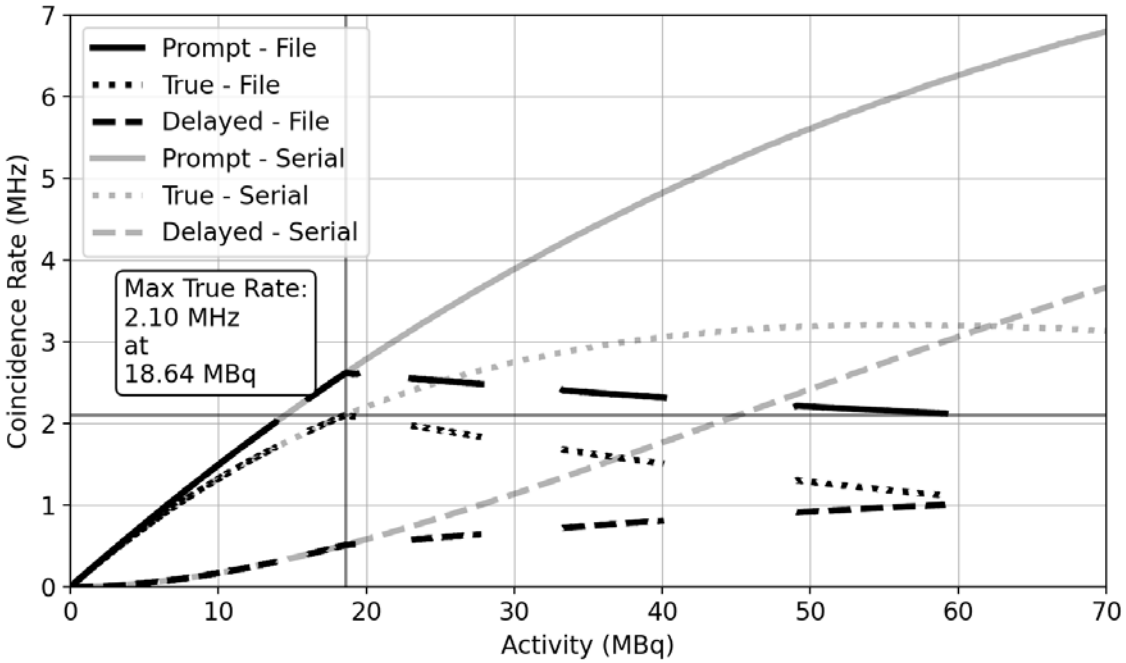

Figure 10.6: Coincidence data rate variation as a function of particle activity as calculated from the recorded data files. The gaps in the data are due to manually starting and stopping the acquisition to bypass the maximum file size allowed by the system.

10.4 Tracking Accuracy and Spatial Resolution

Finally, the tracking accuracy of the system was tested using a ^{18}F point source with approximately 20 ± 1 MBq of activity. The source was mounted to a platter rotated using IKA STARVISC 200-2.5 digitally controlled mixer with a 1 % accurate speed controller. The point source was mounted at a radius of 6.37 ± 0.01 cm, placed close to the central transaxial plane, and rotated at 120 ± 1, 480 ± 5, 720 ± 7, and 900 ± 9 rpm or 0.80 ± 0.01, 3.20 ± 0.03, 4.80 ± 0.04, and 6.00 ± 0.06 m/s, respectively. Each of these tests produced a 1.66 ± 0.01 MHz coincidence rate and was processed using the Birmingham Method (see Section 2.1) with f = 0.3, 0.4, 0.5, and 0.6 and N = 100, 200, 300, and 400. Using the simple relationship $N = R\Delta t$ from Section 2.2, using N = 100, 200, 300, and 400 produces a position every 0.060 ± 0.001, 0.120 ± 0.001, 0.181 ± 0.001, and 0.241 ± 0.001 ms at the 1.66 ± 0.01 MHz coincidence rate.

Table 10.1: The fitted rotational speeds and the root-mean-square deviations of the 120 ± 1 rpm dataset fitted to a model of a particle rotating on a tilted circular orbit. The calculated distance travelled by the particle for the given f, N, and fitted speed at the 1.66 ± 0.01 MHz coincidence rate is also listed for further analysis.

f	Sample Size (N)	Fitted Speed (rpm)	RMS Error (mm)	Distance Travelled per Sample (mm)
0.3	100	121.3 ± 0.7	1.154	0.049 ± 0.001
	200	120.7 ± 0.5	0.902	0.097 ± 0.001
	300	120.6 ± 0.5	0.760	0.146 ± 0.001
	400	120.6 ± 0.4	0.680	0.194 ± 0.001
0.4	100	121.4 ± 0.6	1.039	0.049 ± 0.001
	200	120.7 ± 0.5	0.825	0.097 ± 0.001
	300	120.6 ± 0.4	0.706	0.146 ± 0.001
	400	120.6 ± 0.4	0.715	0.194 ± 0.001
0.5	100	121.4 ± 0.6	1.042	0.049 ± 0.001
	200	120.7 ± 0.5	0.786	0.097 ± 0.001
	300	120.6 ± 0.4	0.673	0.146 ± 0.001
	400	120.6 ± 0.4	0.597	0.194 ± 0.001
0.6	100	121.5 ± 1.3	2.216	0.049 ± 0.001
	200	120.6 ± 0.8	1.331	0.097 ± 0.001
	300	120.6 ± 0.6	1.064	0.146 ± 0.001
	400	120.6 ± 0.5	0.861	0.194 ± 0.001

The positions/track produced by the Birmingham Method were then fitted to a model of a rotating particle on a tilted circular orbit. The root-mean-square error on the fit, the fit calculated rotational speeds, and the distance travelled per sample according to the fit rotation speed are shown in Tables 10.1, 10.2, 10.3, and 10.4 for the 120 ± 1 , 480 ± 5 , 720 ± 7 , and 900 ± 9 rpm datasets respectively. From the fit data, it is very apparent that the centre of rotation is located at $(4.0 \pm 0.5\,,\ 7.6 \pm 0.5\,,\ 129.7 \pm 0.4\,)$ mm. The x and y offsets show that

Table 10.2: The fitted rotational speeds and the root-mean-square deviations of the 480 ± 5 rpm dataset fitted to a model of a particle rotating on a tilted circular orbit. The calculated distance travelled by the particle for the given f, N, and fitted speed at the 1.66 ± 0.01 MHz coincidence rate is also listed for further analysis.

f	Sample Size (N)	Fitted Speed (rpm)	RMS Error (mm)	Distance Travelled per Sample (mm)
0.3	100	480.3 ± 2.7	1.140	0.192 ± 0.003
	200	480.1 ± 2.0	0.830	0.384 ± 0.004
	300	480.1 ± 1.7	0.697	0.580 ± 0.004
	400	480.1 ± 1.5	0.615	0.772 ± 0.004
0.4	100	480.3 ± 2.5	1.029	0.192 ± 0.003
	200	480.1 ± 1.8	0.746	0.384 ± 0.004
	300	480.1 ± 1.5	0.630	0.580 ± 0.004
	400	480.1 ± 1.3	0.552	0.772 ± 0.004
0.5	100	480.3 ± 2.5	1.036	0.192 ± 0.003
	200	480.1 ± 1.7	0.710	0.384 ± 0.004
	300	480.1 ± 1.4	0.584	0.580 ± 0.004
	400	480.1 ± 1.3	0.521	0.772 ± 0.004
0.6	100	480.3 ± 5.3	2.218	0.192 ± 0.004
	200	480.1 ± 3.0	1.268	0.384 ± 0.004
	300	480.1 ± 2.3	0.953	0.580 ± 0.004
	400	480.1 ± 1.9	0.791	0.772 ± 0.005

the system was located with a systematic error within 1 cm of the centre axis, this offset error is a result of the difficulty of positioning anything accurately within the cylindrical volume of the SuperPEPT. As there are no markers, the system was positioned using a measuring tape. The y axis offset is so large due to the necessity to use a normal length shaft to mount the rotating disk with the tracer on. Initially a long shaft was used, but with the extra length, the whole system was not stable enough and began to oscillate at even the

Table 10.3: The fitted rotational speeds and the root-mean-square deviations of the 720 ± 7 rpm dataset fitted to a model of a particle rotating on a tilted circular orbit. The calculated distance travelled by the particle for the given f, N, and fitted speed at the 1.66 ± 0.01 MHz coincidence rate is also listed for further analysis.

f	Sample Size (N)	Fitted Speed (rpm)	RMS Error (mm)	Distance Travelled per Sample (mm)
0.3	100	720.0 ± 4.2	1.164	0.288 ± 0.005
	200	719.7 ± 3.1	0.867	0.576 ± 0.005
	300	719.9 ± 2.7	0.758	0.869 ± 0.006
	400	720.0 ± 2.7	0.738	1.157 ± 0.007
0.4	100	720.0 ± 3.8	1.048	0.288 ± 0.005
	200	719.7 ± 2.9	0.800	0.576 ± 0.005
	300	719.9 ± 2.5	0.682	0.869 ± 0.006
	400	720.0 ± 2.4	0.677	1.157 ± 0.006
0.5	100	720.0 ± 3.8	1.057	0.288 ± 0.005
	200	719.7 ± 2.7	0.752	0.576 ± 0.005
	300	719.9 ± 2.4	0.658	0.869 ± 0.006
	400	720.0 ± 2.4	0.653	1.157 ± 0.006
0.6	100	720.0 ± 7.8	2.177	0.288 ± 0.006
	200	719.7 ± 4.7	1.299	0.576 ± 0.006
	300	719.9 ± 3.6	1.000	0.869 ± 0.007
	400	720.0 ± 3.2	0.886	1.157 ± 0.007

low speeds. Therefore, a normal length shaft was used which prevented the disk from sitting directly on the centre transaxial plane of the scanner causing another systematic error in the system. However, as all the datasets were collected without repositioning the mixer, all of them show the same positional offset. Furthermore, the fit extracted the radius of rotation of the system to be 6.4 ± 0.2 cm which is within error to the measured radius of rotation of 6.37 ± 0.01 cm. Perhaps the greatest source of error on these results was the systematic

Table 10.4: The fitted rotational speeds and the root-mean-square deviations of the 900 ± 9 rpm dataset fitted to a model of a particle rotating on a tilted circular orbit. The calculated distance travelled by the particle for the given f, N, and fitted speed at the 1.66 ± 0.01 MHz coincidence rate is also listed for further analysis.

f	Sample Size (N)	Fitted Speed (rpm)	RMS Error (mm)	Distance Travelled per Sample (mm)
0.3	100	901.6 ± 5.4	1.191	0.361 ± 0.006
	200	901.2 ± 4.2	0.931	0.721 ± 0.007
	300	900.9 ± 3.9	0.876	1.088 ± 0.008
	400	900.9 ± 3.6	0.790	1.448 ± 0.009
0.4	100	901.5 ± 4.9	1.082	0.361 ± 0.006
	200	901.2 ± 3.9	0.864	0.721 ± 0.007
	300	900.9 ± 3.7	0.819	1.088 ± 0.008
	400	900.9 ± 3.3	0.740	1.448 ± 0.008
0.5	100	901.6 ± 4.9	1.076	0.361 ± 0.006
	200	901.2 ± 3.7	0.825	0.721 ± 0.007
	300	900.9 ± 3.6	0.791	1.088 ± 0.008
	400	900.9 ± 3.2	0.718	1.448 ± 0.008
0.6	100	901.5 ± 9.5	2.102	0.361 ± 0.007
	200	901.2 ± 5.8	1.284	0.721 ± 0.008
	300	900.9 ± 4.8	1.061	1.088 ± 0.009
	400	900.9 ± 4.2	0.927	1.448 ± 0.009

error caused by the 1 % accuracy of the mixer's speed controller where the 900 rpm setting had an error of 9 rpm. All of these errors so far were systematic in nature. The statistical errors in this analysis are simply due to the counting statistics and random fluctuations during the measurement and are represented by the RMS error on the fit. However, as the fit was conducted using thousands of rotations each containing a few thousand positions each calculated based on hundreds of LORs, this error has a relatively low contribution to the

overall error on the result.

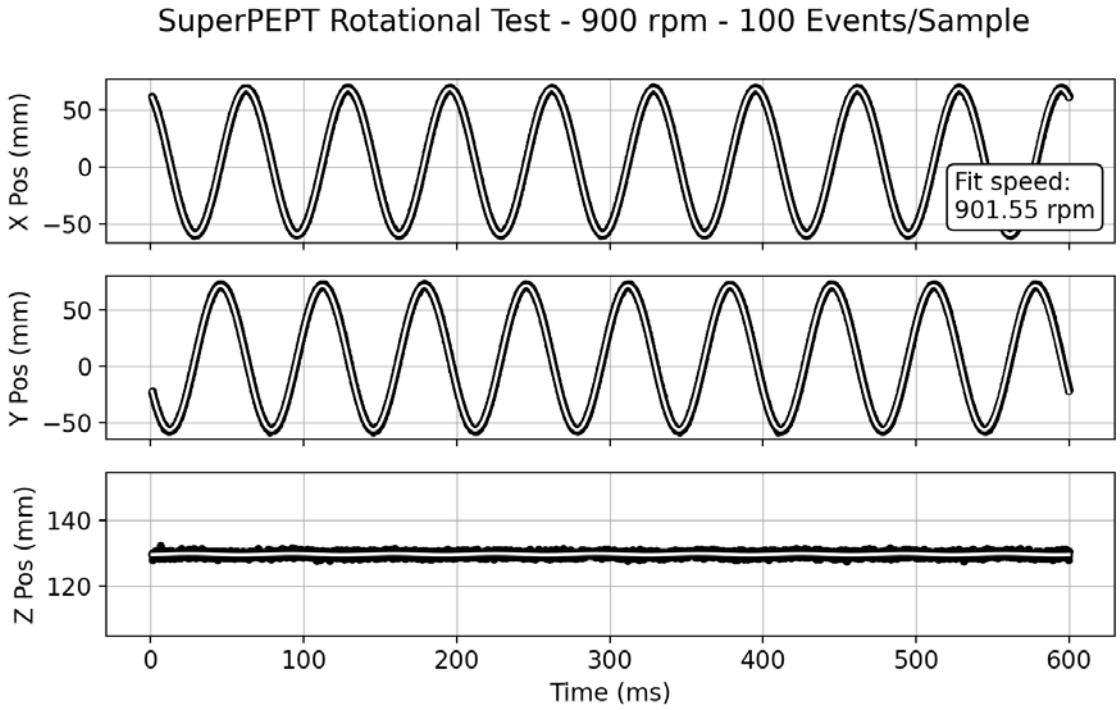

Figure 10.7: Position of the tracer particle rotated at 900 rpm on the transaxial plane of the scanner and processed using the Birmingham Method with $N = 100$ and $f = 0.4$. The black dots are the positions over time of the tracer particle produced by the Birmingham Method. The while line is the result of the fitted function of a particle rotating on a tilted circular orbit in 3D. The errors are smaller than the markers used to display the data points.

As can be seen in those tables, the precision on the location of the particle using a small sample size, N, is independent of the speed as the distance travelled by the particle is always relatively small in each of the samples. At lower speeds, the precision increases with increasing sample size. At higher speeds, the precision begins to plateau even when the sample size is increased and it will get worse. That is because the particle travels a significant distance during that large of a sample size at the higher speeds. Furthermore, the effect of f on the precision is clearly evident. Using a larger value of f means that the final size of the group at which the iteration is stopped is larger, and vice versa. Therefore, the precision decreases when the f is too small and the algorithm begins to reject true LORs and when f is too large and the algorithm does not reject enough of the noise/bad LORs from

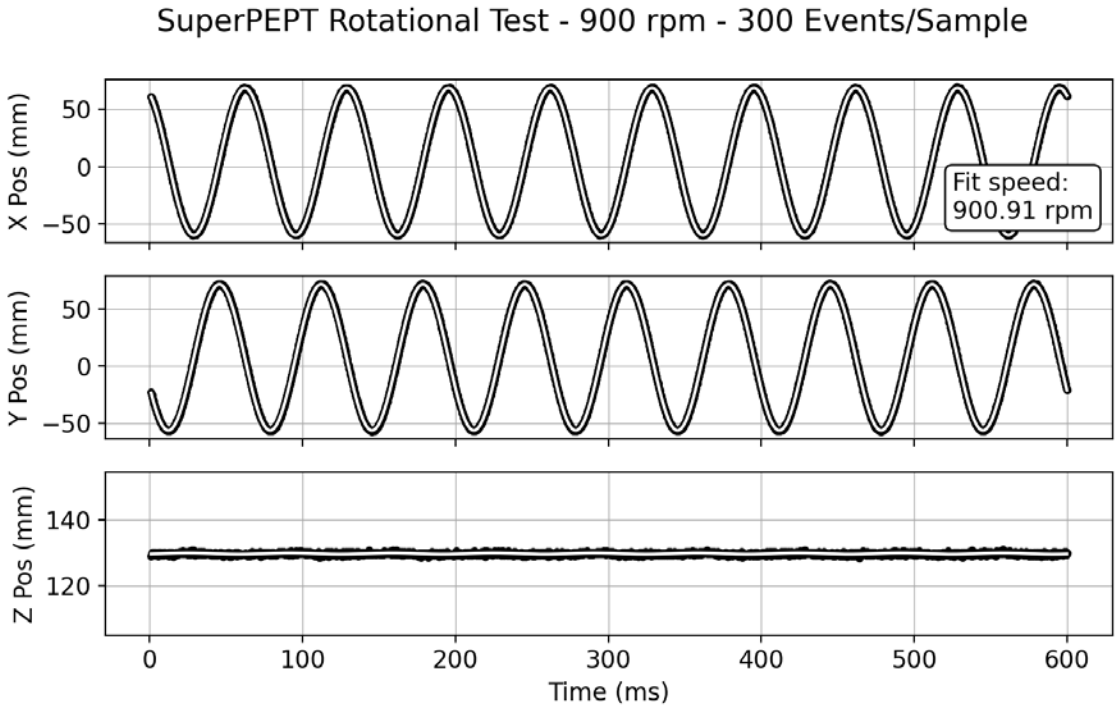

Figure 10.8: Position of the tracer particle rotated at 900 rpm on the transaxial plane of the scanner and processed using the Birmingham Method with $N = 300$ and $f = 0.4$. The black dots are the positions over time of the tracer particle produced by the Birmingham Method. The while line is the result of the fitted function of a particle rotating on a tilted circular orbit in 3D. The errors are smaller than the markers used to display the data points.

each sample. From this data, it can be reasonably extrapolated that the most reasonable f for processing this dataset is somewhere between 0.4 and 0.5.

Figures 10.7 and 10.8 show the 900 rpm positions produced using f of 0.4 and 100 and 300 sample sizes, respectively. Here the increasing precision with sample size can be seen as the frequency of rotation calculated by the fit comes closer to the set rpm. Finally, using Equation 2.5 in Section 2.2, the spatial resolution of SuperPEPT is calculated to be approximately 5 mm within the central region of the scanner [30].

Chapter Eleven

Fluidised Bed Flotation Cell Analysis Using LaMA PEPT

The LaMA PEPT is a large, flexible, and reconfigurable system that can be used for PEPT of very large and unusually shaped engineering systems. Due to the complexity and space required to assemble and configure the system properly, it is rarely used at the PIC for day-to-day acquisitions even in one of its smallest configurations. To date, the full set of 48 buckets has only been used once to study the performance and behaviour of a fluidised bed floatation cell that was over 2 m tall. To accommodate the shape of the cell, a custom support frame made out of aluminium structural profiles has been constructed to support the buckets following the cell's geometry as shown in Figure 11.1.

My contribution to this experiment lie in the assembly, usage, and initial data preparation and processing. This includes the design, manufacture, and assembly of the aluminium structural profile support frame, the assembly and testing of the LaMA PEPT for this experiment, management of the tracer particle through its retrieval and subsequent deposition in the system, operation of the LaMA PEPT for all the experimental days including data management, and the initial processing of the list mode data into a human readable format

Figure 11.1: View of the custom-built support frame for the LaMA PEPT to surround the FLSmith CoarseAIR™ system in a two-head design [329]. The data, clock, and power cables are visible connected to the modules from the side-views of the system.

which included programming and accurate measurements of the positions of each of the modules for the postprocessing program. I also performed multiple quality check on the data by quickly but fully processing parts of the acquired datasets and I gave a brief introduction to our Python data processing tools. The assembly and operation of the fluidised bed floatation cell and subsequent data analysis was conducted by Diego Mesa.

11.1 The Experiment

The FLSmith CoarseAIR™ fluidised bed flotation cell (FBFC) is a novel system designed for the separation of valuable minerals from coarse (diameter greater than 250 µm) tailings of a mineral processing plant. Currently, the coarse tailings are ground down into very fine powders that then can be processed using standard froth floatation. Froth floatation involves the attachment of fine particles to air bubbles forming bubble-particle aggregates that exhibit low apparent density and float to the top of the cell where they can be collected. In those systems, coarse particles fail to attach to air bubbles, easily separate from them, and/or lack the buoyancy to flow to the top. Being able to float coarse particles bypasses

the need for additional grinding which is a very energy inefficient process. In an FBFC, the coarse particles are first suspended in the fluidised bed portion of the system with the use of upward-flowing water. Then, injected air is allowed to bubble through the bed where the suspended hydrophobic valuable minerals attach themselves to the bubbles and are encouraged to flow upward into a teeter bed. The design of the teeter bed uses the low apparent density of the bubble-particle aggregates rather than their buoyancy to float them to the top to be collected. Although the system design was validated through the use of Computational Fluid Dynamics (CFD) simulations, there was a lack of experimental fluid dynamic data verifying the simulations, until this experiment. The results of the acquisitions and the validation of the CoarseAIR™ system are described in detail by Mesa et al. [329].

11.2 The Results

The experiment was a success and confirmed the basic principle and functionality of the system. Hydrophobic particles, almost immediately upon entering the system, attached themselves to bubbles and predominantly stayed on top of the fluidisation region; occasionally dropping down and recirculating. On the other hand, hydrophilic particles preferred to stay in the fluidisation region, recirculating constantly. Upon reaching the lamella plates, the hydrophobic particles, sometimes after a few tries, entered this region and continued upwards to be collected; hydrophilic particles seldomly reached this region and when they did they eventually stooped rising and floated all the way down. Three strengths of fludisation were also tested and showed how upward motion is accentuated, the fluidisation region is expanded, and hydrophilic particles started to behave more erratically. Overall, LaMA performed very well during the experiment. As shown in Figure 11.2, it was able to accurately represent the track of the tracer in all parts of the system giving an insight into the particle behaviours. The boundary area between the two coincidence systems was only

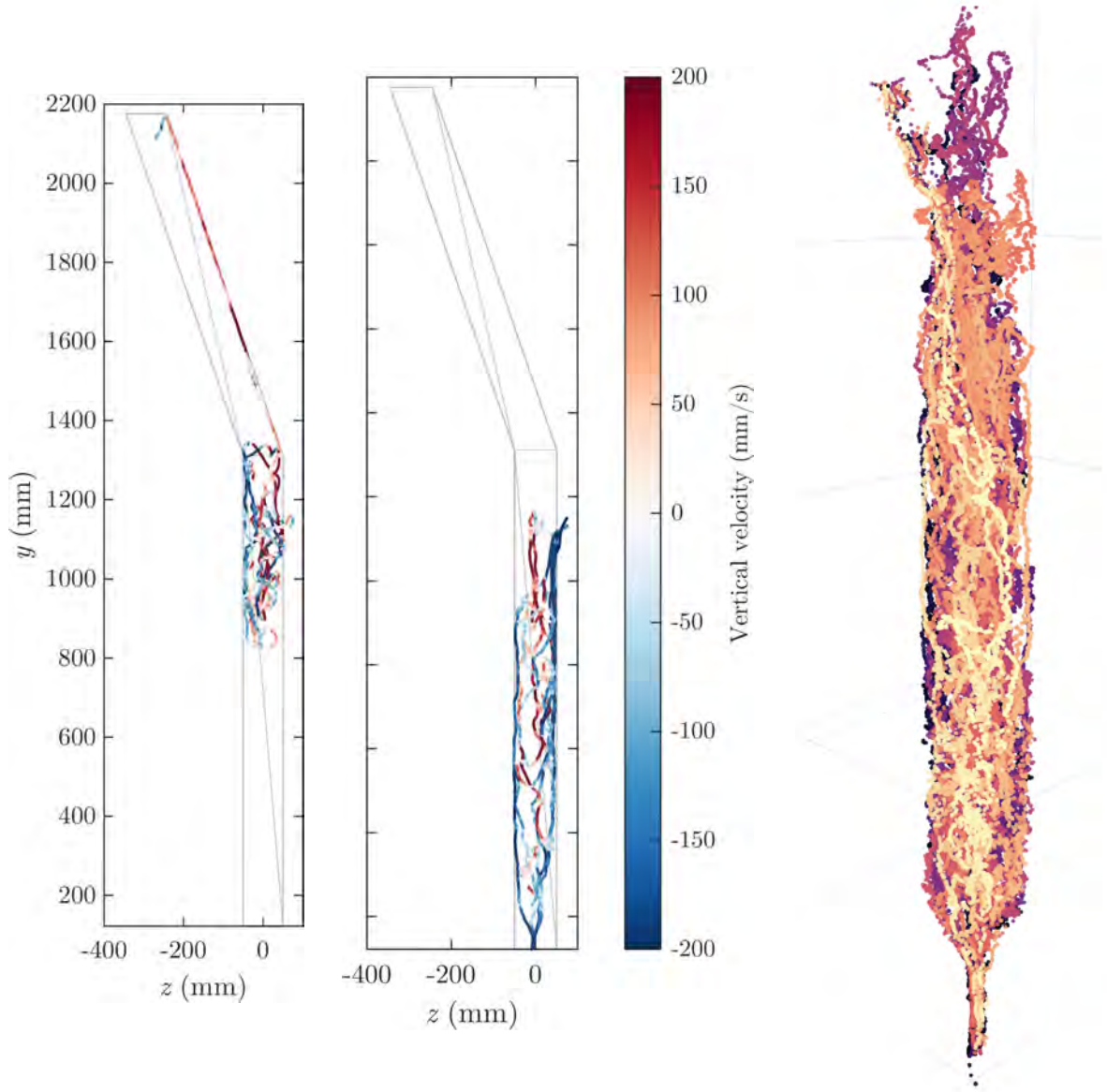

Figure 11.2: From the left: A single track of a hydrophilic particle in the system displaying the desired effect of flowing upwards and out of the system. A single track of a hydrophobic particle in the system displays the desired effect of staying in the system and not overflowing out the top [329]. An integrated mass of tracks of hydrophobic particles in the system displaying the circulating motion in the fluidised bed.

slightly noticeable but as it was located in the area whose behaviour can be observed in a different area, the small loss did not cause any problems in data processing and analysis. This means the positioning and/or the programming of the positions of each of the modules and the time synchronisation of the two coincidence processors was spot on. Furthermore,

the system was able to accurately track particles reaching vertical speeds up to 4 m/s in the fluidised bed part of the system and 2 m/s in the lamella part the experiment.

Chapter Twelve

Conclusions

During the past three years, detailed research has been undertaken into the applications and modification of past PET scanner technology into modern PEPT systems. An initial in-depth study of the principles of PET and PEPT was conducted followed by a detailed historical analysis of the development of these systems and their main components. From the parts of various ECAT series of PET scanners available at the Positron Imaging Centre, a comprehensive timeline of technological advancements and changes was presented about the ECAT lineage. A thorough analysis of these systems revealed the details of their construction and data acquistion and processing pipeline. As confirmed through experimentation, the various parts of the ECAT series of scanners can be interchanged between the various systems, with some limitations. Detector blocks can almost universally be exchanged in any of the systems while bucket controller boards can be exchanged between systems that use the same number of detector blocks per bucket. Finally, the data structures found through the various parts of the systems were discussed such that they could be intercepted and decoded. With that knowledge, modern PEPT systems, SuperPEPT and LaMA for PEPT, were hand-crafted for future use at the University of Birmingham Positron Imaging Centre.

The most advanced, dedicated PEPT system to date, SuperPEPT, has exceeded ex-

pectations. It has displayed superior sensitivity, a very high 2.1 MHz data rate, a large 40.00 cm diameter and 53.50 cm long field-of-view, and a 5 mm PEPT spatial resolution providing the best tracking accuracy available currently in PEPT. The system not only proved itself in its initial characterisation but it has been used at the PIC for several unpublished, research projects on multiphase flow, fluid dynamics, and mixing not discussed here. This system will be the staple of high-resolution PEPT experiments at the PIC.

The Large Modular Array for PEPT, on the other hand, provides flexibility and field-of-view not found anywhere else. Due to its modular nature, the camera can be assembled around cumbersome pieces of industrial equipment or transported and assembled on-site when the equipment cannot be moved. While the system can be difficult to manage at times, once running, it was able to acquire proof-of-concept data for a fluidised bed floatation cell for which no validated simulation program exists.

Support software associated with the detector systems has also been written. Packages used to process the raw scanner data into real-world positions, debugging software helping connect with the scanner serial interface, and data visualisation software for clearer checking of the system were developed.

12.1 Further Work

Although a lot of hard work has gone into this thesis, there is still a lot that can be done and improved. The most important consideration is to apply the systems presented here today to new experiments, studies, and research areas. SuperPEPT should be used for more experiments at the PIC than it is currently used for, taking some of the load from the ADAC Forte system, and for experiments that would benefit from using tiny tracer particles with low amounts of activity or for tracking larger and faster tracer particles. Furthermore,

LaMA should be used for more studies of ever larger and oddly shaped pieces of industrial equipment.

Further development of SuperPEPT is also needed to fully cover all the exposed electronics. Especially with the large number of liquid-based experiments, the covers should be water-proof or -resistant. However, covering the electronics would require them to be directly cooled, perhaps using a water-based system. With some further experimentation and specialised data boards, it may be possible to snoop on the fibre optic data transmission lines to bypass the proprietary data acquisition computer. With the current knowledge of the data structure being sent over them, this would allow for the development of a customised high-speed data acquisition system. The system would then be able to record all the list mode data at high activities which is limited by the current system.

LaMA could benefit from upgrades to its processing hardware. The old Windows Vista PC should be replaced with a modern Windows PC which could be used for possible live data viewing. That modern PC could then also be used for preprocessing of data for easier processing later on. Further, the racks holding the coincidence processors should be replaced with lighter, modern versions with a powerful fan cooling system.

As discussed, the high-voltage distribution components tend to easily break in these ageing detector blocks which need to be repaired. Therefore, a system needs to be developed at the PIC to easily troubleshoot and repair individual detector blocks as well as bucket electronics for the longevity of the PEPT system.

Further software development should also be considered. Standardisation of various data file types using file extensions would be beneficial with so many PEPT systems present at the PIC each one producing its own type of raw data files and the data being moved at various stages of processing in various binary or ASCII formats.

Finally, there are still ECAT scanner parts left at the PIC. It should be possible to develop at least one more PEPT system from them.

Appendix One

Example Python Code for SuperPEPT

Crystal Position Calculation

```
import numpy as np
import plotly.express as px
import pandas as pd

# Unless stated otherwise, all dimensions are in mm and stored angular values are in
    degrees
# This is an unoptimised demonstration code written with the intent to be easily human-
    readable

# Known data
HR_pitch_ax = 4.85
HR_pitch_tx = 4.51
HR_det_height = HR_pitch_ax * 8
HR_det_width = HR_pitch_tx * 8
Centre_gon = 32 # Number of sides
Centre_space = 4.78 # Measured space between centre section detectors

# For quick degree to radiant conversion
pi_180 = np.pi / 180

# Set interaction depth for all crystal element centres
z_depth = -10 # mm

```

```
# Centre section geometry calculations
# Get the inradius
Centre_external_angle = 360 / Centre_gon
cent_space_ang = Centre_external_angle / 2
cent_space_side = (Centre_space / 2) / np.cos(cent_space_ang * pi_180)
Centre_side_length = HR_det_width + (2 * cent_space_side)
Centre_inrad = (Centre_side_length / 2) * (1 / np.tan(np.pi / Centre_gon))
Centre_height = 3 * HR_det_height

# Calculate the small offset
Centre_small_ang_offset = (Centre_external_angle / 2) - ((np.arctan((HR_det_width / 2) /
    Centre_inrad)) * (180 / np.pi))

# Known data for end sections
AR_pitch_ax = 6.75
AR_pitch_tx = 6.75
AR_det_height = AR_pitch_ax * 8
AR_det_width = AR_pitch_tx * 8
End_gon = 24
Space_end = 45 # Space between the centre section and the end section

# End geom calculations
End_dets_height = 106.5
End_det_ang_halfheight = 106.5 / 4
End_det_small_angle = np.arccos((End_dets_height / 2) / AR_det_height) # Stored in
    radiants
End_det_inrad_offset = End_det_ang_halfheight * np.tan(End_det_small_angle)

End_inrad = (AR_det_width / 2) * (1 / np.tan(np.pi / End_gon))
End_inrad += End_det_inrad_offset
End_external_angle = 360 / End_gon

# Calculated position data frame
df = pd.DataFrame(columns = ['BP', 'Rn', 'Sn', 'Pn', 'col', 'row', 'crystal', 'x', 'y',
    'z'])

# Iterate over all possible crystal elements
for bucket_pair in range(12):
  for ring_no in range(4):
    for segment_no in range(48):
```

```
59        for plane_no in range(8):
60
61          col_no = segment_no % 8
62          crys_no = col_no + (plane_no * 8)
63          data = [bucket_pair, ring_no, segment_no, plane_no, col_no, plane_no, crys_no]
64
65          # Determine in which section the crystal element is located in
66          mode = 0 # Assume centre section
67          if bucket_pair in [1, 4, 7, 10]:
68            if segment_no > 23: mode = 1 # It is in the top-end section (odd buckets)
69            else: mode = 2 # It is in the bottom end section
70
71          # Centre section
72          if mode == 0:
73            # Calculate the position in the detector block frame
74            x = (col_no - 3.5) * HR_pitch_tx
75            y = (plane_no - 3.5) * HR_pitch_ax
76            z = z_depth
77            w = 1
78            pos = np.array([x, y, z, w])
79
80            # Calculate the detector sector and angle
81            d_sec = ([0,2,3,5,6,8,9,11].index(bucket_pair) * 4) + ring_no
82            d_ang = ((d_sec + 0.5) * Centre_external_angle) - Centre_small_ang_offset
83
84            # Rotate the detector to face up properly around the x-axis
85            a = 90 * pi_180
86            Rx = np.array( [[1, 0, 0, 0],
87                      [0, np.cos(a), -np.sin(a), 0],
88                      [0, np.sin(a), np.cos(a), 0],
89                      [0, 0, 0, 1]])
90            pos = np.dot(Rx, pos) # Apply the rotation
91
92            # Rotate the detector around the z-axis so it faces correctly inwards
93            c = -d_ang * pi_180
94            Rz = np.array( [[np.cos(c), -np.sin(c), 0, 0],
95                      [np.sin(c), np.cos(c), 0, 0],
96                      [0, 0, 1, 0],
97                      [0, 0, 0, 1]])
98            pos = np.dot(Rz, pos) # Apply the rotation
```

```
99
100           # Apply the translation and store data
101           d_x = Centre_inrad * np.cos((90 - d_ang) * pi_180)
102           d_y = Centre_inrad * np.sin((90 - d_ang) * pi_180)
103           d_z = (2.5 * HR_det_height) - ([3,4,5,0,1,2].index(int(np.floor(segment_no /
      8))) * HR_det_height)
104           trans_mat = np.array([  [1,0,0,d_x],
105                                   [0,1,0,d_y],
106                                   [0,0,1,d_z],
107                                   [0,0,0,1  ]])
108           pos = np.dot(trans_mat, pos) # Apply the translation
109           data += [pos[0], pos[1], pos[2]]
110           df.loc[len(df.index)] = data # Store data
111
112         # Top-end section (odd buckets)
113         elif mode == 1:
114           # Calculate the position in the detector block frame
115           x = (col_no-3.5) * AR_pitch_tx
116           y = (plane_no-3.5) * AR_pitch_ax
117           z = z_depth
118           w = 1
119           pos = np.array([x, y, z, w])
120
121           # Calculate the quadrant, detector sector, and angle
122           d_sec = int(np.floor(segment_no / 8))
123           if bucket_pair in [1,7]:
124             if ring_no > 1:
125               d_sec = np.abs(d_sec - 5)
126           else:
127             d_sec -= 3
128             if ring_no < 2:
129               d_sec = np.abs(d_sec - 5)
130
131           quadrant = int((bucket_pair - 1) / 3)
132           d_ang = ((d_sec + 0.5) * End_external_angle) + (quadrant * 90)
133
134           # Rotate the detector block upside down around the z-axis
135           # This end section only
136           c = 180 * pi_180
137           Rz = np.array([[np.cos(c), -np.sin(c), 0, 0],
```

```
                    [np.sin(c), np.cos(c), 0, 0],
                    [0, 0, 1, 0],
                    [0, 0, 0, 1]])
        pos = np.dot(Rz, pos) # Apply the rotation

        # Rotate the detector block to face up properly around the x-axis
        a = (90 * pi_180)
        if ring_no % 2 == 0:
          a -= End_det_small_angle
        else:
          a += End_det_small_angle
        Rx = np.array([[1, 0, 0, 0],
                  [0, np.cos(a), -np.sin(a), 0],
                  [0, np.sin(a), np.cos(a), 0],
                  [0, 0, 0, 1]])
        pos = np.dot(Rx, pos) # Apply the rotation

        # Rotate the detector around the z-axis so it faces correctly inwards
        c = -d_ang * pi_180
        Rz = np.array([[np.cos(c), -np.sin(c), 0, 0],
                    [np.sin(c), np.cos(c), 0, 0],
                    [0, 0, 1, 0],
                    [0, 0, 0, 1]])
        pos = np.dot(Rz, pos) # Apply the rotation

        # Apply translation matrix and store data
        d_x = End_inrad * np.cos((90 - d_ang) * pi_180)
        d_y = End_inrad * np.sin((90 - d_ang) * pi_180)
        d_z = Centre_height + Space_end + End_det_ang_halfheight
        if ring_no % 2 != 0:
          d_z += 2 * End_det_ang_halfheight
        trans_mat = np.array([[1,0,0,d_x],
                          [0,1,0,d_y],
                          [0,0,1,d_z],
                          [0,0,0,1 ]])
        pos = np.dot(trans_mat, pos) # Apply the translation
        data += [pos[0], pos[1], pos[2]]
        df.loc[len(df.index)] = data # Store data

      # Bottom end section (even buckets)
```

```
178         elif mode == 2:
179           # Calculate the position in the detector block frame
180           x = (col_no - 3.5) * AR_pitch_tx
181           y = (plane_no - 3.5) * AR_pitch_ax
182           z = z_depth
183           w = 1
184           pos = np.array([x, y, z, w])
185
186           # Calculate the quadrant, detector sector, and angle
187           d_sec = int(np.floor(segment_no / 8))
188           if bucket_pair in [4,10]:
189             d_sec = np.abs(d_sec - 2)
190           if ring_no < 2:
191             d_sec = np.abs(d_sec - 5)
192
193           quadrant = int((bucket_pair - 1) / 3)
194           d_ang = ((d_sec + 0.5) * End_external_angle) + (quadrant * 90)
195
196           # Rotate the detector block around the x-axis to face up properly
197           a = (90 * pi_180)
198           if ring_no%2 == 0:
199             a += End_det_small_angle
200           else:
201             a -= End_det_small_angle
202           Rx = np.array([[1, 0, 0, 0],
203                   [0, np.cos(a), -np.sin(a), 0],
204                   [0, np.sin(a), np.cos(a), 0],
205                   [0, 0, 0, 1]])
206           pos = np.dot(Rx, pos) # Apply the rotation
207
208           # Rotate the detector block around the z-axis so it faces correctly inwards
209           c = -d_ang * pi_180
210           Rz = np.array([[np.cos(c), -np.sin(c), 0, 0],
211                       [np.sin(c), np.cos(c), 0, 0],
212                       [0, 0, 1, 0],
213                       [0, 0, 0, 1]])
214           pos = np.dot(Rz, pos) # Apply the rotation
215
216           # Apply translation matrix and store data
217           d_x = End_inrad * np.cos((90 - d_ang) * pi_180)
```

```
            d_y = End_inrad * np.sin((90 - d_ang) * pi_180)
            d_z = Centre_height + Space_end + End_det_ang_halfheight
            if ring_no%2 != 0:
              d_z += 2 * End_det_ang_halfheight
            d_z = -d_z
            trans_mat = np.array([[1,0,0,d_x],
                                  [0,1,0,d_y],
                                  [0,0,1,d_z],
                                  [0,0,0,1  ]])
            pos = np.dot(trans_mat, pos) # Apply the transformation
            data += [pos[0], pos[1], pos[2]]
            df.loc[len(df.index)] = data # Store data

# Plot the crystal element centre positions on an interactive 3D plot
fig = px.scatter_3d(df, x = 'x', y = 'y', z = 'z', color = 'crystal',
            color_discrete_sequence = px.colors.sequential.Rainbow)
fig.update_traces(marker_size = 2)
fig.show()
```

References

[1] G. F. Knoll. *Radiation Detection and Measurment*. 4th ed. John Wiley & Sons, Inc, 2010. ISBN: 978-0-470-13148-0.

[2] M. D. Harpen. "Positronium: Review of symmetry, conserved quantities and decay for the radiological physicist". In: *Medical Physics* **31** (1) (2003), pp. 57–61. DOI: 10.1118/1.1630494.

[3] D. A. Chesler. "Three-Dimensional Activity Distribution from Multiple Positron Scintigraphs". In: *18th Annual Meeting Abstracts for Scientific Program: Papers to be Presented Orally*. Vol. 12. Journal of Nuclear Medicine, 1971, pp. 347–348.

[4] D. A. Chesler. "Positron Tomography and Three-Dimensional Reconstruction Technique". In: *Tomographic Imaging in Nuclear Medicine: The Proceedings of a Symposium Held September 15-16, 1972*. Ed. by G. S. Freedman. New York, New York, USA: Society of Nuclear Medicine, 1973, pp. 176–183.

[5] D. A. Chesler, B. Hoop, and G. L. Brownell. "Transverse Section Imaging of Myocardium With $^{13}NH_4$". In: *Abstracts of Works in Progress Papers Presented at 20th Annual Society of Nuclear Medicine Meeting*. Vol. 14. Journal of Nuclear Medicine, 1973, p. 623.

[6] R. Gordon, R. Bender, and G. T. Herman. "Algebraic Reconstruction Techniques (ART) for three-dimensional electron microscopy and X-ray photography". In: *Journal*

of Theoretical Biology **29** (3) (1970), pp. 471–481. ISSN: 0022-5193. DOI: 10.1016/0022-5193(70)90109-8.

[7] G. N. Hounsfield. "Computerized Transverse Axial Scanning (Tomography). 1. Description of System". In: *British Journal of Radiology* **46** (552) (1973), pp. 1016–1022. ISSN: 0007-1285 (Print) 0007-1285 (Linking). DOI: 10.1259/0007-1285-46-552-1016.

[8] G. N. Hounsfield. *Computed Medical Imaging*. Lecture. Dec. 1979.

[9] A. M. Cormack. "Representation of a Function by Its Line Integrals, with Some Radiological Applications". In: *Journal of Applied Physics* **34** (9) (1963), pp. 2722–2727. ISSN: 0021-8979 1089-7550. DOI: 10.1063/1.1729798.

[10] A. M. Cormack. "Representation of a Function by Its Line Integrals, with Some Radiological Applications. II". In: *Journal of Applied Physics* **35** (10) (1964), pp. 2908–2913. ISSN: 0021-8979 1089-7550. DOI: 10.1063/1.1713127.

[11] A. M. Cormack. *Early Two-Dimensional Reconstruction and Recent Topics Stemming From It*. Lecture. Dec. 1979.

[12] S. R. Cherry and M. Dahlbom. *PET: Physics, Instrumentation, and Scanners*. New York, New York, USA: Springer, 2006, p. 130. ISBN: 978-0-387-32302-2. DOI: 10.1007/0-387-34946-4. URL: https://web.archive.org/web/20170808134424id_/http://eknygos.lsmuni.lt/springer/360/1-117.pdf.

[13] H. M. Dent, W. F. Jones, and M. E. Casey. "A Real Time Digital Coincidence Processor for Positron Emission Tomography". In: *IEEE Transactions on Nuclear Science* **33** (1) (1986), pp. 556–559. ISSN: 0018-9499. DOI: 10.1109/tns.1986.4337164.

[14] D. Brasse, P. E. Kinahan, C. Lartizien, C. Comtat, M. Casey, and C. Michel. "Correction Methods for Random Coincidences in Fully 3D Whole-Body PET: Impact on Data and Image Quality". In: *Journal of Nuclear Medicine* **46** (5) (2005), pp. 859–867.

[15] G. Tarantola, F. Zito, and P. Gerundini. "PET Instrumentation and Reconstruction Algorithms in Whole-Body Applications". In: *Journal of Nuclear Medicine* **44** (5) (2003), pp. 756–769.

[16] T. Lewellen and J. Karp. "PET Systems". In: *Emission Tomography: The Fundamentals of PET and SPECT*. Ed. by M. N. Wernick and J. N. Aarsvold. San Diego, California, USA: Elsevier Academic Press, 2004. Chap. 10, pp. 179–194. ISBN: 978-0-12-744482-6. URL: https://www.sciencedirect.com/book/9780127444826/emission-tomography.

[17] M. J. Berger, J. S. Coursey, M. A. Zucker, J. Chang, S. M. Seltzer, and P. M. Bergstrom. *Stopping-Power & Range Tables for Electrons, Protons, and Helium Ions (STAR)*. Online Database. Last accessed on 2024-02-05. 2017. DOI: 10.18434/T4NC7P. URL: https://www.nist.gov/pml/stopping-power-range-tables-electrons-protons-and-helium-ions.

[18] National Nuclear Data Center. *NuDat Database*. Online Database. Last accessed on 2024-02-05. 2024. URL: https://www.nndc.bnl.gov/nudat3/.

[19] D. R. Schaart. "Physics and Technology of Time-of-Flight PET Detectors". In: *Physics in Medicine and Biology* **66** (9) (2021), 09TR01. ISSN: 1361-6560 (Electronic) 0031-9155 (Linking). DOI: 10.1088/1361-6560/abee56.

[20] Berkeley Nucleonics Corporation. *High resolution low background $CeBr_3$ scintillators*. Data Sheet. San Rafael, California, 2021. URL: https://www.berkeleynucleonics.com/sites/default/files/products/resources/cebr3_datasheet_bnc.pdf.

[21] N. S. Kozlova, O. A. Busanov, E. V. Zabelina, A. P. Kozlova, and V. M. Kasimova. "Optical properties and refractive indices of $Gd_3Al_2Ga_3O_{12}$:Ce^{3+} crystals". In: *Crystallography Reports* **61** (3) (2016), pp. 474–478. ISSN: 1063-7745. DOI: 10.1134/S1063774516030160.

[22] Radiation Monitoring Devices, Inc. *GLuGAG Gamma-Neutron Ceramic Scintillation Detector*. Last accessed on 2024-08-30. 2024. URL: https://www.rmdinc.com/product-category/emerging-products/glugag-gamma-neutron-ceramic-scintillation-detector/.

[23] S. Surti and J. S. Karp. "Advances in Time-of-Flight PET". In: *Physica Medica* **32** (1) (2016), pp. 12–22. ISSN: 1724-191X (Electronic) 1120-1797 (Print) 1120-1797 (Linking). DOI: 10.1016/j.ejmp.2015.12.007.

[24] M. Schmand, L. Eriksson, M. E. Casey, M. S. Andreaco, C. Melcher, K. Wienhard, G. Flugge, and R. Nutt. "Performance Results of a New DOI Detector Block for a High Resolution PET-LSO Research Tomograph HRRT". In: *1997 IEEE Nuclear Science Symposium Conference Record*. Vol. 2. Albuquerque, New Mexico, USA: IEEE, Nov. 1997, pp. 934–938. ISBN: 0-7803-4258-5. DOI: 10.1109/NSSMIC.1997.670463.

[25] C. R. Bemrose, P. Fowles, M. R. Hawkesworth, and M. A. O'Dwyer. "Application of Positron Emission Tomography to Particulate Flow Measurement in Chemical Engineering Processes". In: *Nuclear Instruments and Methods in Physics Research Section A: Accelerators, Spectrometers, Detectors and Associated Equipment* **273** (2-3) (1988), pp. 874–880. ISSN: 01689002. DOI: 10.1016/0168-9002(88)90111-8.

[26] M. R. Hawkesworth, M. A. O'Dwyer, J. Walker, P. Fowles, J. Heritage, P. A. E. Stewart, R. C. Witcomb, J. E. Bateman, J. F. Connolly, and R. Stephenson. "A Positron Camera for Industrial Application". In: *Nuclear Instruments and Methods in Physics Research Section A: Accelerators, Spectrometers, Detectors and Associated Equipment* **253** (1) (1986), pp. 145–157. ISSN: 01689002. DOI: 10.1016/0168-9002(86)91138-1.

[27] D. J. Parker, C. J. Broadbent, P. Fowles, M. R. Hawkesworth, and P. McNeil. "Positron Emission Particle Tracking - A Technique for Studying Flow Within Engineering Equipment". In: *Nuclear Instruments and Methods in Physics Research Section A: Ac-*

celerators, Spectrometers, Detectors and Associated Equipment **326** (3) (1993), pp. 592–607. ISSN: 01689002. DOI: 10.1016/0168-9002(93)90864-e.

[28] C. R. K. Windows-Yule, M. T. Herald, A. L. Nicuşan, C. S. Wiggins, G. Pratx, S. Manger, A. E. Odo, T. Leadbeater, J. Pellico, and R. T. M. de Rosales. "Recent advances in positron emission particle tracking: a comparative review". In: *Reports on Progress in Physics* **85** (1) (2022), p. 016101. DOI: 10.1088/1361-6633/ac3c4c.

[29] D. J. Parker, D. M. Hampel, and Tz. Kokalova Wheldon. "Performance Evaluation of the Current Birmingham PEPT Cameras". In: *Applied Sciences* **12** (14) (2022), p. 6833. ISSN: 2076-3417. DOI: 10.3390/app12146833.

[30] D. M. Hampel, S. Manger, D. J. Parker, and Tz. Kokalova Wheldon. "SuperPEPT: A New Tool for Positron Emission Particle Tracking; First Results". In: *Nuclear Instruments and Methods in Physics Research Section A: Accelerators, Spectrometers, Detectors and Associated Equipment* **1028** (2022), pp. 1–9. ISSN: 01689002. DOI: 10.1016/j.nima.2021.166254.

[31] W. Crookes. "The Bakerian Lecture.—On the Illumination of Lines of Molecular Pressure, and the Trajectory of Molecules". In: *Philosophical Transactions of the Royal Society of London* **170** (1879), pp. 135–164. ISSN: 0261-0523 2053-9223. DOI: 10.1098/rstl.1879.0065.

[32] W. Morgan. "Electrical Experiments Made in Order to Ascertain the Non-Conducting Power of a Perfect Vacuum". In: *Philosophical Transactions of the Royal Society of London* **75** (1785), pp. 272–278. ISSN: 0261-0523 2053-9223. DOI: 10.1098/rstl.1785.0014.

[33] J. J. Thomson. "Cathode Rays". In: *The London, Edinburgh, and Dublin Philosophical Magazine and Journal of Science* **44** (269) (1897), pp. 293–316. ISSN: 1941-5982 1941-5990. DOI: 10.1080/14786449708621070.

[34] U. Pidvalna, R. Plyatsko, and L. Vassyl. “Ivan Puluj and the Discovery of X-Rays”. In: *Proceedings of the Shevchenko Scientific Society. Medical Sciences* **64** (1) (2021), pp. 180–190. ISSN: 27088634 27088642. DOI: 10.25040/ntsh2021.01.18.

[35] J. Puluj. „Über die Entstehung der Röntgen’schen Strahlen und ihre photographische Wirkung“. In: *Sitzungsberichte der Kaiserlichen Akademie der Wissenschaften. Mathematisch-Naturwissenschaftliche Classe. Abt. 2, Mathematik, Physik, Chemie, Physiologie, Meteorologie, physische Geographie und Astronomie* **105** (1896), S. 228–239. URL: https://viewer.acdh.oeaw.ac.at/viewer/!image/MN_2Abt_a_105_1896/1/.

[36] J. Puluj. „Nachtrag zur Abhandlung: ‘Über die Entstehung der Röntgen’schen Strahlen und ihre photographischen Wirkung‘“. In: *Sitzungsberichte der Kaiserlichen Akademie der Wissenschaften. Mathematisch-Naturwissenschaftliche Classe. Abt. 2, Mathematik, Physik, Chemie, Physiologie, Meteorologie, physische Geographie und Astronomie* **105** (1896), S. 243–246. URL: https://viewer.acdh.oeaw.ac.at/viewer/!image/MN_2Abt_a_105_1896/1/.

[37] W. C. Röntgen. „Ueber eine neue Art von Strahlen. Vorläufige Mitteilung.“ In: *Sitzungsberichten der Würzburger Physikalisch-medicinischen Gesellschaft Würzburg* **1895** (1896), S. 132–141. URL: https://digital.zbmed.de/gesundheitspflege/periodical/pageview/6245157.

[38] W. C. Röntgen. “On a New Kind of Rays”. In: *Nature* **53** (1369) (1896), pp. 274–276. ISSN: 0028-0836 1476-4687. DOI: 10.1038/053274b0.

[39] W. C. Röntgen. „Ueber eine neue Art von Strahlen. 2. Mitteilung“. In: *Sitzungsberichten der Würzburger Physikalisch-medicinischen Gesellschaft Würzburg* **1896** (1897), S. 11–19. URL: https://digital.zbmed.de/gesundheitspflege/periodical/pageview/6255460.

[40] W. C. Röntgen. „Weitere Beobachtungen über die Eigenschaften der X-Strahlen“. In: *Mathematische und Naturwissenschaftliche Mitteilungen aus den Sitzungsberichten der Königlich Preußischen Akademie der Wissenschaften zu Berlin* **1897** (1897), S. 392–408. URL: https://archive.org/details/bub_gb_ChgYAAAAYAAJ.

[41] P. Peters. “W. C. Roentgen and the Discovery of X-rays”. In: *A Global TextBook of Radiology*. Ed. by H. Pettersson. Series on Diagnostic Imaging. Oslo, Sweden: The NICER Institute, 1995. Chap. 1, pp. 1–11. ISBN: 82-990882-3-2.

[42] J. Reinarz. *Edwards, John Francis Hall- (1858–1926), Surgeon and Radiographer*. Dictionary. 2013. DOI: 10.1093/ref:odnb/104431. URL: https://www.oxforddnb.com/view/10.1093/ref:odnb/9780198614128.001.0001/odnb-9780198614128-e-104431.

[43] P. K. Spiegel. “The First Clinical X-Ray Made in America–100 Years”. In: *American Journal of Roentgenology* **164** (1) (1995), pp. 241–243. ISSN: 0361-803X (Print) 0361-803X (Linking). DOI: 10.2214/ajr.164.1.7998549.

[44] I. I. Mayba, R. Gaida, R. A. Kyle, and M. A. Shampo. “Ukrainian Physicist Contributes to the Discovery of X-Rays”. In: *Mayo Clinic Proceedings* **72** (7) (1997), p. 658. ISSN: 0025-6196 (Print) 0025-6196 (Linking). DOI: 10.1016/s0025-6196(11)63573-8.

[45] A. Feldman. “A Sketch of the Technical History of Radiology from 1896 to 1920”. In: *Radiographics* **9** (6) (1989), pp. 1113–1128. ISSN: 0271-5333 (Print) 0271-5333 (Linking). DOI: 10.1148/radiographics.9.6.2685937.

[46] J. A. Fleming. “Instrument for Converting Alternating Electric Currents Into Continuous Currents”. U.S. pat. 803684. Marconi Wireless Telegraph Co America. 1905.

[47] R. F. Mould. “William David Coolidge (1873–1975). Biography with Special Reference to X-Ray Tubes”. In: *NOWOTWORY. Journal of Oncology* **67** (4) (2017), pp. 273–280. ISSN: 2300-2115 0029-540X. DOI: 10.5603/njo.2017.0045.

[48] W. D. Coolidge. "Vacuum-Tube". U.S. pat. 1203495. General Electric Company. 1916.

[49] P. U. Villard. « Sur la réflexion et la réfraction des rayons cathodiques et des rayons déviables du radium ». In : *Comptes rendus hebdomadaires des séances de l'Académie des sciences* **130** (1900), p. 1010-1012. URL : https://gallica.bnf.fr/ark:/12148/cb343481087/date.r=comptes+rendus+academie.langEN.

[50] E. Rutherford. "The Magnetic and Electric Deviation of the Easily Absorbed Rays from Radium". In: *The London, Edinburgh, and Dublin Philosophical Magazine and Journal of Science* **5** (26) (1903), pp. 177–187. ISSN: 1941-5982 1941-5990. DOI: 10.1080/14786440309462912.

[51] E. Rutherford and E. N. da C. Andrade. "The Wave-Length of the Soft γ Rays from Radium B". In: *The London, Edinburgh, and Dublin Philosophical Magazine and Journal of Science* **27** (161) (1914), pp. 854–868. ISSN: 1941-5982 1941-5990. DOI: 10.1080/14786440508635156.

[52] T. Sidot. « Sur les propriétés de la blende hexagonale ». In : *Comptes rendus hebdomadaires des séances de l'Académie des sciences* **63** (1866), p. 188-189. URL : https://gallica.bnf.fr/ark:/12148/cb343481087/date.r=comptes+rendus+academie.langEN.

[53] A. Romer. *The Restless Atom: The Awakening of Nuclear Physics*. Science Study Series. Garden City, New York, USA: Anchor Books, 1960, p. 175.

[54] W. Crookes. "Certain Properties of the Emanations of Radium". In: *The Chemical News* **87** (1903), p. 241. URL: https://archive.org/details/chemicalnewsand29unkngoog.

[55] W. Crookes. "The Emanations of Radium". In: *Proceedings of the Royal Society of London* **71** (467-476) (1903), pp. 405–408. ISSN: 0370-1662 2053-9126. DOI: 10.1098/rspl.1902.0116.

[56] E. Regener. „Über Zählung der α-Teilchen durch die Szintillation und die Grösse des elektrischen Elementarquantums.“ In: *Verhandlungen der Deutschen Physikalischen Gesellschaft zu Berlin* **10** (1908), S. 78–83. URL: https://archive.org/details/verhandlungende39unkngoog.

[57] E. Rutherford, J. Chadwick, and C. Ellis. *Radiations from Radioactive Substances*. Cambridge, England: Cambridge University Press, 1930. ISBN: 9780511707179. DOI: 10.1017/CBO9780511707179.

[58] E. Rutherford and H. Geiger. “An Electrical Method of Counting the Number of α-Particles from Radio-Active Substances”. In: *Proceedings of the Royal Society of London. Series A, Containing Papers of a Mathematical and Physical Character* **81** (546) (1908), pp. 141–161. ISSN: 0950-1207 2053-9150. DOI: 10.1098/rspa.1908.0065.

[59] J. S. Townsend. “The Conductivity Produced in Gases by the Motion of Negatively Charged Ions”. In: *The London, Edinburgh, and Dublin Philosophical Magazine and Journal of Science* **1** (2) (1901), pp. 198–227. ISSN: 1941-5982 1941-5990. DOI: 10.1080/14786440109462605.

[60] H. Geiger and E. Rutherford. “Photographic Registration of α Particles”. In: *The London, Edinburgh, and Dublin Philosophical Magazine and Journal of Science* **24** (142) (1912), pp. 618–623. ISSN: 1941-5982 1941-5990. DOI: 10.1080/14786441008637365.

[61] H. Geiger. „Über eine einfache Methode zur Zählung von α- und β-Strahlen“. In: *Verhandlungen der deutschen physikalischen Gesellschaft zu Berlin* **15** (1913), S. 534–539. URL: https://archive.org/details/verhandlungen-der-deutschen-physikalischen-gesellschaft-vol-15.

[62] H. Geiger und O. Klemperer. „Beitrag zur Wirkungsweise des Spitzenzählers“. In: *Zeitschrift für Physik* **49** (11-12) (1928), S. 753–760. ISSN: 1434-6001 1434-601X. DOI: 10.1007/bf01328628.

[63] H. Geiger und W. Müller. „Das elektronenzahlrohr i wirkungsweise und herstellung eines zahlrohrs“. In: *Physikalische Zeitschrift* **29** (22) (1928), S. 839–841. URL: https://archive.org/details/physikalische-zeitschrift-vol-29.

[64] H. Geiger und W. Müller. „Elektronenzählrohr zur Messung schwächster Aktivitäten“. In: *Naturwissenschaften* **16** (31) (1928), S. 617–618. ISSN: 0028-1042 1432-1904. DOI: 10.1007/BF01494093.

[65] A. Trost. „Über Zählrohre mit Dampfzusatz“. In: *Zeitschrift für Physik* **105** (4) (1937), S. 399–444. DOI: 10.1007/BF01333374.

[66] S. H. Liebson and H. Friedman. “Self-Quenching Halogen-Filled Counters”. In: *Review of Scientific Instruments* **19** (5) (1948), pp. 303–306. ISSN: 0034-6748 (Print) 0034-6748 (Linking). DOI: 10.1063/1.1741256.

[67] C. E. Wynn-Williams. “A Thyratron “Scale of Two” Automatic Counter”. In: *Proceedings of the Royal Society of London. Series A, Containing Papers of a Mathematical and Physical Character* **136** (829) (1932), pp. 312–324. ISSN: 0950-1207 2053-9150. DOI: 10.1098/rspa.1932.0083.

[68] L. De Forest. “Oscillation-Responsive Device”. U.S. pat. 836070. Individual. 1906.

[69] L. De Forest. “Wireless Telegraphy”. U.S. pat. 841386. Individual. 1906.

[70] L. De Forest. “The Audion; A New Receiver for Wireless Telegraphy”. In: *Transactions of the American Institute of Electrical Engineers* **25** (1906), pp. 735–763. ISSN: 0096-3860 2330-9431. DOI: 10.1109/t-aiee.1906.4764762.

[71] L. De Forest. “Space Telegraphy”. U.S. pat. 879532. DE FOREST RADIO TELEPHONE Co. 1907.

[72] T. H. Lee. *Planar Microwave Engineering: A Practical Guide to Theory, Measurement, and Circuits*. 1st ed. Cambridge, England: Cambridge University Press, 2004.

ISBN: 9780521835268. URL: https://www.cambridge.org/highereducation/books/planar-microwave-engineering/CA50D727AD97C3F4789065F1F9DB0771.

[73] E. H. Armstorng. "Operating Features of the Audion". In: *Annals of the New York Academy of Sciences* **27** (1) (1917), pp. 215–243. ISSN: 0077-8923 1749-6632. DOI: 10.1111/j.1749-6632.1916.tb55188.x.

[74] I. Langmuir. "The Pure Electron Discharge and Its Applications in Radio Telegraphy and Telephony". In: *Proceedings of the IRE* **3** (3) (1915), pp. 261–286. ISSN: 0096-8390. DOI: 10.1109/jrproc.1915.216680.

[75] J. Elster und H. Geitel. „Ueber die Entladung negativ electrischer Körper durch das Sonnen- und Tageslicht". In: *Annalen der Physik und Chemie* **274** (12) (1889), S. 497–514. ISSN: 0003-3804 1521-3889. DOI: 10.1002/andp.18892741202.

[76] L. R. Koller. "Photoelectric Emission from Thin Films of Caesium". In: *Physical Review* **36** (11) (1930), pp. 1639–1647. ISSN: 0031-899X. DOI: 10.1103/PhysRev.36.1639.

[77] N. R. Campbell. "The Photoelectric Emission of Thin Films". In: *The London, Edinburgh, and Dublin Philosophical Magazine and Journal of Science* **12** (75) (1931), pp. 173–185. ISSN: 1941-5982 1941-5990. DOI: 10.1080/14786443109461791.

[78] R. W. Engstrom. *Photomultiplier Handbook: Theory, Design, Application*. 10-89. Lancaster, Pennsylvania, USA: RCA/Burle, 1980. URL: https://psec.uchicago.edu/links/Photomultiplier_Handbook.pdf.

[79] H. Iams and B. Salzberg. "The Secondary Emission Phototube". In: *Proceedings of the IRE* **23** (1) (1935), pp. 55–64. ISSN: 0096-8390. DOI: 10.1109/jrproc.1935.227243.

[80] B. K. Lubsandorzhiev. "On the History of Photomultiplier Tube Invention". In: *Nuclear Instruments and Methods in Physics Research Section A: Accelerators, Spectrometers, Detectors and Associated Equipment* **567** (1) (2006), pp. 236–238. ISSN: 01689002. DOI: 10.1016/j.nima.2006.05.221.

[81] С. Э. Хайкин. «О Рабомах Л. А. Кубецкого». В: *Радиофронт* **12** (7) (июль 1936), с. 10—12. URL: https://msevm.ru/library/rf/1936/index.htm.

[82] Л. А. Кубецкий. «Проблемы вторичной эмиссии». В: *Радиофронт* **12** (7) (июль 1936), с. 13—18. URL: https://msevm.ru/library/rf/1936/index.htm.

[83] L. A. Kubetsky. "Multiple Amplifier". In: *Proceedings of the IRE* **25** (4) (1937), pp. 421–433. ISSN: 0096-8390. DOI: 10.1109/jrproc.1937.229045.

[84] V. K. Zworykin, G. A. Morton, and L. Malter. "The Secondary Emission Multiplier-A New Electronic Device". In: *Proceedings of the IRE* **24** (3) (1936), pp. 351–375. ISSN: 0096-8390. DOI: 10.1109/jrproc.1936.226435.

[85] J. R. Pierce. "Electron Multiplier Design". In: *Bell Laboratories Record* **16** (9) (1938), pp. 305–309. URL: https://www.worldradiohistory.com/Archive-Bell-Laboratories-Record/30s/.

[86] J. A. Rajchman and E. W. Pike. *Electrostatic Focusing in Secondary Emission Multipliers*. Technical Report TR-362. Radio Corporation of America, Sept. 1937.

[87] J. A. RAJCHMAN. « Le courant résiduel : dans les multiplicateurs d'électrons électrostatiques ». In : *Archives des sciences physiques et naturelles* **20** (1938), p. 231-289. DOI : 10.5169/seals-742942.

[88] J. A. Rajchman and R. L. Snyder. "An Electrically-Focused Multiplier Phototube". In: *Electronics* **1940** (12) (Dec. 1940), pp. 20–23, 58, 60. URL: https://www.worldradiohistory.com/Electronics%20_Master_Page.htm.

[89] P. Görlich. „Über zusammengesetzte, durchsichtige Photokathoden". In: *Zeitschrift für Physik* **101** (5-6) (1936), S. 335–342. ISSN: 1434-6001 1434-601X. DOI: 10.1007/bf01342330.

[90] V. K. Zworykin and J. A. Rajchman. "The Electrostatic Electron Multiplier". In: *Proceedings of the IRE* **27** (9) (1939), pp. 558–566. ISSN: 0096-8390. DOI: 10.1109/jrproc.1939.228753.

[91] Z. Bay. "Electron-Multiplier as an Electron-Counting Device". In: *Nature* **141** (3563) (1938), p. 284. ISSN: 0028-0836 1476-4687. DOI: 10.1038/141284a0.

[92] R. H. Morgan. "An Exposure Meter for Roentgenography". In: *The American Journal of Roentgenology and Radium Therapy* **47** (5) (1942), pp. 777–784. URL: https://archive.org/details/sim_ajr-american-journal-of-roentgenology_1942-05_47_5_0.

[93] S. C. Curran and W. R. Baker. *A Photoelectric Alpha-Particle Detector*. Technical Report MDDC-1296. University of California Radiation Laboratory, Nov. 1944. URL: https://books.google.co.uk/books?id=vN-UQ1UZK8QC.

[94] S. C. Curran and W. R. Baker. "Photoelectric Alpha-Particle Detector". In: *Review of Scientific Instruments* **19** (2) (1948), p. 116. ISSN: 0034-6748 (Print) 0034-6748 (Linking). DOI: 10.1063/1.1741210.

[95] M. Blau and B. Dreyfus. "The Multiplier Photo-Tube in Radioactive Measurements". In: *Review of Scientific Instruments* **16** (9) (1945), pp. 245–248. ISSN: 0034-6748 1089-7623. DOI: 10.1063/1.1770379.

[96] J. W. Coltman and F. H. B. Marshall. "Photomultiplier Radiation Detector". In: *Nucleonics* **1** (3) (1947), pp. 58–64. URL: https://archive.org/details/sim_nucleonics_1947-11_1_3.

[97] R. Sherr. "Scintillation Counter for the Detection of α-Particles". In: *Review of Scientific Instruments* **18** (10) (1947), pp. 767–770. ISSN: 0034-6748 1089-7623. DOI: 10.1063/1.1740842.

[98] H. Kallmann. „Kann man Elektronen sehen?“ In: *Natur und Technik* **1947** (7) (1947), S. 13–15.

[99] M. Deutsch. "Naphthalene Counters for Beta and Gamma Rays". In: *Nucleonics* **2** (3) (1948), pp. 58–59. URL: https://archive.org/details/sim_nucleonics_1948-03_2_3.

[100] R. Hofstadter. "Alkali Halide Scintillation Counters". In: *Physical Review* **74** (1) (1948), pp. 100–101. ISSN: 0031-899X. DOI: 10.1103/PhysRev.74.100.

[101] R. Hofstadter. "The Detection of Gamma-Rays with Thallium-Activated Sodium Iodide Crystals". In: *Physical Review* **75** (5) (1949), pp. 796–810. ISSN: 0031-899X. DOI: 10.1103/PhysRev.75.796.

[102] R. Hofstadter and J. A. McIntyre. "Gamma-Ray Measurements with NaI(Tl) Crystals". In: *Physical Review* **79** (2) (1950), pp. 389–391. ISSN: 0031-899X. DOI: 10.1103/PhysRev.79.389.2.

[103] R. Hofstadter. "Means for Detecting Ionizing Radiations". U.S. pat. 2585551. Individual. 1952.

[104] W. H. Jordan and P. R. Bell. "Scintillation Counters". In: *Nucleonics* **5** (4) (1949), pp. 30–41. URL: https://archive.org/details/sim_nucleonics_1949-10_5_4.

[105] R. J. Moon. "Inorganic Crystals for the Detection of High Energy Particles and Quanta". In: *Physical Review* **73** (10) (1948), pp. 1210–1210. ISSN: 0031-899X. DOI: 10.1103/PhysRev.73.1210.

[106] P. A. M. Dirac. "The Quantum Theory of the Electron". In: *Proceedings of the Royal Society of London. Series A, Containing Papers of a Mathematical and Physical Character* **117** (778) (1928), pp. 610–624. ISSN: 0950-1207 2053-9150. DOI: 10.1098/rspa.1928.0023.

[107] H. Weyl. "Gravitation and the Electron". In: *Proceedings of the National Academy of Sciences of the United States of America* **15** (4) (1929), pp. 323–334. ISSN: 0027-8424 (Print) 1091-6490 (Electronic) 0027-8424 (Linking). DOI: 10.1073/pnas.15.4.323.

[108] P. A. M. Dirac. "A Theory of Electrons and Protons". In: *Proceedings of the Royal Society of London. Series A, Containing Papers of a Mathematical and Physical Character* **126** (801) (1930), pp. 360–365. ISSN: 0950-1207 2053-9150. DOI: 10.1098/rspa.1930.0013.

[109] J. R. Oppenheimer. "Note on the Theory of the Interaction of Field and Matter". In: *Physical Review* **35** (5) (1930), pp. 461–477. ISSN: 0031-899X. DOI: 10.1103/PhysRev.35.461.

[110] H. Weyl. *The Theory of Groups and Quantum Mechanics*. 2nd ed. New York, New York, USA: Dover Publications, Inc., 1950. URL: https://archive.org/details/ost-chemistry-quantumtheoryofa029235mbp.

[111] P. A. M. Dirac. "Quantised Singularities in the Electromagnetic Field". In: *Proceedings of the Royal Society of London. Series A, Containing Papers of a Mathematical and Physical Character* **133** (821) (1931), pp. 60–72. ISSN: 0950-1207 2053-9150. DOI: 10.1098/rspa.1931.0130.

[112] D. Skobelzyn. „Über eine Art der Sekundärstrahlung der γ-Strahlen". In: *Zeitschrift für Physik* **24** (1) (1924), S. 393–399. ISSN: 1434-6001 1434-601X. DOI: 10.1007/bf01327255.

[113] D. Skobelzyn. „Über den Rückstoßeffekt der zerstreuten γ-Strahlen". In: *Zeitschrift für Physik* **28** (1) (1924), S. 278–286. ISSN: 1434-6001 1434-601X. DOI: 10.1007/bf01327184.

[114] D. Skobelzyn. „Über eine neue Art sehr schneller β-Strahlen". In: *Zeitschrift für Physik* **54** (9-10) (1929), S. 686–702. ISSN: 1434-6001 1434-601X. DOI: 10.1007/bf01341600.

[115] D. Skobeltzyn. "Positive Electron Tracks". In: *Nature* **133** (3349) (1934), pp. 23–24. ISSN: 0028-0836 1476-4687. DOI: 10.1038/133023a0.

[116] B. A. Li and C. N. Yang. "C. Y. Chao, Pair Creation and Pair Annihilation". In: *International Journal of Modern Physics A* **04** (17) (1989), pp. 4325–4335. ISSN: 0217-751X 1793-656X. DOI: 10.1142/s0217751x89001813.

[117] C. D. Anderson. *The Production and Properties of Positrons*. Lecture. Dec. 1936.

[118] C. D. Anderson. "The Positive Electron". In: *Physical Review* **43** (6) (1933), pp. 491–494. ISSN: 0031-899X. DOI: 10.1103/PhysRev.43.491.

[119] P. M. S. Blackett and G. P. S. Occhialini. "Some Photographs of the Tracks of Penetrating Radiation". In: *Proceedings of the Royal Society of London. Series A, Containing Papers of a Mathematical and Physical Character* **139** (839) (1933), pp. 699–726. ISSN: 0950-1207 2053-9150. DOI: 10.1098/rspa.1933.0048.

[120] G. Hevesy. "The Absorption and Translocation of Lead by Plants: A Contribution to the Application of the Method of Radioactive Indicators in the Investigation of the Change of Substance in Plants". In: *The Biochemical Journal* **17** (4-5) (1923), pp. 439–445. ISSN: 0264-6021 (Print) 1470-8728 (Electronic) 0264-6021 (Linking). DOI: 10.1042/bj0170439.

[121] W. G. Myers. "Georg Charles de Hevesy: The Father of Nuclear Medicine". In: *Journal of Nuclear Medicine* **20** (6) (1979), pp. 590–594.

[122] G. De Hevesy. *Adventures in Radioisotope Research*. New York, New York, USA: Pergamon Press, 1962. URL: https://archive.org/details/adventuresinradi01heve.

[123] G. De Hevesy. *Some Applications of Isotopic Indicators*. Lecture. Dec. 1944.

[124] J. A. Christiansen, G. De Hevesy et Sv. Lomholt. « Recherches, par une méthode radiochimique, sur la circulation du bismuth dans l'organisme ». In : *Comptes rendus hebdomadaires des séances de l'Académie des sciences* **178** (1924), p. 1324-1326. URL : https://gallica.bnf.fr/ark:/12148/cb343481087/date.r=comptes+rendus+academie.langEN.

[125] J. A. Christiansen, G. De Hevesy et Sv. Lomholt. « Recherches, par une méthode radiochimique, sur la circulation du plomb dans l'organisme ». In : *Comptes rendus hebdomadaires des séances de l'Académie des sciences* **179** (1924), p. 291-293. URL : https://gallica.bnf.fr/ark:/12148/cb343481087/date.r=comptes+rendus+academie.langEN.

[126] F. Guerra and N. Robotti. "Enrico Fermi's Discovery of Neutron-Induced Artificial Radioactivity:The Influence of His Theory of Beta Decay". In: *Physics in Perspective* **11** (4) (2009), pp. 379–404. ISSN: 1422-6944 1422-6960. DOI: 10.1007/s00016-008-0415-1.

[127] F. Joliot and I. Curie. "Artificial Production of a New Kind of Radio-Element". In: *Nature* **133** (3354) (1934), pp. 201–202. ISSN: 0028-0836 1476-4687. DOI: 10.1038/133201a0.

[128] I. Curie. *Artificial Production of Radioactive Elements*. Lecture. Dec. 1935.

[129] F. Joliot. *Chemical Evidence of the Transmutation of Elements*. Lecture. Dec. 1935.

[130] E. Fermi. «Radioattività indotta da bombardamento di neutroni». In: *La Ricerca scientifica ed il progresso tecnico nell'economia nazionale* **1** (5) (1934), p. 283. URL: http://digitale.bnc.roma.sbn.it/tecadigitale/giornale/TO00193681/1934/V.1.

[131] E. Fermi, E. Amaldi, O. D'Agostino, F. Rasetti, and E. Segrè. "Artificial Radioactivity Produced by Neutron Bombardment". In: *Proceedings of the Royal Society of London. Series A, Containing Papers of a Mathematical and Physical Character* **146** (857) (1934), pp. 483–500. ISSN: 0950-1207 2053-9150. DOI: 10.1098/rspa.1934.0168.

[132] E. Fermi. *Artificial Radioactivity Produced by Neutron Bombardment*. Lecture. Dec. 1938.

[133] O. Chiewitz and G. Hevesy. "Radioactive Indicators in the Study of Phosphorus Metabolism in Rats". In: *Nature* **136** (3445) (1935), pp. 754–755. ISSN: 0028-0836 1476-4687. DOI: 10.1038/136754a0.

[134] J. L. Heilbron and R. W. Seidel. *Lawrence and His Laboratory A History of the Lawrence Berkeley Laboratory, Volume I*. California Studies in the History of Science. Berkeley, California, USA: University of California Press, 1989. ISBN: 9780520064263. URL: https://publishing.cdlib.org/ucpressebooks/view?docId=ft5s200764&brand=ucpress.

[135] E. O. Lawrence. "Method and Apparatus for the Acceleration of Ions". U.S. pat. 1948384. 1932.

[136] Anonymous. "Distinguished Nuclear Pioneer-1970 John Hundale Lawrence, M.D". In: *Journal of Nuclear Medicine* **11** (6) (1970), pp. 292–293.

[137] E. O. Lawrence and M. S. Livingston. "The Production of High Speed Light Ions Without the Use of High Voltages". In: *Physical Review* **40** (1) (1932), pp. 19–35. ISSN: 0031-899X. DOI: 10.1103/PhysRev.40.19.

[138] E. O. Lawrence. *The Evolution of the Cyclotron*. Lecture. Dec. 1951.

[139] J. E. Williams. "Donner Laboratory: The Birthplace of Nuclear Medicine". In: *Journal of Nuclear Medicine* **40** (1) (1999), 16N–20N.

[140] J. J. Livingood, F. Fairbrother, and G. T. Seaborg. "Radioactive Isotopes of Manganese, Iron and Cobalt". In: *Physical Review* **52** (2) (1937), pp. 135–135. ISSN: 0031-899X. DOI: 10.1103/PhysRev.52.135.

[141] J. J. Livingood and G. T. Seaborg. "Radioactive Isotopes of Iron". In: *Physical Review* **54** (1) (1938), pp. 51–55. ISSN: 0031-899X. DOI: 10.1103/PhysRev.54.51.

[142] J. G. Hamilton. "The Rates of Absorption of Radio-Sodium in Normal Human Subjects". In: *Proceedings of the National Academy of Sciences of the United States of America* **23** (9) (1937), pp. 521–527. ISSN: 0027-8424 (Print) 1091-6490 (Electronic) 0027-8424 (Linking). DOI: 10.1073/pnas.23.9.521.

[143] J. G. Hamilton. "The Rates of Absorption of the Radioactive Isotopes of Sodium, Potassium, Chlorine, Bromine, and Iodine in Normal Human Subjects". In: *American Journal of Physiology* **124** (3) (1938), pp. 667–678. DOI: 10.1152/ajplegacy.1938.124.3.667.

[144] J. J. Livingood and G. T. Seaborg. "Radioactive Iodine Isotopes". In: *Physical Review* **53** (12) (1938), pp. 1015–1015. ISSN: 0031-899X. DOI: 10.1103/PhysRev.53.1015.2.

[145] J. J. Livingood and G. T. Seaborg. "Radioactive Isotopes of Iodine". In: *Physical Review* **54** (10) (1938), pp. 775–782. ISSN: 0031-899X. DOI: 10.1103/PhysRev.54.775.

[146] E. Segrè and G. T. Seaborg. "Nuclear Isomerism in Element 43". In: *Physical Review* **54** (9) (1938), pp. 772–772. ISSN: 0031-899X. DOI: 10.1103/PhysRev.54.772.2.

[147] G. T. Seaborg and E. Segrè. "Nuclear Isomerism in Element 43". In: *Physical Review* **55** (9) (1939), pp. 808–814. ISSN: 0031-899X. DOI: 10.1103/PhysRev.55.808.

[148] World Nuclear Association. *Radioisotopes in Medicine*. Last accessed on 2023-11-11. July 2023. URL: https://world-nuclear.org/information-library/non-power-nuclear-applications/radioisotopes-research/radioisotopes-in-medicine.aspx.

[149] P. Richards. "A Survey of the Production at Brookhaven National Laboratory of Radioisotopes for Medical Research". In: *Fifth Nuclear Congress, U.S. Papers*. United States Atomic Energy Comission, 1960, pp. 41–52. DOI: 10.2172/4054270.

[150] W. Tucker, M. Greene, A. Weiss, and A. Murrenhoff. *Methods of Preparation of Some Carrier-Free Radioisotopes Involving Sorption on Alumina*. Technical Report BNL-3746. Brookhaven National Laboratory, May 1958. DOI: 10.2172/4305138.

[151] P. Richards, W. D. Tucker, and S. C. Srivastava. "Technetium-99m: An Historical Perspective". In: *The International Journal of Applied Radiation and Isotopes* **33** (10) (1982), pp. 793–799. ISSN: 0020-708X (Print) 0020-708X (Linking). DOI: 10.1016/0020-708x(82)90120-x.

[152] P. Richards. *Technetium-99m: The Early Days*. Technical Report BNL-43197. Brookhaven National Laboratory, Sept. 1989. URL: https://www.osti.gov/biblio/5612212.

[153] A. H. Snell. "Abstract #5: A New Radioactive Isotope of Fluorine". In: *Physical Review Proceedings of the American Physical Society Minutes of the Pasadena Meeting, December 18 and 19, 1936*. Vol. 51. American Physical Society, 1937, pp. 142–150. DOI: 10.1103/PhysRev.51.142.

[154] J. Pacák, Z. Točík, and M. Černý. "Synthesis of 2-Deoxy-2-fluoro-D-glucose". In: *Journal of the Chemical Society D: Chemical Communications* (2) (1969), p. 77. ISSN: 0577-6171. DOI: 10.1039/c29690000077.

[155] T. Ido, C-N Wan, V. Casella, J. S. Fowler, A. P. Wolf, M. Reivich, and D. E. Kuhl. "Labeled 2-deoxy-D-glucose Analogs. 18F-labeled 2-deoxy-2-fluoro-D-glucose, 2-deoxy-2-fluoro-D-mannose and 14C-2-deoxy-2-fluoro-D-glucose". In: *Journal of Labelled Compounds and Radiopharmaceuticals* **14** (2) (1977), pp. 175–183. ISSN: 0362-4803 1099-1344. DOI: 10.1002/jlcr.2580140204.

[156] S. Ruben, W. Z. Hassid, and M. D. Kamen. "Radioactive Carbon in the Study of Photosynthesis". In: *Journal of the American Chemical Society* **61** (3) (1939), pp. 661–663. ISSN: 0002-7863 1520-5126. DOI: 10.1021/ja01872a034.

[157] C. A. Tobias, J. H. Lawrence, F. J. W. Roughton, W. S. Root, and M. I. Gregersen. "The Elimination of Carbon Monoxide from the Human Body with Reference to the Possible Conversion of CO to CO_2". In: *American Journal of Physiology* **145** (2) (1945), pp. 253–263. ISSN: 0002-9513 (Print) 0002-9513 (Linking). DOI: 10.1152/ajplegacy.1945.145.2.253.

[158] G. Antoni. "Development of Carbon-11 Labelled PET Tracers-Radiochemical and Technological Challenges in a Historic Perspective". In: *Journal of Labelled Compounds and Radiopharmaceuticals* **58** (3) (2015), pp. 65–72. ISSN: 1099-1344 (Electronic) 0362-4803 (Linking). DOI: 10.1002/jlcr.3258.

[159] S. Ruben and M. D. Kamen. "Radioactive Carbon of Long Half-Life". In: *Physical Review* **57** (6) (1940), pp. 549–549. ISSN: 0031-899X. DOI: 10.1103/PhysRev.57.549.

[160] S. Ruben and M. D. Kamen. "Long-Lived Radioactive Carbon: C^{14}". In: *Physical Review* **59** (4) (1941), pp. 349–354. ISSN: 0031-899X. DOI: 10.1103/PhysRev.59.349.

[161] M. D. Kamen. "Early History of Carbon-14: Discovery of this Supremely Important Tracer was Expected in the Physical Sense but Not in the Chemical Sense". In: *Science* **140** (3567) (1963), pp. 584–590. ISSN: 0036-8075 (Print) 0036-8075 (Linking). DOI: 10.1126/science.140.3567.584.

[162] W. Davis. *Carbon-14 Production in Nuclear Reactors*. Technical Report ORNL/NUREG/TM-12. Oak Ridge National Laboratory, 1977. DOI: 10.2172/7114972.

[163] H. C. Dudley and M. D. Levine. "Studies of the Toxic Action of Gallium". In: *Journal of Pharmacology and Experimental Therapeutics* **95** (4) (1949), pp. 487–493.

[164] H. C. Dudley, K. E. Henry, and B. F. Linfsley. "Studies of the Toxic Action of Gallium II". In: *Journal of Pharmacology and Experimental Therapeutics* **98** (4) (1950), pp. 409–417.

[165] H. C. Dudley, G. E. Maddox, and H. C. La Rue. "Studies of the Metabolism of Gallium". In: *Journal of Pharmacology and Experimental Therapeutics* **96** (2) (1949), pp. 135–138.

[166] H. C. Dudley, J. I. Munn, and K. E. Henry. "Studies of the Metabolism of Gallium II". In: *Journal of Pharmacology and Experimental Therapeutics* **98** (1) (1950), pp. 105–110.

[167] H. C. Dudley and H. H. Marrer. "Studies of the Metabolism of Gallium III. Deposition in and Clearance from Bone". In: *Journal of Pharmacology and Experimental Therapeutics* **106** (2) (1952), pp. 129–134.

[168] H. C. Dudley, G. W. Imirie, and J. T. Istock. "Deposition of Radiogallium (Ga^{72}) in Proliferating Tissues". In: *Radiology* **55** (4) (1950), pp. 571–578. ISSN: 0033-8419 (Print) 0033-8419 (Linking). DOI: 10.1148/55.4.571.

[169] E. R. King, L. W. Brady, and H. C. Dudley. "Therapeutic Trials of Radiogallium; A Report of Four Cases". In: *American Medical Association Archives of Internal Medicine* **90** (6) (1952), pp. 785–789. ISSN: 0888-2479 (Print) 0888-2479 (Linking). DOI: 10.1001/archinte.1952.00240120060006.

[170] F. R. Lang. "A Study of the Use of Radioactive Gallium in Medicine". In: *Annals of Internal Medicine* **35** (6) (1951), pp. 1237–1249. ISSN: 0003-4819 (Print) 0003-4819 (Linking). DOI: 10.7326/0003-4819-35-6-1237.

[171] G. A. Andrews, S. W. Root, and H. D. Kerman. "Clinical Studies with $Gallium^{72}$". In: *Radiology* **61** (4) (1953), pp. 570–588. DOI: 10.1148/61.4.534.

[172] H. D. Bruner, R. L. Hayes, and J. D. Perkinson. "Preliminary Data on $Gallium^{67}$". In: *Radiology* **61** (4) (1953), pp. 602–613. DOI: 10.1148/61.4.534.

[173] Y. Yano and H. O. Anger. "A $Gallium^{68}$ Positron Cow for Medical Use". In: *Journal of Nuclear Medicine* **5** (6) (1964), pp. 484–487.

[174] Y. Yano and H. O. Anger. *A $Gallium^{68}$ Positron Cow for Medical Use*. Technical Report UCRL-11387. Donner Laboratory and Donner Pavilion, Lawrence Radiation Laboratory, University of Califonia, Oct. 1964. DOI: 10.2172/4029450.

[175] G. I. Gleason. "A Positron Cow". In: *International Journal of Applied Radiation and Isotopes* **8** (2-3) (1960), pp. 90–94. ISSN: 0020-708X (Print) 0020-708X (Linking). DOI: 10.1016/0020-708x(60)90052-1.

[176] M. W. Greene and W. D. Tucker. "An Improved Gallium-68 Cow". In: *The International Journal of Applied Radiation and Isotopes* **12** (1-2) (1961), pp. 62–63. ISSN: 0020708X. DOI: 10.1016/0020-708x(61)90034-5.

[177] R. L. Hayes. "The Medical Use of Gallium Radionuclides: A Brief History with Some Comments". In: *Seminars in Nuclear Medicine* **8** (3) (1978), pp. 183–191. ISSN: 0001-2998 (Print) 0001-2998 (Linking). DOI: 10.1016/s0001-2998(78)80027-0.

[178] F. Rösch. "^{68}Ge/^{68}Ga Generators: Past, Present, and Future". In: *Theranostics, Gallium-68, and Other Radionuclides A Pathway to Personalized Diagnosis and Treatment*. Recent Results in Cancer Research. Heidelberg, Germany: Springer, 2011, pp. 3–16. ISBN: 978-3-642-27993-5. DOI: 10.1007/978-3-642-27994-2_1.

[179] W. H. Blahd. "Ben Cassen and the Development of the Rectilinear Scanner". In: *Seminars in Nuclear Medicine* **26** (3) (1996), pp. 165–170. ISSN: 0001-2998 (Print) 0001-2998 (Linking). DOI: 10.1016/s0001-2998(96)80021-3.

[180] H. C. Allen, R. L. Libby, and B. Cassen. "The Scintillation Counter in Clinical Studies of Human Thyroid Physiology Using I^{131}". In: *Journal of Clinical Endocrinology & Metabolism* **11** (5) (1951), pp. 492–511. ISSN: 0021-972X (Print) 0021-972X (Linking). DOI: 10.1210/jcem-11-5-492.

[181] B. Cassen and L. Curtis. *The in vivo Delineation of Thyroid Glands With an Automatically Scanning Recorder*. Technical Report UCLA-130. University of California Los Angeles, Apr. 1951. URL: https://babel.hathitrust.org/cgi/pt?id=mdp.39015095215607&seq=1.

[182] B. Cassen, L. Curtis, C. W. Reed, and R. Libby. "Instrumentation for I^{131} Use in Medical Studies". In: *Nucleonics* **9** (2) (1951), pp. 46–50. URL: https://archive.org/details/sim_nucleonics_1951-08_9_2.

[183] G. Hotchkiss. "Electrosensitive Recording Paper for Facsimile Telegraph Apparatus and Graphic Chart Instruments". In: *Western Union Technical Review* **3** (1) (1949), pp. 6–16. URL: http://www.samhallas.co.uk/repository/telegraph/wu_tech_review_v3_no1.pdf.

[184] W. E. Goodwin, F. K. Bauer, T. F. Barrett, and B. Cassen. "A Method Using I^{131} for the Determination of Abnormal Thyroid Morphology". In: *American Journal of Roentgenology, Radium Theraphy and Nuclear Medicine* **68** (6) (1952), pp. 963–970. URL: https://archive.org/details/sim_ajr-american-journal-of-roentgenology_1952-12_68_6.

[185] W. E. Goodwin, B. Cassen, and F. K. Bauer. "Thyroid Gland Weight Determination from Thyroid Scintigrams with Postmortem Verification". In: *Radiology* **61** (1) (1953), pp. 88–92. ISSN: 0033-8419 (Print) 0033-8419 (Linking). DOI: 10.1148/61.1.88.

[186] F. K. Bauer and W. H. Blahd. "Treatment of Hyperthyroidism with Individually Calculated Doses of I^{131}". In: *American Medical Association Archives of Internal Medicine* **99** (2) (1957), pp. 194–201. ISSN: 0888-2479 (Print) 0888-2479 (Linking). DOI: 10.1001/archinte.1957.00260020030005.

[187] E. T. Yuhl and L. A. Stirrett. "Clinical Evaluation of the Hepatic Radioactivity Survey". In: *Annals of Surgery* **138** (6) (1953), pp. 857–862. ISSN: 0003-4932 (Print) 1528-1140 (Electronic) 0003-4932 (Linking). DOI: 10.1097/00000658-195312000-00006.

[188] D. E. Kuhl, R. H. Chamberlain, J. Hale, and R. O. Gorson. "A High-Contrast Photographic Recorder for Scintillation Counter Scanning". In: *Radiology* **66** (5) (1956), pp. 730–739. ISSN: 0033-8419 (Print) 0033-8419 (Linking). DOI: 10.1148/66.5.730.

[189] W. J. MacIntyre and C. C. Harris. "The Decline and Fall of the Rectilinear Scanner: Nuclear Medicine Instrumentation 1970–1995". In: *Journal of Nuclear Medicine Technology* **23** (4) (1995), 16S–20S.

[190] H. N. Wagner. "Hal Anger: Nuclear Medicine's Quiet Genius". In: *Journal of Nuclear Medicine* **44** (11) (2003), 26N–34N.

[191] M. R. Powell. "H. O. Anger and his Work at the Donner Laboratory". In: *Seminars in Nuclear Medicine* **9** (3) (1979), pp. 164–168. ISSN: 0001-2998 (Print) 0001-2998 (Linking). DOI: 10.1016/s0001-2998(79)80026-4.

[192] A. Gottschalk. "The Early Years With Hal Anger". In: *Seminars in Nuclear Medicine* **26** (3) (1996), pp. 171–179. ISSN: 0001-2998 (Print) 0001-2998 (Linking). DOI: 10.1016/s0001-2998(96)80022-5.

[193] D. E. Copeland and E. W. Benjamin. "Pinhole Camera for Gamma-Ray Sources". In: *Nucleonics* **5** (2) (1949), pp. 44–49. URL: https://archive.org/details/sim_nucleonics_1949-08_5_2.

[194] H. O. Anger. "Use of a Gamma-Ray Pinhole Camera for in vivo Studies". In: *Nature* **170** (4318) (1952), pp. 200–201. ISSN: 0028-0836 (Print) 0028-0836 (Linking). DOI: 10.1038/170200b0.

[195] H. O. Anger. "A Multiple Scintillation Counter *in vivo* Scanner". In: *American Journal of Roentgenology, Radium Theraphy and Nuclear Medicine* **70** (4) (1953), pp. 605–612. URL: https://archive.org/details/sim_ajr-american-journal-of-roentgenology_1953-10_70_4.

[196] H. O. Anger. "In vivo Radiation Scanner". U.S. pat. 2776377. Individual. 1954.

[197] H. O. Anger. "Whole-Body Scanner Mark II". In: *13th Annual Meeting Proceedings*. Vol. 7. Journal of Nuclear Medicine, 1966, pp. 331–332.

[198] R. K. Mortimer, H. O. Anger, and C. A. Tobias. *The Gamma-Ray Pinhole Camera With Image Amplifier*. Technical Report UCRL-2524. Lawrence Berkeley National Laboratory, Mar. 1954. DOI: 10.2172/4396790.

[199] H. O. Anger. *A New Instrument for Mapping Gamma-Ray Emitters*. Technical Report UCRL-3653. University of California Radiation Laboratory, Jan. 1957. URL: https://escholarship.org/uc/item/2vs8p969.

[200] H. O. Anger. *The Scintillation Camera: A New Instrument for Mapping the Distribution of Radioactive Isotopes*. Technical Report UCRL-3845. University of California Radiation Laboratory, July 1957. URL: https://escholarship.org/uc/item/6v39x1x6.

[201] H. O. Anger. *Mapping the Distribution of Gamma-Ray-Emitting Isotopes With the Scintillation Camera*. Technical Report UCRL-3992. University of California Radiation Laboratory, Mar. 1958. URL: https://escholarship.org/uc/item/0bp4r2rq.

[202] H. O. Anger. "Radiation Image Device". U.S. pat. 3011057. Individual. 1958.

[203] H. O. Anger. "Scintillation Camera". In: *Review of Scientific Instruments* **29** (1) (1958), pp. 27–33. ISSN: 0034-6748 1089-7623. DOI: 10.1063/1.1715998.

[204] H. O. Anger. *Scintillation and Positron Cameras*. Technical Report UCRL-8640. University of California Radiation Laboratory, Aug. 1959. URL: https://escholarship.org/uc/item/066209b1.

[205] H. O. Anger. *Scintillation Camera With Multichannel Collimators*. Technical Report UCRL-11335. Lawrence Radiation Laboratory, University of Califonia, Mar. 1964. URL: https://escholarship.org/uc/item/95w4w2sf.

[206] H. O. Anger. *Scintillation Camera with 11-Inch Crystal*. Technical Report UCRL-11184. Donner Laboratory and Donner Pavilion, Lawrence Radiation Laboratory, University of Califonia, Jan. 1963. URL: https://escholarship.org/uc/item/7ws068mn.

[207] H. O. Anger. *Scintillation Camera with Multichannel Collimators*. Technical Report UCRL-11387. Donner Laboratory and Donner Pavilion, Lawrence Radiation Laboratory, University of Califonia, Oct. 1964. DOI: 10.2172/4029450.

[208] L. V. Dos Remedios, P. M. Weber, and H. O. Anger. "A New 80-Lens Oscilloscope Camera for Routine Dynamic Organ Scintigraphy". In: *Journal of Nuclear Medicine* **17** (4) (1974), pp. 290–296.

[209] H. O. Anger. *Scintillation Camera Image Recording*. Technical Report UCRL-11336. Lawrence Radiation Laboratory, University of Califonia, Mar. 1964. URL: https://escholarship.org/uc/item/9vc358w5.

[210] H. O. Anger. *Eighty-Lens Optical Camera for Recording Dynamic Studies With the Scintillation Camera*. Technical Report UCRL-20699. Lawrence Radiation Laboratory, University of Califonia, May 1971. URL: https://escholarship.org/uc/item/7rh2z57h.

[211] H. O. Anger. *Multiplane Tomographic Gamma-Ray Scanner*. Technical Report UCRL-18338. Lawrence Radiation Laboratory, University of Califonia, June 1968. URL: https://escholarship.org/uc/item/9z28682k.

[212] D. E. Kuhl and R. Q. Edwards. "Image Separation Radioisotope Scanning". In: *Radiology* **80** (4) (1963), pp. 653–662. ISSN: 0033-8419 1527-1315. DOI: 10.1148/80.4.653.

[213] H. O. Anger. "Tomographic Gamma Ray Apparatus and Method". U.S. pat. 3979594. Individual. 1972.

[214] H. O. Anger. "Multi-Angle Nuclear Imaging Apparatus and Method". U.S. pat. 4197460. United States Department of Energy. 1977.

[215] H. O. Anger. *Scintillation Camera and Multiplane Tomographic Scanner*. Technical Report UCRL-18705. Lawrence Radiation Laboratory, University of Califonia, Jan. 1969. URL: https://escholarship.org/uc/item/4j65h22h.

[216] H. O. Anger and J. McRae. *Transmission Scintiphotography*. Technical Report UCRL-18123. Lawrence Radiation Laboratory, University of Califonia, Mar. 1968. URL: https://escholarship.org/uc/item/2097z4bn.

[217] J. McRae and H. O. Anger. *Transmission Scintiphotography and its Applications*. Technical Report UCRL-18339. Lawrence Radiation Laboratory, University of California, July 1968. URL: https://escholarship.org/uc/item/8hv5k8fr.

[218] S. DeBenedetti, C. E. Cowan, W. R. Konneker, and H. Primakoff. "On the Angular Distribution of Two-Photon Annihilation Radiation". In: *Physical Review* **77** (2) (1950), pp. 205–212. ISSN: 0031-899X. DOI: 10.1103/PhysRev.77.205.

[219] F. R. Wrenn, M. L. Good, and P. Handler. "The Use of Positron-Emitting Radioisotopes for the Localization of Brain Tumors". In: *Science* **113** (2940) (1951), pp. 525–527. ISSN: 0036-8075 (Print) 0036-8075 (Linking). DOI: 10.1126/science.113.2940.525.

[220] W. H. Sweet. "The Uses of Nuclear Disintegration in the Diagnosis and Treatment of Brain Tumor". In: *The New England Journal of Medicine* **245** (23) (1951), pp. 875–878. ISSN: 0028-4793 (Print) 0028-4793 (Linking). DOI: 10.1056/NEJM195112062452301.

[221] G. L. Brownell. *A History of Positron Imaging*. Lecture. Oct. 1999.

[222] G. L. Brownell and W. H. Sweet. "Localisation of Brain Tumors with Positron Emitters". In: *Nucleonics* **11** (11) (1953), pp. 40–45. URL: https://archive.org/details/sim_nucleonics_1953-11_11_11.

[223] W. H. Sweet and G. L. Brownell. "Localization of Intracranial Lesions by Scanning With Positron-Emitting Arsenic". In: *Journal of the American Medical Association* **157** (14) (1955), pp. 1183–1188. ISSN: 0002-9955 (Print) 0002-9955 (Linking). DOI: 10.1001/jama.1955.02950310009002.

[224] S. Rankowitz, J. S. Robertson, W. A. Higinbotham, and M. J. Rosenblum. *Positron Scanner for Locating Brain Tumors*. Technical Report BNL-6041. Brookhaven National Laboratory, Mar. 1961. DOI: 10.2172/4736421.

[225] T. Jones and D. Townsend. "History and Future Technical Innovation in Positron Emission Tomography". In: *Journal of Medical Imaging* **4** (1) (2017), p. 011013. ISSN: 2329-4302 (Print) 2329-4310 (Electronic) 2329-4302 (Linking). DOI: 10.1117/1.JMI.4.1.011013.

[226] H. O. Anger. "Stereo Positron Camera for Determining the Spatial Distribution of Radioactive Material in a Test Body". U.S. pat. 3329814. Individual. 1965.

[227] A. Gottschalk and H. O. Anger. *Sensitivity of the Positron Scintillation Camera for Detecting Simulated Brain Tumors*. Technical Report UCRL-11033. Donner Laboratory and Donner Pavilion, Lawrence Radiation Laboratory, University of Califonia, Sept. 1963. URL: https://escholarship.org/uc/item/9jj75521.

[228] H. O. Anger and A. Gottschalk. "Localization of Brain Tumors With the Positron Scintillation Camera". In: *Journal of Nuclear Medicine* **4** (4) (1963), pp. 326–330. URL: https://archive.org/details/sim_journal-of-nuclear-medicine_1963_4_contents.

[229] A. Gottschalk and H. O. Anger. "The Sensitivity of the Positron Scintillation Camera for Detecting Simulated Brain Tumors With Gallium 68-EDTA". In: *American Journal of Roentgenology, Radium Therapy and Nuclear Medicine* **92** (1) (1964), pp. 174–176. URL: https://archive.org/details/sim_ajr-american-journal-of-roentgenology_1964-07_92_1.

[230] A. Gottschalk, K. R. McCormack, J. E. Adams, and H. O. Anger. "A Comparison of Results of Brain Scanning Using Ga^{68}-Edta and the Positron Scintillation Camera, with Hg^{203}-Neohydrin and the Conventional Focused Collimator Scanner". In: *Radiology* **84** (1965), pp. 502–506. ISSN: 0033-8419 (Print) 0033-8419 (Linking). DOI: 10.1148/84.3.502.

[231] H. O. Anger and D. C. Vandyke. "Human Bone Marrow Distribution Shown *in vivo* by Iron-52 and the Positron Scintillation Camera". In: *Science* **144** (3626) (1964),

pp. 1587–1589. ISSN: 0036-8075 (Print) 0036-8075 (Linking). DOI: 10.1126/science.144.3626.1587.

[232] D. Van Dyke, H. O. Anger, and M. Pollycove. *Effect of Erythropoietic Stimulation on Marrow Distribution in Man, Rabbit and Rat As Shown with Fe^{59} and Fe^{52}*. Technical Report UCRL-11184. Donner Laboratory and Donner Pavilion, Lawrence Radiation Laboratory, University of Califonia, Jan. 1963. URL: https://escholarship.org/uc/item/7ws068mn.

[233] G. L. Brownell, C. A. Burnham, S. Wilensky, S. Aronow, H. Kazemi, and D. Strieder. "New Developments in Positron Scintigraphy and the Application of Cyclotron-Produced Positron Emitters". In: *Proceedings of a Symposium on Medical Radioisotope Scintigraphy*. Vol. 1. Vienna, Austria: International Atomic Energy Agency, 1968, pp. 163–176.

[234] C. A. Burnham, S. Aronow, and G. L. Brownell. "A Hybrid Positron Scanner". In: *Physics in Medicine and Biology* **15** (3) (1970), pp. 517–528. ISSN: 0031-9155 (Print) 0031-9155 (Linking). DOI: 10.1088/0031-9155/15/3/012.

[235] D. E. Kuhl and R. Q. Edwards. "The Mark III Scanner: A Compact Device for Multiple-View and Section Scanning of the Brain". In: *Radiology* **96** (3) (1970), pp. 563–570. ISSN: 0033-8419 (Print) 0033-8419 (Linking). DOI: 10.1148/96.3.563.

[236] D. E. Kuhl, R. Q. Edwards, A. R. Ricci, R. J. Yacob, T. J. Mich, and A. Alavi. "The Mark IV System for Radionuclide Computed Tomography of the Brain". In: *Radiology* **121** (2) (1976), pp. 405–413. ISSN: 0033-8419 (Print) 0033-8419 (Linking). DOI: 10.1148/121.2.405.

[237] D. E. Kuhl and R. Q. Edwards. "Cylindrical and Section Radioisotope Scanning of the Liver and Brain". In: *Radiology* **83** (5) (1964), pp. 926–936. ISSN: 0033-8419 (Print) 0033-8419 (Linking). DOI: 10.1148/83.5.926.

[238] D. E. Kuhl, J. Hale, and W. L. Eaton. "Transmission Scanning: A Useful Adjunct to Conventional Emission Scanning for Accurately Keying Isotope Deposition to Radiographic Anatomy". In: *Radiology* **87** (2) (1966), pp. 278–184. ISSN: 0033-8419 (Print) 0033-8419 (Linking). DOI: 10.1148/87.2.278.

[239] D. E. Kuhl, R. Q. Edwards, A. R. Ricci, and M. Reivich. "Quantitative Section Scanning Using Orthogonal Tangent Correction". In: *Journal of Nuclear Medicine* **14** (4) (1973), pp. 196–200.

[240] T. F. Budinger and G. T. Gullberg. "Three-Dimensional Reconstruction in Nuclear Medicine Emission Imaging". In: *IEEE Transactions on Nuclear Science* **21** (3) (1974), pp. 2–20. ISSN: 0018-9499 1558-1578. DOI: 10.1109/tns.1974.6499234.

[241] H. O. Anger. "Gamma-Ray Camera for Imaging Radioisotope Distribution in a Transverse Section of a Rotating Subject". U.S. pat. 3432660. US Atomic Energy Commission. 1968.

[242] C. A. Burnham and G. L. Brownell. "A Multi-Crystal Positron Camera". In: *IEEE Transactions on Nuclear Science* **19** (3) (1972), pp. 201–205. ISSN: 0018-9499. DOI: 10.1109/tns.1972.4326726.

[243] G. L. Brownell, C. A. Burnham, B. Hoop, and D. E. Bohning. "Quantitative Dynamic Studies Using Short-Lived Radioisotopes and Positron Detection". In: *Proceedings of the Symposium on Dynamics Studies with Radioisotopes in Clinical Medicine and Research*. Vienna, Austria: International Atomic Energy Agency, 1970, pp. 161–172.

[244] R. Nutt. "1999 ICP Distinguished Scientist Award. The History of Positron Emission Tomography". In: *Molecular Imaging and Biology* **4** (1) (2002), pp. 11–26. ISSN: 1536-1632 (Print) 1536-1632 (Linking). DOI: 10.1016/s1095-0397(00)00051-0.

[245] J. Ambrose. "Computerized Transverse Axial Scanning (Tomography). 2. Clinical Application". In: *British Journal of Radiology* **46** (552) (1973), pp. 1023–1047. ISSN: 0007-1285 (Print) 0007-1285 (Linking). DOI: 10.1259/0007-1285-46-552-1023.

[246] B. J. Perry and C. Bridges. "Computerized Transverse Axial Scanning (Tomography). 3. Radiation Dose Considerations". In: *British Journal of Radiology* **46** (552) (1973), pp. 1048–1051. ISSN: 0007-1285 (Print) 0007-1285 (Linking). DOI: 10.1259/0007-1285-46-552-1048.

[247] D. A. Chesler and S. J. Riederer. "Ripple Suppression During Reconstruction in Transverse Tomography". In: *Physics in Medicine and Biology* **20** (4) (1975), pp. 632–636. ISSN: 0031-9155 (Print) 0031-9155 (Linking). DOI: 10.1088/0031-9155/20/4/011.

[248] B. Hoop, D. J. Hnatowich, G. L. Brownell, T. Jones, K. A. McKusick, R. G. Ojemann, J. A. Parker, R. Subramanyam, and J. M. Taveras. "Techniques for Positron Scintigraphy of the Brain". In: *Journal of Nuclear Medicine* **17** (6) (1976), pp. 473–479.

[249] D. A. Chesler, C. Hales, D. J. Hnatowich, and B. Hoop. "Three-Dimensional Reconstruction of Lung Perfusion Image with Positron Detection". In: *Journal of Nuclear Medicine* **16** (1) (1975), pp. 80–82.

[250] G. L. Brownell and S. Cochavi. "Transverse Section Imaging With Carbon-11 Labeled Carbon Monoxide". In: *Journal of Computer Assisted Tomography* **2** (5) (1978), pp. 533–538. ISSN: 0363-8715 (Print) 0363-8715 (Linking). DOI: 10.1097/00004728-197811000-00001.

[251] J. S. Robertson, R. B. Marr, M. J. Rosenblum, V. Radeka, and Y. L. Yamamoto. *32-Crystal Positron Transverse Section Detector*. Technical Report BNL-17237. Brookhaven National Laboratory, Jan. 1973. DOI: 10.2172/4622519.

[252] C. J. Thompson, Y. L. Yamamoto, and E. Meyer. "A Position Imaging System for the Measurement of Regional Cerebral Blood Flow". In: *SPIE Proceedings: Application of Optical Instrumentation in Medicine V*. Vol. 96. Bellingham, Wshington, USA: Society for Photo-Optical Instrumentation Engineers, 1976, pp. 263–268. DOI: 10.1117/12.965421.

[253] Y. L. Yamamoto, C. J. Thompson, E. Meyer, J. S. Robertson, and W. Feindel. "Dynamic Positron Emission Tomography for Study of Cerebral Hemodynamics in a Cross Section of the Head Using Positron-Emitting ^{68}Ga-EDTA and ^{77}Kr". In: *Journal of Computer Assisted Tomography* **1** (1) (1977), pp. 43–56. ISSN: 0363-8715 (Print) 0363-8715 (Linking). DOI: 10.1097/00004728-197701000-00007.

[254] M. M. Ter-Pogossian, M. E. Phelps, E. J. Hoffman, and N. A. Mullani. "A Positron-Emission Transaxial Tomograph for Nuclear Imaging (PETT)". In: *Radiology* **114** (1) (1975), pp. 89–98. ISSN: 0033-8419 (Print) 0033-8419 (Linking). DOI: 10.1148/114.1.89.

[255] M. E. Phelps, E. J. Hoffman, N. A. Mullani, and M. M. Ter-Pogossian. "Application of Annihilation Coincidence Detection to Transaxial Reconstruction Tomography". In: *Journal of Nuclear Medicine* **16** (3) (1975), pp. 210–224.

[256] M. E. Phelps, E. J. Hoffman, N. A. Mullani, C. S. Higgins, and M. M. Ter-Pogossian. "Design Considerations for a Positron Emission Transaxial Tomograph (PETT III)". In: *IEEE Transactions on Nuclear Science* **23** (1) (1976), pp. 516–522. ISSN: 0018-9499. DOI: 10.1109/tns.1976.4328298.

[257] E. J. Hoffman, M. E. Phelps, N. A. Mullani, C. S. Higgins, and M. M. Ter-Pogossian. "Design and Performance Characteristics of a Whole-Body Positron Transaxial Tomograph". In: *Journal of Nuclear Medicine* **17** (6) (1976), pp. 493–502.

[258] C. W. Williams, M. C. Crabtree, and S. G. Burgiss. "Design and Performance Characteristics of a Positron Emission Computed Axial Tomograph–ECAT®-II". In: *IEEE*

Transactions on Nuclear Science **26** (1) (1979), pp. 619–627. ISSN: 0018-9499. DOI: 10.1109/tns.1979.4329699.

[259] M. E. Phelps, E. J. Hoffman, S. C. Huang, and D. E. Kuhl. "ECAT: A New Computerized Tomographic Imaging System for Positron-Emitting Radiopharmaceuticals". In: *Journal of Nuclear Medicine* **19** (6) (1978), pp. 635–647. ISSN: 0161-5505 (Print) 0161-5505 (Linking).

[260] S. E. Derenzo, T. F. Budinger, J. L. Cahoon, W. L. Greenberg, R. H. Huesman, and T. Vuletich. "The Donner 280-Crystal High Resolution Positron Tomograph". In: *IEEE Transactions on Nuclear Science* **26** (2) (1979), pp. 2790–2793. ISSN: 0018-9499. DOI: 10.1109/tns.1979.4330537.

[261] S. E. Derenzo, T. F. Budinger, R. H. Huesman, J. L. Cahoon, and T. Vuletich. "Imaging Properties of a Positron Tomograph with 280 BGO Crystals". In: *IEEE Transactions on Nuclear Science* **28** (1) (1981), pp. 81–89. ISSN: 0018-9499 1558-1578. DOI: 10.1109/tns.1981.4331144.

[262] M. J. Weber and R. R. Monchamp. "Luminescence of $Bi_4Ge_3O_{12}$: Spectral and Decay Properties". In: *Journal of Applied Physics* **44** (12) (1973), pp. 5495–5499. ISSN: 0021-8979 1089-7550. DOI: 10.1063/1.1662183.

[263] O. H. Nestor and C. Y. Huang. "Bismuth Germanate: A High-Z Gamma-Ray and Charged Particle Detector". In: *IEEE Transactions on Nuclear Science* **22** (1) (1975), pp. 68–71. ISSN: 0018-9499. DOI: 10.1109/tns.1975.4327617.

[264] Z. H. Cho and M. R. Farukhi. "Bismuth Germanate as a Potential Scintillation Detector in Positron Cameras". In: *Journal of Nuclear Medicine* **18** (8) (1977), pp. 840–844.

[265] C. J. Thompson, Y. L. Yamamoto, and E. Meyer. "Positome II: A High Efficiency Positron Imaging Device for Dynamic Brain Studies". In: *IEEE Transactions on Nu-*

clear Science **26** (1) (1979), pp. 583–589. ISSN: 0018-9499. DOI: 10.1109/tns.1979.4329694.

[266] C. W. Williams, M. C. Crabtree, M. R. Burke, R. M. Keyser, S. G. Burgiss, E. J. Hoffman, and M. E. Phelps. "Design of the Neuro-ECAT®: A High-Resolution, High Efficiency Positron Tomograph for Imaging the Adult Head or Infant Torso". In: *IEEE Transactions on Nuclear Science* **28** (2) (1981), pp. 1736–1740. ISSN: 0018-9499. DOI: 10.1109/tns.1981.4331510.

[267] E. J. Hoffman, M. E. Phelps, and S. C. Huang. "Performance Evaluation of a Positron Tomograph Designed for Brain Imaging". In: *Journal of Nuclear Medicine* **24** (3) (1983), pp. 245–257. ISSN: 0161-5505 (Print) 0161-5505 (Linking).

[268] Axis Imaging News. *CTI: PET's Pet Project*. Last accessed on 2023-10-02. 2006. URL: https://axisimagingnews.com/radiology-products/imaging-equipment/ct/cti-pets-pet-project.

[269] W. F. Jones, M. E. Casey, L. G. Byars, and S. G. Burgiss. "A VMEBUS Based, Real Time Sorter Design for Positron Emission Tomography". In: *IEEE Transactions on Nuclear Science* **33** (1) (1986), pp. 601–604. ISSN: 0018-9499 1558-1578. DOI: 10.1109/tns.1986.4337174.

[270] E. J. Hoffman, A. R. Ricci, L. M. A. M. van der Stee, and M. E. Phelps. "ECAT III – Basic Design Considerations". In: *IEEE Transactions on Nuclear Science* **30** (1) (1983), pp. 729–733. ISSN: 0018-9499. DOI: 10.1109/tns.1983.4332366.

[271] E. J. Hoffman, M. E. Phelps, S. C. Huang, P. E. Collard, L. M. Bidaut, R. L. Schwab, and A. R. Ricci. "Dynamic, Gated and High Resolution Imaging with the ECAT III". In: *IEEE Transactions on Nuclear Science* **33** (1) (1986), pp. 452–455. ISSN: 0018-9499. DOI: 10.1109/tns.1986.4337141.

[272] C. Burnham, J. Bradshaw, D. Kaufman, D. Chesler, and G. L. Brownell. "One Dimensional Scintillation Cameras for Positron ECT Ring Detectors". In: *IEEE Transactions on Nuclear Science* **28** (1) (1981), pp. 109–113. ISSN: 0018-9499. DOI: 10.1109/tns.1981.4331149.

[273] C. A. Burnham, J. F. Bradshaw, D. E. Kaufman, D. A. Chesler, and G. L. Brownell. "Positron Source Position Sensing Detector and Electronics". U.S. pat. 4531058. The Massachusetts General Hospital. 1982.

[274] G. L. Brownell, C. A. Burnham, D. A. Chesler, J. Bradshaw, D. Kaufman, and S. Weise. "PCR-I High Resolution Positron Tomograph Using Analog Coding". In: *IEEE Transactions on Medical Imaging* **3** (1) (1984), pp. 10–17. ISSN: 0278-0062 (Print) 0278-0062 (Linking). DOI: 10.1109/TMI.1984.4307645.

[275] G. L. Brownell, C. A. Burnham, C. W. Stearns, D. A. Chesler, A. -L Brownell, and M. R. Palmer. "Developments in High-Resolution Positron Emission Tomography at MGH". In: *International Journal of Imaging Systems and Technology* **1** (2) (1989), pp. 207–217. ISSN: 0899-9457 1098-1098. DOI: 10.1002/ima.1850010210.

[276] C. A. Burnham, D. E. Kaufman, D. A. Chesler, C. W. Stearns, D. R. Wolfson, and G. L. Brownell. "Cylindrical PET Detector Design". In: *IEEE Transactions on Nuclear Science* **35** (1) (1988), pp. 675–679. ISSN: 0018-9499 1558-1578. DOI: 10.1109/23.12810.

[277] C. A. Burnham, D. E. Kaufman, D. A. Chesler, Y. Chen, M-C. Gregoire, and G. L. Brownell. "MGH Cylindrical PET Detector Characteristics". In: *Conference Record of the 1991 IEEE Nuclear Science Symposium and Medical Imaging Conference*. Vol. 3. Santa Fe, New Mexico, USA: IEEE, 1991, pp. 1644–1647. ISBN: 0-7803-0513-2. DOI: 10.1109/NSSMIC.1991.259193.

[278] C. A. Burnham, D. E. Kaufman, D. A. Chesler, M-C. Gregoire, and G. L. Brownell. "MGH Cylindrical PET Operational Characteristics". In: *Conference Record of the*

1992 IEEE Conference on Nuclear Science Symposium and Medical Imaging. Vol. 2. Orlando, Florida, USA: IEEE, 1992, pp. 895–897. ISBN: 0-7803-0884-0. DOI: 10.1109/NSSMIC.1992.301015.

[279] Anonymous. *New Imaging Systems in Nuclear Medicine*. Report DOE/ER/60519-4. Massachusetts General Hospital, 1989. DOI: 10.2172/5942371.

[280] M. E. Casey and R. Nutt. "A Multicrystal Two Dimensional BGO Detector System for Positron Emission Tomography". In: *IEEE Transactions on Nuclear Science* **33** (1) (1986), pp. 460–463. ISSN: 0018-9499. DOI: 10.1109/tns.1986.4337143.

[281] J. M. Roney and C. J. Thompson. "Detector Identification with Four BGO Crystals on a Dual PMT". In: *IEEE Transactions on Nuclear Science* **31** (5) (1984), pp. 1022–1027. ISSN: 0018-9499. DOI: 10.1109/tns.1984.4333434.

[282] A. R. Ricci, E. J. Hoffman, M. E. Phelps, S. C. Huang, D. Plummer, and R. Carson. "Investigation of a Technique for Providing a Pseudo-Continuous Detector Ring for Positron Tomography". In: *IEEE Transactions on Nuclear Science* **29** (1) (1982), pp. 452–456. ISSN: 0018-9499. DOI: 10.1109/tns.1982.4335885.

[283] M. E. Casey, R. Nutt, and T. D. Douglas. "Two Dimensional Photon Counting Position Encoder System and Process". U.S. pat. 4743764. Computer Technology and Imaging, Inc. 1984.

[284] CTI. *An Introduction to ECAT Technology*. Pamphlet. Knoxville, Tennessee, 2000.

[285] M. E. Casey, R. Nutt, and T. D. Douglass. "Two-Dimensional Photon Counting Position Encoder System and Process". U.S. pat. 4749863. Computer Technology and Imaging, Inc. 1985.

[286] T. J. Spinks, T. Jones, M. C. Gilardi, and J. D. Heather. "Physical Performance of the Latest Generation of Commercial Positron Scanner". In: *IEEE Transactions on*

Nuclear Science **35** (1) (1988), pp. 721–725. ISSN: 0018-9499 1558-1578. DOI: 10.1109/23.12819.

[287] CTI. *Model 931 ECAT Scanner Technical Description*. Manual. CTI, Inc, 1986.

[288] Siemens Gammasonics. *Three-Dimensional Positron Emission Tomography (PET) ECAT Scanner*. Pamphlet. 1987.

[289] CTI. *ECAT 931 Drawings/Schematics Package*. Schematic. 1986.

[290] D. W. Townsend, T. Sprinks, T. Jones, A. Geissbuhler, M. Defrise, M. C. Gilardi, and J. Heather. "Three Dimensional Reconstruction of PET Data From a Multi-Ring Camera". In: *IEEE Transactions on Nuclear Science* **36** (1) (1989), pp. 1056–1065. ISSN: 0018-9499 1558-1578. DOI: 10.1109/23.34605.

[291] T. J. Spinks, T. Jones, D. L. Bailey, D. W. Townsend, S. Grootoonk, P. M. Bloomfield, M. C. Gilardi, M. E. Casey, B. Sipe, and J. Reed. "Physical Performance of a Positron Tomograph for Brain Imaging With Retractable Septa". In: *Physics in Medicine and Biology* **37** (8) (1992), pp. 1637–1655. ISSN: 0031-9155 (Print) 0031-9155 (Linking). DOI: 10.1088/0031-9155/37/8/002.

[292] C. Degueldre and L. Quaglia. "Performance Evaluation of a New Whole Body Positron Tomograph: The ECAT 951/31 R". In: *1992 14th Annual International Conference of the IEEE Engineering in Medicine and Biology Society*. Vol. 5. Paris, France: IEEE, Oct. 1992, pp. 1831–1833. DOI: 10.1109/IEMBS.1992.5762061.

[293] CTI. *ECAT 951R Drawings/Schematics Package*. Schematic. 1990.

[294] Siemens Gammasonics. *ECAT EXACT Service Manual*. Manual. Siemens Gammasonics, Inc, 1992.

[295] Siemens Medical Systems. *ECAT EXACT Operating instructions*. Manual. Siemens Medical Systems, Inc, 1996.

[296] K. Wienhard, L. Eriksson, S. Grootoonk, M. Casey, U. Pietrzyk, and W. D. Heiss. "Performance Evaluation of the Positron Scanner ECAT EXACT". In: *Journal of Computer Assisted Tomography* **16** (5) (1992), pp. 804–813. ISSN: 0363-8715 (Print) 0363-8715 (Linking). DOI: 10.1097/00004728-199209000-00024.

[297] K. Wienhard, M. Dahlbom, L. Eriksson, C. Michel, T. Bruckbauer, U. Pietrzyk, and W. D. Heiss. "The ECAT EXACT HR: Performance of a New High Resolution Positron Scanner". In: *Journal of Computer Assisted Tomography* **18** (1) (1994), pp. 110–118. ISSN: 0363-8715. DOI: 10.1097/00004728-199401000-00023.

[298] H. Watabe, K. Matsumoto, M. Senda, and H. Iida. "Performance of List Mode Data Acquisition with ECAT EXACT HR and ECAT EXACT HR+ Positron Emission Scanners". In: *Annals of Nuclear Medicine* **20** (3) (2006), pp. 189–194. ISSN: 0914-7187 (Print) 0914-7187 (Linking). DOI: 10.1007/BF03027429.

[299] D. L. Bailey, H. Young, P. M. Bloomfield, S. R. Meikle, D. Glass, M. J. Myers, T. J. Spinks, C. C. Watson, P. Luk, A. M. Peters, and T. Jones. "ECAT ART - A Continuously Rotating PET Camera: Performance Characteristics, Initial Clinical Studies, and Installation Considerations in a Nuclear Medicine Department". In: *European Journal of Nuclear Medicine* **24** (1) (1997), pp. 6–15. ISSN: 0340-6997 (Print) 0340-6997 (Linking). DOI: 10.1007/BF01728302.

[300] D. W. Townsend, M. Wensveen, L. G. Byars, A. Geissbuhler, H. J. Tochon-Danguy, A. Christin, M. Defrise, D. L. Bailey, S. Grootoonk, and A. Donath. "A Rotating PET Scanner Using BGO Block Detectors: Design, Performance and Applications". In: *Journal of Nuclear Medicine* **34** (8) (1993), pp. 1367–1376. ISSN: 0161-5505 (Print) 0161-5505 (Linking).

[301] D. W. Townsend, L. G. Byars, M. Defrise, A. Geissbuhler, R. P. Maguire, J. Missirner, R. Roddy, T. Brun, M. A. Mintun, and R. Nutt. "Design and Performance of a Rotating Positron Tomograph, RPT-2". In: *1993 IEEE Conference Record Nuclear Science*

Symposium and Medical Imaging Conference. Vol. 2. San Francisco, California, USA: IEEE, Oct. 1993, pp. 1058–1062. DOI: 10.1109/NSSMIC.1993.701812.

[302] Siemens Medical Systems. *ECAT ART Gantry Service Manual*. Manual. Siemens Medical Systems, Inc, 1996.

[303] T. Beyer, D. W. Townsend, T. Brun, P. E. Kinahan, M. Charron, R. Roddy, J. Jerin, J. Young, L. Byars, and R. Nutt. "A Combined PET/CT Scanner for Clinical Oncology". In: *Journal of Nuclear Medicine* **41** (8) (2000), pp. 1369–1379.

[304] D. W. Townsend, J. P. J. Carney, J. T. Yap, and N. C. Hall. "PET/CT Today and Tomorrow". In: *Journal of Nuclear Medicine* **45** (1 suppl) (2004), 4S–14S. ISSN: 0161-5505.

[305] D. W. Townsend, T. Beyer, and T. M. Blodgett. "PET/CT Scanners: A Hardware Approach to Image Fusion". In: *Seminars in Nuclear Medicine* **33** (3) (2003), pp. 193–204. ISSN: 0001-2998 (Print) 0001-2998 (Linking). DOI: 10.1053/snuc.2003.127314.

[306] G. Brix, J. Zaers, L. C. Adam, M. E. Bellemann, H. Ostertag, H. Trojan, U. Haberkorn, J. Doll, F. Oberdorfer, and W. Lorenz. "Performance Evaluation of a Whole-Body PET Scanner Using the NEMA Protocol". In: *Journal of Nuclear Medicine* **38** (10) (1997), pp. 1614–1623.

[307] Siemens Gammasonics. *ECAT EXACT HR+ Scanner*. Manual. Siemens Gammasonics, Inc, 1996.

[308] T. J. Spinks, T. Jones, P. M. Bloomfield, D. L. Bailey, M. Miller, D. Hogg, W. F. Jones, K. Vaigneur, J. Reed, J. Young, D. Newport, C. Moyers, M. E. Casey, and R. Nutt. "Physical Characteristics of the ECAT EXACT3D Positron Tomograph". In: *Physics in Medicine and Biology* **45** (9) (2000), pp. 2601–2618. ISSN: 0031-9155 (Print) 0031-9155 (Linking). DOI: 10.1088/0031-9155/45/9/313.

[309] C. L. Melcher and J. S. Schweitzer. "Cerium-Doped Lutetium Oxyorthosilicate: A Fast, Efficient New Scintillator". In: *IEEE Transactions on Nuclear Science* **39** (4) (1992), pp. 502–505. ISSN: 0018-9499 1558-1578. DOI: 10.1109/23.159655.

[310] K. Takagi and T. Fukazawa. "Cerium-Activated Gd_2SiO_5 Single Crystal Scintillator". In: *Applied Physics Letters* **42** (1) (1983), pp. 43–45. ISSN: 0003-6951 1077-3118. DOI: 10.1063/1.93760.

[311] C. D. Brandle, A. J. Valentino, and G. W. Berkstresser. "Czochralski Growth of Rare-Earth Orthosilicates (Ln_2SiO_5)". In: *Journal of Crystal Growth* **79** (1-3) (1986), pp. 308–315. ISSN: 00220248. DOI: 10.1016/0022-0248(86)90454-9.

[312] C. L. Melcher. "Lutetium Orthosilicate Single Crystal Scintillator Detector". U.S. pat. 4958080. Schlumberger Technology Corp. 1990.

[313] C. L. Melcher. "Lutetium Orthosilicate Single Crystal Scintillator Detector". U.S. pat. 5025151. 1990.

[314] S. R. Cherry, Y. Shao, R. W. Silverman, K. Meadors, S. Siegel, A. Chatziioannou, J. W. Young, W. Jones, J. C. Moyers, D. Newport, A. Boutefnouchet, T. H. Farquhar, M. Andreaco, M. J. Paulus, D. M. Binkley, R. Nutt, and M. E. Phelps. "MicroPET: A High Resolution PET Scanner for Imaging Small Animals". In: *IEEE Transactions on Nuclear Science* **44** (3) (1997), pp. 1161–1166. ISSN: 0018-9499 1558-1578. DOI: 10.1109/23.596981.

[315] Y. Shao, S. R. Cherry, S. Siegel, R. W. Silverman, and S. Majewski. "Evaluation of Multi-Channel PMTs for Readout of Scintillator Arrays". In: *Nuclear Instruments and Methods in Physics Research Section A: Accelerators, Spectrometers, Detectors and Associated Equipment* **390** (1-2) (1997), pp. 209–218. ISSN: 01689002. DOI: 10.1016/s0168-9002(97)00379-3.

[316] CTI Molecular Imaging, Inc. *Form 10-K/A Annual Report*. Annual Report. United States Securities and Exchange Commission, Sept. 2003. URL: https://www.sec.gov/Archives/edgar/data/1129552/000095014404000579/g86899e10vkza.htm.

[317] CTI Molecular Imaging, Inc. *Form 10-K/A Annual Report*. Annual Report. United States Securities and Exchange Commission, Sept. 2004. URL: http://getfilings.com/o0000950144-04-012040.html.

[318] M. E. Casey, L. Eriksson, M. Schmand, M. S. Andreaco, M. Dahlbom, R. Nutt, and M. Paulus. "Investigation of LSO Crystals for High Spatial Resolution Positron Emission Tomography". In: *IEEE Transactions on Nuclear Science* **44** (3) (1997), pp. 1109–1113. ISSN: 0018-9499 1558-1578. DOI: 10.1109/23.596973.

[319] W. H. Wong. "A Positron Camera Detector Design with Cross-Coupled Scintillators and Quadrant Sharing Photomultipliers". In: *IEEE Transactions on Nuclear Science* **40** (4) (1993), pp. 962–966. ISSN: 0018-9499 1558-1578. DOI: 10.1109/23.256693.

[320] M. Schmand, K. Wienhard, M. E. Casey, L. Eriksson, W. F. Jones, J. H. Reed, J. Treffert, M. Lenox, P. Luk, J. Bao, J. W. Young, K. Baker, S. D. Miller, C. Knoess, S. Vollmar, N. Richerzhagen, G. Flugge, W. D. Heiss, and R. Nutt. "Performance Evaluation of a New LSO High Resolution Research Tomograph-HRRT". In: *1999 IEEE Nuclear Science Symposium. Conference Record. 1999 Nuclear Science Symposium and Medical Imaging Conference*. Vol. 2. Seattle, Washington, USA: IEEE, Oct. 1999, pp. 1067–1071. ISBN: 0-7803-5696-9. DOI: 10.1109/NSSMIC.1999.845845.

[321] K. Wienhard, M. Schmand, M. E. Casey, K. Baker, J. Bao, L. Eriksson, W. F. Jones, C. Knoess, M. Lenox, M. Lercher, P. Luk, C. Michel, J. H. Reed, N. Richerzhagen, J. Treffert, S. Vollmar, J. W. Young, W. D. Heiss, and R. Nutt. "The ECAT HRRT: Performance and First Clinical Application of the New High Resolution Research Tomograph". In: *IEEE Transactions on Nuclear Science* **49** (1) (2002), pp. 104–110. ISSN: 0018-9499 1558-1578. DOI: 10.1109/tns.2002.998689.

[322] M. A. Lodge, R. D. Badawi, R. Gilbert, P. E. Dibos, and B. R. Line. "Comparison of 2-Dimensional and 3-Dimensional Acquisition for ^{18}F-FDG PET Oncology Studies Performed on an LSO-Based Scanner". In: *Journal of Nuclear Medicine* **47** (1) (2006), pp. 23–31. ISSN: 0161-5505 (Print) 0161-5505 (Linking).

[323] E. W. Weisstein. *Inradius*. Last accessed on 2024-08-30. 2003. URL: https://mathworld.wolfram.com/Inradius.html.

[324] A. Sánchez-Crespo and S.A. Larsson. "The influence of photon depth of interaction and non-collinear spread of annihilation photons on PET image spatial resolution". In: *European Journal of Nuclear Medicine and Molecular Imaging* **33** (8) (2006), pp. 940–947. ISSN: 1619-7089. DOI: 10.1007/s00259-005-0024-z.

[325] D. J. Parker, T. W. Leadbeater, X. Fan, M. N. Hausard, A. Ingram, and Z. Yang. "Positron Imaging Techniques for Process Engineering: Recent Developments at Birmingham". In: *Measurement Science and Technology* **19** (9) (2008), p. 094004. ISSN: 0957-0233 1361-6501. DOI: 10.1088/0957-0233/19/9/094004.

[326] D. J. Parker, T. W. Leadbeater, X. Fan, M. N. Hausard, A. Ingram, and Z. Yang. "Positron Emission Particle Tracking Using a Modular Positron Camera". In: *Nuclear Instruments and Methods in Physics Research Section A: Accelerators, Spectrometers, Detectors and Associated Equipment* **604** (1-2) (2009), pp. 339–342. ISSN: 01689002. DOI: 10.1016/j.nima.2009.01.085.

[327] T. W. Leadbeater and D. J. Parker. "A High Speed PC-Based Data Acquisition and Control System for Positron Imaging". In: *Nuclear Instruments and Methods in Physics Research Section A: Accelerators, Spectrometers, Detectors and Associated Equipment* **604** (1-2) (2009), pp. 355–358. ISSN: 01689002. DOI: 10.1016/j.nima.2009.01.184.

[328] T. W. Leadbeater. "The Development of Positron Imaging Systems for Applications in Industrial Process Tomography". PhD Thesis. 2009. URL: https://etheses.bham.ac.uk/id/eprint/521/1/Leadbeater09PhD_A1b.pdf.

[329] D. Mesa, D. M. Hampel, S. J. Neethling, Tz. Kokalova Wheldon, and P. R. Brito-Parada. "Characterisation of the Multiphase Fluid Dynamics of the CoarseAIR™ Fluidised Bed Flotation Cell Using the Large Modular Array (LaMA) for Positron Emission Particle Tracking (PEPT)". In: *Minerals Engineering* (2024). in press.

Nuclear Inst. and Methods in Physics Research, A 1028 (2022) 166254

Contents lists available at ScienceDirect

Nuclear Inst. and Methods in Physics Research, A

journal homepage: www.elsevier.com/locate/nima

SuperPEPT: A new tool for positron emission particle tracking; first results

D.M. Hampel [a,b,c,*], S. Manger [d,b], D.J. Parker [a,b], Tz. Kokalova Wheldon [a,b]

[a] School of Physics and Astronomy, University of Birmingham, Edgbaston, Birmingham, B15 2TT, UK
[b] Positron Imaging Centre, University of Birmingham, Edgbaston, Birmingham, B15 2TT, UK
[c] National Physical Laboratory, Hampton Road, Teddington, TW11 0LW, UK
[d] School of Chemical Engineering, University of Birmingham, Edgbaston, Birmingham, B15 2TT, UK

ARTICLE INFO

Keywords:
PEPT
PET
SuperPEPT
ECAT
Sensitivity
Particle tracking

ABSTRACT

Positron emission particle tracking (PEPT) is a powerful technique for studying flow inside engineering systems by tracking radioactively-labelled particles. A positron camera is used to record coincidence data arising from positron annihilation; since the precision of PEPT depends on the recorded data rate, the camera sensitivity is crucial. We report first results from a new positron camera, SuperPEPT, which has been constructed using components from CTI/Siemens ECAT EXACT 31, ART, and EXACT HR+ scanners and has a versatile geometry with a large field-of-view (FOV). These results were obtained using just two of the three detector sections but already show sensitivity and data rates much higher than achievable with previous positron cameras.

1. Introduction

Positron emission tomography (PET) is a widely used functional medical imaging technique based on the simultaneous detection of the back-to-back photons originating from positron–electron annihilation. Coincident detection of the two photons arising from a single annihilation within the field-of-view (FOV) of the camera results in a line-of-response (LOR) between the two detecting elements along which the annihilation has occurred [1,2]. Acquiring these events over a set period of time; applying corrections for attenuation, system sensitivity variations, and random coincidences; and later processing using tomographic image reconstruction methods yields three-dimensional images representing the distribution of radioactivity within the observed system.

The use of a radioactively labelled fluid in medical PET studies creates images used to study metabolic functions within the body, growth and spread of tumours, and many functional disorders. By contrast, positron emission particle tracking (PEPT), a technique generally used for engineering studies, involves tracking a radioactively-labelled particle. The particle is located many times per second as it travels within a closed system in the FOV of the camera. PEPT relies on acquiring listmode data, which are then divided into groups of either a set number of LORs or a set time step before being processed using a triangulation algorithm into positions, creating a track.

There are many PEPT triangulation algorithms available to process the data. One of the simpler algorithms for single-particle tracking is the Birmingham PEPT algorithm. Iteratively the centre of all the LORs in a group is calculated and outlying LORs are discarded. Eventually, the newly calculated position should not vary much from the previous one after the algorithm reaches a predetermined stop parameter. At this point the position of the particle is said to be final [1]. The rejected LORs correspond to corrupt coincidences due to random or scattered coincidences. Scattered coincidences arise due to the scattering of photons in the surroundings while random coincidences are due to photons from two different annihilations arriving in coincidence, which are especially prominent at high positron activities due to the differences in scaling between true and random coincidence rates. If there were no corrupt coincidences, a few LORs would be enough to give a very accurate position of the particle. Hence, in order to locate a particle frequently and accurately, a high data rate of true coincidence events is highly desirable.

For over 30 years, the University of Birmingham Positron Imaging Centre (PIC) has been involved in the development of PEPT algorithms and data acquisition systems. In the beginning, the centre used a multiwire proportional chamber positron camera to validate and establish the PEPT principle [3]. Currently, the PIC operates an ADAC Forte positron camera [4] and a modular positron camera system [5] constructed by reconfiguring components from CTI/Siemens ECAT 931 and 951 PET scanners. This paper reports the initial results from the latest project, constructing a high sensitivity PEPT system ("SuperPEPT") using components from CTI/Siemens ECAT EXACT HR+, ECAT EXACT 31, and ECAT ART PET scanners.

* Corresponding author at: School of Physics and Astronomy, University of Birmingham, Edgbaston, Birmingham, B15 2TT, UK.
E-mail address: d.hampel@pgr.bham.ac.uk (D.M. Hampel).

https://doi.org/10.1016/j.nima.2021.166254
Received 30 September 2021; Received in revised form 16 December 2021; Accepted 17 December 2021
Available online 27 December 2021

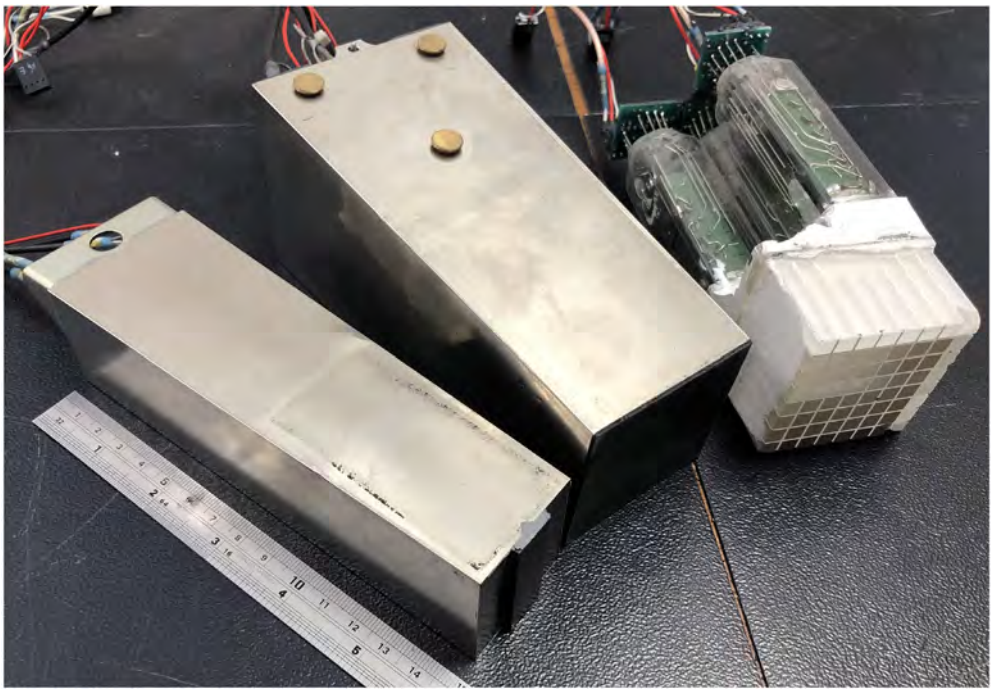

Fig. 1. (Colour on-line) A selection of CTI/Siemens ECAT detector blocks. From left to right, detector blocks from an ECAT EXACT HR+, an ECAT EXACT/ART, and an ECAT 951 PET scanner. A damaged ECAT 951 block is shown without its cladding and one PMT missing. Its 8 × 8 BGO element array can clearly be seen.

2. The CTI/Siemens ECAT PET scanners

2.1. Scanner architecture

The CTI/Siemens ECAT series of PET scanners were the first PET systems to use the block detector architecture developed by Casey and Nutt in the 1980s [6]. They were constructed according to a modular scheme, making it easy to reconfigure them into PEPT systems.

The basic element of each scanner is the detector block, comprising a cuboidal crystal of bismuth germanate (BGO) scintillator, subdivided into an 8 × 8 array of detector elements and viewed by a 2 × 2 array of photomultiplier tubes (PMTs), as can be seen in Fig. 1. Due to the variation in cut depth separating the individual detector elements in the array, by comparing the light detected by each of the four PMTs the crystal element in which a gamma-ray interacted can be uniquely determined, so that just 4 channels of electronics are needed for 64 detector elements.

In the scanner, blocks operate in groups, referred to as buckets. The bucket consists of multiple blocks connected to a set of electronics and controlled by a bucket controller. Each PMT output signal is amplified, then processed by a constant fraction discriminator, integrated, and digitised. The processor on the bucket controller board interprets the signals to obtain correct crystal identifiers and passes this digitised data to a centralised coincidence processor using a serial data connection. Using a separate serial communication connection the bucket controller receives commands from the centralised gantry controller, which can change many parameters such as discriminator levels, amplifier gains, and integration times; this connection also supplies a single clock signal to all the bucket controllers to provide timing information.

The coincidence processor receives hit information from all the buckets and resolves them within 12 ns coincidence windows to identify prompt coincidences (two hits occurring within the resolving time of the system) or delayed coincidences (within the same resolving time after one signal has been delayed, to determine the contribution of random coincidences). To improve efficiency, the coincidence processor only checks certain bucket combinations, based on the geometry of the original scanner. Coincidence data from the coincidence processor are then passed to a data acquisition system for storage, either as sinograms (histograms representing numbers of events as a function of angle and offset) or in listmode.

In essence then, each ECAT scanner comprised a number of buckets (typically 24 or 32), connected to a gantry controller and a coincidence processor, together with power supplies (±5 V for the electronics and 1.5 kV for the PMT bias) [7–10].

2.2. Scanner models

The ECAT EXACT 31 and EXACT 47 scanners produced in the early 1990s were the successors to the original ECAT 930 and 950 series scanners. They differed only in the number of rings: the EXACT 31 had 2 rings each with 12 buckets, which is 96 blocks in each ring, whereas the EXACT 47 had 3 rings (36 buckets in total). The crystal in the EXACT block (shown in Fig. 1) is divided into an 8 × 8 array of 6.35 mm × 6.35 mm and 20 mm long elements, and each bucket contained 4 such blocks. In a major improvement over the previous series, the EXACT system featured a compact, single board coincidence processor made possible due to the introduction of custom, digital, very large scale integrated (VLSI), application-specific integrated circuits (ASICs) that eliminated hundreds of small discrete integrated chips [7].

The ECAT ART (Advanced Rotating Tomograph) was a mid-1990s PET scanner. To reduce cost, instead of using full rings of detectors the ART had a partial ring geometry made up of two opposing banks of detectors, which rotated about the FOV. Following the introduction of custom ASICs in the coincidence processor, the bucket controllers were also updated with this technology. This made it possible for each bucket to interface with up to 12 blocks, greatly decreasing the space taken up by electronics in the head assemblies. However, the detector blocks used were the same as the ones used in the ECAT EXACT scanners. Each bank comprised two buckets with 12 detector blocks and one bucket with 9 detector blocks; that is 66 blocks in the whole scanner. The coincidence processor was vastly different in the ART, needing to account for the rotation of the gantry while acquiring data. Soon after its release, the ECAT ART was combined with a computed tomography (CT) scanner to develop the first PET/CT scanner system [8,9,11].

The ECAT EXACT HR+ scanner was introduced in the late 1990s as a higher resolution system. (Note in order to avoid confusion in

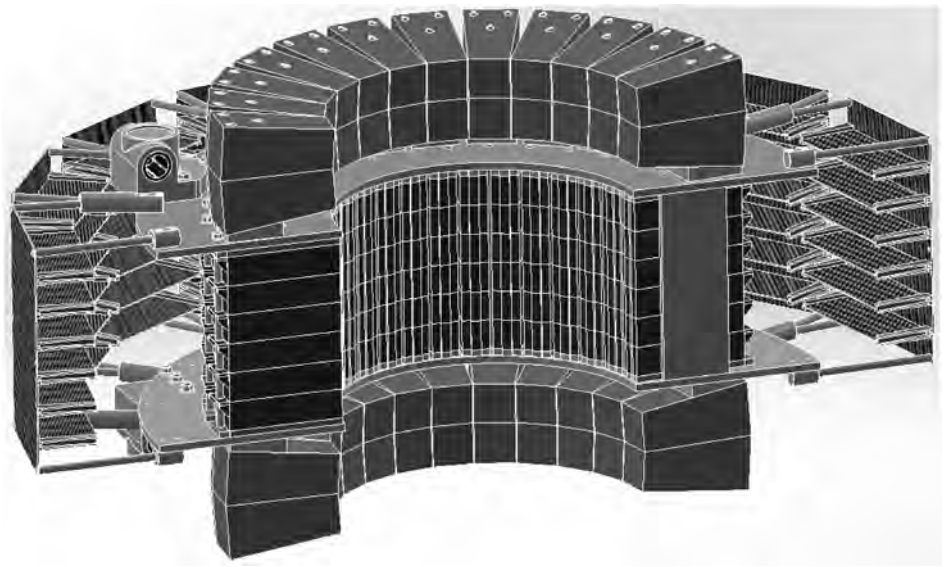

Fig. 2. A cross section of SuperPEPT. The end sections comprised of the EXACT blocks are marked in dark grey and the central section comprised of the HR+ blocks is marked in black.

the present paper we reserve the term EXACT for the EXACT 31 and components thereof and henceforth use HR+ for the EXACT HR+.) The HR+ was one of the last fixed ring PET scanners without an integrated CT scanner. It was a major improvement from the previous models due to its smaller element sizes, giving increased spatial resolution of the system, and increased coincidence data rates. The crystal in the detector block shown in Fig. 1 is divided into an 8 × 8 array of 4.05 mm × 4.39 mm and 30 mm long elements. It uses the same bucket controller boards as the ART, each of which interfaces with 12 blocks. Due to the smaller block size, 24 bucket controller boards were used to create a fixed, full ring tomograph made up of 4 detector rings with 72 blocks each; that is 288 blocks in total. The scanner featured an improved "lossless" coincidence processor which compared all possible coincidences between allowed buckets without applying any priority rules [9,10].

Over the years, the Positron Imaging Centre has acquired an EXACT 31 from the University of Aberdeen, an ART from Hammersmith Hospital, and a HR+ from Hammersmith Imanet. Components from all three of these scanners have been incorporated into SuperPEPT.

3. SuperPEPT

SuperPEPT, shown in Fig. 2, has a cylindrical geometry with an inner diameter of approximately 40 cm and is constructed in three sections. The centre section comprises 192 HR+ blocks, in 6 rings (32 blocks per ring), and has an axial extent of 234 mm. The two end sections each comprise 48 EXACT blocks, in 2 rings (24 blocks per ring) and are 110 mm wide. Axial gaps of 45 mm separate the end sections from the centre section, so that the overall length is approximately 544 mm.

This geometry is dictated by the capacity of the HR+ coincidence processor to handle coincidences between a maximum of 24 buckets. Sixteen ART/HR+ bucket controllers serve the central section, where the HR+ blocks provide the best spatial resolution. By adding two end sections composed of a smaller number of the larger EXACT blocks, each served by 4 bucket controllers, the axial FOV is increased by a more than a factor of 2. The width of the gaps between the central section and the end sections is partly dictated by mechanical issues associated with the mounting of the outer blocks to the frame, but as shown below leads to a sensitivity which varies smoothly along the axis.

As shown in Fig. 3, SuperPEPT is mounted on a custom-built gantry, which allows it to operate with its axis either vertical (e.g. for studying stirred tanks) or horizontal (e.g. for studying pipeline flow). To facilitate setting up the equipment under study, the detector sections are constructed in two semi-circular halves, which can be slid apart by up to 60 cm.

Communications over the serial link with the bucket controllers are transmitted by the HR+ gantry controller board and the data are transmitted to the HR+ coincidence processor. Four ±5 V power supplies (one pair for each half ring) and a 1.5 kV HV power supply complete the gantry electronics.

The coincidence processor is designed to accept coincidences between a bucket and the 14 buckets which would have been opposite it in the original scanner configuration. Thus, for example, bucket 0 is in coincidence with buckets 6–19. The buckets were numbered as follows: the central section comprises buckets 0–1, 4–7, 10–13, 16–19, and 22–23; buckets 2, 8, 14, and 20 make up one end section, and buckets 3, 9, 15, and 21 the other end section. In this way, each bucket in the central section is in coincidence with the 10 buckets opposite in the central section (10/16 of the ring) and with the two buckets opposite in each of the end sections (2/4 of the ring). Once both end sections are operational, coincidences will also be possible between them. Within these bucket combinations, the coincidence processor was set to accept all possible combinations of planes.

Data acquisition is performed by a modern PowerPC-based system (Scintron 7.2) purchased from MiE GmbH, which records coincidence data to disk as listmode files. The PowerPC is controlled from a Windows PC using a software suite provided by the manufacturer. Subsequently the listmode data are transferred from the PowerPC and decoded using locally written, custom software to give LORs in SuperPEPT geometry. A serial communication connection allows commands to be sent to the coincidence processor and bucket controllers for the purpose of setting up and calibration.

4. Results and discussion

The following data have been acquired using the central and just one of the end sections of SuperPEPT. The second end section is fully assembled but not yet in use as some electronic components are currently being sourced. For the following measurements, the lower-level discriminator (LLD) energy was set to 150 keV and the upper-level discriminator (ULD) energy was set to 650 keV. Since the PEPT algorithms discriminate effectively against scattered photons, a low LLD value can be used, increasing the effective sensitivity of the system. Fig. 4

Fig. 3. (Colour on-line) SuperPEPT in its current state of development. The ring assembly is supported by the gantry frame which is able to rotate the central axis of the camera between vertical and horizontal positions (currently in its horizontal position). The data and clock cables running to the coincidence processor and the gantry controller can also be seen; yet to be permanently mounted on the gantry. One of the end sections made up of the EXACT blocks can be seen with its four bucket controller boards on the sides.

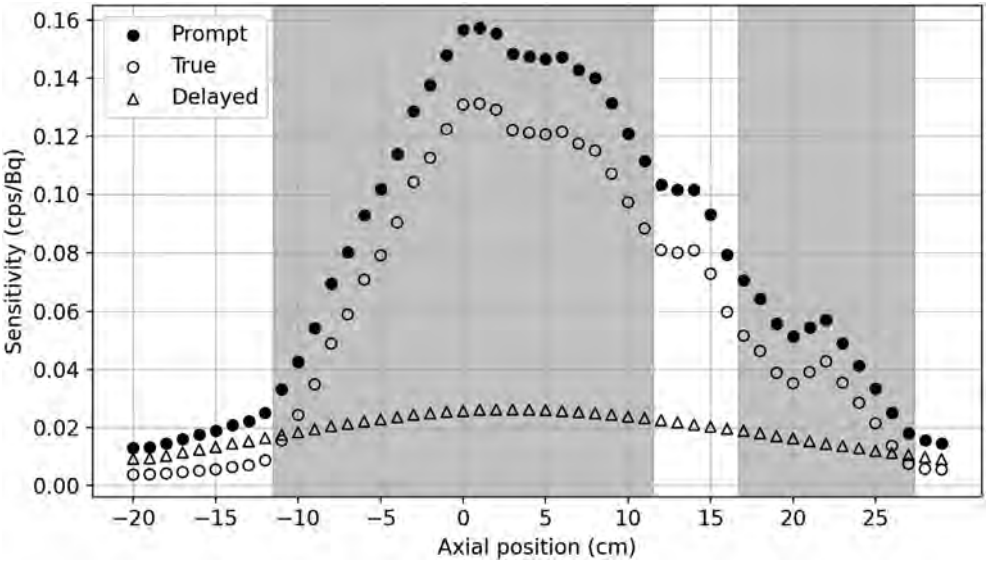

Fig. 4. Absolute sensitivity variation as a function of position along the central axis from the centre of the central section, as recorded using a ^{18}F point source of approximately 20 MBq initial activity. From left to right, the shaded areas represent the length of the central and end sections, respectively.

shows the variation in absolute sensitivity (measured as coincidence-rate per unit activity of the tracer in cps per Bq) along the central axis. The true coincidence rate was obtained by subtracting delayed from prompt coincidence rates. These data were measured using a ^{18}F point source of approximately 20 MBq initial activity (the exact activity, corrected for radioactive decay was used to determine the sensitivity). Using this activity, the prompt coincidence data include a significant contribution of random coincidences. By subtracting the measured number of delayed coincidences, the number of true coincidences has been determined and is plotted. In Fig. 5 the true coincidence rate is subdivided according to the section the events were detected in.

From the figures, it can be seen that the addition of the end section greatly extends the axial FOV out to about 23 cm from the centre. That is because the true coincidence sensitivity remains at least 30% of the maximum value in that range. Once the second end section becomes operational, SuperPEPT will have a useful axial FOV of at least 46 cm.

Figs. 6 and 7 show the variation in radial sensitivity as a function of distance from the centre of the mid-plane of the central section.

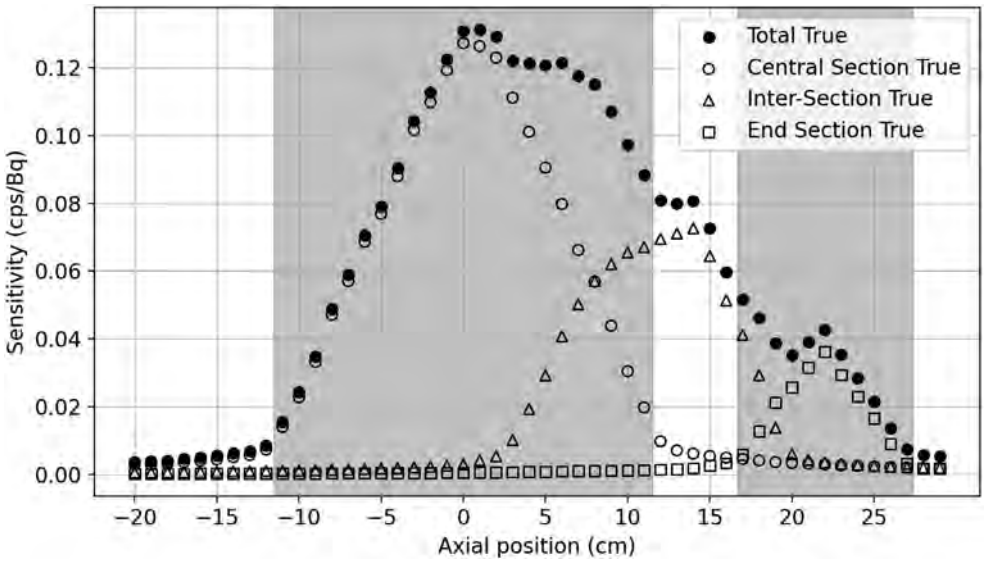

Fig. 5. Absolute sensitivity variation as a function of position along the central axis, as recorded using a ^{18}F point source of approximately 20 MBq initial activity. From left to right, the shaded areas represent the length of the central and end sections, respectively. Contributions from each section to the total true count is shown. The inter-section true coincidence rate is made up of true coincidences which LOR starts in one section and ends in another.

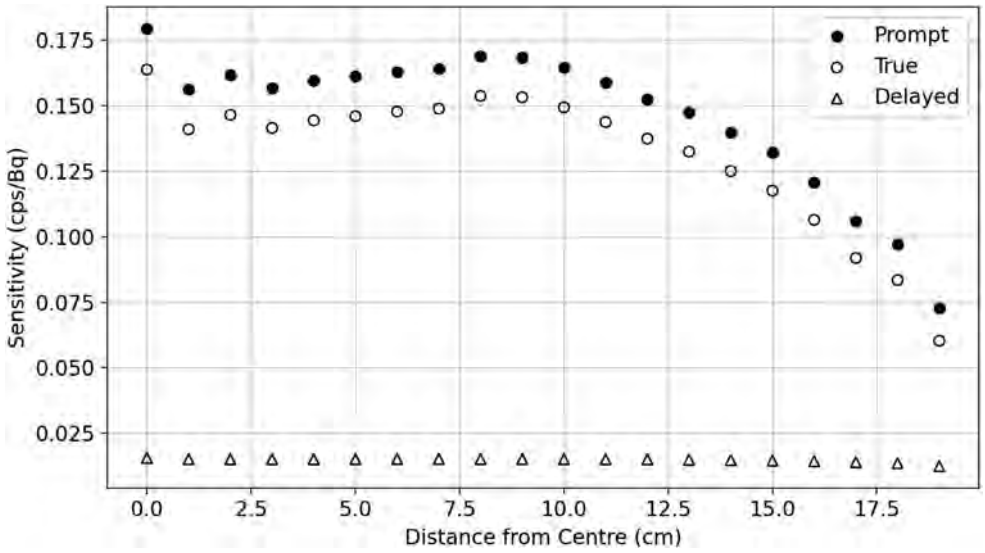

Fig. 6. Absolute sensitivity variation as a function of radial distance from the centre of the mid-plane of the central section, as recorded using a ^{18}F point source of approximately 10 MBq initial activity.

These data were measured using a ^{18}F point source of approximately 10 MBq initial activity. The sensitivity of the system peaks at the centre and then gradually decreases towards the edge of the ring. With only a factor of two difference in sensitivity, experimental apparatus with a diameter of up to 38 cm can be comfortably studied within SuperPEPT. A rise in sensitivity at approximately 8.5 cm from the centre is observed as coincidences between the central and end sections become significant. The sharp increase in sensitivity at the centre of the ring is due to the gaps between the detectors in the central section aligning. Assuming for simplicity that these gaps account for 12% of the circumference of each ring, when the source is on axis opposite gaps align and their effect is to reduce the sensitivity by 12% compared to a gapless system. In contrast, once the source is located off-axis alignment is lost and the effect of the gaps is equivalent to randomly reducing the detection efficiency for each photon by 12%, resulting in an overall reduction in coincidence sensitivity of almost 23%.

Next, the coincidence rates as a function of activity of a decaying, approximately centrally positioned ^{11}C source were recorded. The source initial activity was approximately 120 MBq which made it difficult to position as accurately as the less active ^{18}F point sources. Fig. 8 shows the coincidence rates as measured and reported by the coincidence processor via the serial communications connectionlink. As can be seen, the maximum rate of true coincidences, as limited by the increasing rate of random/delayed coincidences and the electronics, is 2.8 MHz at about 55 MBq of activity. However, Fig. 9 shows the actual data rates as reconstructed from the listmode data files. Due to hardware limitations, the actual maximum true rate of coincidences is 2.0 MHz at about 21.1 MBq. The coincidence rates closely match those reported by the coincidence processor until the hardware data write limit comes into effect.

The tracking accuracy of the system was tested using a ^{18}F point source of approximately 20 MBq initial activity mounted on a circular platter at a radius of 6.37 cm, rotated using an IKA STARVISC 200-2.5 digitally controlled mixer with a 1% accurate speed controller, and positioned on the transaxial plane of the centre section. The particle was rotated at 120, 480, 720, and 900 revolutions per minute (rpm) or

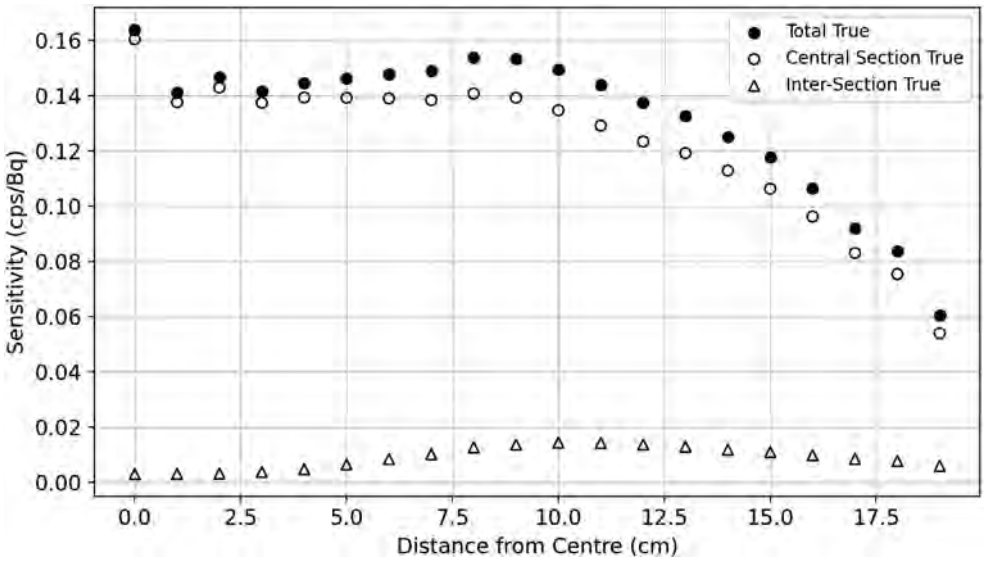

Fig. 7. Absolute sensitivity variation as a function of radial distance from the centre of the mid-plane of the central section, as recorded using a ^{18}F point source of approximately 10 MBq activity. Contributions from each section to the total true count is shown. The inter-section true coincidence rate is made up of true coincidences which LOR starts in one section and ends in another. End section true sensitivity is not shown as no end section true coincidences are observed along the mid-plane of the central section.

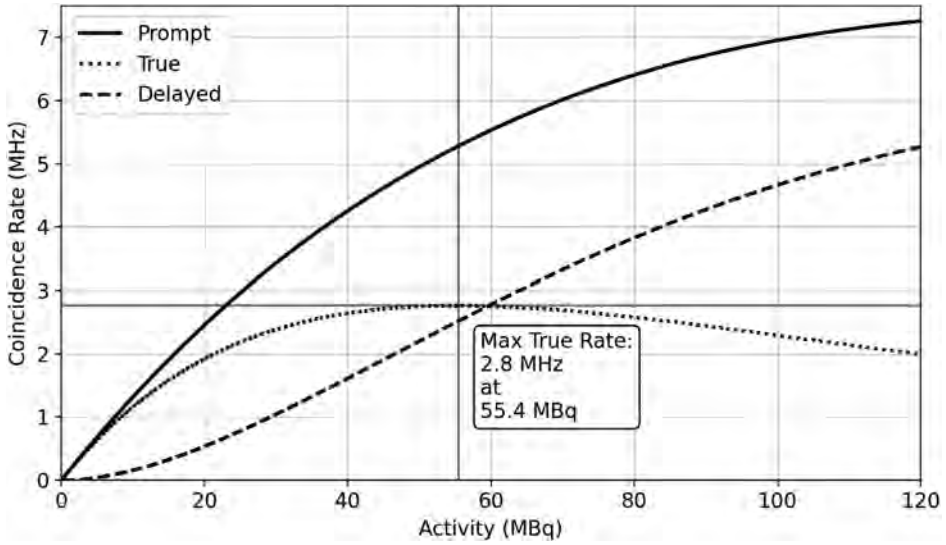

Fig. 8. Coincidence rates as a function of activity of a ^{11}C source of approximately 120 MBq initial activity approximately placed in the centre of the central section. These data were obtained by polling the coincidence processor for its current data rates.

0.80, 3.22, 4.83, and 6.03 m/s, respectively. The rate of coincidences was around 1.66 MHz for all acquisitions. The data were processed into locations using the Birmingham PEPT algorithm, which requires two parameters, N and f. Here, N is the initial number of events (sample size) used to determine each location and f is the fraction of these which remain after corrupts events have been iteratively discarded. In the present case, values of $f = 0.4$ and $N = 100$, 200, and 300 were adopted; at 1.66 MHz these correspond to determining the position every 0.06, 0.12 and 0.18 ms respectively. Using this information, the distance travelled by the particle during each sample is shown in Table 1.

The positional data were then fitted to a model of a rotating particle on a tilted circular orbit. The root-mean-square deviations (δ) along with the fitted rotational speeds for each of the fits are shown in Table 1. Using that table, it can be seen that the precision of locating a particle using a small sample size is almost independent of the rotational speed. This is due to the distance travelled by the particle during the sample being relatively small. At the lower speeds, the precision increases with increasing sample size. However, at higher speeds the precision levels off and would potentially get worse as the movement of the particle during a sample becomes increasingly significant. Figs. 10 and 11 show the positional data and the fit results of a particle rotating at 900 rpm and processed using 100 and 300 sample size, respectively. The increasing precision with increasing sample size can clearly be seen as the frequency of rotation calculated by the fit comes closer to 900 rpm. The small difference in frequency of rotation is well within the 1% error of the set speed of the mixer.

For the case where the particle remains almost stationary during the measurement interval, the precision of location is expected to show proportionality to $\frac{1}{\sqrt{fN}}$. This relationship can be used to define an effective spatial resolution W_{PEPT} for the PEPT system, such that $W_{PEPT} = \sqrt{fN}\delta$ [4]. On this basis, SuperPEPT is found to have a value for W_{PEPT} of approximately 5 mm near the centre of the FOV, degrading slightly as the source moves off axis.

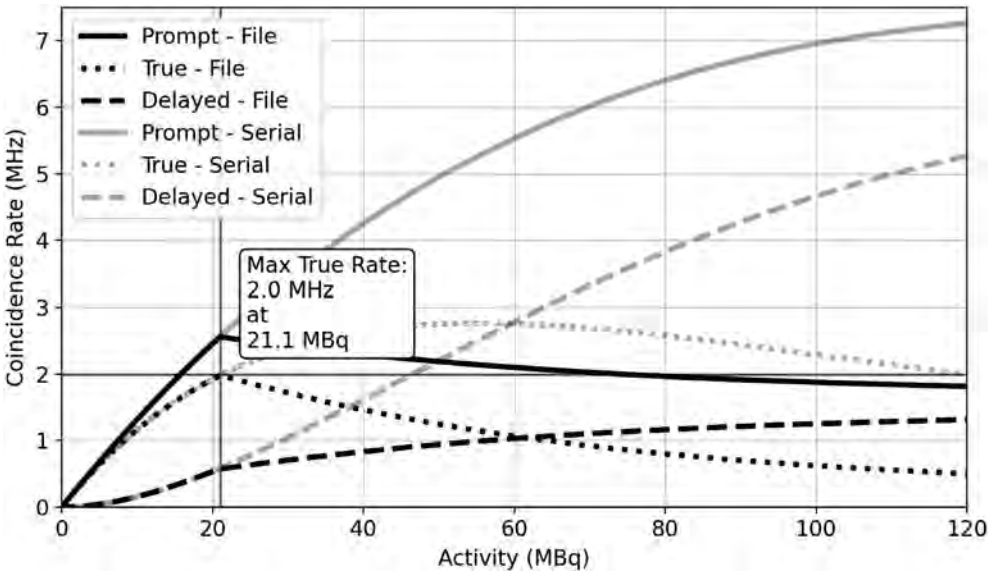

Fig. 9. Coincidence rates as a function of activity of a ^{11}C point source of approximately 120 MBq initial activity approximately placed in the centre of the central section. These data were extracted from the acquired listmode data files. The data obtained by polling the coincidence processor are overlaid in light grey for reference.

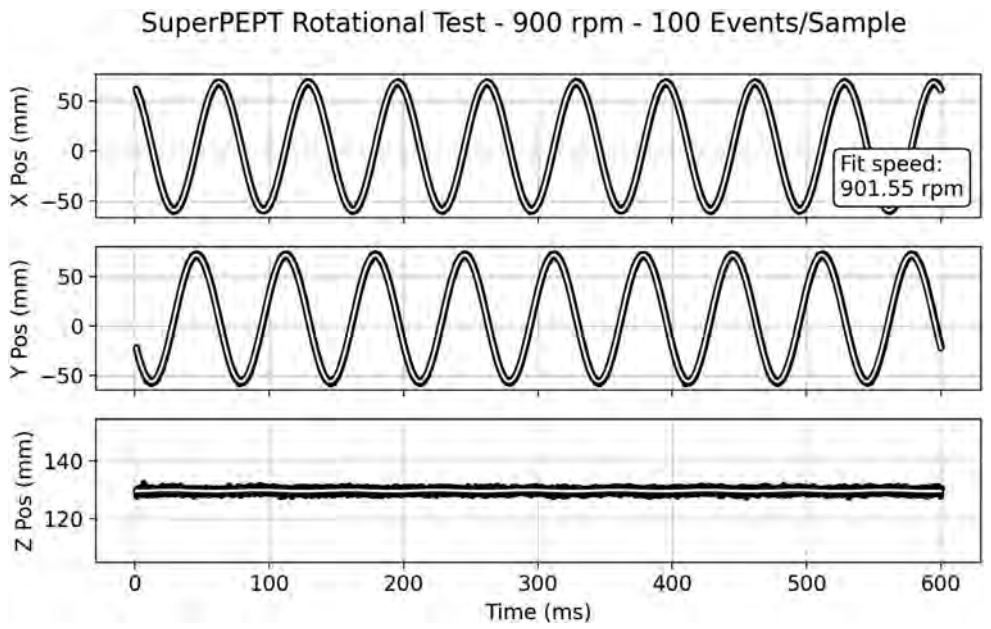

Fig. 10. Position as a function of time of a ^{18}F point source of approximately 20 MBq initial activity rotating at 900 rpm on the transaxial plane of the centre section. The data were processed using N of 100 and f of 0.4 using the Birmingham PEPT algorithm. The positional data were fitted to a model of a rotating particle on a tilted circular orbit.

4.1. Comparison to the ADAC Forte and the modular camera

To date, most PEPT studies performed at the Positron Imaging Centre use the ADAC Forte positron camera. It consists of a pair of NaI(Tl) scintillator gamma camera heads operating in coincidence with a maximum face-to-face separation of 80 cm. Its characteristics were reported by Parker et al. [4]. Operating with a face-to-face separation of 60 cm, its absolute sensitivity for a central point source is approximately 0.02 cps/Bq, so that SuperPEPT represents a factor of more than 7 increase in sensitivity. Also, the useful data rate from the Forte is limited to around 200 kHz, whereas SuperPEPT can operate at around 2 MHz. The spatial resolution of SuperPEPT is also somewhat better than for the Forte, which is characterised by a value of W_{PEPT} around 7 mm near the centre of the FOV. These properties mean that SuperPEPT is capable of much better tracking: fast-moving tracers can be located much more frequently and with increased precision, opening new possibilities for flow studies, including the use of smaller, less active tracer particles.

Another PEPT system available at the Positron Imaging Centre is the modular positron camera [5], constructed using parts from a CTI/Siemens ECAT 931 PET scanner. Sixteen buckets were mounted in individual boxes and can be rearranged into many different geometries dependent on individual experiment requirements. The modular camera system, in one of its most sensitive ring arrangements, demonstrated absolute sensitivity of about 0.03 cps/Bq for a centrally positioned point source. It also demonstrated a useful data rate of around 300 kHz. Therefore, SuperPEPT represents a factor of more than 5 increase in sensitivity and more than 6 increase in useful data rate. The performance of the modular camera system, especially the spatial resolution, varies strongly with the set-up geometry, but compared to all modular

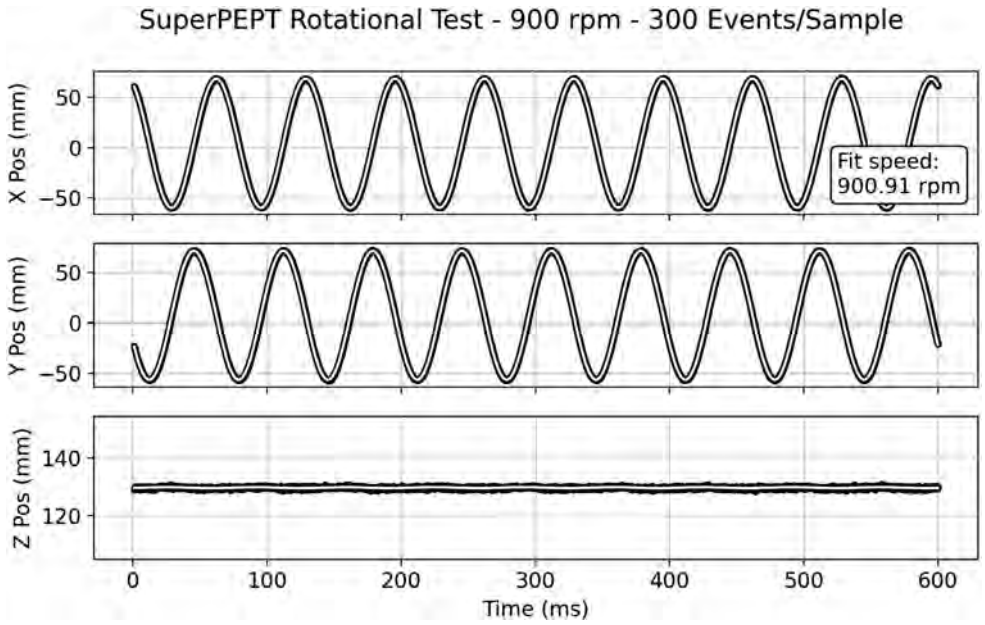

Fig. 11. Position as a function of time of a ^{18}F point source of approximately 20 MBq initial activity rotating at 900 rpm on the transaxial plane of the centre section. The data were processed using N of 300 and f of 0.4 using the Birmingham PEPT algorithm. The positional data were fitted to a model of a rotating particle on a tilted circular orbit.

Table 1
Root-mean-square deviations and fitted rotational speeds of the data to a model of a rotating particle on a tilted circular orbit along with the calculated distance travelled by the particle within the set events per sample in the Birmingham PEPT algorithm at 1.66 MHz coincidence rate.

Set Speed (rpm)	Events per Sample (N)	Fitted Speed (rpm)	RMS Error (mm)	Distance Travelled per Sample (mm)
120	100	121.4	1.04	0.05
	200	120.7	0.83	0.10
	300	120.6	0.71	0.15
480	100	480.3	1.03	0.19
	200	480.1	0.75	0.39
	300	480.1	0.63	0.58
720	100	720.0	1.05	0.29
	200	719.7	0.79	0.58
	300	719.9	0.69	0.87
900	100	901.6	1.08	0.36
	200	901.2	0.86	0.72
	300	900.9	0.82	1.09

camera configurations, SuperPEPT is capable of significantly better particle tracking.

5. Summary and future plans

These initial results show that SuperPEPT represents a significant improvement in PEPT instrumentation, with sensitivity more than seven times higher than the ADAC Forte in addition to improved spatial resolution.

These results were obtained using only two of the three sections of SuperPEPT. In the near future, the second end section will be commissioned. As well as greatly extending the axial FOV, this should further enhance the central sensitivity, through the addition of coincidences between the two end sections.

Some further work is also needed to make protective covers for the electronics and to make the software more user-friendly.

When fully operational, SuperPEPT is expected to significantly extend the scope of PEPT studies. The increased sensitivity opens the possibility of performing accurate tracking with much less activity, for example, using much smaller tracer particles, while existing tracer particles can be tracked at much higher speeds and/or with increased precision.

CRediT authorship contribution statement

D.M. Hampel: Software, Formal analysis, Investigation, Data curation, Writing – Original Draft, Writing – review & editing, Visualisation. **S. Manger:** Software, Data curation. **D.J. Parker:** Conceptualisation, Funding acquisition, Project administration, Supervision, Writing – review & editing. **Tz. Kokalova Wheldon:** Supervision, Writing – review & editing, Resources, Project administration.

Declaration of competing interest

The authors declare that they have no known competing financial interests or personal relationships that could have appeared to influence the work reported in this paper.

Acknowledgements

Financial support for construction of SuperPEPT was provided by EPSRC, UK under Programme Grant EP/R045046/1.

References

[1] D. Parker, C. Broadbent, P. Fowles, M. Hawkesworth, P. McNeil, Positron emission particle tracking - a technique for studying flow within engineering equipment, Nucl. Instrum. Methods Phys. Res. A 326 (3) (1993) 592–607, http://dx.doi.org/10.1016/0168-9002(93)90864-e.
[2] G.F. Knoll, Radiation Detection and Measurement, 4, Wiley, 2010.
[3] M. Hawkesworth, M. ÒDwyer, J. Walker, P. Fowles, J. Heritage, P. Stewart, R. Witcomb, J. Bateman, J. Connolly, R. Stephenson, A positron camera for industrial application, Nucl. Instrum. Methods Phys. Res. A 253 (1) (1986) 145–157, http://dx.doi.org/10.1016/0168-9002(86)91138-1.
[4] D. Parker, R. Forster, P. Fowles, P. Takhar, Positron emission particle tracking using the new Birmingham positron camera, Nucl. Instrum. Methods Phys. Res. A 477 (1–3) (2002) 540–545, http://dx.doi.org/10.1016/s0168-9002(01)01919-2.

[5] D. Parker, T. Leadbeater, X. Fan, M. Hausard, A. Ingram, Z. Yang, Positron emission particle tracking using a modular positron camera, Nucl. Instrum. Methods Phys. Res. A 604 (1–2) (2009) 339–342, http://dx.doi.org/10.1016/j.nima.2009.01.085.

[6] M.E. Casey, R. Nutt, A multicrystal two dimensional BGO detector system for positron emission tomography, IEEE Trans. Nucl. Sci. 33 (1) (1986) 460–463, http://dx.doi.org/10.1109/tns.1986.4337143.

[7] Siemens Gammasonics Inc, Nuclear PET group, in: ECAT EXACT Service Manual 17 60 334, first ed., 1992.

[8] CTI PET Systems Inc, Ecat ART system service manual 35 50 733, C, 1996.

[9] Siemens Medical Systems, Inc, Nuclear medicine group, in: ECAT ART Gantry Service Manual 35 49 792, first ed., 1996.

[10] Siemens Gammasonics Inc., Nuclear PET group, in: ECAT EXACT HR+ Scanner 35 49 735, first ed., 1998.

[11] T. Beyer, D.W. Townsend, T. Brun, P.E. Kinahan, M. Charron, R. Roddy, J. Jerin, J. Young, L. Byars, R. Nutt, A combined PET/CT scanner for clinical oncology, J. Nucl. Med. 41 (2000) 1369–1379.

applied sciences

MDPI

Article

Performance Evaluation of the Current Birmingham PEPT Cameras

David J. Parker *, Dawid M. Hampel and Tzanka Kokalova Wheldon

School of Physics and Astronomy, University of Birmingham, Birmingham B15 2TT, UK; d.hampel@pgr.bham.ac.uk (D.M.H.); t.wheldon@bham.ac.uk (T.K.W.)
* Correspondence: d.j.parker@bham.ac.uk

Abstract: Positron emission particle tracking (PEPT), a powerful technique for studying fluid and granular flows, has been developed at Birmingham over the last 30 years. In PEPT, a "positron camera" is used to detect the pairs of back-to-back photons emitted from positron annihilation. Accurate high-speed tracking of small tracer particles requires a positron camera with high sensitivity and data rate. In this paper, we compare the sensitivity and data rates obtained from the three principal cameras currently used at Birmingham. The recently constructed SuperPEPT and MicroPEPT systems have much higher sensitivity than the longstanding ADAC Forte and can generate data at much higher rates, greatly extending the potential for PEPT studies.

Keywords: PEPT; positron camera; particle tracking

check for updates

Citation: Parker, D.J.; Hampel, D.M.; Kokalova Wheldon, T. Performance Evaluation of the Current Birmingham PEPT Cameras. *Appl. Sci.* **2022**, *12*, 6833. https://doi.org/10.3390/app12146833

Academic Editor: Cristian FOCSA

Received: 31 May 2022
Accepted: 30 June 2022
Published: 6 July 2022

Publisher's Note: MDPI stays neutral with regard to jurisdictional claims in published maps and institutional affiliations.

1. Introduction

Positron emission particle tracking (PEPT) [1] was first developed at Birmingham in the late 1980s as a variant of the medical imaging modality positron emission tomography (PET) more suited to studying flows in engineering and the physical sciences. In PEPT, a tracer particle is labelled by incorporating a radionuclide, which decays by positive beta-decay, generating a positron that rapidly annihilates with an electron to produce a pair of 511 keV photons that are emitted back-to-back, almost exactly 180° apart. Simultaneously detecting these two photons in position-sensitive detectors mounted either side of the field of view (FOV), defines a line of response (LOR) passing close to the annihilation point, so that after detection of only a small number of such coincidence events, the location of the tracer particle can be determined by triangulation. Since the 511 keV photons are highly penetrating, fast and accurate, tracking can be performed even inside dense optically opaque systems (for example, inside the metal casings of industrial equipment).

Over the last 30 years, PEPT has been extensively used to study a very wide range of granular and fluid flows [2]. In the case of granular flows, the tracer particle is either identical to the bulk particles or closely matches their properties; for studying fluid flow, a small neutrally buoyant tracer particle is generally used.

There is constant pressure to extend the use of PEPT to track smaller particles and/or achieve more detailed tracking at high speeds. As discussed in the next section, such developments depend on developing detector systems ("positron cameras") with high sensitivity capable of recording coincidence events at high data rates. This paper briefly compares the capabilities of three positron cameras currently in use at Birmingham.

For simplicity, this paper focusses on tracking a single labelled particle. In recent years, great strides have also been made in the simultaneous tracking of multiple particles—various software approaches have recently been reviewed [3]—and these techniques will clearly benefit from the hardware developments reported below.

2. Simple Characterisation of PEPT Systems

In PEPT, the location of the radioactively labelled tracer particle is determined from triangulation of a number of detected LORs. Because of fundamental uncertainties in the decay process (the distance travelled by the positron before annihilation, and the slight acollinearity of the resulting photons) as well as limitations of the detector systems (e.g., finite crystal sizes), these LORs will exhibit a distribution of distances from the tracer location, which can be characterised by a standard deviation w. Simplistically, provided the tracer does not move significantly during the measurement, using N LORs, its position can be determined with an uncertainty of order $\frac{w}{\sqrt{N}}$.

The data also include a background of invalid events, such as random coincidences or events where one or both of the photons have scattered before detection. The Birmingham PEPT algorithm iteratively discards these invalid events, whose LORs do not pass close to the tracer position, so that only a fraction f of the detected events are useful for locating the tracer. By taking a sufficiently large sample of LORs, a stationary tracer can be located with arbitrary precision given by $\frac{w}{\sqrt{fN}}$. This relationship can be used to determine an effective value of w for the positron camera; note that in most cases the distribution of LORS will be anisotropic so that the tracer can be located better in one direction than another, but it is still useful to represent the overall 3D uncertainty by a single value.

For a moving tracer there will be an optimum sample size, large enough to give adequate statistics but not so large that the tracer moves significantly during the time interval used for location. One way of approaching this is to set this time interval Δt such that the tracer moves a distance roughly equal to the corresponding stationary location precision:

$$v\Delta t \approx \frac{w}{\sqrt{fN}} = \frac{w}{\sqrt{fR\Delta t}}, \tag{1}$$

where v is the tracer speed and R is the data rate (events per second). Rearranging this equation gives

$$\Delta t \approx \left[\frac{w^2}{v^2 fR}\right]^{1/3} \tag{2}$$

and hence an uncertainty of roughly $\left[\frac{vw^2}{fR}\right]^{1/3}$ obtained by using

$$N = R\Delta t \approx f^{-1/3}\left[\frac{Rw}{v}\right]^{2/3}. \tag{3}$$

These simple approximations work quite well provided the number of events used per location is reasonably large (>>10). For example, the ADAC Forte camera (described below) is capable of recording up to 10^5 events per second and has an intrinsic spatial resolution of around 9 mm. Assuming that 50% of the detected events are useful (f = 0.5) one might expect that a tracer moving at 1 m/s could be located every 1 mm along its path with an uncertainty of around 1 mm—this corresponds to a sample size N = 100 and reflects what is often achieved in practice. At lower data rates and/or higher tracer speeds, the data become sparser and the algorithm finds it harder to discriminate against invalid events.

Data rate R is therefore crucial for tracking at high speeds. We define the sensitivity Γ of the positron camera as the limit, as source activity A tends to zero of the fraction of positrons emitted by the source, which result in detected events, so that $R = \Gamma A$. For a symmetrical system and a source at the centre of its FOV, this sensitivity can be expressed as the product $\Omega\varepsilon^2$, where Ω is the fraction of the total 4π solid angle covered by detectors and ε is the quantum efficiency of these detectors for detecting 511 keV photons—this expression relies on the fact that for a central source, if one photon is emitted in a direction so as to strike a detector, its partner will automatically strike the opposite detector. For an off-centre source, this is no longer true, so the sensitivity falls: as shown in Figure 1, movement along the axis linking the detectors leads to a relatively small drop in sensitivity

but moving transversely, the sensitivity falls approximately linearly and reaches zero at the edge of the FOV.

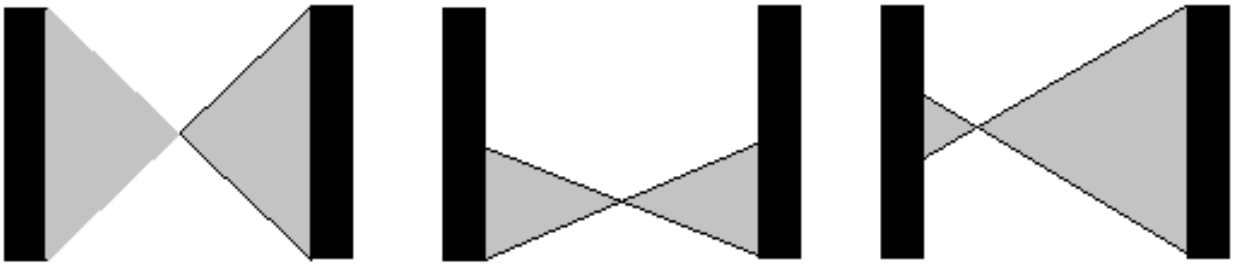

Figure 1. The solid angle for detecting pairs of back-to-back photons is maximum for a source at the centre of the FOV (**left**). As the source moves transverse to the detectors, the angular acceptance falls approximately linearly (**centre**). Movement of the source along the axis between the detectors leads to a smaller reduction in angular acceptance, which is limited by the solid angle of the farther detector (**right**).

As activity increases, the linear relationship between activity and recorded true coincidence rate fails due to the increasing effects of deadtime. Furthermore, since the random coincidence rate is proportional to A^2, the data include an increasing background of random coincidences. The maximum useful data rate for a system is determined by a combination of these two effects, both of which are directly dependent on the singles data rates of individual detectors. If the solid angle is divided into n independent identical detectors (for example the "buckets" of a PET scanner), the singles rate in each is equal to $2A\Omega\varepsilon/n$ (the factor 2 arises from the fact that two photons are emitted in each annihilation), so that for a central source, the ratio of singles rate to coincidence rate is equal to $2/n\varepsilon$. To maximise the possible count rate, it is necessary to use multiple detectors each with high efficiency.

In summary, the key parameters of a PEPT imaging system are the intrinsic spatial resolution and the data rate. It is also important that the fraction f of useful events is as large as possible: for most systems f is indeed large for a low activity bare tracer, but reduces when the tracer is surrounded by material or for more active tracers when the proportion of random coincidences becomes significant.

Since there are practical limits on the activity which can be generated in a small tracer particle, to achieve a high data rate requires high sensitivity, which implies large solid angle and also high efficiency detectors. Because of the dependence on singles rates, the ultimate data rate that can be achieved is particularly dependent on having high efficiency.

In many cases, compromises are required in order to cover the required field of view. Often this involves spacing out detectors, so that they have gaps between them—it should be noted that this is equivalent to using detectors of correspondingly lower efficiency, with all the consequent drawbacks.

3. Development of Positron Cameras at Birmingham

3.1. History of Birmingham PEPT Systems

PEPT was first developed at Birmingham in the 1980s using a "positron camera" comprising a pair of position sensitive multiwire proportional chambers (MWPCs) [4]. The major weakness of this system was its low sensitivity—each MWPC had a quantum efficiency of only 7% for detecting 511 keV photons, so that the overall efficiency for detecting a pair of such photons, both incident on detectors, was less than 0.5%. The maximum useful data rate from this camera was only around 3 kHz. Moreover, because each detector had multiple interaction planes, the data included a significant fraction of events which had scattered in a previous plane before detection, so even for a bare source f was less than 0.4 [1].

In 1999, this camera was replaced by a Forte camera (ADAC Laboratories) [5] comprising a pair of gamma camera heads, each containing a crystal of sodium iodide 16 mm thick and with a quantum efficiency for detecting 511 keV photons of approximately 23%. The Forte, which is still in regular use, has a similar geometry to the original MWPC system, consisting of a pair of rectangular detectors, with active area 51 cm × 38 cm, which are mounted either side of the system of interest with a face-to-face separation adjustable between 25 cm and 80 cm. A typical operating separation of 50 cm corresponds to a geometric acceptance of approximately 0.3 for a central source, but as discussed above, this falls off linearly as the source moves off centre.

Most medical PET scanners use rings composed of high efficiency scintillation crystals to image a relatively narrow slice of a human patient or a laboratory animal. Crystals are grouped into modules ("buckets") each with its own set of electronics. Since these systems are inherently modular, it is in principle straightforward to reconfigure them to give a geometry more suitable for PEPT studies of engineering systems. In the early 2000s, the Birmingham group started reconfiguring the detectors from early CTI/Siemens ECAT PET scanners to develop PEPT systems. A modular positron camera was developed comprising 16 modules, each containing four scintillator detectors [6]. The detectors were blocks of bismuth germanate (BGO), each approximately 50 × 60 mm^2 in area and 30 mm thick. Each block was cut into an 8 × 8 array of crystal elements, each 6.3 × 6.8 mm^2, and was coupled to four photomultiplier tubes (PMTs) in such a way that comparing the four PMT outputs allowed the crystal element to be uniquely identified.

The capability of this system was compared to that of the Forte when operated in a similar geometry [6]: the boxes were stacked two wide by four high giving two rectangular detector arrays each approximately 66 × 35 cm^2 and separated by 50 cm. Despite the much higher efficiency of the BGO crystals, because of the gaps between blocks, the sensitivity in this geometry is only a little higher than for the Forte. Much more recently, a large modular array (LaMA) for PEPT was constructed comprising 48 buckets.

The great advantages of these modular systems are their transportability and flexible geometry, enabling tracking to be performed on large-scale industrial equipment, but at the cost of reduced sensitivity due to the gaps between blocks. It has been clear for some time that much better results would be obtained by developing a dedicated high sensitivity system with a field of view large enough to accommodate laboratory-scale equipment. Two such systems have recently been constructed at Birmingham: SuperPEPT and MicroPEPT. They are briefly described in the next sections; then we present an experimental comparison of these systems with the ADAC Forte.

3.2. SuperPEPT

SuperPEPT was constructed principally by reconfiguring components from an ECAT HR+ PET scanner. As originally configured, this scanner comprised 24 buckets, each consisting of 12 high resolution BGO blocks, each approximately 32 × 35 × 30 mm^3 and subdivided into 64 pixels 4.0 × 4.4 mm^2. To extend the FOV, in SuperPEPT we have replaced some of these high-resolution blocks with the lower resolution blocks from an EXACT31 scanner, which are 52 × 52 × 20 mm^3 and divided into 64 6.4 × 6.4 mm^2 pixels.

As shown in Figure 2, SuperPEPT comprises three cylindrical sections: a central section made with the original high-resolution HR+ blocks and two end sections made with the same electronics but the lower resolution EXACT31 blocks. The internal diameter is approximately 40 cm throughout. The central section consists of 16 buckets, configured as six rings of detector blocks with 32 blocks per ring, and has an axial length of 234 mm. Each end section consists of four buckets of EXACT31 blocks, configured in two rings (24 blocks per ring) and has an axial length of 110 mm. Axial gaps of 45 mm between the central section and the end sections bring the overall axial length to 544 mm.

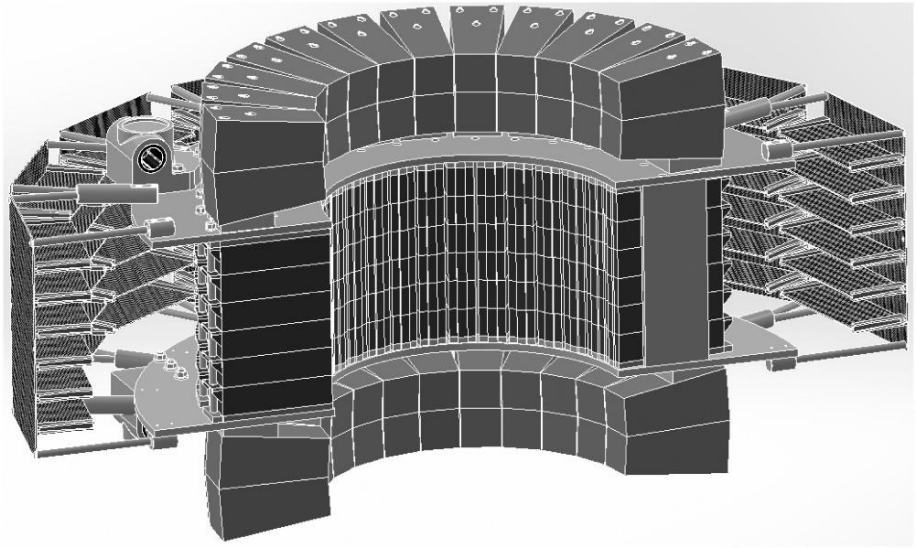

Figure 2. Diagram of SuperPEPT. Reprinted from [7], Copyright (2022), with permission from Elsevier.

To increase the effective efficiency of the detectors, all the blocks were operated with a lower-level discriminator (LLD) value of 150 keV rather than the value of 350 keV usually adopted for PET imaging. Data from the HR+ coincidence processor are acquired in listmode using a new data-acquisition system (Scintron 7.2, from MiE GmbH, Seth, Germany). Initial results from SuperPEPT operating with only the central section and one end section were recently reported [7]. Since then, the second end section has been brought into use. A full report on the performance of the complete system will be published shortly; meanwhile, this paper presents its key parameters.

SuperPEPT has an overall FOV of 40 cm diameter and 54 cm axially, comparable to the ADAC Forte. For a source at the centre of the FOV, the central section has a geometrical acceptance of approximately 0.5 and the addition of the end sections increases this to approximately 0.67.

3.3. MicroPEPT

As well as clinical systems intended for imaging slices of the human body, equipment manufacturers have recently devoted considerable investment to developing pre-clinical PET systems designed for high resolution imaging of small animals. Some time ago, Birmingham acquired a microPET P4, manufactured by Concorde Microsystems Inc., and used this to develop a prototype MicroPEPT system, intended to provide high resolution tracking over a smaller FOV than that of SuperPEPT.

The characteristics of the original P4 were reported by Tai et al. [8]. Its detectors are blocks of lutetium oxyorthosilicate (LSO) scintillator, $19 \times 19 \times 10$ mm^3, which (in a similar way to the BGO blocks of the ECAT systems) are each cut into an 8×8 array of crystal elements, giving a pixel size of 2.4×2.4 mm^2, and connected via a bundle of optical fibres to a position-sensitive PMT. In the P4, these blocks were mounted in sets of four in cassettes, and the scanner contained a total of 42 cassettes, arranged in a single ring with internal diameter 26 cm, corresponding to 32 individual crystal rings covering an axial field of view of 7.8 cm. Because the PMTs are wider than the crystals to which they are coupled, each cassette splays out as shown in Figure 3.

To produce a system with a longer axial field of view more suitable for PEPT, at Birmingham the 42 cassettes were rearranged in two adjacent rings to make a camera whose axial FOV is comparable to its diameter. Because of the way the cassettes splay out, the cassettes in the two rings are angled in either side of the central mounting plate, creating gaps between them; although, at the two extremes, the crystals butt together to create a ring with internal diameter 130 mm, in the centre plane the internal diameter is 165 mm and there are gaps approximately 5 mm wide between the crystals (Figure 4).

Figure 3. MicroPET cassette as used in constructing MicroPEPT: the four LSO crystals on the left of the picture are connected via light guides to position sensitive PSDs on the right.

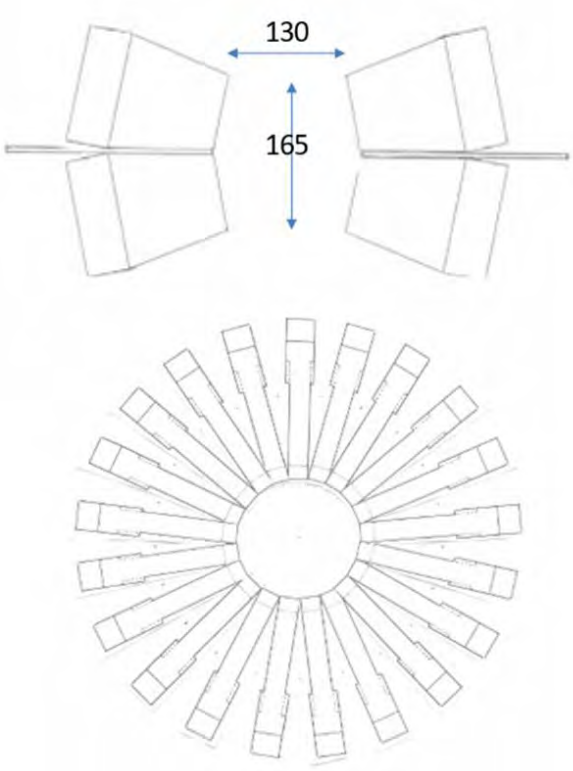

Figure 4. MicroPEPT geometry: the 42 cassettes are mounted in two rings, above and below the central mounting plate, with the detectors in the upper ring staggered relative to those in the lower ring.

MicroPEPT operates with a coincidence resolving time of 6 ns; in order to increase their effective efficiency, the blocks were operated with an LLD value of 200 keV rather than the usual 350 keV.

4. Materials and Methods

As a simple characterisation of the three scanners, data were measured for sources mounted at the centre of the FOV in each case. This represents a "best case" scenario, but is useful as a basis for comparing their performance.

The sensitivity and count rate performance of the three cameras were investigated by making repeated measurements using a centrally mounted ^{11}C source. ^{11}C sources were produced by activating small pieces of graphite using a beam of 28 MeV protons from the Birmingham MC40 Cyclotron. The initial activity of each source was measured using a Capintec CRC-15R Radioisotope Calibrator, and subsequent activities were calculated based on the known half-life of 20.38 min, where the elapsed time was measured to within 10 s. The principal uncertainty on all these measurements arises from the accuracy of the CRC-15R's calibration, which should be correct to within 2%. Note that any error in calibration will affect all the measurements in the same way, so comparison of the relative sensitivities of the systems is unaffected.

For each set of measurements, a ^{11}C source of initial activity around 50 MBq was mounted at the centre of the FOV of the camera under study. In each case, its location was determined using the Birmingham PEPT algorithm and was confirmed to lie within 5 mm of the central point. As the ^{11}C source decayed over a period of up to 3 h (down to an activity of approximately 100 kBq), 10 s data files were recorded at intervals, and were then analysed to determine the data rates.

Both MicroPEPT and SuperPEPT simultaneously record both the usual prompt coincidences and also "delayed" coincidences in which the signal from one of the two detectors has been delayed by significantly more than the resolving time before checking for the presence of a coincidence. These delayed coincidences correspond only to random coincidences, whereas the prompt coincidences comprise both true coincidences and random coincidences. Hence the rate of true coincidences can be determined by subtracting the delayed coincidences from the prompt coincidences. In the case of the ADAC Forte only prompt coincidences are recorded, so information on the random coincidence rate is not explicitly available.

The active region of the ^{11}C sources was somewhat extended (up to 5 mm in diameter) so to assess the tracking performance of each camera point, sources containing ^{18}F were used. ^{18}F was produced in solution by irradiating water enriched in ^{18}O with a beam of 10.8 MeV protons from the Birmingham MC40 Cyclotron and was then absorbed into a bead of ion-exchange resin <1 mm in diameter. The activity of each particle labelled in this way was measured using the Capintec CRC-15R. The source was then mounted in the FOV and the PEPT algorithm used to confirm that it was within 5 mm of the centre of the the FOV (within 2 mm in the case of MicroPEPT). Data were recorded for different levels of activity and were analysed using the original Birmingham PEPT algorithm [1] taking the sample size N as 1000 and varying the value of f so as to minimise the 3D standard deviation of the set of resulting locations.

5. Results

5.1. ADAC Forte

Figure 5 shows the count rate data measured for a ^{11}C source mounted at the centre of the FOV of the ADAC Forte operating at a face-to-face separation of 50 cm. As the activity tends to zero, the data approach the straight line corresponding to a sensitivity of 0.014. Combining this value with the angular acceptance of 0.3 implies that each detector has a quantum efficiency of approximately 22% for detecting 511 keV photons, almost identical to the value of 23% reported when this camera was first evaluated.

As seen in Figure 5, as the activity increases, the data rate quickly drops below that expected for a sensitivity of 0.014, due to the effects of dead-time in the detectors and data acquisition hardware. The data rate saturates at a little over 120 kHz. A source of activity 15 MBq mounted centrally gives a data rate of approximately 110 kHz, and this can be regarded as the maximum desirable activity for use with this system.

As currently set up, this camera does not report the rate of random coincidences, but based on previous measurements [5], the randoms rate is expected to be relatively low (<10%) even for an activity of 15 MBq.

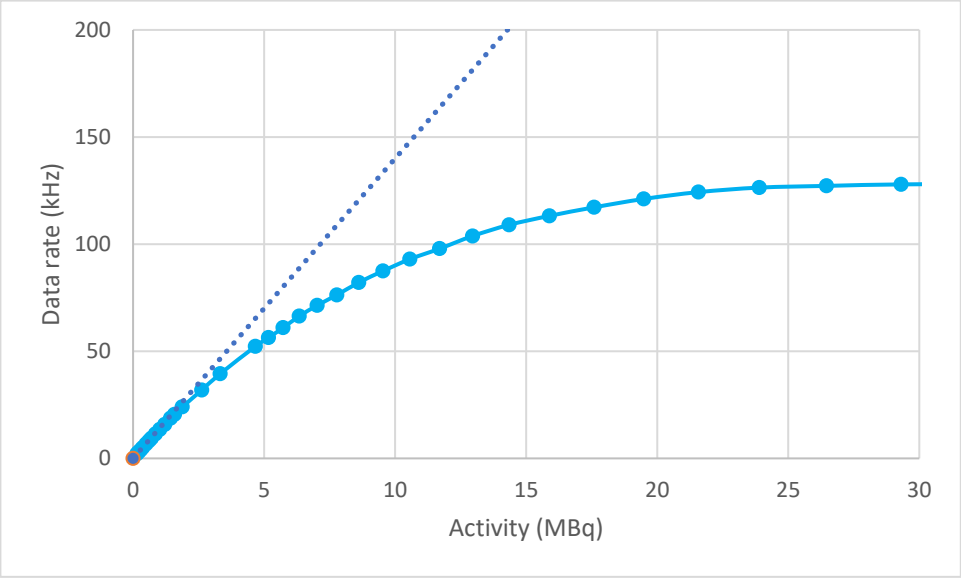

Figure 5. Coincidence data rate recorded from the ADAC Forte for a central ^{11}C source of varying activity. The dotted line corresponds to a sensitivity of 1.4%.

Using the Birmingham PEPT algorithm to analyse data from a low activity ^{18}F point source mounted at the centre of the FOV, the optimum value of f was found to be approximately 0.6, and the effective value of w was found to be approximately 8.5 mm. This value is fortuitously similar to the spatial resolution often quoted for the detector heads of this camera, but corresponds to a completely different quantity. When a gamma-ray interacts in one of the heads, the PMTs localise the centroid of the resulting light with a spatial resolution of around 8 mm (FWHM of the 2D distribution). On the other hand, w represents the standard deviation in 3D of the LORs around the source and is dominated by the uncertainty in the direction linking the detector heads.

As the activity increases, the data quality deteriorates slightly: at an activity of 7.5 MBq the optimum value of f is around 0.45 and the corresponding w value is 9.5 mm.

5.2. SuperPEPT

Figure 6 shows the data rates measured from SuperPEPT using a central ^{11}C source of varying activity. The kink at around 13 MBq is due to the bandwidth of the data acquisition, which can record a maximum data rate of 3.1 MHz (sum of prompt and delayed coincidences). (In fact, the true limit is actually lower: the system can buffer approximately 1.5×10^9 events at 3.1 MHz, but thereafter can only record at a little over 2 MHz).

At low activity, the prompt coincidence rate is consistent with a sensitivity of 22% for a central source. Combining this with the total angular acceptance of 0.67 implies an average detector efficiency of approximately 57%. This figure represents an average over the mix of HR+ and EXACT31 blocks. Discarding events involving either of the end sections, the sensitivity measured using just the central section is approximately 16% and combining this with the angular acceptance of 0.5 for this central section again implies an effective detector efficiency of 57% for this central section. The actual efficiency of the HR+ blocks operated with a LLD value of 150 keV is somewhat higher than this. So as to achieve the internal diameter of 40 cm the HR+ are mounted with gaps of approximately 4 mm between them, and no allowance was made for these gaps in calculating the angular acceptance of this cylindrical section.

As the activity increases, the effective sensitivity drops due to increasing dead time. Note that the important rate is that of true coincidences—fortuitously, when considering the total prompt coincidence rate the effect of dead-time is almost balanced by the increasing contribution of random coincidences. Although its presence is clear, dead time is actually quite modest—at an activity of 10 MBq the true coincidence rate (approximately 1.87 MHz)

is only 15% lower than that predicted on the basis of 22% sensitivity. Moreover, at this activity, random coincidences contribute only 11% of the total prompt coincidence rate.

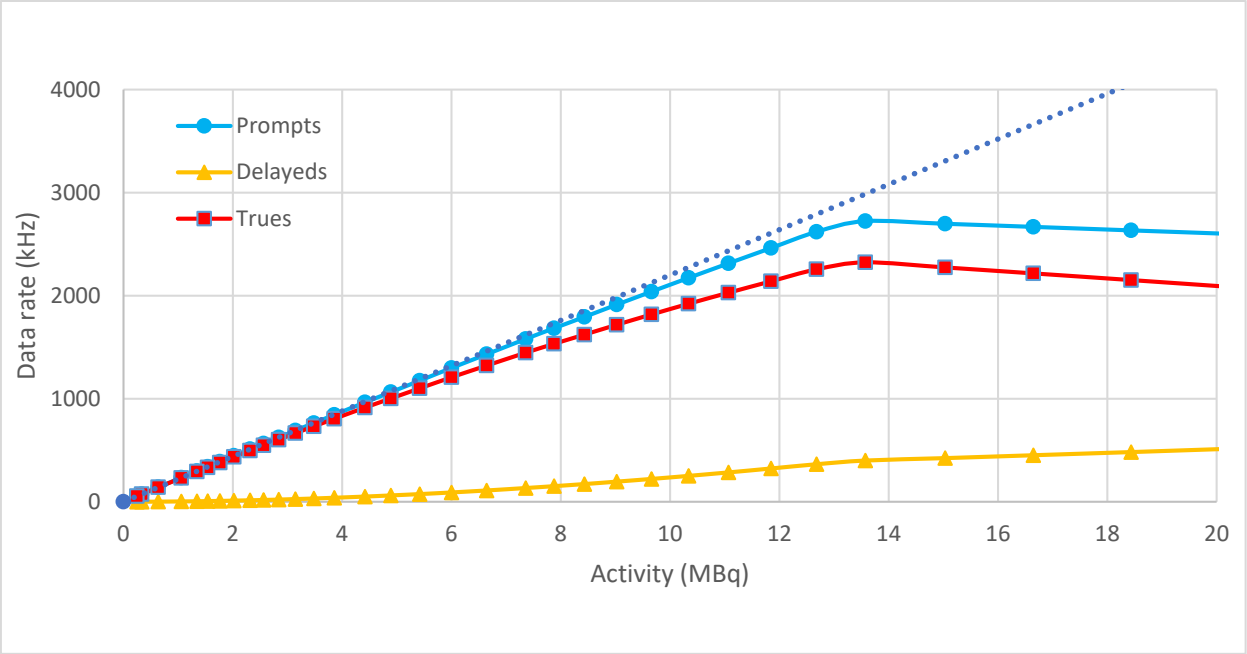

Figure 6. Data rates measured from SuperPEPT for a central ^{11}C source of varying activity. The upper set of points shows the total coincidence rate, the lower set the delayed coincidence rate, and the middle set the rate of true coincidences given by the difference prompt minus delayed. The dotted line corresponds to a sensitivity of 22%.

Using the Birmingham PEPT algorithm to process the point source data measured at low activity, optimum precision of location was found with a value $f \approx 0.6$, and corresponds to an effective value of $w \approx 6$ mm. Almost identical results were found even at activities up to 12 MBq (data rates well over 2 MHz).

Using the formulae derived in Section 2, these values imply that a 10 MBq tracer can be located with an uncertainty of around 0.3 mm every 0.3 ms if moving at 1 m/s, and with an uncertainty of around 0.65 mm every 6.5 ms if moving at 10 m/s.

5.3. MicroPEPT

Figure 7 shows the data rates measured from MicroPEPT using a central ^{11}C source of varying activity. The MicroPEPT data acquisition system can record up to 3.4 M events/s (prompt + delayed coincidences)—for a central source this limit is reached at an activity of approximately 50 MBq, and above this activity the true coincidence rate drops as random coincidences gradually take a larger fraction of the available rate.

At low activity, the rate data are consistent with a sensitivity of 5.4% for a central source. As the activity increases, the effective sensitivity (trues rate as a fraction of source activity) gradually reduces due to increasing dead-time, and the data also contain a significant fraction of random coincidences, but reliable tracking is still possible.

Using the Birmingham PEPT algorithm to process the point source data measured at low activity, optimum precision of location was found with a value $f \approx 0.50$, and corresponds to an effective value of $w \approx 3$ mm. Almost identical results were found even at activities up to 20 MBq (data rates up to 1 MHz).

Using the formulae derived in Section 2, these values imply that a 20 MBq tracer can be located with an uncertainty of around 0.25 mm every 0.25 ms if moving at 1 m/s, and with an uncertainty of around 0.6 mm every 6 ms if moving at 10 m/s.

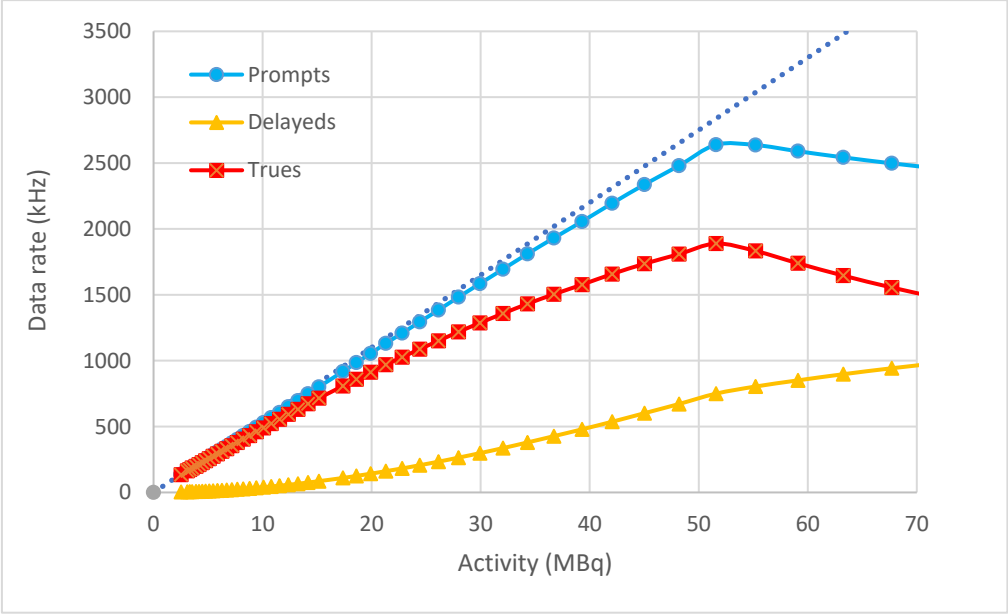

Figure 7. Data rates measured from MicroPEPT for a central ^{11}C source of varying activity. The upper set of points shows the total coincidence rate, the lower set the delayed coincidence rate, and the middle set the rate of true coincidences given by the difference prompt delayed. The dotted line corresponds to a sensitivity of 5.4%.

6. Discussion

The key parameters of the three positron cameras are compared in Table 1.

Table 1. Comparison of the three positron cameras.

Camera	FOV	Sensitivity at Centre	Effective w Value	Maximum True Coincidence Rate
ADAC Forte	51 cm × 38 cm × 50 cm *	1.4%	8.5 mm	0.12 MHz
SuperPEPT	40 cm diameter 54 cm axially	22%	6 mm	2.3 MHz
MicroPEPT	13 cm diameter 16.5 cm axially	5.4%	3 mm	2 MHz

* Separation adjustable from 25–80 cm: data reported here are for a separation of 50 cm.

Figure 8 compares the data rates of the three systems as a function of source activity for a central source. For both SuperPEPT and MicroPEPT, the value plotted is the true coincidence rate, obtained as the difference between the rates of prompt and delayed coincidences. The curve for the ADAC Forte shows the total prompt coincidence rate, so overestimates the trues rate.

Both SuperPEPT and MicroPEPT have much higher sensitivity than the Forte and are capable of delivering much higher data rates, enabling much more precise tracking of fast-moving tracers.

The sensitivity of MicroPEPT is approximately four times lower than that of SuperPEPT. This lower sensitivity is balanced by improved spatial resolution ($w \approx 3$ mm for MicroPEPT, $w \approx 6$ mm for SuperPEPT) so that for the same source activity, the precision of tracking achieved by the two systems is very similar. However, the data rate of SuperPEPT falls off above an activity of approximately 13 MBq due to the limited bandwidth of the data acquisition system, whereas that of MicroPEPT continues to increase up to 50 MBq activity, so that if tracer activity is not a limitation, MicroPEPT is able to achieve better tracking than SuperPEPT (over its much more limited FOV). In future, SuperPEPT might benefit from employing a data acquisition system with higher bandwidth, but it already represents a dramatic improvement on previous PEPT systems.

For simplicity, all the results presented here are for a single tracer particle mounted at the centre of the FOV. For an off-centre source, the absolute data rates will be lower, but the comparison between the three systems remains broadly similar. SuperPEPT and MicroPEPT also offer great potential for simultaneous tracking of multiple tracer particles.

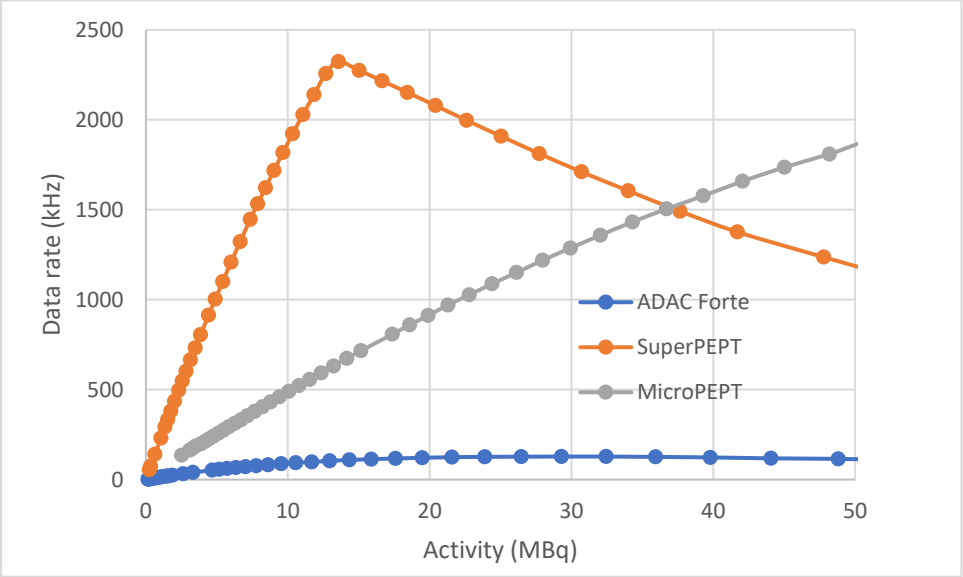

Figure 8. Comparison of the data rates recorded for central ^{11}C sources of varying activity using the three cameras. For SuperPEPT and MicroPEPT, the curves show the rate of true coincidences, obtained as the difference between the measured rates of prompt and delayed coincidences; for the ADAC Forte the total prompt coincidence rate is plotted.

Author Contributions: Funding acquisition, D.J.P.; Investigation, D.J.P. and D.M.H.; Methodology, D.J.P.; Software, D.M.H.; Supervision, T.K.W.; Writing—original draft, D.J.P.; Writing—review & editing, D.J.P., D.M.H. and T.K.W. All authors have read and agreed to the published version of the manuscript.

Funding: Financial support for construction of SuperPEPT and MicroPEPT was provided by EPSRC, UK under Programme Grant EP/R045046/1.

Institutional Review Board Statement: Not applicable.

Informed Consent Statement: Not applicable.

Data Availability Statement: Not applicable.

Conflicts of Interest: The authors declare no conflict of interest.

References

1. Parker, D.J.; Broadbent, C.J.; Fowles, P.; Hawkesworth, M.R.; McNeil, P. Positron emission particle tracking—A technique for studying flow within engineering equipment. *Nucl. Instrum. Methods Phys. Res. Sect. A* **1993**, *326*, 592–607. [CrossRef]
2. Windows-Yule, C.R.K.; Seville, J.P.K.; Ingram, A.; Parker, D.J. Positron emission particle tracking of granular flows. *Annu. Rev. Chem. Biomol. Eng.* **2020**, *11*, 367–396. [CrossRef] [PubMed]
3. Windows-Yule, C.R.K.; Herald, M.T.; Nicusan, A.L.; Wiggins, C.S.; Pratx, G.; Manger, S.; Odo, A.E.; Leadbeater, T.; Pellico, J.; de Rosales, R.T.M.; et al. Recent advances in positron emission particle tracking: A comparative review. *Rep. Prog. Phys.* **2022**, *85*, 016101. [CrossRef] [PubMed]
4. Hawkesworth, M.R.; O'Dwyer, M.A.; Walker, J.; Fowles, P.; Heritage, J.; Stewart, P.A.E.; Witcomb, R.C.; Bateman, J.E.; Connolly, J.F.; Stephenson, R. A positron camera for industrial application. *Nucl. Instrum. Methods Phys. Res. Sect. A* **1986**, *253*, 145–157. [CrossRef]
5. Parker, D.J.; Forster, R.N.; Fowles, P.; Takhar, P.S. Positron emission particle tracking using the new Birmingham positron camera. *Nucl. Instrum. Methods Phys. Res. Sect. A* **2002**, *477*, 540–545. [CrossRef]
6. Parker, D.J.; Leadbeater, T.W.; Fan, X.; Hausard, M.N.; Ingram, A.; Yang, Z. Positron emission particle tracking using a modular positron camera. *Nucl. Instrum. Methods Phys. Res. Sect. A* **2009**, *604*, 339–342. [CrossRef]

7. Hampel, D.M.; Manger, S.; Parker, D.J.; Kokalova Wheldon, T.K. SuperPEPT: A new tool for positron emission particle tracking; first results. *Nucl. Instrum. Methods Phys. Res. Sect. A* **2022**, *1028*, 166254. [CrossRef]
8. Tai, Y.C.; Chatziioannou, A.; Siegel, S.; Young, J.; Newport, D.; Goble, R.N.; Nutt, R.E.; Cherry, S.R. Performance evaluation of the microPET P4: A PET system dedicated to animal imaging. *Phys. Med. Biol.* **2001**, *46*, 1845–1862. [CrossRef]

IEEE Access
Multidisciplinary | Rapid Review | Open Access Journal

Received 8 December 2022, accepted 4 March 2023, date of publication 10 March 2023, date of current version 17 March 2023.

Digital Object Identifier 10.1109/ACCESS.2023.3255505

APPLIED RESEARCH

Monte Carlo Model of the Large Modular Array for Positron Emission Particle Tracking

MATTHEW HERALD[1], DAWID HAMPEL[2], TZANY KOKALOVA WHELDON[2,3], JONATHAN SEVILLE[1,3], AND CHRISTOPHER WINDOWS-YULE[1,3]

[1]School of Chemical Engineering, University of Birmingham, B15 2TT Birmingham, U.K.
[2]School of Physics and Astronomy, University of Birmingham, B15 2TT Birmingham, U.K.
[3]Positron Imaging Centre, University of Birmingham, B15 2TT Birmingham, U.K.

Corresponding author: Matthew Herald (mxh1092@bham.ac.uk)

This work was supported in part by the Engineering and Physical Science Research Council under Grant EP/T034327/1, and in part by the Advanced Imaging and Numerical Modelling of Segregation and Transport of Plastics in Fluidised Beds: Toward a Circular Economy for Plastics.

ABSTRACT Positron emission particle tracking (PEPT) is a non-invasive technique used to study fluid, granular, and multi-phase systems of interest to academia and industry. PEPT employs position-sensitive radiation detectors to record gamma rays in coincidence and track the movement of discrete sources. A modular detector array, the Large Modular Array (LaMA), has been constructed at the University of Birmingham's Positron Imaging Centre (PIC) to enable custom detector geometries. To estimate the LaMA's performance characteristics prior to experimentation, assist in developing optimised camera geometries, and determine ideal PEPT tracer characteristics a Monte Carlo model of LaMA is created and subsequently validated with experimental measurements. Validation is achieved through comparisons of the spatial resolution and count-rate response following the National Electrical Manufacturers Association (NEMA) industry standard protocol. Notably, the model's pulse-processing chain is autonomously calibrated to match experimental measurements using a recently developed technique which applies an evolutionary algorithm. The results show the simulated spatial resolution of the validated model matches the experiment to within 5%. Additionally, the total, true, and corrupted count-rates are reproduced to a mean error of 3.41%. This calibrated detector model strengthens the PIC's modelling capabilities. To facilitate future research, this model has been made publicly available through the PIC's GitHub repository.

INDEX TERMS Digital twin, GATE, Monte Carlo, positron emission particle tracking.

I. INTRODUCTION

Positron emission particle tracking (PEPT) is an imaging technique used to study opaque engineering and scientific systems using flow-following tracers labelled with positron-emitting radionuclides [1]. Positrons annihilate with electrons in close proximity to the labelled tracer, producing back-to-back 511 keV gamma-rays which can be detected with position-sensitive radiation detectors such as gamma cameras or positron emission tomography (PET) scanners [2]. Reconstruction of the labelled tracer position requires detecting both annihilation photons in coincidence to form a line-of-response (LoR) and applying a PEPT algorithm on a sample of LoRs to find the most likely annihilation point [3]. By detecting the tracer successively, a time-dependent trajectory is developed which can be analysed to determine system properties such fully three-dimensional velocity fields, tracer re-circulation times, and diffusivity [1]. PEPT has been used extensively over the last 30 years to study a variety of equipment ranging from coffee roasters, washing machines, and liquid metal castings [4], [5], [6].

To perform a PEPT measurement, equipment must first be moved to a lab and placed in the field-of-view (FOV) of a position-sensitive detector. At the University of Birmingham's Positron Imaging Centre (PIC), detectors like the ADAC Forte and SuperPEPT have been acquired or built specifically for PEPT measurements [7]. The Forte dual-headed positron camera was acquired because the two

The associate editor coordinating the review of this manuscript and approving it for publication was Giovanni Merlino.

detector heads can be separated up to between 250 mm and 800 mm, which enables the accommodation of a variety of equipment while optimising detector sensitivity. This system can record LoRs up to approximately 100 kHz [8]. Additionally, SuperPEPT, which has recently been constructed using components from CTI/Siemens ECAT EXACT 31, ART, and EXACT HR+ scanners has a cylindrical geometry of about 400 mm in diameter and 544 mm in length. The diameter can be separated up to 600 mm to place an experiment in the FOV, but must be closed again to record data. SuperPEPT records LoRs up to 2500 kHz, a factor of 20 higher than the Forte, enabling improved spatiotemporal resolution of PEPT trajectories [9].

However, there are instances where experimental equipment is too large or consists of awkward geometries which cannot be easily fit into the FOV of existing systems. To address this, a modular detector array, named the Large Modular Array (LaMA), has been designed to be assembled around experimental systems in custom geometries [10]. LaMA consists of building block, called 'boxes', which contain four ECAT951 block detectors. These boxes can be placed in nearly any configuration and connected to a coincidence processor, allowing flexible geometries to be designed for imaging large-scale industrial equipment [11]. Since the LaMA is reconfigured in a different geometry for each experiment, the performance characteristics of the camera are difficult to predict. As such, estimating the spatiotemporal resolution of the expected trajectories, designing an optimised geometry, and selecting an appropriate tracer activity for a given experiment can be challenging.

In this work we describe and validate a Monte Carlo model of the LaMA which will be used to help optimise experiments in the future. This model is created using the Geant4 Application for Tomographic Emission (GATE), a Monte Carlo radiation transport software which emulates the detector geometry, radioactive sources, and electronic pulse-processing of particles interacting with the detector [12], [13]. The performance of the camera in a simple geometry is characterised following the industry-standard National Electrical Manufacturers Association (NEMA) protocol [14]. Notably, the pulse-processing model is calibrated by through a recently developed method which compares the simulated and real performance characteristics and tunes parameters of the pulse-processing model using an evolutionary algorithm [15], [16], [17].

A. THE LARGE MODULAR ARRAY (LaMA)

The idea for the LaMA was developed at the PIC in the early 2000s, growing out of the need to have a detector system which could image large or awkward industrial systems and potentially be able to be transported to equipment which could not be moved. One feature that was identified as being key to this future system was being modular so that custom geometries could be tailored to each experiment. To this end, initially, three CTI/Siemens ECAT ring scanners were acquired and dismantled to retrieve the block detectors which could then be reassembled into a new geometries [10].

Each block detector consists of an 8×8 bismuth germanate (BGO) crystal array, with each crystal measuring 6.25 mm in width, 6.75 mm in height, and 30 mm in thickness. The BGO crystals are optically coupled to a 5 mm thick glass light guide and four photo-multiplier tubes (PMTs), each 100 mm in length. Using the 192 block detectors extracted from the PET scanners, a modular unit consisting of four blocks was designed. Each of these units are termed a 'box' and 48 boxes were constructed in total. Each box is approximately 360 mm in width, 95 mm in height (including spacers), and 460 mm in thickness with each of the four block detectors spaced 90 mm apart from centre-to-centre. A single box is shown on the left side of Fig. 1 and a stack of four boxes is shown on the right. These modular units are the fundamental building blocks of LaMA. Currently, up to 32 boxes can be connected to a single coincidence processor unit to form a detector array. By using more than one coincidence processor and merging the data streams in post-processing, all 48 boxes can be used simultaneously, but coincidences can only be formed between boxes connected to a shared coincidence processor.

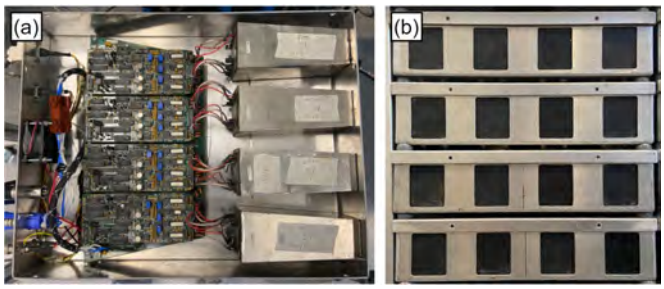

FIGURE 1. (a) A view inside a single box where four block detectors are mounted. (b) A stack of four boxes. The geometry used in this work is two stacks of four boxes separated by 500 mm.

B. Geant4 APPLICATION FOR TOMOGRAPHIC EMISSION (GATE)

GATE is a Monte Carlo radiation transport and detector simulation software designed for emulating the geometries, sources, and pulse-processing chain of imaging systems [12]. Many different types of detectors and imaging modalities have been modelled using GATE, including other detector systems used for PEPT such as the ADAC Forte and Siemens Inveon [13], [18], [19]. GATE is a useful tool for modelling PEPT experiments because it provides output comparable to real detectors and serves as 'sandbox' through which changes in the detector or source properties can be assessed, synthetic data can be processed to verify imaging techniques, or limits of techniques can be investigated without expending the considerable time and resources required for physical experimentation. Of special importance for the model presented in this work, a GATE model of a PEPT detector and experimental geometry can be used to the assess impact of changes in the geometry to the sensitivity of the system and affect this has on

tracer trajectories quantified through estimates of their spatial and temporal resolution [20], [21], [22].

One useful feature of GATE is the 'parameterisation' of the simulation scripts which allows users to quickly change aspects of the simulation through the command line. Using this, the source activity, placement of LaMA's boxes, and the values for parameters of the digitizer can be edited without having to manually change the file. In this work, we use GATE to first replicate the geometry of the LaMA and the source, then calibrate the digitizer through evolutionary an evolutionary algorithm which is able to edit the pulse-processing settings of the detector through parameterised simulation scripts. The fitness of a set of candidate solutions with tune-able digitizer parameters is then compared through the ability of the GATE model to replicate the experimentally measured performance characteristics.

C. EVOLUTIONARY ALGORITHMS

When calibrating simulated models to experimental measurements, the complex relationship between variables, noisy measurements, and the large number of solutions that need to be tried to explore the solution space leads to a difficult optimisation problem with many false local minima [23]. When there are several parameters which need to be optimised, such as encountered in a digitizer model, traditional approaches like design-of-experiments become too unwieldy and gradient-based optimisers struggle to overcome local minima in a multi-dimensional and noisy solution space. This has led most GATE models to be calibrated manually using estimates of the optimal parameters provided by manufacturers of the detectors [24], [25]. This type of manual tuning is both subjective and also not guaranteed to produce the optimal calibration.

However, a type of optimisation algorithm that has been shown to excels in these cases are evolutionary algorithms [15], [26]. Evolutionary algorithms emulate biological evolution by using a group of simulations to act as a population with varied features. In this way, the fitness of individual simulations against a selective pressure can be quantified. To improve the fitness of the next generation of simulations, the fittest simulations are allowed to reproduce which allows their features to be transferred and some random mutations added to increase diversity, potentially introducing beneficial features.

In this work, the Covariance Matrix Adaptation using Evolutionary Strategy (CMA-ES), which is a stochastic optimiser for robust non-linear non-convex numerical optimisation, is used to perform the model calibration [16]. While CMA-ES generates, assesses, and updates solutions to parameters of the digitizer, an additional software is used to couple CMA-ES to the GATE simulation. This software is the Autonomous Characterisation and Calibration via Evolutionary Simulation (ACCES) which is a Python interface to the CMA-ES algorithm specifically designed for general calibration simulations and has been previously used to calibrate a GATE model of the ADAC Forte [15], [17]. More details about our use of this software to calibrate the LaMA digitizer are provided in Section II-C.

II. METHODS

A. CHARACTERISATION EXPERIMENTS

Two sets of characterisation experiments are conducted to measure the spatial resolution and count-rate response of the LaMA in a simple geometry. These two characteristics are the most important detector characteristics in regard to PEPT experiments because spatial resolution predominately influences the ability to resolve a point-like source and the digitizer model controls the count-rate response curve. Thus, these two characteristics ultimately determine the spatial and temporal resolution of a PEPT tracer, which are the characteristics of interest for users of PEPT algorithms [7].

In order to characterise LaMA's performance characteristics, a single, simple geometry was chosen. This geometry is a dual-headed stack of four boxes on either side of a source. The two stacks are separated by 500 mm. This configuration is used because of the low number of boxes required and also because of the large solid angle it creates with the source, allowing three-dimensional tracking of a point source, which is important for PEPT algorithms. Additionally, by choosing a simple geometry and achieving a calibration with the GATE model, it is expected that when the system is scaled up for future experiments the GATE model will remain accurate. The LoRs collected from these experiments are processed according to the NEMA protocol and in all cases the centre of the FOV is defined as 0, 0, 0 mm.

1) SPATIAL RESOLUTION

The spatial resolution of the detector is defined as the full-width half-maximum (FWHM) of the point-spread-function (PSF) for a small point-like source in the detector's FOV. The source used for this experiment is a 1 mm sphere of anionic exchange resin, volumetrically activated with fluorine-18 in a solution of water produced by the University of Birmingham MC40 cyclotron [27]. For imaging, the source was placed in a small plastic sample holder and fixed to a block of polystyrene foam at six locations ranging from the centre of the FOV and locations at 1/4th of the FOV. These locations and the source activities at the time of the experiment are listed in Table 1. The source and the LaMA geometry are shown in Fig. 2.

TABLE 1. Spatial resolution test parameters.

X (mm)	Y (mm)	Z (mm)	Initial Activity (MBq)	End Activity (MBq)
0	0	0	2.26	2.07
0	77.5	0	2.06	1.91
86.25	0	0	1.88	1.69
0	0	125	1.39	1.20
0	77.5	125	1.19	1.05
86.25	0	125	1.00	0.86

To produce projection images, the LoRs collected from the experiment were first voxelised into a three-dimensional array with a 1 mm voxel size using the voxelisation method

FIGURE 2. The spatial resolution tests are conducted using a 1 mm diameter resin bead placed inside a plastic sample holder and taped to a piece of polystyrene foam.

implemented in the `pept` Python package [28]. Two-dimensional slices from this array were extracted which contain the voxel with the maximum number of LoR crossings. From these slices. A one-dimensional profile was drawn through the maximum voxel and the FWHM was extracted from each position. Following the NEMA protocol, the spatial resolution is calculated using (1-4).

$$Res_{Trans_{Center}} = (Res_{y_{x=0,y=0,z=0}} + Res_{x_{x=0,y=0,z=0}} + Res_{y_{x=1/4,y=0,z=0}} + Res_{x_{x=1/4,y=0,z=0}})/4 \quad (1)$$

$$Res_{Trans_{1/4}} = (Res_{y_{x=0,y=1/4,z=1/4}} + Res_{x_{x=0,y=1/4,z=1/4}} + Res_{y_{x=0,y=1/4,z=0}} + Res_{x_{x=0,y=1/4,z=0}})/4 \quad (2)$$

$$Res_{Axial_{Center}} = (Res_{z_{x=0,y=0,z=0}} + Res_{z_{x=1/4,y=0,z=0}})/2 \quad (3)$$

$$Res_{Axial_{1/4}} = (Res_{z_{x=0,y=0,z=1/4}} + Res_{z_{x=1/4,y=0,z=1/4}})/2 \quad (4)$$

2) COUNT-RATE RESPONSE

The count-rate experiment measures the LoR count-rate of the detector in response to a central source which is imaged over several half-lives. The total, true, and scattered plus random LoRs count-rates are extracted using the NEMA protocol and recorded at regular intervals as a function of source activity. The scattered plus random count-rate is termed the corrupted count-rate since the LoRs do not pass through the positron annihilation point due to scattering or originating from separate annihilation events and thus are treated as noise in a PEPT experiment.

The phantom is a hollow, high-density polyethylene cylinder measuring 120 mm in height and 50 mm in diameter with an inner cavity measuring 100 mm in height by 12 mm in diameter. This cavity is filled with a well-mixed solution of fluorine-18 and water. Initially, the activity of the phantom was approximately 80 MBq. This activity was chosen such that the expected count-rate will exceed the maximum rate at which LoRs can be recorded by the detector, then, as the source decays, the count-rate response curves can be developed. The phantom was imaged over several half-lives until the activity reached near that of the background. The phantom and detector geometry are shown in Fig. 3.

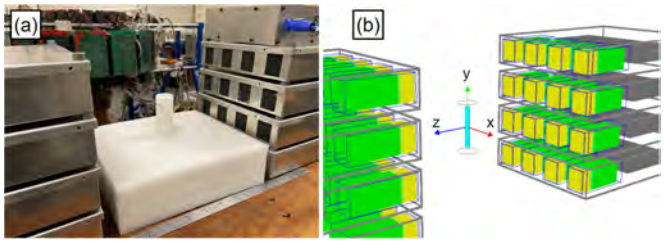

FIGURE 3. (a) The count-rate experiment is conducted with the high-density polyethylene phantom placed in the centre of FOV and imaged over several half-lives. (b) A GATE model of the same experiment is conducted.

Similarly to Section II-A1, projection images are produced by voxelising LoRs into a three-dimensional array with a 1 mm voxel size. Two-dimensional slices are extracted in the plane parallel to the detector face (XY plane) which contains the maximum voxel. The slice is then transformed into a one-dimensional profile by summing the voxels in the Y-axis which are along the cylinder's axis. The average source activity, $\bar{A}$, for each projection image is determined by (5) which calculates the average activity by using the initial activity, A_0, the initial and final time of the acquisition, t_0 and t_f, as well as the decay constant for fluorine-18, λ. The true counts are considered to be the LoRs $\pm$ 20 mm from the peak of the profile from which the background on either side of the 40 mm window is averaged and subtracted from the counts in the window. The remaining counts outside the window and including the background are considered corrupted counts.

$$\bar{A} = \frac{A_0}{t_f - t_0} \int_{t_0}^{t_f} \exp(-\lambda t)\, dt \quad (5)$$

B. GATE MODEL

The design of a GATE model for the LaMA presents several challenges since it must be easily customised to rapidly prototype new geometries, only allow specific coincidences to be formed between boxes connected to a single coincidence processor, and be able to emulate the noise, data buffer, and spatial blurring inherent in the system. Achieving these goals is accomplished using the tools available in the GATE software in addition to custom data post-processing. The geometry, digitizer, and post-processing are described in the following sections. A downloadable version of the LaMA GATE model and post-processing software is provided through a GitHub repository: LaMA Model.

1) GEOMETRY MODEL

Since any LaMA geometry is built using boxes, to build a model of the LaMA, only a single box needs to be described which can later be copied, translated, and rotated to any position and orientation using GATE's generic repeater function. The dimensions for each box are found in Section I-A and these are replicated in GATE. Material definitions for BGO, aluminium frame, and glass light guide are already included in the GATE materials database and definitions for the PMTs and electronics are added. Importantly, the four ECAT951 block detectors are included in each box and the 8 × 8 BGO crystal array in each block is defined as the 'Sensitive Detector' (SD) through which GATE records the interactions of particles. The model of a single box is shown in Fig. 4 from various viewpoints. The order in which the repeated boxes are listed determines their volume number, which will become important later when defining which pairs of boxes are valid for recording coincidences.

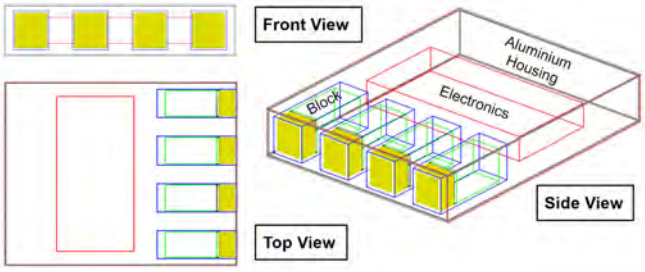

FIGURE 4. A model of a box for the LaMA consisting of four ECAT951 block detectors each with an 8 × 8 array of BGO crystals. The box is shown from various viewpoints and has major components labelled.

2) DIGITIZER MODEL

While a geometric model ensures the interactions of the source's radiation field with the detector are accurately recorded, the system's pulse-processing chain must also be properly modelled in order to emulate the detector's response. In GATE, implementing a linear pulse-processing chain to particle interactions is the role of the digitizer. The digitizer is a series of steps and filters which transform the observable information (time, energy, position) of a particle interaction with the SD into a form similar or identical to the real detector output [29]. This includes grouping interactions, flow-logic, and data-loss to mimic the real behaviour of the imaging system [30]. The digitizer for the LaMA is shown in Fig. 5.

For the LaMA, we apply a typical digitizer model for a PET system, but also implement a post-processing stage to implement aspects of the detector not directly possible through GATE [19]. This is needed to force the detector to only record coincidences between pairs of boxes which are associated with each other in the real coincidence processor, implement a random spatial-blurring of LoRs to match the experimentally observed spatial resolution, and implement a bandwidth limitation to cap the rate at which LoRs are written to file. The post-processing steps for the LaMA GATE model digitizer are the final three steps before the final simulated detector response is produced, as shown in Fig. 5.

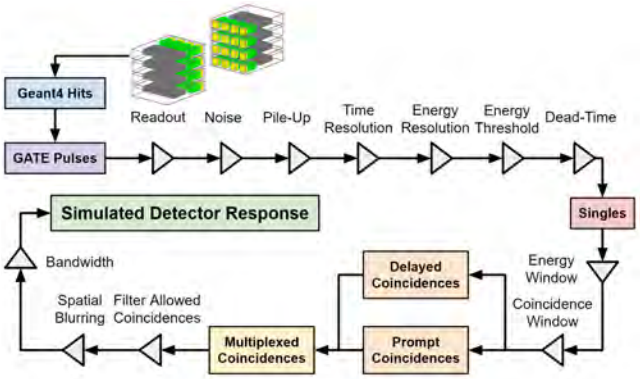

FIGURE 5. The pulse-processing digitizer of the LaMA GATE model.

C. DIGITIZER OPTIMISATION

Even if every detail of the LaMA were known, there are differences between simulation and experiment which require aspects of the digitizer to be calibrated [10], [31]. While this could be achieved through manual calibration, for this we work we use a recently developed method which applies an evolutionary algorithm to achieve a calibration to experimental performance characteristics autonomously [15].

Six stages of the digitizer are chosen to be calibrated because of the effect they have on replicating the count-rate response. These are the noise frequency, pile-up time, time resolution, lower-level energy discriminator, upper-level energy discriminator, and the non-paralysable singles dead-time. The noise frequency is the rate at which random events are generated simply by having the detectors running and is a combination of the background activity and electronic noise. The pile-up time is the time after an event is detected when other events in close succession can be added to the signal. The time resolution is the probability of precision by which two events can be distinguished in time, as defined by an FWHM. The lower and upper energy discriminators are the thresholds between which an event can trigger the dead-time and be recorded. The singles dead-time is a non-paralysable dead-time model, described by (6) which limits the rate of recording single events [32].

$$\frac{\lambda_{out}}{\lambda_{in}} = \frac{1}{(1 + \lambda_{in}\tau)} \tag{6}$$

In order to use an evolutionary algorithm to calibrate a GATE model, there must a metric through which the fitness of candidate solutions to the parameters of the digitizer can be assessed. This is achieved through a cost function, shown in (7), which is the product of the percent differences between the experiment and simulation's total, true, and corrupted count-rate response over a range of source activities, calculated using (8-10). Using this metric reduces the agreement between the experiment and simulation down to a single value

which can be optimised through minimisation of (7).

$$\varepsilon = \varepsilon_{Tot}\varepsilon_{True}\varepsilon_{Corrupt} \quad (7)$$

$$\varepsilon_{Tot} = \sum |(R_{Tot_{exp}} - R_{Tot_{sim}})/R_{Tot_{exp}}| \quad (8)$$

$$\varepsilon_{True} = \sum |(R_{True_{exp}} - R_{True_{sim}})/R_{True_{exp}}| \quad (9)$$

$$\varepsilon_{Corrupt} = \sum |(R_{Corrupt_{exp}} - R_{Corrupt_{sim}})/R_{Corrupt_{exp}}| \quad (10)$$

Parameter combinations are generated following a multivariate normal distribution with the initial uncertainty defined as the range between the upper and lower bounds of the solution space for each parameter. To stop the optimisation, the user must provide either the number of generations, called epochs, of simulations desired or provide a target uncertainty in the calibrated parameters. In this optimisation, we used 100 epochs with 100 parameter value combinations per epoch as the terminating criteria because this provides greater than 10 times the factorial of the number of free-parameters in the optimisation, sufficiently constraining the problem.

Each combination is simulated over 10 different activities, ranging from 2 MBq to 80 MBq, until 5 million LoRs are recorded at each activity. This number of LoRs provides sufficient counts such that an accurate measurement of each respective count-rate can be extracted from the projection images. The bounds of the parameters and their initial guesses are provided in Table 2. The optimisation is conducted on the University of Birmingham's high-performance computing system, BlueBEAR, on Icelake cores with 16 GB of memory each. After the optimisation is finished, the calibrated parameters are extracted and a new set of simulations are conducted with 20 activities over the same activity range until 30 million LoRs are recorded, reducing statistical error even further. These simulations are presented and compared in Section III.

TABLE 2. Digitizer parameter bounds and initial guesses for calibration.

Parameter	Lower Bound	Upper Bound	Initial Guess
Singles Dead-Time (ns)	0	10000	5000
Noise Frequency (ns)	1000	10000	5500
Pileup Time (ns)	0	1000	500
Lower Level Disc. (keV)	0	400	200
Upper Level Disc. (keV)	700	2200	1450
Time Resolution (ns)	0	30	15

III. RESULTS AND DISCUSSION

In this section, we present the results of the characterisation experiments as well as the results of the digitizer calibration. For spatial resolution, six tracer positions were imaged over several minutes then the FWHM of the 1-dimensional PSF is extracted. The FWHM at these positions are used to compute the transaxial and axial spatial resolutions in the centre of the FOV and at 1/4th of the FOV. Next, the experiments are reproduced in simulation and the crystal blurring is adjusted until the best match between the experiment and simulation was achieved. The crystal blurring that best agrees with the experiment 2 times the crystal dimensions

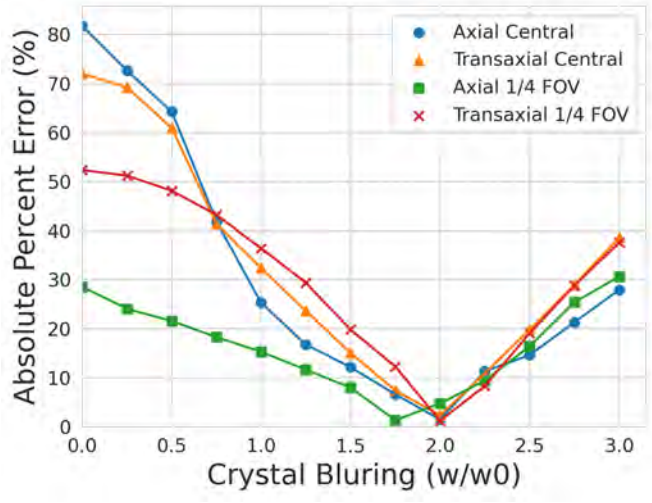

FIGURE 6. The spatial blurring is calibrated by finding the crystal blurring that minimises the absolute percent error.

TABLE 3. Results and comparisons of the spatial resolution tests for the experiment and simulation.

Spatial Resolution	Experiment (mm)	Simulation (mm)	Percent Error (%)
Central Transaxial	8.26	8.38	1.44
1/4th FOV Transaxial	8.95	9.37	4.72
Central Axial	21.83	22.34	2.32
1/4th FOV Axial	24.09	23.80	-1.20

(6.25 mm by 6.75 mm), as evidenced in Fig. 6. The experimental and simulated results are presented in Table 3 and compared through their respective percent differences.

Following the spatial resolution characterisation and crystal blurring calibration, the count-rate response experiments were analysed to be used as a comparison for the ACCES optimisation. The optimisation takes place over 100 epochs with 100 parameter value combinations tried every epoch. This results in 10,000 cost function evaluations which took approximately three days to complete running the BlueBEAR high-performance computing system. At the end of the optimisation, the final mean parameter values were extracted. The value for these parameters and their uncertainty are provided in Table 4. Additionally, the history of these parameters during the optimisation (uncertainties and mean values) is presented in Fig. 7, demonstrating that before the end of the optimisation, each parameter reaches a stable value, meaning that the parameters have been calibrated.

All parameters produced reasonable calibrations within the upper and lower bounds given to the optimiser. Interestingly, the optimised value for the time resolution falls within the 12 ns ± 2 ns measured in a previous characterisation of the LaMA [31]. This provides additional evidence that the calibrated parameters correspond to physical reality and are global solutions, not simply local solutions.

The parameter with the highest uncertainty is the upper level energy discriminator. We believe this is due to the relatively small impact of this parameter on the calibration. To illustrate this, take for example the the singles dead-time which has the lowest uncertainty. The singles dead time has

a strong pressure to be calibrated because this is applied to nearly all events which are detected. meaning small changes in the calibrated values will causes large differences in the simulated count-rate response. On the other hand, the upper energy discriminator acts on a much smaller set of events and can only be applied to events that have piled up on one another. Since the upper energy discriminator is set to 1990 keV, this means that at least four 511 keV events must be grouped together and this happens only a limited number of times in a simulation. As a result, there is not a strong pressure to calibrate this value. While this results in a higher uncertainty, because of the lower effect of this parameter on the overall response of the model this value is considered adequately calibrated.

TABLE 4. Digitizer calibration results and uncertainty.

Parameter	Calibrated Values	Uncertainty
Singles Dead-Time (ns)	6630	± 57.9
Noise Frequency (ns)	1970	± 9.39
Pileup Time (ns)	637	± 6.91
Lower Level Disc. (keV)	324	± 7.99
Upper Level Disc. (keV)	1990	± 85.5
Time Resolution (ns)	13.7	± 0.084

When the new set of simulations is conducted with the calibrated digitizer, the results match the experiment to a mean absolute difference of 3.41% over all three count-rates

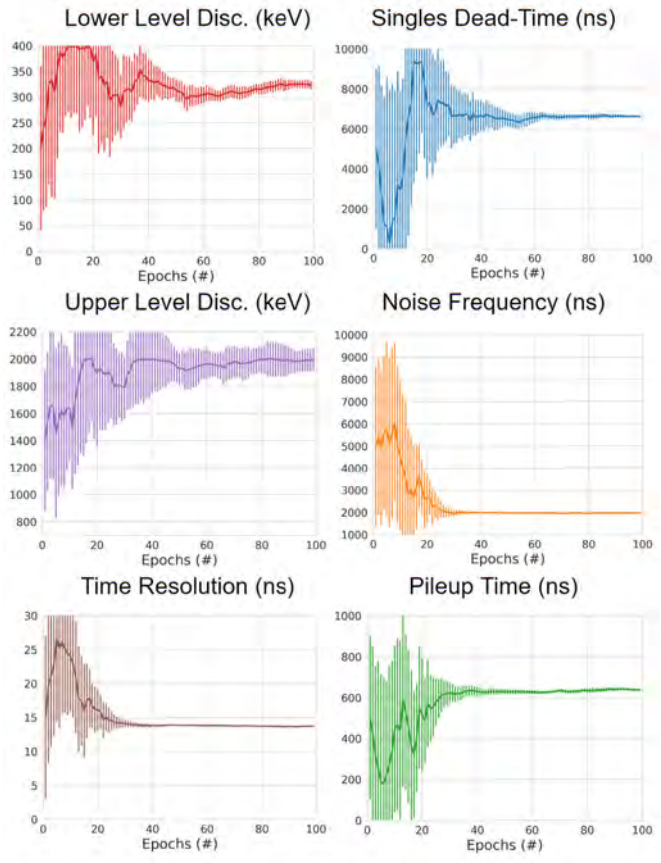

FIGURE 7. Subplots showing the mean values of calibrated parameters with the error bars as the standard deviation of solutions.

with the total, true, and corrupted count-rates being 2.31%, 2.18%, and 5.72%, respectively. The experimental and simulated count-rate response is shown in Fig. 8. To quantify the calibration further, it is also important to observe how the fraction of true and corrupted counts behave as a function of source activity. These results are presented in Fig. 9, showing that their behaviour is approximately the same overall activities with the true and corrupted count fractions reconstructed to 1.91% and 3.72% error, respectively.

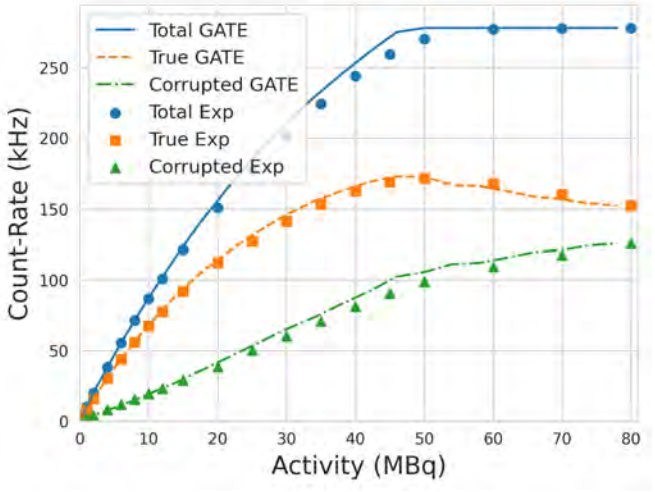

FIGURE 8. Results of the count-rate experiment and comparison of the ACCES calibrated GATE model.

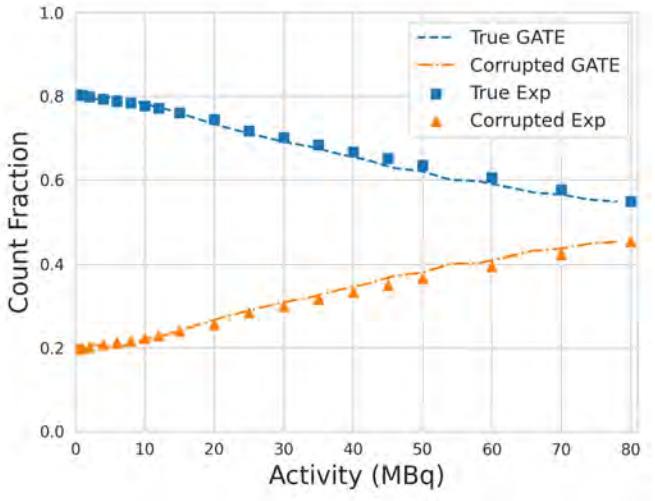

FIGURE 9. Results of the count-rate experiment in terms of the true and corrupt count fractions and comparison with the ACCES calibrated GATE model.

In summary, the GATE model of the LaMA has been characterised by experiments testing the spatial resolution and count-rate response and the digitizer pulse-pulse processing model has been calibrated using an evolutionary algorithm. In addition to calibrating the amount of crystal spatial blurring, six free-parameters of the pulse-processing digitizer model were calibrated using evolutionary simulation,

ultimately producing simulated results which match the observed real behaviour of the detector system. The ACCES software was used to perform this optimisation autonomously, needing only the number of solutions to try for each epoch, the bounds of the solution space for each parameter, and a terminating criterion.

IV. CONCLUSION

In this work, we have introduced a Monte Carlo model of the Positron Imaging Centre's LaMA and validated the model against experimental measurements. This model will bolster the modelling capabilities of the Positron Imaging Centre, complementing the existing Monte Carlo model of the ADAC Forte. A model of LaMA is particularly useful because the camera is typically configured into new geometries for every experiment in order to capture the relevant system behaviour. Prior to this model, it was not possible to quantitatively estimate the spatial resolution and count-rate response because these characteristics depend on a complex relationship between source activity, detector geometry, and gamma-ray scattering. Using this model, not only can the spatial resolution and count rate response be estimated, but moreover the tracer activity which maximises the true count-rate and the detector geometry which maximises the camera sensitivity for a given experiment can be identified.

CONFLICT OF INTEREST

The authors declare that there is no conflict of interest.

ACKNOWLEDGMENT

The authors would like to thank Andrei Nicusan for developing and maintaining the `pept` Python Library and Access Optimization Tools. The computations described in this article were performed using the University of Birmingham's BlueBEAR service, which provides High-Performance Computing to the University's research community. See their website for more details.

REFERENCES

[1] K. Windows-Yule, L. Nicusan, M. T. Herald, S. Manger, and D. Parker, *Positron Emission Particle Tracking*. Bristol, U.K.: IOP Publishing, 2022.

[2] C. R. K. Windows-Yule, J. P. K. Seville, A. Ingram, and D. J. Parker, "Positron emission particle tracking of granular flows," *Annu. Rev. Chem. Biomol. Eng.*, vol. 11, no. 1, pp. 367–396, Jun. 2020.

[3] D. J. Parker, C. J. Broadbent, P. Fowles, M. R. Hawkesworth, and P. McNeil, "Positron emission particle tracking—A technique for studying flow within engineering equipment," *Nucl. Instrum. Methods Phys. Res. A, Accel. Spectrom. Detect. Assoc. Equip.*, vol. 326, no. 3, pp. 592–607, Mar. 1993.

[4] M. Al-Shemmeri, K. Windows-Yule, E. Lopez-Quiroga, and P. J. Fryer, "Coffee bean particle motion in a spouted bed measured using positron emission particle tracking (PEPT)," *J. Food Eng.*, vol. 311, Dec. 2021, Art. no. 110709.

[5] C. R. Jones, A. Corona, C. Amador, and P. J. Fryer, "Dynamics of fabric and dryer sheet motion in domestic clothes dryers," *Drying Technol.*, vol. 40, no. 10, pp. 2087–2104, 2021.

[6] A. Dybalska, A. J. Caden, D. J. Parker, J. Wedderburn, and W. D. Griffiths, "Liquid metal flow studied by positron emission tracking," *Metall. Mater. Trans. B*, vol. 51, no. 5, pp. 1912–1917, Oct. 2020.

[7] D. J. Parker, D. M. Hampel, and T. K. Wheldon, "Performance evaluation of the current Birmingham PEPT cameras," *Appl. Sci.*, vol. 12, no. 14, p. 6833, Jul. 2022.

[8] D. Parker, R. Forster, P. Fowles, and P. Takhar, "Positron emission particle tracking using the new Birmingham positron camera," *Nucl. Instrum. Methods Phys. Res. A, Accel. Spectrom. Detect. Assoc. Equip.*, vol. 477, nos. 1–3, pp. 540–545, Jan. 2002.

[9] D. M. Hampel, S. Manger, D. J. Parker, and T. K. Wheldon, "SuperPEPT: A new tool for positron emission particle tracking; first results," *Nucl. Instrum. Methods Phys. Res. A, Accel. Spectrom. Detect. Assoc. Equip.*, vol. 1028, Apr. 2022, Art. no. 166254.

[10] D. J. Parker, T. W. Leadbeater, X. Fan, M. N. Hausard, A. Ingram, and Z. Yang, "Positron emission particle tracking using a modular positron camera," *Nucl. Instrum. Methods Phys. Res. A, Accel. Spectrom. Detect. Assoc. Equip.*, vol. 604, nos. 1–2, pp. 339–342, Jun. 2009.

[11] W. D. Griffiths, D. J. Parker, X. Fan, and M. Hausard, "Tracking inclusions in aluminium alloy castings using positron emission particle tracking (PEPT)," *Mater. Sci. Technol.*, vol. 26, no. 5, pp. 528–533, May 2010.

[12] S. Jan et al., "GATE: A simulation toolkit for PET and SPECT," *Phys. Med. Biol.*, vol. 49, no. 19, pp. 4543–4561, Oct. 2004.

[13] D. Sarrut et al., "Advanced Monte Carlo simulations of emission tomography imaging systems with gate," *Phys. Med. Biol.*, vol. 66, no. 10, May 2021, Art. no. 10TR03.

[14] *Performance Measurements of Positron Emission Tomographs (PET) 2018*, National Electrical Manufacturers Association, Rosslyn, VA, USA, 2018.

[15] M. Herald, A. Nicuşan, T. K. Wheldon, J. Seville, and C. Windows-Yule, "Autonomous digitizer calibration of a Monte Carlo detector model through evolutionary simulation," *Sci. Rep.*, vol. 12, no. 1, p. 19535, Nov. 2022.

[16] N. Hansen, K. Nozawa, L. Rolshoven, M. Chan, Y. Akimoto, and D. Brockhoff, "CMAES/pycma: R3.2.2," Zenodo, Tech. Rep., Mar. 2022.

[17] A.-L. Nicusan, D. Werner, J. A. Sykes, J. Seville, and K. Windows-Yule, "ACCES: Autonomous characterisation and calibration via evolutionary simulation," GitHub, San Francisco, CA, USA, Tech. Rep., Feb. 2022.

[18] M. Herald, T. Wheldon, and C. Windows-Yule, "Monte Carlo model validation of a detector system used for positron emission particle tracking," *Nucl. Instrum. Methods Phys. Res. A, Accel. Spectrom. Detect. Assoc. Equip.*, vol. 993, Mar. 2021, Art. no. 165073.

[19] S. Lee, J. Gregor, and D. Osborne, "Development and validation of a complete GATE model of the Siemens Inveon trimodal imaging platform," *Mol. Imag.*, vol. 12, no. 7, Oct. 2013, Art. no. 7290.2013.00058.

[20] M. Herald, Z. Bingham, R. Santos, and A. Ruggles, "Simulated time-dependent data to estimate uncertainty in fluid flow measurements," *Nucl. Eng. Des.*, vol. 337, pp. 221–227, Oct. 2018.

[21] C. R. K. Windows-Yule, M. T. Herald, A. L. Nicusan, C. S. Wiggins, G. Pratx, S. Manger, A. E. Odo, T. Leadbeater, J. Pellico, R. T. M. D. Rosales, A. Renaud, I. Govender, L. B. Carasik, A. E. Ruggles, T. Kokalova-Wheldon, J. P. K. Seville, and D. J. Parker, "Recent advances in positron emission particle tracking: A comparative review," *Rep. Prog. Phys.*, vol. 85, no. 1, Jan. 2022, Art. no. 016101.

[22] M. T. Herald, J. A. Sykes, D. Werner, J. P. K. Seville, and C. R. K. Windows-Yule, "DEM2GATE: Combining discrete element method simulation with virtual positron emission particle tracking experiments," *Powder Technol.*, vol. 401, Mar. 2022, Art. no. 117302.

[23] S. Shalev-Shwartz, O. Shamir, and S. Shammah, "Failures of gradient-based deep learning," in *Proc. 34th Int. Conf. Mach. Learn.*, vol. 70, D. Precup and Y. W. Teh, Eds., Aug. 2017, pp. 3067–3075.

[24] M. Strugari, D. DeBay, S. Beyea, and K. Brewer, "NEMA NU 1–2018 performance characterization and Monte Carlo model validation of the Cubresa Spark SiPM-based preclinical SPECT scanner," *EJNMMI Phys.*, Aug. 2022.

[25] A. Tiwari, M. Merrick, S. A. Graves, and J. Sunderland, "Monte Carlo evaluation of hypothetical long axial field-of-view PET scanner using GE discovery MI PET front-end architecture," *Med. Phys.*, vol. 49, no. 2, pp. 1139–1152, Feb. 2022.

[26] Y. Kwon, S. Kang, Y.-S. Choi, and I. Kim, "Evolutionary design of molecules based on deep learning and a genetic algorithm," *Sci. Rep.*, vol. 11, no. 1, p. 17304, Aug. 2021.

[27] D. J. Parker, "Positron emission particle tracking and its application to granular media," *Rev. Sci. Instrum.*, vol. 88, no. 5, May 2017, Art. no. 051803.

[28] A. L. Nicuşan and C. R. K. Windows-Yule, "Positron emission particle tracking using machine learning," *Rev. Sci. Instrum.*, vol. 91, no. 1, Jan. 2020, Art. no. 013329.
[29] S. Kerhoas-Cavata and D. Guez, "Modeling electronic processing in GATE," *Nucl. Instrum. Methods Phys. Res. A, Accel. Spectrom. Detect. Assoc. Equip.*, vol. 569, no. 2, pp. 330–334, Dec. 2006.
[30] D. Guez, F. Bataille, C. Comtat, P.-F. Honore, S. Jan, and S. Kerhoas, "Counting rates modeling for PET scanners with GATE," *IEEE Trans. Nucl. Sci.*, vol. 55, no. 1, pp. 516–523, Feb. 2008.
[31] T. W. Leadbeater, "The development of positron imaging systems for applications in industrial process tomography," Ph.D. thesis, Univ. Birmingham, Birmingham, U.K., Jul. 2009.
[32] S. Usman and A. Patil, "Radiation detector deadtime and pile up: A review of the status of science," *Nucl. Eng. Technol.*, vol. 50, no. 7, pp. 1006–1016, Oct. 2018.

MATTHEW HERALD was born in the USA. He received the B.S. degree in nuclear engineering from the University of Tennessee, Knoxville, in 2019. He is currently pursuing the Ph.D. degree in chemical engineering with the University of Birmingham, under the supervision of Christopher Windows-Yule.

He is a member of the Institue of Physics and currently works for Jacobs as a Physicist. His work revolves around developing Monte Carlo models of position-sensitive detectors and simulating positron emission particle tracking experiments to optimize data acquisition. He has developed a model of the ADAC Forte dual-headed positron camera and used this in an international collaboration of other institutes using positron emission particle tracking algorithms to benchmark their performance on a common, known data set. He is the coauthor on the first book written about positron emission particle tracking which was written to be used by students, users, and researchers.

DAWID HAMPEL was born in Poland, but spent most of his primary education in the USA. He received the M.Eng. degree (Hons.) in nuclear engineering from the University of Birmingham, Birmingham, U.K., in 2019, where he is currently pursuing the Ph.D. degree in cyclotron production and radiochemical purification methods of emerging radionuclides for cancer diagnosis and treatment while developing positron emission particle tracking detector arrays.

His early work includes the development of Geant4 radiation transport simulations and simulations of numerous nuclear reactions in TALYS and EMPIRE. He is the Co-Developer of UoB-TIP Toolkit used to ease the analysis of nuclear reaction data and OLab an online, interactive nuclear laboratory both used with the University of Birmingham. His current work involves the development and improvement of PEPT detector arrays in both hardware and software levels. He is working with the Positron Imaging Centre, he has built and tested SuperPEPT and redeveloped and modernized the Large Modular Array (LaMA) for PEPT with contributions to other systems used at the site.

Mr. Hampel is a member of the Institute of Physics.

TZANY KOKALOVA WHELDON received the Ph.D. degree in nuclear physics from Freie Universitaet, Berlin, Germany.

She is currently a full-time Professor of nuclear physics with the University of Birmingham and the Director of the Positron Imaging Centre. Her work spans the full breadth of nuclear physics from experimental nuclear astrophysics and machine learning, medical isotopes, applications, and industry-related nuclear decommissioning. She carries out research, teaches, and supervises eight Ph.D. students, and key roles mentoring women. She has travelled extensively, performing experiments with laboratories in Australia, the USA, and Europe. She was a recipient of the Daphne Jackson Fellowship and won a Timewise Power Returner Award celebrating, in 2020, her ability to combine career success at a senior level whilst working flexibly.

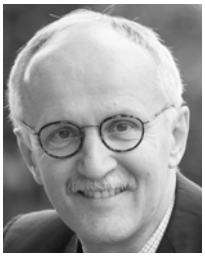

JONATHAN SEVILLE was born in Yorkshire, U.K. He received the degree in chemical engineering from the University of Cambridge and University of Surrey.

Before starting his academic career, he worked for several years for the research division of Courtaulds Ltd. Since 2017, he has been a Professor of formulation engineering with the University of Birmingham. Previously, he was the Executive Dean of Engineering and Physical Sciences with the University of Surrey (2011–2016), the Dean of Engineering with the University of Warwick (2008–2011), and the Head of the Department of Chemical Engineering, University of Birmingham (1998–2008). He is an experienced researcher in chemical engineering, particularly in processes involving particulate solids, and has pioneered the use of radioactive tracers to image flow in industrial equipment. He has around 200 publications and authored or edited five books on aspects of particle technology. Among the numerous companies which have supported his research are Unilever, Procter and Gamble, GSK, Merck Sharp and Dohme, and Pfizer. He is a fellow of the Royal Academy of Engineering and was President of the Institution of Chemical Engineers (IChemE), in 2016–2017.

CHRISTOPHER WINDOWS-YULE was born in Worcestershire. He received the B.S. and Ph.D. degrees in physics from the University of Birmingham.

Previously, he was a Postdoctoral Researcher with the University of Twente, The Netherlands. He is currently an Associate Professor with the University of Birmingham's School of Chemical Engineering. His research interests include imaging and numerical modeling of particulate and multiphase systems, employing a diverse range of techniques, notably discrete element method (DEM) modeling, computational fluid dynamics (CFD), and positron emission particle tracking (PEPT). His research aims to address significant contemporary challenges in science, medicine and industry by exploiting the synergy of experimental techniques, numerical simulation, and machine-learning methodologies. His current projects include work, funded by EPSRC, the Royal Academy of Engineering and the Royal Society, developing novel plastic recycling methods, work funded by the British Heart Foundation aiming to develop novel methods of blood-flow imaging for the diagnosis of cardiovascular disease, and diverse industry-funded projects. He is a Turing Fellow, a two-time Royal Academy of Engineering Industrial Fellow, and a Founding Member of the U.K. Young Academy.

Characterisation of the multiphase fluid dynamics of the CoarseAIR™ fluidised bed flotation cell using the Large Modular Array (LaMA) for positron emission particle tracking (PEPT)

Diego Mesa[a,*], Dawid M. Hampel[b,*], Stephen J. Neethling[a], Tzany Kokalova Wheldon[b] and Pablo R. Brito-Parada[a]

[a]Advanced Mineral Processing Research Group, Royal School of Mines, Imperial College London, United Kingdom
[b]Positron Imaging Centre, School of Physics and Astronomy, University of Birmingham, United Kingdom

ARTICLE INFO

Keywords:
CoarseAIR™ flotation cell
positron emission particle tracking (PEPT)
Large Modular Array (LaMA)
multiphase fluid dynamics
fluidised bed flotation cell

ABSTRACT

Fluidised bed flotation cells (FBFCs) present a compelling solution for coarse particle flotation, enabling an increase in the target particle size in comminution circuits, with the corresponding energy savings. Despite their potential and strong industrial interest, the three-phase fluid dynamics of large-scale FBFCs remain unexplored due to measurement complexities and size restrictions. This paper presents the first quantification of the fluid dynamics of the CoarseAir™-100, a 2m tall laboratory-scale FBFC. Measurements were obtained using positron emission particle tracking (PEPT), a non-invasive technique that tracks the motion of a radiolabelled tracer. Leveraging the Large Modular Array (LaMA) PEPT system, consisting of 48 buckets, each housing four detector blocks, this study is the largest PEPT experiment to date. Particle tracks of hydrophobic and hydrophilic tracers were obtained under different fluidisation and airflow rates. Hydrophobic tracers exhibited buoyant behaviour despite their large size of up to 700 µm, while hydrophilic tracers engaged in recirculation patterns with rapid downward motion near the walls. The intricate motion of particles in the lamella plates was experimentally quantified, revealing an average path tortuosity of 7.3, providing essential information for design. These results represent a major advance in our understanding of fluidised bed flotation cells, contributing to the refinement of design and scale-up strategies for FBFCs.

1. Introduction

Froth flotation is the most important and widely used technique in the mineral processing industry, being a key step in the production of critical raw materials. The flotation process requires the particles to be reduced in size in order to partially liberate the surface of the valuable minerals for bubble-particle attachment. However, the grinding process is highly inefficient [1, 2], using up to 70% of the total energy consumption of a typical mining operation [1, 3]. It has been reported that approximately 3% of the world's electricity is consumed in mineral comminution [3–5]. Consequently, significant efforts have been directed towards the flotation of coarse particles in order to reduce grinding requirements.

Coarse material in froth flotation is usually defined as particles with a diameter greater than 250 µm. The flotation of coarse material is challenging due to the high probability of detachment of particles from the surface of the bubbles [2, 6], which is enhanced by the turbulent regime of conventional flotation cells. Moreover, even if coarse particles remain attached to the bubbles, the low buoyancy of the particle-bubble aggregates hinders coarse flotation efficiency [2, 5, 7].

Several new designs of flotation equipment have been proposed to tackle these two specific challenges of coarse flotation [2]. Among them, the most promising designs consist of fluidised bed flotation cells, including Eriez's HydroFloat™ [8–11], Jord's NovaCell™ [12, 13], and most recently FLSmidth's CoarseAIR™ [14]. Two comprehensive reviews of fluidised bed flotation cells for coarse flotation can be found in Kromah et al. [5] and Janishar Anzoom et al. [15].

Fluidised bed flotation cells operate under the principle of hindered settling, which involves the suspension of particles in a teeter bed [5, 16]. The upward flow of water generates a fluidised bed of suspended particles. The injected air bubbles attach to the exposed hydrophobic surface of the coarse particles, forming bubble-particle aggregates with low apparent density. These aggregates still lack the required buoyancy to ascend independently, as highlighted for conventional flotation cells. However, in fluidised bed flotation, these aggregates can rise to the top of the teeter bed because of their lower density and ultimately overflow from the cell.

To prevent the detachment of coarse particles, fluidised bed flotation cells need to have quiescent regimes, avoiding zones of turbulent mixing. Although there are several publications of Computational Fluid Dynamics (CFD) simulations for different fluidised bed flotation cells [10, 17–20], there is a distinct lack of experimental fluid dynamics data associated with this type of equipment. Han et al. [21] conducted an experiment in a three-phase fluidised bed flotation column, where the solid phase was represented by steel balls. However, their results obtained with image analysis are limited to general observations such as bed fluctuation ratio, gas holdup and bubble size distribution, and do not explore the dynamics of the fluids and particles involved.

d.mesa@imperial.ac.uk (D. Mesa); d.hampel@pgr.bham.ac.uk (D.M. Hampel)

ORCID(s): 0000-0002-2417-9821 (D. Mesa); 00-0002-3453-4778 (D.M. Hampel); 0000-0003-0881-3332 (S.J. Neethling); 0000-0002-2035-3749 (T. Kokalova Wheldon); 0000-0001-6252-246X (P.R. Brito-Parada)

This gap in the literature is not an isolated issue for three-phase fluidised bed flotation cells. The experimental characterisation of flotation multiphase fluid dynamics is a challenging problem, which has only recently been tackled using positron emission particle tracking (PEPT).

1.1. Positron emission particle tracking (PEPT)

Positron emission particle tracking, or PEPT, is a non-invasive technique utilised to monitor the position of a tracer particle over time [22]. This technique uses penetrating radiation and is not dependent on optical properties, making it suitable for tracking a particle within opaque and dense systems such as a flotation cell. This is a key advantage over other experimental techniques, such as Particle Image Velocimetry (PIV), which are typically limited to single or dilute two-phase systems, as they are based on optical properties.

In PEPT experiments, a tracer particle radiolabelled with a short-lived, positron-emitting isotope is tracked using a positron-sensitive detector array such as a positron emission tomography (PET) camera. The positron emitted by the tracer annihilates with an electron from local matter, producing a pair of 511 keV almost back-to-back γ-rays. If the PET camera detects both γ-rays from the pair in coincidence within a set coincidence time window, the annihilation event can be located somewhere along the path between the two detectors, forming a line of response (LOR). With multiple LORs, the location of a moving tracer particle can be triangulated with time, providing time series data on the tracer's location, which can be used to determine the tracer velocity.

In the last decade, PEPT has been increasingly used to evaluate the fluid dynamics of complex multiphase mineral processing applications, including froth flotation [23–26]. Although there have been many developments on its use and capabilities, PEPT is still a novel and specialised technique, available in a handful of laboratories worldwide, due to the need for a cyclotron to produce radioactive material. Another limitation for its widespread use has been the maximum size of equipment that can be positioned within a PET camera.

PEPT experiments involve placing the equipment of interest within the field-of-view (FOV) of a positron-sensitive detector. Commonly, these detectors correspond to repurposed PET cameras from hospitals, with FOV not greater than the space required for a patient to fit through the bore, *i.e.* under 0.15 m^3 or 0.8 m^2 by 0.15 m deep. However, some experimental equipment will not fit within the FOV of existing detectors. To address this challenge, a large modular array of detectors, called LaMA, has been recently designed at the University of Birmingham Positron Imaging Centre (PIC) to be assembled around experimental systems in custom geometries [27, 28].

This work presents an experimental study aimed at quantifying the fluid dynamics of a 2 m tall fluidised bed flotation cell using PEPT. The LaMA detector was assembled around the geometry of the experimental system in a custom configuration, which enabled the imaging of a large-scale laboratory prototype of the cell. To the authors' knowledge, this is the largest PEPT experiment to date in terms of the height of the field-of-view. The objective of this study is to investigate the complex fluid dynamics of the fluidised bed flotation cell, which plays a critical role in the separation of coarse mineral particles.

2. Materials and methods

2.1. CoarseAIR fluidised bed flotation cell – laboratory-scale prototype

The experiments were performed using the CoarseAIR™-100 (CA100), a 2.3 m high fluidised bed flotation cell with a capacity of just under 20 L, as depicted in Figure 1. The CoarseAIR™ cell, based on the REFLUX™ classifier design [29], comprises a lower fluidised bed and an upper system of inclined channels called lamella plates. Small air bubbles are generated by injecting pressurised air into the fluidisation water. The feed suspension is injected at an intermediate height. The whole tank experiences a positive water bias, with small/light particles flowing upwards through the inclined channels, whereas the larger/heavier particles sink into the lower fluidised bed. Hydrophobic particles attach to the bubbles, forming bubble-particle clusters with low apparent density, and thus collect toward the top of the cell. Further details about the cell design and metallurgical performance can be found in Crompton et al. [14].

The cell was operated semi-continuously, with an initial batch of mineral pulp fed. The tailings were recycled, while the concentrate was collected into a separate tank, being filtered to recycle the fluidisation water. High-pressure air was injected at 80 PSI into the fluidisation water to produce small bubbles. Symmetric inlets introduced the aerated fluidisation water into the fluidisation chamber at the bottom of the cell (see Figure 1a). The cell included instrumentation for adjusting fluidisation and airflow rates, providing control over the operating conditions.

2.2. Large Modular Array (LaMA) for PEPT

The Large Modular Array (LaMA) is a flexible, geometrically reconfigurable PEPT system developed upon the CTI/Siemens ECAT PET scanner architecture. The system was first tested and assembled in the late 2000s at the PIC [30] but only consisted of 16 buckets or modules based on the ECAT 931 scanner. Soon afterwards, it was fitted with parts from the upgraded ECAT 951 scanner and did not undergo any major development until its major expansion and modification in 2021.

Today the array consists of 48 buckets based on the 951 series detectors and electronics which can interface with one of the two available independent coincidence processors (CP), one from ECAT 951 and one from ECAT 931. Each bucket is contained within a square aluminium enclosure measuring 360 mm wide, 95 mm tall, and 460 mm deep and contains four bismuth germanate (BGO) scintillator detector blocks spaced 88 mm apart, centred upon the front face of the bucket as shown in Figure 2. Each detector block

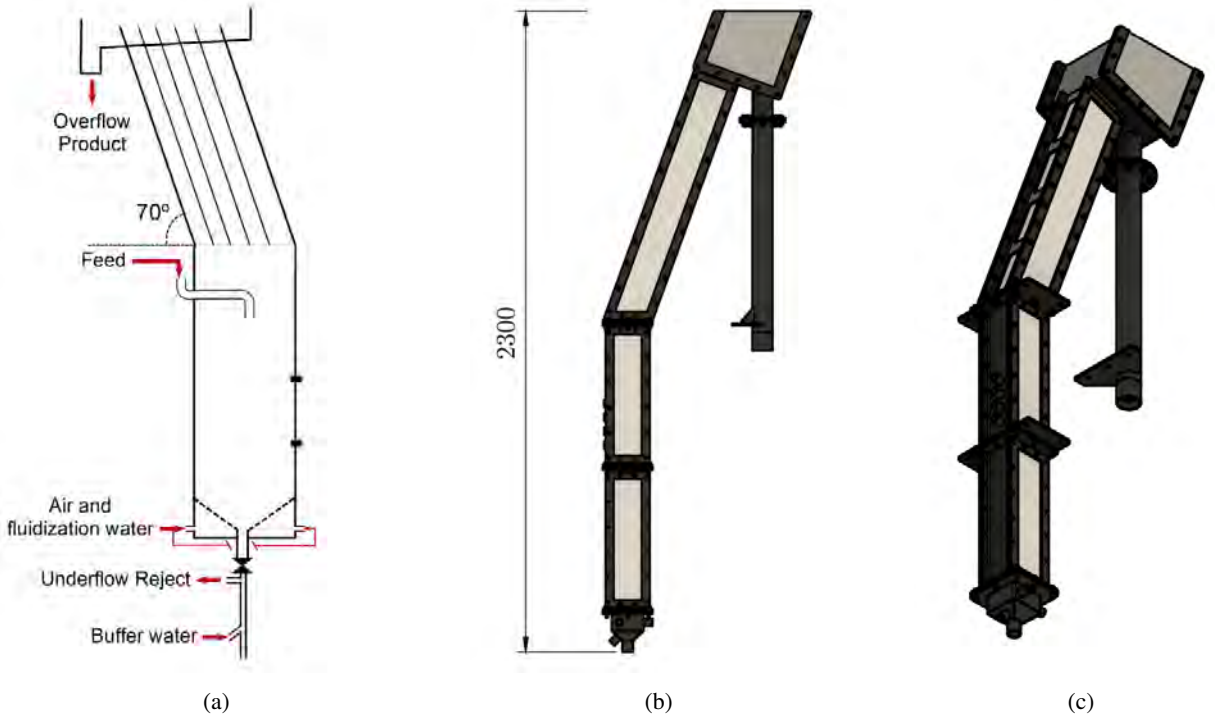

Figure 1: Schematic of the CoarseAIR™ fluidised bed flotation cell, showing (a) the main sections, inlets and outlets (adapted from Crompton et al. [14]), (b) a lateral view of the cell, and (c) an isometric view of the laboratory-scale prototype used in this work. The box at the bottom is the fluidisation chamber, where a mix of water and air is injected at high pressure. The vertical section is the fluidised bed and the slanted section hosts lamella plates that aim to improve the separation efficiency.

crystal is approximately 50 x 50 mm^2 in area and 30 mm thick, subdivided into an 8 x 8 array of crystal elements, and is viewed by four photomultiplier tubes. The 951 series bucket controller then processes the output from each of the photomultiplier tubes for each of the four detector blocks to determine within which crystal element the gamma ray has interacted. These positional data are then sent to the CP to determine if an interaction has occurred in any of the other buckets within the 12 ns coincidence resolving time.

To use all of the 48 buckets, two CPs are used as each one can only accept inputs from 2 to 32 buckets. Therefore, the buckets can be distributed between the two CPs according to the experiment's geometrical requirements. The coincidence data are then recorded from each CP by custom-designed acquisition boards that also add a timestamp to each event. This timestamp allows the data produced by the two CPs to be combined during post-processing to continuously track the movement of a tracer as it travels between the areas viewed by each of the CPs. Therefore, this extends the FOV of the system beyond what is possible with just a single scanner's worth of electronics.

Due to the modular nature of the array, LaMA can be built after the equipment is set up to closely surround it and follow any awkward geometry. To view the full 2.3 m tall fluidised bed flotation cell, a flat plane design was chosen where the buckets were stacked in two tall columns exactly 500 mm apart, as seen in Figure 5b. The fluidisation chamber, fluidised bed, and its intersection with the angled

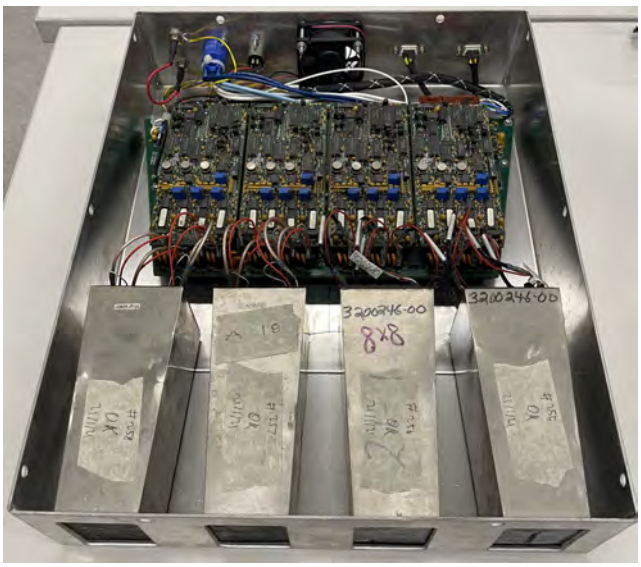

Figure 2: A LaMA bucket with its lid removed displaying four detector blocks and a bucket controller board from the ECAT 951 PET scanner.

lamella plates were viewed by 32 buckets connected to the 951 series CP and the remaining upper lamella plates were viewed by 16 buckets connected to the 931 series CP. This bucket arrangement essentially divided the system into two sections. The first section provided accurate particle tracking within the fluidised bed and at the lamellae intersection

while the second section further extended the FOV to include the rest of the lamellae. The whole arrangement was supported by a custom-designed frame made to follow the angled lamellae of the cell built from aluminium profile extrusions, as shown in Figure 5c.

2.3. Materials and reagents

Copper tailings were used as the mineral feed, sourced by FLSmidth. The tailings received were sieved and deslimed, discarding the fraction under 75 µm. After desliming, the P80 of the sample was 250 µm, as shown in Figure 3. A 50:50 mixture of MIBC and X133 was used as frother. PAX and diesel were used as the copper-ore collectors.

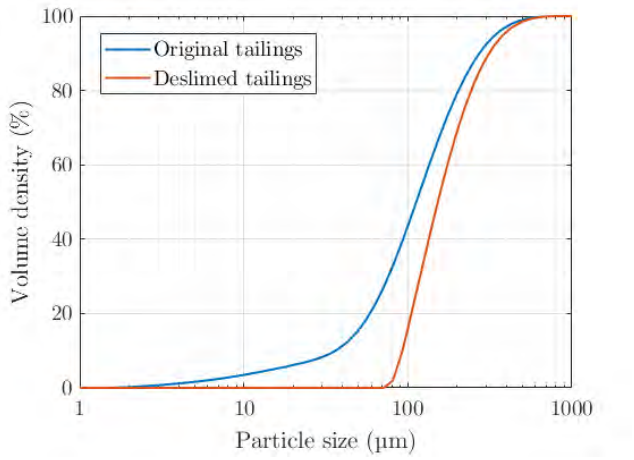

Figure 3: Particle size distribution of the tailings material. The blue line represents the cumulative distribution by volume of the tailings as received, and the red line represents the particle size distribution after desliming.

2.4. PEPT tracers

For these measurements directly activated tracers were used. The activation was performed using an 11.2 MeV proton beam at the Birmingham Cyclotron Facility [31, 32]. The chalcopyrite particles were prepared at the Positron Imaging Centre at the School of Physics and Astronomy in Birmingham, which is in the same building as the Cyclotron and used straight after the irradiation for the measurements. The technique of directly activated tracers for PEPT is outlined in Fan et al. [33]. The activated chalcopyrite particles were dispersed in a concentrated solution of collectors (PAX + diesel) and utilised as proxies for hydrophobic (valuable) particles. When the chalcopyrite particles were directly introduced into the cell without any treatment in collectors, they behaved as hydrophilic (gangue) particles.

The chalcopyrite particles used as tracers had a specific gravity of 4200 and varied in diameter, ranging between 300 to 700 µm. The activity of the tracers used ranged between 2.5 to 4.5 MBq.

2.5. Experimental procedure

PEPT experiments were conducted utilising LaMA for particle tracking as shown in Figure 5. Experiments were

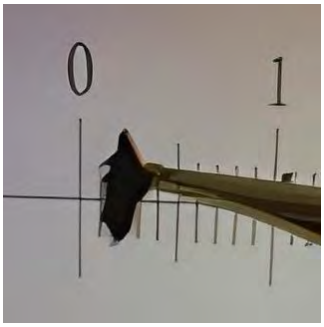

Figure 4: Chalcopyrite particles were directly activated to be used as tracers. The particles we used as hydrophobic and hydrophilic tracers, depending on their treatment with collectors.

duplicated on different days, using different tracers and material feed. Each experiment used only one tracer at a time, testing hydrophobic and hydrophilic tracers.

The airflow and fluidisation rates were set constant for most of the experiments, with a superficial gas velocity (J_G) of 0.17 cm/s and a superficial water velocity of fluidisation (J_{W_f}) of 0.19 cm/s, following the "Normal" operating conditions defined by FLSmidth (see Table 1). Airflow and fluidisation rates were also varied to assess the effect of these operating conditions on the fluid dynamics of the system. These variability tests, however, were only performed for hydrophilic tracers, as tracer recirculation allowed for longer experiments to be run.

Table 1
Operating conditions assessed in PEPT tests. Superficial gas velocity (J_G) and superficial water velocity of fluidisation (J_{W_f}) were varied at three levels.

Operating condition	J_G (cm/s)	J_{W_f} (cm/s)
Low	0.11	0.13
Normal	0.17	0.19
High	0.23	0.25

A feed with a solid content of 50%$_{w/w}$ was prepared in an external agitated tank, using 3 kg of tailings samples 100% ≥ 75µm and 3 litres of tap water. The pulp was conditioned by adding 10 g/t of diesel and agitating for 5 minutes, followed by the addition of 90 g/t of PAX and 3 minutes of agitation. Finally, 40 g/t of the frother mix was added to the pulp. The conditioned pulp was injected into the CA100 cell from the middle injection point using a peristaltic pump. The fluidisation water tank was conditioned with the frother mix at a dosage of 20 ppm$_{v/v}$. Figure 6 presents a schematic representation of the process flow diagram used during experiments.

The positron-emitting tracers were recovered at the end of each experiment. On the occasions when the tracer overflowed with the concentrate (hydrophobic tracers), these were recovered by placing a sieve in the concentrate pipe, being manually re-injected into the cell for further testing.

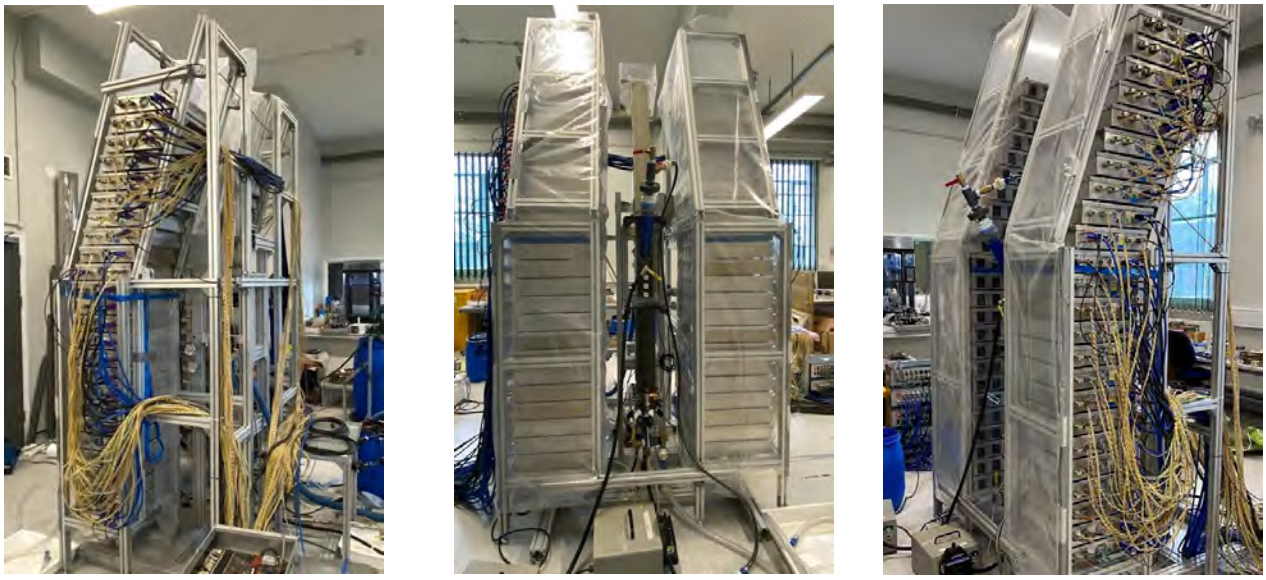

(a) (b) (c)

Figure 5: Large Modular Array (LaMA) for PEPT in an ad-hoc configuration for the CoarseAIR™ fluidised bed experiments. Photographs obtained during experiments in the Positron Imaging Centre at the University of Birmingham.

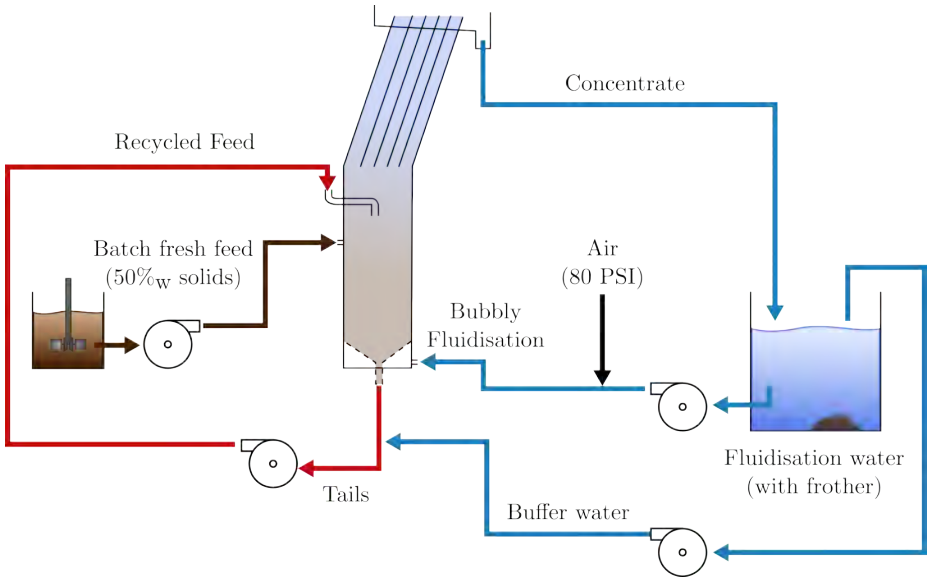

Figure 6: Process flow diagram of the CA100™ setup for continuous PEPT experiments.

Conversely, when the tracer reported to the tailings, it was recycled back into the cell by the peristaltic pumps.

2.6. PEPT data analysis using PEPT-ML

The experimental PEPT data were analysed using the machine learning-based algorithm PEPT-ML, proposed by Nicuşan and Windows-Yule [34] to determine the position of the tracer for each of the detected positron annihilation events. In this algorithm, the data is split into a series of individual samples, each containing a given N number of LORs. For every sample of LORs, PEPT-ML computes cutpoints or the midpoint of the shortest line segment that is perpendicular to a pair of LORs for every possible pair of LORs in a sample that is also shorter than a set maximum distance. These cutpoints are then clustered using a Hierarchical Density-Based Spatial Clustering of Applications with Noise (HDBSCAN) algorithm, and the centres of the clusters are extracted in so-called "1-pass clustering". These centres can then be further split into samples of a given size and clustered again using the HDBSCAN algorithm in "2-pass clustering". The trajectory of every particle using the centres from the previous step is then constructed.

When extracting post-processed data from tracer trajectories, it is often important to sample data at fixed timesteps. Being a Lagrangian technique, PEPT tracers can be located

more frequently in more sensitive areas of the FOV of a PEPT camera, especially in LaMA where sensitivity varies due to the spaces between the detector blocks. Therefore, it is necessary to use interpolation to convert the "randomly" sampled positions into regular timesteps. These interpolated tracks are then used to calculate the tracer velocity.

All individual tracks were analysed, quantifying the motion and velocity of the tracers. Representative two-minute tracks of each tracer are shown and discussed in Section 3.1, while Section 3.2 focuses on particle dynamics in the slanted lamella plates.

Over one hour of PEPT data was used to create a time-averaged 3D Eulerian grid with voxel dimensions of 10mm by 10mm by 10mm. Slanted voxels were used in the lamella plates' region for consistency. The central slice of the cell, represented by all the voxels in the yz plane with $x \in [-10, 10]$ mm, was analysed in Section 3.3, focusing on the vertical velocity and the residence time in terms of passes. For the velocity data, its different vectorial components for each voxel were represented by a kernel-smoothed distribution, as described in Mesa et al. [23] and Cole et al. [26]. The peak of the distribution, representing the most likely velocity, was used as the representative value for each voxel, eliminating the effect of outliers. The measurement of passes refers to the number of times the tracer passed through a voxel (relative to entering and exiting the cell), normalised by the passes in the slice [24].

3. Results and discussion

3.1. Analysis of individual tracks

Representative two-minute tracks, one for each tracer type, are discussed in this section. Figure 7 shows the position with time of the tracer on each Cartesian component, where x represents the depth of the cell (ranging between -50 and 50 mm), y represents the vertical direction (between 0 and 2100 mm) and z the horizontal component (-300 to 50 mm). The tracers were fed into the cell at a height of $y \approx$ 1000 mm. The tracers would move within the cell and finally would either overflow as a concentrate or sink towards the tailings.

The configuration of LaMA, as described in Section 2.2, was such that two groups of cameras were used. This separation of LaMA into two sections is evidenced in Figure 7a in the slight gap between the tracks when crossing a height of $y \approx 1500$ mm (close to 60 s on the track). The hydrophobic tracer shown in Figure 7a floated and reported to the concentrate after approximately 90 seconds. The tracer was then sieved from the concentrate using a Geiger counter to identify its location and fed back into the cell for further testing.

The hydrophilic tracers, on the other hand, were recycled from the tailings back into the cell, allowing long experiments to be performed. In the particular two-minute track shown in Figure 7b, it is observed that on most occasions the hydrophilic tracer sunk directly to the tailings for recycling. However, between the times 30-110 s, it can be observed that the hydrophilic tracer was suspended in the cell, even rising back near the injection point, before sinking and recirculating again.

Figure 8 shows the velocity Cartesian components of the tracer motion. The highest velocities were reached on the vertical axis y, as expected, achieving speeds close to 400 mm / s. The vertical velocity can be directly linked to the upward motion related to the rise of a tracer attached to a bubble or the sinking motion of a gangue particle, thus most attention has been paid to this component of the overall velocity.

To better understand the motion and velocity of the tracks, a 2D representation (yz plane) is shown in Figure 9. The motion of the tracer is represented by the track, and the colour of the line represents the vertical velocity.

The hydrophobic tracer shown in Figure 9a entered the cell and circulated in the upper section of the columnar body, with fluctuating vertical speeds below 400 mm/s. At around one minute of tracking, the hydrophobic tracer was collected towards the lamella plates. In the lamella plates, the tracer reached a vertical velocity of 200 mm/s, with fluctuating velocities in the x and z directions. The motion within the lamella plates is further explored in Section 3.2.

In the case of the hydrophilic tracer, Figure 9b evidences a rapid downward movement near the wall near the injection point, as the recirculating flow is injected with a downward angle at a high velocity. In the two minutes tracked, the hydrophilic tracer recirculated four times, with a residence time of under one minute. The third time the tracer entered the cell in this 2-minute track, it had a longer residence time, circulating within the columnar section of the cell, reaching positive vertical velocities of 300 mm/s.

The analysis of multiple tracks such as those shown in Figures 7 to 9 suggests that the hydrophilic particles moved predominantly downward, with a short residence time. This effect could imply that the design of the recirculation inlet of this laboratory-scale CA100, combined with the operation of the recirculation pump, had a direct effect on the operation of the cell, altering the stability of the fluidised bed. Similarly, the analysis of multiple hydrophobic tracks shows that coarse valuable particles are quickly floated by the CA100. Generalised observations of flow patterns are discussed in Section 3.3, where long tracks are analysed using Eulerian representations.

3.2. Particle motion in the lamella plates

Multiple tracks obtained with hydrophobic tracers are shown in Figure 10. These tracks correspond to approximately 15 minutes of operation, obtained during independent experimental runs on two different days, with different tracers.

Once a hydrophobic particle entered the lamella plates, its movement in the component z was controlled by the spacing between plates. The motion in the xy plane, however, denoted a tortuous path towards the top of the cell. The central subfigure in Figure 10, shows that the tracer did not move in a straight line upward once it entered the

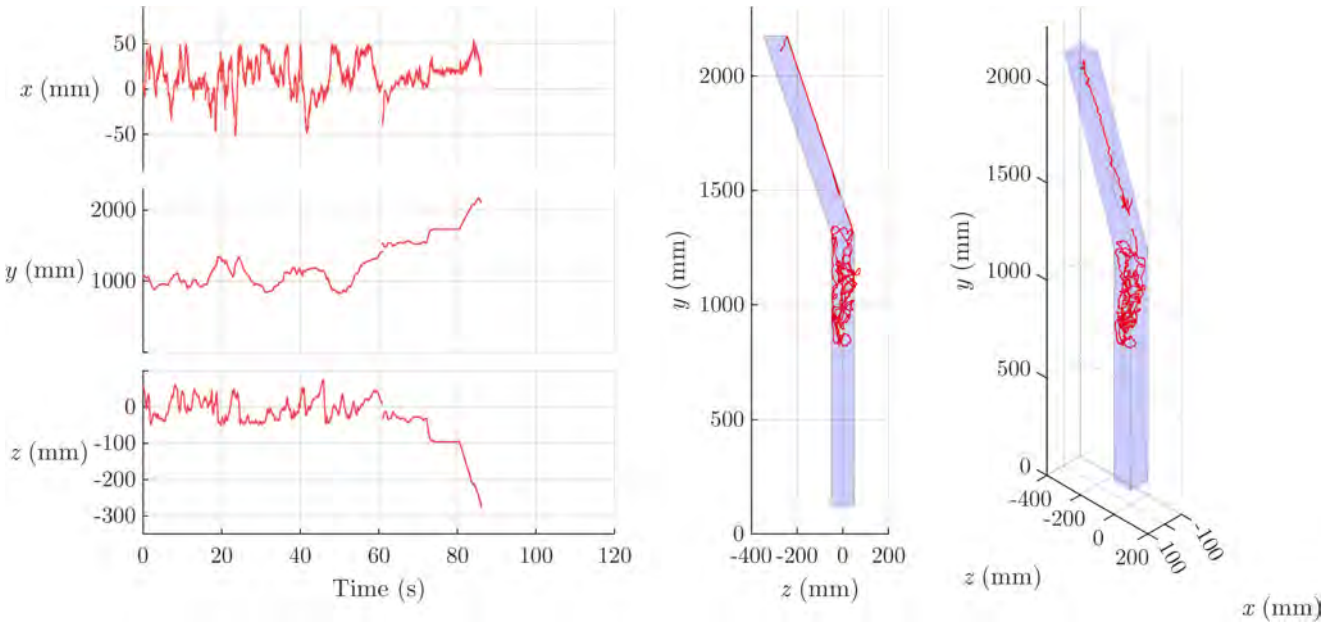

(a) Hydrophobic tracer

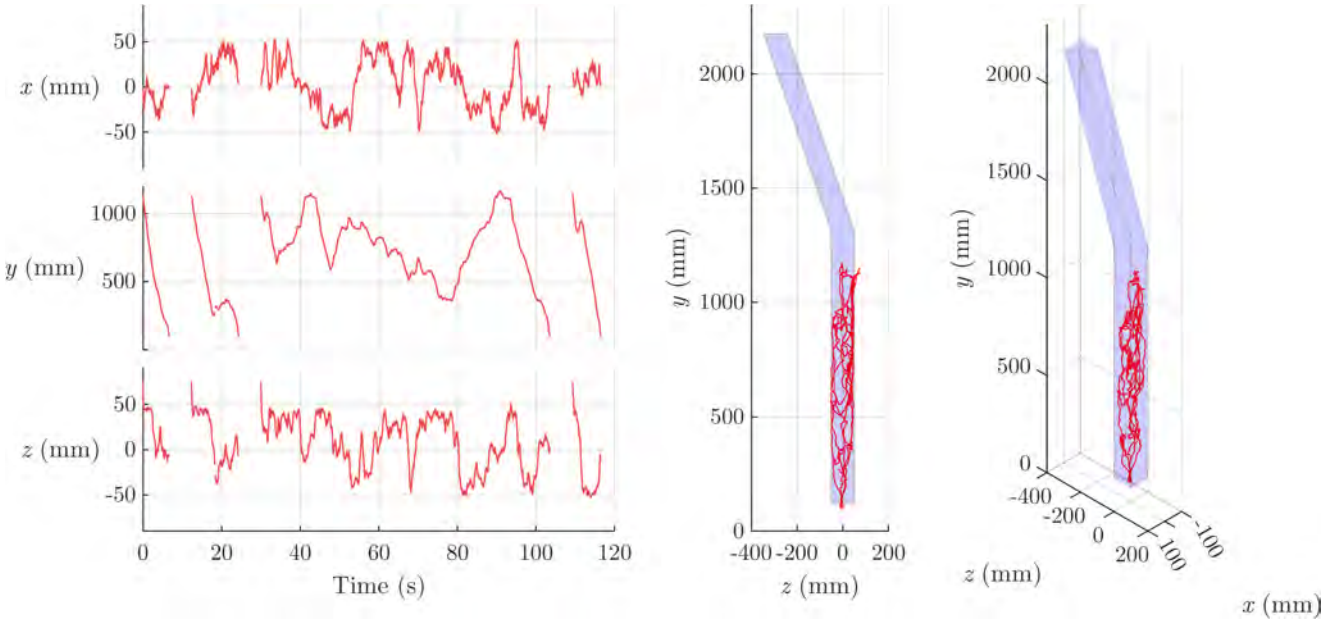

(b) Hydrophilic tracer

Figure 7: Representative two-minute tracks of flotation with (a) a hydrophobic and (b) a hydrophilic tracer.

lamella plates. On the contrary, the tracer covered most of the available width of the cell (x component), evidencing downward motion near the walls.

The tortuosity of each track in the lamella plates region was calculated as the ratio between the 3D arc-length of the track and the Eulerian distance between the points of entry and overflow. Consequently, a tortuosity value of 1 would represent a straight path in the region between two lamella plates, while values over 1 represent more convoluted tracks. The average path tortuosity in the lamella plates was 7.3, ranging between 2 and 19. Tortuosity variability may have been caused by differences in tracer size and shape, subtle geometrical differences between lamella plates, or differences in the size and number of bubbles to which the tracer was attached.

3.3. Eulerian representation analysis

For the analysis of the time-averaged velocity data, the tracer velocity ($\vec{v}$) was decomposed into its vectorial components, namely the depth ($\vec{v_x}$), vertical ($\vec{v_y}$) and horizontal ($\vec{v_z}$) velocities, and were represented by the peak of the velocity distribution in each voxel. Eulerian representations of the vertical velocities of the hydrophilic and hydrophobic tracers are shown in Figure 11. The central slices in depth

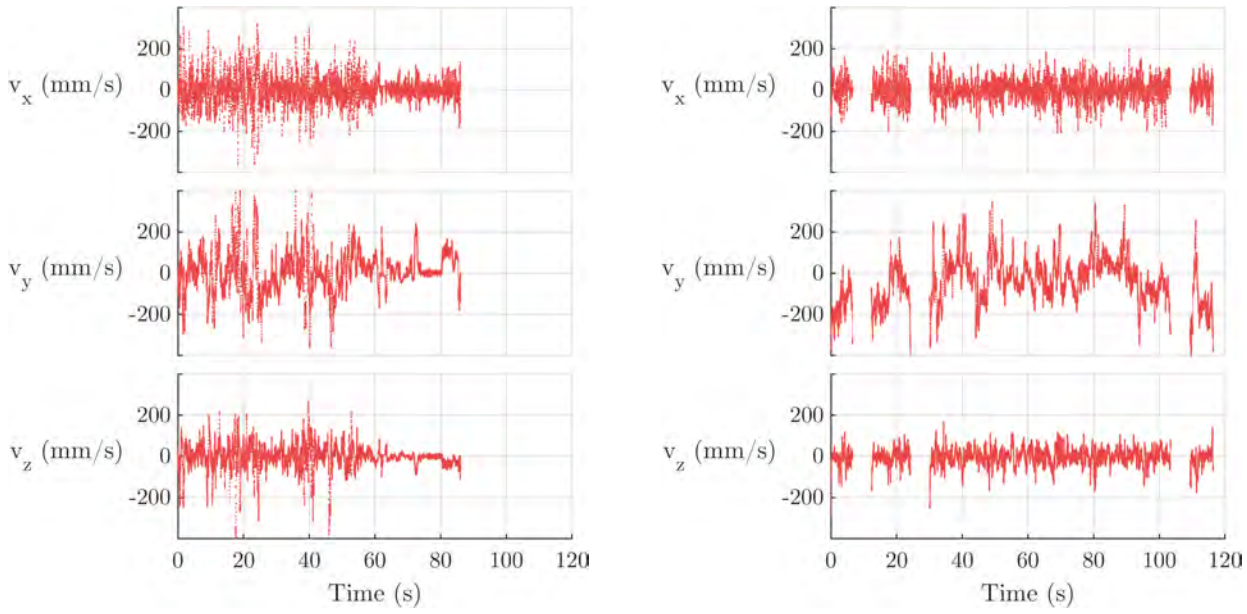

(a) Hydrophobic tracer (b) Hydrophilic tracer

Figure 8: Velocity components of the representative two-minute tracks obtained with (a) a hydrophobic and (b) a hydrophilic tracer.

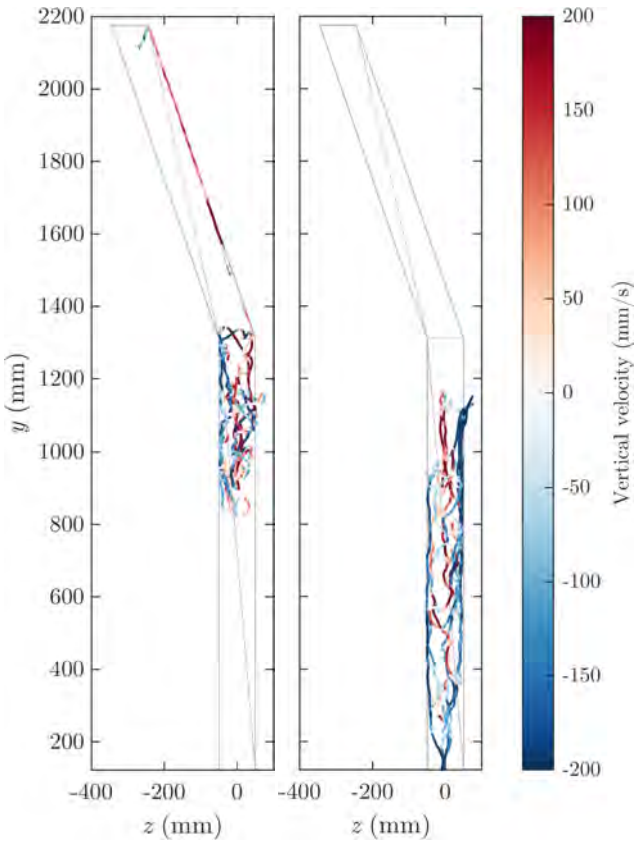

(a) Hydrophobic tracer (b) Hydrophilic tracer

Figure 9: Lateral view of the representative two-minute tracks obtained with (a) hydrophobic and (b) hydrophilic tracer. The vertical velocity $\vec{v}_y$ is represented by the colour bar.

($x \in [-10, 10]$ mm) were chosen as these are farther away from the walls, allowing the analysis of bulk behaviour. This slice effectively entails the merging of two yz slices of 10 mm thickness ($x \in [-10, 0] \cup [-10, 0]$ mm), which is possible due to the symmetry of the flotation cell along the vertical dimension, allowing to increase the number of data points within each voxel [23].

Figure 11a shows that hydrophobic particles move throughout the whole cell until they attach to a bubble and are collected toward the lamella plates. As observed in Section 3.1, the tracer tends to rise near the centre of the cell and sink near the walls, which may be an indication of convective flows in the cell. In this central slice, it is observed that the hydrophobic particles tend to ascend using only the central lamella plates.

In the case of hydrophilic particles (Figure 11b), the velocity profile evidences a rapid downward movement near the wall closer to the injection point, as the recirculating flow is injected downward at high velocity. Therefore, it is plausible that the design of the recirculation inlet combined with the operation of the recirculation pump directly affects the operation of the cell, altering the stability of the fluidised bed. As in the case of hydrophobic particles, an upward motion is observed in the middle of the cell, which is related to the fluidisation water injection from the bottom.

Notably, in over one hour of continuous operation, the hydrophilic tracer was never wrongly recovered, which translates to a great selectivity. Furthermore, and despite the large size of the tracer (> 300 µm), the hydrophobic tracer rarely reported to tailings, implying that high recoveries can be achieved with CA100. These metallurgical observations are well aligned with the results obtained by Crompton et al.

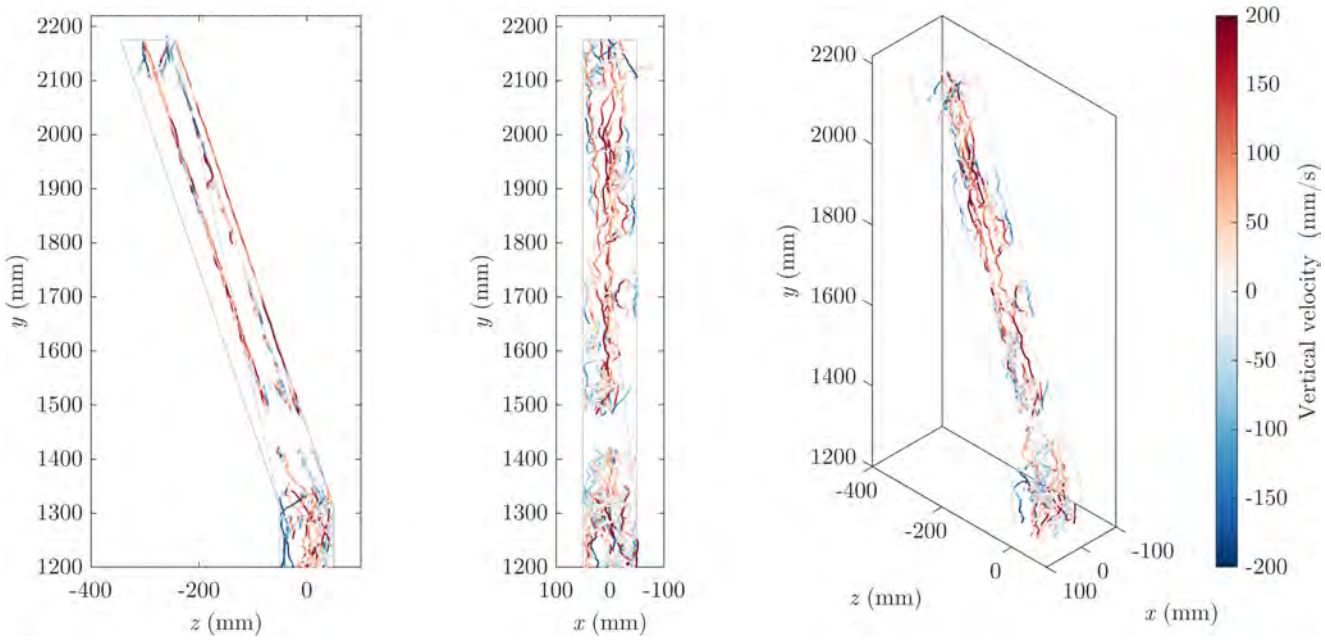

Figure 10: Particle dynamics in the inclined lamella plates.

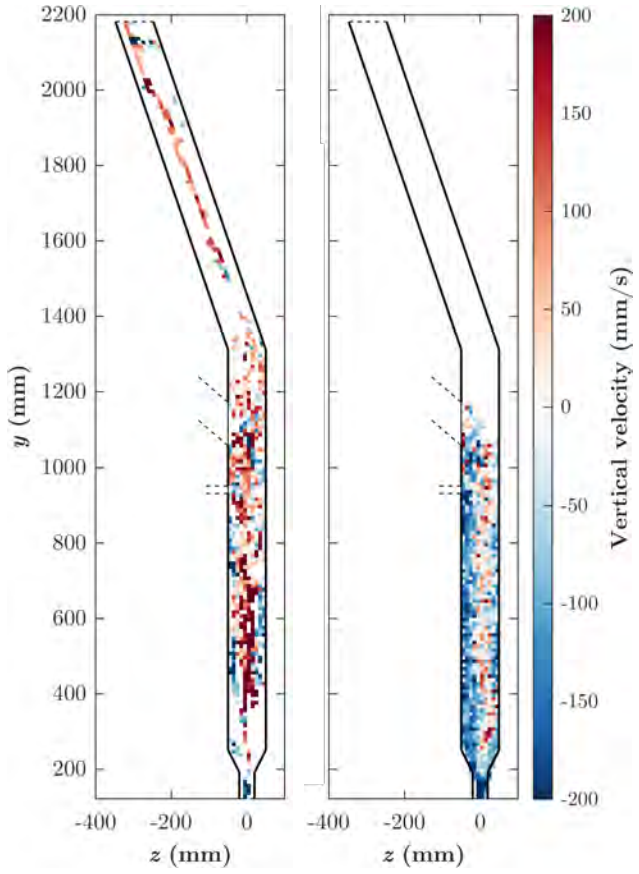

(a) Hydrophobic tracers (b) Hydrophilic tracers

Figure 11: Eulerian representation of the time-average vertical velocity of (a) hydrophobic and (b) hydrophilic particles. The Eulerian representations considered multiple tracks, with a voxel size of 10 mm by 10 mm by 10 mm, sliced in the middle plane of the cell ($x \in [-10, 10]$ mm).

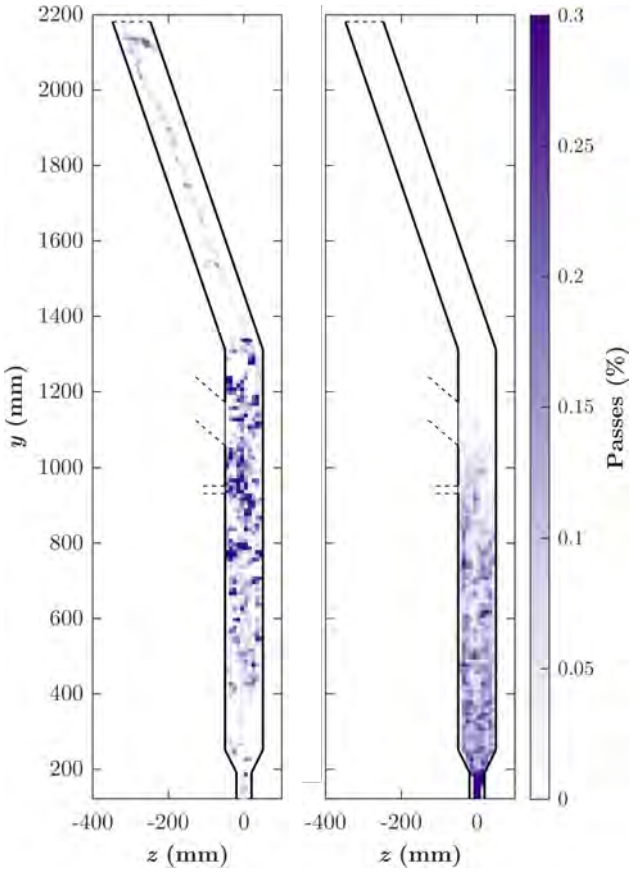

(a) Hydrophobic tracers (b) Hydrophilic tracers

Figure 12: Eulerian representation of the time-average Location density of (a) hydrophobic and (b) hydrophilic particles. The Eulerian representations considered multiple tracks, with a voxel size of 1 cm^3, sliced at the middle plane of the cell ($x \in [-10, 10]$ mm).

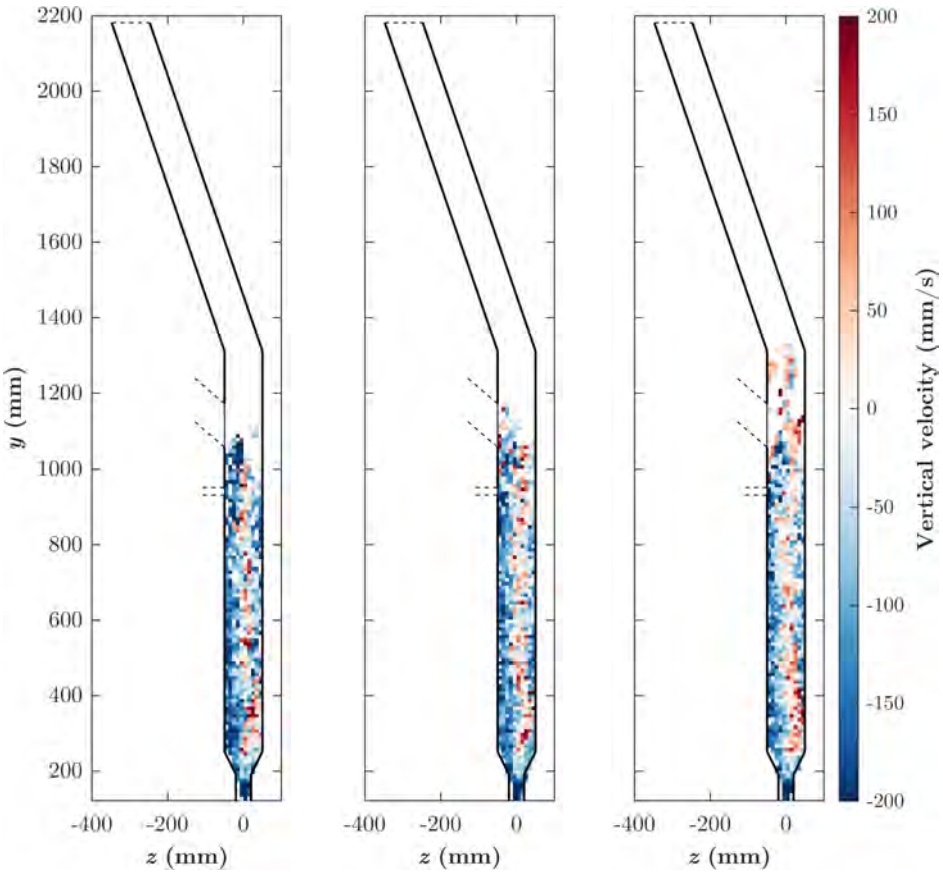

(a) Low fluidisation (b) Normal fluidisation (c) High fluidisation

Figure 13: Effect of the operating conditions on the vertical velocity of the hydrophilic tracers, shown in time-averaged Eulerian representations of the middle plane of the cell ($x \in [-10, 10]$ mm). The operating conditions correspond to (a) Low fluidisation: $J_G = 0.11$ cm/s and $J_{W_f} = 0.13$ cm/s, (b) Normal fluidisation: $J_G = 0.17$ cm/s and $J_{W_f} = 0.19$ cm/s, and (c) High fluidisation: $J_G = 0.23$ cm/s and $J_{W_f} = 0.25$ cm/s.

[35] with the CA100, where a cumulative recovery of over 80% was reported for valuable particles ≤ 600 µm.

The normalised passes of the tracers per each voxel are shown in Figure 12. The hydrophobic particles (Figure 12a) tend to circulate several times in the upper section of the columnar body, presenting a relatively uniform occupancy. The number of passes in the lamella plates is considerably lower, implying that once tracers entered into this slanted section, they tended to move upwards relatively fast, despite the tortuosity described in Section 3.2. Notably, the hydrophobic tracers only used the central and top lamella plates, which could be related to an effect of the feed/recirculation flow displacing the ascending particles towards the opposite wall.

The hydrophilic tracer (Figure 12b) shows a higher pass count at the bottom of the tank. This behaviour evidences that, although large hydrophilic particles tend to move downwards, there is still mixing and suspension of these particles due to the fluidisation water.

3.4. Effect of operating conditions

Three different operating conditions were tested for the hydrophilic tracers, varying the airflow and fluidisation rate, into "Low", "Normal" and "High", as described in Table 1. The results obtained are shown in Figure 13.

Although the overall behaviour of the hydrophilic tracer for the different operating conditions is similar in terms of motion, some differences can be appreciated, both in terms of vertical velocity values and the occupied zones. At the highest airflow and fluidisation rates tested (Figure 13c), the hydrophilic particles evidenced a faster upward motion in the centre of the tank. Moreover, this upward flow occupied a larger portion of the tank when compared to the normal operating conditions (Figures 11b and 13b), while also reaching higher into the tank, closer to the lamella plates.

A lower fluidisation Figure 13a, on the other hand, resulted in a more pronounced downward motion dominating the behaviour of hydrophilic particles. The level of the bed seems to have been affected as well, reaching a lower level than in normal conditions, although the difference is less pronounced than in the case of High v/s Normal comparison.

4. Conclusions

This study represents a substantial advancement in our understanding of the fluid dynamics of fluidised bed flotation cells (FBFCs), specifically focusing on the CoarseAir™-100. The Large Modular Array (LaMA) PEPT system was used to perform the largest positron emission particle tracking experiment to date, shedding light on the complex fluid dynamics within large-scale fluidised bed flotation cells.

The study allowed us to carry out a quantitative assessment of the flotation of hydrophobic tracers as they preferentially floated towards the concentrate despite their coarse size, while hydrophilic tracers exhibited a distinctive recycling mechanism, moving from tailings back into the cell. Detailed Cartesian tracking of individual particle paths unveiled intricate motion patterns within the system. The analysis of hydrophobic tracer dynamics within the inclined lamella plates revealed tortuous paths, emphasising the significant influence of design and geometry on particle movement.

Decomposing time-averaged velocity data through Eulerian representation provided further insights into the behaviour of hydrophobic and hydrophilic particles. Hydrophobic particles moved throughout the cell, displaying an ascending motion primarily through central and top lamella plates. In contrast, hydrophilic particles exhibited rapid downward and upward movements, reflecting the impact of operating conditions on fluidisation dynamics.

Exploration of different operating conditions highlighted the variations in the behaviour of hydrophilic tracers. Higher airflow and fluidisation rates accentuated upward motion, expanding the occupancy of hydrophilic particles in the central region of the tank.

This work significantly contributes to the knowledge base of fluidised bed flotation cells. The acquired experimental data not only enhance our understanding of particle dynamics but also provide a benchmark for validating multiphase simulations and evaluating alternative designs.

Acknowledgements

The authors acknowledge funding from FLSmidth. The authors thank Mr. Yui Ming Kan, technician at the Positron Imaging Centre, for his help during the experiments. The authors also thank Dr Ben Phoenix and the Birmingham Cyclotron team for their help with the direct activation of the tracers used.

CRediT authorship contribution statement

Diego Mesa: Methodology, Software, Formal analysis, Investigation, Data Curation, Writing - Original Draft, Visualisation. **Dawid M. Hampel:** Methodology, Software, Formal analysis, Investigation, Data Curation, Writing - Original Draft, Visualisation. **Stephen J. Neethling:** Resources, Project administration, Funding acquisition. **Tzany Kokalova Wheldon:** Conceptualisation, Resources, Methodology, Writing - Review & Editing, Supervision, Project administration. **Pablo R. Brito-Parada:** Conceptualisation, Resources, Writing - Review & Editing, Supervision, Project administration, Funding acquisition.

References

[1] Ahmad Hassanzadeh. A survey on troubleshooting of closed-circuit grinding system. *Canadian Metallurgical Quarterly*, 57(3):328–340, July 2018. ISSN 0008-4433. doi: 10.1080/00084433.2018.1464618. URL https://doi.org/10.1080/00084433.2018.1464618. Publisher: Taylor & Francis _eprint: https://doi.org/10.1080/00084433.2018.1464618.

[2] Ahmad Hassanzadeh, Mehdi Safari, Duong H. Hoang, Hamid Khoshdast, Boris Albijanic, and Przemyslaw B. Kowalczuk. Technological assessments on recent developments in fine and coarse particle flotation systems. *Minerals Engineering*, 180:107509, April 2022. ISSN 0892-6875. doi: 10.1016/j.mineng.2022.107509. URL https://www.sciencedirect.com/science/article/pii/S0892687522001194.

[3] V. Deniz. Comparisons of Dry Grinding Kinetics of Lignite, Bituminous Coal, and Petroleum Coke. *Energy Sources, Part A: Recovery, Utilization, and Environmental Effects*, 35(10):913–920, May 2013. ISSN 1556-7036. doi: 10.1080/15567036.2010.514591. URL https://doi.org/10.1080/15567036.2010.514591. Publisher: Taylor & Francis _eprint: https://doi.org/10.1080/15567036.2010.514591.

[4] S. Chehreh Chelgani, M. Parian, P. Semsari Parapari, Y. Ghorbani, and J. Rosenkranz. A comparative study on the effects of dry and wet grinding on mineral flotation separation–a review. *Journal of Materials Research and Technology*, 8(5):5004–5011, September 2019. ISSN 2238-7854. doi: 10.1016/j.jmrt.2019.07.053. URL https://www.sciencedirect.com/science/article/pii/S223878541930849X.

[5] V. Kromah, S. B. Powoe, R. Khosravi, Ali Asimi Neisiani, and S. Chehreh Chelgani. Coarse particle separation by fluidized-bed flotation: A comprehensive review. *Powder Technology*, 409:117831, September 2022. ISSN 0032-5910. doi: 10.1016/j.powtec.2022.117831. URL https://www.sciencedirect.com/science/article/pii/S0032591022007161.

[6] Jianlong Wang, Anh V. Nguyen, and Saeed Farrokhpay. A critical review of the growth, drainage and collapse of foams. *Advances in Colloid and Interface Science*, 228:55–70, February 2016. ISSN 0001-8686. doi: 10.1016/j.cis.2015.11.009. URL https://www.sciencedirect.com/science/article/pii/S0001868615002171.

[7] Graeme J. Jameson. Advances in Fine and Coarse Particle Flotation. *Canadian Metallurgical Quarterly*, 49(4):325–330, October 2010. ISSN 0008-4433. doi: 10.1179/cmq.2010.49.4.325. URL https://doi.org/10.1179/cmq.2010.49.4.325. Publisher: Taylor & Francis _eprint: https://doi.org/10.1179/cmq.2010.49.4.325.

[8] J. N. Kohmuench, G. H. Luttrell, and M. J. Mankosa. Coarse particle concentration using the HydroFloat Separator. *Mining, Metallurgy & Exploration*, 18(2):61–67, May 2001. ISSN 2524-3470. doi: 10.1007/BF03402873. URL https://doi.org/10.1007/BF03402873.

[9] Shadrack Fosu, Bellson Awatey, William Skinner, and Massimiliano Zanin. Flotation of coarse composite particles in mechanical cell vs. the fluidised-bed separator (The HydroFloat™). *Minerals Engineering*, 77:137–149, June 2015. ISSN 0892-6875. doi: 10.1016/j.mineng.2015.03.011. URL https://www.sciencedirect.com/science/article/pii/S0892687515001016.

[10] Md. Tariqul Islam and Anh V. Nguyen. Parametric investigations of different variables on liquid–solid fluidization in a HydroFloat cell using computational fluid dynamics. *Chemical Engineering Research and Design*, 159:13–26, July 2020. ISSN 0263-8762. doi: 10.1016/j.cherd.2020.03.028. URL https://www.sciencedirect.com/science/article/pii/S0263876220301301.

[11] Massimiliano Zanin, Eddie Chan, and William Skinner. Modelling the fluidised bed in HydroFloat™ for improved process control. *Powder Technology*, 388:241–250, August 2021. ISSN 0032-5910. doi: 10.1016/j.powtec.2021.04.089. URL https://www.sciencedirect.com/science/article/pii/S0032591021003764.

[12] Graeme J. Jameson and Cagri Emer. Coarse chalcopyrite recovery in a universal froth flotation machine. *Minerals Engineering*, 134: 118–133, April 2019. ISSN 0892-6875. doi: 10.1016/j.mineng.2019.01.024. URL https://www.sciencedirect.com/science/article/pii/S089268751930041X.

[13] Graeme J. Jameson, Lonn Cooper, Kitty K. Tang, and Cagri Emer. Flotation of coarse coal particles in a fluidized bed: The effect of clusters. *Minerals Engineering*, 146:106099, January 2020. ISSN 0892-6875. doi: 10.1016/j.mineng.2019.106099. URL https://www.sciencedirect.com/science/article/pii/S0892687519305102.

[14] Luke J. Crompton, Md Tariqul Islam, and Kevin P. Galvin. Investigation of Internal Classification in Coarse Particle Flotation of Chalcopyrite Using the CoarseAIRTM. *Minerals*, 12(6):783, June 2022. ISSN 2075-163X. doi: 10.3390/min12060783. URL https://www.mdpi.com/2075-163X/12/6/783. Number: 6 Publisher: Multidisciplinary Digital Publishing Institute.

[15] Sayed Janishar Anzoom, Ghislain Bournival, and Seher Ata. Coarse particle flotation: A review. *Minerals Engineering*, 206:108499, January 2024. ISSN 0892-6875. doi: 10.1016/j.mineng.2023.108499. URL https://www.sciencedirect.com/science/article/pii/S0892687523005137.

[16] Barry A. Wills and James A. Finch. Froth Flotation. In *Wills' Mineral Processing Technology*, pages 265–380. Elsevier, 2016. ISBN 978-0-08-097053-0. doi: 10.1016/B978-0-08-097053-0.00012-1. URL https://linkinghub.elsevier.com/retrieve/pii/B9780080970530000121.

[17] Mohsen Hamidipour, Jinwen Chen, and Faïçal Larachi. CFD study on hydrodynamics in three-phase fluidized beds—Application of turbulence models and experimental validation. *Chemical Engineering Science*, 78:167–180, August 2012. ISSN 0009-2509. doi: 10.1016/j.ces.2012.05.016. URL https://www.sciencedirect.com/science/article/pii/S0009250912002977.

[18] J.E. Dickinson and K.P. Galvin. Fluidized bed desliming in fine particle flotation – Part I. *Chemical Engineering Science*, 108:283–298, April 2014. ISSN 00092509. doi: 10.1016/j.ces.2013.11.006. URL https://linkinghub.elsevier.com/retrieve/pii/S0009250913007355.

[19] K. P. Galvin and J. E. Dickinson. Fluidized bed desliming in fine particle flotation – Part II: Flotation of a model feed. *Chemical Engineering Science*, 108:299–309, April 2014. ISSN 0009-2509. doi: 10.1016/j.ces.2013.11.027. URL https://www.sciencedirect.com/science/article/pii/S000925091300763X.

[20] K. P. Galvin, N. G. Harvey, and J. E. Dickinson. Fluidized bed desliming in fine particle flotation – Part III flotation of difficult to clean coal. *Minerals Engineering*, 66-68:94–101, November 2014. ISSN 0892-6875. doi: 10.1016/j.mineng.2014.02.008. URL https://www.sciencedirect.com/science/article/pii/S0892687514000557.

[21] Jikang Han, Taishan Liu, Yanfeng Li, Peng Chen, Mao Yin, Mengqi Ma, and Geoffrey M Evans. Bed hydrodynamics of a new three-phase fluidized bed flotation column with steel ball particles. *Minerals Engineering*, 184:107669, June 2022. ISSN 0892-6875. doi: 10.1016/j.mineng.2022.107669. URL https://www.sciencedirect.com/science/article/pii/S0892687522002795.

[22] D.J. Parker, C.J. Broadbent, P. Fowles, M.R. Hawkesworth, and P. McNeil. Positron emission particle tracking - a technique for studying flow within engineering equipment. *Nuclear Instruments and Methods in Physics Research Section A: Accelerators, Spectrometers, Detectors and Associated Equipment*, 326(3):592–607, March 1993. ISSN 01689002. doi: 10.1016/0168-9002(93)90864-E. URL https://linkinghub.elsevier.com/retrieve/pii/016890029390864E.

[23] Diego Mesa, Katie Cole, Michael R. van Heerden, and Pablo R. Brito-Parada. Hydrodynamic characterisation of flotation impeller designs using Positron Emission Particle Tracking (PEPT). *Separation and Purification Technology*, 276:119316, December 2021. ISSN 1383-5866. doi: 10.1016/j.seppur.2021.119316. URL https://www.sciencedirect.com/science/article/pii/S138358662101025X.

[24] Diego Mesa, Michael van Heerden, Katie Cole, Stephen J. Neethling, and Pablo R. Brito-Parada. Hydrodynamics in a three-phase flotation system – Fluid following with a new hydrogel tracer for Positron Emission Particle Tracking (PEPT). *Chemical Engineering Science*, 260:117842, October 2022. ISSN 0009-2509. doi: 10.1016/j.ces.2022.117842. URL https://www.sciencedirect.com/science/article/pii/S0009250922004262.

[25] K. Cole, Pablo R. Brito-Parada, Kathryn Hadler, Diego Mesa, Stephen J. Neethling, Alexander M. Norori-McCormac, and Jan J. Cilliers. Characterisation of solid hydrodynamics in a three-phase stirred tank reactor with positron emission particle tracking (PEPT). *Chemical Engineering Journal*, 433:133819, April 2022. ISSN 1385-8947. doi: 10.1016/j.cej.2021.133819. URL https://www.sciencedirect.com/science/article/pii/S1385894721053924.

[26] K. Cole, Daniel J. Barker, Pablo R. Brito-Parada, Andy Buffler, Kathryn Hadler, Isobel Mackay, Diego Mesa, Angus J. Morrison, Stephen Neethling, Alexander Norori-McCormac, Barry Shean, and Jan Cilliers. Standard method for performing positron emission particle tracking (PEPT) measurements of froth flotation at PEPT Cape Town. *MethodsX*, page 101680, March 2022. ISSN 2215-0161. doi: 10.1016/j.mex.2022.101680. URL https://www.sciencedirect.com/science/article/pii/S2215016122000644.

[27] David J. Parker, Dawid M. Hampel, and Tzanka Kokalova Wheldon. Performance Evaluation of the Current Birmingham PEPT Cameras. *Applied Sciences*, 12(14):6833, January 2022. ISSN 2076-3417. doi: 10.3390/app12146833. URL https://www.mdpi.com/2076-3417/12/14/6833. Number: 14 Publisher: Multidisciplinary Digital Publishing Institute.

[28] Matthew Herald, Dawid Hampel, Tzany Kokalova Wheldon, Jonathan Seville, and Christopher Windows-Yule. Monte Carlo Model of the Large Modular Array for Positron Emission Particle Tracking. *IEEE Access*, 11:25982–25990, 2023. ISSN 2169-3536. doi: 10.1109/ACCESS.2023.3255505. Conference Name: IEEE Access.

[29] K. P. Galvin, J. Zhou, A. J. Price, P. Agrwal, and S. M. Iveson. Single-stage recovery and concentration of mineral sands using a REFLUX™ Classifier. *Minerals Engineering*, 93:32–40, July 2016. ISSN 0892-6875. doi: 10.1016/j.mineng.2016.04.010. URL https://www.sciencedirect.com/science/article/pii/S0892687516301029.

[30] D J Parker, T W Leadbeater, X Fan, M N Hausard, A Ingram, and Z Yang. Positron imaging techniques for process engineering: recent developments at Birmingham. *Measurement Science and Technology*, 19(9):094004, September 2008. ISSN 0957-0233, 1361-6501. doi: 10.1088/0957-0233/19/9/094004. URL https://iopscience.iop.org/article/10.1088/0957-0233/19/9/094004.

[31] MC40 Cyclotron Facility - The Birmingham Centre for Nuclear Education and Research. URL https://www.birmingham.ac.uk/research/activity/nuclear/about-us/facilities/mc40-cyclotron-facility.aspx.

[32] David Parker and Carl Wheldon. The Birmingham MC40 Cyclotron Facility. *Nuclear Physics News*, 28(4):15–20, October 2018. ISSN 1061-9127. doi: 10.1080/10619127.2018.1463021. URL https://doi.org/10.1080/10619127.2018.1463021. Publisher: Taylor & Francis _eprint: https://doi.org/10.1080/10619127.2018.1463021.

[33] X. Fan, D. J. Parker, and M. D. Smith. Labelling a single particle for positron emission particle tracking using direct activation and ion-exchange techniques. *Nuclear Instruments and Methods in Physics Research Section A: Accelerators, Spectrometers, Detectors and Associated Equipment*, 562(1):345–350, June 2006. ISSN 0168-9002. doi: 10.1016/j.nima.2006.03.015. URL https://www.sciencedirect.com/science/article/pii/S0168900206005341.

[34] A. L. Nicuşan and C. R. K. Windows-Yule. Positron emission particle tracking using machine learning. *Review of Scientific Instruments*, 91 (1):013329, January 2020. ISSN 0034-6748. doi: 10.1063/1.5129251. URL https://aip.scitation.org/doi/10.1063/1.5129251. Publisher: American Institute of Physics.

[35] Luke J. Crompton, Md. Tariqul Islam, and Kevin P. Galvin. Assessment of the partitioning of coarse hydrophobic particles in the product concentrate of the CoarseAIR™ flotation system using a novel mechanical cell reference method. *Minerals Engineering*, 198: 108088, July 2023. ISSN 0892-6875. doi: 10.1016/j.mineng.2023.

108088. URL https://www.sciencedirect.com/science/article/pii/S0892687523001024.